Transactions of the ASME®

Transactions of the ASME, Journal of Engineering for Gas Turbines and Power (ISSN 0742-4795) is published quarterly (Jan., Apr., July, Oct.) for $125.00 per year by The American Society of Mechanical Engineers, 345 East 47th Street, New York, NY 10017. Second class postage paid at New York, NY and additional mailing offices. POSTMASTER: Send address changes to Transactions of the ASME, Journal of Engineering for Gas Turbines and Power, c/o THE AMERICAN SOCIETY OF MECHANICAL ENGINEERS, 22 Law Drive, Box 2300, Fairfield, NJ 07007-2300.
CHANGES OF ADDRESS must be received at Society headquarters seven weeks before they are to be effective. Please send old label and new address.
PRICES: To members, $36.00, annually: to nonmembers, $125.00.
Add $15.00 for postage to countries outside the United States and Canada.

INDEXED by Applied Mechanics Reviews and Engineering Information, Inc.
Canadian Goods & Services Tax Registration #126148048

Journal of Engineering for Gas Turbines and Power

Published Quarterly by The American Society of Mechanical Engineers
VOLUME 113 • NUMBER 4 • OCTOBER 1991

TECHNICAL PAPERS

(Contents continued on page 481)

Contents (continued)

Combined Cycle Plants With Frame 9F Gas Turbines

P. Lugand

C. Parietti

Power Plants Division,
CTM Engineering Departments,
GEC ALSTHOM SA,
Belfort, France

The new 200 MW class MS 9001F gas turbines allow combined cycle plants to reach even higher output levels and greater efficiency ratings. Size factor and higher firing temperatures, with a three-pressure level steam reheat cycle, offer plant efficiencies in excess of 53 percent. Heat recovery steam generators have been designed to accommodate catalytic reduction elements limiting flue gas NO_x emissions to as low as 10 ppm VD (15 percent O_2). A range of steam turbine models covers the different possible configurations. Various arrangements based on the 350 or 650 MW power generation modules can be optimally configured to the requirements of each site.

1 Frame 9F Gas Turbine

The arrival of the 200 MW gas turbine onto the energy market ushers in a new generation of large combined cycle plants for the power industry. The 350 MW output level is obtained by associating the 9F gas turbine with a 120 MW steam turbine in a VEGA 109F. The 650 MW level is achieved by two 9F models with a 250 MW steam turbine (VEGA 209F). Higher plant output levels can be reached by multiplying those modular VEGA blocks to the power configuration required (Fig. 1).

The new MS 9001F gas turbine differs from the 9E model not only in terms of performance but also in size, weight and constructional arrangements (Table 1). Architecture of the 9F machine features attractive in-line arrangement of its axial air intake and gas exhaust. Its dry low-NO_x combustor, the principle of which is to maintain lean combustion throughout the combustor with short residence times, limits NO_x emissions without steam injection while conserving turbine performance.

Table 2 shows the main characteristics and performance values of the 9E and 9F models. The thermodynamic cycle of the 9F machine is identical to that of the 60 Hz 7F model, notably as concerns its firing temperature of 1260°C.

2 Steam Cycles for 9F-Based Combined Cycle Applications

With the increased exhaust gas temperatures and flow rates of the 9F gas turbine, combined cycle applications can feature enhanced thermodynamic characteristics and steam reheat designs.

Several steam cycles are envisaged and can be adopted to meet the different application requirements of utility owners: two-pressure cycles; simplified one-pressure cycles; enhanced two-pressure or three-pressure reheat cycles.

The steam temperature has been fixed at 540°C allowing use of commonly available materials. A steam temperature of 565°C could have been selected, in application of experience with conventional thermal plants, but such an increase, although improving efficiency, would imply operational constraints and possibly an availability penalty.

As regards the two-pressure combined cycle plants, it will be recalled that the net efficiency (LHV) of a VEGA 209E plant with a frame 9E gas turbine is 50 percent. This value reaches 52 percent for a VEGA 209F. The efficiency improvement afforded by the new frame 9F gas turbine in the same conditions is thus seen to be 2 percentage point, i.e., 4 percent (Table 3). The thermodynamic cycle switches from 70 bar/

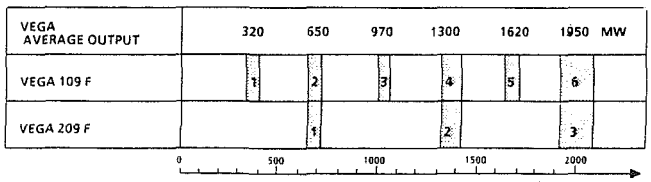

Fig. 1 Frame 9F VEGA plant output levels

Table 1 Construction differences between frames 9E and 9F (VEGA viewpoint)

GT model	Exhaust type	Thrust bearing	Generator position	Outline dimensions (m)		GT weight (t)	Rotor weight (t)
				Width	Length (GT + gen.)		
9001 E	Radial	Exhaust side	Exhaust side	Ø 3.8	25	220	28 + 22
9001 F	Axial	Suction side	Suction side	Ø 4.7	27	300	85

Table 2 9E and 9F gas turbine characteristics and performance: simple cycle

GT model	Firing temperature °C	Exhaust gas		Compressor ratio	Gross output MW	Net efficiency (LHV) %
		Flow kg/s	Temp. °C			
9001 E	1104	408.6	529	12.1	116.9	33.1
9001 F	1260	612.2	583	13.5	212.2	34.1

Natural gas - base load - ISO conditions
Gross output at generator terminals - Net efficiency : at outlet terminals of transformers

Contributed by the International Gas Turbine Institute and presented at the 35th International Gas Turbine and Aeroengine Congress and Exposition, Brussels, Belgium, June 11–14, 1990. Manuscript received by the International Gas Turbine Institute January 23, 1990. Paper No. 90-GT-345.

Table 3 9E and 9F VEGA performance characteristics

	Steam turbine inlet		Gross output (MW)			Net output MW	Net efficiency %
	Pressure bar	Temp. °C	Gas turbine	Steam turbine	Total		
209 E Two-pressure	70/6	510/210	2 x 115.3	127.1	357.7	352.4	50
209 F Two-pressure	100/6	540/190	2 x 210.1	237.1	657.3	646.4	52

Natural gas - ISO conditions - Condenser pressure : 50 mbar
Net values (LHV) at outlet terminal of main transformers

Table 4 VEGA 109F steam cycle options

	Steam turbine inlet		Gross output (MW)			Net output MW	Net efficiency %
	Pressure bar	Temp. °C	Gas turbine	Steam turbine	Total		
Simplified cycle One pressure	65	540	210.7	106.4	317.1	312.3	50.3
Two-pressure cycle	100/6	540/190	210.1	117.1	327.2	321.7	51.8
Enhanced cycle Two-pressure reheat	110/ 30/7	540/ 540/240	210	121	331	325.7	52.4
Enhanced cycle Three-pressure reheat	110/ 30/6	540/ 540/235	209.7	124	333.7	328.3	52.8

Natural gas - ISO conditions - Condenser pressure : 50 mbar
Net values (LHV) at outlet terminal of main transformers

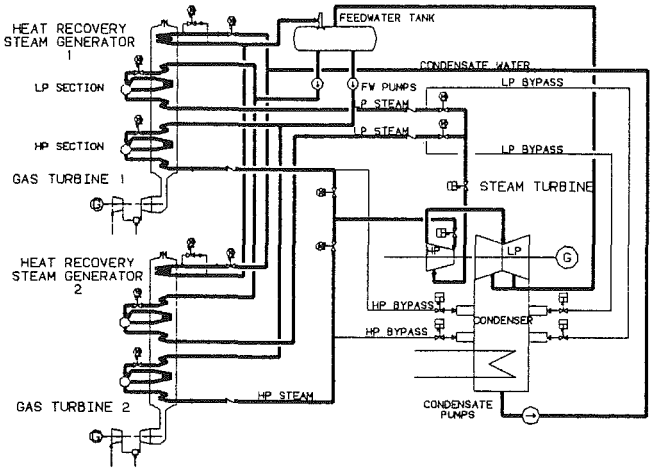

Fig. 2 Two-pressure VEGA 209F

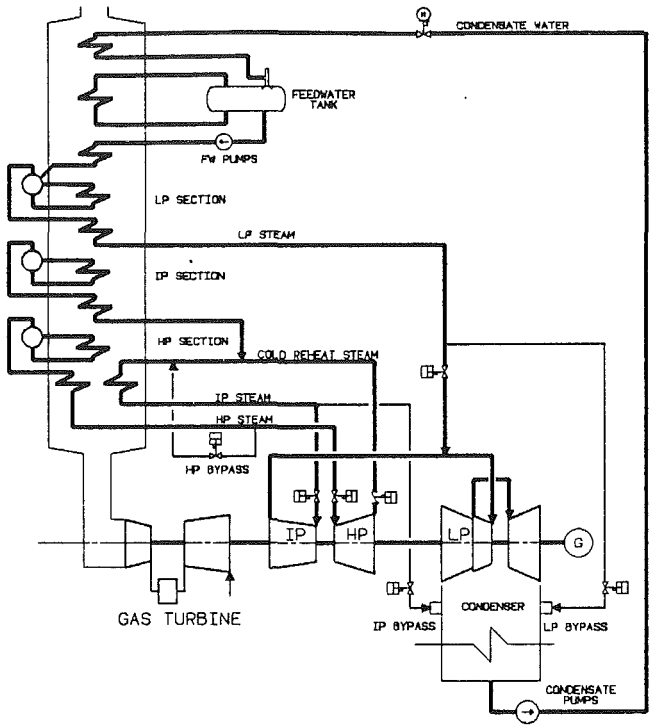

Fig. 3 Single shaft three-pressure reheat VEGA 109F

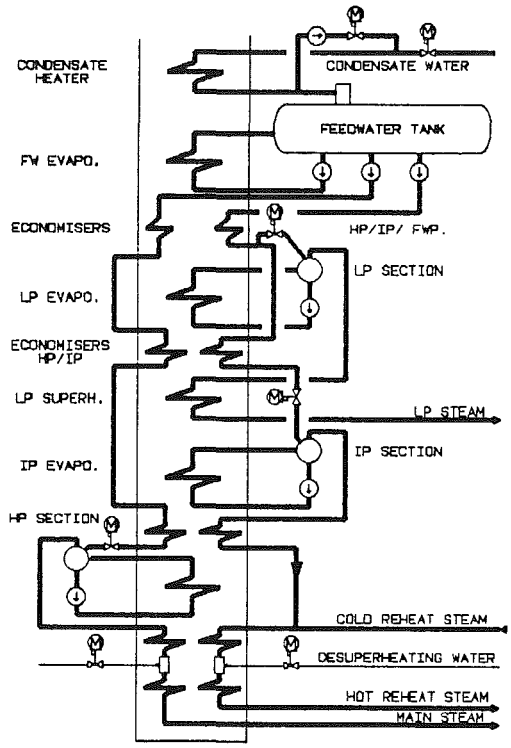

Fig. 4 HRSG steam-water schematic: three-pressure reheat VEGA 109F and 209F

510°C to 100 bar/540°C. The steam–water loop (Fig. 2) includes a condensate heater installed in the flue gas stream and a deaerator fed with turbine bleed steam. The LP and HP feedwater circuits are independent. Flue gas temperature at stack exit is approximately 90°C.

The size effect of the steam turbine modules is such that the net efficiency difference between a VEGA 109F and 209F cycle is about 0.2 percentage point (see two-pressure cycle values in Tables 3 and 4).

The simplified one-pressure cycle can be of interest for base or medium load plants. The system does not include a feedwater deaerator and deaeration is perfomed in the condenser hotwell. The flue gas leaves the stack at a temperature of about 150°C. The decrease in net efficiency, compared to the two-pressure cycle, is about 1.5 percentage point (Table 4).

Introducing steam reheat at 540°C in a two-pressure cycle improves efficiency by 0.6 percentage point. Introducing a third pressure provides a further gain in efficiency of 0.4 percentage point. For these reheat cycles the optimum HP pressure is about 110 bar, with the reheat pressure at about 30 bar. Table 4 recapitulates all these values.

The steam–water loop of the VEGA 109F three-pressure, reheat cycle is shown in Fig. 3. The condensate is heated at the tail end of the boiler flue gas stream. The deaerator is supplied with steam by a low-temperature evaporator located downstream of the boiler LP economizer (Fig. 4).

Combined cycle performance varies with site conditions. To illustrate this, consider a 350 MW three-pressure reheat VEGA 109F unit on a North European site with ambient air design temperatures of 8.6°C and cooling water at 10°C. The net

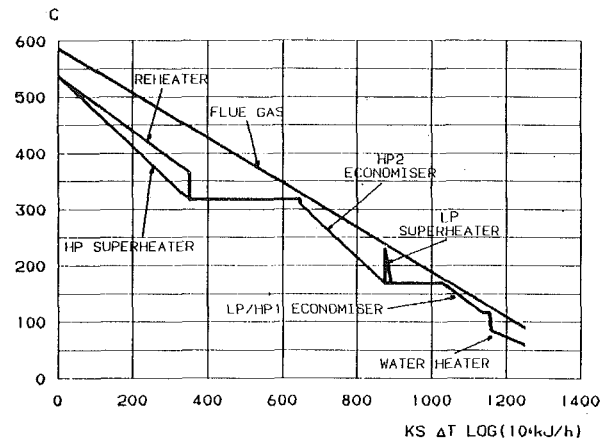

Fig. 5 Steam and water temperature diagram: two-pressure reheat VEGA 109F and 209F

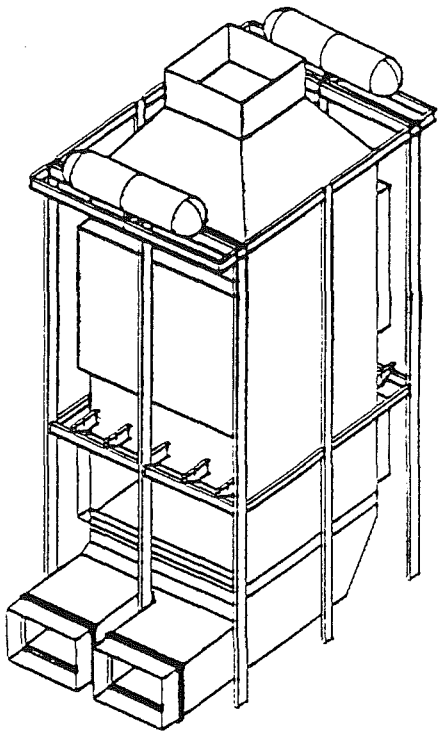

Fig. 6 Frame 9F VEGA plant HRSG

efficiency improves by 0.8 percentage point, reaching 53.6 percent. The unit produces an extra 13 MW.

The 9F gas turbine's variable compressor inlet guide vane system maintains part-load efficiency of the combined cycle at loads between 70 and 100 percent.

3 Heat Recovery Steam Generator

As an example, Fig. 5 shows flue gas and steam–water temperature evolutions for the two-pressure reheat cycle. The optimum pinch point value determined by an economic study based on current European economic conditions is 8 to 9°C.

The vertical HRSG (Fig. 6) is of the assisted circulation type. The exchangers hang from beams. The casing, supported independently of the exchangers, is of the warm type for flue gas temperatures of up to 400°C and of the hot type beyond.

In certain countries, it will be necessary to install an in-boiler $deNO_x$ module of the selective catalytic reduction (SCR) type to reduce NO_x emissions further down to 10 ppm. The catalysts use titanium dioxide and vanadium pentoxide. The reducing

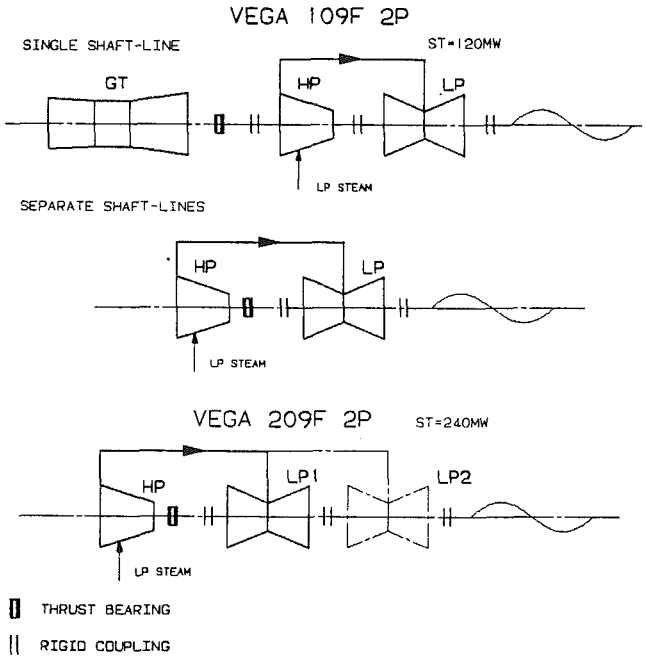

Fig. 7 Nonreheat steam turbine models

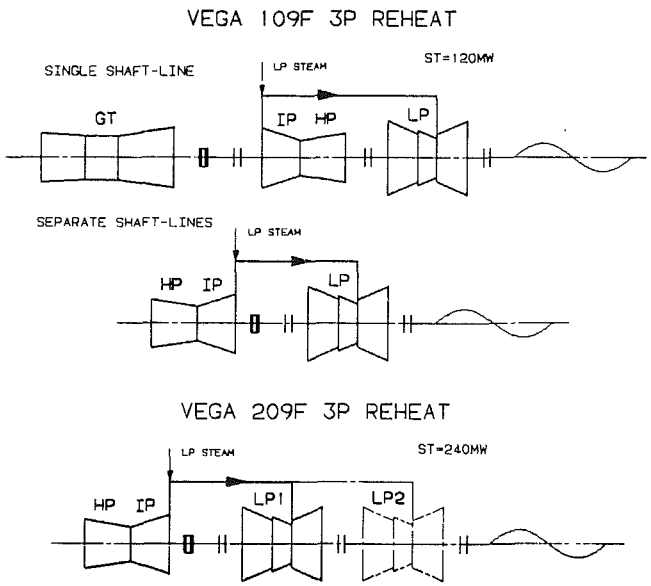

Fig. 8 Reheat steam turbine models

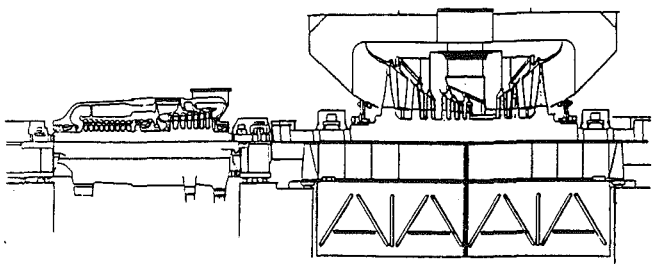

Fig. 9 250 MW steam turbine for three-pressure reheat VEGA 209F

agent is ammonia. The catalyst module is installed in the gas stream 370°C temperature zone and rests on supporting girders. Space is accommodated above the $deNO_x$ equipment for access, removal, and replacement of the catalysts.

The steam–water circuits downstream from the deaerator are independent. To optimize heat recovery, the different ex-

changers are placed in parallel in the flue gas stream (Fig. 4): the HP1 and IP1 economizers; the HP2 and IP2 economizers; and the superheaters and reheaters.

Superheat and reheat steam temperatures are controlled by feedwater injection. Similarly, the condensate heater inlet temperature is controlled by recirculation maintaining a temperature of 60°C when the combined cycle is operating on very low sulfur-content natural gas, and 110°C when operating on light distillate.

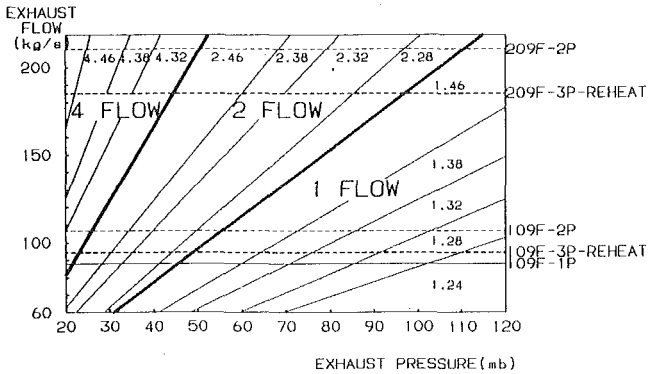

Fig. 10 Steam turbine LP exhaust selection

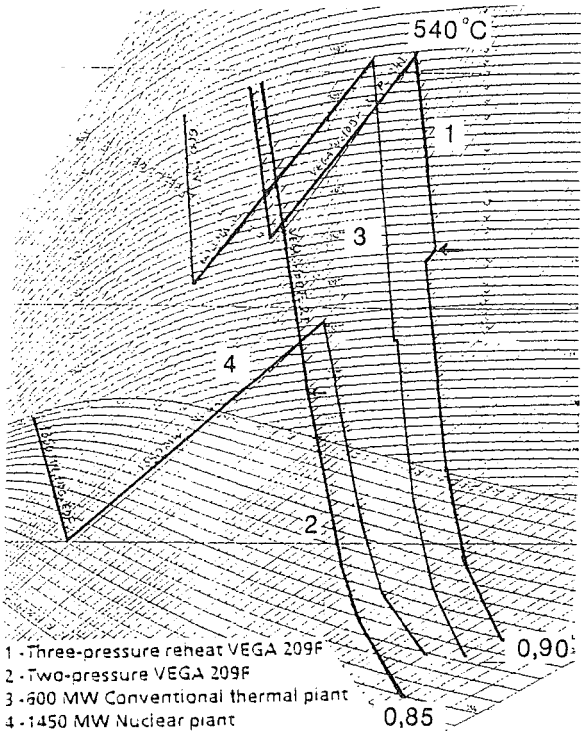

Fig. 11 Turbine steam expansion lines

4 Steam Turbine

The main objectives in the design of the steam turbines are high performance, operating flexibility, utilization of standard experience-proven components, and modular design and construction with a minimum number of large components capable of covering the widest possible range of different types of machines.

Figures 7 and 8 show the schematic arrangements of the nonreheat and reheat steam turbine models. It will be observed that identical models are deployed for both single-shaft and multishaft installation configurations of the VEGA 109F. The 120 MW steam turbine for the VEGA 109F 2P unit will be single-casing single-flow for condenser pressures higher than 55 mbar.

The reheat turbines (Fig. 9) all have a combined HP/IP casing. The standardized LP casing design features a single-flow IP section between the two LP flows. A one-flow design is selected for high condenser pressures.

Selection from a range of standard steel blades for the last LP stage covers the vacuum range from 20 to 120 mbar for the 120 MW and 250 MW turbines. Figure 10 indicates the vacuum range covered by each blade for single-flow, double-flow, and four-flow designs.

All the HP casings are double-shell type. On account of the steam conditions (100–110 bar/540°C) and the starting flexibility required of the turbines, an internal steam circuit ensures the necessary cooling of the HP and IP casings. Moderate HP rotor body diameter is another feature further promoting operation flexibility.

Figure 11 compares turbine steam expansion lines for different cycles: VEGA 209F 3P reheat cycle; VEGA 209F 2P cycle; 600 MW conventional thermal; and 1450 MW nuclear.

For each cycle, acceptable steam moisture content values are achieved at the bottom end of the expansion line (between 10 and 15 percent for very low condenser pressures).

5 VEGA Plant Installation Arrangements

GT-HRSG In-Line Arrangement. The in-line arrangement of the gas turbine and heat recovery steam generator is identical in all our combined cycle configurations (Fig. 12). The HRSG is located in line with the gas turbine exhaust hood.

The installation has no exhaust gas bypass system. The entire flue gas flow exhausts through the HRSG as soon as the turbine is started. This option is itself a criterion having an impact on equipment and operation definition but, above all, it allows suppression of the large size high-temperature service bypass dampers.

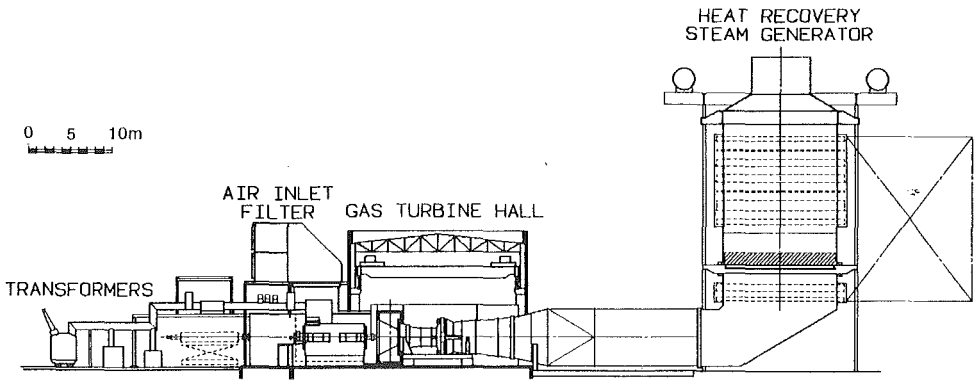

Fig. 12 9F gas turbine/HRSG installation elevation

The low-standing gas turbine (axis 3.6 m above the ground) and the associated traveling crane form a compact specialized assembly integrating its own maintenance facilities. The generator is located underneath the air intake filter; its rotor can be removed by a mobile lifting device.

VEGA 109F Installation Configurations. For the 350 MW module, two arrangements are possible: a single-shaft arrangement with the gas turbine and the steam turbine driving a single generator, and a multishaft arrangement with two separate shaftlines, each turbine driving its own generator.

The single-shaft VEGA 109F is a compact module particularly well suited to replication. For a 1300 MW unit, for example, four VEGA 109 modules would be installed in identical fashion and in parallel (Fig. 13). The ground surface occupied is 24,500 m^2. In this single-shaft arrangement, the steam turbine is located between the gas turbine and the generator, thus conserving its ease of maintenance. The complete shaftline has only one thrust bearing providing clearance to accommodate longitudinal expansions of the machines. Its location is between the gas turbine and the steam turbine. The lube oil system serves both turbines. Compressor air inlet ducting may be of the vertical type, comprising a withdrawable section to allow passage of the overhead traveling crane or may be arranged horizontally, with the air intake filter installed at ground level.

The ground-installed single-shaft configuration with its axis at 3.6 m (Fig. 14) is particularly well suited to the simple nonreheat cycles. The steam turbine exhausts into two half-condensers situated either side of the turbine (Fig. 15). Each half-condenser rests on neoprene pads and connection with the turbine is by flexible joint and articulated rods.

Reheat cycle units require available space underneath the shaftline to accommodate the boiler-to-turbine steam piping. Figure 14 shows a raised installation of the shaftline with the condenser located under the steam turbine.

The VEGA 109F multishaft arrangement is an appropriate configuration when constructing the combined cycle unit in two phases. The first step consists in installing the gas turbine-generator set to operate in simple cycle mode for peaking service. The second step is to add the steam plant (HRSG + steam turbine-generator). For steam turbines with a single-flow LP casing (condenser pressures of about 50 mbar) turbine exhaust may be of the axial type (Fig. 16).

VEGA 209F Installation Arrangements. The integrated configuration (Fig. 17) constitutes an independent 650 MW module. The axes of the gas turbines and the steam turbine lie in parallel. The steam turbine is located between the two gas turbines and is installed in classical fashion, on a concrete foundation table. All the gas turbines and the steam turbine have their own traveling crane and a transversal access bay for maintenance.

The electrical part (power transmission and the electrical building) is distinct from the steam part (HRSG and steam piping). A common central control and electrical building is provided for the gas and steam turbines. This VEGA 209F covers 11,500 m^2 of ground.

In another configuration termed longitudinal (Fig. 18), the gas turbines are identical and installed in parallel. The steam plant machine room is installed on the side. This arrangement has the merit of avoiding interference between equipment during construction. The ground space requirement is 13,000 m^2.

Indoor or Outdoor Installation. The frame 9F gas turbine is normally enclosed in an aesthetic "superpackage" phonic housing, which also constitutes the maintenance quarters for periodic maintenance of the combustor. For major overhauls of the gas turbine, the roof of this enclosure can be removed within a few minutes. Outdoor installation of the superpackaged gas turbine is also possible. The noise level in this configuration with one gas turbine in service is 63 dB(A) at a distance of 90 m.

In countries where climatic conditions are severe, certain utility owners prefer to install their gas turbines indoors. To do so does not require any acoustical treatment of the turbine building.

The steam turbine and associated mechanical equipment are installed indoors, as is the traditional practice. Noise abatement is achieved by phonic hooding of the equipment concerned.

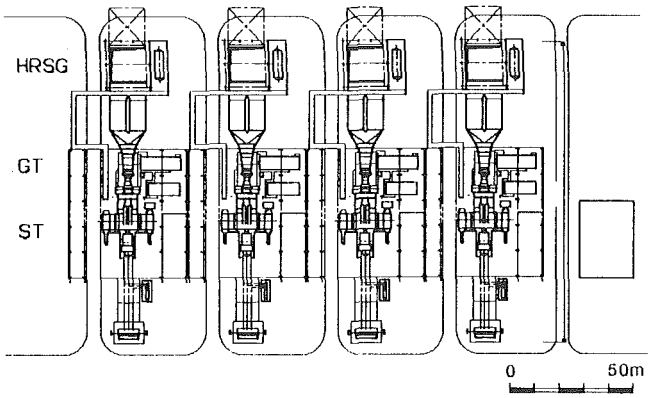

Fig. 13 1300 MW unit with four VEGA 109F single-shaft modules

6 Operation of 9F-Based VEGA Units

Steam Bypass System. Since our base designs do not feature an exhaust gas bypass system, operation of the VEGA plant in simple-cycle mode is achieved by dumping the inevitable steam generated by the HRSG to the condenser, after expansion and desuperheating. For the VEGA 209F units, steam bypass systems are provided for each gas turbine/HRSG module to allow independence of operation during transients (startups, trips, and shutdowns).

For the reheat cycles three steam bypass systems are provided as schematically shown in Fig. 3: one HP bypass, between the superheated steam circuit and the reheat circuit; one IP bypass, between the reheat circuit and the condenser; and one LP bypass between the LP steam circuit and the condenser.

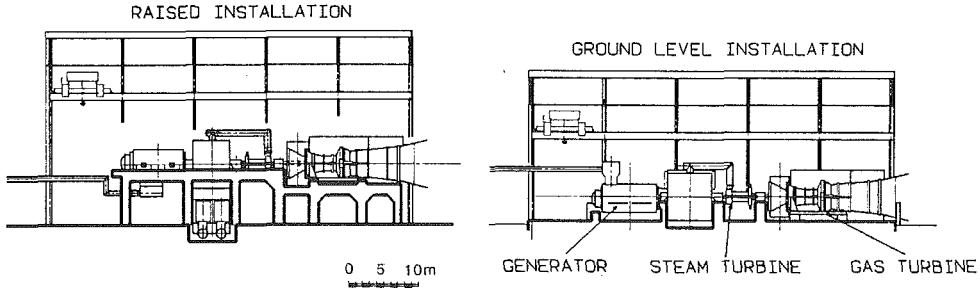

Fig. 14 Single-shaft VEGA 109F alternative installation arrangements

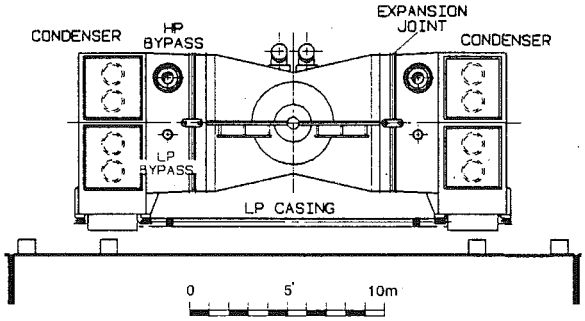

Fig. 15 Single-shaft VEGA 109F dual condenser installation arrangement

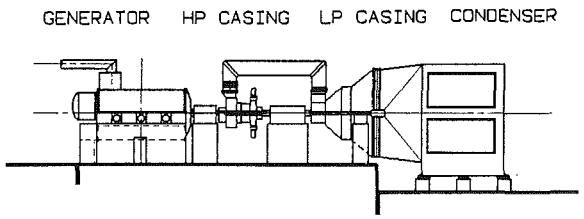

Fig. 16 120 MW axial exhaust steam turbine for multishaft VEGA 109F

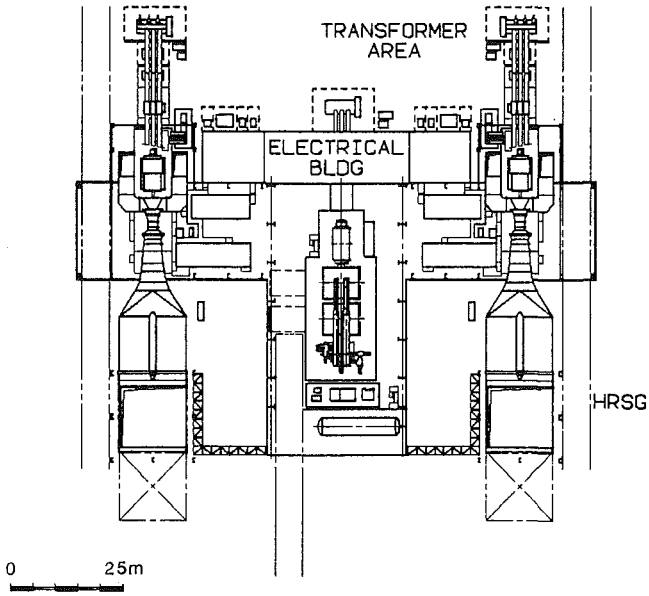

Fig. 17 650 MW VEGA 209F integrated installation arrangement

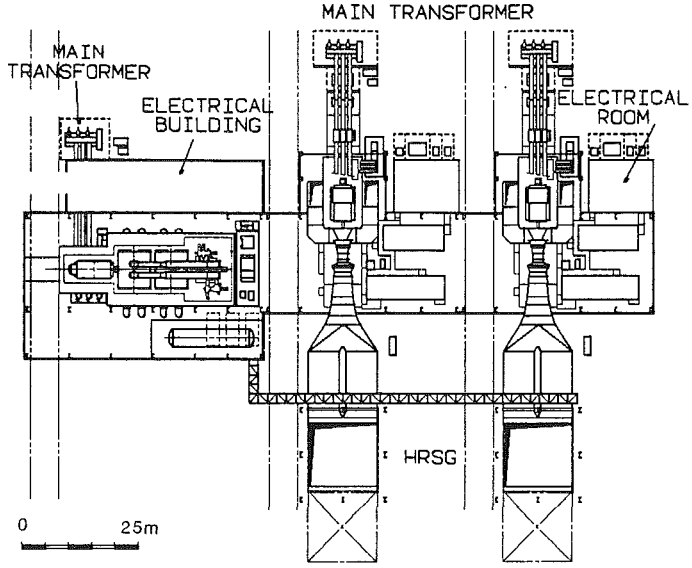

Fig. 18 650 MW VEGA 209F longitudinal installation arrangement

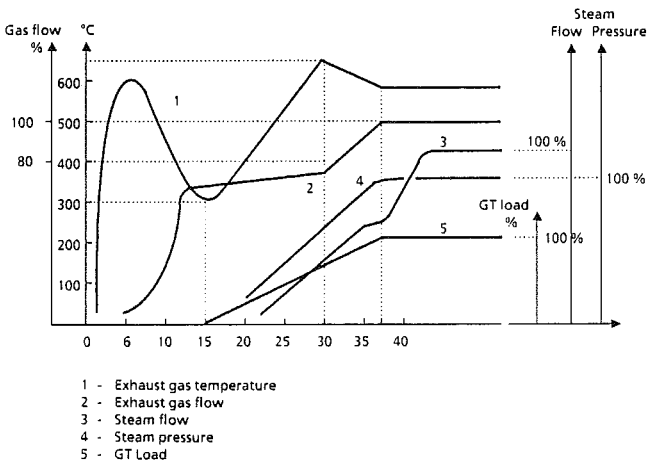

Fig. 19 VEGA 209F GT and HRSG cold startup curves

For the nonreheat cycles (Fig. 2) only the HP and LP steam circuits need a bypass to the condenser.

Gas Turbine Simple Cycle Operation. Extended operation of the gas turbines without the steam turbine in service implies the need to dump the steam produced by the HRSGs. This is accomplished by installing an auxiliary condenser complete with associated auxiliary piping and bypass valves.

Steam Turbine General Operation. The steam turbine operates in sliding pressure mode on the HP/IP side (HP and IP steam admission valves wide open) and in fixed pressure mode LP side. This provides high operating flexibility and ensures steady comportment of the steam turbine during rapid load change conditions.

Startup of 9F-Based VEGA Units. One prerequisite to startup of all VEGA 9F combined cycle units, whatever their configuration, is the need to establish condenser vacuum. As a result, externally sourced auxiliary steam is required for feeding the turbine gland seals.

Startup of the gas turbine is in two successive phases: initial run-up to approximately 2500 rpm by means of an external drive source, and self-sustained run-up to 3000 rpm.

For the single-shaft configuration there are two drive possibilities to start the gas turbine.

One way is to use the generator as a synchronous motor, with the generator powered at variable voltage and frequency through a static frequency convertor (SFC), itself fed from the external network. The other way is to drive the gas turbine by means of the steam turbine using auxiliary steam from an independent source.

Startup of the single-shaft configured combined cycle is in three main phases: startup of the shaftline (SFC or steam turbine drive). Steam temperature and pressure increase. The steam bypass systems dump steam to the condenser and warm the circuits; coupling and loading via the gas turbine; steam turbine operation. Loading of the single-shaft power set continues.

During these startup phases specific measures are taken to protect the steam turbine, such as casing warm-up and injection of cooling steam into the last stages.

In a VEGA 209F configuration, startup of each gas turbine is performed using the static frequency convertor. The steam

turbine, which is independent, is started in a second step as soon as the characteristics of the steam produced by the HRSG are acceptable. The startup sequences and evolution of the thermodynamic parameters are shown in Fig. 19. Coupling of the gas turbine takes place within 15 min. after starting and full loading requires another 22 min. Cold startup time for a VEGA 209F is achieved within approximately 3 h of starting the first gas turbine. A warm startup after an 8-h shutdown takes about 50 min.

7 Conclusion

Combined cycle plants built around the frame 9F gas turbine fit easily into electric grids in countries that have reached unit output levels in the 350 to 650 MW range and make use of natural gas.

As is the case for all combined cycle projects, progressive investment remains feasible. Initial expenditure concerns the gas turbine(s) that in simple cycle mode will produce 2/3 of the final output of the VEGA plant.

9F VEGA plants can of course also burn coal gas. Integrated Gasification Combined Cycle (IGCC) plants based on different possible gasification processes offer an additional source of fuel for combined cycle plants and further the concept of progressive investment.

References

Boissenin, Y., 1989, "Combined Cycle Power Plants: a Practical Guide to the Right Choice," presented at the ASME COGEN-TURBO 3rd Conference & Exhibition, Nice, France, Aug. 30–Sept. 1.

Brandt, D. E., 1988, "The Design and Development of an Advanced Heavy-Duty Gas Turbine," ASME JOURNAL OF ENGINEERING FOR GAS TURBINES AND POWER, Vol. 110, pp. 243–250.

Lugand, P., and Paren, J., 1988, "VEGA: A Versatile Range of Combined-Cycle Power Plants," presented at the ALSTHOM Gas Turbine Congress, Cannes.

Fully Loaded Factory Test of the CW251B12 Gas Turbine Engine

I. S. Diakunchak
Gas and Steam Turbine Engineering,
Power Generation Canadian Division,
Westinghouse Canada Inc.,
Hamilton, Ontario, Canada

The fully loaded factory test of the CW251B12 45 MW class industrial gas turbine is described in this paper. This gas turbine is the latest uprating of the W251 series of engines. The main objectives of the factory test were the verification of the performance and the mechanical integrity of the new engine model. A brief description of the main features of the engine, the application of the first unit, the test facility, and the engine instrumentation used in the test is included. Details of the engine performance test results, telemetry test data results, and the hot end component metal temperature measurements are provided.

Introduction

The CW251B12 engine is the latest model of the successful series of heavy-duty, single-shaft, industrial gas turbines designed for 50 and 60 Hz utility and industrial service in simple cycle, combined cycle, and cogeneration applications. The engine is capable of operation on a wide range of gaseous and liquid fuels, as well as dual-fuel operation. It has provision for water or steam injection for NO_x emissions reduction to the desired level. The expected "introductory" output power of the new model was 45 MW, and the output power of the "mature" engine was 48 MW. The uprated performance was achieved by compressor redesign for increased inlet flow and efficiency and a modest increase in firing temperature. To accommodate the firing temperature increase, cooling modifications were made to the first-stage turbine stator and blade.

The application of the first CW251B12 engine is in a cogeneration plant (Diakunchak and Nevin, 1989). This plant consists of the gas turbine-generator set, supplementary fired Heat Recovery Steam Generator (HRSG), and a steam turbine-generator set. The gas turbine inlet system includes a self-clean pulse-type filter and a silencer. A compressor water wash system, which is located in the inlet manifold, has on-line misting and off-line soak capabilities. The gas turbine drives the generator through a speed reducing gear box. The gas turbine exhaust gases are ducted into a supplementary fired HRSG, which produces steam for process and for generation of additional electricity in the steam turbine-generator set.

To verify the new engine model performance and mechanical integrity, a fully loaded factory test was carried out on the first CW251B12 engine. The objectives of the factory test were as follows:

1 To verify engine performance over its entire operating range.

2 To determine the optimum inlet guide vane setting.

3 To verify the redesigned compressor performance, to determine the compressor surge margin and stall characteristics, and to map the compressor performance at different inlet guide vane staggers.

4 To establish engine performance with water injection.

5 To verify the vibration characteristics of the new compressor components.

6 To verify the mechanical integrity of the hot end components at the increased firing temperature.

Engine Description

The CW251B12 engine (Diakunchak, 1989) is a single-shaft, two-bearing design, incorporating proven design concepts of the earlier models, as well as new features, which will result in improved performance and reliability.

The longitudinal cross section of the CW251B12 engine is shown on Fig. 1. The engine incorporates cold end power drive and axial exhaust. The single rotor shaft is supported by two bearings of the inherently stable tilting pad type. The thrust bearing is a Glacier directionally lubricated, double-acting, tilting shoe type. The engine consists of three cylinders, which are horizontally split to facilitate field maintenance without rotor removal. The front part of the compressor forms one cylinder; the back end of the compressor, the combustor, and the turbine are in the second cylinder; and the third cylinder incorporates the exhaust diffuser. The compressor rotor is manufactured by shrinking 19 disks on to a hollow shaft. The three turbine disks are bolted together and then joined to the compressor rotor by a torque tube and a center coupling.

Compared to its immediate predecessor, the CW251B12 compressor has new inlet guide vanes, new airfoils on the first two stages, and restaggered stators on all but two of the downstream stages. The compressor redesign objectives were 4 percent increase in inlet flow and 1 percent increase in overall efficiency. The performance improvement was to be achieved by a 12.7 mm (0.5 in.) increase in compressor inlet outer radius, double circular arc airfoil profiles on the first two stages, and optimized restagger of most of the downstream stators (Marson, 1989). The double circular arc profiles, in conjunction with thinner airfoil cross sections, were incorporated in the design of the new airfoils so as to give lower surface Mach

Contributed by the International Gas Turbine Institute and presented at the 35th International Gas Turbine and Aeroengine Congress and Exposition, Brussels, Belgium, June 11–14, 1990. Manuscript received by the International Gas Turbine Institute January 15, 1990. Paper No. 90-GT-363.

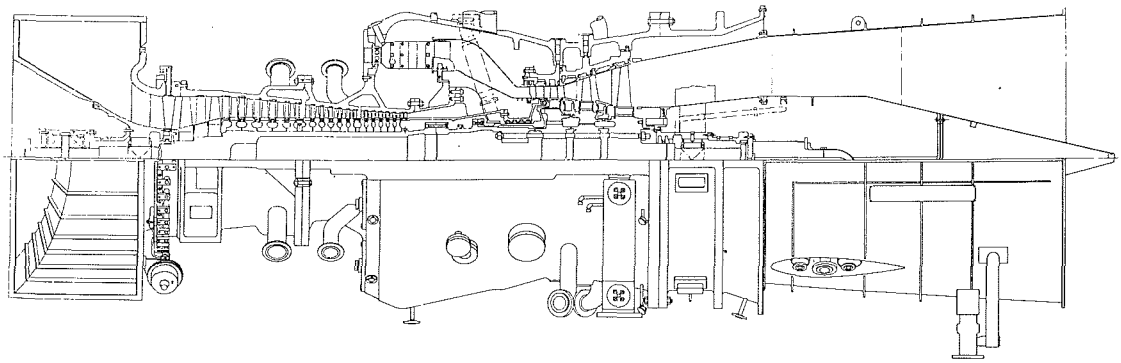

Fig. 1 Longitudinal cross section of CW251B12 engine

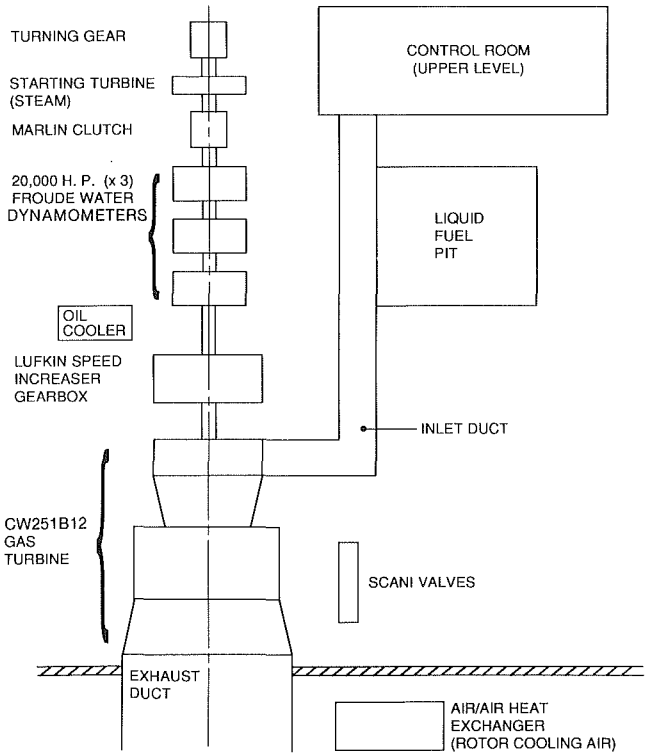

Fig. 2 Test house schematic

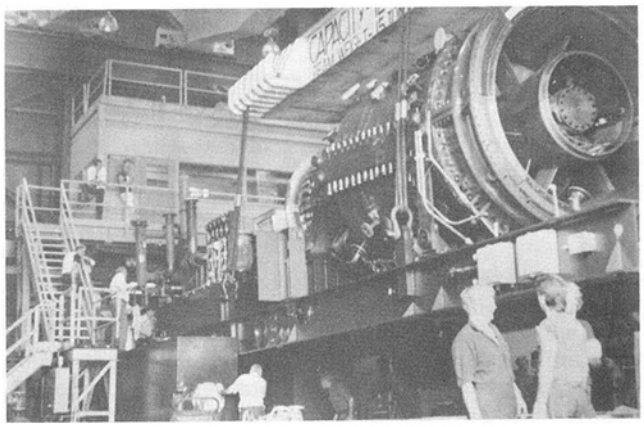

Fig. 3 CW251B12 engine in test house

numbers, improved airfoil choke margin, and hence improved compressor performance.

The combustion system consists of eight axially oriented, cylindrically shaped baskets. Provision is made for injecting steam or water for NO_x suppression. At the exit from the combustor baskets are located film-cooled goose-neck style transition ducts, which direct the hot combustion gases into the turbine.

The three-stage turbine incorporates two modifications in the CW251B12 application. The cooling of the first-stage stator is enhanced by film cooling the shrouds with compressor delivery air. To provide the film cooling, two rows of holes on the outer platform and one row on the inner platform are electrochemically machined at 30 deg to the surface. To improve the first-stage turbine blade service life at the increased firing temperature the blade cooling design is upgraded by adding turbulators to the radial cooling holes. The turbulators, or "ribs," promote turbulence in the cooling flow and therefore increase heat transfer. The cooling holes are cast with marginally larger diameter than in the original design and then the "ribs" are produced by electrochemical machining.

Test Facility

The CW251B12 Prototype factory test was carried out in a test facility, which was equipped to absorb engine output power considerably in excess of base load. Three Froude DA790 high-speed hydraulic dynamometers were connected in series. Although the nominal rating of the dynamometers was 20,000 hp, in actual practice each could absorb considerably higher power (up to a total of 90,000 hp at 7300 rpm gear box output speed). A speed increasing Lufkin double helical gear box connected the engine to the dynamometers. The engine was started by a 1000 hp Westinghouse CE120 steam turbine, which was connected to the front dynamometer. The inlet air was brought to the engine through a vertical stack incorporating a 1.46 m (57.5 in.) ASME air meter, which was located above the test house roof. From the inlet stack the air passed through a rectangular duct with a trash screen and then through a 90 deg cascaded bend into the engine inlet manifold. The engine exhaust gases passed into a 3.05 m (10 ft) diameter exhaust duct and then into a vertical stack, which contained turning vanes and a silencer. The exhaust stack was located on the opposite side of the test house from the inlet stack and was considerably higher to ensure that the exhaust gases would not contaminate the inlet air flow. The gas turbine and dynamometer controls were located in a room situated above the engine starting package (see Fig. 2). Figure 3 shows the CW251B12 engine installed in the test house.

Data Acquisition and Reduction

To collect the vast quantities of test measurements available during an engine test, a high-speed electronic data acquisition system was used. This system (see Fig. 4) consisted of two Autodata 10 data recorders, which collected the raw data from the engine and converted some of the measurements into en-

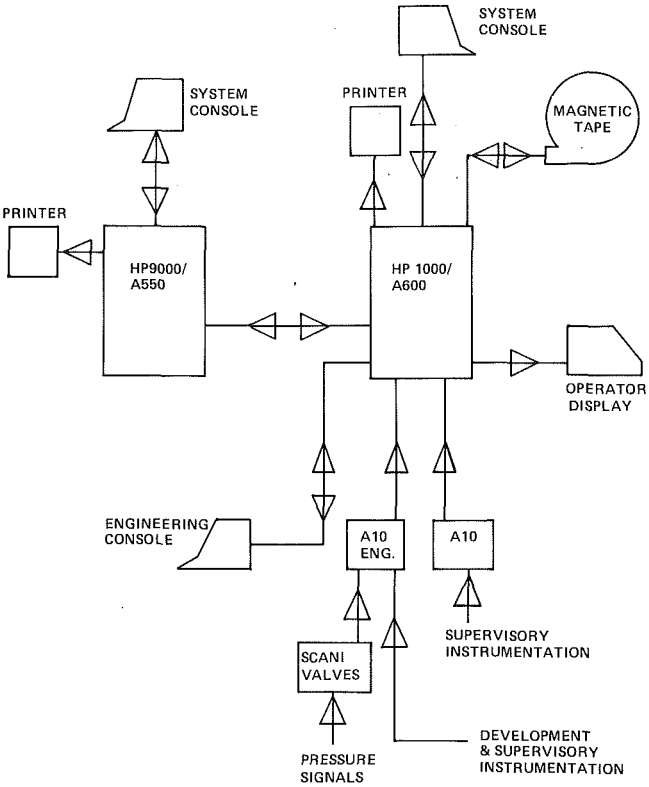

Fig. 4 Data acquisition system

gineering units. The Autodata 10, dedicated to detail data collection, transmitted the measured data to the HP1000 minicomputer, which controlled the data acquisition, adjusted the data for calibration corrections, converted the rest of the measurements into engineering units, and stored the data permanently on a disk. Several peripheral pieces of equipment were employed for viewing the raw data converted to appropriate units, as it was collected. Special recording equipment was used to record continuously compressor blade and diaphragm vibration, compressor rotating stall, important compressor parameters during engine startup and combustor basket temperature during water injection tests.

The detailed engine and component test data analysis was carried out by the HP9000 computer, which accessed the test data files stored in the HP1000. The test analysis computer program, which was used for the detailed performance analysis, consisted of the following modules:

1 Calculation of compressor inlet air flow, compressor bleed flow, fuel flow, lube oil flows, cooling air flows, and air flows throughout the engine.

2 Compressor performance calculation, including nondimensional performance parameters, compressor work, and compressor efficiencies based on several definitions.

3 Combustor performance calculation, including combustor efficiency and pressure drop.

4 Calculation of mechanical losses, including bearing losses, gear box losses and radiation losses.

5 Turbine performance calculation, including turbine work, efficiency and swallowing capacity.

6 Exhaust diffuser performance.

7 Overall heat balance calculation, including calculation of the firing temperature from the accurately measured exhaust temperature, the estimated turbine work and the measured cooling air flows injected into the turbine. This "back end" firing temperature was used as a check on the "front end" calculation, which was based on the measured compressor exit temperature, measured fuel flow and the estimated combustor inlet flow.

8 Correction of the factory test measured output power and heat rate to standard conditions for an engine at a site installation and comparison with the expected site performance of the engine.

Engine Instrumentation

A large number of instruments was incorporated into the engine for the determination of the engine and component performance, measurement of metal and cavity temperatures throughout the engine, and measurement of vibration characteristics of critical components. Approximately 500 individual readings were collected at each test point. The following performance-related parameters were measured:

1 Air meter pressure drop, for estimation of compressor inlet air flow.

2 Four static pressures and 16 thermocouples at compressor inlet manifold, for determination of compressor inlet conditions.

3 Four static pressures just upstream of the inlet guide vanes, for inlet scroll calibration.

4 Static pressures and temperatures throughout the compressor, for detailed compressor performance analysis.

5 Four total pressure and temperature rakes at compressor diffuser exit, for measurement of radial distributions at compressor exit.

6 Static pressure and temperature in the combustor cylinder, for determination of combustor inlet conditions.

7 Thermocouple rakes at exit from one transition duct.

8 Four static pressures at the inlet to the first-stage turbine vane, for estimation of turbine inlet total pressure.

9 Four static pressures at turbine exit and at exhaust diffuser exit, for determination of turbine exit total pressure and exhaust diffuser performance.

10 Eight thermocouples at turbine exit.

11 Sixteen thermocouples at exhaust diffuser exit, for accurate determination of engine exit temperature.

12 Fuel flow, lube oil flows.

13 Cooling air orifice pressure drops, for cooling air flow estimation.

14 Engine and dynamometer speeds.

15 Dynamometer torques.

16 Total pressure, static pressure, temperature, and flow angle traverses at turbine exit and exhaust diffuser exit.

The measurements associated with engine mechanical integrity verification were: bearing temperatures, thrust bearing load cell readings, vibration readings, combustor basket and transition duct metal temperatures, first-stage turbine blade metal temperature, first and second-stage turbine stator metal temperatures, and cavity temperatures in critical areas of the engine. The second-stage compressor blade strain gage data were continuously recorded via telemetry equipment. Strain gage data was also collected on the first two compressor diaphragms.

Test Program

The main components of the CW251B12 Prototype factory test program were:

1 Shakedown, starting, ignition tests.

2 Vibration monitoring, overspeed trip, trim balance.

3 Hot end metal temperature measurement, including first-stage turbine blade metal temperature measurement by means of optical pyrometry.

4 Second-stage compressor blade and first and second stage compressor diaphragm strain gage measurement.

5 Inlet guide vane optimization.

6 Compressor performance and mapping.

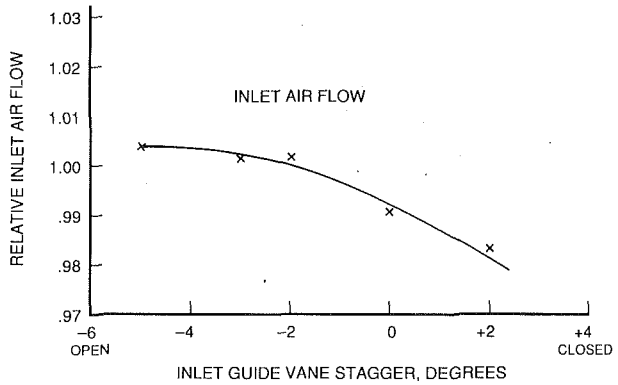

Fig. 5 Inlet guide vane optimization, air flow

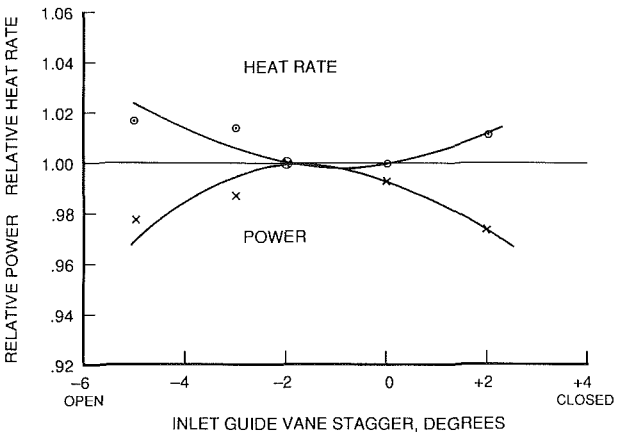

Fig. 6 Inlet guide vane optimization, power and heat rate

7 Compressor rotating stall and surge tests.
8 Engine performance.
9 Water injection tests.
10 Exhaust flow traverses.

Number 2 distillate fuel oil was used in the factory tests. The total engine running time was close to 50 hours. Pertinent test information was continuously collected throughout the duration of the tests. Detailed test data analysis was carried out at approximately 40 discrete test points, the majority of which were at base load firing temperature.

Test Results

Compressor Performance. The factory test of the CW251B12 engine demonstrated over a wide range of operating conditions that the engine performed better than expected. The major contributor to this performance improvement was the redesigned compressor, which exceeded its design goals.

The starting characteristics of the redesigned compressor were similar to those of the original design. The engine starting sequence was as follows: The inlet guide vanes were fully closed on startup and the two compressor bleed valves were open, the starter motor increased the compressor speed to about 1050 rpm, the engine was ignited, the speed increased further until at 3500 rpm the starter motor was disengaged, by 5100 rpm first the seventh stage and then the thirteenth stage bleed valves were closed, and finally the speed was increased to the synchronous speed value, the inlet guide vanes were opened and the engine loaded up.

The inlet guide vane optimization tests were carried out by running the engine at the base load firing temperature and taking test data at different inlet guide vane staggers. There

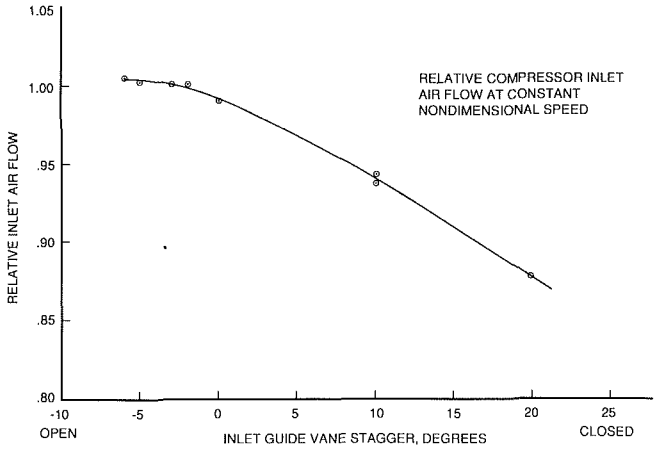

Fig. 7 Inlet air flow variation

was a continuous increase in compressor inlet air flow as the inlet guide vanes were opened up to −5 deg. This is shown on Fig. 5, which is a plot of the variation of the relative nondimensional mass flow, corrected to constant nondimensional speed, with inlet guide vane stagger. The peak compressor efficiency occurred at about 0 deg to −2 deg inlet guide vane setting.

Because the inlet guide vane optimization tests took a substantial amount of time, there was a variation in ambient conditions. In addition, there was some variation in the firing temperature. Therefore, the measured power and heat rate were corrected to constant ambient conditions and firing temperature to produce the information shown on Fig. 6. This graph shows that at inlet guide vane stagger of −2 deg the output power is about 1/2 percent higher than at 0 deg and that the heat rate is virtually the same. Thus based on output power and compressor inlet air flow considerations, the −2 deg inlet guide vane stagger was selected as optimum.

A substantial number of temperature and pressure measurements were taken at the compressor inlet, in between the airfoil rows, and at compressor exit. This information will be analyzed in considerable detail to provide an accurate assessment of the redesigned compressor performance. Bulk compressor data were collected at discrete test points over the complete range of inlet guide vane stagger. These data will be employed in the generation of the compressor characteristics at different inlet guide vane staggers.

The compressor performance, especially inlet mass flow, was better than originally assumed in the estimation of the CW251B12 engine performance, and considerably better than in the CW251B10 compressor. As the testing progressed, there was a small reduction in compressor inlet flow due to fouling, since the factory test facility did not incorporate an inlet filtration system. Compressor fouling was confirmed by a visual inspection when the engine was opened up after the completion of testing. Figure 7 shows the referred compressor inlet flow at constant nondimensional speed plotted against inlet guide vane stagger. At 0 deg inlet guide vane stagger, the inlet flow is about 5.5 percent higher than in the original compressor. At the optimum stagger of −2 deg, the flow is higher by a further 0.7 percent. Compared to the mass flow value used in the original estimation of the CW251B12 engine performance, the inlet mass flow was 3.7 percent higher. Thus the redesigned compressor exceeded its design target by a considerable margin. The increase in compressor efficiency was also better than expected, but by only a small amount.

The compressor surge test indicated that the new compressor surge margin was similar to that of the original design.

Engine Performance. Based on the average of the optimum inlet guide vane stagger test results, corrected to ISO conditions

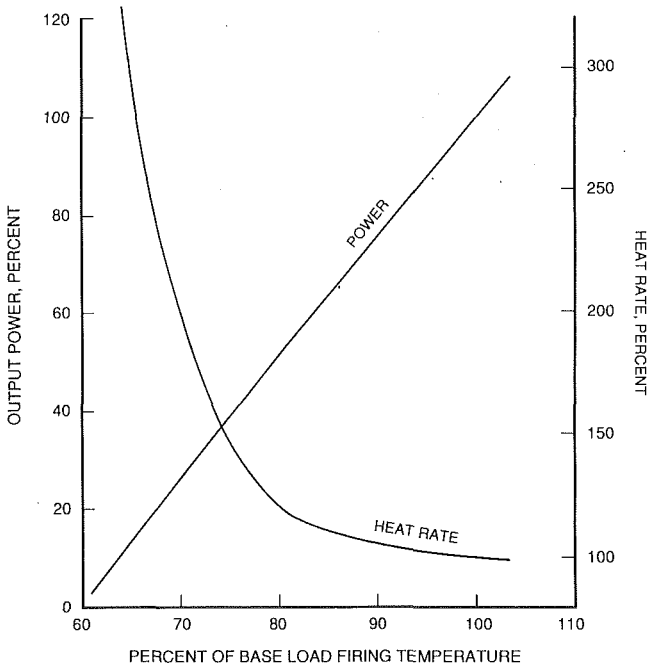

Fig. 8 Output power and heat rate variation with firing temperature

and the introductory CW251B12 baseload firing temperature of 1130°C (2065°F), the estimated margin on output power was about 4.5 percent compared to the original CW251B12 performance prediction. The corresponding estimate of the heat rate improvement was 2.4 percent. The exhaust temperature was within about 4°C (7°F) of the original estimate. As was pointed out previously, most of the improvement was due to better than originally assumed compressor performance. Some of the engine performance improvement was believed to be due to a small increase in turbine efficiency, which resulted from a reduction in blade tip clearances. The tip clearance reduction was made possible by the incorporation of abradable stationary tip shrouds. Figure 8 shows the relative variation of output power and heat rate with firing temperature, where the output power and heat rate are normalized to the values at the base load firing temperature.

Water injection tests showed that for the CW251B12 engine operating on No. 2 distillate oil fuel, the NO_x emission can be reduced by about 80 percent at an injection rate of water to fuel of about one. For each percent (of inlet air flow) water injection the output power increased by about 6 percent.

Exhaust Traverses. Figure 9 shows the results of the turbine exit plane traverse taken at approximately the baseload operating condition. The flow conditions are reasonably smooth across the annulus, except near the outer radius, where the tip leakage effects can be seen. It should be pointed out that the improved turbine blade tip clearance has reduced the tip flow gradients compared to those measured on the CW251B10 engine (Diakunchak and Nevin, 1986).

Mechanical Integrity Tests. Telemetry tests were carried out on the second-stage compressor blade to determine its vibration characteristics. Static vibration tests carried out on this blade indicated a potential interference of Mode 2 with eighth harmonic excitation. To alleviate this problem the blade was modified at the leading edge tip. Both the modified and the unmodified blades were strain gaged. The telemetry test data showed that there was very little difference in the vibratory stresses between the modified and the unmodified blades. The maximum vibratory stress measured at the tip (on the nodal line) was about $\pm$ 15 $\times$ 10^6 N/m^2 ($\pm$ 2100 psi). At blade hub the maximum stress was about $\pm$ 10 $\times$ 10^6 N/m^2 ($\pm$ 1430 psi).

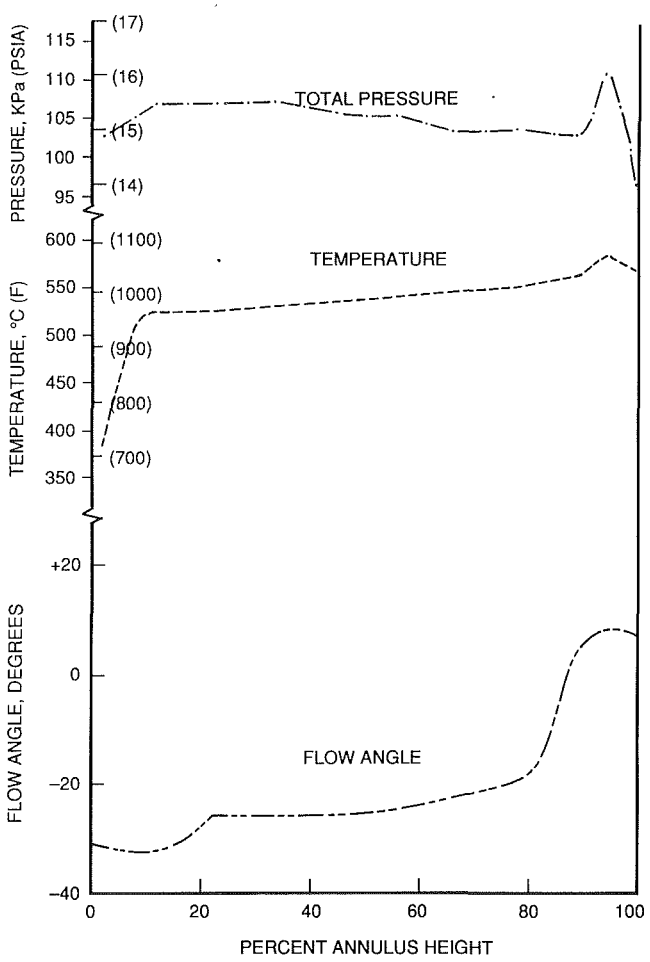

Fig. 9 Turbine exit traverse results at base load

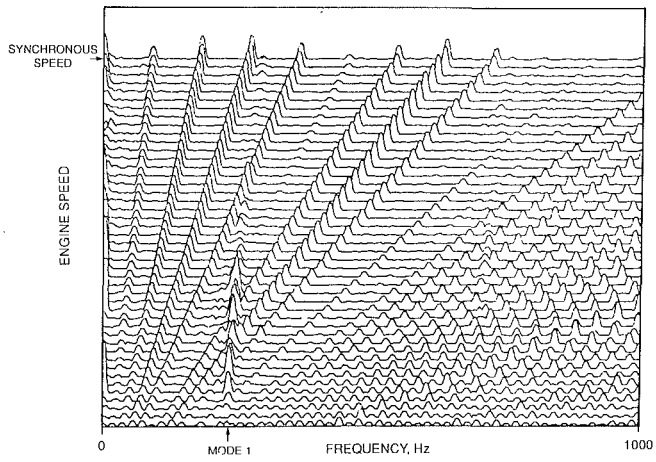

Fig. 10 Second-stage compressor blade waterfall frequency plot

The above stress levels were considered very low and therefore satisfactory. Figure 10 shows a typical "waterfall" plot for the modified second-stage blade. Strain gage test data from the first and second-stage compressor diaphragms also showed that the margins on the vibratory stresses were more than adequate.

The combustor basket thermocouple measurements indicated low metal temperatures. The average basket metal temperature was 730°C (1350°F), with a few hot spots measured up to a maximum of 787°C (1450°F). The transition duct metal temperatures were also satisfactory. The maximum metal tem-

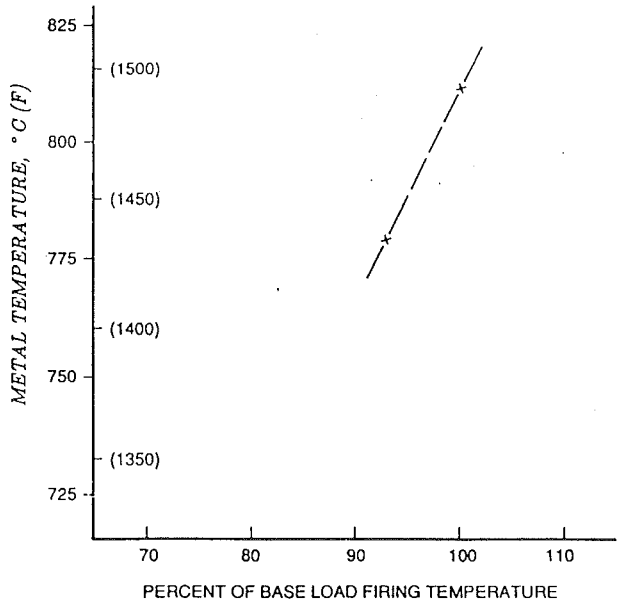

Fig. 11 First-stage turbine blade optical pyrometer test results

perature was 893°C (1600°F), with most of the transition duct surface being below this value.

The first-stage turbine blade optical pyrometer tests provided metal temperature measurements on the blade pressure surface, at three quarters of blade span from the hub, near the leading edge. The measured average temperature was about 816°C (1500°F), or about 56°C (100°F) lower than in the original blade design. The low measured blade metal temperature was attributed to the effectiveness of the turbulators. Figure 11 shows the average first-stage blade metal temperature measured by the optical pyrometer plotted against relative firing temperature.

The average first-stage turbine stator metal temperature was about 838°C (1540°F), with a maximum of about 900°C (1650°F). The average second-stage metal temperature was about 782°C (1440°F). This was similar to the measurements obtained on the CW251B10 engine, at similar firing temperature.

Disk cavity temperatures in the hot end, bearing temperatures, and loadings on the thrust bearing indicated no problems in the CW251B12 engine application. In summary, the mechanical integrity tests demonstrated that the CW251B12 engine will meet its reliability objectives.

Posttest Observations. After the completion of the tests the engine was opened up for inspection and instrumentation removal. The compressor blades and stators were found to be in good condition, but fouled with dirt. Minor diaphgram seal rubs were evident on the middle stages. There were light blade tip rubs, also on the middle stages, generally at the horizontal joint (see Fig. 12).

The combustion baskets, fuel nozzles, transition ducts, and

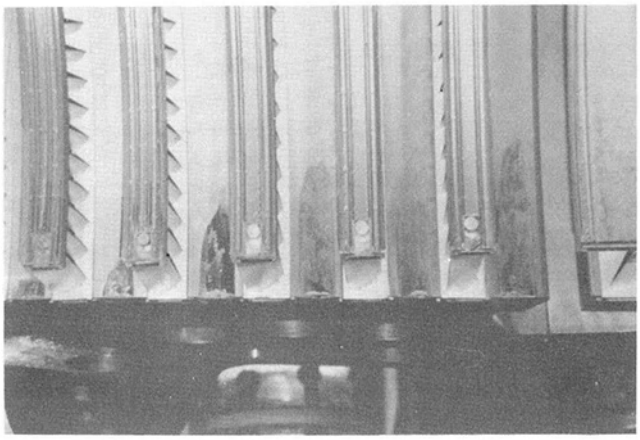

Fig. 12 View of compressor cylinder after test

turbine airfoils were in good condition. The first-stage turbine blades had experienced tip rubs, indicating good tip sealing. There were no tip rubs on the second and third-stage blades. All honeycomb blade hub seals had some rubs. The journal and thrust bearing pads were in excellent condition.

The results of the mechanical tests and the posttest inspection verified the mechanical integrity of the new compressor hardware and the hot end components. This will ensure that the CW251B12 engine reliability objectives will be achieved in field service.

Conclusions

1 The redesigned compressor exceeded its design goals.

2 The compressor inlet mass flow was about 5.5 percent higher and the efficiency about 1 percent higher than in the original design.

3 The CW251B12 engine output power was 4.5 percent better and the heat rate 2.4 percent better than the original predictions.

4 The results of the test measurements and posttest inspection verified the mechanical integrity of the CW251B12 engine.

5 Based on the successful factory test, the CW251B12 engine rating will be increased from 45 MW to 46.5 MW and the heat rate will be reduced from 11290 kJ/kW h (10,700 Btu/kW h) to 11018 kJ/kW h (10,550 Btu/kW h)

References

Diakunchak, I. S., and Nevin, D. R., 1986, "Fully Loaded Factory Performance Test of the CW251B10 Gas Turbine Engine," ASME Paper No. 86-GT-71.

Diakunchak, I. S., 1989, "The CW251B12 Gas Turbine Engine," ASME Paper No. 89-GT-119.

Diakunchak, I. S., and Nevin, D. R., 1989, "The CW251B12 Engine in a Cogeneration Application," *Proceedings of the Eighth NRCC Symposium on Industrial Applications of Gas Turbines*, Ottawa, Canada.

Marson, E., 1989, "Compressor Uprating for CW251B12 Gas Turbine," ASME Paper No. 89-GT-141.

D. T. Entenmann
Manager, Stress and Dynamics.

W. E. North
Fellow Engineer.

Westinghouse Electric Corporation,
Technology & Strategic Operations Div.,
Orlando, FL 32826

I. Fukue
Manager, Gas Turbine Design Section.

A. Muyama
Design Engineer.

Mitsubishi Heavy Industries, Ltd.,
Takasago Machinery Works,
Takasago, Japan

Shop Test of the 501F—A 150 MW Combustion Turbine

The 501F is a 150 MW-class 60 Hz engine jointly developed by Westinghouse Electric Corporation and Mitsubishi Heavy Industries, Ltd. This paper describes the full-load shop test program for the prototype engine, as carried out in Takasago, Japan. The shop test included a full range of operating conditions, from startup through full load at the 1260°C (2300°F) design turbine inlet temperature. The engine was prepared with more than 1500 instrumentation points to monitor flow path characteristics, metal temperatures, displacements, pressures, cooling circuit characteristics, strains, sound pressure levels, and exhaust emissions. The results of this shop test indicate the new 501F engine design and development effort to be highly successful. The engine exceeds power and overall efficiency expectations, thus verifying the new concepts and design improvements.

Introduction

The 501F engine, jointly developed by Westinghouse Electric Corporation and Mitsubishi Heavy Industries, Ltd. (MHI) is the latest, largest, and most advanced in a long line of single-shaft heavy-duty industrial combustion turbines. This engine combines the proven design features of the W501D5 [1] with advanced cooling schemes, including technology used in the MF111 [2], as well as the low-NO_x combustion technology of the MW701D [3]. This results in a highly efficient and powerful combustion turbine that will be available for 1990 operation and can satisfy the needs for both simple and combined cycle application in the foreseeable future. It will operate on all conventional combustion turbine fuels, incorporating dual fuel nozzles and technology when requested, and also with coal derived low Btu gas produced in an integrated gasification combined cycle power plant (IGCC) [4]. The engine incorporates a highly efficient 16-stage axial compressor, low-NO_x combustion system, and a four-stage turbine with a flow path designed utilizing fully three-dimensional analysis techniques. The plant performance characteristics presented in Table 1 are for a turbine inlet temperature[1] of 1260°C (2300°F) for the mature rating and 1210°C (2210°F) for the initial rating. A general description of the engine is presented in [5, 6].

As an integral part of any engine development program, testing includes advanced technology component verification testing, full-load shop testing, and prototype field testing. This paper describes the component and shop test programs. The shop test results are presented here with respect to the overall design considerations. Detailed shop test data evaluation is continuing and will serve as the basis for further design improvements, some of which are noted herein. The results of these studies will be the subjects of further publications.

[1]Hereinafter referred to as TIT or RIT (rotor inlet temperature).

Contributed by the International Gas Turbine Institute and presented at the 35th International Gas Turbine and Aerospace Congress and Exposition, Brussels, Belgium, June 11–14, 1990. Manuscript received by the International Gas Turbine Institute January 26, 1990. Paper No. 90-GT-362.

Table 1 501F design plant performance

		Initial	Mature
Power, net kW		135,000	145,000
Heat rate, kJ/kW-h		10,706	10,548
	Btu/kW-h	10,150	10,000
Air flow, kg/s		413.6	413.6
	lb/s	912	912
Pressure ratio		14:1	14.2:1
Exhaust temperature,	°C	545	571
	°F	1013	1061

Engine Design Features

A longitudinal section of the 501F engine is shown in Fig. 1. A summary of the basic design features is presented below, with those features unique to the 501F listed separately. The pre-501F list is a modification of that presented in [7].

Pre-501F Features

- Cold end generator drive to eliminate the need for a flexible coupling.
- Horizontally split casings to facilitate field maintenance with the rotor in place.
- Two-bearing rotor with the compressor and turbine portions joined by a center coupling.
- Variable inlet guide vane (IGV) to provide exhaust temperature control for heat recovery applications and to improve starting characteristics.
- Compressor diaphragms and dovetail rooted blades removable with the rotor in place.
- Three axisymmetric compressor bleeds for turbine cooling with two used to avoid surge during starting.
- Combustors and transitions removable without lifting cylinder covers.

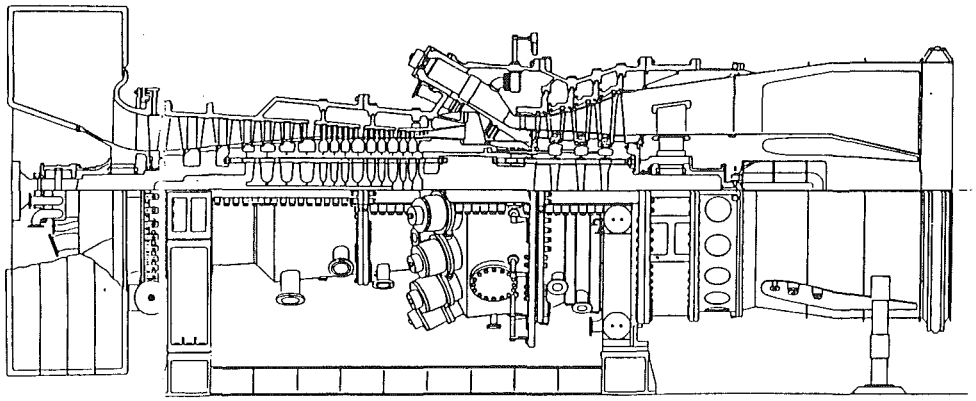

Fig. 1 501F longitudinal section

- Turbine rotor with bolted, CURVIC[2] coupled disks.
- Fir-tree rooted turbine blades removable on-site with rotor in place.
- Multiple turbine blade ring concept to provide field service of stators with the rotor in place.
- Cooled stage 1 and 2 vane segments and cooled stage 1 and 2 blades.
- Stage 1 vanes removable without lifting cylinder cover.
- Tangential exhaust casing struts to maintain rotor alignment.

501F Additional Features

- Compressor blade locking feature that is visibly inspectable.
- Blade rings in compressor section to optimize cylinder to rotor alignment.
- Advanced hybrid combustor system, or premixed system, incorporating low-NO_x features.
- Combustor transition cooling scheme, which takes benefits of asymmetric external cooling characteristics of combustor shell flow.
- Bolted compressor rotor design, which eliminates a main coupling joint, as found on the W501D5 design, to increase rotor dynamic stability margin as well as facilitate fabrication and maintenance of the rotor.
- Cooled stage 3 vane segment and turbine blade to improve reliability.
- 16-stage newly designed, highly efficient axial flow compressor incorporating larger diameter rear stages to help balance spindle thrust and two exit guide vanes, instead of one, to straighten the flow leaving the compressor.
- Turbine flow path design utilizing fully three-dimensional flow analysis.
- Journal bearings consist of two-element tilting pad bearings for load carrying and an upper half fixed bearing to eliminate top pad fluttering concerns and related local babbitt spragging.
- Leading edge groove (LEG) direct lubricated thrust bearing to reduce the required oil flow and its mechanical loss.
- Integral "Z" tip shrouds in third and fourth-stage rotors to minimize the potential for flow-induced nonsynchronous vibration.
- Use of segmented isolation rings in the turbine vane segment support scheme to minimize blade ring distortion.
- State-of-the-art turbine blade and vane segment cooling schemes to increase reliability and overall engine efficiency.

Component Verification Test Program

Prior to the engine shop test, critical components unique to the 501F engine were tested to assure performance and reliability, using special test rigs and facilities.

The tests included:

(A) Rotating blade vibration test
(B) Turbine aerodynamic test
(C) Combustion test
(D) Turbine cooled parts heat transfer tests

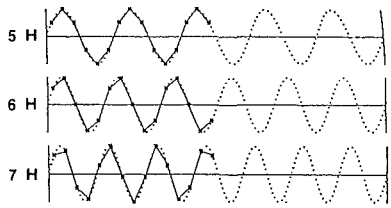

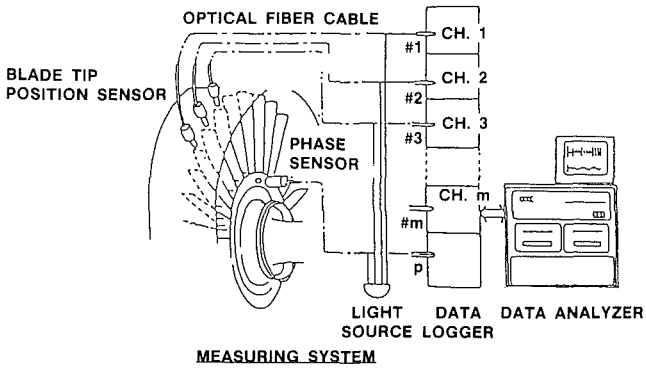

Fig. 2 Optical fiber blade vibration monitoring system

Rotating Blade Vibration Test. Natural frequency and vibratory stresses of compressor and turbine blades for selected stages were checked during a high-speed rotor balancing test to assure that those blades were well tuned. During the test, the actual fully bladed rotor was driven by an electric motor up to 110 percent of rated speed in a vacuum room. The frequencies and amplitudes of compressor blade vibration for the first, second, fourth, and seventh stages were measured using a noncontact optical fiber monitoring system. This system showed the movement of each individual blade tip by monitoring the position of each blade tip from several different locations circumferentially and analyzing this information through a synchronizing process. The schematic of this measuring system is shown in Fig. 2. In the turbine, strain gages were applied directly to the blades of each stage and the meas-

[2]Trademark of Gleason Works.

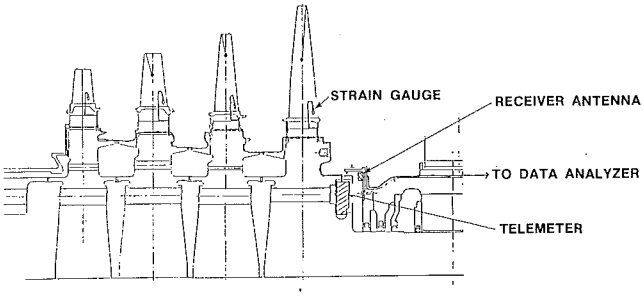

Fig. 3 Telemetry system

ured strain signals were transmitted to a data acquisition system through the telemetry system shown in Fig. 3. After analyzing all measured data, it was confirmed that no further tuning was necessary for the blades.

Turbine Aerodynamic Test. In order to verify the turbine aerodynamic performance for each stage, the following tests were carried out using special test rigs:

- The stage-averaged loss coefficients were measured in a two-dimensional cascade test by varying Mach number and incidence angle.
- The engine pressure ratio is largely dependent on the flow coefficient of the row 1 vane nozzle, so an annular cascade test using a scale model of the assembled row 1 vanes was carried out to determine the flow coefficient.
- 501F turbine airfoils were designed utilizing fully three-dimensional analysis techniques. From the above tests, however, the effects of the three-dimensional design on performance could not be estimated. Therefore, model turbine tests using scaled row 4 vanes and blades were conducted. The test rigs are shown in Fig. 4. The test results displayed in Fig. 5 show that the stage efficiency goal was met.

The data confirmed that the original design objectives were satisfied.

Combustion Test. Two types of combustor were used for the shop test: a diffusion type, which was similar to the Westinghouse W501D5 standard combustor, and MHI's advanced premixed type combustor for distillate oil fuel.

Prior to the shop test, basic characteristics of both combustors, such as flame propagation, exhaust emission, pattern factor, combustor wall temperature, dynamic pressure oscillation, etc., were checked in both atmospheric and high-pressure tests, and if necessary, those combustors were modified to achieve the design target. Figure 6 shows the high-pressure combustion test facility.

In addition to the above test, mechanical vibratory tests, a flow visualization test around the combustor, and acoustic resonance tests were conducted to assure the reliability of the combustion system.

Turbine Cooled Parts Heat Transfer Test. Many advanced cooling technologies are incorporated into 501F hot parts to maintain the metal temperatures within desirable levels. Some of these technologies have already been utilized in MHI's advanced 13-MW high-temperature gas turbine MF111, and over 100,000 hours of MF111 operating experience showed the benefit and reliability of those technologies.

Figure 7 shows the comparison of cooling design between MF111 and 501F. In order to verify the effectiveness of cooling technologies that are unique to the 501F, such as eight rows of pin fin cooling in the stage 1 vane segment, and showerhead cooling for both rotating blade and stationary vanes, scale model tests were carried out. These test results were incorporated into the cooling design of 501F hot parts.

Prior to the shop test, the cooling effectivenesses of the final configurations of both row 1 vanes and blades were confirmed in hot cascade tests. In these tests, prototype vanes and blades

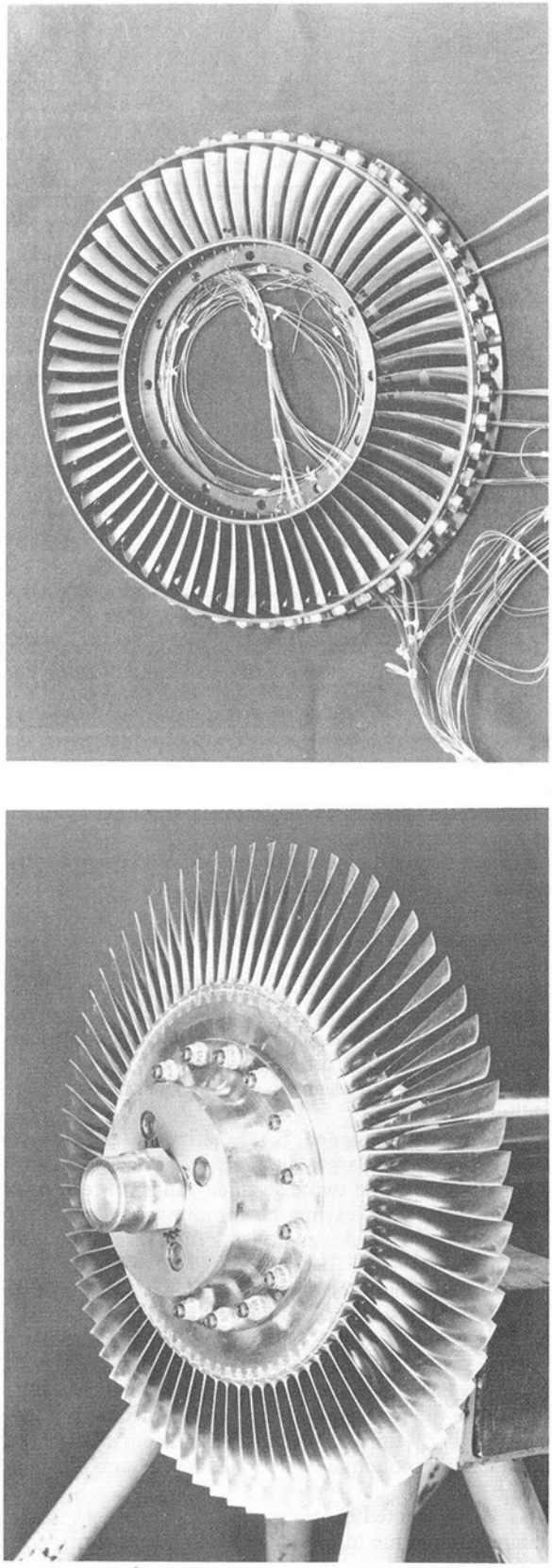

Fig. 4 Model test rotor

were positioned at the downstream end of the test combustor to simulate the actual engine operating conditions. Metal temperatures at various locations in the vanes and blades were measured and confirmed to compare favorably with the design allowables.

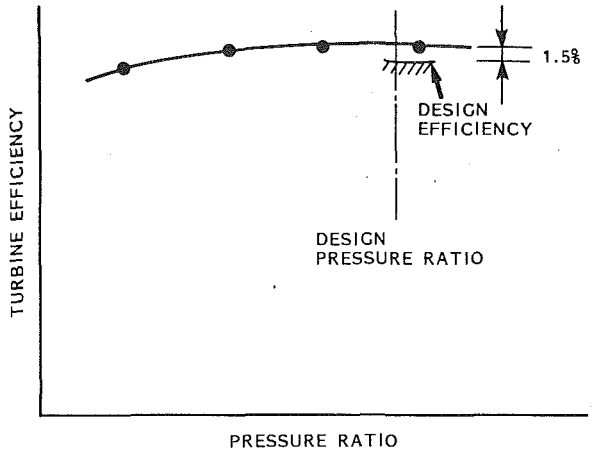

Fig. 5 Turbine row 4 model test

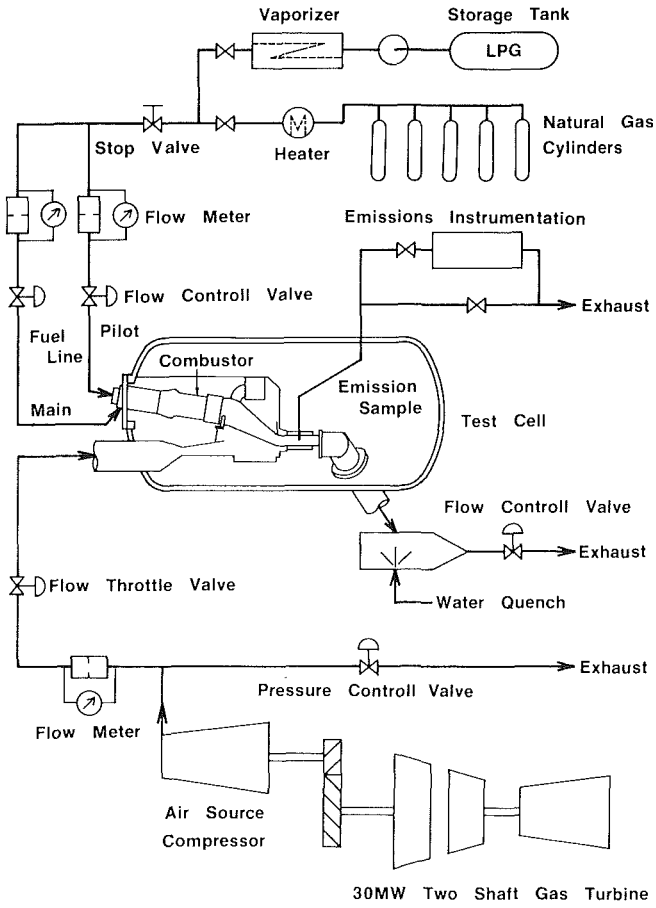

Fig. 6 Schematic of combustion test facility

Shop Test Program

The objective of the full-load shop test was to verify the following characteristics as well as develop the optimum setting schedules for system components:

1 Starting characteristics—Confirm characteristics including light-off, acceleration, vibration, and surge margin.

2 Performance—Verify individual compressor and turbine as well as overall gas turbine performance. Parameters included airflow, power output, heat rate, and exhaust temperature.

3 Exhaust Emissions—Emission testing included sampling for nitrogen oxides (NO_x), nitric oxide (NO), carbon monoxide (CO), unburned hydrocarbons (UHC), Bacharach smoke number (BSN), carbon dioxide (CO_2), and oxygen (O_2).

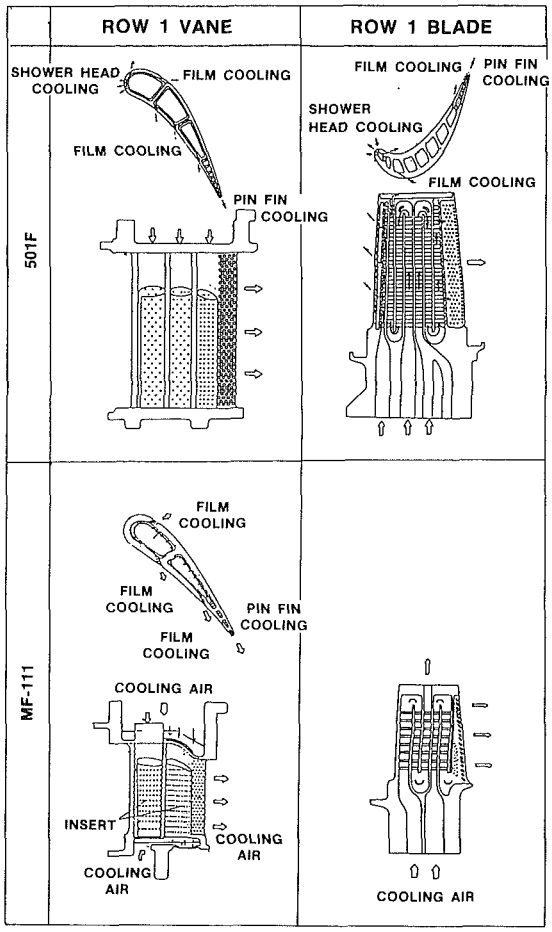

Fig. 7 Cooling scheme for 501F and MF-111

4 Hot Parts Metal Temperatures—Confirmed that the hot parts metal temperatures were below the associated allowables at 1260°C (2300°F) RIT during full-load operation. Components monitored include combustor baskets, combustor transitions, turbine vanes and blades, and turbine row 1 ring segment.

5 Mechanical Characteristics—Vibratory stresses of the compressor and turbine blades, bearing temperatures, casing temperatures, and disk cavity temperatures were monitored continuously during the test. In addition, axial and radial growths were monitored at strategic locations in the engine to verify design calculations.

The major features of the shop test facility and engine installation are listed below:

1 The prototype 501F engine was coupled with a 162MVA generator.

2 All the auxiliaries associated with the test were shop facilities, including the starting system, lube oil system, coolers, and inlet and exhaust ducts.

3 Distillate oil was used as the fuel.

4 Two types of combustor were used. A diffusion combustor, similar to the W501D5, was used for initial startup and a premixed combustor was used for rated operation.

5 The gas turbine and generator were installed in the test stand without packaged auxiliaries.

6 The control systems and supervisory instrumentation were shop available equipment.

7 The compressor air supply ducting system employed a bellmouth inlet to measure air flow.

8 The electrical power generated was absorbed by a water rheostat with cooling towers.

Figure 8 presents an overall general arrangement of the test facility, showing the major components: gas turbine, gener-

ator, exciter, starter, G/T control room, special instrumentation room, cooling air cooler, water rheostat, and air intake and exhaust stacks. The gas turbine generator was a three-phase cylindrical synchronous alternator rated at 162,000 KVA. The starting system included a 1450 kW (1945 hp) electric motor.

Monitoring System During Engine Operation. As mentioned previously, in addition to the supervisory instrumentation, more than 1500 special instrumentation points were applied to the engine during the full load shop test. Included were advanced instrumentation systems such as an Accufiber probe for measuring turbine inlet temperature, an optical pyrometer for monitoring turbine row 1 blade metal temperature, and an optical fiber for compressor blade vibration monitoring.

A summary of the special instrumentation is shown in Fig. 9.

All measured pressure data were converted to electric signals through scanivalves and stored in a data logger. Dynamic pressure fluctuation and vibratory stresses were analyzed using an "FFT" (Fast Fourier Transform) analyzer with the frequencies and amplitude monitored during "real time" with the engine operating.

Data critical to the continued operation of the engine, such as metal temperatures of hot parts and cavity temperatures, were also monitored on computer display together with associated alarm limits.

The turbine inlet temperature of the operating engine was calculated from measured data using a heat balance calculation program. The required data for this calculation were automatically transferred from the data logger during engine operation.

The following information was obtained with the engine monitoring system during the shop test.

1 Performance—Air flow, inlet temperature and pressure, exhaust temperature and pressure, fuel flow, generator output, compressor surge margin and stage efficiency, turbine stage and diffuser efficiency.

2 Metal Temperatures—Combustor basket, transition piece, row 1 turbine blade, row 1-4 turbine vane segments, row 1 ring segment, bearings, outer casings, blade rings, exhaust cylinder.

3 Stress/Vibration—Compressor blades and diaphragms, combustor baskets, transition pieces and associated supports, turbine blades, exhaust struts. In addition to casing vibration, both lateral and torsional rotor vibration were monitored.

4 Others—Thrust load, cooling air flow network, mechanical loss, air and gas temperatures of various cavities, exhaust emissions, rotor/casing displacement, noise level, and lube oil flow and temperature.

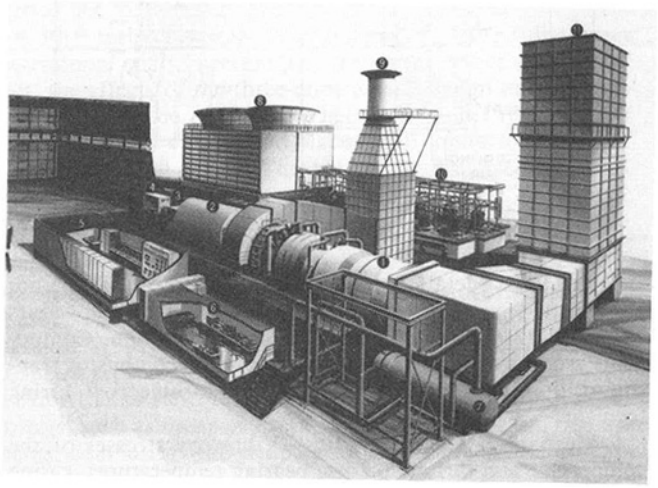

Fig. 8 General arrangement of 501F shop test

Test Results

The test program results are summarized below for the areas of starting and acceleration, overall performance, combustion emissions, hot parts temperatures, and vibratory stresses.

Starting and Acceleration. The shop test starting schedule included ignition at 610 rpm, starter motor disengagement at 2400 rpm, and bleed valve closure at 3310 rpm with the IGV position held constant at 19 deg. The elapsed time from starting button to synchronizing speed was about 20 min. At ignition speed, two combustors located at the bottom of the engine were ignited. Cross-flame tubes produced complete ignition in 40 to 50 s. Compressor rotating stall was cleared at approximately 2000 rpm. Throughout the starting sequence, compressor operating characteristics were very stable, thus indicating sufficient margin against surging during starting.

When the starting motor was disengaged, the responses of exhaust gas temperature and engine speed were monitored to confirm that the engine could easily accelerate from 2400 rpm without assistance.

(A) PERFORMANCE	(B) METAL TEMP.	(C) STRESS/VIBRATION	(D) OTHERS
1 AIR FLOW	8 COMBUSTOR BASKET	16 COMPRESSOR BLADE	24 COOLING AIR NETWORK
2 INLET TEMP. & PRESS	9 TRANSITION PIECE	17 COMPRESSOR VANE	• FLOW
3 EXHAUST TEMP. & PRESS	10 TURB. ROW 1 BLADE	18 COMBUSTOR BASKET	• TEMPERATURE
4 FUEL FLOW	11 TURB. ROW 1-4 VANE	19 TRANSITION PIECE	• PRESSURE
5 GENERATOR OUTPUT	12 BEARING METAL	20 TURBINE BLADE	25 TRUST LOAD
6 COMPRESSOR	13 OUTER CASING	21 ROTOR VIB.	26 EXHAUST EMISSION
(SURGE MARGIN	14 INNER CASING	22 CASING VIB.	27 ROTOR/CASING EXPANSION
(STAGE EFF.	15 EXHAUST CYLINDER	23 ROTOR TORSIONAL VIB.	28 NOISE
7 TURBINE			29 LUBE OIL TEMP.
(STAGE EFF.			
(DIFFUSER EFF.			

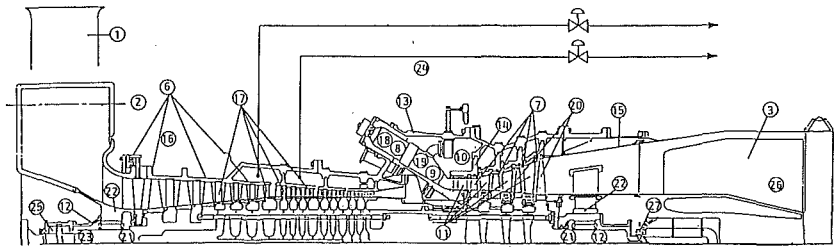

Fig. 9 501F prototype special measurements

Overall Performance. Performance data measured during the full-load shop test were analyzed and corrected from shop test conditions to standard ambient conditions. The results show that the measured power output and exhaust gas flow exceeded the predicted values by more than 2 percent. In addition, the heat rate was slightly better than predicted and the exhaust gas temperature was higher than the predicted value by approximately 10°C (18°F). When the performance values shown in Table 1 were developed, some margin was incorporated. It has now been verified that measured performance exceeded the predicted values. New performance ratings will be established following completion of a full shop test data evaluation.

Combustion/Emission. Nitrogen oxides (NO_x), carbon monoxide (CO), unburned hydrocarbons (UHC), and other emissions were measured for both the diffusion type and the premixed type combustors using oil fuel. When using the premixed-type combustor, it was found that the setting schedules of inlet guide vane and bypass valve would affect the combustion stability significantly. Figure 10 shows the dynamic pressure fluctuation measured inside the premixed combustor. Stable combustion was assured throughout engine startup and operation by selecting the optimum schedule of IGV and bypass valve settings. Figure 11 presents the NO_x emission level of the premixed-type combustor compared with that for the conventional diffusion type combustor at dry conditions. The NO_x level of the premixed-type combustor was less than half that for the diffusion type combustor at full load conditions.

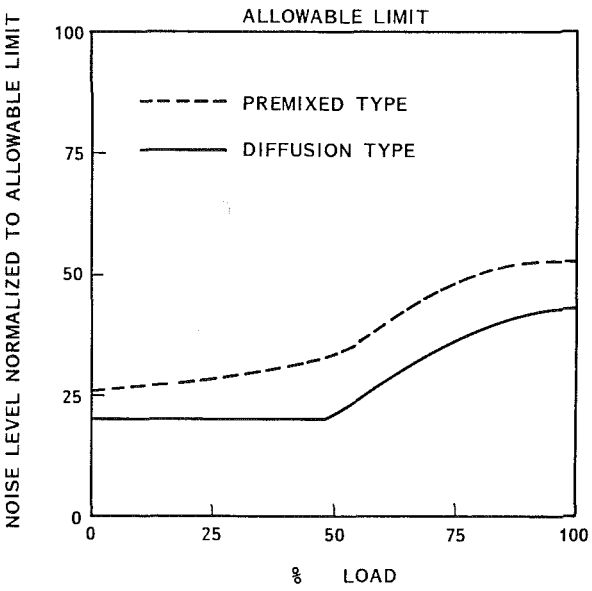

Fig. 10 Combustor noise level

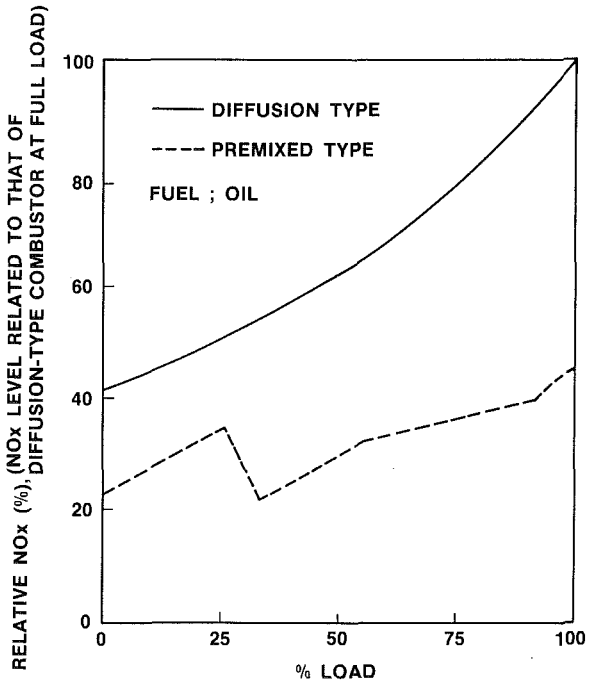

Fig. 11 NO_x emission

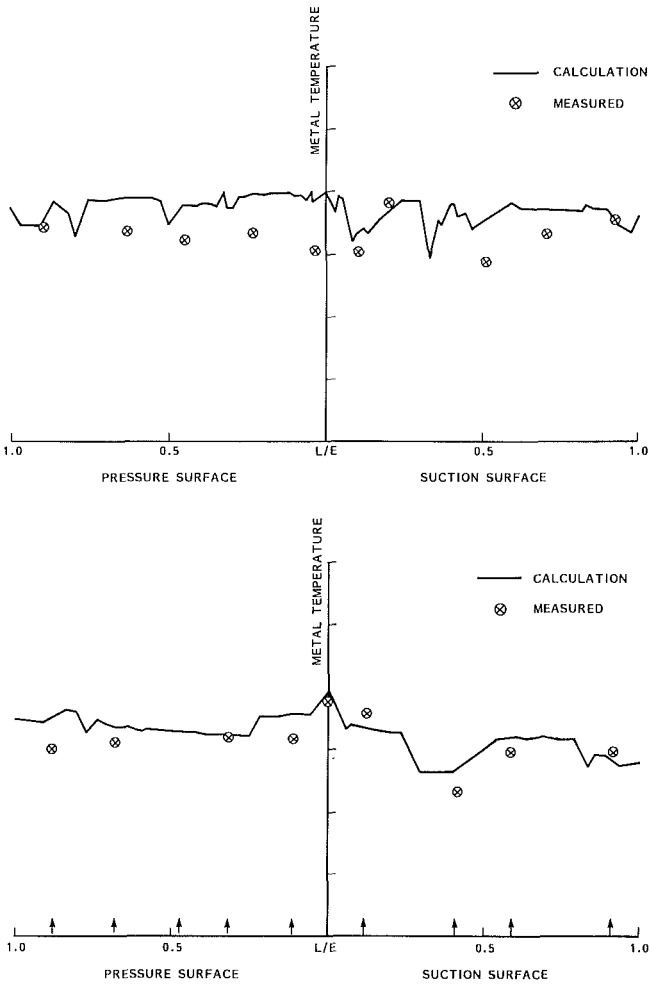

Fig. 12 Row 1 and 2 vane metal temperature

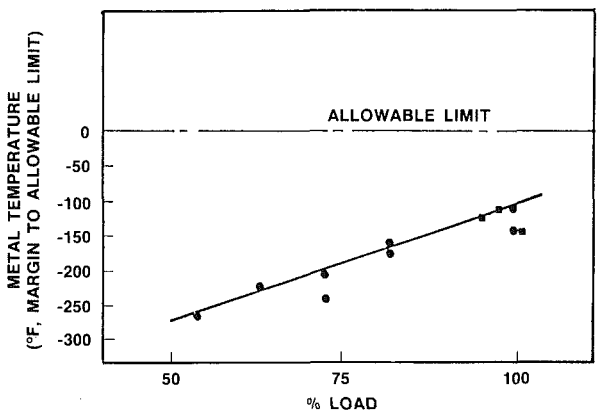

Fig. 13 Turbine row 1 blade metal temperature

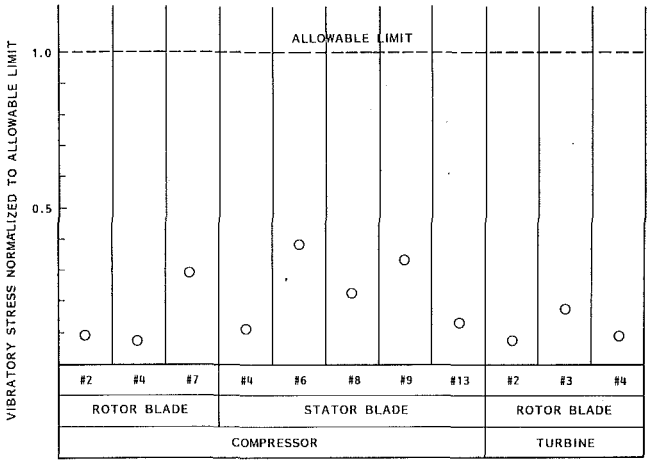

Fig. 14 Summary of vibratory stress

Hot Part Temperatures. Figures 12 and 13 present hot part temperatures measured at the 1260°C (2300°F) full-load condition. Figure 12 shows metal temperatures for rows 1 and 2 vane segments at midheight normalized to the calculation results. The temperatures were obtained from thermocouples mounted on the surface of the vane airfoils. It was confirmed that the measured temperatures were within an acceptable range of the expected values; thus the calculation techniques for the cooled vane designs were considered verified.

Figure 13 shows the row 1 turbine blade metal temperature at 60 percent blade height. The temperatures presented in the figure were obtained through the use of a pyrometer and confirm an adequate design margin.

Evaluation of hot parts data is continuing and will provide the basis for further design improvements, if so indicated.

Vibratory Stresses. Figure 14 presents vibratory stresses as measured during the test along with corresponding design allowables. Vibratory stresses of other stationary components such as combustor transitions and tangential struts were also measured. All measured stresses are within the design allowables.

Summary

Overall, the 501F shop test was an outstanding success. Performance was better than anticipated at 100 percent load, as presented in Table 1. Hot parts metal temperatures were verified to be consistent with design values. A starting motor of 1450 kW (1945 hp) was verified to be adequate via successful starting and acceleration testing. The new premixed combustion system proved successful for oil firing, and mechanical characteristics, such as vibratory stresses of blades and diaphragms, such as vibratory stresses of blades and diaphragms, thrust force, axial/radial growth, and bearing metal temperatures were confirmed to be within the design limits at various operating conditions.

References

1 Scalzo, A. J., Holden, P. C., and Howard, G. S., "The Westinghouse W501D Combustion Turbine Engine," ASME Paper No. 81-GT-32, 1981.

2 Akita, E., et al., "Development and Testing of the 13 MW Class Heavy Duty Gas Turbine MF-111," ASME Paper No. 87-GT-37, 1987.

3 Aoyama, K., and Mandai, S., "Development of a Dry Low NO_x Combustor for a 120-MW Gas Turbine," ASME JOURNAL OF ENGINEERING FOR GAS TURBINES AND POWER, Vol. 106, 1984, pp. 795-800.

4 Hendry, R. L., and Pillsbury, P. W., "Commercial Demonstration of the DOW Gasification Process in an Integrated Combined Cycle Cogeneration Application," *Proceedings of the American Power Conference*, 1987.

5 Scalzo, A. J., McLaurin, L. D., Howard, G. S., Mori, Y., Hiura, H., and Sato, T., "A New 150-MW High-Efficiency Heavy-Duty Combustion Turbine," ASME JOURNAL OF ENGINEERING FOR GAS TURBINES AND POWER, Vol. 111, 1989, pp. 211-217.

6 Scalzo, A. J., Antos, R. J., and Fukue, I., "Operating Experience Complements New Technology in Design of Advanced Combustion Turbine," ASME Paper No. 88-JPGC/GT-1, 1988.

7 Scalzo, A. J., Howard, G. S., and Holden, P. C., "Field Test of the W501D A 100 MW Combustion Turbine," ASME Paper No. 83-GT-174, 1983.

MS3002 Advanced Tech Upgrade Application and Operating Experience

C. M. Grondahl
Principal Engineer,
Turbine Technology Dept.,
General Electric Co.,
Schenectady, NY 12345

M. E. Guiler
Manager,
Compressor Dept.,
Texas Eastern Pipeline Co.,
Kingwood, TX 77339

Modernization of MS3002 gas turbines produced by GE from 1951 to 1973 has been accomplished with the application of advanced technology components in a redesigned turbine hot section. Texas Eastern installed the first modernization package in 1986 and now has 10 units in service totalling more than 135,000 operating hours. This paper presents the user's motivation to refurbish 30-year-old gas turbines, including details of the uprate installation and subsequent operating experience. Specifics of the advanced technology components in these units are provided including their impact on unit performance and reliability.

Introduction

First introduced in 1951, the GE MS3002 gas turbine has undergone performance improvements with each successive model, as shown in Fig. 1. Earlier models "A" through "G" were all built with essentially the same compressor air flow and major turbine components. Improvements in performance were achieved through application of high-temperature alloys and increases in turbine firing temperature. The current production model "J" and its predecessor model "H" (introduced in 1969) are based on a redesigned turbine section featuring a higher compression ratio and supported by four bearings instead of the five used in the earlier units. With the exception of the compressor, few model "H" or "J" components fit physically into the earlier models. After many thousands of fired hours, major components such as turbine wheels were approaching the end of their useful lives, and parts for early models had become less readily available.

Texas Eastern began purchasing GE MS3002 model "C" gas turbines in 1955 for use in gas pipeline pumping stations, and by 1962 the fleet had grown to 21. By 1985 individual turbines had accumulated between 169,000 and 241,000 fired hours, while thermal efficiencies averaged about 27 percent. However, these turbines had a composite wheel design and they would require inspection or replacement at the next major overhaul interval. Texas Eastern had two options: It could replace components in the turbines, although some components were not readily available, or it would have to replace the turbines completely.

General Electric offered a third alternative for operators of more than 200 MS3002 models "A" through "G" with the commitment in 1984 to design a new turbine section for these units. Shown in Fig. 2 it is an extensive modernization renewing the high maintenance hot gas path components based on a new aero design using 1980s technology to provide substantial improvements in performance and extended maintenance intervals. With a guaranteed 32 percent thermal efficiency (at specified conditions) and projected reliability of a new machine, Texas Eastern chose to uprate 10 of their MS3002 model Cs in 1986.

The discussion that follows describes the generic uprate, applicable to all models "A" through "G," as well as the Texas Eastern application.

Uprate Performance Goals

Advanced technology developments for MS3002 models "A" through "G" began with a new aerodynamic cycle based on Texas Eastern's requirement for fuel efficiency improvement at the original Model "C" output rating of 8000 hp. The resulting turbine design, however, provides fuel efficiency and increased output options over the entire operating range for both regenerative and simple cycle designs. Figures 3 and 4

MS3002 MODELS A THRU J PERFORMANCE HISTORY

MODEL	SHIP DATES	HP RANGE*	HEAT RATE** (BTU/HP-HR)	FIRING TEMP (°F) RC	FIRING TEMP (°F) SC	AIR FLOW* (10^3 LBS/HR)
3002A, B	1951-56	5,000-6,700	10,100	1,450	1,450	355
3002C	1955-59	TO 7,600	9,280	1,500	1,500	355
3002D	1961-63	TO 8,000	9,070	1,550	--	360
3002E, G	1963-66	TO 8,500	8,900	1,575	1,525	371
3002F	1966-73	TO 9,300	8,490	1,625	1,575	371
3002H, J	1969-	TO 14,600	7,410	1,750	1,730	415

* RATINGS FOR MODELS A THRU G ARE BASED ON NEMA (1000 FT ALTITUDE AND 80°F) CONDITIONS AND MODELS H & J ARE BASED ON ISO (SEA LEVEL AND 59°F) CONDITIONS. TO CONVERT FROM NEMA TO ISO RATINGS FOR APPROXIMATE COMPARISON, MULTIPLY NEMA RATING BY 1.12. INCLUDES 0/0 INCHES H_2O INLET/EXHAUST PRESURE DROPS

** HEAT RATES GIVEN ARE FOR REGENERATIVE CYCLE AND ARE LOWER HEATING VALUE. TO CONVERT TO % THERMAL EFFICIENCY, DIVIDE 2547 BTU/HP-HR BY HEAT RATE (BTU/HP-HR) AND MULTIPLY BY 100

Fig. 1

Contributed by the International Gas Turbine Institute and presented at the 35th International Gas Turbine and Aeroengine Congress and Exposition, Brussels, Belgium, June 11-14, 1990. Manuscript received by the International Gas Turbine Institute January 24, 1990. Paper No. 90-GT-350.

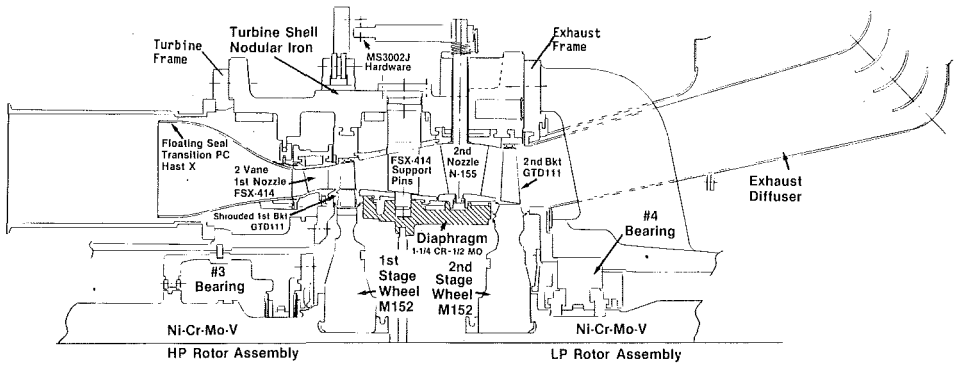

Fig. 2 MS3002 modernization and upgrade program

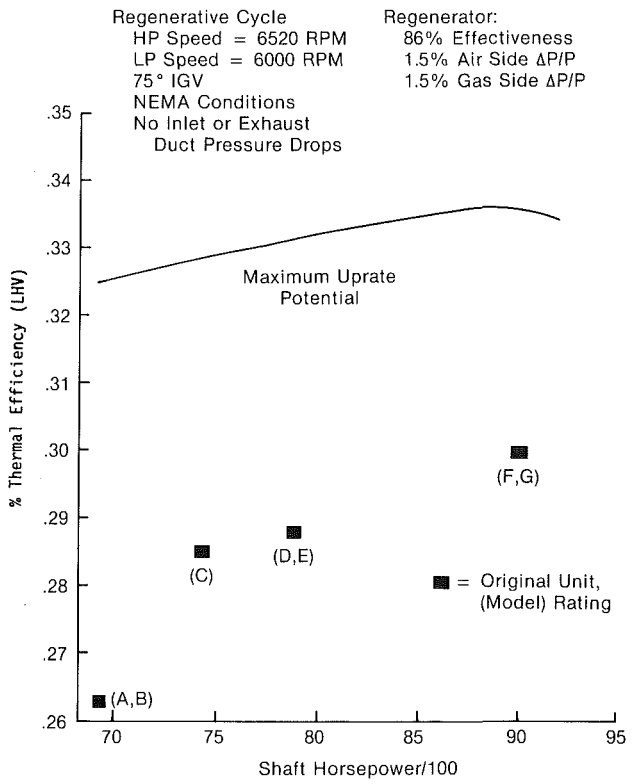

Fig. 3 MS3002 regenerative cycle thermal efficiency improvement

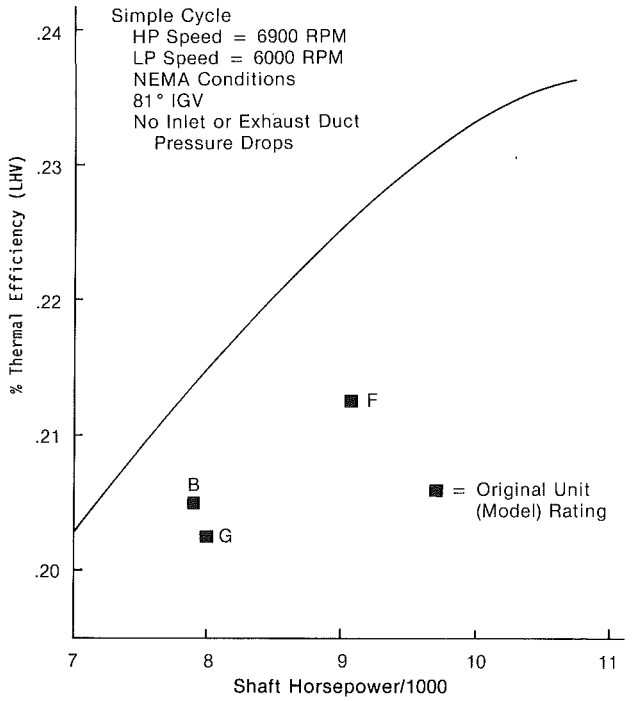

Fig. 4 MS3002 models A through G: simple-cycle performance uprate capability

show the uprate performance capability for regenerative and simple-cycle turbines firing at 1628°F and 1643°F, respectively.

combustion system, number of compressor stages, and/or exhaust diffuser arrangement of some units may reduce their uprate performance potential.

The following design parameters were established:

	Regeneration Cycle	Simple Cycle
Nominal compressor shaft speed	6520 rpm	6900 rpm
Minimum compressor shaft speed	5900 rpm	5900 rpm
Maximum 100 percent load shaft speed (with 105 percent continuous operating capability)	6000 rpm	6000 rpm
Maximum exhaust temperature	1000°F	1000°F
Maximum firing temperature	1628°F	1643°F
Maximum IGV angle	75 deg	81 deg
Minimum IGV angle	63 deg	75 deg

A major design objective was commonality of new components for all the models to maximize and ensure availability of these parts. This was achieved in every respect, with the exception of some minor interface seals and piping for specific applications.

Models "A" through "G" can now be uprated to the maximum regenerative or simple cycle horsepower shown in Figs. 3 and 4 with the associated thermal efficiencies. However, the

Figures 3 and 4 are based on the nominal compressor shaft speed at maximum load shaft speed, firing temperature, IGV angle and exhaust temperature at NEMA conditions with no inlet or exhaust pressure drop. Regenerator effectiveness of 86 percent is assumed for the regenerative cycle.

The following Texas Eastern uprate design-point parameters result in a thermal efficiency of 32 percent, at original NEMA output of 8000 hp. Texas Eastern's objective was moderni-

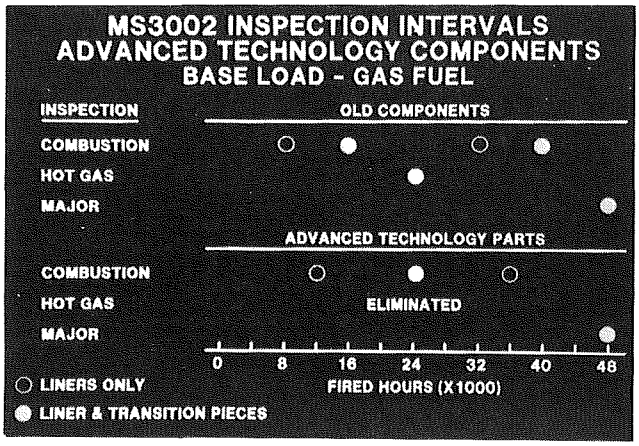

Fig. 5

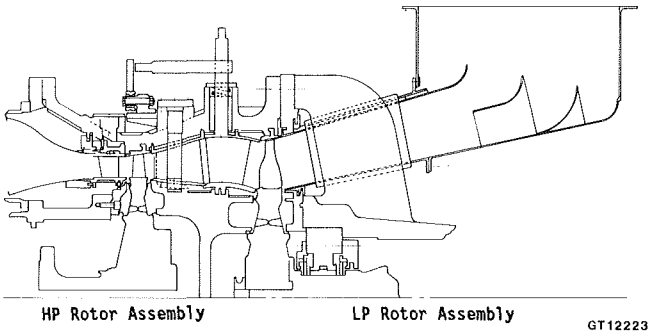

Fig. 6

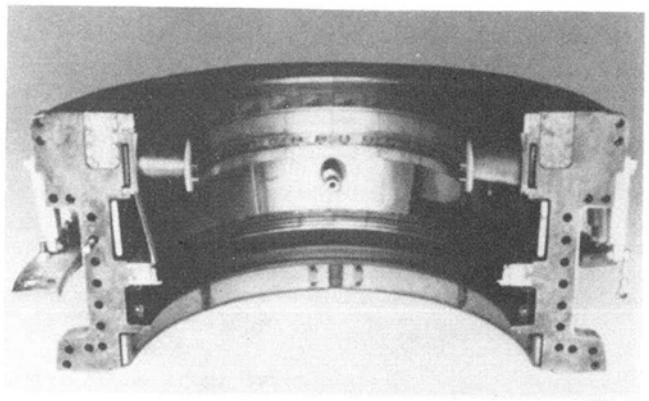

Fig. 7 Air-cooled turbine shell arrangement

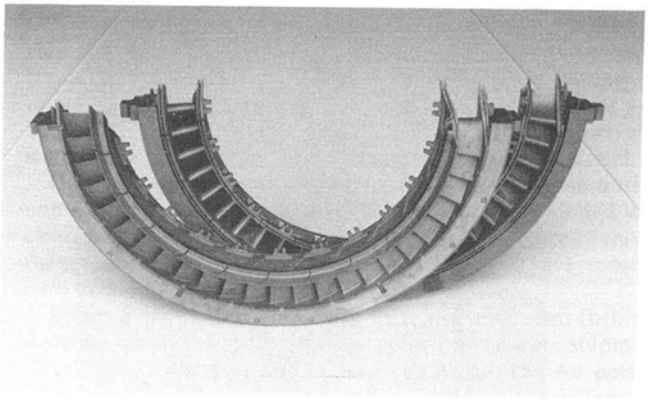

Fig. 8 MS3002 stage 1 turbine nozzle

zation of turbines at their original horsepower, minimizing changes in the load compressor and permits.

Compressor shaft speed	6280 rpm
Load shaft speed	5700 rpm
IGV angle	75 deg
Firing temperature	1600°F
Exhaust temperature	1000°F
NEMA conditions	
Inlet pressure drop	0
Exhaust pressure drop	0
Regenerator effectiveness	86 percent

Maintenance Goals

When uprating MS3002 units with advanced technology components, major inspections are only required every 48,000 fired hours (based on baseload operation with natural gas). Combustion inspection intervals have been extended up to 50 percent, with liner inspections recommended at 12,000 fired hours and transition piece inspections at 24,000 fired hours. Hot gas path inspections have been eliminated with the uprate. Inspection interval improvements based on advanced technology parts are shown in Fig. 5.

MS3002 Uprate With Advanced Technology Components

The new MS3002 aerodynamic design resulted in significant design change of gas path components in order to meet performance goals. Maintenance and reliability objectives also contribute to the turbine design, as shown in Fig. 2. A typical original design turbine section is shown in Fig. 6.

In the new design, the original water-cooled, welded turbine shell was replaced with an air-cooled, nodular iron cast shell, which is arranged in the factory, complete with first and second-stage shrouds, second-stage nozzle partitions, and interstage diaphragm. Figure 7 shows the turbine arrangement partially assembled. The turbine shell is designed as a drop-in replacement for the original with respect to turbine frame and exhaust frame vertical bolting.

Extra stock is provided on the turbine shell to accommodate resurfacing of mating flanges that may have distorted during service. The aft turbine shell flange area is air cooled with tenth-stage extraction air from the axial flow compressor. This cooling air is then delivered, in series, to the interstage diaphragm for aft and forward wheel space cooling. Elsewhere in the turbine shell, insulation packs are used to control temperatures.

Tubes for removable thermocouples enter the interstage wheel spaces via support pins. Borescope inspection holes through the turbine shell and shrouds make it possible to view first and second-stage turbine buckets.

The 32 variable second-stage nozzle partitions and shafts are integrally cast from N155 alloy. The control ring is roller supported from the turbine shell. At Texas Eastern, dual hydraulic cylinders mounted on the turbine shell use existing 300 psi hydraulic oil to drive the control ring and position second-stage nozzle partitions. New linkages provide feedback to the existing control system on Texas Eastern units. Other uprate applications integrate controls upgrade packages and, in some cases, use different hydraulic actuators.

Increased Nozzle Life. Several new design factors resulted in increased nozzle life. The first-stage turbine nozzle (Fig. 8) consists of 24 two-vane segments (Fig. 9) cast from FSX-414 material. The reduction from the original seven vanes per segment significantly increases the number of calculated thermal cycles to sidewall crack initiation, a design similar to first-stage nozzles in the latest GE gas turbine products.

Air cooling, which controls metal temperatures and associated thermal strain, also contributes to long nozzle life. A sheet metal core plug distributes impingement cooling on the

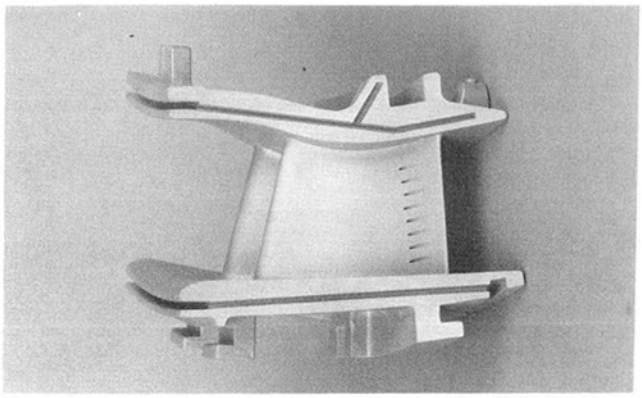

Fig. 9 Two-vane nozzle segment

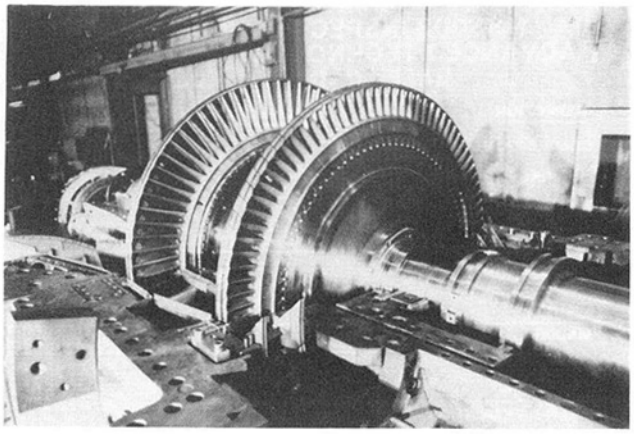

Fig. 11 MS3002 stage 1 and 2 rotors

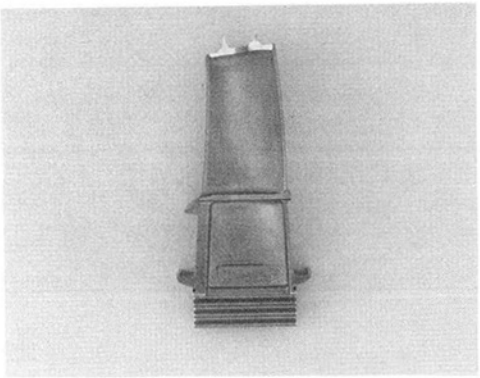

Fig. 10 First-stage bucket

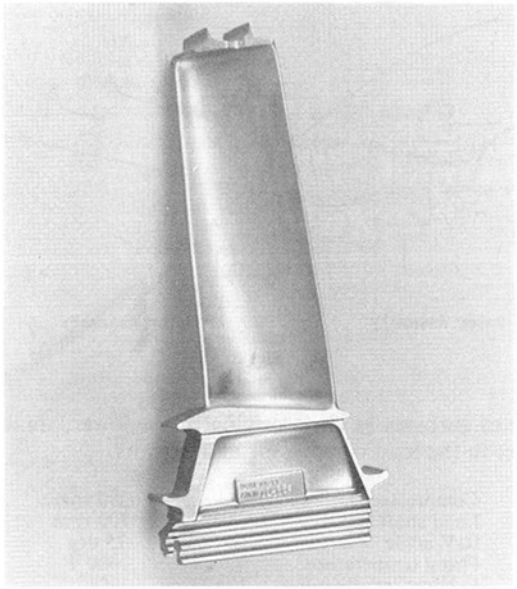

Fig. 12 Second-stage bucket

interior of each vane, and cooling air exits the vane from holes near the trailing edge on the suction side.

Nozzle sidewall contours accommodate a larger gas path diameter, which was required to achieve performance objectives. The nozzle is supported from the turbine frame by a new nozzle support ring, which contains the stator seals and two thermocouple wells for monitoring wheel space temperature.

Rotor Replacement. The MS3002 uprate package calls for replacement of the existing high-pressure (HP) rotor with an M152-alloy first-stage wheel, new buckets, shaft, rotor shim, and bolts. Replacement of the original composite wheels was a specific requirement of Texas Eastern.

Cast of GTD111 alloy, the 92 first-stage buckets are solid to minimize damage by foreign objects, and are designed with an integral shroud to maximize performance (see Fig. 10). A three-tang dovetail wheel attachment is used; axial constraint is achieved with twist locks. The shaft is a one-piece design similar to those found on later model "F" machines.

A modification to #3 bearing seals is required on some models to fit the uprate shaft. Figure 11 shows the uprate HP and low-pressure (LP) rotor assemblies in a unit with upper casings removed.

A new LP rotor design is also required, with an M152-alloy second-stage wheel, new buckets, shaft, and associated hardware. The 80 shrouded second-stage buckets are also cast of GTD111 alloy (Fig. 12) and the same dovetail attachment in stage one is used for the second stage, but is employed 10 deg off axis to accommodate bucket airfoil geometry. Axial constraint is achieved by snap ring similar to other current production turbines.

The shaft fits in the existing #4 and #5 bearing and is equipped with a new overspeed bolt assembly, speed ring and coupling hub. The uprate wheel and shaft geometry requires new wheel space seals and #4 bearing forward side seal. The change in the mass of the rotor as the result of these advanced design and materials modifications is relatively small, resulting in very little change to the rotor dynamics.

Frame Modifications. Uprate modifications to the exhaust frame include a new, extended diffuser to improve efficiency (Fig. 13) and minor changes on both the inner and outer side walls to better match the second stage bucket exit annulus. The forward vertical flange is skim cut to remove any existing distortion and potential leakage when assembled to the new turbine shell. Similar relief is cut on the aft surfaces of the turbine frame that join the turbine shell and nozzle support ring.

Other modifications to the turbine frame provide replacement insulation packs, resizing combustion can mounting bolts, and provisions to accommodate uprate transition pieces. In some models there were changes to sealing air piping for bearings #2 and #3.

Combustion System Upgrade. The gas turbine combustion system is extensively upgraded as illustrated in Fig. 14. Hastelloy X is used for the combustion liners, and other changes for the liners include louvered design and features found on later models, such as the hula seal on the transition piece and splash-plate cooling at crossfire tube locations.

The liner length, extended to the combustion elbow, eliminates a short #2 liner originally used in the turbines. Complete

MS3002 Upgrade Exhaust Diffuser

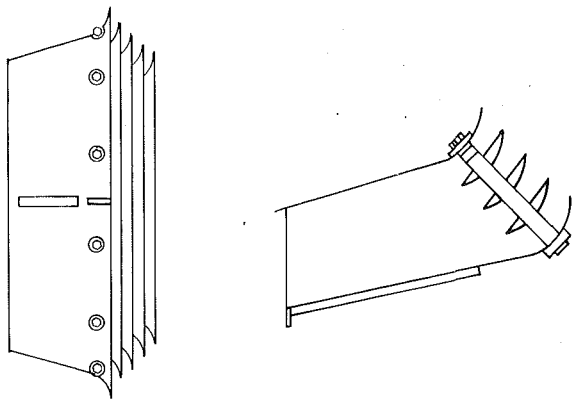

Fig. 13

MS3002 Upgraded Combustion System

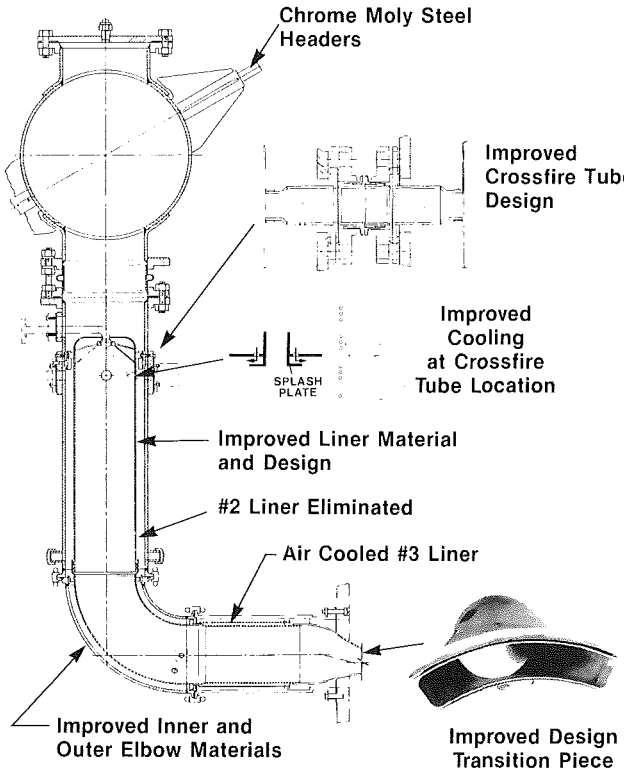

Fig. 14

inner and outer elbow assemblies are supplied, upgraded with Hastelloy-X material for the inner elbow and chrome-molybdenum alloy for the outer elbow in regenerative cycle applications. The #3 liner, extending from the elbow to transition piece, is air cooled.

The uprate transition piece incorporates the latest in duct shape design and is fabricated from heavy-gage Hastelloy-X material. Other transition piece features include new side seals, a floating outer seal, and increased corner radii, to help extend life expectancy. The transition piece exit radii provide an improved gas path flow match with the first-stage nozzle entrance, which remains unchanged from the original design. The improved transition pieces can be used with early MS3002 units even without the other uprate modifications.

Crossfire tube assemblies were replaced with a three-piece design similar to those used on later MS3002 models. Carbon steel headers, approaching the end of their useful lives, were replaced with upgraded headers made from chrome-molybdenum alloy. They were equipped with later model access covers. Fuel nozzle tips were replaced with new gas hole sizing to match uprated fuel flow requirements.

Control system modification on Texas Eastern units provides overtemperature protection using fast-acting extended exhaust thermocouples and the TEMPRO Option I package. Some machines were also equipped with the TEMCON I and II electronic modules, which eliminate pneumatic components from the fuel regulator control system. Other MS3002 uprates have incorporated more sophisticated controls systems, using microprocessor-based GE Mark IV Speedtronic controls.

Uprate Installation

During the upgrades of the Texas Eastern units, the turbines were removed from their bases and sent to a GE service shop for disassembly, inspection, and the installation of the advanced technology components. The turbine frame and exhaust frame flange surfaces were machined to restore flatness of joints. Uprate components, such as the exhaust diffuser and insulation packs, were installed and compressor rotors and stators were rebladed with the latest replacement material.

Optical alignment of bearings and casing was done during unit assembly on a special base. Casings were doweled and clearances checked upon installation of rotors. Figure 15 shows the turbine rotors in the lower half. All casing bolts are replaced with current GE design standard 12-point nuts.

Because of lift limitation at the site, the upgraded turbines were disassembled at the service center for separate shipment of rotors, compressor and turbine subassemblies. An optical alignment of turbine sole plates was made on site before installation of the upgraded turbines. Upgraded combustion headers, elbows, and liners were field assembled to the turbines, and cooling and sealing air piping, hydraulic oil and fuel piping modifications were installed. A field alignment of the turbine load equipment was performed, and control modification installation and checks complete the uprate.

Six of Texas Eastern's earliest MS3002 units were uprated in 1986, two more in 1987, and two in 1988.

Operating Experience

Performance tests conducted on Texas Eastern units have established that the uprates met the guaranteed 32 percent thermal efficiency (regenerative cycle) at 8000 hp and reference conditions. Power was measured by torque meter and fuel flow was measured by turbine flow meter and orifice differential pressure. Relative to the initial estimate, the compressor (HP set) speed was increased approximately 200 rpm to 6280 rpm, while maintaining constant exhaust temperature, to provide rated output. There have also been several minor turbine design changes introduced in the last of Texas Eastern's initial order of 10 uprates to enhance performance.

The first two of Texas Eastern's uprated MS3002's have each accumulated over 22,000 fired hours and all units are operating reliably. A few changes were required, primarily on the first four units, that were attributed to the learning curve of an extensive modernization program conducted without benefit of fired factory tests.

Summary

The MS3002 advanced technology uprate has modernized ten Texas Eastern turbines with major new components, improving performance and extending maintenance levels.

Texas Eastern's management is pleased with the efficiency and reliability obtained through GE's uprate program and has purchased five additional uprate packages that will be in service in 1990.

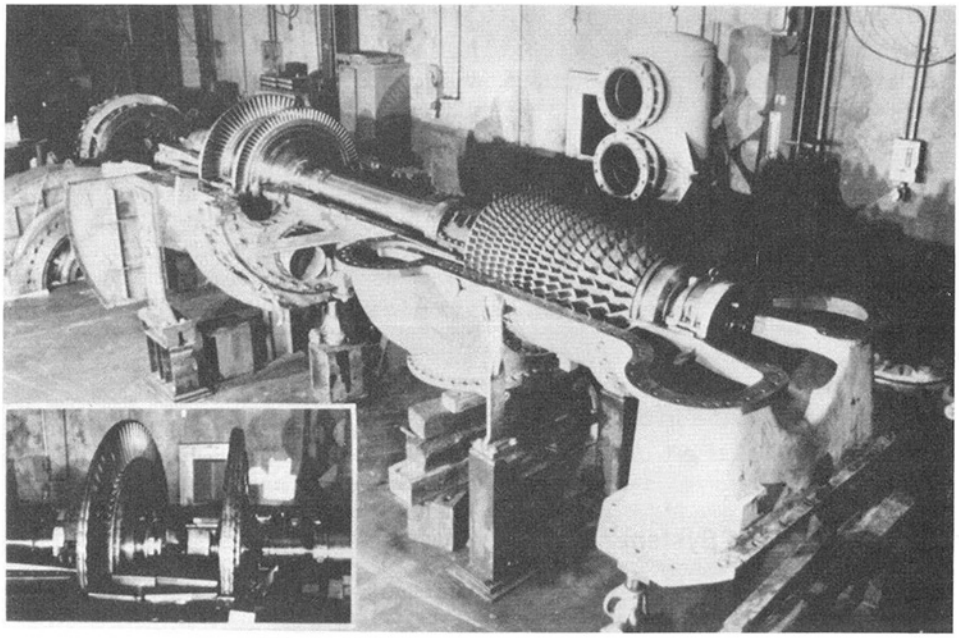

Fig. 15 MS3002 turbine and compressor rotors

References

Freeman, M. A., 1987, "MS3002 Gas Turbine Modernization With Advanced Technology Parts," GER-3527.

Hawthorne, P. R., and Davis, R. A., 1989, "Life Extension and Performance Enhancement of an Industrial Gas Turbine Through Upgrading," ASME Paper No. 89-GT-8.

Johnston, J. R., 1988, "Performance and Reliability Improvements for Heavy-Duty Gas Turbines," GER-3571.

C. Wu
Department of Mechanical Engineering,
U.S. Naval Academy,
Annapolis, MD 21402

R. L. Kiang
David Taylor Research Center,
Annapolis, MD 21402

Power Performance of a Nonisentropic Brayton Cycle

Work and power optimization of a Brayton cycle are analyzed with a finite-time heat transfer analysis. This work extends the recent flurry of publications in heat engine efficiency under the maximum power condition by incorporating nonisentropic compression and expansion. As expected, these nonisentropic processes lower the power output as well as the cycle efficiency when compared with an endoreversible Brayton cycle under the same conditions.

Introduction

In its simplest form, an analysis of a thermodynamic cycle assumes all processes are reversible. In the analysis of the Carnot cycle, for instance, the two isothermal processes are assumed to be reversible. This means the heat transfer between the source and the working medium and that between the working medium and the sink must be carried out at an infinitesimal pace. Likewise, the two adiabatic processes in that cycle are assumed to be reversible. That means no entropy generation is allowed during those two processes. Because of these idealistic assumptions, the high efficiencies of these reversible heat engines are seldom approached by working engines.

In an attempt to obtain a more realistic Carnot efficiency, Curzon and Ahlborn (1975) incorporated finite rates of heat transfer to and from a Carnot engine. After maximizing the power output, they derived a simple expression for the efficiency that was an improvement over the well-known Carnot efficiency. They cited cases for which the efficiencies of existing engines were well described by their results.

Since Curzon and Ahlborn's work, the study of irreversible thermodynamic cycles has been undertaken by many researchers. Rubin (1979a) defined an endoreversible engine. In his model, all the losses are associated with transfer of heat to and from the engine; there are no internal losses within the engine itself. Andresen et al. (1977a, 1977b, 1984) and Salamon et al. (1984) developed thermodynamics in finite time to find the extremes in work and in power for imperfect heat engines. A step Carnot cycle was defined and potentials for finite-time processes were constructed to determine the optimal performance of a real engine. Mozurkewich and Berry (1983) studied optimization of a real heat engine based on a dissipative system. Band et al. (1982) determined the optimal motion of a piston in a cylinder that was coupled to a heat bath from which the rate of heat transfer was finite. Rubin (1978) explored standards of performance for real energy conversion processes and reviewed the argument against the use of standards derived from infinitely slow reversible processes. Rubin and Andresen (1982) also found the optimal configurations for a class of heat engines with finite cycling times and suggested that figures of merit based on these optimal configurations might be more useful than those based on reversible processes. Rubin (1979b) then treated the thermodynamic variables of the working fluid as dynamic variables and used mathematical techniques from optimization theory to analyze the same class of irreversible heat engines examined by Curzon and Ahlborn (1975). Wu (1987) applied the finite-time analysis to an ocean thermal energy conversion (OTEC) system. Wu (1988) also extended the results of Curzon and Ahlborn on the Carnot cycle by incorporating a heat source and heat sink of finite capacities. Using similar techniques, Wu (1989) investigated the power optimization of a Rankine heat engine.

This general theme of renewed analyses of heat engines under maximum power output has been applied to all of the standard thermodynamic cycles; the Brayton cycle has received its fair share of attention. Bejan (1988) considered an ideal Brayton cycle operating between an infinite heat source and an infinite heat sink. He demonstrated that in order to maximize the power output, the temperature extremes that mark the two constant-pressure processes have to bear definite relationships with the heat source and the heat sink temperatures. Leff (1987) has shown that the imposition of maximum work adds further constraints on the Brayton cycle temperatures. More recently, Wu and Kiang (1990) examined the performance of a work and power maximized Brayton cycle using finite-time analysis. The power maximization introduces additional constraints on the cycle temperatures such that the power output is a function of the source and the sink temperatures only. In this paper, we extend that analysis to incorporate nonisentropic compression and expansion to increase the degree of realism further.

Closed-Cycle Gas Turbines

The Brayton cycle to be analyzed is a closed cycle. A corresponding closed-cycle gas turbine engine has both advantages and disadvantages when compared with the more familiar open-cycle gas turbine engines. The advantage of a closed-cycle gas turbine is that it provides a good control of the turbine over a wide range of loads with essentially no loss in overall system thermal efficiency at reduced loads. This is accomplished by varying the pressure in the closed system. The compressor power requirement and the output of the turbine are both

Contributed by the Advanced Energy Systems Division for publication in the JOURNAL OF ENGINEERING FOR GAS TURBINES AND POWER. Manuscript received by the Advanced Energy Systems Division April 3, 1990; revision received October 15, 1990.

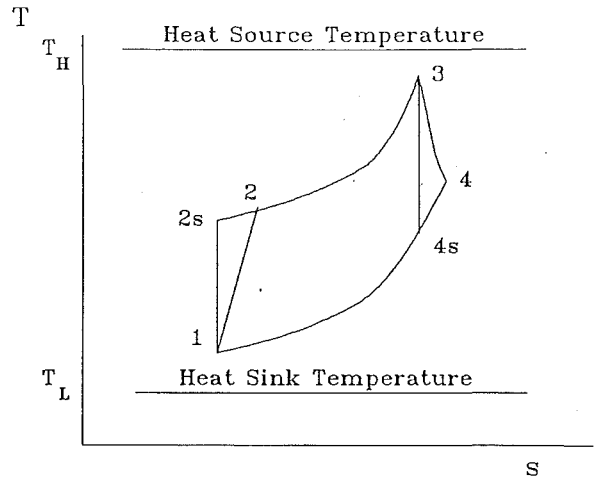

Fig. 1 Closed Brayton cycle with heat source and heat sink

directly proportional to the mass flow of the gas, provided the system's pressure level is varied while the turbine inlet temperature is held constant (Fraas, 1982). A closed-cycle gas turbine can also be operated with dirty fuel or even low-grade coal. Because the hot gas leaving the turbine is at a relatively high pressure of 3 to 30 times atmospheric pressure, it makes the use of a regenerator with a closed cycle more economically attractive than with an open-cycle gas turbine. The principal disadvantage of a closed-cycle gas turbine is the additional heat exchangers needed between the working fluid and a heat source, and between the working fluid and a heat sink.

More than a few closed-cycled gas turbines were or have been in operation around the world (Harmon, 1976). In addition to the heat exchangers linking the engine to the heat source and the heat sink, most of these operational engines incorporate an intercooler and some a precooler, to increase the overall plant efficiency. An analysis of a realistic closed Brayton cycle would have to include the effects of finite heat source and sink, the added processes of intercooling and precooling, and the nonisentropic nature of the compression and the expansion processes. In this paper, the effect of nonisentropic compression and expansion will be quantified.

Optimization of a Nonisentropic Brayton Cycle

A Brayton cycle operating between an infinite heat source and an infinite heat sink is shown in Fig. 1. In this T–s diagram, the process between 1 and 2s is an isentropic compression representing the work done by an ideal compressor. Process 1–2 takes into account the nonisentropic nature of a real compressor. Process 2s–3 is an isobaric expansion; 3–4s is an isentropic expansion representing the process in an ideal turbine; 3–4 represents a nonisentropic expansion of a real turbine; and 4s–1 is an isobaric compression. Let us consider the nonisentropic cycle 1-2-3-4-1. The thermodynamic equations of interest are:

$$Q_{\text{in}} = C_p(T_3 - T_2) \tag{1}$$

$$Q_{\text{out}} = C_p(T_4 - T_1) \tag{2}$$

$$W = C_p[(T_3 - T_2) - (T_4 - T_1)], \tag{3}$$

$$\eta = 1 - \frac{T_4 - T_1}{T_3 - T_2}. \tag{4}$$

The compressor and turbine efficiencies are defined as

$$\eta_c = \frac{T_{2s} - T_1}{T_2 - T_1}, \tag{5}$$

$$\eta_T = \frac{T_3 - T_4}{T_3 - T_{4s}}.$$

In this analysis, we shall consider the compressor and turbine efficiencies given. Thus, T_2 and T_4 can be solved in terms of T_{2s} and T_{4s}:

$$T_2 = T_1 + \frac{T_{2s} - T_1}{\eta_c}, \tag{7}$$

$$T_4 = T_3 - \eta_T(T_3 - T_{4s}) \tag{8}$$

Substituting Eqs. (7) and (8) into Eq. (3), then using the isentropic relations between pressures and temperatures, one obtains an alternate expression for the work:

$$W = C_p\eta_T T_3\left(1 - \frac{1}{r_p^{\frac{k-1}{k}}}\right) - \frac{C_p T_1}{\eta_c}\left(r_p^{\frac{k-1}{k}} - 1\right) \tag{9}$$

where k is the ratio of specific heats and denotes r_p, the pressure ratio of the compressor, p_2/p_1. We assume an ideal gas working fluid so the k is a constant. This expression for W indicates that work output is function of T_1, T_3, and r_p. W can be maximized with respect to the pressure ratio by taking

$$\partial W/\partial r_p = 0 \tag{10}$$

and solving for the optimum r_p. The result is

$$(r_p)_{\text{opt}} = \left(\frac{P_2}{P_1}\right)_{\text{opt}} = \left(\eta_c\eta_T\frac{T_3}{T_i}\right)^{\frac{k}{2(k-1)}} \tag{11}$$

The corresponding maximum work is

$$W_{\max} = C_p\eta_T T_3\left[1 - \left(\eta_c\eta_T\frac{T_3}{T_1}\right)^{-1/2}\right] - \frac{C_p T_1}{\eta_c}\left[\left(\eta_c\eta_T\frac{T_3}{T_1}\right)^{1/2} - 1\right] \tag{12}$$

The six temperatures around a Brayton cycle are not independent of one another. T_2 and T_4 can be expressed in terms of the other four via Eqs. (7) and (8). We now show that T_{2s} and T_{4s} can be expressed in terms of T_1 and T_3 for a work-optimized Brayton cycle.

The fact that 2s-3 and 4s-1 are constant pressure processes puts a constraint on the four temperatures:

$$T_1T_3 = T_{2s}T_{4s}. \tag{13}$$

This equation can readily be obtained by applying the isentropic relations between pressures and temperatures. Equation (11) adds another constraint on the temperatures if one converts the pressure ratio to a temperature ratio by the isentropic relation. Thus, work optimization dictates that

$$T_{2s} = (\eta_c\eta_T T_1T_3)^{1/2}. \tag{14}$$

Substituting Eq. (14) into Eq. (13) leads to

$$T_{4s} = [(T_1T_3)]/(\eta_c\eta_T)]^{1/2}. \tag{15}$$

Nomenclature

A = surface area of heat exchanger
k = ratio of specific heats
LMTD = log mean temperature difference
P = power
Q_{in} = heat input
Q_{out} = heat output
s = entropy
T = temperature
t = time
U = overall heat transfer coefficient
W = work
η = efficiency

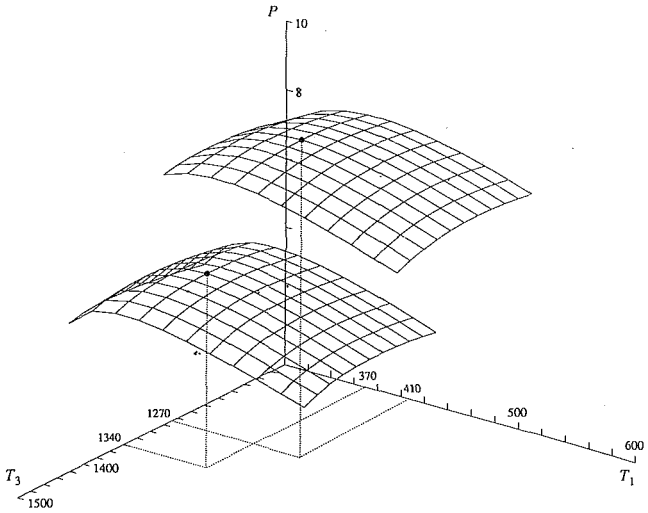

Fig. 2 Power output as functions of T_1 and T_3; upper surface: component efficiency = 1.0; lower surface: component efficiency = 0.9

Finally, substituting Eqs. (14) and (15) into Eqs. (7) and (8), we have T_2 and T_4 expressed in terms of T_1 and T_3:

$$T_2 = \left(1 - \frac{1}{\eta_c}\right) T_1 + \left(T_1 T_3 \frac{\eta_T}{\eta_c}\right)^{1/2}, \tag{16}$$

$$T_4 = (1 - \eta_T) T_3 + \left(T_1 T_3 \frac{\eta_T}{\eta_c}\right)^{1/2}. \tag{17}$$

Let us now turn our attention to power. The power output over one cycle is

$$P = \frac{W}{t} = \frac{C_p[(T_3 - T_2) - (T_4 - T_1)]}{t}, \tag{18}$$

where

$$t = t_{12} + t_{23} + t_{34} + t_{41}. \tag{19}$$

It is generally accepted that the gas transit time through the compressor or the turbine is relatively short, so that the compression and the expansion processes can be considered adiabatic, if not isesntropic. On the other hand, the much slower gas velocity through a heat exchanger coupled with the inherent limitation on the maximum heat flux achievable in a heat exchanger make the gas contact time much larger than the transit time through the compressor or the turbine. In other words, t_{12} and t_{34} can be considered negligible when compared with t_{23} and t_{41}. The total cycle time is then approximated by

$$t \approx t_{23} + t_{41}. \tag{20}$$

t_{23} and t_{41} can be obtained by analyzing the heat transfer between the heat source and the system, and that between the system and the heat sink. Referring to Fig. 1,

$$Q_{\text{in}} = U_H A_H (\text{LMTD}_H) t_{23}, \tag{21}$$

$$Q_{\text{out}} = U_L A_L (\text{LMTD}_L) t_{41}, \tag{22}$$

where U is the overall heat transfer coefficient and A is the surface area of the heat exchanger. The subscripts H and L refer to the heat source and the heat sink, respectively. The log mean temperature differences are defined as

$$\text{LMTD}_H = \frac{(T_H - T_2) - (T_H - T_3)}{\ln [(T_H - T_2)/(T_H - T_3)]}, \tag{23}$$

$$\text{LMTD}_L = \frac{(T_1 - T_L) - (T_4 - T_L)}{\ln [(T_1 - T_L)/T_4 - T_L)]}. \tag{24}$$

We now eliminate Q_{in} between Eqs. (1) and (21), and Q_{out} between Eqs. (2) and (22), and then solve for t_{23} and t_{41}. With

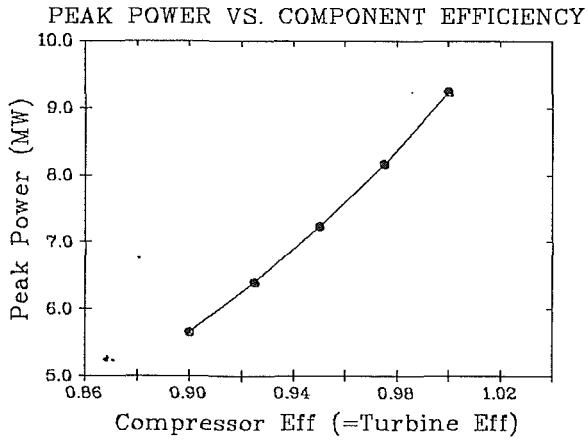

Fig. 3 Peak power versus component efficiency

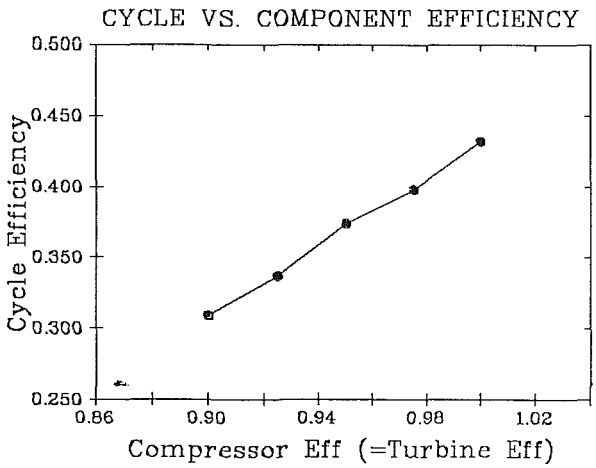

Fig. 4 Cycle efficiency vesus component efficiency

Eq. (20), the expression for power, Eq. (18), can be written as

$$P = \frac{(T_3 - T_2) - (T_4 - T_1)}{\dfrac{T_3 - T_2}{U_H A_H (\text{LMTD}_H)} + \dfrac{T_4 - T_1}{U_L A_L (\text{LMTD}_L)}} \tag{25}$$

Although Eq. (25) contains all four temperatures T_1, T_2, T_3, and T_4, the reader is reminded that T_2 and T_4 can be expressed in terms of T_1 and T_3 because of Eqs. (16) and (17). For given T_H and T_L, P is a function of T_1 and T_3 only. Power from this nonisentropic Brayton cycle can in principle be maximized by requiring

$$\partial P/\partial T_1 = 0 \text{ and } \partial P/\partial T_3 = 0, \tag{26}$$

Since the expression for P is too complex to yield simple analytical solutions for the optimum T_1 and T_3, a numerical example will be given instead in the next section.

Comparison With the Isentropic Cycle

The equations derived in the last section also apply to an isentropic Brayton cycle provided one sets η_c and η_T to unity ($\eta_c = \eta_T = 1$ restores internal reversibilities, thus making such a cycle an endoreversible cycle). Thus, for an endoreversible cycle, the optimum pressure ratio for maximum work is

$$(r_p)_{\text{opt}} = (T_3/T_1)^{\frac{k}{2(k-1)}} \tag{27}$$

and the two temperature constraints lead to

$$T_{2s} = (T_1 T_3)^{1/2}, \tag{28}$$

$$T_{4s} = (T_1 T_3)^{1/2}. \tag{29}$$

The expression for power remains the same as that of Eq. (25). Equations (27)–(29) replicate the results obtained by Wu and Kiang (1990) in which an endoreversible Brayton cycle was examined.

To see the effect of η_c and η_T on the maximum power output, we resort to two numerical examples. We choose the following arbitrary but realistic values:

$$U_H A_H = 0.1 \text{ MW/K} \tag{30}$$

$$U_L A_L = 0.1 \text{ MW/K} \tag{31}$$

$$T_L = 300 \text{ K} \tag{32}$$

$$T_H = 1500 \text{ K} \tag{33}$$

Equation (25), coupled with Eqs. (16) and (17), is then solved numerically for given pairs of T_1 and T_3. The maximum power and the corresponding T_1 and T_3 are then identified. These calculations were done for two cases. Case 1 is the endoreversible case in which the efficiencies of the compressor and the turbine are both 100 percent. In this case, the optimal T_1 and T_3 are found to be 410 K and 1270 K, respectively. The peak power output is 9.240 MW. Case 2 assumes equal compressor and turbine efficiencies and they are equal to 90 percent. In this case, the optimal T_1 and T_3 are 370 K and 1340 K, respectively. The peak power is now only 5.653 MW, down significantly from the isentropic case. The results of these numerical calculations are shown in Fig. 2.

Degradation of Peak Power and Efficiency

To illustrate further the dependence of the peak power on the component efficiencies, the above calculations were repeated for several intermediate compressor and turbine efficiencies. Again, for ease of presenting the results graphically, we assume that the compressor and the turbine efficiencies are equal. Omitting the variances in optimal T_1 and T_3, Fig. 3 shows the degradation in peak power as the component efficiency is reduced. The two end points are the results of Case 1 and Case 2 of the last section. In addition to the peak power, the cycle efficiency can also be calculated by the use of Eq. (4). The results are shown in Fig. 4. The cycle efficiencies in this figure represent the theoretical upper bounds provided the cycle is operated under the conditions given in Eqs. (30)–(33). The points in Figs. 3 and 4 are meant to illustrate the relatively severe degradation of the cycle power and efficiency when the degree of nonisentropicity, as reflected in the component efficiencies, is increased. As is seen, a 10 percent drop in both the compressor and the turbine efficiency reduces the power output by nearly 40 percent, and reduces the cycle efficiency by nearly 30 percent.

Conclusions

Using finite-time analysis, a nonisentropic Brayton cycle operating between an infinite heat source and an infinite heat sink has been studied. The nonisentropic nature of the compression and expansion processes is taken into account by the introduction of the compressor and the turbine efficiencies. It is shown that for a work and power maximized Brayton cycle operating under given source and sink temperatures, the cycle temperatures, T_1–T_4, are completely constrained. The power output and the cycle efficiency are strong functions of the component efficiencies.

References

Andresen, B., Salamon, P., and Berry, R. S., 1977a, "Thermodynamics in Finite Time Extremals for Imperfect Heat Engines," *J. Chem. Phys.*, Vol. 66, pp. 1571–1577.

Andresen, B., Salamon, P., Nitzan, A., and Berry, R. S., 1977b, "Thermodynamics in Finite Time. I. The Step Carnot Cycle," *Phys. Rev.*, Vol. A15, pp. 2086–2093.

Andresen, B., Salamon, P., and Berry, R. S., 1984, "Thermodynamics in Finite Time," *Phys. Today*, Vol. 37(9), pp. 62–70.

Band, Y. B., Kafri, O., and Salamon, P., 1982, "Finite Time Thermodynamics: Optimal Expansion of a Heated Working Fluid," *J. Appl. Phys.*, Vol. 53(1), pp. 8–28.

Bejan, A., 1988, *Advanced Engineering Thermodynamics*, Wiley, New York, pp. 411–414.

Curzon, F. L., and Ahlborn, B., 1975, "Efficiency of a Carnot Engine at Maximum Power Output," *Am. J. Phys.*, Vol. 43, pp. 22–24.

Fraas, A. R., 1982, *Engineering Evaluation of Energy Systems*, McGraw-Hill, New York.

Harmon, R. A., 1976, "Operational Status and Current Trends in Gas Turbines for Utility Applications in Europe," Fossil Energy Organization of U.S. Energy Research and Development Administration, Report No. TIC-FE/WAPO-0016-1, Aug. 16, pp. 53–80.

Leff, H. S., 1987, "Thermal Efficiency at Maximum Work Output: New Results for Old Heat Engines," *Am. J. Phys.*, Vol. 55(7), pp. 602–610.

Mozurkewich, M., and Berry, R. S., 1983, "Optimization of a Heat Engine Based on a Dissipative System," *J. Appl. Phys.*, Vol. 54(7), pp. 3651–3661.

Rubin, M. H., 1978, "Figures of Merit for Energy Conversion Processes," *Am. J. Phys.*, Vol. 46, pp. 637–639.

Rubin, M. H., 1979a, "Optimal Configuration of a Class of Irreversible Heat Engines. I," *Phys. Rev.*, Vol. A19, pp. 1272–1276.

Rubin, M. H., 1979b, "Optimal Configuration of a Class of Irreversible Engines. II," *Phys. Rev.*, Vol. A19, pp. 1277–1289.

Rubin, M. H., and Andresen, B., 1982, "Optimal Staging of Endoreversible Heat Engines," *J. Appl. Phys.*, Vol. 53(1), pp. 1–7.

Salamon, P., Andresen, B., Salamon, P., and Berry, R. S., 1984, "Thermodynamics in Finite Time," *Phys. Today*, Vol. 37(9), pp. 62–70.

Wu, C., 1987, "Performance Bound for Real OTEC Heat Engines," *J. Ocean Engrg.*, Vol. 14(4), pp. 349–354.

Wu, C., 1988, "Power Optimization of a Finite-Time Carnot Heat Engine," *J. Energy*, Vol. 13(9), pp. 681–687.

Wu, C., 1989, "Power Optimization of a Finite-Time Rankine Heat Engine," *Int. J. Heat Fluid Flow*, Vol. 10(2), pp. 134–138.

Wu, C., and Kiang, R. L., 1990, "Work and Power Optimization of a Finite-Time Brayton Cycle," *Int. J. Ambient Energy*, Vol. 11, No. 3, pp. 129–136.

Thermodynamic Optimization of Irreversible Power Cycles With Constant External Reservoir Temperatures

L. W. Swanson
Assistant Professor,
Department of Engineering,
University of Denver,
Denver, CO 80208
Assoc. Mem. ASME

An extended version of the Bejan model of irreversible power plants is proposed using a log-mean temperature difference (LMTD) representation for both the high and low-temperature heat exchangers. The analysis focuses on minimizing the irreversibilities associated with the hot and cold heat exchangers. The results indicate that the maximum power output, external conductance allocation ratio, and second law efficiency are functions of the number total heat exchanger transfer units (N), and are asymptotic to Bejan's original results as $N \to O$. This asymptote represents a global power output maximum and occurs for either extremely high cycle flow rates or cycle phase change processes in both heat exchangers. The LMTD representation also shows that under optimal conditions, more conductance should be allocated to the low-temperature heat exchanger as N increases.

Introduction

Understanding the role that specific irreversibilities play in the global performance of thermodynamic power cycles is important in defining ways to reduce cycle energy use, increase overall efficiency, and reduce capital and operating costs. Traditionally, the second-law efficiency has been a measure of how close the power cycle operates to the maximum first-law efficiency, namely the ideal Carnot efficiency. It is well known that the ideal Carnot efficiency is based on the assumption that the process is reversible and therefore requires that the heat exchange processes between the cycle and both the hot and the cold temperature reservoirs are in thermal equilibrium. This assumption is unrealistic for practical power cycles because it demands either an infinite amount of contact time or an infinite amount of heat exchange area between the cycle and its thermal reservoirs. The Carnot efficiency does, however, reflect a global characteristic of the ideal system (maximum efficiency), which is easily determined and is therefore useful for design purposes.

The notion that more realistic global cycle characteristics can be defined has compelled thermodynamicists to develop theoretical models that treat power cycles as finite time processes. The finite time models account for isolated well-defined irreversibilities, such as heat exchange processes, which occur in all power cycles. All other irreversibilities associated with the power cycle, such as friction, heat losses through piping, etc., are generally not considered.

Curzon and Ahlborn (1975) took this approach by developing a theoretical model of a Carnot engine, which accounted for irreversibilities in the heat exchange processes between the power cycle and its thermal reservoirs. Newton's law of cooling was used as the heat exchange mechanism for both heat exchangers. The power was maximized with respect to the temperature differences in both the hot exchanger and the cold exchanger. The thermal efficiency was found to be

$$\eta_{I,C-A} = 1 - \left(\frac{T_L}{T_H}\right)^{1/2},$$

which compares favorably with thermal efficiencies for practical power cycles. The analysis also showed that the working fluid temperatures for the isothermal branches of the Carnot cycle were simple functions of the hot and cold conductances and the reservoir temperatures. These results clearly indicate that finite time models for thermodynamic power cycles produce more realistic thermal efficiencies and can be used to define useful global cycle characteristics.

The analysis of Curzon and Ahlborn was generalized to some extent by De Vos (1985) who used heat exchange mechanisms of the form

$$q_{HC} = C_H(T_H^n - T_{HC}^n),$$

and

$$q_{LC} = C_L(T_L^m - T_{LC}^m),$$

where C_H and C_L are the appropriate thermal conductances. This generalized heat exchange mechanism can be applied to local conductive heat exchange ($n, m = 1$), convective heat exchange ($n, m = 1$), or grey body radiative heat exchange ($n, m = 4$). De Vos produced results for several types of hot reservoir driving forces ($n, m = -1, 1, 2, 4$) assuming the cold reservoir was in thermal equilibrium ($T_L = T_{LC}$), and

Contributed by the Advanced Energy Systems Division for publication in the JOURNAL OF ENGINEERING FOR GAS TURBINES AND POWER. Manuscript received by the Advanced Energy Systems Division May 2, 1990; revision received October 23, 1990.

for comparative purposes plotted the corresponding thermal efficiencies as functions of the cold reservoir temperature to hot reservoir temperature ratio. The results showed that as n was increased the thermal efficiency approached the Carnot efficiency. Although De Vos mentioned that the thermal efficiency derived for the radiative driving force has potential application to solar energy conversion, no comparison was made with solar power plant data.

More rigorous theoretical studies of finite time power cycles have been conducted by Salamon and his colleagues (Salamon et al., 1980, 1982; Salamon and Nitzan, 1981; Hoffmann and Salamon, 1987), and Andresen et al. (1984). In general, these studies involved modeling the heat exchange processes using Newton's law of cooling and applying the calculus of variations to minimize an objective function subject to certain constraints. In most of these studies, an entropy generation function was chosen as the objective function. Salamon and Nitzan (1981) have shown that the optimal cycle operation takes place when the working fluid remains at a constant temperature during the heat exchange processes. From a practical point of view, this suggests that the heat exchange mechanisms for the working fluid should involve phase change or extremely large mass flow rates. The large mass flow rates produce small changes in temperature due to the short heat exchange contact time. Imposing a short contact time is somewhat counterintuitive because the absolute maximum efficiency (ideal Carnot efficiency) requires an infinite heat exchange contact time. A second result of this analysis has shown that optimal conditions occur when the adiabatic branches of the cycle take place instantaneously. This result also suggests the need for very large mass flow rates through the turbines and pumps. In general, the conclusions drawn from these analyses can serve as a basis for overall power plant design philosophy; however, imposing these requirements on practical power plants may be difficult.

More recently, Wu (1988, 1989) conducted theoretical studies of finite-time Carnot and Rankine power cycles. Both cycles were modeled using a log-mean temperature difference driving force, an irreversibility factor, and a time factor to simulate the heat exchange processes between the heat engine and surroundings. Power output surfaces were obtained that provided a far more realistic prediction of heat engine efficiency than the standard Carnot cycle efficiency.

Finally, Bejan (1988) devised a model that applied Newton's law of cooling to the heat exchangers of an irreversible power plant composed of a hot-temperature heat exchanger, a cold-temperature heat exchanger, an ideal Carnot cycle, and a heat exchange process characterizing internal cycle irreversibilities. Bejan found that the maximum work can be expressed as a function of the reservoir temperature ratio (T_H/T_L), the total external conductance (C_e), and the cold reservoir temperature (T_L). An external conductance allocation ratio (x) was also defined that specified the relative sizes of the hot and cold heat exchangers. The analysis showed that for maximum work $x = 0.5$, requiring that the total external conductance be equally distributed between the cold and hot heat exchangers. The optimal hot and cold Carnot cycle temperatures (T_{HC}, T_{LC}) were found to be simple functions of the reservoir temperatures. The second law efficiency was expressed in terms of the reservoir temperature ratio, the total external conductance, and the ratio of the internal cycle conductance to the total external conductance (C_i/C_e). C_i accounted for the heat exchange process due to the internal irreversibilities commonly neglected by other studies. Through the use of experimental data for a variety of industrial power plants, the average value of C_i/C_e was found to be equal to 0.04. It is apparent that this approach offers a fresh and profound new way of analyzing irreversible power plants, producing simple global characteristics that can significantly influence design philosophy.

The study in this paper extends the Bejan model of irreversible power plants by applying a log-mean temperature difference (LMTD) driving force to both the hot and the cold-temperature heat exchangers. The LMTD driving force is a practical representation for most heat exchangers (e.g., see Incropera and DeWitt, 1990) and aside from Wu's work (1988, 1989), has not been applied to finite time power cycles. The insights gained by this work will contribute to the current pool of knowledge regarding the effect of specific irreversibilities on the global performance of thermodynamic power cycles.

Analysis

The finite time thermodynamic model developed herein extends the work of Bejan (1988) to a heat transfer mechanism described by a log-mean temperature difference. The log-mean temperature difference evolves naturally in the derivation of thermal energy exchange between two fluid steams with either counterflow or parallel flow heat exchanger configurations. This driving force has also been adapted to a crossflow heat

Nomenclature

C_i = conductance for internal cycle irreversibilities, W/K
C_e = total external conductance, W/K
C_H = hot heat exchanger external conductance, W/K
C_L = cold heat exchanger external conductance, W/K
C_p = specific heat at constant pressure, W s/kg K
$\dot{m}$ = mass flow rate, kg/s
N = total number of transfer units = $N_H + N_L$
N_H = number of hot exchanger transfer units = $C_H/\dot{m}C_p$
N_L = number of cold exchanger transfer units = $C_L/\dot{m}C_p$
q_i = heat transfer rate due to internal cycle irreversibilities, W
q_H = hot-end total heat transfer rate, W
q_L = cold-end total heat transfer rate, W
q_{HC} = hot exchanger heat transfer rate, W
q_{LC} = cold exchanger heat transfer rate, W
T_H = hot reservoir temperature, K
T_L = cold reservoir temperature K
T_{HC} = hot Carnot cycle temperature, K
T_{LC} = cold Carnot cycle temperature, K
$\dot{W}$ = Carnot cycle power output, W
x = external conductance allocation ratio = C_H/C_e
η_I = first-law efficiency = $\dot{W}/q_H$
η_{II} = second-law efficiency = η_I/η_c
η_c = ideal Carnot efficiency = $1 - T_L/T_H$
$\eta_{I,C-A}$ = Curzon-Ahlborn efficiency = $1 - (T_L/T_H)^{1/2}$
τ = reservoir temperature ratio = T_H/T_C
τ_c = Carnot cycle temperature ratio = T_{HC}/T_{LC}

Subscripts

H = hot reservoir
HC = hot end of the Carnot cycle
L = cold reservoir
LC = cold end of the Carnot cycle
max = maximum
opt = optimum
1 = first maximization
2 = second maximization

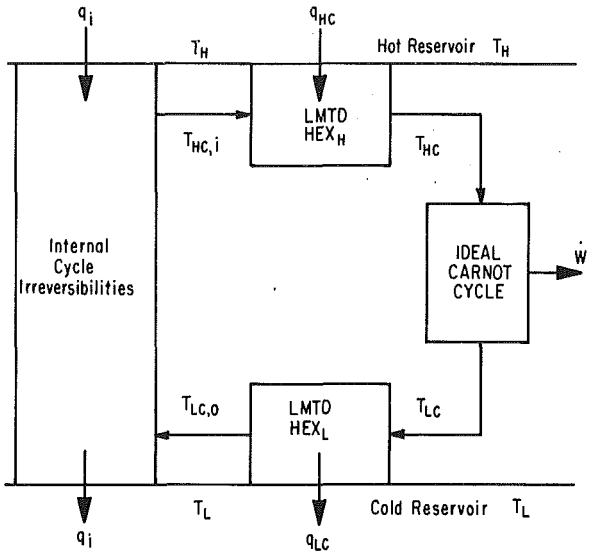

Fig. 1 Schematic of the modified Bejan model of irreversible power cycles

exchanger configuration by use of correction factor to a standard counterflow configuration (e.g., see Incropera and DeWitt, 1990).

Figure 1 shows a schematic of the cycle, which consists of a hot-temperature heat exchanger (HEX_H), a cold-temperature heat exchanger (HEX_L), an ideal Carnot cycle, and a heat exchange process that accounts for internal cycle irreversibilities. The hot exchanger transfers heat into the cycle (q_{HC}), the cold exchanger transfers heat out of the cycle (q_{LC}), and q_i represents the heat transfer due to internal cycle irreversibilities, i.e., friction losses, heat losses through the piping, etc. The reservoir temperatures (T_H, T_L) and the heat capacity flow rate ($\dot{m}C_p$) are assumed to be constant. The working fluid temperature varies as the fluid passes through both the hot and the cold heat exchangers. The working fluid outlet temperature at the hot exchanger, T_{HC}, corresponds to the hot reservoir temperature in the ideal Carnot cycle; the working fluid inlet temperature at the cold exchanger, T_{LC}, corresponds to the cold reservoir temperature in the ideal Carnot cycle. The heat flow path describing the cycle irreversibilities also accounts for the difference in temperature of the internal working fluid at the locations where the fluid temperature is $T_{HC,i}$ and $T_{LC,o}$. Under these assumptions, the transfer of heat in the hot exchanger can be described by

$$q_{HC}=C_H\left[\frac{(T_H-T_{HC,i})-(T_H-T_{HC})}{\ln\dfrac{T_H-T_{HC,i}}{T_H-T_{HC}}}\right], \tag{1}$$

and

$$q_{HC}=\dot{m}C_p(T_{HC}-T_{HC,i}). \tag{2}$$

It is interesting to note that for either an infinite mass flow rate or phase change (infinite specific heat), $\dot{m}C_p \to \infty$ and $T_{HC,i} \to T_{HC}$, forcing Eq. (1) to become indeterminate. Applying l'Hôpital's rule reduces Eq. (1) to Newton's law of cooling,

$$\lim_{\dot{m}Cp\to\infty} q_{HC}=\lim_{T_{HC,i}\to T_{HC}} q_{HC}=C_H(T_H-T_{HC}). \tag{3}$$

Therefore the relationships derived in this work should be asymptotic to Bejan's results as $\dot{m}C_p \to \infty$. The inlet temperature can be eliminated using Eqs. (1) and (2), giving

$$q_{HC}=\frac{C_H}{N_H}(e^{N_H}-1)(T_H-T_{HC}), \tag{4}$$

where

$$N_H=\frac{C_H}{\dot{m}C_p}. \tag{5}$$

N_H is a dimensionless quantity known as the number of hot exchanger transfer units. A similar derivation for the cold exchanger results in

$$q_{LC}=\frac{C_L}{N_L}(1-e^{-N_L})(T_{LC}-T_L), \tag{6}$$

where

$$N_L=\frac{C_L}{\dot{m}C_p}. \tag{7}$$

N_L is the number of cold exchanger transfer units. It should be noted that in terms of the number of transfer units, Eqs. (4) and (6) asymptote to Newton's law of cooling as $N_H \to 0$ and $N_L \to 0$, respectively. The total external conductance C_e is defined as

$$C_e=C_H+C_L, \tag{8}$$

$$C_H=xC_e, \tag{9}$$

$$C_L=(1-x)C_e, \tag{10}$$

where x is the external conductance allocation ratio, which accounts for the distribution of conductance between the hot exchanger and the cold exchanger. Dividing the above three expressions by the heat capacity flow rate produces similar expressions in terms of the number of transfer units,

$$N=N_H+N_L, \tag{11}$$

$$N_H=xN, \tag{12}$$

$$N_L=(1-x)N, \tag{13}$$

where N represents the total number of external transfer units. The first and second laws of thermodynamics for the ideal Carnot cycle are

$$\dot{W}=q_{HC}-q_{LC} \tag{14}$$

and

$$q_{HC}=\frac{T_{HC}}{T_{LC}}q_{LC}. \tag{15}$$

Combining these two expressions produces

$$\dot{W}=q_{LC}\left(\frac{T_{HC}}{T_{LC}}-1\right). \tag{16}$$

Maximum Power Output. This section focuses on maximizing the power output with respect to the Carnot cycle temperature ratio (T_{HC}/T_{LC}) and the external conductance allocation ratio (x). Substituting Eqs. (6), (10), and (13) into Eq. (16) yields a power output function of

$$\dot{W}=\dot{m}C_pT_L(1-e^{-(1-x)N})\left(\frac{T_{LC}}{T_L}-1\right)\left(\frac{T_{HC}}{T_{LC}}-1\right). \tag{17}$$

Substituting Eqs. (4), (6), (12), and (13) into Eq. (15) and rearranging gives

$$\frac{T_{LC}}{T_L}-1=\frac{F(x)\left(\dfrac{\tau}{\tau_c}-1\right)}{1+F(x)}, \tag{18}$$

where

$$F(x)=\frac{e^{xN}-1}{1-e^{-(1-x)N}}, \tag{19}$$

$$\tau=\frac{T_H}{T_L}, \tag{20}$$

$$\tau_c = \frac{T_{HC}}{T_{LC}}. \tag{21}$$

τ is the ratio of reservoir temperatures and τ_c is the ratio of Carnot cycle temperatures. Equation (18) can then be substituted into Eq. (17) producing an expression for the cycle power of

$$\dot{W} = \frac{C_e}{N} T_L(1 - e^{-(1-x)N}) \left(\frac{F(x)}{1+F(x)}\right)\left(\frac{\tau}{\tau_c} - 1\right)(\tau_c - 1). \tag{22}$$

This expression shows that cycle power is dependent on the number of total transfer units, the total external conductance, the external conductance allocation ratio, the reservoir temperature ratio, and the Carnot cycle temperature ratio. The power is now maximized with respect to both the Carnot cycle temperature ratio and the external conductance allocation ratio. Maximizing with respect to the Carnot cycle temperature ratio specifies the optimal Carnot cycle temperature ratio, which can be used to determine the optimal working fluid hot-exchanger outlet temperature and cold-exchanger inlet temperature. Maximizing the power with respect to the external conductance allocation ratio determines the optimal distribution of total external conductance between the hot heat exchanger and the cold heat exchanger. The reservoir temperatures and therefore the reservoir temperature ratio are assumed to be known. The number of total transfer units and total external conductance are parameters that can be determined once the plant power is specified. Maximizing the power with respect to the Carnot temperature ratio produces the same result found by Bejan (1988), $\tau_{c,\text{opt}} = \tau^{1/2}$. Under these conditions the power function becomes

$$\dot{W}_{\max,1} = \frac{C_e}{N} T_L(1 - e^{-(1-x)N}) \left(\frac{F(x)}{1+F(x)}\right)(\tau^{1/2} - 1)^2. \tag{23}$$

Performing a second maximization with respect to the external conductance allocation ratio (x) results in

$$x_{\text{opt}} = \frac{1}{N} \ln\left(\frac{2}{1+e^{-N}}\right). \tag{24}$$

This expression for the optimal external conductance allocation ratio has some interesting asymptotic characteristics; namely,

$$\lim_{N\to 0} x = 0.5, \tag{25}$$

and

$$\lim_{N\to\infty} x = 0. \tag{26}$$

As suggested earlier, x is asymptotic to Bejan's value of 0.5 as the total number of transfer units approaches zero. Recall that this condition requires that the working fluid undergo a phase change process in both heat exchangers or that the working fluid mass flow rate approach infinity. These asymptotes constrain the conductance allocation ratio to $0 < x \leq 0.5$. Thus for a finite number of total exchanger transfer units, more external conductance or transfer units should be allocated to the cold exchanger. Figure 2 shows that the optimal external conductance allocation ratio decreases monotonically as the total number of transfer units increases. Substituting Eq. (24) into Eq. (23) results in a maximum power of

$$\dot{W}_{\max,2} = \frac{1 - e^{-N}}{N} \frac{C_e}{4} T_L(\tau^{1/2} - 1)^2, \tag{27a}$$

or

$$\dot{W}_{\max,2} = \dot{m} C_p \frac{T_L}{4}(1 - e^{-N})(\tau^{1/2} - 1)^2. \tag{27b}$$

Equations (27a) and (27b) provide two different ways of looking at the functional dependence of the maximum power. Assuming the external conductance is constant, Eq. (27a) shows that increasing N is equivalent to decreasing the heat capacity flow rate. This change is definitely undesirable because it not only decreases the maximum power as shown by Fig. 3, but it also requires shifting external conductance from the hot exchanger to the cold exchanger as dictated by Eq. (24). Shifting the conductance may be a difficult and expensive task for operational power plants. If the heat capacity flow rate is assumed to be constant, Eq. (27b) shows that increasing N, which is equivalent to increasing the external conductance, increases the maximum power output. The increase in external conductance under these circumstances should also be distributed according to Eq. (24); however, in this case, conductance is simply added to each exchanger in different amounts. The asymptotes for the maximum power output are:

$$\lim_{N\to 0} \dot{W}_{\max,2} = \frac{C_e}{4} T_L(\tau^{1/2} - 1)^2, \tag{28}$$

and

$$\lim_{N\to\infty} \dot{W}_{\max,2} = \frac{\dot{m} C_p}{4} T_L(\tau^{1/2} - 1)^2. \tag{29}$$

The asymptote given by Eq. (28), which is equal to that derived by Bejan, is independent of the heat capacity flow rate and represents a global power output maximum. Under this condition ($N \approx 0$), the maximum power increases linearly as the total external conductance increases. At the other extreme (N

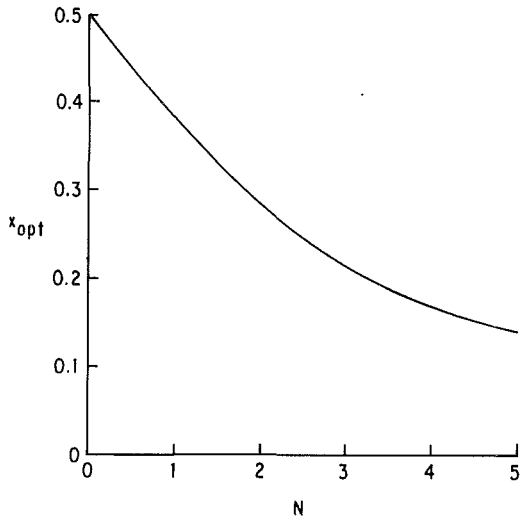

Fig. 2 Optimal external conductance allocation ratio as a function of the total number of transfer units

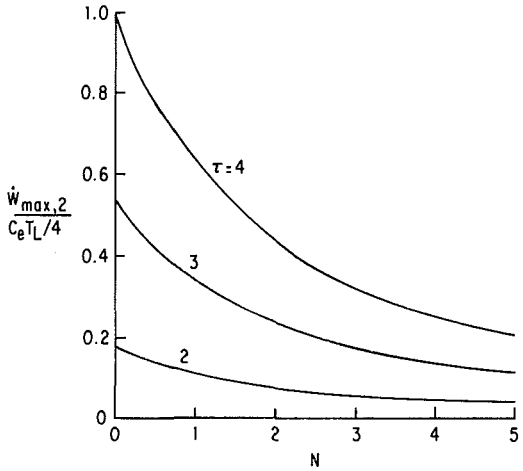

Fig. 3 Dimensionless maximum power as a function of the total number of transfer units

> 5), Eq. (29) shows that the power becomes independent of the total external conductance and increases linearly as the heat capacity flow rate increases.

Optimal Carnot Cycle Temperatures. The optimal Carnot cycle temperatures can readily be determined by applying the first and second laws of thermodynamics given earlier. Substituting Eqs. (4), (6), and (27*a*) into the first law given by Eq. (14) yields

$$\frac{T_H - T_{HC}}{T_H} = \frac{1}{4}\frac{1-e^{-N}}{e^{x_{\text{opt}}N}-1}(1-\tau^{-1/2})^2 + \frac{1-e^{-(1-x_{\text{opt}})N}}{e^{x_{\text{opt}}N}-1}\left(\frac{T_{LC}-T_L}{T_H}\right), \quad (30)$$

Substituting Eqs. (4) and (6) into the second law given by Eq. (15) and noting that $\tau_{c,\text{opt}} = \tau^{1/2}$ gives

$$\frac{T_{LC}-T_L}{T_L} = \tau^{-1/2}\frac{e^{x_{\text{opt}}N}-1}{1-e^{-(1-x_{\text{opt}})N}}\frac{T_H - T_{HC}}{T_H}. \quad (31)$$

Combining Eqs. (30), (31), and (24) produces an optimal hot-end Carnot cycle temperature of

$$T_{HC,\text{opt}} = T_H\left[1-\frac{1}{4}(1+e^{-N})(1-\tau^{-1/2})\right]. \quad (32)$$

Following the same procedure, a similar expression can be derived for the optimal cold-end Carnot cycle temperature,

$$T_{LC,\text{opt}} = T_L\left[1+\frac{1}{4}(1+e^{-N})(\tau^{1/2}-1)\right]. \quad (33)$$

Note that both Eqs. (32) and (33) are asymptotic to Bejan's results as $N \to 0$. Equation (32), plotted in Fig. 4, shows that as the total number of transfer units is increased (increase in external conductance), the hot-end Carnot cycle output temperature increases. This decrease in driving force occurs because conductance is being added to the hot exchanger, regardless of the fact that the distribution of conductance shifts toward the cold heat exchanger. Equation (33), also given in Fig. 4, shows that as the total number of transfer units is increased, the cold-end Carnot cycle temperature decreases. This decrease in driving force is also due to the increase in total external conductance and is larger in magnitude than that for the hot exchanger because of the required relative increase in external conductance allocated to the cold end as dictated by Eq. (24). In general, for a finite number of transfer units, maximizing the power production by increasing the total external conductance requires shifting more external conductance to the cold end while decreasing the driving forces in both the hot and the cold heat exchangers.

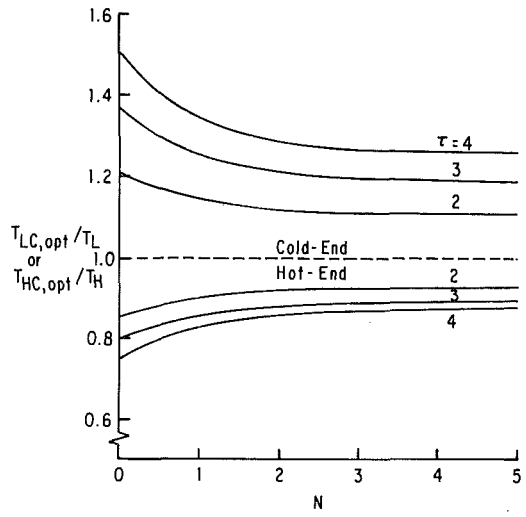

Fig. 4 Optimal Carnot cycle temperature ratios for the hot and cold heat exchangers

Efficiencies. The optimal first-law efficiency is equal to the optimal work, given by Eq. (27*a*), divided by the total heat input; namely,

$$\eta_I = \frac{W_{\max,2}}{q_H}. \quad (34)$$

The total heat input under optimal conditions is given by

$$q_H = q_i + q_{hC} = C_i(T_H - T_C) + \frac{C_e}{N}(e^{x_{\text{opt}}N}-1)(T_H - T_{HC}), \quad (35)$$

where q_i is the heat transfer due to internal cycle irreversibilities (see Fig. 1) and is represented by the simplest heat transfer mechanism, Newton's law of cooling. Using Eq. (27) and the above expression for the total heat transferred into the cycle, the first law efficiency becomes

$$\eta_I = \frac{\frac{1-e^{-N}}{N}(\tau^{1/2}-1)^2}{4\frac{C_i}{C_e}(\tau-1)+\frac{4}{N}(e^{x_{\text{opt}}N}-1)\left(\tau-\frac{T_{HC}}{T_L}\right)}. \quad (36)$$

Substituting Eqs. (24) and (32) into Eq. (36) gives

$$\eta_I = \frac{\frac{1-e^{-N}}{N}(1-\tau^{-1/2})}{4\frac{C_i}{C_e}(1+\tau^{-1/2})+\frac{1-e^{-N}}{N}}. \quad (37)$$

Values for the first-law efficiency are given in Table 1 as a function of the total number of transfer units and the reservoir temperature ratio. The ratio C_i/C_e has been assumed constant and equal to Bejan's value of 0.04, which corresponds to $N = 0$. This value should be a maximum even if C_i is a function of the total number of transfer units, because the internal irreversibilities increase as the heat capacity flow rate increases; therefore, as $N \to 0$, C_i approaches its maximum value. Table 1 shows that the first-law efficiency decreases as the number of transfer units increases. As expected, for a fixed number of transfer units, the efficiency increases as the reservoir temperature ratio increases. The Curzon–Ahlborn efficiency is also given in Table 1 for comparative purposes. If the cycle is

Table 1 First-law efficiency as a function of the total number of transfer units ($\eta_{I,C-A}$ = Curzon–Ahlborn efficiency, η_C = ideal Carnot cycle efficiency)

τ	N	η_I	$\eta_{I,C-A}$	η_C
2	0	0.280	0.293	0.500
	1	0.273		
	2	0.264		
	3	0.255		
	4	0.246		
	5	0.237		
3	0	0.396	0.423	0.667
	1	0.382		
	2	0.365		
	3	0.348		
	4	0.331		
	5	0.315		
4	0	0.463	0.500	0.750
	1	0.444		
	2	0.422		
	3	0.399		
	4	0.377		
	5	0.356		

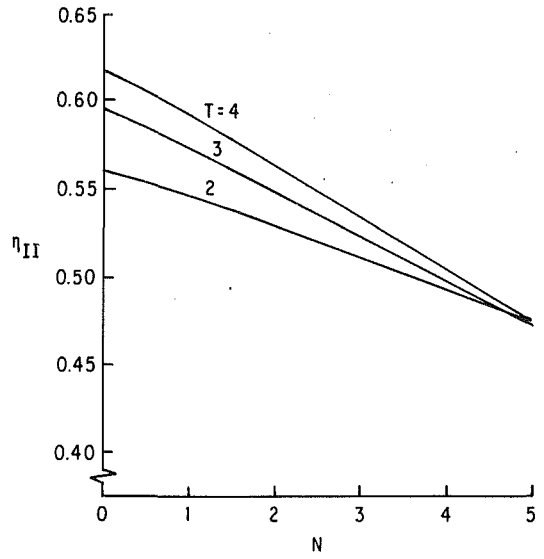

Fig. 5 Optimal second-law efficiency as a function of the total number of transfer units

assumed to be endoreversible (no internal irreversibilities or $C_i/C_e = 0$), Eq. (37) reduces to the Curzon–Ahlborn efficiency. It is important to note that although Eq. (37) is based on an LMTD driving force, the endoreversible efficiency is independent of the total number of transfer units. This result emphasizes the significance and universality of the Curzon–Ahlborn expression. Secondly, incorporating the internal irreversibilities into the efficiency, as proposed by Bejan, produces values less than those given by the Curzon–Ahlborn efficiency (see Table 1), which is in general agreement with experimental data.

The second-law efficiency is defined as the ratio of the first-law efficiency, given by Eq. (37), and the Carnot efficiency, given as

$$\eta_c = 1 - \tau^{-1}. \tag{38}$$

Therefore, the second-law efficiency becomes

$$\eta_{II} = \frac{\dfrac{1-e^{-N}}{N}}{4\dfrac{C_i}{C_e}(1+\tau^{-1/2})^2 + \dfrac{1-e^{-N}}{N}(1+\tau^{-1/2})}. \tag{39}$$

The second-law efficiency is plotted in Fig. 5 and shows trends similar to those for the first-law efficiency: The second-law efficiency decreases as the total number of transfer units increases and increases as the reservoir temperature ratio increases. These trends are not surprising since the Carnot cycle efficiency is constant for any given reservoir temperature ratio.

Conclusions

The study in this paper extends the Bejan model of irreversible power plants by imposing a log-mean temperature difference (LMTD) heat transfer mechanism in the hot and cold temperature heat exchangers. The LMTD representation is commonly used to describe most commercial heat exchangers. The results show that the maximum power output, external conductance allocation ratio, and second-law efficiency are functions of the total number of transfer units, and are asymptotic to Bejan's global power output maximum as $N \to 0$. This asymptote occurs for either extremely high mass flow rates or phase change processes in both heat exchangers. Under optimal conditions, more external conductance should be allocated to the cold-end exchanger as the total number of transfer units increases. The temperature driving forces in both exchangers were found to decrease as the total number of transfer units was increased. This was due to the increase in external conductance under the assumption that the heat capacity flow rate was constant. Both first and second-law efficiencies also decreased as the total number of transfer units was increased, with the first-law efficiency becoming independent of the total number of transfer units and asymptotic to the Curzon–Ahlborn efficiency under endoreversibility conditions.

The results of this analysis provide information that can be used to design or upgrade certain types of power plants. It is obvious that the results given in this paper as well as others sited earlier require further experimental verification under controlled conditions. Most of the data acquired for comparative purposes in previous studies were obtained from operational power plants and lacked the details (i.e., heat capacity flow rates, conductances, etc.) necessary to confirm the trends given in this paper. Secondly, the assumption that the heat capacity flow rate is constant, made in this work as well as in some others, severely limits the generality of these results. This is obvious when considering the boiler heat exchange process (hot-end exchanger) in a Rankine cycle, which uses water as the working fluid. For this cycle, sensible heat is added to the incoming liquid water until the boiling temperature is reached, then a vapor–liquid phase change process occurs, followed by sensible heating of the water vapor until a desired degree of superheat is achieved. During this process the value of the heat capacity flow rate changes three times.

It is apparent that models developed using finite time thermodynamics provide global power cycle characteristics, which are essential to the design process. In view of the continued upward rise in global energy consumption, this method can undoubtedly be used to reduce energy consumption by influencing the design and upgrade philosophy for new and current power plants, respectively.

References

Andresen, B., Salamon, P., and Berry, R. S., 1984, "Thermodynamics in Finite Time," *Physics Today*, Vol. 37, No. 9, pp. 62–70.

Bejan, A., 1988, "Theory of Heat Transfer—Irreversible Power Plants," *International Journal of Heat and Mass Transfer*, Vol. 31, No. 6, pp. 1211–1219.

Curzon, F. L., and Ahlborn, B., 1975, "Efficiency of a Carnot Engine at Maximum Power Output," *American Journal of Physics*, Vol. 43, No. 1, pp. 22–24.

De Vos, A., 1985, "Efficiency of Some Heat Engines at Maximum-Power Conditions," *American Journal of Physics*, Vol. 53, No. 6, pp. 570–573.

Hoffmann, K. H., and Salamon, P., 1987, "Lower Bounds on Dissipation in Composite Systems," *Physical Review A*, Vol. 35, No. 1, pp. 369–373.

Incropera, F. P., and DeWitt, D. P., 1990, *Introduction to Heat Transfer*, 2nd ed., Wiley, New York.

Salamon, P., Nitzan, A., Andresen, B., and Berry, R. S., 1980, "Minimum Entropy Production and the Optimization of Heat Engines," *Physical Review A*, Vol. 21, No. 6, pp. 2115–2129.

Salamon, P., and Nitzan, A., 1981, "Finite Time Optimizations of a Newton's Law Carnot Cycle," *Journal of Chemical Physics*, Vol. 74, No. 6, pp. 3546–3560.

Salamon, P., Band, Y. B., and Kafri, O., 1982, "Maximum Power From a Cycling Working Fluid," *Journal of Applied Physics*, Vol. 53, No. 1, pp. 197–202.

Wu, C., 1988, "Power Optimization of a Finite-Time Carnot Heat Engine," *Energy*, Vol. 13, No. 9, pp. 681–687.

Wu, C., 1989, "Power Optimization of a Finite-Time Rankine Heat Engine," *International Journal of Heat and Fluid Flow*, Vol. 10, No. 2, pp. 134–138.

An Explanation for Observed Compression Ratios in Internal Combustion Engines

S. A. Klein
Mechanical Engineering Department,
University of Wisconsin-Madison,
Madison, WI 53706

Comparisons of the compression ratios, efficiencies, and work of the ideal Otto and Diesel cycles are presented at conditions that yield maximum work per cycle. The compression ratios that maximize the work of the Diesel cycle are found always to be higher than those for the Otto cycle at the same operating conditions, although the thermal efficiencies are nearly identical. The compression ratios that maximize the work of the Otto and Diesel cycles compare well with the compression ratios employed in corresponding production engines.

Introduction

The air-standard Otto and Diesel cycles are used to describe the major processes occurring in internal combustion engines. The two cycles differ only in the energy input process and provide limiting cases for actual engine operation. Thermodynamic analysis shows the efficiency of both cycles to increase with increasing compression ratio. The implication of this result is that the higher the compression ratio, the better. However, spark-ignition internal engines typically operate at a compression ratio less than 10, whereas compression-ignition engines may operate at a compression ratio of 15 or more. An explanation for this difference, offered in most mechanical engineering thermodynamic textbooks, is that the compression ratio in spark-ignition engines is limited to about 10 to prevent pre-ignition of the fuel–air mixture. Compression-ignition engines do not have this limitation and can thereby operate at higher compression ratio, and consequently, higher efficiency. There is, however, another explanation for the observed compression ratios in internal combustion cycles, which is the objective of this paper.

Maximum Work of the Air-Standard Otto Cycle

Although the thermal efficiency of the Otto cycle increases with increasing compression ratio, there is a compression ratio that maximizes the net work per cycle, as seen in Fig. 1. An analytical expression for this optimum compression ratio can easily be derived for the air-standard Otto cycle assuming a constant specific heat ratio. Referring to the T–s diagram in Fig. 2(*a*), W_{net}, the net work of the Otto cycle per unit mass of gas in the cylinder, is

$$W_{net} = W_{1\text{-}2} + W_{3\text{-}4} = C_v(T_1 + T_3 - T_2 - T_4) \quad (1)$$

Assuming processes 1–2 and 3–4 to be isentropic

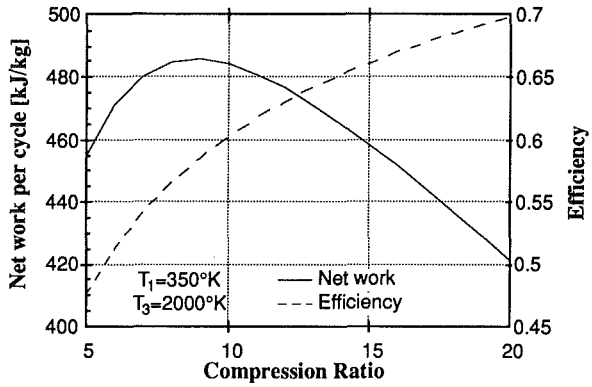

Fig. 1 Net work per cycle (per unit mass of gas) and efficiency versus compression ratio for the air-standard Otto cycle with k = 1.4

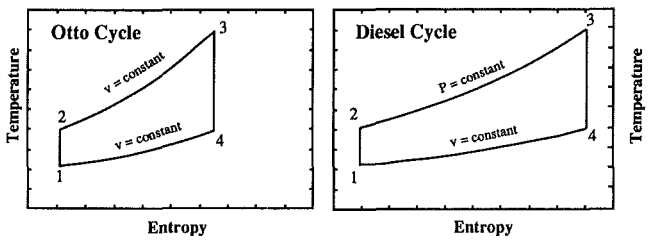

Fig. 2 Temperature-entropy representations of the air-standard (*a*) Otto and (*b*) Diesel cycles operating at maximum net work (drawn to scale) between the same temperature limits

$$T_2 = T_1 r^{k-1} \quad (2)$$

$$T_4 = T_3 / r^{k-1} \quad (3)$$

where r is the compression ratio $= v_1/v_2 = v_4/v_3$.

Eliminating T_2 and T_4 using Eqs. (2) and (3),

$$W_{net} = C_v[T_1(1 - r^{k-1}) + T_3(1 - 1/r^{k-1})] \quad (4)$$

Contributed by the Advanced Energy Systems Division for publication in the JOURNAL OF ENGINEERING FOR GAS TURBINES AND POWER. Manuscript received by the Advanced Energy Systems Division June 22, 1990; revision received September 24, 1990.

T_1, C_v, and k are constants in the following analysis. If T_3 is also assumed constant, the net work depends only on the compression ratio. Setting dW_{net}/dr to zero results in the following expression for r_{max}, the compression ratio that maximizes the net work:

$$r_{max} = (T_1/T_3)^{-1/(2k-2)} \tag{5}$$

The thermal efficiency, η, at maximum net work is

$$\eta_{max} = 1 - \frac{1}{r^{k-1}} = 1 - \sqrt{\frac{T_1}{T_3}} \tag{6}$$

Remarkably, the efficiency at maximum net work for the Otto cycle has the same form as the efficiency derived by Curzon and Alhborn (1975) for the heat transfer limited Carnot cycle as first observed by Leff (1987). It is also worth noting that, when the cycle operates at maximum net work,

$$T_2 = T_4 = \sqrt{T_1 T_3} \tag{7}$$

Maximum Work of the Air-Standard Diesel Cycle

An analysis similar to that presented for the Otto cycle can be made for the air-standard Diesel cycle represented in Fig. 2(*b*). Assuming T_1, C_v, and k to be constants, the net work of the Diesel cycle can be expressed as

$$W_{net} = W_{12} + W_{23} + W_{34} = C_v(T_1(1 - kr^{k-1}) + kT_3 - T_1^{1-k}T_3^k r^{k(1-k)}) \tag{8}$$

As with the Otto cycle, there is a compression ratio that maximizes the net work. Assuming T_3 to be constant, the maximum net work compression ratio for the Diesel cycle is

$$r_{max} = \left(\frac{T_1}{T_3}\right)^{\frac{k}{(1-k^2)}} \tag{9}$$

Again, at maximum net work, $T_2 = T_4$. The thermal efficiency of the Diesel cycle at maximum net work is

$$\eta_{max} = 1 - \frac{(r^{k-1} - 1)}{k(r^{(k^2-1)/k} - r^{k-1})} \tag{10}$$

Although Eq. (10) appears to be quite different from the corresponding efficiency for the Otto cycle (Eq. (6)), the efficiency of the Diesel cycle at maximum net work is very close, but not exactly equal, to $1 - \sqrt{T_1/T_3}$.

Comparison of the Air-Standard Otto and Diesel Cycles for Fixed Cycle Temperatures

If the maximum cycle temperature, T_3, is assumed to be independent of the compression ratio and k and C_v are known constants, the maximum work per cycle and the corresponding efficiency and compression ratio are functions only of the ratio T_3/T_1. Figure 3 presents the work, compression ratio, and thermal efficiency of the Diesel cycle divided by the corresponding quantities for the Otto cycle as a function of T_3/T_1 for $k = 1.40$. The compression ratio that maximizes the work of the Diesel cycle is always higher than that for the Otto cycle

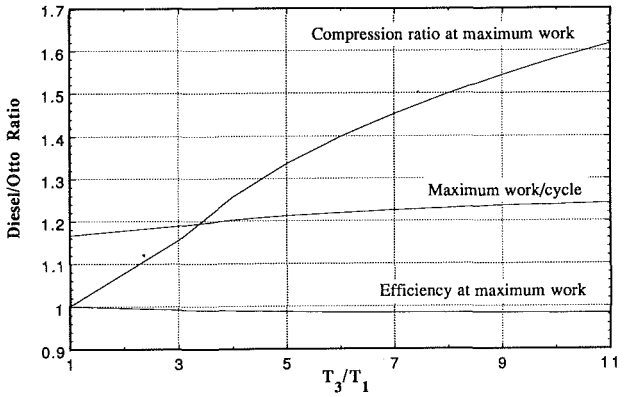

Fig. 3 Diesel/Otto cycle ratios of the maximum work/cycle, compression ratio, and thermal efficiency at maximum work as a function of the maximum/minimum cycle temperatures for $k = 1.40$

at the same value of T_3/T_1. The efficiencies of the two cycles, operated at maximum net work, are very similar, with the Otto cycle having a slightly higher efficiency. The Diesel cycle, however, enjoys significantly higher net work per cycle for the same value of T_3/T_1, as evident from the T–s diagrams in Fig. 2. Similar results have been presented by Leff (1987).

Heat Transfer Considerations

In a real engine, T_3 could not be expected to remain constant as the compression ratio is varied, as assumed in Fig. 1 and in the derivation of Eqs. (5) and (9). Increasing the compression ratio increases T_2, which results in higher values of T_3, assuming the energy release during combustion is unchanged. There are, however, additional relationships between T_3 and the compression ratio, which result from a consideration of heat transfer to the cylinder walls.

Internal combustion engines combust fuel with air in near-stoichiometric proportions. The combustion process is obviously not adiabatic since the maximum temperature in the cycle is far below the adiabatic combustion temperature. The actual heat transfer processes occurring within the cylinder are quite complicated. Regardless, the cylinder wall heat transfer will increase with increasing compression ratio since the difference between the mass-averaged gas and cylinder wall temperatures increase. For a given bore to stroke ratio, increasing the compression ratio also increases the peak gas density (which increases the gas to cylinder wall heat transfer coefficient) and slightly decreases the surface area available for heat transfer.

As a first approximation, the heat transfer to the cylinder walls is assumed to be a linear function of the difference between the average gas and cylinder wall temperatures during the energy release process 2–3. The wall temperature is further assumed to be constant as in Mozurkewich and Berry (1982) and Hoffman et al. (1985). In this case, Q_{23}, the energy transferred to the gas in the cylinder during combustion for the Otto cycle, can be represented

$$Q_{23} = C_v(T_3 - T_2) = \alpha - \beta(T_3 + T_2) \tag{11}$$

where α and β are constants. If the combustion process were

Nomenclature

- C_v = constant-volume specific heat of working fluid (assumed as air)
- k = ratio of constant pressure to constant volume specific heat (assumed to be 1.4)
- r = compression ratio
- Q_{23} = energy added to gas during process 2–3 as a result of combustion
- T_i = temperature at state i
- W = work per unit mass of gas in the cylinder per cycle
- α = heat transfer constant used in Eqs. (11)–(14)
- β = heat transfer constant used in Eqs. (11)–(14)
- η = thermal efficiency defined as the ratio of the net work to energy input

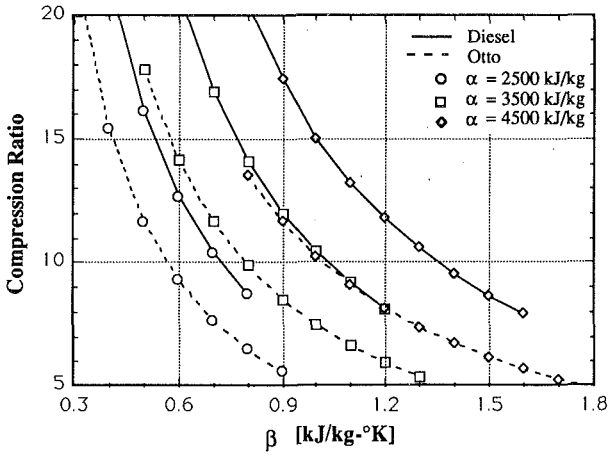

Fig. 4 Comparison of the compression ratios of the Diesel (solid lines) and Otto (dotted lines) at maximum net work for various values of α and β with T_1 = 350 K and k = 1.4

adiabatic (β = 0), the heat transfer to the gas would be equal to α, the heat release during combustion. Fuels used in internal combustion engines release about 50,000 kJ/kg. The air-fuel ratio for stoichiometric conditions is approximately 15. As a result, α should be approximately 3500 kJ/kg air. Values of β must range from about 0.3 to 1.8 in order to achieve maximum gas temperatures of 1500 to 3000 K, as observed in practice.

Eliminating T_3 from Eq. (4) using Eq. (11)

$$W_{\text{net}} = C_v\left(T_1(1-r^{k-1}) + \frac{(\alpha+(C_v-\beta)T_1r^{k-1})(1-r^{1-k})}{C_v+\beta}\right) \tag{12}$$

Setting dW_{net}/dr to zero results in the compression ratio at maximum power for the Otto cycle with heat transfer considerations.

$$r_{\max} = \left(\frac{\alpha}{2T_1\beta}\right)^{1/(2k-2)} \tag{13}$$

It can again be shown that, at this compression ratio, T_2 is equal to T_4.

Considering heat transfer to the cylinder walls for the Diesel cycle with the same heat transfer model used for the Otto cycle,

$$Q_{23} = C_p(T_3 - T_2) = \alpha - \beta(T_3 + T_2) \tag{14}$$

A simple analytical expression for the compression ratio at maximum net work that does not involve T_3 is not apparent. However, the maximum net work compression ratio for the Diesel cycle can be determined numerically.

The compression ratios that result in maximum work for the Otto and Diesel cycles are plotted in Fig. 4 as a function of α and β with T_1 = 350 K and k = 1.4. The values of β for each value of α are such that the maximum gas temperature lies in the range of 1500 to 3000 K, as observed in actual engines. For given values of α and β, the compression ratio that maximizes the work of the Diesel cycle is always higher than that of the Otto cycle.

Conclusions

The air-standard Otto and Diesel cycles are very simplistic and cannot possibly represent the complex processes occurring in internal combustion engines. Furthermore, compromises in the performance of modern engines are made in order to meet emission standards. Nevertheless, the results observed in Figs. 3 and 4 show that the maximum work compression ratios for the Otto cycle are significantly lower than those for the Diesel cycle, as observed in practice. Further, these compression ratios compare reasonably well with the compression ratios employed in production engines.

Power output is surely a major design consideration in the determination of the compression ratio for internal combustion engines. The point of this paper is that the choice of compression ratio in internal combustion engines is dictated to some extent by the desire to maximize engine power output. Preignition is certainly a design consideration in spark-ignition engines. However, the characteristics of gasoline are an economic consequence of engine power–compression ratio tradeoffs. The textbook explanation of factors limiting the compression ratio of spark-ignition engines misses this point.

References

Curzon, F. L., and Alhborn, B., 1975, "Efficiency of a Carnot Engine at Maximum Power Output," *Am. J. Phys.*, Vol. 43, pp. 22–24.

Hoffman, K. H., Watowich, S. J., and Berry, R. S., 1985, "Optimal Paths for Thermodynamic Systems: The Ideal Diesel Cycle," *J. Appl. Phys.*, Vol. 58(6), pp. 2125–2134.

Leff, H. S., 1987, "Thermal Efficiency at Maximum Work Output: New Results for Old Heat Engines," *Am. J. Phys.*, Vol. 55, pp. 602–610.

Mozurkewich, M., and Berry, R. S., 1982, "Optimal Paths for Thermodynamic Systems: The Ideal Otto Cycle," *J. Appl. Phys.*, Vol. 53(1), pp. 34–42.

Optimum Heat Power Cycles for Specified Boundary Conditions

O. M. Ibrahim

S. A. Klein

J. W. Mitchell

Solar Energy Laboratory,
University of Wisconsin-Madison,
Madison, WI 53706

Optimization of the power output of Carnot and closed Brayton cycles is considered for both finite and infinite thermal capacitance rates of the external fluid streams. The method of Lagrange multipliers is used to solve for working fluid temperatures that yield maximum power. Analytical expressions for the maximum power and the cycle efficiency at maximum power are obtained. A comparison of the maximum power from the two cycles for the same boundary conditions, i.e., the same heat source/sink inlet temperatures, thermal capacitance rates, and heat exchanger conductances, shows that the Brayton cycle can produce more power than the Carnot cycle. This comparison illustrates that cycles exist that can produce more power than the Carnot cycle. The optimum heat power cycle, which will provide the upper limit of power obtained from any thermodynamic cycle for specified boundary conditions and heat exchanger conductances is considered. The optimum heat power cycle is identified by optimizing the sum of the power output from a sequence of Carnot cycles. The shape of the optimum heat power cycle, the power output, and corresponding efficiency are presented. The efficiency at maximum power of all cycles investigated in this study is found to be equal to (or well approximated by) $\eta = 1 - \sqrt{T_{L,in}/\phi T_{H,in}}$ where ϕ is a factor relating the entropy changes during heat rejection and heat cddition.

Introduction

Carnot (1824) introduced the concepts of reversibility and the principle that the thermal efficiency of a reversible cycle is determined solely by the temperatures of the heat source and heat sink. The maximum possible efficiency is obtained when only reversible processes are involved. Reversible heat transfer processes require thermal energy to be transferred with infinitesimal temperature differences. For finite heat exchange areas and heat transfer coefficients, the rate of heat exchange in reversible processes approaches zero, and the total energy transfer in finite time is zero. As a result, as a cycle approaches thermodynamic reversibility, its output power becomes infinitesimally small.

Consider a simplified model of a Carnot cycle[1] where all of the irreversibilities are associated with the transfer of heat to and from the power cycle equipment. There are no internal losses within the cycle itself. The heat source and heat sink are first considered to be at constant temperatures T_H and T_L, respectively. Because of the finite heat transfer conductance of materials, the cycle operates between T_h and T_l as shown in Fig. 1 to provide temperature differences, the driving forces for heat transfer between the cycle and the hot and cold reservoirs. Figure 2 shows a plot of power versus efficiency for

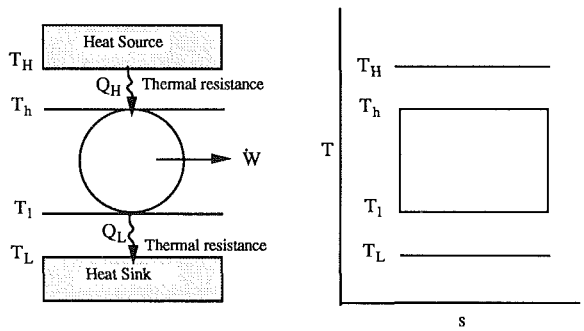

Fig. 1 Carnot cycle coupled to heat source and heat sink with infinite heat capacitance rates

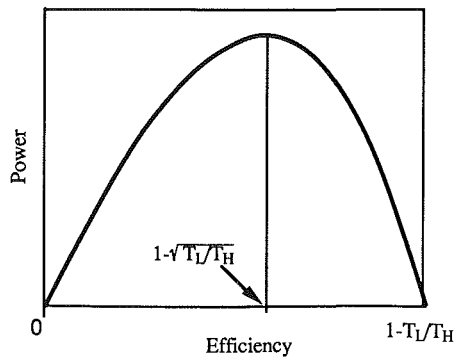

Fig. 2 Power/efficiency tradeoffs for the Carnot cycle

[1]In this paper, the term "Carnot cycle" is used to refer to a cycle having two adiabatic and two isothermal processes. The processes may be irreversible and as a result the cycle may not achieve the Carnot cycle efficiency.

Contributed by the Advanced Energy Systems Division for publication in the JOURNAL OF ENGINEERING FOR GAS TURBINES AND POWER. Manuscript received by the Advanced Energy Systems Division September 6, 1990; revision received January 30, 1991.

the cycle. Finite power can only be achieved by operating at less than the maximum efficiency. A point of maximum power exists, and at this point the efficiency is given by

$$\eta = 1 - \sqrt{T_L/T_H} \tag{1}$$

The existence of a maximum power point for this simple cycle and the limitation of the efficiencies of real processes resulting from finite heat transfer rate constraints were recognized by El-Wakil (1962), and by Curzon and Ahlborn (1975). They considered a Carnot cycle with heat transfer limitations and derived expressions for the maximum power and the cycle efficiency at the maximum power. Their studies were limited to the case in which the heat transfer fluid streams have infinite thermal capacitance rates (mass flow rate – specific heat product), i.e., the source and sink were assumed to be isothermal. Curzon and Ahlborn's study has inspired many subsequent studies. Leff (1987a) shows that the Brayton, Otto, Diesel and Atkinson cycles also produce maximum power at an efficiency of $\eta = 1 - \sqrt{T_L/T_H}$. Gordon (1988) has investigated the maximum power-efficiency relations for solar-driven cycles. Bejan (1988) considered an irreversible power plant model, accounting for the heat loss through the plant to the surroundings. Several papers deal with optimum power of the Carnot cycle operating between finite thermal capacitance rates heat source and sink, e.g., Ondrechen et al. (1983) and Wu (1988). Lee et al. (1990) analytically present the optimum power and the efficiency of a finite time Carnot heat engine operating between two reservoirs with finite heat-capacity rates. They show that the efficiency at maximum power depends only on the inlet temperatures of the cold and hot reservoirs. To achieve their results, a periodic cycle is considered with heat exchange contact time being among the independent variables. Rubin (1979a) extended the Curzon and Ahlborn model by consideration of cycles in which the reservoir temperatures are controllable parameters varying between the temperatures of the coldest and hottest reservoirs. Using a Lagrange optimization method, he shows that the efficiency at maximum power depends only on the coldest and hottest reservoir temperatures. Rubin (1979b) considered a reciprocating engine with heat exchange contact time being among the independent variables. The engine is a standard engine with a cylinder and piston, which is used to do work on the outside world. The working fluid is a perfect gas. He used optimum-control theory to find the possible optimum controls and the optimum trajectories for this type of engine.

Ondrechen et al. (1981) investigated a reversible cycle using an ideal gas working fluid providing maximum power using a finite thermal capacitance rate heat source. They considered a series of sequential Carnot cycles where each sequential cycle operates at its maximum power point. The heat sink was assumed to be isothermal and the heat exchangers were assumed infinitely large. Leff (1987b) used a second law availability analysis to obtain the maximum work available for the case where both heat source and heat sink have finite thermal capacitance rates. However, no study has identified the nature of a power cycle that produces maximum power for the case where heat exchanger area and heat transfer coefficients are finite, the cycle is internally irreversible, and the working fluid is not restricted to an ideal gas.

Although the Carnot cycle is the most efficient cycle, there exist cycles that can produce more power than the Carnot cycle for the same boundary conditions when heat transfer constraints are considered. The goal of this paper is to identify the optimum power cycle, i.e., the cycle that produces the maximum power for specified external boundary conditions. Although still somewhat idealized, the cycle that provides maximum power for specified external boundary conditions gives a more reasonable design goal than do reversible cycles that generate zero power. In this analysis, heat exchanger areas and heat transfer coefficients are finite and the cycle may be internally irreversible. Analytical and numerical techniques are used to determine the maximum power. The shape of optimum power cycle, i.e., the working fluid temperature as a function of entropy, $T(s)$, along with power output and efficiency, are presented for given heat source, heat sink, and heat exchanger conductances.

Irreversible Power Cycle Model

The irreversibilities that constrain the performance of a power cycle can be considered as external and internal. External irreversibilities arise from temperature differences that occur between the cycle and the heat source and sink. Internal irreversibilities result primarily because of fluid and mechanical friction. External irreversibilities are considered in previous studies (e.g., Curzon and Ahlborn, 1975).

There are several ways to account for internal irreversibilities. Howe (1982) derived an equation for the efficiency at maximum power for an irreversible Carnot cycle, accounting for internal irreversibilities, by multiplying the thermal efficiency of a reversible cycle by a factor (ψ) less than one (equal to one when the cycle is internally reversible).

$$\eta = \psi[1 - T_l/T_h] \tag{2}$$

El-Wakil (1962) accounted for internal irreversibilities by relating the entropy change during heat rejection for reversible and irreversible cycles.

Nomenclature

C_p = specific heat capacity at constant pressure, kJ/kg K
C_v = specific heat capacity at constant volume, kJ/kg K
$\dot{C}$ = heat capacitance rate (mass flow rate-specific heat product), kW/K
k = heat capacity ratio = C_p/C_v
i = fraction of unavailable energy that occurs with internal irreversibilities (El-Wakil, 1962)
$\dot{m}$ = mass flow rate, kg/s
N = number of cycles
NTU = number of transfer units = $UA/\dot{C}$
$\dot{Q}$ = rate of heat transfer, kW
P = pressure, N/m^2
s = entropy, kJ/kg K
$\dot{S}$ = entropy transfer rate (mass flow rate-entropy product), kW/K
T = temperature, K
UA = heat exchanger conductance (total heat transfer coefficient area product), kW/K
$\dot{W}$ = power, kW
ϵ = heat exchanger effectiveness
η = thermal efficiency
λ = Lagrange multiplier
ψ = a factor relating the efficiency of an irreversible cycle to a reversible one (Howe, 1982)
ϕ = a factor relating the entropy change during heat rejection and heat addition

Subscripts

A = area
B = Brayton
C = Carnot
H = heating fluid, heat source, hot-side heat exchanger
h = high
L = cooling fluid, heat sink, cold-side heat exchanger
l = low
i = cycle
in = inlet
min = minimum
max = maximum
op = optimum
p = production
total = total
wf = working fluid

$$\Delta \dot{S}_L'/\Delta \dot{S}_L = 1 + i \tag{3}$$

where i = fraction of unavailable energy that occurs with internal irreversibilities; $\Delta \dot{S}_L'$ = entropy change during heat rejection for irreversible cycles; ΔS_L = entropy change during heat rejection for reversible cycles. Equation (3) leads to the following expression for the thermal efficiency for an irreversible cycle:

$$\eta = 1 - (i+1)T_l/T_h \tag{4}$$

Thermodynamic analysis of a Carnot cycle results in

$$\dot{W} = \dot{Q}_H - \dot{Q}_L \tag{5}$$

$$\frac{\dot{Q}_H}{T_h} - \frac{\dot{Q}_L}{T_l} \leq 0 \tag{6}$$

where $\dot{Q}_L$ is the rate of heat rejected, $\dot{Q}_H$ is the rate of heat supplied, and $\dot{W}$ is the power output. Equation (6) is known as the "Clausius Inequality."

In this study, a simple model relating the entropy change during heat rejection and heat addition is considered. An irreversibility factor (ϕ) is defined such that the entropy inequality for internally irreversible cycles, Eq. (6), can be written as an equality:

$$\frac{\dot{Q}_H}{T_h} - \phi \frac{\dot{Q}_L}{T_l} = 0 \tag{7}$$

ϕ is equal to one when the cycle is internally reversible and less than one when the cycle is internally irreversible. The entropy production, S_p, is related to ϕ by the following equation:

$$\dot{S}_p = (1-\phi)\frac{\dot{Q}_L}{T_l} \tag{8}$$

Introducing ϕ makes it possible to derive an analytical solution for an internally irreversible Carnot cycle similar to the solution obtained for the internally reversible one. In the following analysis, ϕ is assumed to be constant. The thermal efficiency for the irreversible cycle then can be written as

$$\eta = 1 - \frac{T_l}{\phi T_h} \tag{9}$$

The fact that η should be greater than zero requires that $\phi \geq T_l/T_h \geq T_L/T_H$, which sets a lower limit for ϕ. All of the above expressions for the thermal efficiency for irreversible cycles are related in the following manner:

$$\phi = \frac{1}{1+i} \tag{10}$$

$$\psi = \frac{1 - T_l/\phi T_h}{1 - T_l/T_h} \tag{11}$$

Maximum Power of a Carnot Cycle

Carnot Cycle Coupled to Heat Source and Sink With Infinite Thermal Capacitance Rates. When the Carnot cycle is coupled to an isothermal heat source and sink as shown in Fig. 3, the rates at which heat is supplied and rejected are given by:

$$\dot{Q}_H = UA_H(T_H - T_h) \tag{12}$$

$$\dot{Q}_L = UA_L(T_l - T_L) \tag{13}$$

where UA_H and UA_L are, respectively, the hot-side and cold-side heat exchanger conductance (heat transfer coefficient-area product). The energy and the entropy balances on the cycle are then given by

$$\dot{W} = UA_H(T_H - T_h) - UA_L(T_l - T_L) \tag{14}$$

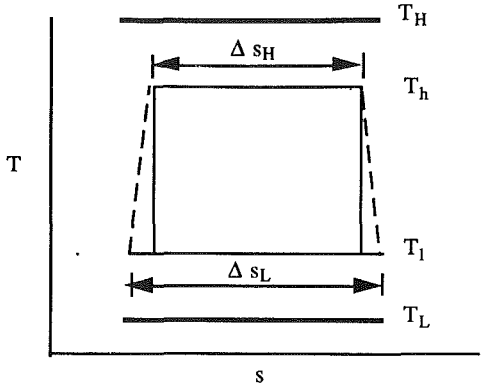

Fig. 3 Carnot cycle with irreversible expansion and compression coupled to heat source and heat sink with infinite heat capacitance rates

$$g = \frac{UA_H(T_H - T_h)}{T_h} - \phi\frac{UA_L(T_l - T_L)}{T_l} = 0 \tag{15}$$

where g is the entropy constraint function.

The values of T_h and T_l that result in the maximum power are found using the method of Lagrange multipliers. A Lagrange multiplier, λ, is defined such that:

$$\partial \dot{W}/\partial T_h = \lambda \partial g/\partial T_h \tag{16}$$

$$\partial \dot{W}/\partial T_l = \lambda \partial g/\partial T_l \tag{17}$$

Evaluating the partial derivatives allows Eqs. (16) and (17) to be written as:

$$1 = \lambda T_H/T_h^2 \tag{18}$$

$$1 = \lambda \phi T_L/T_l^2 \tag{19}$$

Solving Eqs. (15), (18), and (19) leads to the following relation for the unknown cycle temperatures:

$$T_l/T_h = \sqrt{\phi T_L/T_H} \tag{20}$$

The efficiency at the maximum power point is then given by:

$$\eta = 1 - \sqrt{T_L/(\phi T_H)} \tag{21}$$

The values of T_h and T_l that result in the maximum power are:

$$T_h = \left[\frac{\phi UA_L\sqrt{T_L/\phi} + UA_H\sqrt{T_H}}{\phi UA_L + UA_H}\right]\sqrt{T_H} \tag{22}$$

$$T_l = \left[\frac{\phi UA_L\sqrt{T_L/\phi} + UA_H\sqrt{T_H}}{\phi UA_L + UA_H}\right]\sqrt{\phi T_L} \tag{23}$$

The maximum power for a single Carnot cycle coupled to an isothermal heat source and heat sink is then:

$$\dot{W}_{\max} = \frac{\phi UA_L}{\phi UA_L + UA_H} UA_H[\sqrt{T_H} - \sqrt{T_L/\phi}]^2 \tag{24}$$

The Lagrange multiplier method locates an extremum point, which may be a minimum or a maximum. A verification that $\dot{W}_{\max}$ in Eq. (24) is a maximum is possible by obtaining the sign of the second derivative of $\dot{W}_{\max}$ with respect to any free variable (e.g., T_h, T_l) or by examination of a plot of $\dot{W}_{\max}$ versus the variable, as in Fig. 4.

Equation (21) shows that the efficiency of a Carnot cycle at a maximum power depends only on the temperature of the heat reservoirs and the irreversibility factor ϕ. If $\phi = 1$, the efficiency reduces to the relationship of El-Wakil (1962), and Curzon and Ahlborn (1975). The effects of internal irreversibility on the power/efficiency tradeoffs are shown in Fig. 4. The internal irreversibilities decrease both the maximum power and the efficiency at the maximum power.

The variation of power with the cold-side heat exchanger conductance ratio, defined as the fraction of total heat ex-

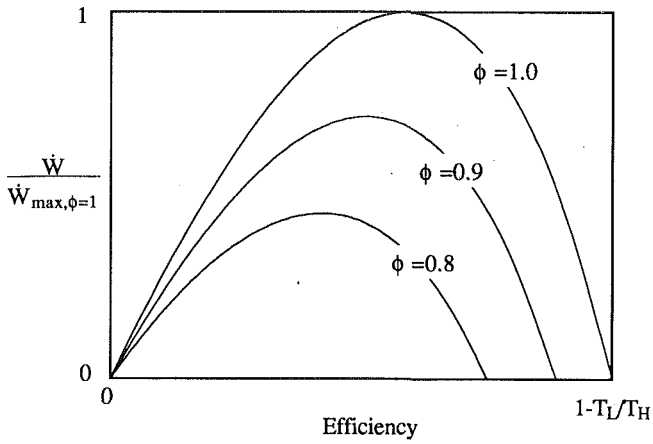

Fig. 4 Power/efficiency tradeoffs for the Carnot cycle showing the effects of internal irreversibility ($UA_H = UA_L$)

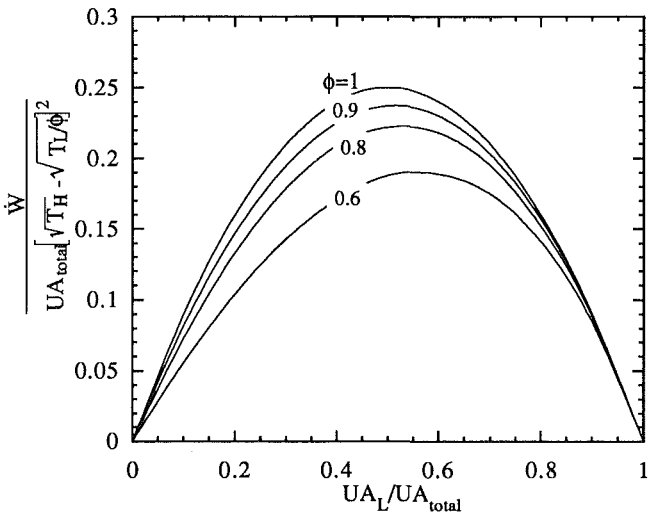

Fig. 5 Variation of power output with cold-side heat exchanger conductance ratio

changer conductance used at the cold-side heat exchanger, is shown in Fig. 5. There exists an optimum balance between the conductances of the hot-side and cold-side heat exchangers. The total heat exchanger conductance, $UA_{total} = UA_L + UA_H$, should be split evenly when the cycle is internally reversible, as concluded by Bejan (1988). However, as the internal irreversibility increases, the cold-side heat exchanger should be increasingly larger than the hot-side heat exchanger to obtain maximum power because the internal irreversibility increases the heat rejection. A larger cold-side heat exchanger reduces the external irreversibility by allowing the cycle to reject energy at a lower temperature.

Carnot Cycle Coupled to Heat Source and Sink With Finite Thermal Capacitance Rates. When the Carnot cycle is coupled to a source and sink with finite thermal capacitance rates, the rates at which heat is supplied and rejected can be expressed as (Kays and London, 1964)

$$\dot{Q}_H = \dot{C}_H \epsilon_H (T_{H,in} - T_h) \tag{25}$$

$$\dot{Q}_L = \dot{C}_L \epsilon_L (T_l - T_{L,in}) \tag{26}$$

where $T_{H,in}$ = inlet temperature of the heating fluid; $T_{L,in}$ = inlet temperature of the cooling fluid; $\dot{C}_H$ = thermal capacitance rate of the heating fluid; $\dot{C}_L$ = heat capacitance rate of the cooling fluid; ϵ_H = effectiveness of the hot-side heat exchanger = $1 - \exp(-\mathrm{NTU}_H)$; ϵ_L = effectiveness of the cold-side heat exchanger = $1 - \exp(-\mathrm{NTU}_L)$. Using the method of Lagrange multipliers, similar to the analysis for infinite thermal capacitance rates, the optimum power for a single Carnot cycle coupled to source and sink streams with finite thermal capacitance rates is

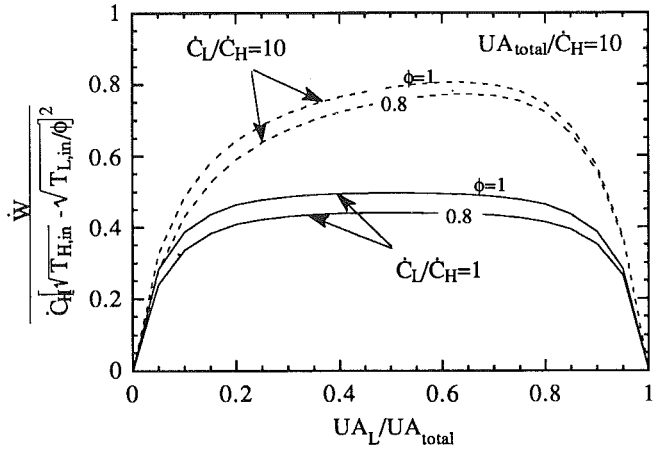

Fig. 6 Variation of power output with cold-side heat exchanger conductance ratio

$$\dot{W}_{max} = \frac{\phi \dot{C}_L \epsilon_L}{\phi \dot{C}_L \epsilon_L + \dot{C}_H \epsilon_H} \dot{C}_H \epsilon_H [\sqrt{T_{H,in}} - \sqrt{T_{L,in}/\phi}]^2 \tag{27}$$

Equation (27) reduces to Eq. (24) in the limit of high capacity rates whereupon $\epsilon_H \dot{C}_H \to UA_H$ and $\epsilon_L \dot{C}_L \to UA_L$.

The efficiency at the maximum power point is given by:

$$\eta = 1 - \sqrt{T_{L,in}/\phi T_{H,in}} \tag{28}$$

Equations (21) and (28), which are very similar, demonstrate that for both finite and infinite capacitance rates, the efficiency of a Carnot cycle at maximum power depends only on the inlet temperatures of the heat reservoirs.

The variation of the power with the cold-side heat exchanger conductance ratio is shown in Fig. 6. The optimum ratio is a function of the irreversibility factor, the thermal capacitance rates of the heat source and heat sink, and the total conductance. As the internal irreversibilities increase, the optimum cold-side heat exchanger conductance ratio increases. When $\dot{C}_L/\dot{C}_H = 1$, the total heat exchanger conductance, UA_{total}, should be split evenly when the cycle is internally reversible; however, as $\dot{C}_L/\dot{C}_H$ increases, the optimum cold-side conductance ratio (UA_L/UA_{total}) increases.

Maximum Power of a Closed Brayton Cycle

A simple closed Brayton cycle, composed of two adiabatic and two constant-pressure processes, is considered with an ideal gas having constant thermal capacitance rate ($\dot{C}_{wf}$). The shape of the closed Brayton cycle on temperature-entropy coordinates is a function of the thermal capacitance rate of the working fluid, $\dot{C}_{wf}$. As $\dot{C}_{wf}$ becomes infinitely large, the Brayton cycle maximum power approaches the Carnot cycle maximum power, since the constant pressure processes approach isothermal behavior. The effect of the Brayton cycle shape on cycle power output is presented in this section to show that there exist cycles that can produce more power than the Carnot cycle for the same boundary conditions.

Brayton Cycle Coupled to Heat Source and Sink With Infinite Thermal Capacitance Rates. The Brayton cycle coupled to heat source and heat sink with infinite thermal capacitance rates is sketched in Fig. 7. The rates at which heat is supplied and rejected are given by:

$$\dot{Q}_H = \dot{C}_{wf} \epsilon_H (T_H - T_1) = \dot{C}_{wf} (T_2 - T_1) \tag{29}$$

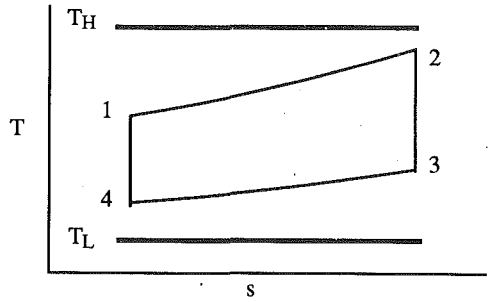

Fig. 7 Brayton cycle coupled to heat source and sink with infinite heat capacitance rates

$$\dot{Q}_L = \dot{C}_{wf}\epsilon_L(T_3 - T_L) = \dot{C}_{wf}(T_3 - T_4) \tag{30}$$

Thermodynamic analysis of a closed Brayton cycle provides

$$\dot{W} = \dot{C}_{wf}\epsilon_H(T_H - T_1) - \dot{C}_{wf}\epsilon_L(T_3 - T_L) \tag{31}$$

$$\dot{C}_{wf}\ln[T_2/T_1] - \dot{C}_{wf}\ln[T_3/T_4] = 0 \tag{32}$$

Using the method of Lagrange multipliers, the maximum power and the efficiency at maximum power for a closed internally reversible Brayton cycle coupled to an isothermal heat source and heat sink are given by:

$$\dot{W}_{\max} = \frac{\dot{C}_{wf}\epsilon_H\epsilon_L}{\epsilon_H + \epsilon_L - \epsilon_H\epsilon_L}\left[\sqrt{T_H} - \sqrt{T_L}\right]^2 \tag{33}$$

$$\eta = 1 - \sqrt{T_L/T_H} \tag{34}$$

The efficiency of the Brayton cycle can be expressed in terms of pressure ratio (P_L/P_H) only:

$$\eta = 1 - [P_L/P_H]^{(k-1)/k} \tag{35}$$

Therefore, at the maximum power point:

$$\sqrt{T_L/T_H} = [P_L/P_H]^{(k-1)/k} \tag{36}$$

A comparison of the maximum power of this Brayton cycle and the Carnot cycle is shown in Fig. 8. As $\dot{C}_{wf}$ increases, the maximum power of the Brayton cycle increases and asymptotically approaches the Carnot cycle maximum power. The maximum power of the Carnot cycle is always greater than the maximum power of Brayton cycle for the case where the heat source and heat sink are isothermal. The Carnot cycle provides better temperature matching with the isothermal heat source and heat sink, which reduces the external irreversibility.

Brayton Cycle Coupled to Heat Source and Sink With Finite Thermal Capacitance Rates. When the Brayton cycle is coupled to a heat source and sink with finite thermal capacitance rates (Fig. 9), the rates at which heat is supplied and rejected are given by:

$$\dot{Q}_H = \dot{C}_{H,\min}\epsilon_H(T_{H,\text{in}} - T_1) = \dot{C}_{wf}(T_2 - T_1) \tag{37}$$

$$\dot{Q}_L = \dot{C}_{L,\min}\epsilon_L(T_3 - T_{L,\text{in}}) = \dot{C}_{wf}(T_3 - T_4) \tag{38}$$

where the effectivenesses of hot-side heat exchanger ϵ_H, and cold-side heat exchanger ϵ_L, for counterflow heat exchangers are defined as (Kays and London, 1964):

$$\epsilon_H = \frac{1 - \exp[-\text{NTU}_H(1 - \dot{C}_{H,\min}/\dot{C}_{H,\max})]}{1 - (\dot{C}_{H,\min}/\dot{C}_{H,\max})\exp[-\text{NTU}_H(1 - \dot{C}_{H,\min}/\dot{C}_{H,\max})]} \tag{39}$$

$$\epsilon_L = \frac{1 - \exp[-\text{NTU}_L(1 - \dot{C}_{L,\min}/\dot{C}_{L,\max})]}{1 - (\dot{C}_{L,\min}/\dot{C}_{L,\max})\exp[-\text{NTU}_L(1 - \dot{C}_{L,\min}/\dot{C}_{L,\max})]} \tag{40}$$

where $\dot{C}_{H,\min}$ and $\dot{C}_{H,\max}$ are, respectively, the smaller and the larger of the two capacitance rates $\dot{C}_H$ and $\dot{C}_{wf}$. $\dot{C}_{L,\min}$ and $\dot{C}_{L\max}$ are, respectively, the smaller and the larger of $\dot{C}_L$ and

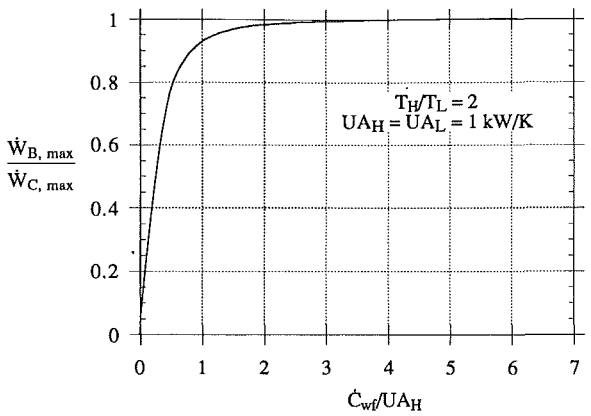

Fig. 8 Comparison of the maximum power of internally reversible Brayton and Carnot cycles when the heat source and the heat sink heat capacitance rates are infinite

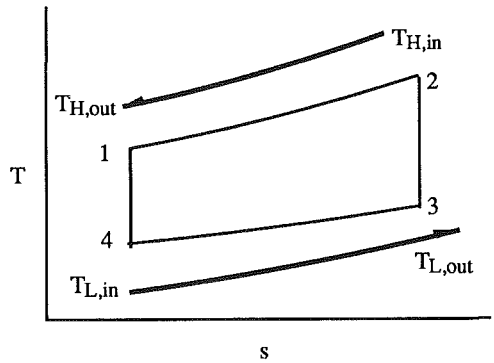

Fig. 9 Brayton cycle coupled to heat source and sink with finite heat capacitance rates

$\dot{C}_{wf}$. The number of heat transfer units, NTU_H and NTU_L, are based on the minimum thermal capacitance rates.

Energy and entropy balances on an internally reversible closed Brayton cycle are:

$$\dot{W} = \dot{C}_{H,\min}\epsilon_H(T_{H,in} - T_1) - \dot{C}_{L,\min}\epsilon_L(T_3 - T_{L,in}) \tag{41}$$

$$\dot{C}_{wf}\ln[T_2/T_1] - \dot{C}_{wf}\ln[T_3/T_4] = 0 \tag{42}$$

Using the method of Lagrange multipliers, similar to the analysis for the case of isothermal heat reservoirs, the optimum power and the efficiency at maximum power:

$$\dot{W}_{\max} = \frac{\dot{C}_{H,\min}\epsilon_H\dot{C}_{L,\min}\epsilon_L\left[\sqrt{T_{H,in}} - \sqrt{T_{L,in}}\right]^2}{\dot{C}_{H,\min}\epsilon_H + \dot{C}_{L,\min}\epsilon_L - \dot{C}_{H,\min}\epsilon_H\dot{C}_{L,\min}\epsilon_L/\dot{C}_{wf}} \tag{43}$$

$$\eta = 1 - \sqrt{T_{L,in}/T_{H,in}} \tag{44}$$

The effect of the heat capacitance rate of the working fluid ($\dot{C}_{wf}$) on the maximum power of the internally reversible Brayton cycle is shown in Fig. 10. The Brayton cycle can produce more power than the maximum power of the Carnot cycle for the same boundary conditions and the same heat exchanger conductances. The increased power of the Brayton cycle can be attributed to the lower entropy production during the heat transfer processes, due to more favorable matching of the working fluid and external stream temperatures. The optimum value of working fluid thermal capacitance rate, $\dot{C}_{wf,op}$, is always bounded by $\dot{C}_L \geq \dot{C}_{wf,op} \geq \dot{C}_H$. When $\dot{C}_L = \dot{C}_H$, $\dot{C}_{wf,op}/\dot{C}_H = 1$, the maximum power of the Brayton cycle asymptotically approaches the Carnot maximum power as $\dot{C}_{wf}$ increases.

Optimum Heat Power Cycles

It has been shown that the Brayton cycle can produce more

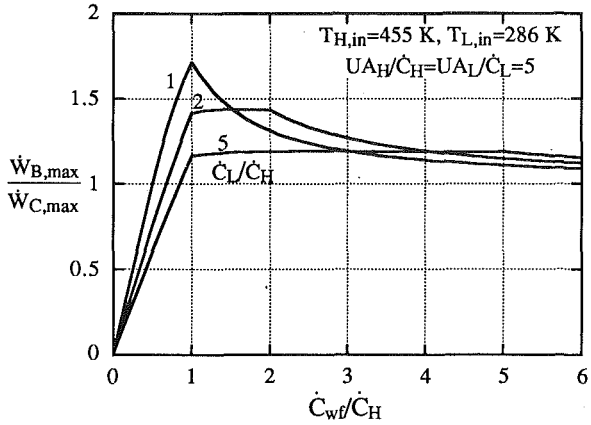

Fig. 10 Comparison of the maximum power of internally reversible Brayton and Carnot cycles when the heat source and the heat sink heat capacitance rates are finite

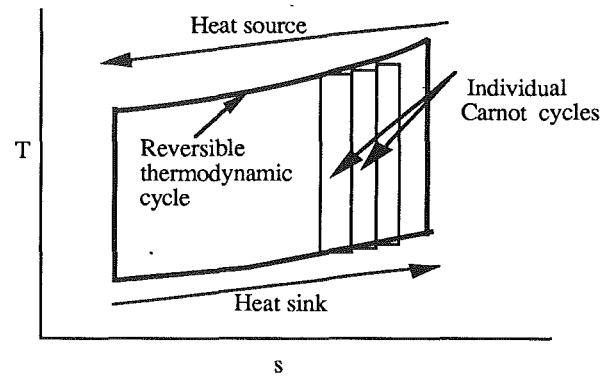

Fig. 11 A thermodynamic cycle can be broken into a sequence of Carnot cycles

power than an equivalent Carnot cycle when the heat source and heat sink have finite thermal capacitance rates. Other cycles, such as the Otto and Diesel cycles, can also produce more power than the Carnot cycle. The purpose of this section is to identify the internally reversible cycle that will result in the upper limit of the maximum power for specified boundary conditions.

Any internally reversible thermodynamic cycle can be broken into a sequence of internally reversible Carnot cycles as shown in Fig. 11. An infinite number of infinitesimal cycles have the same heat interactions with the heat source and heat sink, and the same power output as the original cycle. Starting from a sequence of Carnot cycles, the optimum power cycle can be identified by dividing the total heat exchange conductance equally between the cycles. As the number of cycles in sequence approaches infinity, the performance and shape of the sequence approaches the performance and shape of the optimum power cycle. Ondrechen et al. (1981) considered sequential Carnot cycles to find the maximum power from a heat source with finite thermal capacitance rates and infinitely large heat exchangers. However, they determined the sum of the maximum power for each cycle in the sequence. Operating each cycle in the sequence at maximum power does not necessarily result in the system consisting of all cycles in the sequence producing maximum power. In this study, the goal is to optimize the sum of the power output from all cycles, rather than optimizing the power output from each individual cycle in the sequence as done by Ondrechen et al.

An energy balance on all the Carnot cycles in Fig. 11 is

$$\dot{W}=\sum_{i}^{N}[\dot{Q}_{H,i}-\dot{Q}_{L,i}] \tag{45}$$

An entropy balance for each cycle i in the sequence can be expressed as

$$\frac{\dot{Q}_{H,i}}{T_{h,i}}-\frac{\dot{Q}_{L,i}}{T_{l,i}}=0 \quad [i=1, N] \tag{46}$$

Optimum Power Cycle Coupled to Heat Source and Sink With Infinite Thermal Capacitance Rates. When sequential Carnot cycles are coupled to an isothermal heat source and heat sink, the power from the N-Carnot cycles is given by:

$$\dot{W}=\sum_{i=1}^{N}[UA_{H,i}(T_H-T_{h,i})-UA_{L,i}(T_{l,i}-T_L)] \tag{47}$$

The shape of the optimum cycle is determined by maximizing $\dot{W}$ with respect to $T_{h,i}$ and $T_{l,i}$, subject to the following constraints:

$$\frac{UA_{H,i}(T_H-T_{h,i})}{T_{h,i}}-\frac{UA_{L,i}(T_{l,i}-T_L)}{T_{l,i}}=0 \quad [i=1,N] \tag{48}$$

Using the method of Lagrange multipliers, the efficiency at the maximum power point for any cycle i in the sequence is found, as discussed previously, to be

$$\eta=1-\sqrt{T_L/T_H} \tag{49}$$

The values of $T_{h,i}$ and $T_{l,i}$ that result in the maximum power are:

$$T_{h,1}=T_{h,2}=\ldots=T_{h,i}=\left[\frac{UA_L\sqrt{T_L}+UA_H\sqrt{T_H}}{UA_L+UA_H}\right]\sqrt{T_H} \tag{50}$$

$$T_{l,1}=T_{l,2}=\ldots=T_{l,i}=\left[\frac{UA_L\sqrt{T_L}+UA_H\sqrt{T_H}}{UA_L+UA_H}\right]\sqrt{T_L} \tag{51}$$

The maximum power for sequential Carnot cycles coupled to an isothermal heat source and heat sink is then:

$$\dot{W}_{max}=\sum_{i}^{N}\frac{UA_{L,i}}{UA_{L,i}+UA_{H,i}}UA_{H,i}[\sqrt{T_H}-\sqrt{T_L}]^2$$
$$=\frac{UA_L}{UA_L+UA_H}UA_H[\sqrt{T_H}-\sqrt{T_L}]^2 \tag{52}$$

Equations (22), (23), (50), and (51) show that all individual cycles have the same upper and lower temperatures, and they are the same as the upper and lower temperatures resulting from the power optimization of a single cycle. The maximum power, efficiency, and the shape of N-cycles in a sequence are the same as those of a single cycle. For an isothermal heat source and heat sink, the maximum power cycle is the Carnot cycle. This conclusion is consistent with the results shown in Fig. 8, which show that the Brayton cycle always produces less power than the maximum power of the Carnot cycle for the case where the heat source and heat sink are isothermal.

Optimum Power Cycle Coupled to Heat Source and Heat Sink With Finite Thermal Capacitance Rates. When the sequential Carnot cycles are coupled to a heat source and sink with finite thermal capacitance rates, the power from the N-Carnot cycles is given by:

$$\dot{W}=\sum_{i=1}^{N}[\dot{C}_H\epsilon_H(T_{H,in,i}-T_{h,i})-\dot{C}_L\epsilon_L(T_{l,i}-T_{L,in,i})] \tag{53}$$

The shape of the optimum cycle is determined by maximizing $\dot{W}$ with respect to $T_{h,i}$ and $T_{l,i}$ subject to the following constraints:

$$\frac{\dot{C}_H\epsilon_H(T_{H,in,i}-T_{h,i})}{T_{h,i}}-\frac{\dot{C}_L\epsilon_L(T_{l,i}-T_{L,in,i})}{T_{l,i}}=0 \quad (i=1, N) \tag{54}$$

$$T_{H,in,i+1}=T_{H,in,i}-\epsilon_H(T_{H,in,i}-T_{h,i}) \quad (i=1, N-1) \tag{55}$$

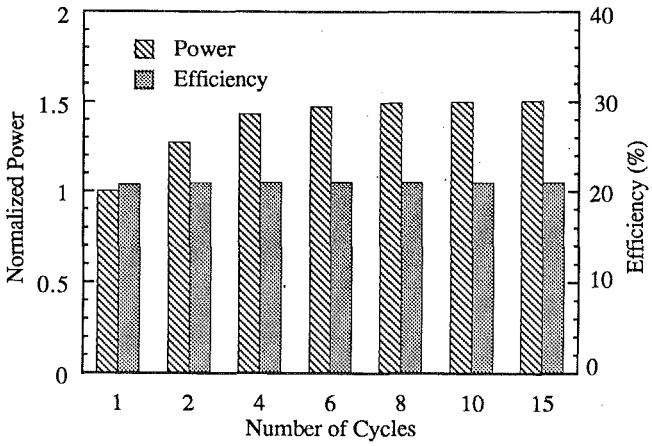

Fig. 12 Maximum power and corresponding efficiency versus the number of Carnot cycles in sequence for $T_{L,in} = 286$ K, $T_{H,in} = 455$, $C_L/C_H = 10$, and $UA_H = UA_L$ ($NTU_H = 10$)

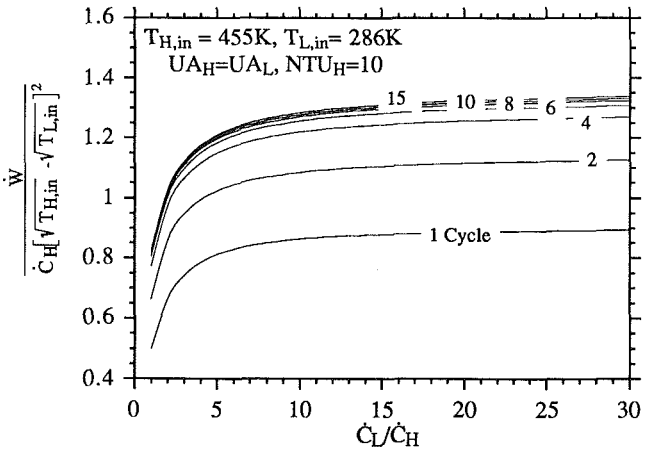

Fig. 13 Variation of maximum power with heat capacitance rate ratio

$$T_{L,in,i-1} = T_{L,in,i} + \epsilon_L (T_{l,i} - T_{L,in,i}) \tag{56}$$

$T_{H,in,i}$ and $T_{L,in,i}$ are the source and sink inlet temperatures for a Carnot cycle in the sequence where $T_{H,in,1}$ and $T_{L,in,N}$ are specified inlet source and sink temperatures. As the cycles in the sequence extract and reject heat, the source temperature decreases and sink temperature increases in the flow direction. $\epsilon_{H,i}$ and $\epsilon_{L,i}$ are the effectivenesses of the hot-side and cold-side heat exchangers of each cycle, which are assumed to be equal in this analysis.

An analytical solution is not apparent for this optimization problem. However, the optimum heat power cycle with finite thermal capacitance rate heat source and heat sink can be determined numerically. Consider a hot fluid stream entering the boiler at 455 K, and a cold fluid stream entering the condenser heat exchanger at 286 K.

The required number of Carnot cycles in sequence that will sufficiently identify the cycle is considered for the case where $NTU_H = 10$ and $\dot{C}_L/\dot{C}_H = 10$. Figure 12 shows the efficiency at maximum power as the number of Carnot cycles in sequence increases from 1 to 15. The efficiency at maximum power is approximately independent of the number of Carnot cycles in the sequence. The efficiency of the optimum heat power cycle is almost the same as the maximum power efficiency of a single Carnot cycle operating between the same external streams (the 1 percent difference noted in this case can be due to the numerical techniques and roundoff error). However, the maximum power increases significantly as the number of Carnot cycles in sequence increases from 1 to 15. The difference between the maximum power obtained from 10 cycles in sequence and 15 cycles in sequence is very small (less that 1 percent),

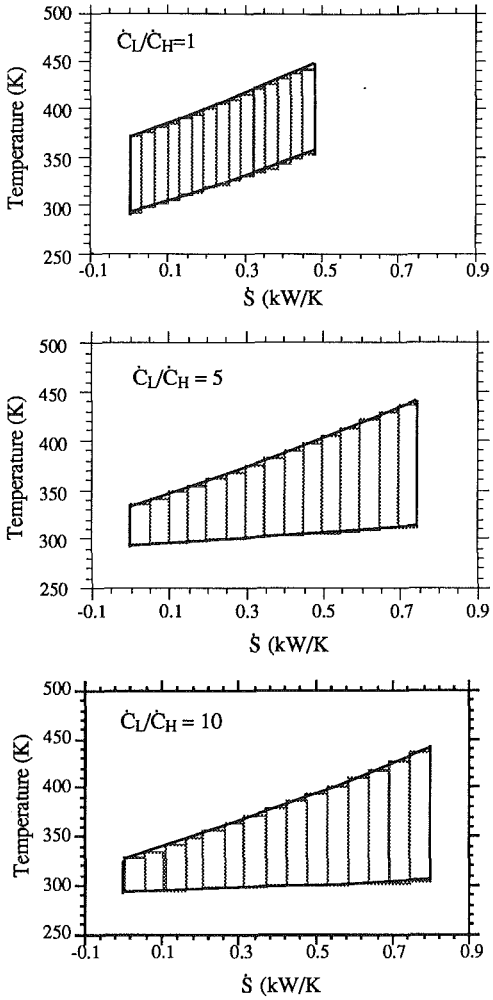

Fig. 14 Variation of the maximum power cycle shape with heat capacitance rate ratio for $T_{L,in} = 286$ K, $T_{H,in} = 455$, and $UA_H = UA_L$ ($NTU_H = 10$)

which indicates that the 15 cycles approximate the optimum heat power cycle.

The effect of thermal capacitance rates ratio ($\dot{C}_L/\dot{C}_H$) on the maximum power for different number of Carnot cycles in sequence is shown in Fig. 13. As the thermal capacitance rate ratio increases, the power output increases rapidly at first and then levels off for thermal capacitance rates ratios greater than 5 approaching an asymptotic limit. However, there is no significant variation in the power output as $\dot{C}_L/\dot{C}_H$ is increased above 10.

Figure 14 shows the shape of the optimum heat power cycles in a T-$\dot{S}$ diagram. The slopes of the heating and cooling processes, as well as the cycle temperatures, vary with the thermal-capacitance rate ratio. Similar graphs can be constructed to show the effects of heat exchanger conductances on the optimum power cycle shape. The shape of the optimum heat power cycles varies from rectangular for infinitely small heat exchangers to triangular for infinitely large heat exchangers.

Conclusions

The optimum power produced by the closed Brayton, Otto, and other familiar cycles can be greater than the optimum power produced by the Carnot cycle for the same working conditions and heat exchanger conductances. The heat power cycle that produces the maximum power for specified boundary conditions provides a useful tool for studying power cycles and forms the basis for making design improvements. The shape of the optimum heat power cycle varies with the external

boundary conditions such as the type of heat source and heat sink, and heat exchanger conductance.

If the heat source and sink have infinite heat capacitance rates (i.e., isothermal), the heat transfer processes for the optimum cycle cycle are isothermal, i.e., the Carnot cycle is the optimum cycle. However, if the heat source and the heat sink have finite heat capacitance rates, the heat transfer processes for the optimum cycle cycle are not isothermal, but rather occur over a range of temperatures. This variable temperature at both the cooling and heating processes can be achieved either by varying the pressure during the phase change of a pure fluid or by keeping the pressure constant during the phase change of a nonazeotropic binary mixture. The thermodynamic advantages of the cycles proposed by Kalina (e.g., Kalina, 1983), which uses ammonia–water as working fluid may be explained in this manner.

For both finite and infinite capacitance rates, the efficiency at maximum power of internally reversible Carnot and Brayton cycles is equal to $1-\sqrt{T_{L,in}/T_{H,in}}$. Moreover, the efficiency of the optimum heat power cycles is found to be well approximated by the same form. Because this efficiency depends only on the inlet temperatures of the heat reservoirs, it can be obtained easily and used as a design tool. In the case of internal irreversibility, the efficiency at maximum power is no longer given by this simple form. Rather it is given by a more complicated form, which depends on how the internal irreversibility is modeled. In this study, a simple model relating the entropy change during heat rejection and heat addition is used. The result is a modification to the efficiency at maximum power, which is found to be equal to or well approximated by $\eta=1-\sqrt{T_{L,in}/\phi T_{H,in}}$, where ϕ is a factor relating the entropy changes during heat rejection and heat addition.

References

Bejan, A., 1988, "Theory of Heat Transfer—Irreversible Power Plants," *Int. J. Heat Mass Transfer*, Vol. 31, No. 6, pp. 1211–1219.

Carnot, S., 1824, *Reflection on the Motive Power of Fire, and on Machines Fitted to Develop That Power*, Bachelier, Paris; also in E. Mendoza, ed., 1960, *Reflections on the Motive Power of Fire and Other Papers on the Second Law of Thermodynamics*, Dover, New York.

Curzon, F. L., and Ahlborn, B., 1975, "Efficiency of a Carnot Engine at Maximum Power Output," *Am. J. Phys.*, Vol. 43, pp. 22–24.

El-Wakil, M. M., 1962, *Nuclear Power Engineering*, McGraw-Hill, New York.

Gordon, J. M., 1988, "On Optimized Solar-Driven Heat Engines," *Solar Energy*, Vol. 40, No. 5, pp. 457–461.

Howe, J. P., 1982, "The Maximum Power, Heat Demand and Efficiency of a Heat Engine Operating in Steady State at Less Than Carnot Efficiency," *Energy*, Vol. 7, No. 4, pp. 401–402.

Kalina, A., 1983, "Combined Cycle and Waste Heat Recovery Power Systems Based on a Novel Thermodynamic Energy Cycle Utilizing Low-Temperature Heat for Power Generation," ASME Paper No. 83-JPGC-GT-3.

Kays, W. M., and London, A. L., 1964, *Compact Heat Exchangers*, McGraw-Hill, New York.

Lee, W. Y., Kim, S. S., and Won, S. H., 1990, "Finite-Time Optimization of a Heat Engine," *Energy*, Vol. 15, No. 11, pp. 979–985.

Leff, H. S., 1987a, "Thermal Efficiency at Maximum Work Output: New Results for Old Heat Engines," *Am. J. Phys.*, Vol. 55, No. 7.

Leff, H. S., 1987b, "Available Work From a Finite Source and Sink: How Effective is a Maxwell's Demon?" *Am. J. Phys.*, Vol. 55, No. 8, pp. 701–705.

Lu, P., 1980, "On Optimum Disposal of Waste Heat," *Energy*, Vol. 5, pp. 993–998.

Ondrechen, M. J., Andresen, B., Mozurkewich, M., and Berry, R. S., 1981, "Maximum Work From a Finite Reservoir by Sequential Carnot Cycles," *Am. J. Phys.*, Vol. 49, No. 7, pp. 681–684.

Ondrechen, M. J., Rubin, M. H., and Band, Y. B., 1983, "The Generalized Carnot Cycle: A Working Fluid Operating in Finite Time Between Finite Heat Sources and Sinks," *J. Chem. Phys.*, Vol. 78, No. 7, pp. 4721–4727.

Rubin, M. H., 1979a, "Optimum Configuration of a Class of Irreversible Heat Engines. I," *Phys. Rev. A*, Vol. 19, No. 3, pp. 1272–1276.

Rubin, M. H., 1979b, "Optimum Configuration of a Class of Irreversible Heat Engines. II," *Phys. Rev. A*, Vol. 19, No. 3, pp. 1277–1289.

Wu, C., 1988, "Power Optimization of a Finite-Time Carnot Heat Engine," *Energy*, Vol. 13, No. 9, pp. 681–687.

Thermal-Hydraulic Analysis of the Fort St. Vrain Modular Vault Dry Store System

S. M. Cho

A. H. Seltzer

Foster Wheeler Energy Corporation,
Livingston, NJ 07039

M. Blackbourn

GEC ALSTHOM Engineering Systems Ltd.,
Leicester, United Kingdom

A passive, natural thermosyphon, air-cooled modular vault dry store (MVDS) system is being constructed for the storage of nuclear spent fuel for the Fort St. Vrain (FSV) Nuclear Power Station. In support of this FSV-MVDS system, thermal-hydraulic design analyses have been performed. The objective of the analyses is to determine flow and temperature distributions within the system and thus to ensure that the maximum fuel element temperatures shall not exceed specified design limit values under various loading and unloading conditions. This paper presents the method of analysis and discusses the resulting thermal-hydraulic characteristics of the MVDS system.

Introduction

The modular vault dry store (MVDS) system provides a secure method of storing nuclear spent fuel in a dry environment. The MVDS system covers the circumstances where fuel, which has already been stored in an existing reactor facility such as a pool for an appropriate period of time, may be required to be further stored for up to several decades before being sent to a permanent storage facility. Therefore the MVDS can be used as a monitored retrieval storage (MRS) or independent spent fuel storage installation (ISFSI).

The schematics of the MVDS and its natural circulation cooling system are shown in Figs. 1 and 2, respectively. The MVDS design can hold irradiated fuel assemblies from both light water and gas-cooled reactors in individual vertical storage tubes retained within a concrete structure forming the storage vault. The vault provides the necessary shielding for the stored fuel and integral air flow ducts for a natural thermal buoyancy cooling system. The decay heat from fuel assemblies warms the air within the vault, and the warmed air within the vault moves upward and passes to the environment via the separate vault outlet ducts. Cooler air is then drawn into the vault and over the outside of the storage tubes to maintain an air flow consistent with the heat load (number of fuel assemblies) within the vault. It is a passive, natural thermosyphon, air-cooled heat exchanger.

The MVDS system is designed to be "modular" so it can be erected and then progressively extended to store any number of fuel assemblies and it can also be expanded in capacity at a later date. The MVDS facility is completely independent from the reactor plant and can be sited wherever it is convenient.

The MVDS concept has been proven in service since 1971 at the Wylfa gas-cooled reactor station in North Wales, United Kingdom. This facility has been expanded twice for a total current storage capacity of over 900 tons. Information on this operating facility may be obtained from Lawson (1967) and Maxwell and Deacon (1979). The first US MVDS storage facility is currently being built for the Fort St. Vrain (FSV) Nuclear Power Station of the Public Service Company of Colorado by Foster Wheeler Energy Corporation of USA and GEC ALSTHOM Engineering Systems Limited of England. The FSV MVDS will store 1482 spent fuel blocks from the reactor core within six vault modules, each module containing 45 storage tubes and each tube containing six stacked spent

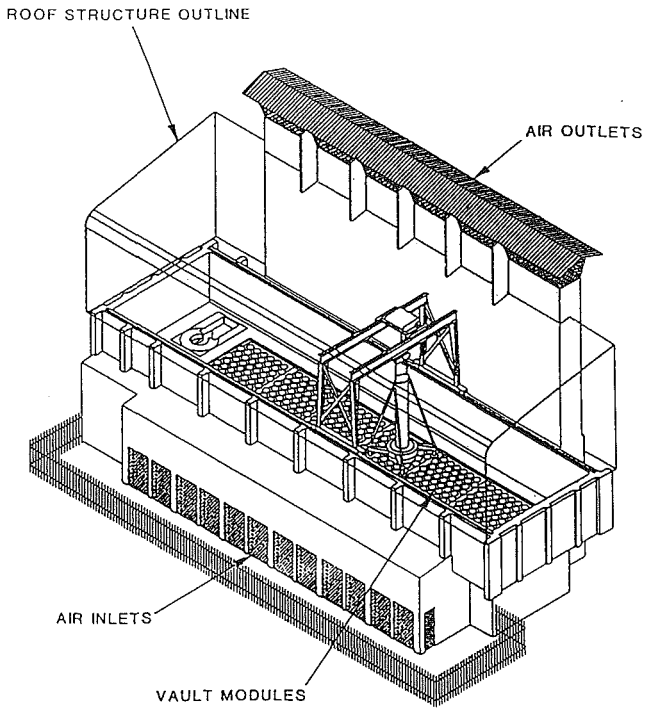

Fig. 1 Fort St. Vrain modular dry store system

Contributed by the Nuclear Engineering Division and presented at the Joint ASME/AIChE National Heat Transfer Conference, Minneapolis, Minnesota, July 28–31, 1991. Manuscript received by the Nuclear Engineering Division December 18, 1990.

fuel elements. The module and storage tube arrangements are schematically shown in Fig. 3. It is designed to comply fully with US Nuclear Regulatory Commission's licensing requirements of 10CFR72 and satisfies the design criteria of ANSI 57.9. It is designed for a lifetime of 40 years. General MVDS design configurations and the FSV MVDS design concept may be found from Blackbourn and Atkinson (1987), Cundill et al. (1986), Deacon (1981), Holt (1990a, 1990b), and Lehr et al. (1990).

This paper presents the method and results of thermal-hydraulic analyses that have been performed in support of the design of the Fort St. Vrain MVDS. The goal of the analyses is to determine flow and temperature distributions within the MVDS and thus to ensure that the maximum fuel element temperatures shall not exceed specified design values. Various fuel loading and unloading conditions and associated thermal-hydraulic characteristics of the MVDS are discussed.

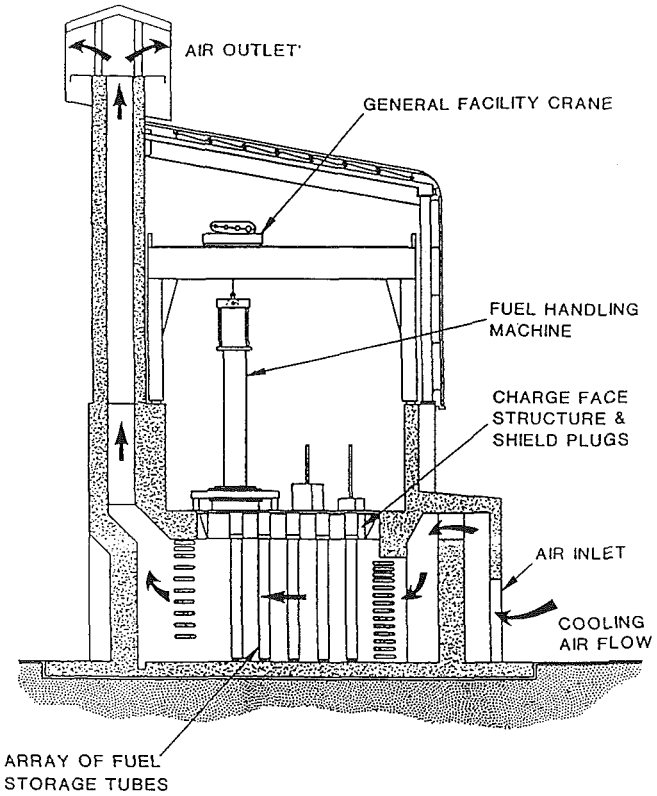

Fig. 2 MVDS cross section (illustrating equipment layout and the natural thermal buoyancy cooling system across the vault)

Thermal Hydraulic Analysis Method

As shown in Fig. 2, the MVDS cooling system consists of, starting from the air inlet: the inlet duct, inlet collimators, shielded storage tubes containing irradiated fuel, outlet collimators, and outlet duct. The inlet and outlet ducts are contoured in a way that provides radiation shielding and prevents any direct impact of outside missiles on the fuel storage tubes. The comb-shaped inlet and outlet collimators provide radiation shielding and also help direct air flow across the storage tube bundle. Air flow is circulated through the MVDS by a buoyant force generated inside the vault as a result of the decay heat released from the spent fuel inside the storage tubes. All the decay heat from the spent fuel is indirectly rejected to the environment by highly reliable passive heat transfer processes. The primary heat rejection from the spent fuel to the storage tubes is by radiation, convection, and conduction. The storage tubes are sealed and provide a secure and reliable containing boundary between the active fuel and the environment. The secondary heat rejection process from the outside of the storage tubes to the environment is produced by a self-regulating natural thermosyphon, buoyancy-driven cooling flow of ambient air over the outside of the storage tubes. In this section, the analysis methods of the primary and secondary heat rejection mechanisms are presented.

Natural Circulation Air Cooling System Thermal Hydraulics. The buoyancy-driven natural circulation air cooling of the spent fuel-containing storage tubes was analyzed using the COMMIX-1B computer code. The COMMIX-1B code is a transient, multidimensional, single-phase computer program

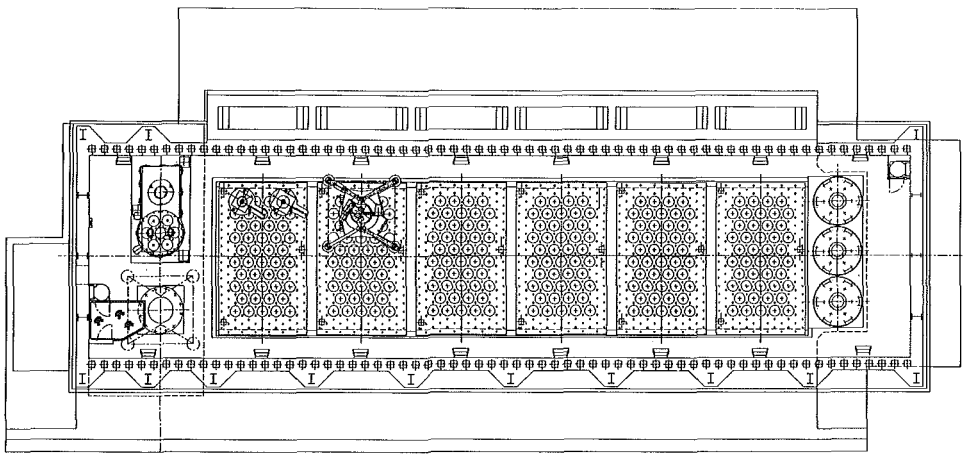

Fig. 3 Fort St. Vrain MVDS module and fuel storage tube arrangements

Nomenclature

F_1, F_2, F_3, F_4 = factors defined in Eq. (1)
G_{max} = maximum mass flux
Gr = Grashof number
K = pressure loss coefficient
N = number of tube rows
Nu = Nusselt number
Re = Reynolds number
Δp = pressure drop or loss
ρ = fluid density

Subscripts

b = bulk fluid condition
n = nth tube row
r = refer to Eq. (2)

for thermal-hydraulic analysis of nuclear reactor components. Although developed for nuclear reactor applications, the code is general enough to be used to analyze a wide range of processes in engineering systems. COMMIX-1B solves the conservation equations of mass, momentum, and energy as a boundary-value problem in space and an initial-value problem in time. The staggered grid system is used to describe the field variables at the center of a cell and flow variables at the surface of a cell.

The COMMIX-1B code uses the "new" porous-media formulation method via local volume averaging. This formulation utilizes the concepts of volume porosity, directional surface permeability (directional because surface permeability is an anisotropic vector quantity), distributed resistance, and distributed heat source or sink. (Volume porosity is defined as the ratio of the volume occupied by the fluid in a control volume to the total control volume. Surface permeability is defined as the ratio of area allowed for fluid flow through a control surface to the total control surface area.) The use of the new porous-media formulation methodology makes the COMMIX-1B code suitable for the analysis of the MVDS natural cooling system. Details of COMMIX-1B development and verifications may be found from ANL (1985) and Sha (1982).

A two-dimensional (Cartesian) COMMIX-1B model was constructed of the Fort St. Vrain MVDS cooling system, which is shown schematically in Fig. 2. One dry store module (with internal cooling passage dimensions of 4.9 m height, 3.4 m width, 7.2 m length) containing 45 fuel storage tubes is modeled. There are 10 rows of storage tubes in this module: five tubes in odd-numbered rows and four tubes in even-numbered rows. Each storage tube is made of carbon steel and is 448 mm in diameter and 4.9 m long, and the tubes are arranged in a triangular pattern. The model includes the inlet fence, the inlet screen and 180 deg turn, the inlet collimators, the fuel storage tube array, the outlet collimators, the outlet plenum, the outlet duct, and the outlet screen. Also included in the model, although not acting as an active air flow path, are the charge hall and its roof.

The grid system of the model consists of 29 nodes in the horizontal direction and 45 nodes in the vertical direction, and starts and ends suitably far away from the MVDS in the quiescent air. There are 1014 total computational cells, 12 irregular surface elements, and 2329 total surface elements. An irregular surface is a surface that is not coincident with any Cartesian grid planes and is modeled with the appropriate surface angles and volumetric and surface porosities. Thus, although these surfaces may look "crude" in the output plots, they are modeled as truly inclined surfaces. The grid system around the MVDS is shown in Fig. 4.

A one-equation turbulence model was used with wall function corrections to both the turbulent kinetic energy equation and the momentum equations for cells adjacent to solid walls (COMMIX-1B, 1985). (Note that the COMMIX-1B code has an option of using a two-equation turbulence model, but this more complex model was not warranted in the present study since its use would not improve the accuracy of the results much, due to the fact that the flow field inside the vault is determined primarily by the distributed flow resistances in the tube array.) An implicit time advancement using a successive-overrelaxation type iteration scheme was employed.

The heat transfer correlations used in the storage tube bundle array are summarized below and are evaluated at the lower bound of the uncertainty band:

Crossflow (*Engineering Sciences Data, 1973*)

$$\mathrm{Nu}_n = \mathrm{Nu}_r F_1 F_2 F_3 F_4 \tag{1}$$

where Nu_n = Nusselt number for nth tube row

$$\mathrm{Nu}_r = a\, Re_b^m\, \mathrm{Pr}_b^{0.34} \tag{2}$$

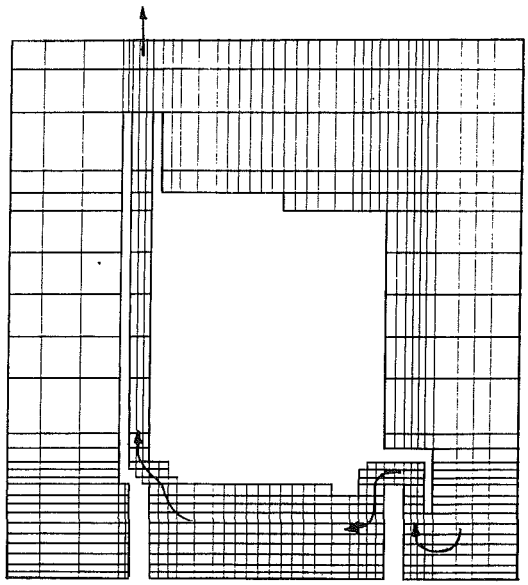

Fig. 4 COMMIX-1B model grid system around MVDS (the actual model extends 4.5 times farther in the horizontal direction and 2.8 times farther in the vertical direction)

a, m = constants as a function of Re_b
Re_b = fluid Reynolds number at bulk fluid condition
Pr_b = fluid Prandtl number at bulk fluid condition
F_1 = fluid property variation factor
F_2 = bank depth factor
F_3 = tube inclination factor
F_4 = nth tube row correction factor

Axial (*Vertical*) *Flow*

$$\mathrm{Nu} = 0.023\ \mathrm{Re}^{0.8}\ \mathrm{Pr}^{1/3} \tag{3}$$

where the characteristic length dimension in the Nusselt (Nu) and Reynolds (Re) numbers is the hydraulic diameter of the tube bundle in the axial flow direction.

Natural Convection Flow

$$\mathrm{Nu} = 0.13\ (\mathrm{GrPr})^{1/3} \tag{4}$$

where Gr is the Grashof number.

Both the forced convection and natural convection heat transfer coefficients are calculated for all heat transfer surfaces, and the larger of the natural convection value and the forced convection value is used in the COMMIX-1B analysis. All surfaces other than the fuel storage tubes are assumed to be thermally insulated.

The two major pressure drop correlations used for the tube bundle crossflow and the inlet and outlet collimators are as follows:

Tube Bundle Crossflow (*Engineering Sciences Data, 1974*)

$$\Delta p = KNG_{\max}^2/(2\rho) \tag{5}$$

where

Δp = pressure drop
N = number of tube rows in crossflow direction
$G_{\max}$ = maximum mass flux between tubes
ρ = fluid density
K = loss coefficient, which depends on row number, fluid property variation, flow bypass, tube inclination, and tube surface roughness, and is given by Engineering Sciences Data (1974).

Inlet and Outlet Collimators (*Idelchik, 1986*)

$$\Delta p = KG_{\max}^2/(2\rho) \tag{6}$$

where K is the pressure loss coefficient, which depends upon the geometry of collimators, including the open flow area, and is given by Idelchik (1986).

Table 1 Summary of thermal-hydraulic analysis results under various vault operating conditions (Air inlet temperature is 38.9°C (102°F) for all cases. All cases, except case 2, are loaded with average fuel.)

Case	Air flow, kg/s	Bulk air outlet temperature, °C	Maximum local air temperature, °C	Maximum tube temperature, °C	Maximum fuel element temperature, °C
1 Fully loaded vault	3.91	44.8	47.3	63.2	83.8
2 Last row only loaded with peak fuel	2.07	40.6	41.1	71.6	105.0
3 Half-full vault	3.16	42.4	44.4	63.3	83.9
4 Quarter-full vault	2.73	41.3	42.9	62.2	82.9
5 Last row only	1.86	40.0	40.5	59.7	80.5

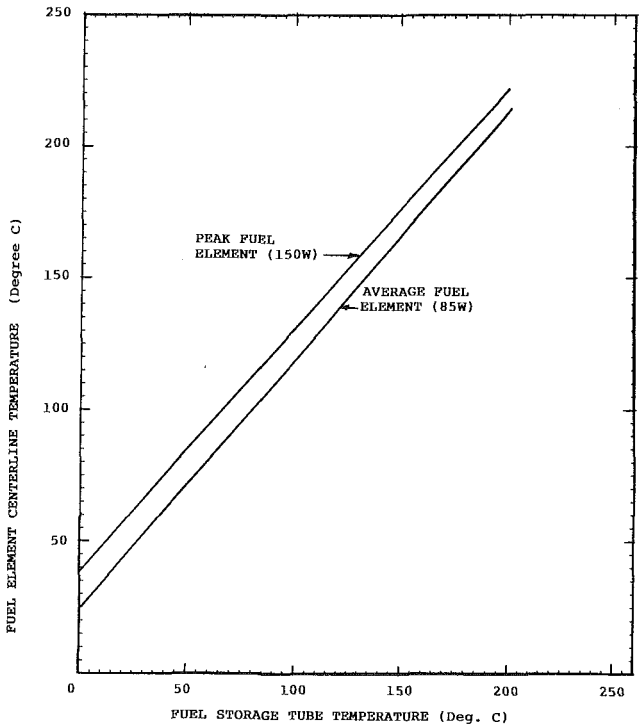

Fig. 5 Fuel element centerline temperature as a function of fuel storage tube temperature

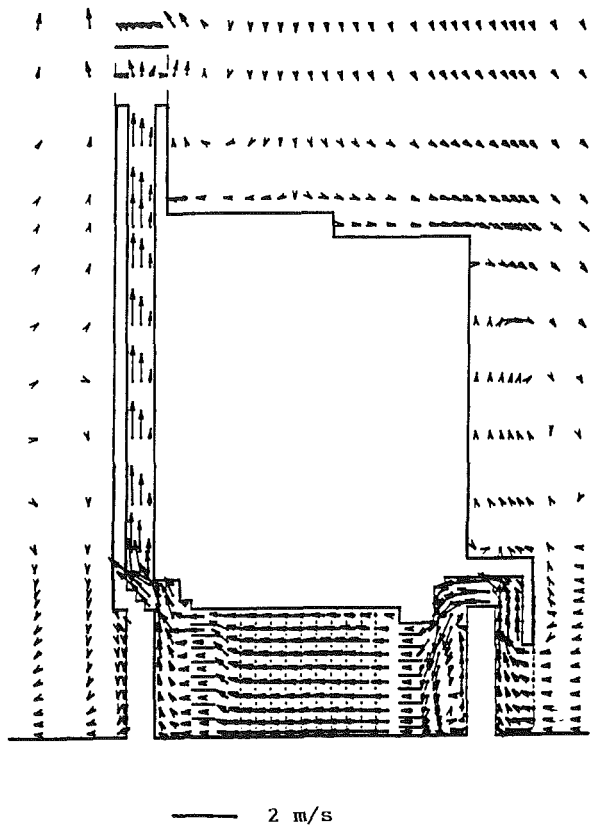

Fig. 6 Air flow distribution under fully loaded vault conditions (case 1)

All other pressure drop correlations are standard ones for friction, area contraction/expansion, and flow turning (SAE, 1989).

Internal Heat Transfer From the Fuel Element to the Storage Tube. The FSV High-Temperature Gas-Cooled Reactor fuel element comprises an hexagonal graphite brick, typically 0.4 m across flats and 0.8 m long. The element contains a large number of uniformly distributed fuel and coolant channels. The fuel decay heat is primarily generated within these fuel channels and is conducted radially through the graphite matrix to the outer surface, from which the heat is transferred by radiation and gaseous conduction/convection to the inside surface of the surrounding storage tube.

The fuel is modeled as a cylinder, with the same cross-sectional area as the hexagonal element and with a uniform volumetric heat source. The element is assumed to be concentric within the storage tube and the heat transfer processes are modeled using classical analytical methods (McAdams, 1954; Eckert and Drake, 1972). The calculation of the fuel element temperatures for two heat outputs and a range of storage tube temperatures is carried out using the SINDA/FLUINT (1986) computer code. The variation of the fuel element centerline temperature as a function of the storage tube temperature is presented in Fig. 5. Results are given for an average fuel element heat output of 85 W (510 W per six-element storage tube) and a peak rated element of 150 W (900 W per storage tube). The storage tube temperatures predicted by the COMMIX-1B analysis are used directly with Fig. 5 to estimate the fuel centerline temperatures. No benefit has been claimed for axial conduction heat transfer in either the storage tube or the fuel element.

Results and Discussion

Five vault loading and unloading cases have been analyzed. In all cases, the model boundary conditions are still air at atmospheric pressure and at a temperature of 38.9°C (102°F) far away from the MVDS. The use of a still air condition is based on the results of wind tunnel tests (Blackbourn and Atkinson, 1987) using a 1/200 scale model of the external building geometry, which demonstrated that a positive wind-induced pressure gradient always exists between the inlet and outlet ducts of each module with wind of any speed from any direction. This positive engineered feature ensures that the vault buoyancy-driven air flow is always enhanced by wind effects, thereby reducing fuel storage tube and fuel temperatures relative to their calm day values. A uniform heat flux profile for the decay heat release from the fuel assembly is assumed along the length of the fuel storage tube. The results of the analyses are summarized in Table 1 and discussed in the following sections.

Case 1: Fully Loaded Vault With Average Fuel. This case simulates a vault module completely full with the 45 fuel stor-

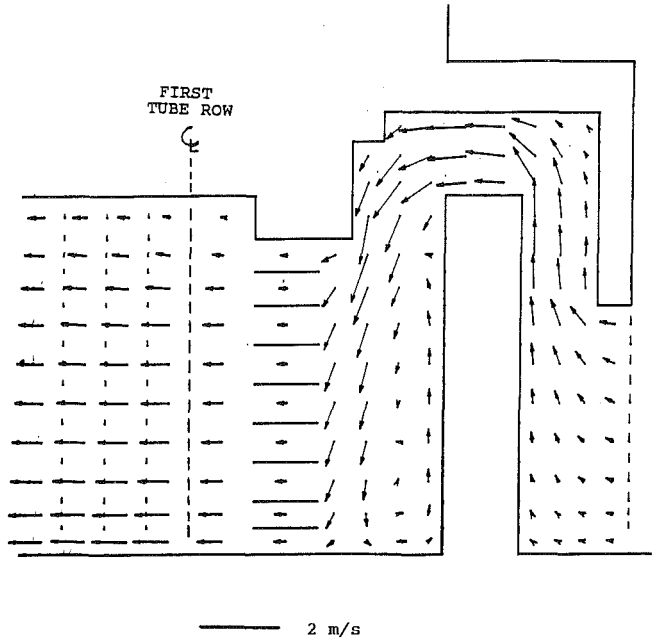

Fig. 7 Air flow distribution at the vault inlet under fully loaded vault conditions (case 1)

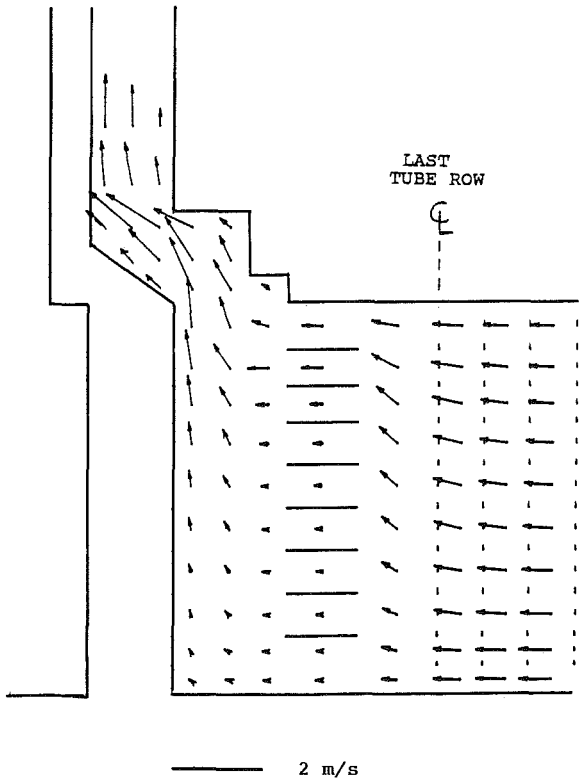

Fig. 8 Air flow distribution at the vault outlet under fully loaded vault conditions (case 1)

age tubes, each containing six 600-day decay average rated fuel elements. The total module heat load is 22,950 W and each individual fuel storage tube heat load is 510 W (six 85 W elements within one storge tube). Figure 6 shows the air flow distribution throughout the vault cooling circuit, with distribution details at the inlet and at the outlet shown in Figs. 7 and 8, respectively. The air velocity vectors show a generally uniform state of flow through the tube bundle.

Figure 9 presents an isotherm plot of the air temperature distribution within the storge tube array. The temperature con-

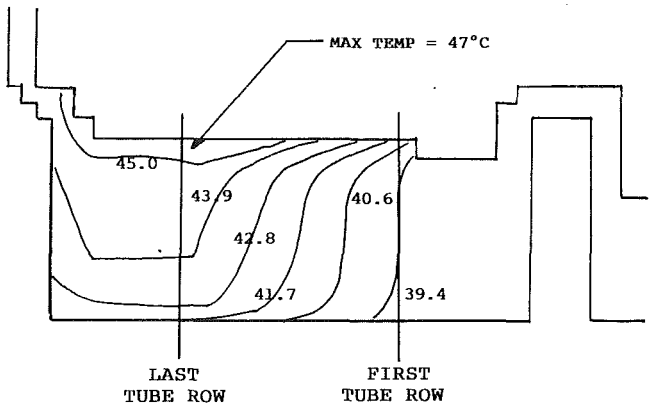

Fig. 9 Air temperature distribution (in °C) in the storage tube array under fully loaded vault conditions (case 1)

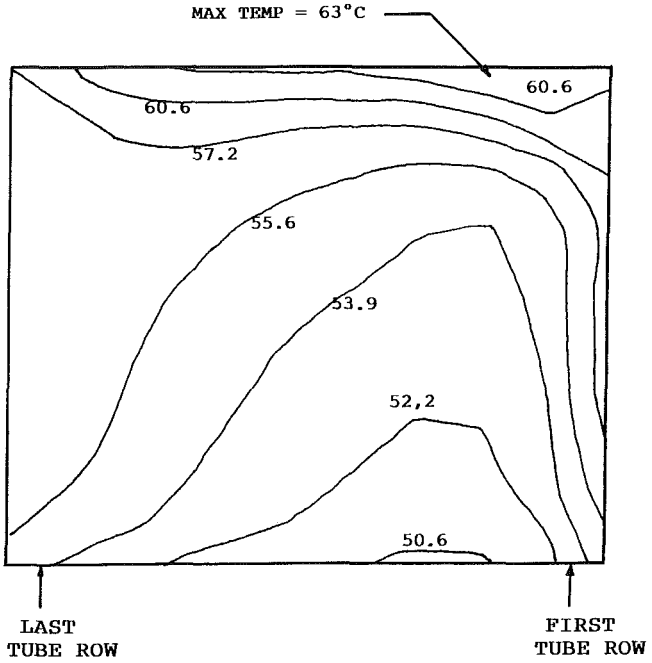

Fig. 10 Storage tube temperature distribution (in °C) under fully loaded vault conditions (case 1)

tours show a gradual increase in air temperature as it passes over the tube bundle and, as expected, the upper region of the vault is slightly warmer than the lower region. The bulk air temperature increases from 38.9°C at the inlet to 44.8°C at the outlet. The maximum local air temperature is predicted at the top of the ninth row and is 47.3°C. The extreme range of air temperature is small, amounting to 8.3°C.

Figure 10 presents the fuel storage tube temperature distribution throughout the ten rows of storage tubes in the array. The contours reflect the reduced convective heat transfer coefficient that exists on the first few tube rows. Turbulence created by the first few rows of storage tubes causes a progressive increase in the heat transfer coefficient (effect of factor F_2 in Eq. (1)). The maximum fuel storage tube temperature of 63.2°C occurs at the top of the third row due to both the heat transfer effect described previously and the slight reduction of flow at the top of the inlet end of the tube bundle resulting from the 180 deg turn of flow passage at the vault inlet (Fig. 7). In reality, the temperatures of the tubes in rows 1 and 10, together with all those tubes adjacent to the vault side walls, will be reduced due to direct radiation heat transfer to the collimators and the surrounding concrete walls. (This radiation heat transfer has not been modeled in the present study.)

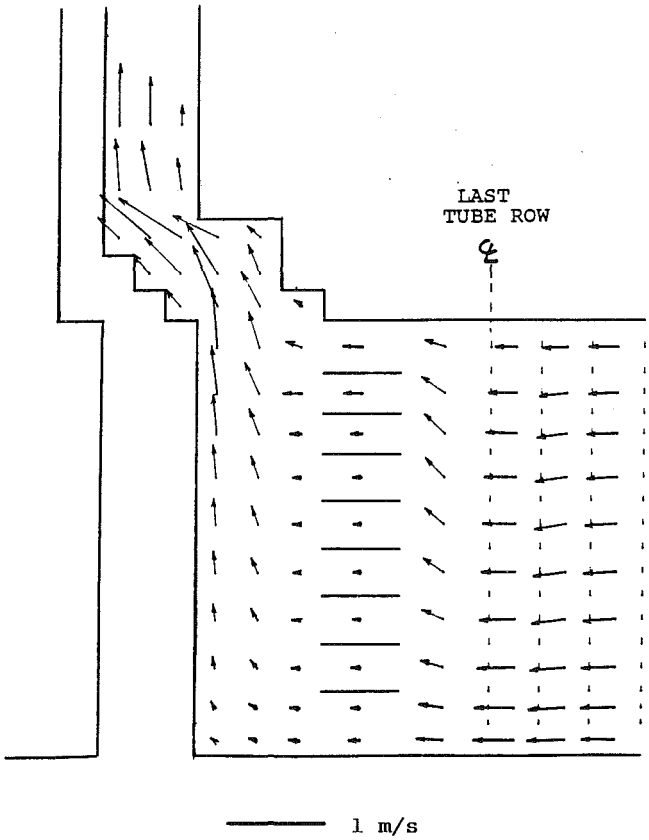

Fig. 11 Air flow distribution in the vault outlet region under partially loaded vault conditions (case 2: peak rated fuel elements in row 10)

The extreme range of predicted fuel storage tube temperatures is small, amounting to only 13°C, which demonstrates that all the fuel storage tubes are well cooled in all parts of the vault. The maximum fuel element centerline temperature of 83.8°C occurs in the top elements of the third tube row. The minimum fuel element temperature of 71.5°C occurs in some of the bottom elements. The extreme range of fuel element temperatures is small, only 12°C. Neither the COMMIX-1B analysis nor the fuel element temperature assessment takes any account of axial conduction in either the fuel elements or the storage tubes. Axial conduction will in practice significantly reduce axial temperature gradients in the system, particularly in the region of the higher temperatures.

Case 2: Partially Loaded Vault With Peak Rated Fuel Elements. This case simulates a hypothetical and extreme, partially loaded situation in which 600-day decay peak rated fuel elements are loaded into the four storage tubes of the tenth and last row (900 W per storage tank with six 150 W elements). All the other storage tubes are empty of fuel.

Figure 11 presents the detail of the air flow distribution in the vicinity of the last tube row. The air velocity vectors show the uniformity of the cooling flow over the last tube row and that the air cooling system flow rate is significant and well established even at this low heat load. The air flow rate of 2.07 kg/s (shown in Table 1) represents 53 percent of the full vault value (Case 1), whereas the heat load is only 16 percent of the full vault value.

Figure 12 presents the temperature distribution over the height of the loaded fuel storage tube. It shows that the air cooling flow effectiveness improves slightly toward the bottom of the vault. The maximum storage tube temperature for this peak rated fuel is 71.6°C at the top of the storage tube and the corresponding maximum fuel element centerline temperature is 105.0°C. The air temperature rise across the vault is only 1.7°C (see Table 1).

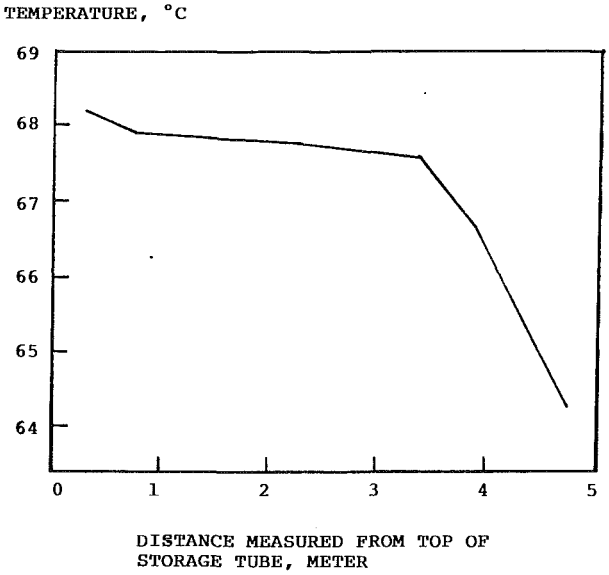

Fig. 12 Axial distribution of storage tube temperature for row 10 under partially loaded vault conditions (case 2)

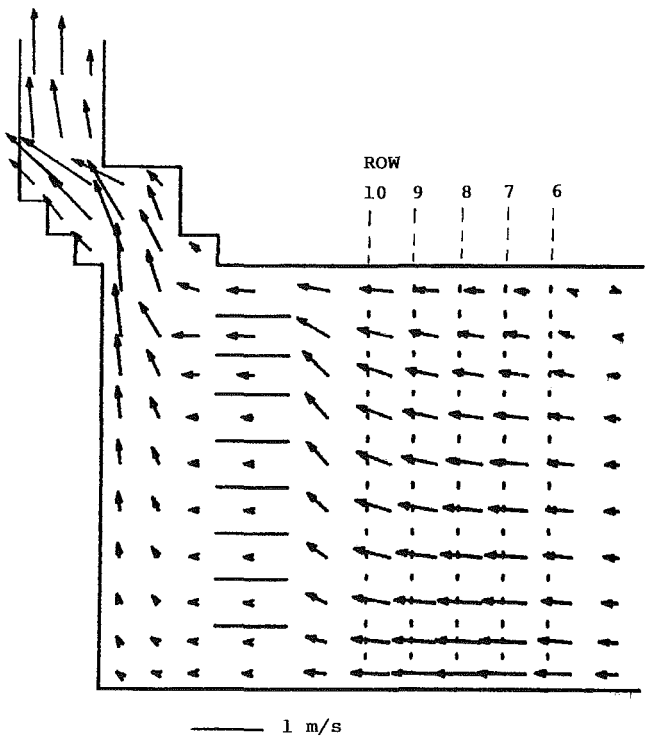

Fig. 13 Air flow distribution in the vault outlet region under half-full vault conditions (case 3)

Case 3: Vault Unloading—Half-Full State. This case simulates a possible unloading situation in which one half of the complement of fuel storage tubes, those in rows 1–5, have been discharged from a vault. In this case, rows 6–10 are occupied with storage tubes containing average fuel (510 W per storage tube). The case could also represent an alternative vault loading pattern in which the operation started with an empty vault and was progressively loaded with fuel elements in storage tubes. In this scenario, the air flow distribution for storage tube rows 6–10 and the corresponding storage tube wall temperature distribution are shown in Figs. 13 and 14, respectively. For this half-loaded vault situation, the air cooling flow rate is 81 percent of the full vault value. The results are summarized in Table 1. The maximum tube wall temperature is predicted at

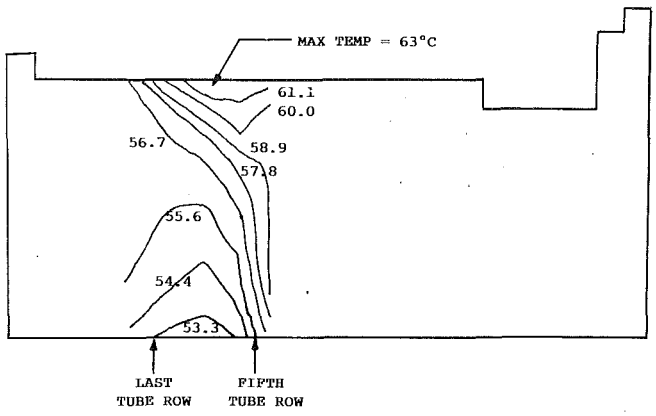

Fig. 14 Storage tube temperature distribution (in °C) under half-full vault conditions (case 3)

the top of row 8 and is 63.3°C. The overall air temperature rise across the half-loaded module is 3.5°C. The maximum centerline temperature for the average rated fuel elements in the vault is 83.9°C.

Case 4: Vault Unloading—Quarter-Full State. This case simulates a similar situation to that described in Case 3 in which only the fuel storage tubes of rows 8–10 are occupied with average fuel (510 W per storage tank). The results are summarized in Table 1 and indicate that the overall air temperature rise across the vault is 2.4°C and the maximum fuel storage tube temperature is 62.2°C occurring at the top of row 9. The maximum fuel element centerline temperature for the average rated fuel is 82.9°C.

Case 5: Vault Unloading—Single-Row State. This case is an extension of Cases 3 and 4 and represents the extreme situation in which a vault contains only a single row of fuel storage tubes; all other possible storage locations are empty. The case assumes that the tenth and last row only is occupied with average rated fuel elements (510 W per storage tube). The results are summarized in Table 1 and indicate a 1.1°C overall air temperature rise and that the maximum storage tube temperature is 59.7°C and occurs at the top of the row. The total vault heat load for this situation is only 2.04 kW, representing 9 percent of the vault full heat load. The air cooling flow rate for this case is 1.86 kg/s, however, representing 48 percent of the full vault cooling flow rate. The maximum fuel element centerline temperature is 80.5°C and occurs in the top element in the storage tube.

Summary of Results

The range of cases presented demonstrates that the MVDS buoyancy-driven air cooling system, or thermosyphon, provides an efficient and reliable cooling over the full range of vault loading/unloading conditions. The thermosyphon system is designed for the maximum vault heat load condition and the results demonstrate that all other conditions are enveloped by this case. The analysis shows that, as the vault heat load reduces, the reduction in the cooling flow rate is always less marked and that even with an extremely small vault heat load, the thermosyphon flow rate is substantial.

The MVDS thermosyphon flow rate is designed to give a small air temperature rise and low storage tube and fuel temperatures. This is the case for all types of fuel stored in an MVDS. Due to the small temperature increase in the cooling air and the design of the collimator features, the distribution of air flow throughout the vault tube array is more or less uniform and the resulting storage tube temperatures are all acceptable for all operating conditions.

The variation in storage tube temperatures, both axially and row-by-row, is very small with consequent small variations in the fuel element temperatures. The maximum temperature of an average rated fuel element is 84°C and that of the peak rated fuel element is 105°C. These temperatures are significantly below the maximum permissible value of 400°C in an air environment. (Similar margins are also available for light water reactor fuel storage situations.)

Conclusions

Thermal hydraulic analyses were conducted for a modular vault dry store system designed for the nuclear spent fuel in the Fort St. Vrain Nuclear Power Station. An extreme range of fuel loading and unloading conditions was studied and the results of the study indicate that the FSV-MVDS buoyancy-driven air cooling system is highly effective. For the heat load range of 9 to 100 percent of design load, the cooling air flow rate remains high, providing typically 48 to 100 percent of the full load value. The overall air temperature increase across the vault is very small with a maximum value of 5.9°C (Case 1). The air velocity distribution in the storage tube array is fairly uniform, resulting in a more or less even temperature distribution for the cooling air and consequently for the storage tube wall. The maximum fuel element temperature is 84°C for average rated fuel elements and 105°C for peak rated fuel elements. These temperatures are well below the maximum permissible temperature of 400°C, imposed by oxidation of the graphite element in an air environment.

The extremely favorable results obtained above are believed to be due to several well-engineered design features of the MVDS systems, which include low-elevation air inlet opening, tall air outlet duct, and horizontal inlet and outlet comb-shaped collimators.

Acknowledgments

This paper is based on work performed by the joint Foster Wheeler-GEC ALSTHOM project team for the design of the Fort. St. Vrain MVDS for the Public Service Company of Colorado.

References

Argonne National Laboratory Publication, 1985, "COMMIX-1B: A Three-Dimensional Transient Single-Phase Computer Program for Thermal Hydraulic Analysis of Single and Multicomponent Systems, Vol. I: Equations and Numerics, Vol. II: User's Manual," Report No. ANL-85-42, NUREG/CR-4348.

Blackbourn, M., and Atkinson, D. C., 1987, "An Open Loop Air Thermosyphon Cooling System for Irradiated Nuclear Fuel in a Modular Vault Dry Store," presented at the ASME Winter Annual Meeting, Boston, MA.

Cundill, B. R., Wheeler, D. J., and Barratt, R. O., 1986, "The Addition of Air-Cooled Dry Vault Storage Facilities to Operating Nuclear Plants," presented at the Third International Spent Fuel Storage Technology Symposium/Workshop, Seattle, WA, Apr. 8–10.

Deacon, D., 1981, "The Long-Term Dry Storage of Irradiated Oxide Fuel and Vitrified Waste," *Nuclear Engineering International*, Aug., pp. 32–36.

Eckert, E. R. G., and Drake, M., 1972, *Analysis of Heat and Mass Transfer*, McGraw-Hill, New York.

Engineering Sciences Data Unit Publication, 1973, "Convective Heat Transfer During Crossflow of Fluids Over Plain Tube Banks," Item No. 73031, London.

Engineering Sciences Data Unit Publication, 1974, "Pressure Loss During Crossflow of Fluids With Heat Transfer Over Plain Tube Banks Without Baffles," Item No. 74040, London.

Holt, A. J., 1990a, "A Modular Vault Dry Storage Facility for Fort St. Vrain," *Nuclear Engineering International*, Oct., pp. 105–107.

Holt, A. J., 1990b, "Recent Developments in Dry Vault Storage of Irradiated Fuel," presented at the International Conference on Spent Fuel Storage Safety, Engineering and Environmental Aspects, IAEA, Vienna, Oct.

Idelchik, I. E., 1986, *Handbook of Hydraulic Resistance*, Hemisphere Publishing Corporation, Washington, DC.

Lawson, D., 1967, "Dry Storage of Irradiated Fuel," *Nuclear Engineering*, Aug., pp. 604–605.

Lehr, M., Ealing, C. J., and Agarwal, B. K., 1990, "Application of Modular

Vault Dry Storage to Public Service of Colorado—Fort St. Vrain," presented at the Spent Fuel Management Seminar III, sponsored by the Institute of Nuclear Materials Management, Washington, DC, Jan. 17–19.

Maxwell, E. O., and Deacon, D., 1979, "Dry Storage of Irradiated Magnox Fuel in Air," *Nuclear Engineering International*, May, pp. 71–75.

McAdams, W. H., 1954, *Heat Transmission*, McGraw-Hill, New York.

Sha, W. T., 1982, "Analytical Thermal Hydraulic Research," Argonne National Laboratory Report, Aug.

SINDA '85/FLUINT, 1986, "System Improved Numerical Differencing Analyzer and Fluid Integrator," Version 2.2., MCT-86-594.

SAE, 1989, *Aerospace Applied Thermodynamics Manual*, Society of Automotive Engineers, New York.

Compressor Coating Effects on Gas Turbine Engine Performance

J. D. MacLeod
Research Officer,
National Research Council,
Ottawa, Ontario, K1A 0R6

J. C. G. Laflamme
421 Tactical Fighter Squadron,
Canadian Forces Europe,
CFB Baden-Soellingen,
Federal Republic of Germany

In an attempt to increase the time between maintenance actions and to improve performance retention of turboprop engines installed in transport and maritime patrol aircraft, the Canadian Department of National Defence is evaluating an erosion and corrosion-resistant blade coating, for use on compressors. As coatings could appreciably alter engine performance by virtue of their application thickness and surface quality, the National Research Council of Canada was asked to quantify any performance changes that could occur. A project was initiated, utilizing a new Allison T56 turboprop engine, to assess not only the performance changes resulting from the coating, but also those from dismantling and reassembling the compressor, since the compressor must be completely disassembled to apply the coating. This paper describes the project objectives, the experimental installation, and the measured effects of the coating application on compressor performance. Performance variations due to compressor rebuilds on both engine and compressor characteristics are discussed. As the performance changes were small, a rigorous measurement uncertainty analysis is included. The coating application process and the affected overhaul procedures are examined. The results of the pre- and postcoating compressor testing are presented, with a discussion of the impact on engine performance.

Background

In 1983, the Canadian Department of National Defence expressed serious concern over the rapidly escalating cost of operation and maintenance of aircraft gas turbine engines. The components of major concern were compressor and turbine blades and vanes. The increasing rate of rejection of these items during overhaul prompted a reassessment of the time between overhaul for certain engine types.

The blades and vanes of gas turbine engines are susceptible to deterioration as a result of erosion and corrosion. The deterioration, in the form of increased surface roughness, loss of material, and alteration of aerodynamic profile, shows up in terms of reduced stall margin, poorer fuel economy, and increased operating temperatures.

Recently, advances have been made in the state of the art in blade-coating technologies. In addition to offering erosion and corrosion protection, these new "super-smooth" coatings are claimed, by their manufacturers, to offer significant aerodynamic performance improvements. Such modern blade coatings have not previously been qualified in T56 engines. Since smoothness effects are a function of blade Reynolds number, which is dependent on engine size and speed, claims based on evaluations on other engines were not applicable. The Engine Laboratory of the National Research Council of Canada (NRCC) was tasked to evaluate the effect of coatings on engine performance and efficiency, and make recommendations for subsequent widespread use of coatings for operational use on T56 engines.

Since the compressor must be disassembled in order to be coated, it was deemed necessary to isolate the effect on performance of the rebuild from that of the coating. Therefore, a program of three consecutive rebuilds was established to quantify the portion of any performance shift that was not attributable to the coating itself. Results, previously presented in [1, 2], show that the effects of the compressor rebuild, although random, can be significant. The parameters most affected include compressor efficiency, airflow, compressor and combustor pressure ratios, and fuel flow.

Experimental Installation

To assess properly the effects of coating the compressor on the performance of a gas turbine engine, a sophisticated test setup with specialized instrumentation was required. A description of the engine, and instrumentation used for this assessment, is included to illustrate the complexity of this project.

Engine Description

The test vehicle for this coating study was an Allison T56-A14LFE single-spool turboprop engine from a CP-140 Aurora patrol aircraft. This engine was an excellent candidate for this study because it has no variable geometry or transient bleed valve operation that might affect the repeatability of the engine data. The T56 engine has a 14-stage compressor, with bleed valves that are only open below the idle speed, a six-can combustor, and a four-stage turbine. The single shaft is coupled to a reduction gearbox mounted forward of the compressor. For the NRCC tests, power was transmitted through the gearbox to a flywheel and a Froude waterbrake dynamometer. A schematic diagram of the engine test configuration is shown in Fig. 1.

The engine control is one of a constant speed design using

Contributed by the International Gas Turbine Institute and presented at the 35th International Gas Turbine and Aeroengine Congress and Exposition, Brussels, Belgium, June 11–14, 1990. Manuscript received at ASME Headquarters December 1990.

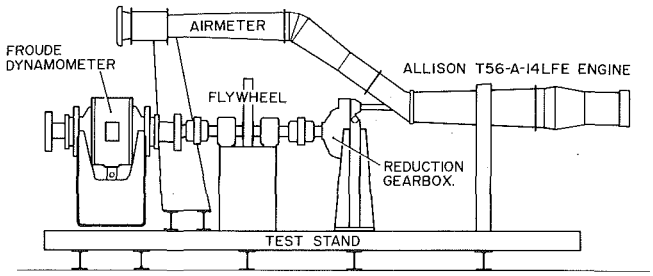

Fig. 1 Schematic of T56 turboprop engine on test stand

a governor to maintain a constant rotor speed of 13820 rpm. Power is controlled by setting the turbine inlet temperature with the power lever angle.

Instrumentation

Instrumentation used on the T56 was divided into two categories: external and internal. The external instrumentation included a high Mach number (0.8) airmeter in front of the engine, compressor inlet pressure and temperature rakes, a tailpipe airmeter mounted after the turbine, vibration sensors on the engine carcass, and turbine-type fuel flowmeters. The high-velocity airmeter facilitated accurate flow measurement because of the large difference between the local total and static pressures. A diffuser mounted behind the airmeter reduced the airspeed to normal engine inlet conditions. The internal instrumentation consisted of total temperature and pressure probes in every stage of the compressor, as well as compressor discharge and turbine inlet pressure and temperature rakes. With this degree of instrumentation, it was possible to monitor not only the condition of the overall engine, but also the performance of its major components, and the individual compressor stages.

The data were recorded using a NEFF 620 data acquisition system controlled by a DEC PDP 11/34 computer. Measurement uncertainty estimates were available for the complete instrumentation package. The complete methodology for fuel flow measurement has been documented in [3].

Summary of Testing, Rebuild, and Coating Procedures

In an attempt to isolate the effects of the compressor coating by monitoring small thermodynamic performance changes, a highly structured test plan was required. To achieve this goal, a test sequence was established that would best suit the requirements of the coating study, as well as the rebuild study, based on the knowledge of how the coating and rebuilding were to be performed.

Test Sequence

To establish the effects of coating the compressor on overall engine performance, it was first important to establish the effects of rebuilding the compressor. A comparison of three rebuilds was chosen. A larger sample would have been preferred; however, there were significant cost and time constraints on the project. The T56 engine chosen for the testing had no flight hours, in order to develop a legitimate "as-new" baseline. Baseline testing of the engine was performed to establish the "as-received" condition of the engine. Performance signatures of the overall engine and its individual components were then quantified.

In the experimental program, the engine was run at a fixed aerodynamically corrected rotational speed to provide a common basis for comparison, i.e., the mechanical speed of the engine was adjusted using the dynamometer, as a function of the ambient temperature. The procedure used for each test run established a series of increasing power settings, for a given corrected rotor speed. At each power setting, the engine was allowed to stabilize for five minutes, then two sets of data were recorded. Typically, up to six power settings (12 data points) were recorded for each test.

After the baseline testing was completed, the engine was sent to the overhaul contractor to be disassembled and rebuilt following normal procedures. On return to NRCC, the engine was retested using the same procedures used in the baseline tests. This process was repeated for a second and a third rebuild. Following the third rebuild testing, the engine was returned to the overhaul contractor for rebuilding and coating of the compressor. The testing after the third rebuild became the reference condition for the postcoating testing.

Rebuild Procedure

The rebuild procedure used for this project consisted of a disassembly, inspection, and reassembly of the compressor section only. The disassembly procedure entailed the removal of the turbine and combustor modules, leaving only the compressor. The compressor casing was then removed from the rotor, and the stator vanes were detached from the casing. The rotor disks were unstacked and all the individual blades were removed. During removal, each blade was numbered, so that it could be returned to its original position upon reassembly. After disassembly, each piece underwent a petroleum solvent wash followed by an inspection to insure that no parts were damaged. Measurements of critical dimensions such as blade clearances, vane axial clearances, and rotor balance condition were recorded before disassembly and after reassembly. Upon reassembly of the compressor case, the stator vane axial clearances were set. The rotor blades were replaced in the same numbered order, and their balance checked. The entire compressor was then mated with the combustor and turbine modules, and a functional test was performed. The engine was then returned to NRCC for testing.

Coating Procedure

The coating chosen for this study was titanium nitride (TiN). Before the application process could begin, the compressor blades and vanes were rigorously cleaned. The vanes were chemically stripped of their nickel–cadmium flashing, and their corrugated seals were removed. Both the blades and vanes were shot-peened using glass beads, followed by a petroleum solvent wash.

The TiN coating was applied using a plasma vapor deposition (PVD) process, where the individual pieces are sprayed and heated in a heated vacuum chamber. The average thickness of the coating was approximately 6–8 μm. Upon completion of the coating process, the corrugated seals were replaced on the vanes, and the compressor was reassembled.

Data Presentation

Data recorded during a test were stored in basic engineering units so that observers could check the data quality visually as the test progressed. After a test was completed, the data were normalized, and used to calculate performance parameters such as pressure and temperature ratios, corrected air and fuel flow, etc. These parameters were then curve-fitted to quadratic equations, using a least-squares method. The independent variable for curve-fitting engine data was corrected turbine inlet temperature. Comparisons between various test runs were then made using the curve-fitted values of each parameter. All data presented in this study were taken at 100 percent corrected rotor speed, or 13,820 rpm. For curve-fit comparisons, the reference value used for the corrected turbine inlet temperature was 2200 R (1220 K).

Effects of Ambient Conditions

The NRCC test cell has no provision for controlling the

ambient inlet air temperature. The engine was therefore operated over a wide range of temperatures experienced over the Canadian seasons. All performance data were corrected to standard day reference conditions for comparison. Previous experience at NRCC [4, 5] and other test facilities [6] suggests that the normal standard day corrections do not ensure that the data will collapse to a single curve. Since temperature lapse rate data were not available for all of the parameters being considered in this study, test data presented here were all recorded at similar ambient temperature conditions.

The use of the long inlet duct on the T56 causes a significant pressure loss and distortion at the compressor face. This pressure loss simulates an altitude of nearly 500 m and a ram pressure ratio (compressor inlet total pressure divided by the static pressure at the exhaust exit plane) of approximately 0.97. The effect of ram pressure ratio on output power was accounted for using the manufacturer's procedures [7].

Since humidity affects the thermodynamic properties of the engine cycle, the atmospheric conditions were monitored to avoid condensation in the inlet air stream and minimize performance corrections [8].

Test Results

For this study, 14 performance parameters were chosen to describe the condition of the engine for each power setting. The selection of appropriate parameters was made to analyze the performance of the overall engine and of its individual components, namely the compressor, combustor, and turbine. To assess the compressor behavior, isentropic efficiency, corrected airflow, corrected speed, and compressor pressure and temperature ratios were examined. For combustor performance, combustor pressure and temperature ratios were analyzed. Isentropic efficiency was chosen as a suitable parameter to describe the performance of the turbine. Corrected fuel flow, corrected output power, and specific fuel consumption were selected to define overall engine behavior, as were engine temperature and pressure ratios.

Since only the compressor was disassembled and coated during this project, the strongest emphasis was in monitoring changes in the compressor performance and in turn, the effects on overall engine performance. Combustor and turbine performance were included to see whether a change in compressor operation affects downstream components.

Data Quality

The quality of the data for each test was determined by the back-to-back repeatability of each of the performance parameters. This was done by comparing the deviations of the individual datapoints from the curve-fitted quadratic equations derived from the data. A mean value of the deviation of the data from its curve was used to estimate the repeatability of each parameter within each test.

To establish the quality of the data recorded (within a rebuild or coating sequence), an analysis of the run-to-run repeatability was performed. This analysis consisted of comparing curve-fitted test data recorded under the same ambient conditions during the same test sequence. A mean deviation between the curve-fits for each of the performance parameters was then used to define the repeatability values within each test sequence.

An estimate of the overall repeatability of each of the parameters was accomplished by adding the back-to-back and run-to-run repeatabilities. With these estimated repeatability values, a true comparison of the rebuild and coating effects could be carried out.

Back-to-Back Repeatability

For each power setting during a test, two complete scans were recorded by the data acquisition system. To assess the back-to-back repeatability, the values of these recorded points were compared to the curve-fit-generated points at a specified turbine inlet temperature. This procedure gave an indication of the steadiness of the engine/data system operation, and the "goodness" of the curve-fit to the actual data points. These deviations are shown in Table 1 for the rebuild study and the coating test series.

Table 1 Back-to-back repeatability

PARAMETER	DEVIATION (%)		EXPECTED RANDOM ERROR (%)
	PRE-COATING	POST-COATING	
Compressor efficiency	0.06	0.07	0.03
Corrected airflow	0.06	0.08	0.10
Corrected fuel flow	0.12	0.05	0.12
Corrected output power	0.16	0.24	1.10
Specific fuel consumption	0.35	0.29	1.10
Corrected speed	0.03	0.02	0.01
Compressor pressure ratio	0.05	0.11	0.06
Compressure temperature ratio	0.02	0.03	0.00
Turbine efficiency	0.20	0.50	0.02
Combustor temperature ratio	0.02	0.03	0.00
Combustor pressure ratio	0.05	0.09	0.08
Engine temperature ratio	0.18	0.18	0.00
Engine pressure ratio	0.22	0.18	0.03
Corrected torque	0.17	0.27	1.10

Reference: Corrected speed = 13820 RPM
Corrected Turbine Inlet Temperature = 2200 ^{o}R (1220 K)

The corrected output power and specific fuel consumption reveal a noticeable scatter, as do the turbine efficiency, engine pressure ratio, and corrected torque. All other parameters indicate very small deviations from their respective curves.

The deviation in the corrected output power and specific fuel consumption are to be expected because each of these parameters was calculated from two or three measured quantities. The scatter in the turbine efficiency is also expected because it is calculated using an approximate value for the specific heat ratio within the turbine. In addition the turbine efficiency is an inverse parabolic function, which may not be conducive to a least-squares curve-fit.

Run-to-Run Repeatability

Within each series of tests (rebuild or coating), at least three complete runs were recorded for each corrected rotor speed condition. Having established the agreement of the test data with the generated curve-fits, the next step was to determine how well these curves collapsed within each test series. To evaluate the run-to-run repeatability of the data within each test series, the values of curve-fitted data were compared from at least two runs taken at similar ambient conditions. These deviations are shown in Table 2 for the rebuild testing and the coating testing.

Close examination of the run-to-run repeatability results showed that most parameters were reasonably reproducible, with the exception of corrected output power and specific fuel consumption. Certain parameters, such as turbine efficiency and engine pressure ratio, had better run-to-run repeatability than back-to-back repeatability. In the case of turbine efficiency, this anomaly presumably results from difficulties in representing the uniquely shaped efficiency function with a quadratic equation.

Combined Repeatability

Before a comparison of the coating effects could be made, it was necessary to estimate the overall or combined repeatability of the data from the pre- and postcoating test series. Since the same equipment, instrumentation suite, data system,

Table 2 Run-to-run repeatability

PARAMETER	DEVIATION (%) PRE-COATING	POST-COATING	EXPECTED RANDOM ERROR (%)
Compressor efficiency	0.16	0.12	0.03
Corrected airflow	0.17	0.12	0.10
Corrected fuel flow	0.22	0.05	0.12
Corrected output power	0.45	0.12	1.10
Specific fuel consumption	0.54	0.17	1.10
Corrected speed	0.11	0.14	0.01
Compressor pressure ratio	0.05	0.17	0.06
Compressure temperature ratio	0.08	0.11	0.00
Turbine efficiency	0.16	0.14	0.02
Combustor temperature ratio	0.06	0.01	0.00
Combustor pressure ratio	0.05	0.12	0.08
Engine temperature ratio	0.14	0.14	0.00
Engine pressure ratio	0.07	0.02	0.03
Corrected torque	0.45	0.14	1.10

Reference: Corrected speed = 13820 RPM
Corrected Turbine Inlet Temperature = 2200 ^{o}R (1220 K)

Table 3 Coating effects

PARAMETER	OVERALL REPEATABILITY (%)	DEVIATION (%)	UNCERTAINTY (%)
Compressor efficiency	0.41	-0.20	0.87
Corrected airflow	0.43	-1.00	0.27
Corrected fuel flow	0.44	+0.23	0.43
Corrected output power	0.97	+0.38	1.42
Specific fuel consumption	1.35	-0.15	1.52
Corrected speed	0.30	-0.10	0.13
Compressor pressure ratio	0.38	-0.86	0.25
Compressure temperature ratio	0.24	-0.17	0.40
Turbine efficiency	1.00	-0.65	0.90
Combustor temperature ratio	0.12	+0.18	0.49
Combustor pressure ratio	0.31	+0.72	0.35
Engine temperature ratio	0.64	+0.39	0.40
Engine pressure ratio	0.49	-0.43	0.12
Corrected torque	1.03	+0.63	1.41

Reference: Corrected speed = 13820 RPM
Corrected Turbine Inlet Temperature = 2200 ^{o}R (1220 K)

and facility were used for each test series, it was unlikely that many of the measurement bias errors would have changed. Thus the population of observed measurements taken at the same environmental conditions for the coated engine test series were combined to form an overall datum with a defined data scatter. If when compared to the data taken under similar environmental conditions for the uncoated engine testing, there was a shift outside the scatter band established during the rebuild study, then a performance shift, caused by the coating process, would be deemed to have occurred.

A statistical approach using the methods described by Abernethy [9] was used to calculate bias and precision errors, and the measurement uncertainty for this experiment. These precision results are shown in Tables 1 and 2 as expected random error. This information was compared to a more basic method using the observed repeatabilities. To accomplish this, a worst case scenario was assumed. In other words, it was assumed that both the back-to-back and run-to-run repeatabilities were acting in the same direction within each test series, and opposing each other between pre- and postcoating testing. Therefore, the overall repeatability would be the sum of all run-to-run and back-to-back repeatabilities. Thus, the method chosen to define the overall repeatabilities always overestimates the more usual statistical value, such as the root-sum-square method. A complete list of the overall repeatabilities for each of the parameters is given in Table 3.

In general, the quality of the test data for the pre- and postcoating tests appeared to be very good, with the possible exception of output power. Overall, the test data recorded for the coating study were considered to be of sufficiently good quality to be used for a practical comparison.

Comparison of Coating Data

Having established the overall repeatabilities of the performance parameters selected for the coating evaluation, the comparison of the pre- and postcoating tests was carried out. The observed shifts in the various performance parameters are given in Table 3. Several of these shifts are shown graphically in Figs. 2-4.

Coating Results

To assess the various effects of the coating, the engine and its individual components were considered separately. The effects on compressor performance were noticed in the corrected airflow (Fig. 2), which showed a decrease of 1.0 percent from the precoating tests. This decrease was more than double the

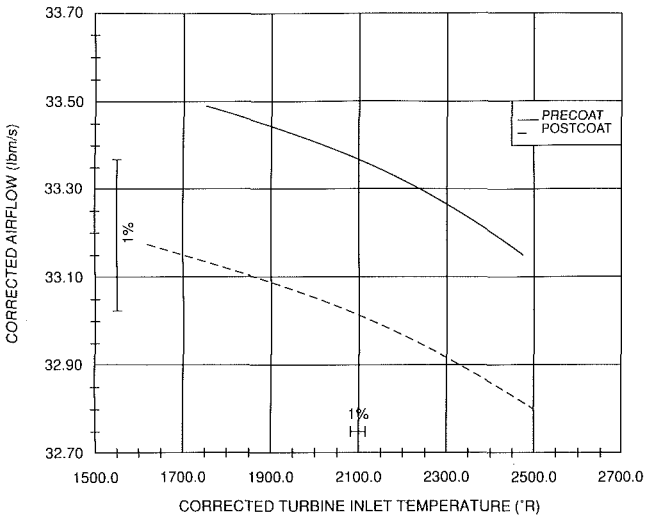

Fig. 2 Corrected airflow versus corrected turbine inlet temperature

pessimistic repeatability of the measured parameter. The compressor pressure ratio (Fig. 3) showed a decrease of 0.86 percent, which was also much larger than the repeatability. The compressor efficiency and compressor temperature ratio did not indicate any significant shifts.

The corrected speed for the pre- and postcoating tests was within 0.1 percent of the target value of 13,820 rpm.

The combustor pressure ratio (Fig. 4) increased by 0.72 percent, which is more than twice the overall repeatability for that parameter. This was expected since the rebuild study [1, 2] had indicated a strong relationship between the exit conditions of the compressor and the combustor pressure losses. The effects on the combustor temperature ratio and the turbine efficiency were negligible.

Concerning the overall engine performance, the corrected fuel flow increased by only 0.23 percent, which is less than the projected repeatability. Shifts in the corrected torque and corrected output power were within the overall repeatability band. The engine temperature and pressure ratios were also unaffected.

Discussion of Coating Results

The results of the performance evaluation of the coats were compared assuming the overall repeatability was the worst combination of all of the back-to-back and run-to-run re-

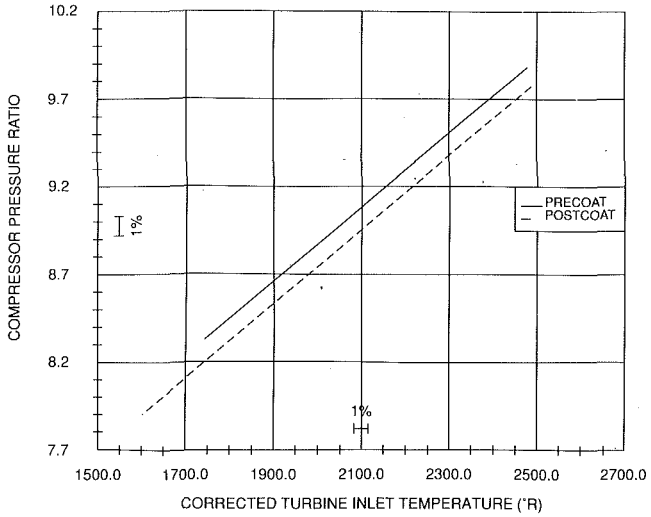

Fig. 3 Compressor pressure ratio versus corrected turbine inlet temperature

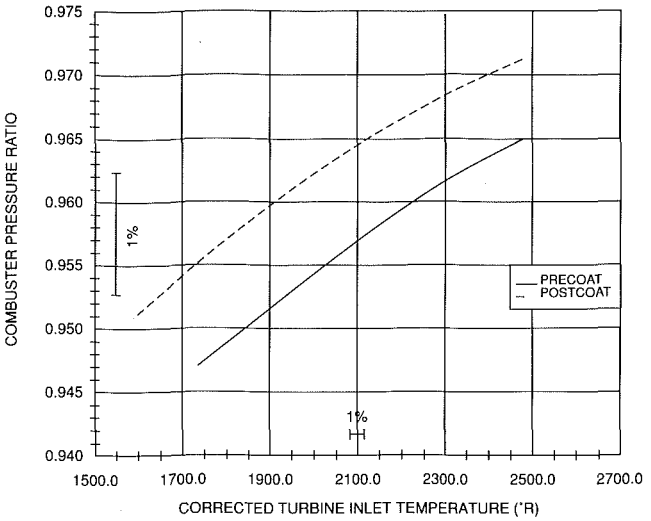

Fig. 4 Combustor pressure ratio versus corrected turbine inlet temperature

peatabilities. A comparison (Table 1) of the back-to-back repeatability to the expected random error shows very close agreement on most parameters, with the exception of torque. The run-to-run repeatability was shown (Table 2) to be slightly greater than the expected random error, indicating some portion of the bias error should be included. On most parameters, the overall repeatability was found to be more pessimistic than the estimated uncertainties (Table 3) calculated using the methods described by Abernathy [9].

The actual cause for the observed shifts in the performance parameters is open for speculation. The results of the rebuild study [1, 2] indicated a close relationship between the blade tip clearances and performance shifts. During the coating and rebuild process, changes in blade tip clearances were measured. A comparison of these clearance changes shows that 10 of 14 compressor stages experienced a decrease in blade tip clearance. This very closely approximates the situation during the first rebuild, where 13 of 14 stages had decreased tip clearances. However, the postcoating testing showed different performance shifts altogether. For example, for the first rebuild the corrected airflow increased 0.77 percent; for the coated compressor, the airflow decreased 1.0 percent. Similarly, compressor pressure ratio and combustor pressure ratio increased during the first rebuild, as opposed to decreasing after coating. This would suggest that the effects of the coating more than counteracted the effects of the rebuild.

The coating itself has no influence on the blade tip clearances in the compressor; however, the aerodynamic behavior around leading and trailing edges on the blades and vanes may be affected by the buildup of coating material in these areas. Shifts in aerodynamic profiles around the leading edge could decrease compressor performance.

Conclusions

The results of the coating study have indicated that the measured performance shifts are less than or equal to the effects of rebuilding the compressor alone. However, the coating results did suggest that the source of the performance change may be different, i.e., leading edge aerodynamic changes instead of blade tip clearance changes.

The most significant effects of the coating are on parameters such as corrected airflow, compressor pressure ratio, and combustor pressure ratio. Whether or not the extent of the effects of coating the compressor have been shown is unknown. A much larger statistical sample would be required to determine the limits of the performance effects.

To the users of coated engine parts, the performance parameters of most concern are output power and specific fuel consumption. The repeatabilities in these parameters are much larger than the observed performance shifts. Therefore, it is unlikely that the effects of the coating would be detected during field use.

Recommendations

It is recommended that field testing of coated compressors be carried out to evaluate the durability of the coating, and to trend the performance retention over the overhaul life of the engine compared to uncoated compressors.

References

1 MacLeod, J. D., and Laflamme, J. C. G., "The Effects of a Compressor Rebuild on Gas Turbine Engine Performance: Final Results," AGARD CP (in preparation), 1989.

2 MacLeod, J. D., and Laflamme, J. C. G., "The Effects of a Compressor Rebuild on Gas Turbine Engine Performance," AGARD CP-448-26, 1988.

3 Grabe, W., "Fuel Flow Measurement in Gas Turbine Testing," National Research Council of Canada, TR-ENG-001, 1988.

4 MacLeod, J. D., "Effect of Inlet Temperature Variation on Gas Turbine Engine Performance," National Research Council of Canada, LM-ENG-007, 1987.

5 Jarvo, J., and Muir, D. E., "Ambient Temperature Effects on Gas Turbine Performance," GasTOPS Report GTL-19-31.2-TR.1, 1989.

6 Greco, L., and Gordon, S., "Allison T56-A-14 Engine—Official Sea Level Low and High Temperature, and Altitude Performance Tests," NAEC-AEL-1836, 1966.

7 *T56-A-14LFE Overhaul Manual*, Vol. I, C-14-33-000/MP-001, 1983.

8 Grabe, W., and Bird, J. W., "Humidity Effects on Gas Turbine Performance," National Research Council of Canada, TR-ENG-003, 1989.

9 Abernethy, R. B., and Thompson, J. W., *Handbook of Uncertainty in Gas Turbine Measurements*, AEDC-TR-73-5, 1973.

A Comparison of Analog and Digital Controls for Rotor Dynamic Vibration Reduction Through Active Magnetic Bearings

R. D. Williams

F. J. Keith
Department of Electrical Engineering.

P. E. Allaire
Department of Mechanical and Aerospace Engineering.

University of Virginia,
Charlottesville, VA 22903

Active magnetic bearings are implemented using analog and digital controllers to achieve vibration reduction for multimass flexible rotors. Various models are developed for the rotor-bearing system, and the first three critical speeds (resonant frequencies) are shown to be unaffected by inclusion of the higher order shaft dynamics in the model. Higher order rotor-bearing models reveal the presence of "shaft modes," the excitation of which is a function of the position of the magnetic bearing proximity probe (these modes are effectively damped by the flexible coupling employed in the test apparatus). Rotor dynamic behavior is investigated for various analog and digital controllers. Rotor response in the presence of proportional-derivative control is similar for both analog and digital control. Higher order digital control algorithms (second derivative and integral) affect the rotor response in a frequency dependent manner: Second derivative feedback is effective at reducing third mode vibration, and integral feedback, while rejecting any steady-state rotor position error, slightly accentuates the vibration at the first critical speed. Increasing the sampling rate of the digital controller has a similar effect to increasing the amount of second derivative feedback employed.

1 Introduction

Significant improvements have been made in many of the components present in rotating machinery over the past few decades. Advances in rotor dynamics and materials technology have allowed machine designers to push equipment such as turbines, compressors, and engines to speeds previously unattainable. In addition, many modern designs specify thinner, less rigid shafts to reduce weight and to increase design flexibility. These advances in machine design have necessiated the development of improved bearings capable of supporting these new high-speed flexible rotors.

Advances in bearing design have generally kept pace with the demands of the new machines. Fluid-film bearings such as the tilting-pad continue to support many difficult rotors. Also, much progress has been made in the past five to ten years on a very different and promising device for handling a variety of rotating machinery problems: the magnetic bearing.

All types of magnetic bearings support and control rotors or other loads through contact-free electromagnetic forces. For rotating machinery, the rotor is suspended and stabilized within a ring of electromagnets whose coil currents are actively controlled. Many variations on the basic design are possible, but all designs eliminate contact between the rotor and the stator under normal operating conditions. Also, because the electromagnets are open loop unstable, all designs require external electronic control to regulate the electromagnetic forces acting on the bearing.

In addition to reducing operational costs and friction losses, magnetic bearings permit active control of the bearing's dynamic characteristics. As these characteristics are strictly a function of an external control algorithm, they can be changed at will and can be made to adapt to changes in the operating conditions of the machine. The wide range of possible dynamic characteristics achievable with a magnetic bearing facilitate the placement of the critical operating speeds of a particular machine, and the magnetic bearing could be optimized for operation at several different speeds by merely changing the control system parameters.

It should be obvious that the controller is fundamental in the design of a magnetic bearing system. This paper presents the results of tests performed to compare analog and digital controls for a radial magnetic bearing. The bearing has an eight-pole layout as illustrated in Fig. 1, and two such bearings are used to support a small, flexible shaft test rotor as shown in Fig. 2. Analog control designs for this particular apparatus have been previously reported [1]. This paper will show the performance of the bearing under the control of a nonideal analog controller. This performance will be compared with that of a simple digital controller. The flexibility and sampling rate limitations of the digital controller will then be explored as additions are made to the basic control algorithm.

Contributed by the International Gas Turbine Institute for publication in the JOURNAL OF ENGINEERING FOR GAS TURBINES AND POWER. Manuscript received by the International Gas Turbine Institute June 1989.

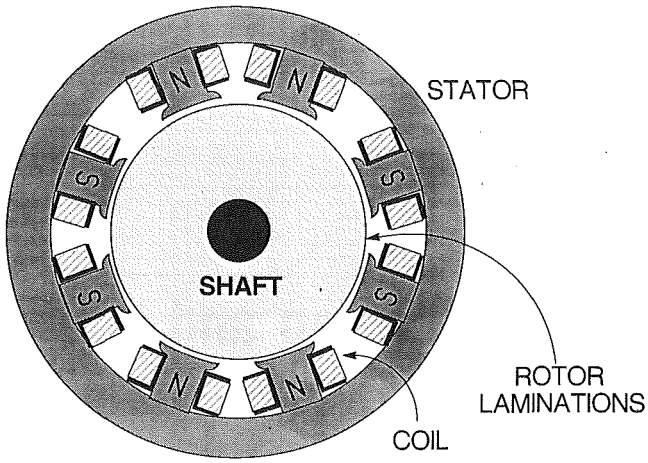

Fig. 1 Cross-sectional view of a typical eight-pole magnetic bearing

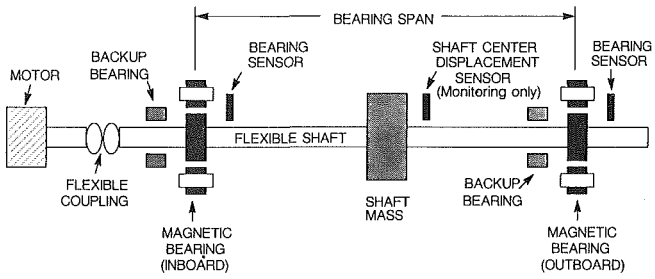

Fig. 2 Experimental rotor

Several researchers have presented results demonstrating the viability of proportional-derivative algorithms for controlling active magnetic bearings [1, 3, 14, and others]. A PD controller was implemented using the same apparatus presented here [19], and results of the previous work are summarized in Section 4.3. In this paper, however, the flexibility of a digitally controlled magnetic bearing is further demonstrated with the implementation of additional, more complex algorithms. In addition, the effect of controller sampling rate on bearing performance, and hence rotor dynamic response, is investigated.

2 Previous Work

Vibration reduction in rotating machinery has received much attention in the literature over the past ten to twenty years. In particular, the idea of using active feedback to control the vibration of a rotating shaft has been pursued by many people. It has been shown that for a single mass rotor on rigid supports, proportional feedback control can increase the critical speed (resonant frequency) of the system while reducing the damping ratio. Also, derivative feedback control can reduce vibration amplitudes and flatten the response peaks at critical speeds [2]. This work was extended to rotors with flexible supports with the control forces exerted at the bearing locations instead of at the rotor mass location, and the results were shown to be similar [3]. The concept of actively controlling conventional bearings has also been investigated and confirmed to be a viable approach for reducing rotor vibrations [4].

Magnetic bearings and dampers are very useful for controlling rotor vibration. The dynamic response effects of a magnetic damper on a rotor supported by convectional bearings have been studied [5]. Also, there have been several studies of the characteristics of systems employing active magnetic bearings to support flexible rotors [6, 7].

The control systems used with active magnetic bearings have received significant attention in the literature, with work reported in both theoretical investigations and experimental testing. State-space control approaches have been pursed with an emphasis placed upon eigenvalue assignment through state feedback [8]. Reinig and Desrochers [9] compare schemes that accommodate unbalance force disturbances in rotating systems: One scheme reduces rotor motion at the bearing to zero at the cost of high bearing forces, and the other allows large rotor orbits at the bearings so that the bearing force is zero. Humphris et al. [1] have investigated the stiffness and damping properties of a magnetic journal bearing as functions of two control algorithms; it was shown that varying amounts of position and velocity feedback affected the stiffness and damping characteristics of the bearing respectively. Hisatani et al. [10] compared analog and digital control designs for single-axis control of a nonrotating rotor and found that simple, fast digital algorithms tended to perform better for their application than slower, more complex ones. Reduced-order control designs were proposed and tested by Salm [11], and system stability is shown to be guaranteed in the presence of observation spillover if certain bearing/position probe collocation requirements are met (spillover is discussed in depth by Balas [12]). The controllers were implemented on independent MC68000 microprocessors. Carmichael et al. [13] compared analog and digital controllers for a single-axis magnetic suspension; the digital control was realized with an 8085 microprocessor. Digital control algorithms were also investigated by Scudiere et al. [14] with a proportional-derivative scheme, which gave an exponential weighing to previous input data points. It was shown that heavily weighting the previous samples gave a smooth but slowly responding output signal while light weighting of the previous samples yielded quick output responses to input changes, but the responses were considerably less damped.

Industrial and scientific applications of active magnetic bearings are becoming greater in number. A 1979 *IEEE Spectrum* article [15] describes several pieces of rotating machinery that include magnetic bearings. In particular, power losses in magnetic bearings are shown to be about two orders of magnitude less than the losses for hydrodynamic bearings when compared for a compressor with a 1000 kg shaft. Magnetic bearings have been successfully employed in cryogenerators [16] and for controlling momentum wheels in satellites [17]. It can be seen from these examples that the magnetic bearing has many potential applications. The advantages of low frictional losses and the ability to operate in a process fluid make the magnetic bearing a viable solution to a variety of engineering problems.

3 A Multimass Rotor

Our multimass rotor, as depicted in Fig. 2, has an infinite number of degrees of freedom (DOFs) as a result of its continuously distributed mass and its continuously flexible nature. The rotor/bearing system must be accurately modeled to permit proper design of the bearing components and controls. To make analysis of the rotor finite-dimensional, it is divided into segments, and finite-element techniques are applied to the segmented elements to generate an equivalent model, which represents the continuous system as lumped point masses interconnected by massless springs (the springs represent the stiffness, or alternately the flexibility of the rotor shaft). The number of DOFs retained in the equivalent system is a function of how much information and complexity is desired in the reduced-order model. For example, subsequent discussions of the mode shapes of this rotor are based on an 18-station (17-segment) model of the rotor while a three-station model is used to generate the transfer functions used for root locus evaluation of system behavior. It will be shown that the first three critical speeds (resonant frequencies) predicted by these two models are very nearly the same. This is shown in Table 1. Thus, we only use the higher order 18-station model when the additional information it provides is needed.

Table 1 Undamped critical speeds from analysis program

Mode	18 Translational DOF's 3 Rotational DOF's	3 Translational DOF's 3 Rotational DOF's	3 Translational DOF's 0 Rotational DOF's
1	1720 RPM	1724 RPM	1725 RPM
2	2476 RPM	2470 RPM	2478 RPM
3	4109 RPM	4104 RPM	4136 RPM
4	17,522 RPM (292 Hz)	34,383 RPM	...
5	26,537 RPM (442 Hz)	50,491 RPM	...
6	42,453 RPM (708 Hz)	59,925 RPM	...

Three different rotor modes were developed for this work: an 18-station model with three rotational degrees of freedom (the rotatory inertia of each of the three lumped masses is included in the model), a three-station model with three rotational DOFs, and a three-station model with no rotational DOFs (none of these models includes the effects of the flexible coupling between the drive motor and the rotor). Comparison of the lowest frequency eigenvalues for the models (the lowest critical speeds) was made, and in all cases the model assumed that the rotor was supported on 300 lb/in. bearings at both the inboard and outboard ends. For the first three critical speeds, all three of the models gave virtually identical results indicating that the first three resonant frequencies were dominant. That is, the critical speeds were predominantly determined by the lumped mass and were relatively unaffected by differences in the modeling of the shaft itself. Modes 4, 5, and 6 were significantly different for the two modeling cases, which were of high enough order to include these modes. This was no surprise, because these higher modes (the "shaft modes") result directly from the effects of the mass distributed between the dominant lumped masses, and the three-station mode assumed that no mass existed between these stations.

In addition to calculating the eigenvalues of the rotor system, the finite element program that we used computes stiffness and mass matrices for the equivalent lumped-mass model. These matrices are calculated on the basis of the modulus of elasticity and the density of the shaft material (in this case, the shaft is made of steel, with $E = 3.0 \times 10^7$ lb/in. and $\rho = 7.32 \times 10^{-4}$lb - sec^2/in^4.), and provide the equivalent stiffnesses and masses for the lumped mass configuration. The finite-element analysis also provides information about the relative displacements at the various points along the shaft for each of the undamped natural frequencies. In other words, we are provided with a "picture" of the shape of the rotor that would be seen if the rotor were experiencing free (as opposed to forced) vibration at one of the resonant frequencies of the system. Figure 3 shows these mode shapes for the first five modes, or critical speeds, of the system. The effects of the flexible coupling are not included in this model. At each of these critical speeds, the rotor will exhibit very different "flexing" characteristics.

From Fig. 3, we see that the relative amplitudes of the fourth and fifth modes at the bearing locations are very nearly zero. Thus, we expect to see very little fourth or fifth mode response at the bearings. Close inspection of Fig. 3 reveals that the position probes providing feedback to the bearing controller, located between stations 6 and 8 for the inboard bearing and between stations 20 and 22 for the outboard bearing, will detect significant amounts of vibration at these frequencies. Thus, the feedback signal to the controller is contaminated by these higher modes, and it no longer accurately reflects the actual behavior of the rotor at the bearing locations. This phenomenon, caused here by the noncollocation of the position probes and the bearings, is referred to as *spillover*, and can destabilize the closed-loop feedback system. In fact, oscillations of ~ 325 Hz and ~ 450 Hz were observed for certain amounts of proportional and derivative feedback when the rotor was supported by the bearings but not rotating. Connection of the rotor to a drive motor through a flexible coupling suppressed these oscillations. In addition to this suppression of the fourth

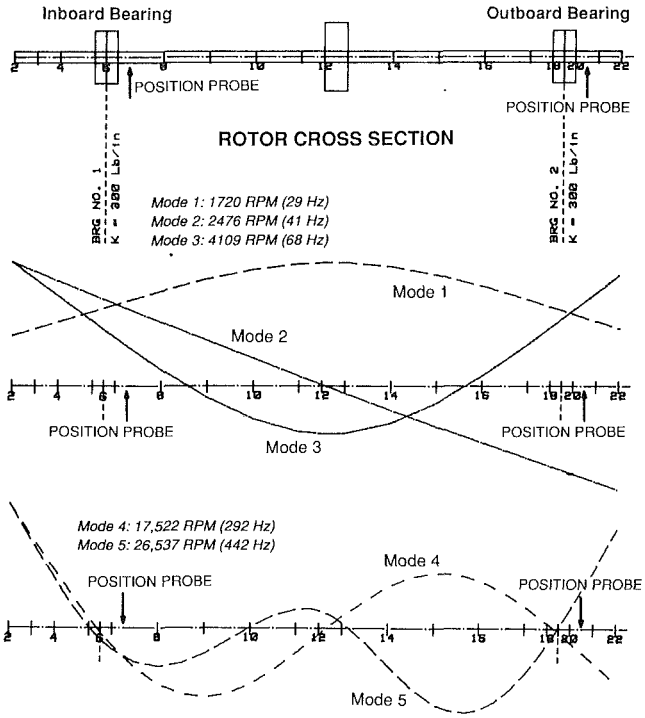

Fig. 3 Undamped synchronous shaft modes for rotor/bearing system (no coupling)

and fifth mode oscillations, the flexible coupling undoubtedly provides some additional vibration reduction for the lower modes as well. The observed frequency of oscillation was directly related to changes of the probe location along the rotor shaft (for example, switching the outboard bearing probe to the inboard side of the bearing caused the oscillation frequency to switch between the two observed frequencies). When it became apparent that the probes should be as close to the bearing as possible, special end collars for the stacked laminations were installed. These allowed the probes to be placed within one inch (axially) of the bearing center-line. Addition of these collars greatly improved the system's ability to reject the higher frequency oscillations. A more complete discussion of spillover can be found in [11] and [12].

4 Dynamic Behavior of a Multimass Rotor in Magnetic Bearings

This work was intended to determine the dynamic behavior of a multimass rotor operating in active magnetic bearings controlled by analog and digital controllers. In particular, we were interested in the vibratory response of the rotor at the bearing locations as the rotor was operated between 0 and 10,000 rpm. This range of operating speeds causes the rotor to pass through its first three resonant frequencies (critical speeds). The effects of various analog and digital controllers on the rotor response at these critical speeds were investigated with concentration on response at a bearing location. For this work, data were taken at the outboard bearing to minimize the effect of the flexible coupling on the results.

4.1 Data Gathering Procedures and Operating Conditions. Before presenting results from the operating rotor system, it seems appropriate to describe briefly the means by which the data were gathered and to summarize the operating conditions that remained constant for all of the results presented here.

The process of gathering data from the running rotor is fairly straightfoward. As the rotor is slowly accelerated from rest to 10,000 rpm, the horizontal and vertical displacements

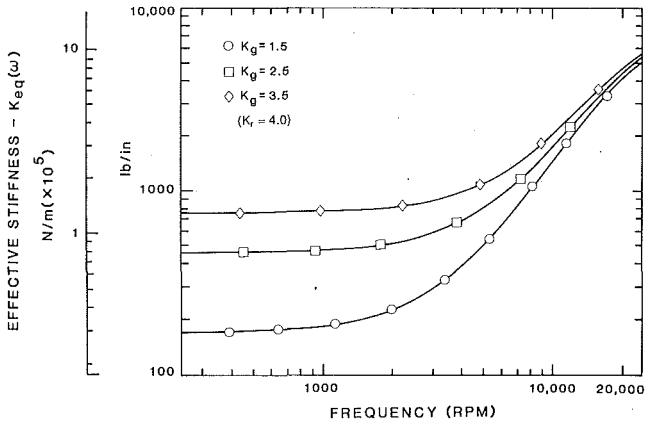

Fig. 4(*a*) Effective bearing stiffness as proportional feedback is varied (analog controller)

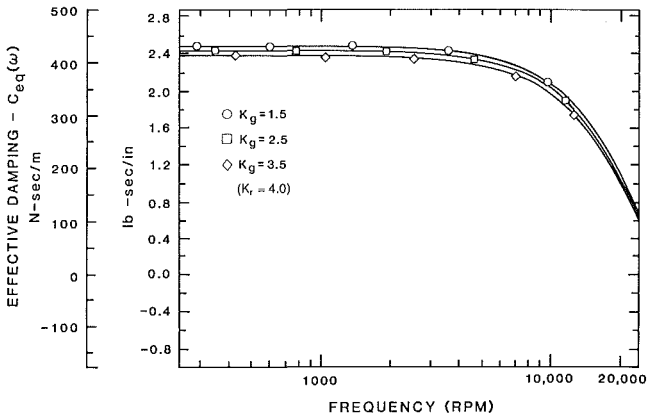

Fig. 4(*b*) Effective bearing damping as proportional feedback is varied (analog controller)

at the bearing are measured by eddy current displacement probes and the probe outputs are periodically sampled and stored as numerical data (data points were taken every 25 rpm from 200 to 10,000 rpm while the rotor speed was increased). In addition to the displacement information obtained, the phase of the peak response relative to an index mark on the rotor is recorded. The phase information is useful when investigating rotor behavior, especially when one is concerned with the behavior near the critical speeds. The source for these measurements is the same position probe used to provide feedback to the magenetic bearing control circuit.

For all the results presented in this paper, the inboard magnetic bearing was controlled by an analog PD controller with the transfer function:

$$G_{PD}(s) = \frac{K_t[R_1C(0.1K_r)s + K_g(1+RCs)(1+R_1C_1s)]}{(1+\tau_s s)(1+RCs)(1+R_1C_1s)(1+\tau_{out}s)(1+\tau_a s)} \quad (1)$$

where

τ_s = 56 μS	(2.8 kHz pole for position probe buffer and low pass filter)
R_1C = 22 mS	(differentiator multiplying constant)
RC = 220 μS	(720 Hz differentiator pole)
R_1C_1 = 100 μS	(1.6 kHz differentiator pole)
K_g, K_r	(proportional and derivative feedback gain constants)
K_t	(Controller loop gain)
τ_{out} = 47 μS	(3.4 kHz output low pass filter pole)
τ_a = 100 μS	(1.6 kHz monitor circuit pole)

with the parameter settings K_g = 2, K_r = 4, K_t = 5. Analog control of the inboard bearing was used for two reasons. We were interested in the effects of controller algorithms on the response at one bearing only, and thus the best results were obtained with all other operating conditions held constant while the characteristics of the outboard bearing were investigated. Also, the personal computer (AT&T PC6300 with 8 MHz 8087 coprocessor) used to implement the various digital control algorithms has limited computational abilities. Simultaneous digital control of both the inboard and outboard bearings restricts the choice of controller parameters that produce a stable system.

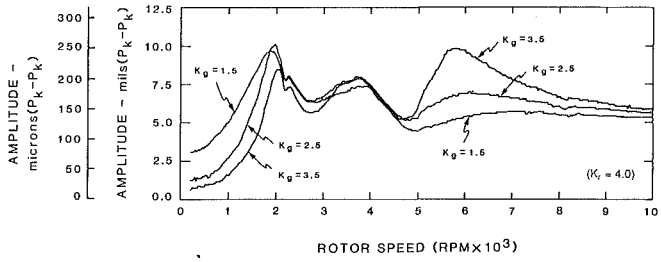

Fig. 5 Vertical displacement at outboard bearing varying proportional feedback (analog controller)

4.2 Results From the Analog PD Controller. As a baseline for comparison and evaluation of the digital controller, we first considered results of controlling the outboard bearing by the analog PD controller just described. In particular, we investigated the effects of varying the K_g and K_r parameters on the rotor response at the outboard bearing, equivalent to changing the stiffness and damping of the bearing.

Figure 4 shows the calculated stiffness and damping characteristics for the outboard bearing as a function of the "stiffness" parameter, K_g. Note that, for the lower frequencies, the predicted curves indeed show the expected changes in the bearing stiffness while the damping curves remain virtually unchanged. In Fig. 5, we see how this changing stiffness is manifested in the vibratory response of the rotor at the bearing. For the slower rotational speeds (0 to ~ 1500 rpm), the bearing response is reduced as the stiffness is increased and the first critical speed increases with increased K_g (this is expected behavior). However, beyond the first critical speed (~ 1900 rpm), the response plots show that the increased bearing stiffness does not guarantee reduced vibration levels at the bearing, and at the third critical the increased stiffness seems to cause a marked *increase* in the amount of rotor vibration. This behavior is counterintuitive, but it is presumed to arise because the forcing function for these tests is a fairly complicated function resulting from shaft modal stiffness relative to bearing stiffness as well as distributed unbalance weights at each of the three rotor lumped masses. Also, note that the inboard bearing and motor coupling were not changed. Predictions of high-frequency rotor behavior in the presence of the changing modal energy distributions that result from these changing stiffness properties must be made on the basis of more than a single degree-of-freedom understanding of the system dynamics.

The calculated stiffness and damping curves resulting form changes in the "damping" parameter, K_r, are presented in Fig. 6. Again, note that the stiffness curves are virtually unaffected by changes in the damping characteristics of the bearing. It is therefore possible to see the effect of varying the damping characteristic of the bearing while holding the stiffness characteristic constant. The rotor response in the presence of this changing damping is shown Fig. 7, and for this series of tests it is clear that the bearing damping is indeed increasing as K_r is increased. Both the amplitude and the Q (amplification factor) of the rotor response decrease for increasing values of K_r. As the bearing damping is increased, the damped resonant frequencies of the system increase consistent with the expec-

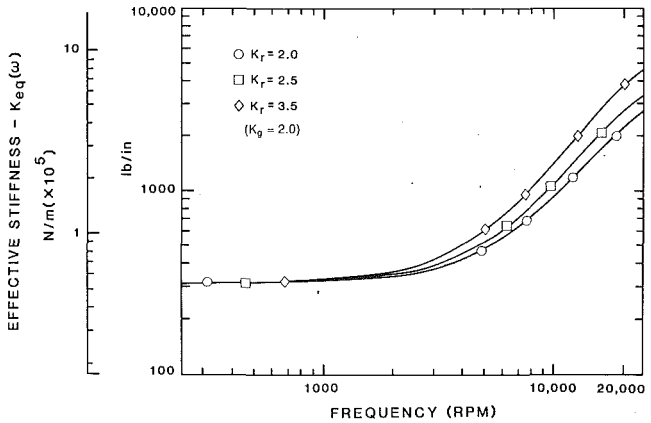

Fig. 6(*a*) Effective bearing stiffness as derivative feedback is varied (analog controller)

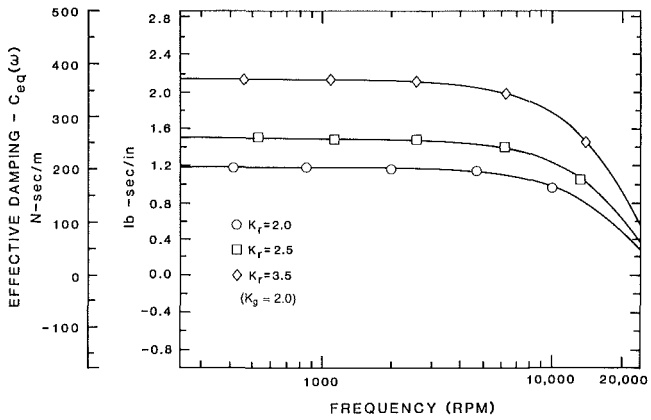

Fig. 6(*b*) Effective bearing damping as derivative feedback is varied (analog controller)

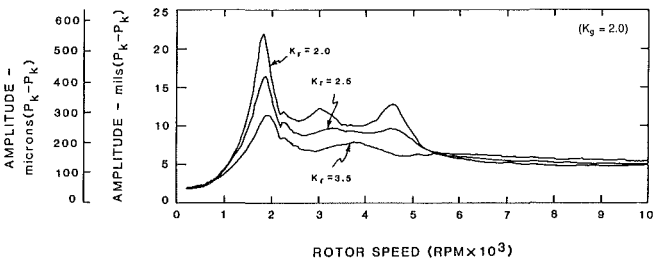

Fig. 7 Vertical displacement at outboard bearing varying derivative feedback (analog controller)

tation that the forcing function for the system results from an unbalanced mass distribution [21].

4.3 Results From the Digital PD Controller. A similar series of tests on the rotor was repeated with the outboard bearing controlled by a digital controller while the inboard bearing remained under analog control. A block diagram for the digital controller is shown in Fig. 8. First, the effect of varying the bearing stiffness via the digital controller parameter K_p was investigated. Figures 9 and 10 show the now familiar bearing stiffness and damping curves and the corresponding rotor plots. For this particular set of tests, the digital control algorithm included some second derivative feedback, which will be justified and explained later (the effects of the second derivative feedback are most evident in the high-frequency portion of the damping curves, where close inspection will detect a gentle rise in the predicted damping at ~ 10,000 rpm before the eventual high frequency rolloff). Inspection of Fig.

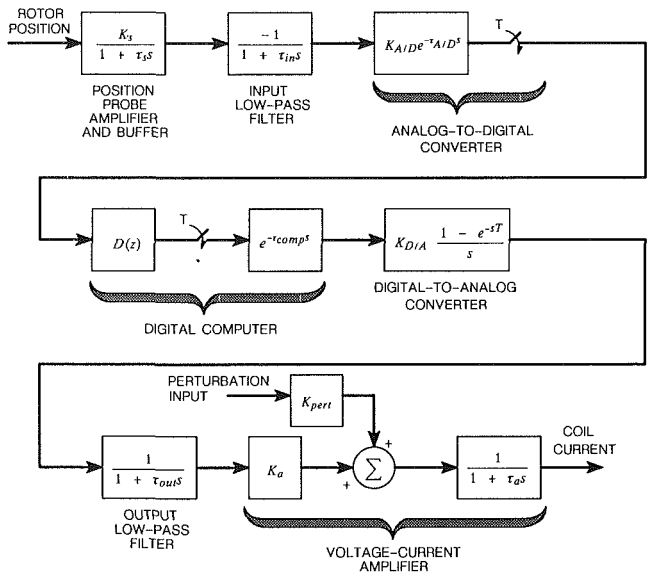

Fig. 8 Detailed block diagram of digital controller

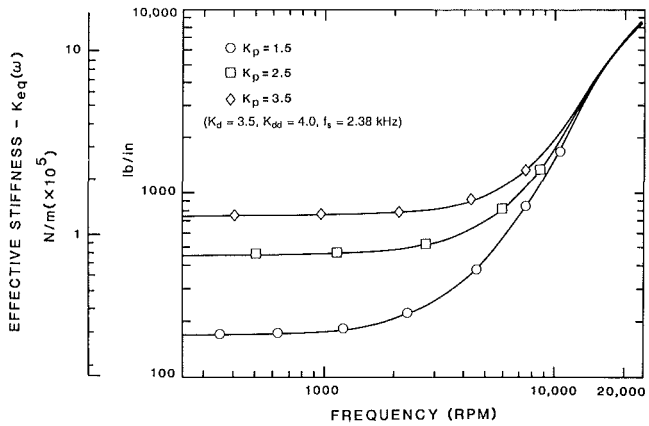

Fig. 9(*a*) Effective bearing stiffness as proportional feedback is varied (digital controller)

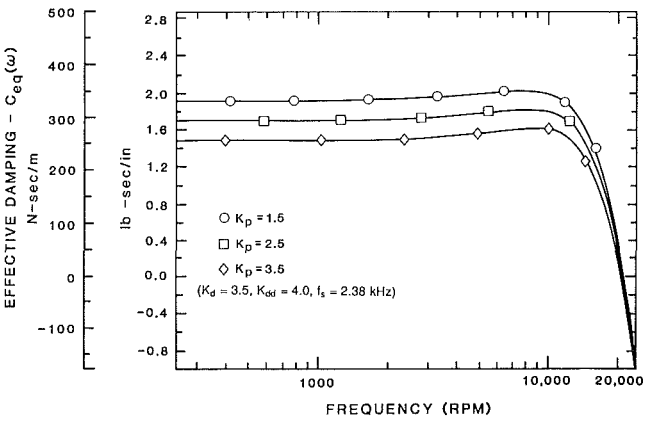

Fig. 9(*b*) Effective bearing damping as proportional feedback is varied (digital controller)

9(*a*) shows that changing K_p does indeed change the predicted stiffness characteristic of the controller, but the changes in this parameter are not as decoupled from changed in the damping characteristic as was true for the similar changes in the analog controller parameters (see Fig. 4). But despite this less ideal behavior, Fig. 9 shows the changing the stiffness via a digital controller has the same effects on the rotor response as chang-

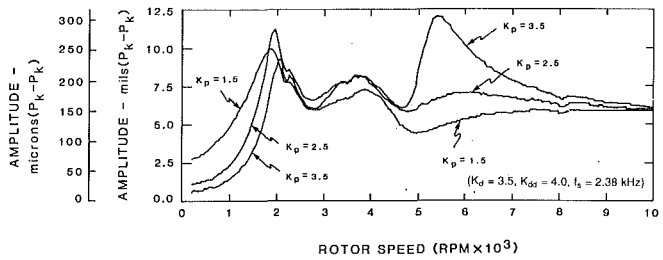

Fig. 10 Vertical displacement at outboard bearing varying proportional feedback (digital controller)

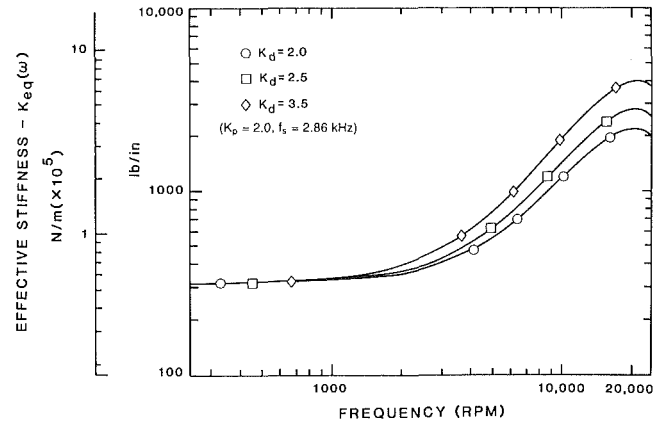

Fig. 11(*a*) Effective bearing stiffness as derivative feedback is varied (digital controller)

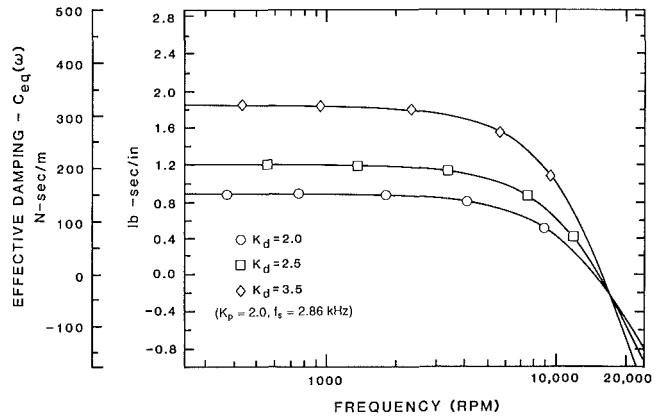

Fig. 11(*b*) Effective bearing damping as derivative feedback is varied (digital controller)

ing the stiffness with an analog controller: The amplitude of vibration is reduced for the slower running speeds, and it is increased for the higher speeds, particularly near the third critical speed.

Variations in the bearing damping via changes in the digital controller's damping parameter, K_d, also yield similar results to those found when the damping was varied using analog control. Figures 11 and 12 show the appropriate curves for these test. Note that changes in the K_d parameter affect the bearing stiffness much less than changes in the K_p parameter affected the damping characteristic in the previous example. The stiffness and damping characteristics are more decoupled for changes in the K_d parameter than for changes in K_p. Again, Fig. 12 shows the effects of increasing bearing damping on rotor response at the bearing: The peak amplitudes of vibration at the criticals are reduced and the critical speeds are moved to higher frequencies.

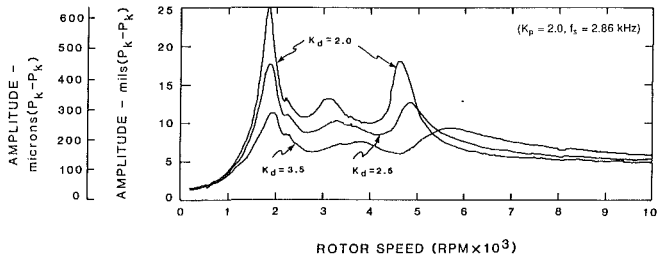

Fig. 12 Vertical displacement at outboard bearing varying derivative feedback (digital controller)

4.4 Summary of Results for PD Controllers. The results of this section demonstrate the adjustable stiffness and damping features of the active magnetic bearing. PD control has been shown effective for controlling an operating rotor in these bearings, and the predicted relationships between the controller parameters (K_g, K_r, for analog, K_p, K_d for digital) have been experimentally verified. PD controllers have been implemented with both analog and digital techniques, and the implementation of similar algorithms has yielded very similar results in terms of the rotor response at the magnetic bearing under test.

On the basis of these results, one would probably conclude that the analog implementation of the PD controller represents the better choice in terms of cost, complexity, and high-frequency performance. The next section demonstrates the advantages of digital implementations when changes in the basic algorithm are desired. Two additional digital controller algorithms were developed and tested on the magnetic bearing rig, and the effects of sampling rate on controller performance were examined.

5 Digital Control Extensions

Analysis of ideal PD controllers compared with equivalent real controller implementations shows that for low frequencies, real implementations approach ideal performance. At higher frequencies, the real controller performance diverges from ideal performance. The crux of the problem for real implementations of PD controllers is that bandwidth limitations prevent these systems from exhibiting the +90 deg high-frequency phase lead characteristic expected for an ideal PD algorithm. Since a truly ideal PD controller cannot be built, it is desirable to identify mechanisms that will cause a real PD controller to behave in a more ideal manner. A solution to this problem helps to overcome the high-frequency phase lag effects by adding phase lead to the controller signal over a range of higher frequencies. Incorporating second derivative feedback into the basic PD controller will achieve this result.

5.1 Inclusion of Second Derivative Feedback. Second derivative feedback is easily added to a digital PD controller without hardware changes. The continuous frequency domain representation of a proportional-derivative-derivative (PDD) controller would be represented by:

$$G_{PDD}(s) = K_p + K_d s + K_{dd} s^2 \tag{2}$$

Using the backward difference approximation for the Laplace variable s yields:

$$D_{PDD}(z) = D_p + \frac{K_d(z-1)}{Tz} + \frac{K_{dd}(z-1)^2}{T^2 z^2} \tag{3}$$

Figure 13 shows the effect of varying second derivative feedback on magnitude and phase responses for the digital PDD controller. Inspection of the figure reveals that second derivative feedback is quite useful as a means of reshaping the high-frequency end of the $K_{eq}(\omega)$ and $C_{eq}(\omega)$ curves. These stiffness and damping curves show that increasing amounts of second derivative feedback cause an upward shift in the high-fre-

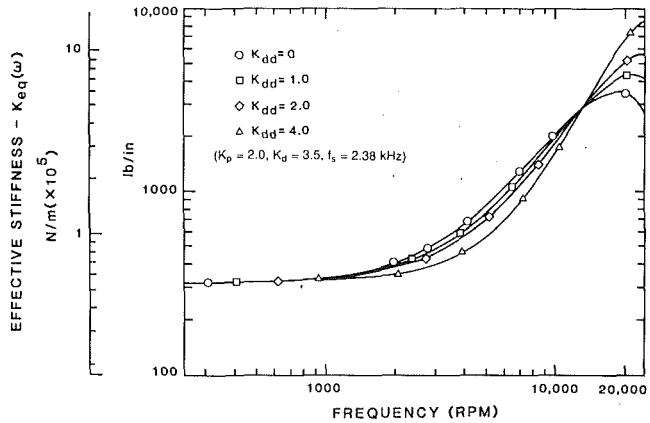

Fig. 13(*a*) Bearing stiffness effect of varying second derivative feedback in a digital PDD controller

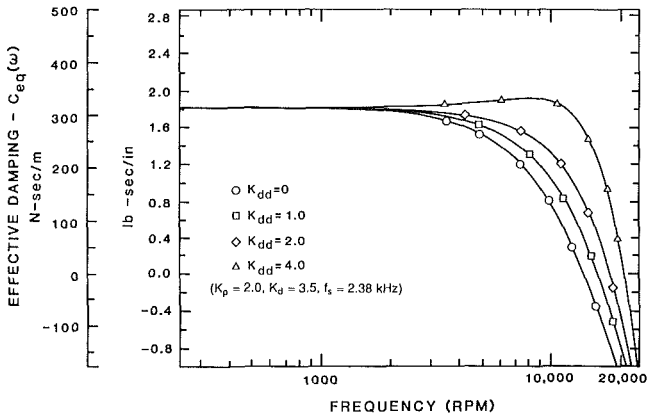

Fig. 13(*b*) Bearing damping effect of varying second derivative feedback in a digital PDD controller

quency portion of the $C_{eq}(\omega)$ curve, even to the point of having $C_{eq}(\omega)$ increase above its low-frequency value before finally rolling off at the higher end of the curve. Thus, second derivative feedback does provide a means of making a PD controller perform in a more ideal manner by providing a wider bandwidth over which the damping curve is flat. Note that this performance improvement is accompanied by steeper rolloffs of the damping curve and noiser output signals, but this may occur above the desired operating speed range of the rotor.

The trends in these damping curves suggest that the rotor will exhibit an increasingly damped response at higher running speeds with almost no effect at the lower speeds as the amount of second derivative feedback is increased. The rotor responses in Fig. 14 clearly fulfill this expectation. As K_{dd} is increased, the second and third critical speeds become increasingly damped while the response at the first critical remains virtually unchanged. The effect at the third critical is more dramatic than the effect of the second, and this supports the conclusion that the damping characteristics of the magnetic bearing are indeed changing as predicted by the calculated damping curve in Fig. 13.

5.2 Inclusion of Integral Feedback. The closed-loop transfer function for the magnetic bearing system has no integration term for either PD of PDD controllers. Therefore, the position error of the rotor in the presence of a static load is not zero. Rather, it is a function of the stiffness of the bearing as determined by K_p. Many applications can benefit from a bearing system that automatically compensates for

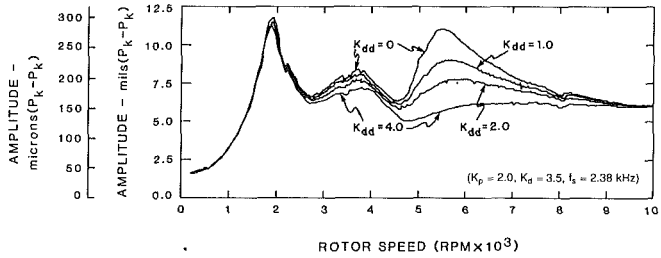

Fig. 14 Vertical displacement at outboard bearing, varying second derivative feedback

changes in static forces on the rotor, and for this reason the addition of an integrator to the PDD controller is examined.

Adding integral feedback to the PDD algorithm is as straightforward as the addition of second derivative feedback, although practical problems such as controller saturation and reset windup must be considered in the actual software coding. Controller saturation occurs when a nonzero d-c input signal is present for long enough to cause the controller output to integrate to its output limit, either positive or negative. Such action can overwhelm the other aspects of the PIDD algorithm, but careful coding of the algorithm can avoid this saturation unless part of the controller circuit is malfunctioning. Reset windup is a numerical saturation phenomenon by which the output of a digital controller tends toward its numerical limit after the computer is reset but before the control loop can be closed. This behavior can be avoided by placing the rotor in support using the PDD algorithm prior to including the integral feedback.

Again the controller is modified without hardware changes. The addition of an integrator yields the following continuous domain representation:

$$G_{\mathrm{PIDD}}(s) = K_p + K_d s + K_{dd} s^2 + \frac{K_i}{s} \tag{4}$$

Converting this to the z domain produces:

$$D_{\mathrm{PIDD}}(z) = K_p + \frac{K_d(z-1)}{Tz} + \frac{K_{dd}(z-1)^2}{T^2 z^2} + K_i T \frac{z}{z-1} \tag{5}$$

The effects of various values of K_i on the shapes of the calculated stiffness and damping curves are illustrated in Fig. 15. There is essentially no change in the stiffness curve because the integral term can only affect the out-of-phase component of the controller signal, and thus cannot affect the real (as opposed to the imaginary) component of the controller transfer function. However, the damping curve is radically changed by the presence of the integrator, and it actually becomes negative for the lowest frequencies. This result might lead one to the conclusion that the system is rendered unstable through the inclusion of an integration term, about this conclusion is incorrect. It is important to remember that these stiffness and damping curves can only be used to predict the bearing response to a harmonic excitation, and that they cannot be used by themselves to predict the stability of the system. However, it is important to note that the low-frequency transition of the damping curve from negative to positive damping must be at a lower frequency than the first critical speed of the rotor-bearing system. Violation of this requirement will result in an unstable system [22].

The damping curves in Fig. 15(*b*) indicate that the integrator should have its predominant effect on the low-frequency portion of the rotor response while leaving the high-frequency portion essentially unchanged. Inspection of Fig. 16 reveals that this is so. Increasing the integrator gain constant increases the amplitude response at the first critical without affecting the second and third criticals significantly. It should also be noted that the presence of significant integrator gain has an

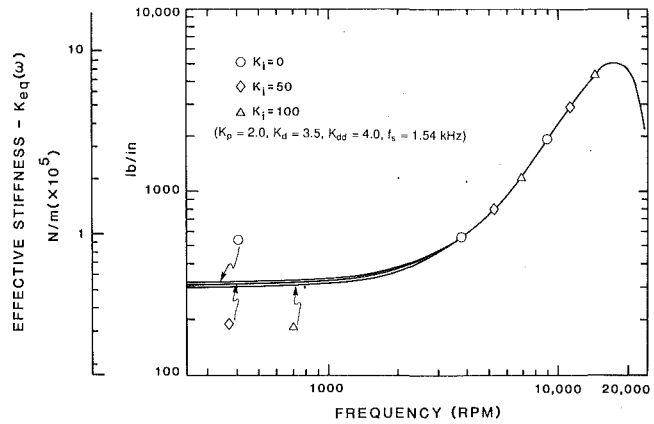

Fig. 15(*a*) Effective bearing stiffness with varying integral feedback (digital PIDD controller)

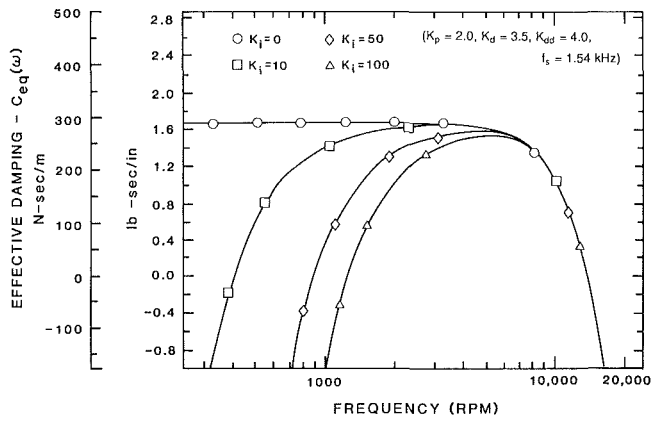

Fig. 15(*b*) Effective bearing damping with varying integral feedback (digital PIDD controller)

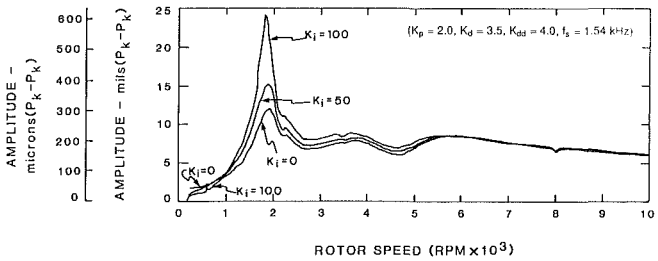

Fig. 16 Vertical displacement at outboard bearing, varying integral feedback (PIDD controller)

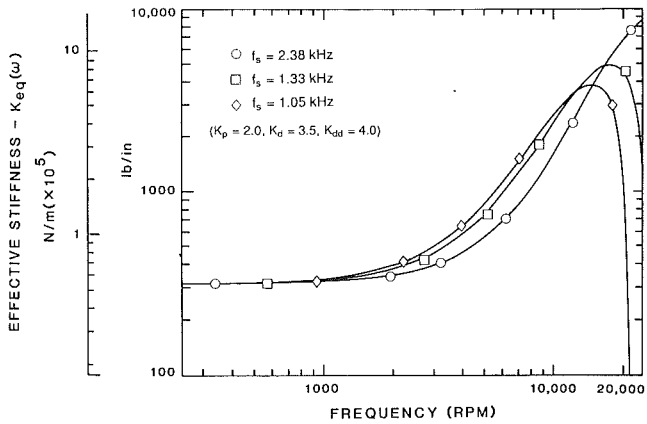

Fig. 17(*a*) Effective bearing stiffness as sampling rate is varied

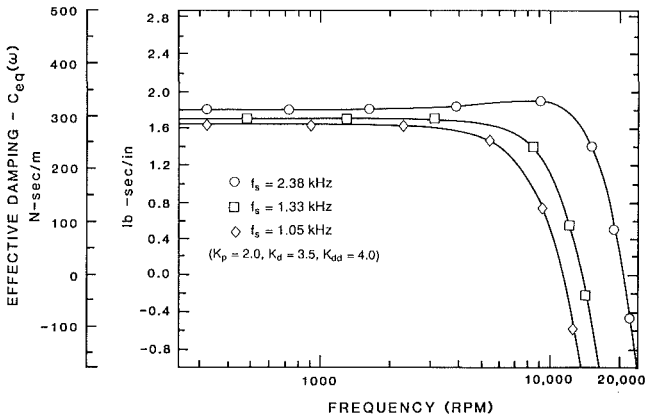

Fig. 17(*b*) Effective bearing damping as sampling rate is varied

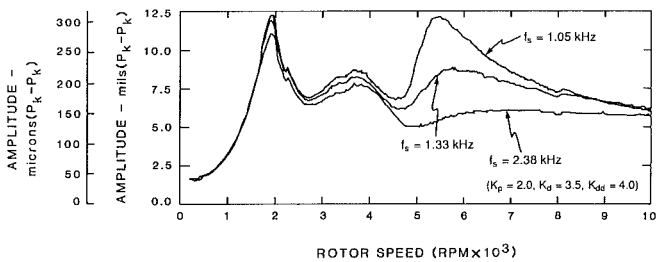

Fig. 18 Vertical displacement at outboard bearing, varying sampling rate

effect similar to increasing bearing stiffness at extremely low frequencies (around 200 rpm). This is due to the fact that a system with a large integrator gain constant will interpret a low-frequency excitation as a slowly changing static load, and it will attempt to integrate this signal to zero. It is important to recognize that the presence of an integrator in the system will accentuate the low-frequency dynamic response as a consequence of having a system that rejects static perturbations.

5.3 Sampling Rate Effects. Digital PD, PDD, and PIDD controllers have been shown to exhibit bearing damping characteristics that drop off at higher frequencies. This rolloff is due to the phase lag introduced into the system by the various low pass filters (as described previously) and delay elements present. Although the A/D conversion time and the computational delay are fixed values, the sampling rate of the controller was varied to permit study of the relationship between the sampling rate and the shape of the effective stiffness and damping curves.

All of the results presented thus far were obtained using the maximum sampling rate (minimum sampling period, T) possible for each controller configuration investigated (these sampling rates are indicated in the respective figures). To investigate sampling rate effects, the sampling rate was intentionally reduced and the predicted and observed responses were compared. Since reducing the sampling rate effectively increases the amount of phase lag introduced by the zero order hold device, a reduction in the sampling rate is expected to cause an earlier rolloff of the damping curve, thus further degrading the high-frequency performance of the magnetic bearing.

This expectation is well founded, as shown in Fig. 17. As the sampling rate is decreased from 2.38 kHz to 1.05 kHz, an obvious degradation in the bearing damping performance for high frequencies occurs. The rotor responses shown in Fig. 18 confirm this trend in the damping curves: As the sampling

period is increased (sampling rate decreased), the amplitude response of the rotor, especially for the higher frequencies, increases noticeably.

The addition of second derivative feedback to the controller signal has essentially the inverse effect of decreasing the sampling rate. Increasing the amount of second derivative feedback pushes the rolloff point of the damping curve to higher frequencies; decreasing the sampling rate of the controller causes the damping curve to roll off at a lower frequency. Thus, as has already been shown, second derivative feedback can be employed to improve the response of a system that has limitations on the maximum allowed sampling rates.

It should be noted that an effect similar to adding second derivative feedback could probably be achieved by employing a hold device higher than zero-order to reconstruct the controller output signal. In fact, use of a first-order-hold device was briefly considered because of its gentler phase rolloff characteristics at low frequencies. This idea was rejected because such devices are quite rare, and a first-order-hold device is essentially a zero-order-hold device with a derivative term included. It was concluded that the additional complexity of a first-order-hold device could not be justified for the level of system desired here in light of the fact that the lag effects of the zero-order-hold device could be overcome through judicious choice of controller algorithms.

Comparison of the effects of second derivative feedback and the effects of sampling rate establish that the characteristic curves predicted for the various controllers being tested are actually manifested at the bearing during operation of the rig. Close inspection of Fig. 13 shows only very slight changes in the predicted low-frequency damping as the amount of second derivative feedback is changed. Accordingly, the corresponding rotor responses in Fig. 14 show only very small changes in the amplitude response at the first critical speed. In Figs. 17 and 18, however, note the larger variations in both the predicted low-frequency damping values and the rotor amplitude responses at the first critical speed. That even subtle predicted differences such as this are evident in the measured responses inspires confidence in the ability to predict bearing characteristics on the basis of these simulated stiffness and damping curves.

Conclusions

The flexibility of digital controllers as applied to magnetic bearings has been demonstrated. This flexibility was exercised by implementing additional software algorithms rather than hardware modifications. The design approach embraced in this paper resulted in a simple means of determining how these new algorithms would affect bearing performance. Second derivative feedback was explored to provide reshaping of the high-frequency portion of the damping curve, and integral feedback was implemented to confirm that the effects of this algorithm on the rotor response would be successfully predicted.

Efforts are currently in progress at the University of Virginia to extend this work to provide more flexible and powerful digital control of magnetic bearings. The additional work includes areas related to both mechanical and electrical aspects of the system. Current areas of exploration include examination of control computer architectures with fault-tolerant parallel structures that complement the multiple axis magnetic bearing control problem, adaptive control, and vibration suppression [20]. Its is anticipated that continued exploration of digital control of magnetic bearings will lead to greater flexibility in rotating machinery design.

Acknowledgments

This work was funded in part by the Center for Innovative Technology of the Commonwealth of Virginia and the Army Research Laboratory.

References

1 Humphris, R. R., Kelm, R. D., Lewis, D. W., and Allaire, P. E., "Effect of Control Algorithms on Magnetic Journal Bearing Properties," ASME JOURNAL OF ENGINEERING FOR GAS TURBINES AND POWER, Vol. 108, No. 4, Oct. 1986, pp. 624–632.

2 Allaire, P. E., Lewis, D. W., and Jain,V. K., "Feedback Control of a Single Mass Rotor on Rigid Supports," *Journal of the Franklin Institute*, Vol. 312, No. 1, 1981, pp. 1–11.

3 Allaire, P. E., Lewis, D. W., and Knight, J. D., "Active Vibration Control of a Single Mass Rotor on Flexible Supports," *Journal of the Franklin Institute*, Vol. 315, No. 3, 1983, pp. 211–222.

4 Stanway, R., and Burrows, C., "Active Vibration Control of a Flexible Rotor on Flexibly-Mounted Journal Bearings," ASME *Journal of Dynamic Systems, Measurement, and Control*, Vol. 103, Dec. 1981, pp. 383–388.

5 Kaya, F., and Roberts, J., "Optimum Vibration Control of Flexible Transmission Shafts," *IMechE J.*, 1984, pp. 525–534.

6 Schweitzer, G., and Ulbrich, H., "Magnetic Bearings—A Novel Type of Suspension," *IMechE J.*, 1980, pp. 151–156.

7 Schweitzer, G., "Characteristics of a Magnetic Rotor Bearing for Active Vibration Control," *IMechE J.*, 1976.

8 Stanway, R., and O'Reilly, J., "State-Variable Feedback Control of Rotor-Bearing Suspension Systems," *IMechE J.*, 1984, pp. 515–524.

9 Reinig, K. D., and Desrochers, A. A., "Disturbance Accommodating Controllers for Rotating Mechanical Systems," ASME *Journal of Dynamic Systems, Measurement, and Control*, Vol. 108, Mar. 1986, pp. 24–31.

10 Hisatani, M., Inoue, Y., and Mitsui, J., "Development of Digitally Controlled Magnetic Bearing," *Bulletin of JSME*, Vol. 29, No. 247, Jan. 1986, pp. 214–220.

11 Salm, J. R., "Active Electromagnetic Suspension of an Elastic Rotor: Modelling, Control, and Experimental Results," presented at the ASME Design Engineering Division Conference on Vibration and Noise, Boston, MA, Sept. 27–30, 1987.

12 Balas, M. J., "Feedback Control of Flexible Systems," *IEEE Transactions on Automatic Control*, Vol. AC-23, No. 4, Aug. 1978, pp. 673–679.

13 Carmichael, A. T., Hinchliffe, S., Murgatroyd, P. N., and Williams, I. D., "Magnetic Suspension Systems With Digital Controller," *Rev. Sci. Instrum.*, Vol. 57, No. 8, Aug. 1986, pp. 1611–1615.

14 Scudiere, M. B., Willems, R. A., and Gillies, G. T., "Digital Controllers for a Magnetic Suspension System," *Rev. Sci. Instrum.*, Vol. 57, No. 8, Aug. 1986, pp. 1616–1626.

15 Habermann, H., and Liard, G., "Practical Magnetic Bearings," *IEEE Spectrum*, Sept. 1979, pp. 26–30.

16 Stolfi, F., and de Jonge, A. K., "Stirling Cryogenerators With Linear Drive," *Philips Technical Review*, Vol. 42, No. 1, Apr. 1985, pp. 1–10.

17 Lange, T., "Optimal Magnetic Bearing Control for High-Speed Momentum Wheels," *J. Guidance*, Nov.-Dec., 1985, pp. 737–742.

18 Cameron, A., *Basic Lubrication Theory*, Langman Group, Ltd, London, 1980.

19 Keith, F., Williams, R., Allaire, P., and Schafer, R., "Digital Control of Magnetic Bearings Supporting a Multimass Flexible Rotor," presented at Magnetic Suspension Technology Workshop, NASA Langley Research Center, Hampton, Virginia, Feb. 2–4. 1988.

20 Yates, S., and Williams, R., "A Fault-Tolerant Multiprocessor Controller for Magnetic Bearings," *IEEE MICRO*, Vol. 8, No. 4, Aug., 1988, pp. 6–17.

21 Meirovitch, L., *Elements of Vibration Analysis*, McGraw-Hill, 1986, pp. 56–58.

22 Keith, F. J., "Digital Control System Design for Active Magnetic Bearings," M. S., Thesis, University of Virginia, May 1988, pp. 93–96.

Acoustic Design of Lightweight Gas Turbine Enclosures

R. D. Rawlinson
Altair Filters International Ltd.,
Alton, Hants, United Kingdom

Acoustic enclosures for the gas turbine industry have to comply with a number of stringent safety requirements including structural strength, fire resistance, and sound insulation. This has led traditionally to heavy enclosure designs. Corrugated enclosure panels offer significant structural advantages because of their increased bending stiffness. Consequently, a corrugated panel of a given thickness can give the same structural strength as a flat panel of substantially greater weight and thickness. However, corrugated panels are intrinsically less effective as a sound insulator than flat panels of the same thickness. This paper examines the implications of corrugated, lightweight panels for acoustic enclosures. It illustrated that, by careful design, the inherent acoustical disadvantages of corrugated panels can be overcome so that thinner, lighter, and more cost-effective enclosures can be used without compromising the overall structural and acoustical design requirements.

Introduction

Gas turbines are used extensively in onshore and offshore environments for power generation, but their use introduces a number of potential hazards. To reduce the risks caused by fire and high noise levels, enclosures, with intake and exhaust silencers, are fitted around the turbines. These enclosures and silencers must be capable of withstanding large static loads produced by equipment sited on top of them, and large dynamic loads due to wind.

Traditionally these enclosures are heavy and expensive, especially when stainless steel or aluminum is required for offshore use. This has led to a consideration of more cost-effective designs, which still comply with the stringent demands of the oil and gas industry.

One approach that is proving successful is the use of a corrugated enclosure design, which employs a thinner steel wall than its flat panel counterpart, without compromising the structural and fire protection requirements. However, corrugated designs are intrinsically less effective as sound insulators than flat panels. These weaknesses must be understood so that multilayered panels based on the corrugated design, can compensate for the deficiencies of unlined, corrugated panels.

This paper presents the results of theoretical predictions and measurements on flat and corrugated panels, which were tested in the unlined condition and then with a sound absorbent lining. The effects of varying the profile of the corrugations is also considered.

The paper considers first the behavior of flat, unlined panels, then describes the physical reasons why corrugated, unlined panels have a different acoustic response to flat panels. The effects of sound absorbent linings on flat and corrugated panels are then considered.

Contributed by the International Gas Turbine Institute and presented at the 35th International Gas Turbine and Aeroengine Congress and Exposition, Brussels, Belgium, June 11-14, 1990. Manuscript received by the International Gas Turbine Institute January 9, 1990. Paper No. 90-GT-54.

Sound Transmission Through Unlined Flat Panels

When a sound wave is incident on a wall or partition, some of the sound energy is transmitted through the wall. The fraction of incident energy that is transmitted is called the transmission coefficient. The accepted index of sound transmission is the sound reduction index, which is sometimes called the transmission loss. This is related to the transmission coefficient by the equation:

$$R = 10 \log_{10}(1/\tau), \text{ dB} \quad (1)$$

The behavior of flat panels has been described extensively in the literature, so only the outline of their theoretical performance is given here (Beranek, 1971; Fahy, 1985). The general behavior of a single skin, isotropic panel is shown in Fig. 1. This characteristic behavior is valid for a wide range of materials including steel and aluminum.

The propagation of audio-frequency waves through panels and walls is primarily due to the excitation of bending waves, which are a combination of shear and compressional waves. When a panel is of finite extent then a number of resonances are set up in the panel, which are dependent on the bending stiffness of the panel. The frequency of the first panel resonance, $f1$, is given by

$$f1 = (\pi/2)\sqrt{(B/m)(1/a^2 + 1/b^2)}, \text{ Hz} \quad (2)$$

The second resonance occurs at the "coincidence" frequency, fc, when the projected wavelength of the incident sound coincides with the wavelength of the bending wave in the panel. The coincidence frequency is given by:

$$f_c = (c^2/2\pi)\sqrt{(m/B)}, \text{ Hz} \quad (3)$$

The amount of sound transmitted by a panel is dependent on the surface weight, the damping of the panel, and the frequency of the sound. For a finite panel exposed to a random noise field, the acoustic behavior is specified mathematically as follows:

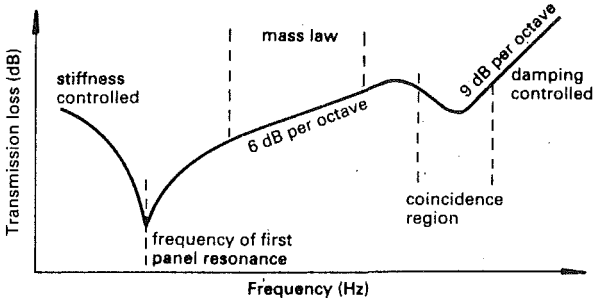

Fig. 1 Sound reduction index for a typical flat, unlined panel

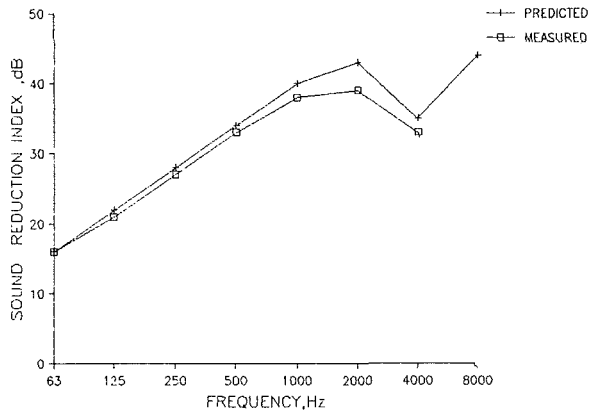

Fig. 2 Predicted and measured sound reduction indices for 3-mm steel

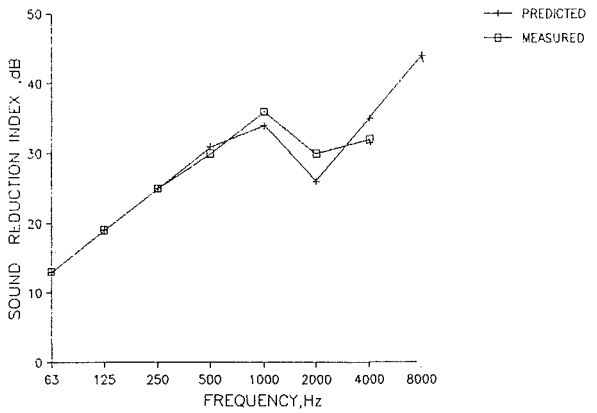

Fig. 3 Predicted and measured sound reduction indices for 6-mm aluminum

$$R = 20\log_{10}S - 20\log_{10}f - 20\log_{10}(4\pi\rho_o c),\ \text{dB},\ f<f1 \quad (4)$$

$$R = 20\log_{10}(mf) - 47,\ \text{dB},\ f1<f<f_c \quad (5)$$

$$R = 20\log_{10}(\pi fm/\rho_o c) + 10\log_{10}(2\eta f/\pi f_c),\ \text{dB},\ f>f_c \quad (6)$$

Table 1 Comparison of predicted and measured sound reduction indices of flat, unlined panels

Material	Measured or Predicted	Sound Reduction Index, dB 63	125	250	500	1000	2000	4000	8000
3mm steel	predicted	16	22	28	34	40	43	35	44
	measured	16	21	27	33	38	39	33	-
6mm steel	predicted	22	28	34	40	43	35	44	53
	measured	22	27	35	39	44	37	42	-
6mm aluminium	predicted	13	19	25	31	34	26	35	44
	measured	13	19	25	30	36	30	32	-

In most practical situations the lowest resonance frequency is below the audio range. Above this frequency a broad frequency range occurs in which the transmission loss is controlled by the surface weight and increases with frequency at the rate of 6 dB per octave. In the coincidence region the transmission loss is limited by the damping of the panel. Above the coincidence frequency the transmission loss increases by 9 dB per octave and is determined by the surface weight and the damping.

Clearly for a high value of sound reduction index over the majority of the audio frequency range (the mass-controlled region) it is better to have a high surface weight, a low bending stiffness, and a high internal damping.

The acoustic performances of some materials have been predicted and are compared to measured values in Table 1. The data for 3-mm steel and 6-mm aluminum are shown in Figs. 2 and 3. Each of the examples shown has the characteristic shape described above and the agreement between the measured and predicted values of transmission loss is good.

Sound Transmission Through Unlined Corrugated Panels

In corrugated panels the characteristics of the panel are not the same in all directions. The moment of inertia across the corrugations differs from that parallel to the corrugations; thus the bending stiffness varies with direction. This affects both the first panel resonance and the coincidence frequency so that the sound transmission characteristics for these panels differs from flat panels with the same thickness.

The first panel resonance is now given by:

$$f1 = (\pi/2m^{0.5}) \times \sqrt{(Bx/a^4(1-\nu^2) + By/b^4(1-\nu^2) + Bxy/a^2b^2)},\ \text{Hz} \quad (7)$$

where Bx and By are the bending stiffnesses in the two principal planes of the panel and Bxy accounts for the torsional rigidity of the plate (Hearman, 1959).

For real panels, measuring several meters in length and height, the frequency of this first resonance may still be in the

Nomenclature

a, b = panel dimensions, m
B, Bx, By, Bxy = bending and torsional stiffnesses
c = speed of sound in air, m/s
d = fiber diameter, μm
f = frequency, Hz
$f1$ = first panel resonance, Hz
f_c, f_{cx}, f_{cy} = coincidence frequency, Hz
l = thickness of absorptive layer, m
ln = natural logarithm
m = mass per unit area, kg/m^2
R = sound reduction index or transmission loss, dB
$R1$ = flow resistivity
S = stiffness
α = attenuation constant for the material, dB/m
η = damping
λ_m = wavelength of sound in the absorptive layer, m
ν = Poisson ratio
ρ_o = density of air
ρ_m = density of absorptive layer
τ = transmission coefficient
ω = angular frequency

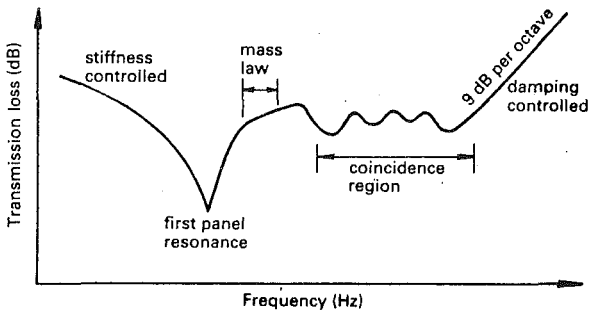

Fig. 4 Sound reduction index for a typical corrugated, unlined panel

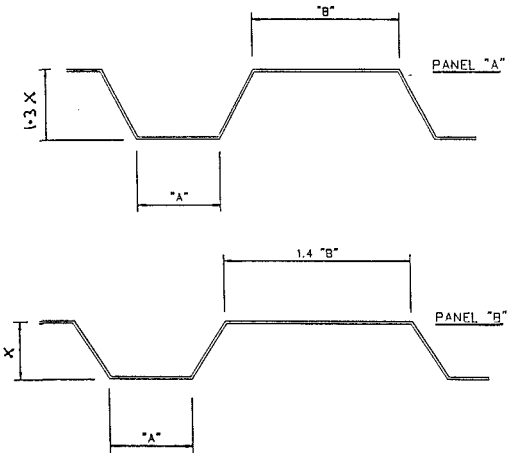

Fig. 5 Two designs of corrugated panels

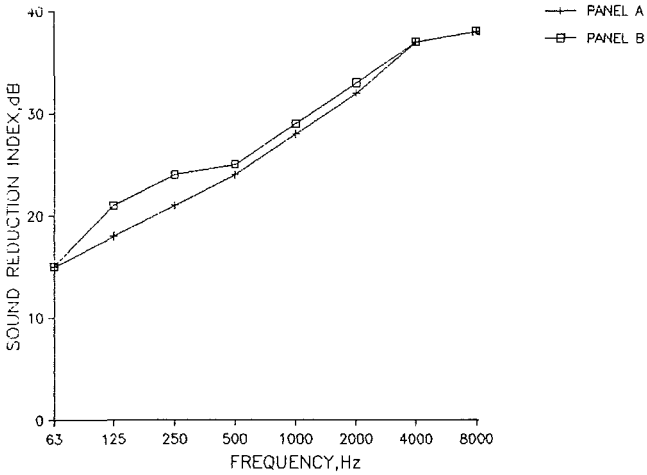

Fig. 6 Predicted transmission loss for two designs of corrugated panels

subaudio range but can be several octaves higher than the first resonance of a flat panel of the same dimensions.

Since the coincidence frequency is determined by the bending stiffness, the presence of two bending stiffnesses gives rise to two critical frequencies, f_{cx} and f_{cy}, where:

$$f_{cx} = (c^2/2\pi)\sqrt{(m/Bx)},\ f_{cy} = (c^2/2\pi)\sqrt{(m/By)}$$

If the ratio of the bending stiffnesses, Bx and By, is less than 1.4, then the effects on the transmission loss of the panel will be small (Beranek, 1971) but in typical panels the ratio of the bending stiffnesses is usually much greater than 1.4. This gives rise to a plateau in the transmission loss curve, which is illustrated in Fig. 4. The plateau may extend over several decades for common corrugated or ribbed panels.

Table 2 Comparison of predicted sound reduction indices of two, unlined corrugated panels.

	Sound Reduction Index, dB							
	63	125	250	500	1000	2000	4000	8000
Panel A	15	18	21	24	28	32	37	38
Panel B	15	21	24	25	29	33	37	38

Table 3 Predicted parameters for three panels (the panels were made of steel measuring 4-m by 2.5-m by 2.5-mm thick)

	Bending Stiffness N.m	First Panel Resonance Hz	Coincidence Frequency Hz
Panel A (corrugated)	240,000:241	30	163:5115
Panel B (corrugated)	90,000:263	18	264:4897
Flat Panel	296	2.9	4825

Table 4 Predicted and measured sound reduction indices for panel A

	Sound Reduction Index, dB							
	63	125	250	500	1000	2000	4000	8000
predicted	15	18	21	24	28	32	37	38
measured	20	23	25	23	23	28	29	29

The sound transmission through orthotropic (corrugated) panels has been investigated by Heckl (1960) who derived the following relationships for the diffuse field sound transmission:

$$\tau = (\rho_o c f_{cx}/\pi\omega m f)(\ln(4f/f_{cx}))^2,\ f_{cx} < f < f_{cy} \quad (8)$$

$$\tau = (\pi\rho_o c/\omega m f)(f_{cx} f_{cy})^{0.5},\ f > f_{cy} \quad (9)$$

f_{cx} and f_{cy} are the two coincidence frequencies and where f_{cx} is the lower of the two values.

The performances of two designs of corrugated panels have been predicted for panels made of 2.5-mm-thick steel with the designs shown in Fig. 5. The predicted transmission losses are given in Table 2 and Fig. 6.

The predicted panel bending stiffnesses and resonant frequencies for the two panels are tabulated in Table 3 for a simply supported panel 4-m wide by 2.5-m high. The values for a flat panel of the same overall dimensions have also been included. The bending stiffness of panel B, in the direction parallel to the corrugations, is slightly less than that for panel A. This causes a shift in the lower critical frequency of about half an octave, which gives rise to a slightly higher transmission loss at lower frequencies.

Transmission loss measurements have been carried out on a partition with the design of panel A. The test was carried out in accordance with the standard ISO 140 (1978). Table 4 and Fig. 7 compare the predicted and measured performances. Both sets of curves show a plateau effect, which is more evident in the measured values. The predicted and measured values are within 4 dB of each other up to 4 kHz, above which the curves differ by about 7 dB. Although the agreement is not as close as for flat panels, it is encouraging. Of more interest is the comparison between the transmission losses of unlined, flat, and corrugated panels with the same thickness. Figure 8 and Table 5 show that the corrugated panel is substantially

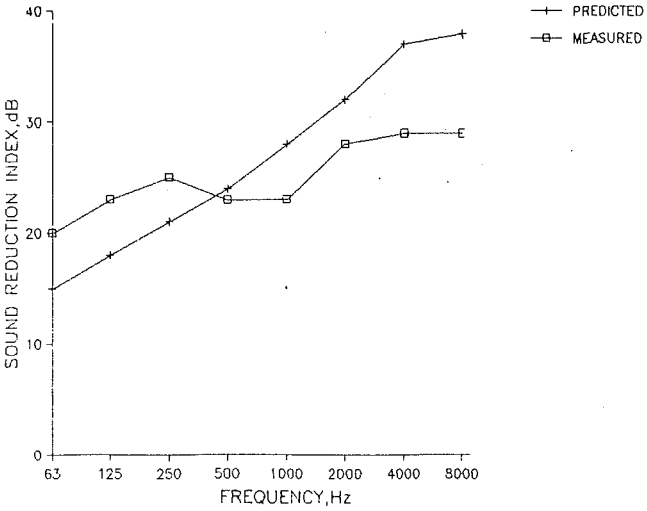

Fig. 7 Predicted and measured sound reduction indices for panel A

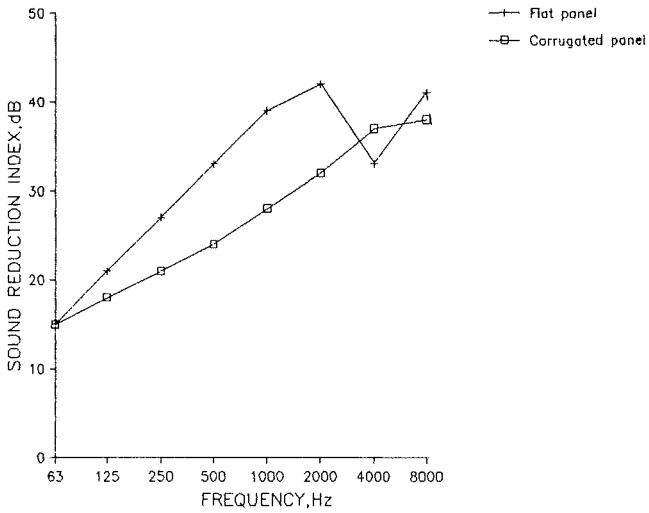

Fig. 8 Predicted performance of flat and corrugated panels

less effective in reducing sound transmission in the midfrequencies compared to the flat panel equivalent.

Clearly, if noise control is a primary consideration, then unlined corrugated panels are not recommended, unless other engineering considerations dictate their use. Corrugated panels offer a considerable increase in bending stiffness, compared to flat panels, which reduces the amount of additional stiffening that would be required for a flat panel. But the volume of material required to produce a corrugated panel is significantly greater than that for a flat panel. For the two corrugated panel designs considered above, panel A contains 23 percent more material than the flat panel, and panel B contains 13 percent more material. Depending on the structural requirements, the additional stiffening required for a flat panel may result in a material saving when a corrugated design is chosen, especially if the flat panel is much thicker to compensate for its inherent low bending stiffness.

The Attenuation of Sound by Absorptive Linings

Sound absorbent linings are frequently fitted in acoustic enclosures to reduce the buildup of reverberant noise inside the enclosure. Typical reductions in the reverberant noise level may be between 3 and 10 dB depending on the application. An additional benefit is the increase in transmission loss of

Table 5 Predicted sound reduction indices for flat corrugated panels (panel thickness of 2.5-mm)

	Sound Reduction Index, dB							
	63	125	250	500	1000	2000	4000	8000
Flat Panel	15	21	27	33	39	42	33	41
Corrugated Panel	15	18	21	24	28	32	37	38

the enclosure panel, which further reduces the noise level outside the enclosure.

The increase in panel transmission loss arises because of several mechanisms. First, if the absorbent lining is sufficiently heavy and the panel is relatively thin, then the added layer may give sufficient additional weight to affect the "mass-law" performance and increase the damping of the panel. At high frequencies the absorbent may be relatively thick in comparison to the wavelength of the sound. The high-frequency sound may be attenuated not only because of the impedance mismatch between the air and the absorbent, but as the sound wave passes through the added layer a significant amount of acoustic energy is converted into heat by viscous losses in the interstices. In practice, the amount of heat generated is minute.

It is possible to distinguish between three frequency regions in which different attenuating mechanisms are predominant (Beranek, 1971). For convenience these are described as regions A, B, and C, where A is the low-frequency region, C is the high-frequency region and B is the transition region. The boundaries between these three regions are defined by the physical characteristics of the absorptive material in terms of the flow resistivity and the material thickness.

The flow resistivity of fibrous absorptive materials is dependent upon the bulk density and fiber diameter by the approximate relationship:

$$R1 = (3.18 \times 10^3)(\rho_m^{1.53}/d^2) \tag{10}$$

The frequency limits of the three regions, A, B, and C, are defined by:

Region A: $10l \lambda_m$
Region B: $10l \lambda_m$, $\lambda l < 9$ dB
Region C: $\alpha l > 9$ dB

The values of λ_m, the wavelength of the sound inside the absorptive layer, and α, the attenuation constant for the material, can be measured or predicted for semirigid materials (Delaney and Bazley, 1969):

$$\alpha = (\omega/c)(0.189(\rho_o f/R1)^{-0.595}) \tag{11}$$

$$\lambda_m = (c/f)(1 + 0.0978(\rho_o f/R1)^{-0.7})^{-1} \tag{12}$$

For an absorptive layer of known thickness and flow resistivity, the attenuation predicted from the equations given above is additive to that produced by the unlined panel.

The predicted and measured acoustic performances of two flat panels and one corrugated panel, each with an absorptive lining, are shown in Table 6 and Figs. 9 and 10.

The predicted performances of the two flat panels are in good agreement with the measured performances over the majority of the frequency range. The largest discrepancies occur at 63 Hz and 8 kHz.

The agreement between the theoretical and measured performances of the corrugated panel is not as good as for the flat panel. The largest discrepancies occur at the lower frequencies with better agreement occurring at high frequencies. This follows the low frequency trend shown in Fig. 8 where

Table 6 Comparison of predicted and measured sound reduction indices of three lined panels

	Measured or Predicted	Sound Reduction Index, dB 63	125	250	500	1000	2000	4000	8000
Panel 1 (flat)	predicted	14	22	31	39	48	47	65	63
	measured	20	21	27	38	48	58	67	66
Panel 2 (flat)	predicted	20	30	40	46	52	60	63	79
	measured	31	34	35	44	54	63	62	68
Panel 3 (corrugated)	predicted	16	19	22	27	36	44	52	56
	measured	22	24	28	32	38	48	52	52

Panel 1: 1.6mm flat steel lined with 100mm thick glassfibre, 49kg/cu.m density

Panel 2: 5mm flat steel lined with 100mm thick glassfibre, 48kg/cu.m density

Panel 3: 2.5mm corrugated steel lined with 50mm thick mineral wool, 64kg/cu.m density

the corrugated panel was unlined and the predicted performance was less than the measured performance by 5 dB. Nevertheless, the agreement is sufficiently close to support the theoretical model.

Discussion

It has been shown that the acoustic performance of lined and unlined panels can be predicted with reasonable accuracy for flat and corrugated panels. It has also been shown that, where noise control is important, unlined corrugated panels are not recommended unless other engineering considerations dictate their use, because corrugated panels are intrinsically less effective as sound insulators than flat panels of the same thickness.

A lining of sound absorptive material can substantially increase the sound reduction index of panels and the additional attenuation depends on the density, fiber diameter, and thickness of the lining. By careful selection of these parameters, the acoustic disadvantages of corrugated panels can be considerably reduced so that corrugated panels can be used confidently in situations where noise control is a primary requirement. The additional bending stiffness of corrugated panels permits a thinner outer skin to be employed and reduces the amount of additional bracing required to provide the structural integrity necessary in the demanding environment offshore. This reduction in overall weight compensates for the additional material used in forming the corrugations.

By careful design of the panel, a corrugation profile can be selected, which provided the most cost-effective solution when structural integrity, weight cost, ease of manufacture, and acoustic performance are considered. When expensive materials, such as stainless steel and aluminum, are employed, the reduction in cost by using a thinner-walled corrugated panel can be considerable.

A further consideration is the fire rating of lined corrugated panels. The normal requirement for bulkheads and decks offshore is the "A-60" class division (SOLAS, 1974). Corrugated panel designs of the type described in this paper have been submitted to, and approved by, the appropriate authorities.

In some situations where a particularly high acoustic performance is called for, the corrugated design lends itself well to a multilayer construction employing an additional inner layer of heavy impervious material. Cheaper materials are used for the additional septum than for the outer skin. The acoustic attenuation of these multilayer designs are comparable to the performance of flat panels employing outer skins of twice the thickness of the corrugated outer skin. Figure 11 compares the measured performances of a traditional 5-mm-thick flat panel design with 100-mm-thick absorptive lining and multilayered panel based on a 2.5-mm-thick corrugated panel lined with a 50-mm absorptive layer.

The nominal surface weights of the two designs are 50 kg/

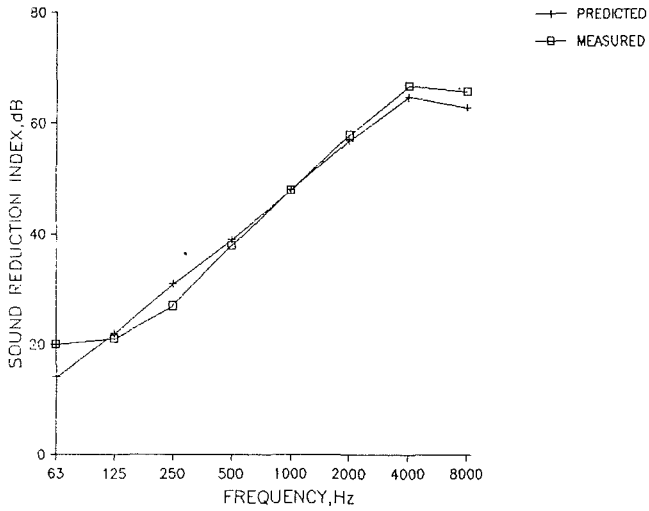

Fig. 9(*a*) Predicted and measured sound reduction index of panel 1

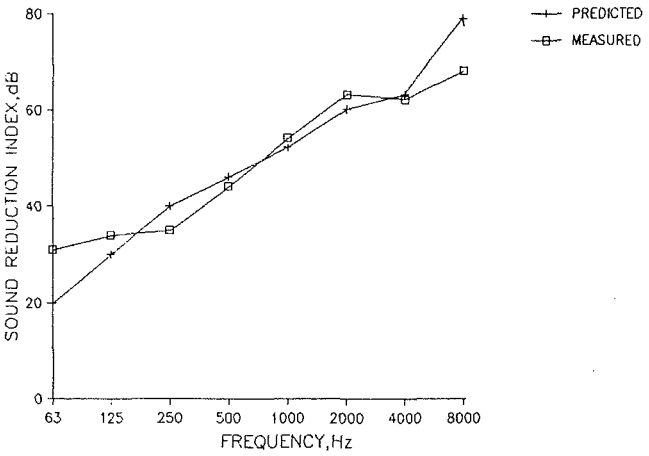

Fig. 9(*b*) Predicted and measured sound reduction index of panel 2

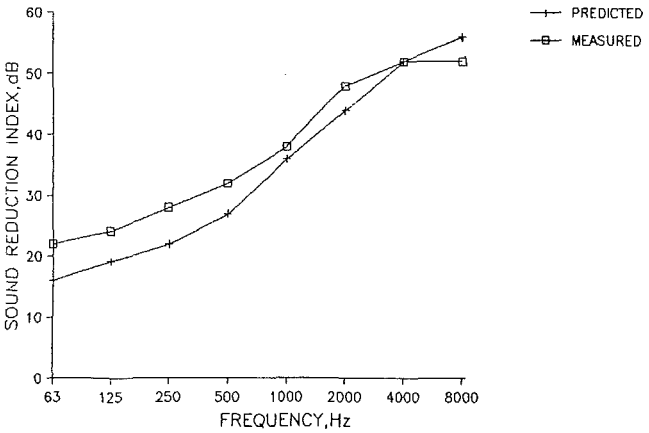

Fig. 10 Predicted and measured sound reduction index of panel 3

m^2 and 40 kg/m^2 for the flat and corrugated panels, respectively. Except at 63 and 125 Hz, the performance of the two panels is very similar.

Conclusion

This paper has shown that the acoustic performance of corrugated and flat steel panels can be predicted. The acoustic behavior of corrugated panels is very different from that of

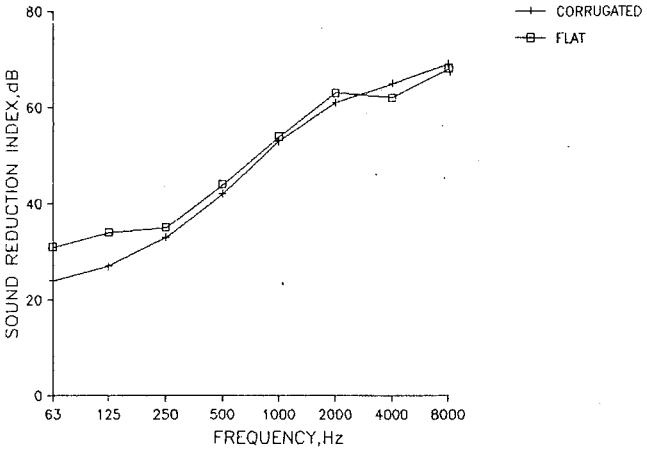

Fig. 11 Predicted sound reduction indices of two high-performance panels

flat panels. This means that if corrugated panels are required, careful consideration must be given to the design, since unlined corrugated panels are unsuitable on their own for noise control applications.

However, the greater bending stiffness of corrugated panels offers many financial and structural advantages in the demanding environment that exists offshore, especially for gas turbines.

By lining the interior of a corrugated panel with a material whose physical parameters have been carefully chosen, the inherent acoustic weaknesses can be overcome. Thus a more cost-effective approach to gas turbine enclosure design can be adopted, which considers the structural integrity, weight, cost, ease of manufacture, and acoustic performance. The resultant designs employ less bracing and thinner outer skins to achieve the same acoustic performance as flat-walled constructions weighing typically 25 percent more than the equivalent corrugated design.

References

Beranek, L. L., 1971, *Noise and Vibration Control*, McGraw-Hill, New York.

Delaney, M. E., and Bazley, E. N., 1969, "Acoustical Characteristics of Fibrous Absorbent Materials," National Physical Laboratory, U.K., Report AC 37.

Fahy, F., 1985, *Sound and Structural Vibration*, Academic Press, London.

Hearman, R. F. S., 1959, "The Frequency of Flexural Vibration of Rectangular Orthotropic Plates With Clamped or Supported Edges," ASME *Journal of Applied Mechanics*, Vol. 26, pp. 537–540.

Heckl, M., 1960, "Untersuchungen an Orthoropen Platten," *Acustica*, Vol. 10.

International Standards Organization, 1978, "Measurement of Sound Insulation in Building Elements," ISO 140.

SOLAS, 1974, "International Convention for the Safety of Life at Sea," Regulation 3, Chap. 11-2.

Steady-State Analysis of a Nonlinear Rotor-Housing System

Y. B. Kim
Graduate Student.

S. T. Noah
Associate Professor.
Mem. ASME

Mechanical Engineering Department,
Texas A&M University,
College Station, TX 77843-3123

The periodic steady-state response of a high-pressure oxygen turbopump (HPOTP) of a space shuttle main engine (SSME), involving a clearance between the bearing and housing carrier, is sought. A harmonic balance method utilizing Fast Fourier Transform (FFT) algorithm is developed for the analysis. An impedance method is used to reduce the number of degrees of freedom to the displacements at the bearing clearance. Harmonic and subharmonic responses to imbalance for various system parameters are studied. The results show that the computational technique developed in this study is an effective and flexible method for determining the stable and unstable periodic response of complex rotor-housing systems with clearance-type nonlinearity.

Introduction

Modern complex rotating machinery contains various sources of strong nonlinearities. These include clearances in bearings, gears and splines, rubbing in splines, seals and rotor blades, squeeze film dampers, and other fluid effects. Observed nonlinear behavior of actual rotor systems includes jump discontinuities (Ehrich, 1966), large subsynchronous motion (Bently, 1979; Muszynska, 1984; Beatty, 1985), quasi-periodic and possible chaos (Neilson and Barr, 1988). As stated by Nataraj and Nelson (1987), future developments in modern machines depend heavily on the ability to identify, understand mathematically, and analyze systems involving nonlinear components.

Quite often, it is essential to determine the steady-state periodic response of rotor systems in the form of self-excited limit cycles or forced motion due to rotating unbalance. Accurate prediction of the nonlinear periodic responses and their stability plays a central role in developing a complete picture of the dynamic behavior of nonlinear rotor systems as function of their parameters.

Several methods have recently been advanced for determining the periodic response of low-order nonlinear rotor systems (Yamamoto, 1954; Childs, 1982; Saito, 1985; Choi and Noah, 1987). For application to larger, multidisk rotor systems, Nataraj and Nelson (1987) developed a periodic solution method based on a collocation approach for the response of the rotor. They utilized a subsystem approach to reduce the size of the resulting system of algebraic equations.

The aim of the present paper is to present a general approach for the determination of the synchronous and subsynchronous response of complex rotor systems. The method is applied to a rotor system interacting through local large nonlinearities with its flexible housing. The present work extends the harmonic balance method developed earlier (Saito, 1985; Choi and Noah, 1987) for a modified Jeffcott rotor model with bearing clearances to the determination of the periodic response of nonlinear multidisk rotor systems with flexible housings.

In the present work, it is shown that the harmonic balance method, as applied to a large, rotor-housing system with bearing clearances, can be made to be highly efficient. This is achieved by using a version of an impedance formulation in which the system is reduced to its displacements at the bearing clearances (see Noah, 1984; Fan and Noah, 1989). In this case, the impedance method is applied to each of the harmonic components of the assumed periodic solution.

Rotor-Housing Model

A typical multidisk rotor interacting with its flexible housing through rolling element bearings with deadband clearances is considered. A bearing with deadband clearance between the outer race and the housing is located at nodes 1 and 10 in Fig. 2. The equations of motion of the rotor using a finite element method can be written in matrix form as

$$[M]_R\{\ddot{R}\} + [C]_R\{\dot{R}\} + [K]_R\{R\} = \{F_c\}_R + \{F_I\}_R \qquad (1)$$

where $[M]_R$ is a mass matrix, including diametral moment of inertias for the disks; $[C]_R$ includes damping and gyroscopic terms. The vector $\{F_c\}_R$ represents the coupling forces acting on the rotor by the housing including nonlinear deadband type bearing reaction forces. $\{F_I\}$ is the vector of the mass imbalance forces of the disks and the displacement vector $\{R\}$ is defined as

$$\{R\} = \{R_{1x}, R_{1y}, \ldots, \beta_{My}, \beta_{Mx}\}$$

where R_i and β_i stand for displacement and rotation, respectively, and the subscript M represents the total node number.

In particular, the forces in the y direction on the bearings with clearances are expressed as

Contributed by the International Gas Turbine Institute and presented at the 35th International Gas Turbine and Aeroengine Congress and Exposition, Brussels, Belgium, June 11-14, 1990. Manuscript received by the International Gas Turbine Institute January 19, 1990. Paper No. 90-GT-328.

$$F_{bmy} = K_{bmy}(R_{my} - H_{ny})\left(1 - \frac{\delta}{\sqrt{(R_{my} - H_{ny})^2 + (R_{mz} - H_{nz})^2}}\right) \tag{2}$$

where m and n denote the bearing node numbers on the rotor and housing, respectively, and y and z denote the y axis and z axis of the rotor and housing coordinates. The rotor displacements are denoted by R while H denotes the housing response. The symbol δ represents the size of the deadband clearance between a bearing and the housing.

The bearing forces, F_{bmy} or F_{bmz}, will vanish if δ is larger than the radial displacement of the rotor relative to the housing, which is the denominator in Eq. (2); otherwise the bearing forces will be as given by Eq. (2). A similar expression can be written for the nonlinear bearing forces in the z direction, which are denoted by F_{bmz}.

The equations of motion for the housing can be written in the matrix form as

$$[M]_H\{\ddot{H}\} + [C]_H\{\dot{H}\} + [K]_H\{H\} = \{F_c\}_H \tag{3}$$

where $\{H\}$ is the vector of the transverse and rotational displacements at each node of the housing model and the subscript H stands for the housing system. $\{F_c\}_H$ denotes the coupling forces on the housing due to the rotor so that

$$\{F_c\}_H = -\{F_c\}_R \tag{4}$$

In order to reduce the system to its displacements at the nonlinear bearing supports, the equations of motion need to be modified. This is achieved using a subsystem approach. The coordinate vector can be modified so that the transverse displacements at the gap are listed first;

$$\{R\} = \{R_{1y,2y,\ldots,Ny}, R_{1z,2z,\ldots,Nz}, R_{(N+1)y,(N+2)y,\ldots,My}, R_{(N+1)z,(N+2)z,\ldots,Mz}\}^T$$

where $(1, 2, \ldots, N)$ is the bearing node number related to nonlinearity while $(N + 1, N + 2, \ldots, M)$ is the other node number involving linear displacements, which will be eliminated in the assembling procedure.

The housing coordinate vector can be rearranged in a similar fashion. After rearranging the coordinate vectors, the matrices $[M]_R$, $[M]_H$, $[C]_R$, $[C]_H$, $[K]_R$, and $[K]_H$, and other force vectors also need to be modified according to their vector components.

Analysis

Extending the procedure developed by Choi and Noah (1987), a steady-state, periodic solution for the motion of the rotor can be represented by a Fourier series expansion. For the displacement of the ith node, one writes

$$R_{iy} = A^i_{0y} + \sum_{n=1}^{N}\left(A^i_{ny}\cos\frac{n\omega t}{\nu} + B^i_{ny}\sin\frac{n\omega t}{\nu}\right) \tag{5a}$$

$$R_{iz} = A^i_{0z} + \sum_{n=1}^{N}\left(A^i_{nz}\cos\frac{n\omega t}{\nu} + B^i_{nz}\sin\frac{n\omega t}{\nu}\right) \tag{5b}$$

where ν is the subharmonic ratio, which is unity for harmonic and superharmonic cases, or an integer for subharmonic cases. Similar equations are written for the displacements H_{iy} and H_{iz} of the housing. Since the motion is periodic and steady state, the nonlinear coupling force can also be written as

$$f_{iy} = C^i_{0y} + \sum_{n=1}^{N}\left(C^i_{ny}\cos\frac{n\omega t}{\nu} + D^i_{ny}\sin\frac{n\omega t}{\nu}\right) \tag{6a}$$

$$f_{iz} = C^i_{0z} + \sum_{n=1}^{N}\left(C^i_{nz}\cos\frac{n\omega t}{\nu} + D^i_{nz}\sin\frac{n\omega t}{\nu}\right) \tag{6b}$$

The nonlinear forces exerted on the housing are of equal and opposite sign to those of Eq. (6). To apply the harmonic balance method, one forms the vectors of the coefficients of cos $n\omega t/\nu$ and sin $n\omega t/\nu$, for $n = 1, 2, \ldots, N$.

The constant coefficients of the displacements of the coupling forces are then written as follows:

For the constant term,

$$[K]_R\begin{pmatrix}\{A^0_m\}\\ \{A^0_s\}\end{pmatrix} = \begin{pmatrix}\{C^0_m\}\\ \{C^0_s\}\end{pmatrix} \tag{7}$$

where

$$\{A^0_m\} = \{A^1_{0y}, A^1_{0z}, \ldots, A^N_{0y}, A^N_{0z}\}^T$$
$$\{A^0_s\} = \{A^{N+1}_{0y}, A^{N+1}_{0z}, \ldots, A^M_{0y}, A^M_{0z}\}^T$$
$$\{C^0_m\} = \{C^1_{0y}, C^1_{0z}, \ldots, C^N_{0y}, C^N_{0z}\}^T$$
$$\{C^0_s\} = \{0, 0, 0, \ldots, 0, 0\}^T$$

and the subscripts "m" and "s" stand for the master and slave part for a reduced algebraic system resulting from applying the harmonic balance method. The reduced slave co-

Nomenclature

$\{A^0_m\}$ = cosine coefficients associated with Master degree of freedom

$\{\Delta A_m\}$ = incremental vector of $\{A^0_m\}$

A^i_{nx}, A^i_{ny} = nth cosine coefficient of the steady-state solution in x, y direction at ith node

$\{A^0_s\}$ = cosine coefficients associated with Slave degree of freedom

B^i_{nx}, B^i_{ny} = nth sine coefficient of the steady-state solution in x, y direction at ith node

$[C]_R$ = rotor damping matrix

$\{C_n\}$ = constant cosine coefficient vector of nonlinear force

C_{nx}, C_{ny} = nth cosine coefficient of nonlinear force in x, y direction

$\{C^0_m\}$ = cosine coefficients of nonlinear force associated with Master degree of freedom

$\{C^0_s\}$ = cosine coefficients of nonlinear force associated with Slave degree of freedom

$\{D_n\}$ = constant sine coefficient vector of nonlinear force

D_{nx}, D_{ny} = nth sine coefficient of nonlinear force in x, y direction

F = bearing force

$\{F_c\}$ = coupling force vector on housing due to rotor

H_{ix}, H_{iy} = x, y rectilinear housing displacement at ith node

$[K]_R$ = rotor stiffness matrix

K_b = bearing stiffness

$[\bar{K}]$ = equivalent constant coefficient stiffness matrix

$[M]_R$ = rotor mass matrix

$\{Q_m\}$ = trigonometric coefficients associated with Master degree of freedom

$\{Q^0_{mn}\}$ = trigonometric coefficients with nth harmonic mode in Master degree of freedom

$\{\Delta Q_n\}$ = incremental vector form of $\{Q^0_{mn}\}$

$\{Q_s\}$ = trigonometric coefficients associated with Slave degree of freedom

$\{R\}$ = rotor displacement vector

R_{ix}, R_{iy} = x, y rectilinear displacement at ith node

$[S]$ = total trigonometric coefficient matrix

$[\bar{S}]$ = equivalent trigonometric coefficient matrix

$[\overline{S_n}]$ = equivalent trigonometric coefficient matrix with nth harmonic mode

ordinates correspond to those coordinates where no coupling forces exist. Therefore, the stiffness matrix of the rotor, $[K]_R$, is partitioned as

$$[K]_R = \begin{pmatrix} [K_{mm}]_R^{(2N\times 2N)} & [K_{ms}]_R^{(2N\times 2L)} \\ [K_{sm}]_R^{(2L\times 2N)} & [K_{ss}]_R^{(2L\times 2L)} \end{pmatrix}$$

where N is the total number of degrees of freedom at the nonlinearity and L is the total number of degrees of freedom associated with linear displacements of the rotor. Equation (7) is expanded as

$$[K_{mm}]_R\{A_m^0\} + [K_{ms}]_R\{A_s^0\} = \{C_m^0\} \tag{8a}$$

$$[K_{sm}]_R\{A_m^0\} + [K_{ss}]_R\{A_s^0\} = \{C_s^0\} \tag{8b}$$

Combining Eqs. (7) and (8), the following equation is obtained

$$[[K_{mm}]_R - [K_{ms}]_R[K_{ss}]_R^{-1}[K_{sm}]_R]\{A_m^0\} = \{C_m^0\} \tag{9}$$

By setting

$$[\bar{K}]_R = [K_{mm}]_R - [K_{ms}]_R[K_{ss}]_R^{-1}[K_{sm}]_R, \quad (2N\times 2N)$$

the final reduced matrix can be written as

$$[\bar{K}]_R\{A_m^0\} = \{C_m^0\} \tag{10}$$

Because of the gap relations already given by Eq. (2), a discrete FFT algorithm will result in $\{C_m^0\}$ being a function of all the Fourier coefficients in Eq. (5) and the corresponding coefficients for the housing displacements. The implicit equation form of the above relation can be expressed as

$$\{C_m^0\} = \{C_m^0(A_{0y}^N, A_{0z}^N, \ldots, A_{ny}^N, A_{nz}^N)\} \tag{11}$$

where N is the total nonlinear degree of freedom number and n represents the retained harmonic terms. The Newton-Raphson (second-order) iterative method is used, and for that purpose an incremental form is written in place of Eq. (10).

If one sets

$$\{A_m^0\} = \{A_m^0\} + \{\Delta A_m\}$$
$$\{C_m^0\} = \{C_m^0\} + \{\Delta C_m\}$$

then

$$[\bar{K}]_R\{\Delta A_m\} - \{\Delta C_m\} = \{C_m^0\} - [\bar{K}]_R\{A_m^0\} \tag{12}$$

This equation is solved sequentially with an equivalent set for the housing at each increment and iteration is used to obtain compatible coefficient increments for the rotor and housing.

Applying the harmonic balance method to the equations of motion (1), the cosine terms leads to

$$-\left(\frac{n\omega}{\nu}\right)^2[M]_R\{A\} + \left(\frac{n\omega}{\nu}\right)[C]_R\{B\} + [K]_R\{A\} = \{C_n\} + \{g_c\} \tag{13}$$

where

$$\{A\} = \{A_{ny}^1, A_{nz}^1, \ldots, A_{ny}^M, A_{nz}^M\}^T$$
$$\{B\} = \{B_{ny}^1, B_{nz}^1, \ldots, B_{ny}^M, B_{nz}^M\}^T \quad (M = N+L)$$
$$\{C_n\} = \{C_{ny}^1, C_{nz}^1, \ldots, C_{ny}^N, C_{nz}^N, 0, 0, \ldots\ldots 0\}^T$$
$$\{g_c\} = \{0, 0, 0, \ldots, (me\omega^2)^{\alpha i}, 0, (me\omega^2)^{\alpha j}, 0, \ldots, 0\}^T$$
$$= \{0\}$$
$$\text{if } n = \nu \ (n = 1, 2, \ldots, N)$$
$$\text{if } n \neq \nu$$

where the α are the nodes at which the disks are located; M is the total node numbers; N is the node on which the nonlinear coupling forces of the rotor to the housing exist. Similar expressions are written for the housing.

For the sine terms, one obtains

$$-\left(\frac{n\omega}{\nu}\right)^2[M]_R\{B\} - \left(\frac{n\omega}{\nu}\right)[C]_R\{A\} + [K]_R\{B\} = \{D_n\} + \{g_s\} \tag{14}$$

where

$$\{D_n\} = \{D_{ny}^1, D_{nz}^1, \ldots, D_{ny}^N, D_{nz}^N, 0, \ldots, 0\}^T$$
$$\{g_s\} = \{0, 0, 0, \ldots, (me\omega^2)^{\alpha i}, 0, (me\omega^2)^{\alpha j}, 0, \ldots, 0\}^T$$
$$= \{0\}$$
$$\text{if } n = \nu \ (n = 1, 2, \ldots, N)$$
$$\text{if } n \neq \nu$$

Combining Eqs. (13) and (14)

$$[S]_R\{Q\} = \{w\} + \{u\} \tag{15}$$

where

$$\{w\} = \{C_{ny}^N, C_{nz}^N, D_{ny}^N, D_{nz}^N, 0, \ldots, 0\}^T$$
$$\{u\} = \{A_{ny}^1, A_{nz}^1, B_{ny}^1, B_{nz}^1, \ldots, B_{ny}^M, B_{nz}^M\}^T$$

Nomenclature (cont.)

$[T]$ = overall coefficient matrix
$\{\bar{U}\}$ = equivalent trigonometric force vector
$\{W_m\}$ = trigonometric coefficients of nonlinear force associated with Master degree of freedom
$\{W_{mn}^0\}$ = trigonometric vector of nonlinear force with nth harmonic mode in Master degree of freedom
$\{\Delta W_{mn}\}$ = incremental vector of $\{W_{mn}^0\}$
e = eccentricity
$\{f_{ix}, f_{iy}\}$ = nonlinear restoring force vector in x, direction at ith node
$\{g_c, g_s\}$ = imbalance force vector of cosine, sine terms
m = disk mass
$\{q\}$ = constant trigonometric coefficient vector of steady-state solution
$\{\Delta r\}$ = overall incremental coefficient vector
$\{u\}$ = total imbalance force vector
$\{\Delta v\}$ = overall incremental coefficient vector of nonlinear force
$\{w\}$ = constant trigonometric coefficient vector of nonlinear force
$\{z\}$ = overall force vector
β_{ix}, β_{iy} = rotational displacement in x, y direction at ith node
δ = gap size
ν = subharmonic ratio

Subscripts

B = bearing-related term
H = housing-related term
L = total number of degrees of freedom associated with linear motion
N = total number of degrees of freedom associated with nonlinear coupling nodes
M = total number of degrees of freedom = $L + N$
R = rotor-related term
m = Master degree of freedom
n = nth harmonic mode
s = Slave degree of freedom
x = x direction
y = y direction

Superscripts

i = ith node
α = node number at which disk is located

To apply the reduction technique, Eq. (15) can be partitioned as follows:

$$\begin{pmatrix} [S_{mm}]_R^{(4N\times 4N)} & [S_{ms}]_R^{(4N\times 4L)} \\ [S_{sm}]_R^{(4L\times 4N)} & [S_{ss}]_R^{(4L\times 4L)} \end{pmatrix} \begin{pmatrix} \{Q_m\} \\ \{Q_s\} \end{pmatrix} = \begin{pmatrix} \{W_n\} \\ 0 \end{pmatrix} + \begin{pmatrix} \{U_m\} \\ \{U_s\} \end{pmatrix} \tag{16}$$

where

$$\{Q_m\} = \{A_{ny}^1, A_{nz}^1, \ldots, B_{ny}^N, B_{nz}^N\}^T$$
$$\{Q_s\} = \{A_{ny}^{N+1}, A_{nz}^{N+1}, \ldots, B_{ny}^M, B_{nz}^M\}^T$$
$$\{W_m\} = \{C_{ny}^1, C_{nz}^1, \ldots, D_{ny}^N, D_{nz}^N\}^T$$
$$\{U_s\} = \{0, 0, \ldots, (me\omega^2)^{\alpha i}, 0, 0, (me\omega^2)^{\alpha i}, 0, \ldots, 0\}^T$$
$$\{U_m\} = \{0, 0, \ldots, 0, 0\}^T$$

Equation (16) can be expanded as

$$[S_{mm}]_R\{Q_m\} + [S_{ms}]_R\{Q_s\} = \{W_m\} + \{U_m\} \tag{17a}$$
$$[S_{sm}]_R\{Q_m\} + [S_{ss}]_R\{Q_s\} = \{U_s\} \tag{17b}$$

From Eq. (17*b*)

$$\{Q_S\} = [S_{ss}]_R^{-1}\{U_s\} - [S_{ss}]_R^{-1}[S_{sm}]_R\{Q_m\} \tag{18}$$

Combining Eqs. (17*a*) and (18), the following equation is obtained:

$$[[S_{mm}]_R - [S_{ms}]_R[S_{ss}]_R^{-1}[S_{sm}]_R]\{Q_m\} = \{W_m\} + \{U_m\} - [S_{ms}]_R[S_{ss}]_R^{-1}\{U_s\} \tag{19}$$

If we set

$$[\overline{S}]_R = [S_{mm}]_R - [S_{ms}]_R[S_{ss}]_R^{-1}[S_{sm}]_R, \quad (4N\times 4N)$$
$$\{\overline{U}\} = [U_m] - [S_{ms}]_R[S_{ss}]_R^{-1}\{U_s\}, \quad (4N\times 1)$$

then Eq. (16) can be rearranged as

$$[\overline{S}]_R\{Q_m\} = \{W_m\} + \{\overline{U}\} \tag{20}$$

To apply a numerical iteration procedure, one can use the following incremental form:

$$\{Q_m\} = \{Q_m\} + \{\Delta Q_m\}$$
$$\{W_m\} = \{W_m\} + \{\Delta W_m\} \tag{21}$$

Substituting Eq. (21) into Eq. (20),

$$[\overline{S}]_R\{\Delta Q_m\} - \{\Delta W_m\} = \{W_m\} + \{\overline{U}\} - [\overline{S}]_R\{Q_m\} \tag{22}$$

Since Eq. (22) is obtained only for one harmonic term, one can expand Eq. (22) for general retained harmonic terms

$$[\overline{S_n}]_R\{\Delta Q_{mn}\} - \{\Delta W_{mn}\} = \{W_{mn}\} + \{\overline{U_n}\} - [\overline{S_n}]_R\{Q_{mn}\}, \tag{23}$$

where $n = 1, 2, \ldots, N$.

Equation (23) represents the cosine and sine incremental terms and Eq. (12) represents the incremental constant term, so one can combine these equations. $\{Q_{mn}\}$ and $\{A_m\}$ contain the final solution forms, which are solved by the Newton–Raphson method. The overall incremental form for the rotor system will be as follows:

$$[T]_R\{\Delta r\} - \{\Delta v\} = \{z\} \tag{24}$$

where

$$\{\Delta r\} = \{\Delta A_{0y}^1, \Delta A_{0z}^1, \Delta A_{0y}^2, \Delta A_{0z}^2, \ldots, \Delta A_{0y}^N, \Delta A_{0z}^N, \Delta A_{1y}^1, \Delta A_{1z}^1, \Delta B_{1y}^1, \Delta B_{1z}^1, \ldots, \Delta B_{1y}^N, \Delta B_{1z}^N, \vdots \Delta A_{ny}^1, \Delta A_{nz}^1, \Delta B_{ny}^1, \Delta B_{nz}^1, \ldots, \Delta B_{ny}^N, \Delta B_{nz}^N\}^T$$

$$\{\Delta v\} = \{\Delta C_{0y}^1, \Delta C_{0z}^1, \Delta C_{0y}^2, \Delta C_{0z}^2, \ldots, \Delta C_{0y}^N, \Delta C_{0z}^N, \Delta C_{1y}^1, \Delta C_{1z}^1, \Delta D_{1y}^1, \Delta D_{1z}^1, \ldots, \Delta D_{1y}^N, \Delta D_{1z}^N, \vdots \Delta C_{ny}^1, \Delta C_{nz}^1, \Delta D_{ny}^1, \Delta D_{nz}^1, \ldots, \Delta D_{ny}^N, \Delta D_{nz}^N\}^T$$

and

$$[T]_R = \begin{pmatrix} [\overline{K}_R & \ldots & \ldots & 0 \\ 0 & [\overline{S_1}]_R & \ldots & 0 \\ \vdots & \vdots & \ddots & \vdots \\ 0 & \ldots & \ldots & [\overline{S_n}]_R \end{pmatrix}$$

where

$$\{z\} = [\{C_m^0\} - [\overline{K}]_R\{A_m^0\}, \{W_{m1}\} - \{\overline{U_1}\} - [\overline{S_1}]_R\{Q_{m1}\}, \{W_{m2}\} - \{\overline{U_2}\} - [\overline{S_2}]_R\{Q_{m2}\}, \ldots, \{W_{mn}\} - \{\overline{U_n}\} - [\overline{S_n}]_R\{Q_{mn}\}]^T$$

$[\overline{K}]_R$ is $(2N \times 2N)$ and $[\overline{S_i}]_R$ is $(4N \times 4N)$ for $(i = 1, 2, \ldots, n)$.

From Eq. (24), $\{\Delta v\}$ is written with partial derivatives of $\{\Delta r\}$ terms since $\{\Delta v\}$ is a function of $\{\Delta r\}$. The partial derivative terms yield the Jacobian matrix, so one can finally obtain the following equation:

$$\{\Delta v\} = [P]\{r\} \tag{25}$$

where

$$[P] = \begin{pmatrix} \frac{\partial C_{0y}^1}{\partial A_{0y}^1} & \frac{\partial C_{0y}^1}{\partial A_{0z}^1} & \frac{\partial C_{0y}^1}{\partial A_{0y}^2} & \cdots & \frac{\partial C_{0y}^1}{\partial B_{nz}^N} \\ \frac{\partial C_{0z}^1}{\partial A_{0y}^1} & \frac{\partial C_{0z}^1}{\partial A_{0z}^1} & \frac{\partial C_{0z}^1}{\partial A_{0y}^2} & \cdots & \frac{\partial C_{0y}^1}{\partial B_{nz}^N} \\ \vdots & \vdots & \vdots & \ddots & \vdots \\ \frac{\partial D_{nz}^N}{\partial A_{0y}^1} & \frac{\partial D_{nz}^N}{\partial A_{0z}^1} & \frac{\partial D_{nz}^N}{\partial A_{0y}^2} & \cdots & \frac{\partial D_{nz}^N}{\partial B_{nz}^N} \end{pmatrix}$$

where the superscript stands for the degree of freedom number while the subscript stands for the retained harmonic term in the y or z direction. The total dimension of the $[P]$ matrix is $2N(1 + 2n) \times 2N(1 + 2n)$ and the size of the unknown vector r is also $2N(1 + 2n)$.

The $[P]$ matrix can be determined using numerical differentiation of the discrete and inverse discrete FFT method. More details on the calculation procedure are given by Choi and Noah (1987). The matrix has to be updated at each iteration step until it converges. The steady-state solution procedure for flexible housing is the same as for the rotor system as outlined above.

After calculating the rotor response using an iteration procedure, the forces due to the nonlinear coupling between rotor and housing are automatically calculated. The nonlinear coupling forces are then applied to the housing system to update the absolute housing displacements and nonlinear coupling forces. Another iteration process is used to obtain once more the updated rotor response and then iterate until both rotor and housing responses have the same steady-state convergent values.

Numerical Results and Discussion

To demonstrate the application and computational efficiency of the harmonic balance method, the method is applied to a modified version of a large generic model utilized previously by Davis et al. (1984) to study the effect of flexibility of the housing on the dynamic behavior of the rotor system. The generic model used in the present paper represents a high-pressure oxygen turbopump (HPOTP) of a space shuttle main engine (SSME). A description of the model is provided in Figs. 1 and 2.

The equations of motion of the rotor and housing are formulated by the finite element method using beam elements. The coupling coefficients at the three disks were arbitrarily selected to include the wear ring seal coupling on the first disk, the impeller-diffuser interaction on the second disk, and the turbine interstage seal coupling coefficients on the third disk.

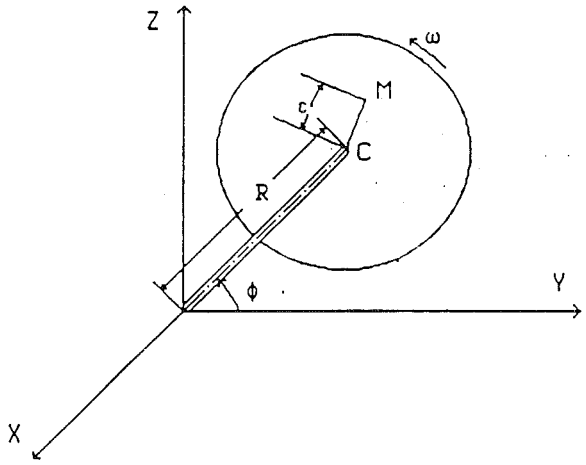

Fig. 1 Rotor coordinate system

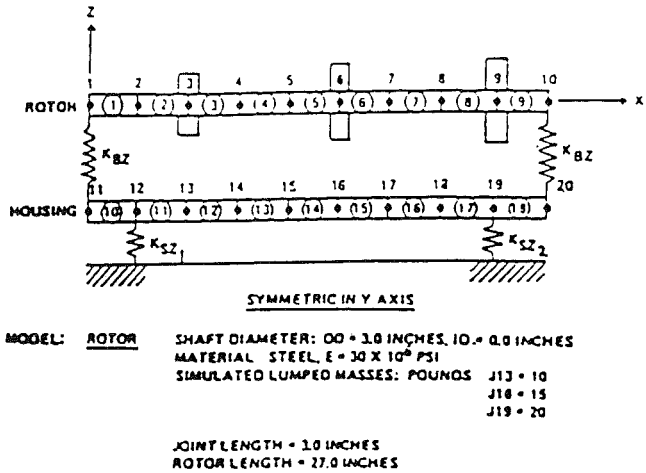

HOUSING

6/1 Housing/Rotor Weight Ratio

$EI = 2\text{-}4 \times 10^8$ LB·IN^3

$KSZ_1 = 4 \times 10^4$ LB/IN

$K_{SY_1} = 5 \times 10^4$ LB/IN

$K_{SZ_2} = 5 \times 10^4$ LB/IN

$K_{SY_2} = 1.5 \times 10^5$ LB/IN

Fig. 2 HPOTP generic model

The rotor is supported at each end by a ball bearing. A clearance exists between the outer race of each bearing and a carrier attached to the housing. The rotor is subjected to imbalance forces and constant direction side forces.

The harmonic balance/FFT method was used to generate forced nonlinear periodic responses in the range 0–40,000 rpm. The results are shown in Fig. 3, in which the fundamental synchronous responses at the two critical speeds are shown to occur around 1900 rad/s and 4300 rad/s. The figure shows the radial displacements of the rotor relative to the housing at the left bearing. The critical speed map is depicted in Fig. 4 for the generic model in the absence of bearing clearances. The gyroscopic terms are included, which are shown to raise the forward critical speeds and lower the backward critical speeds. The figure shows the first two critical speeds to be exactly the same as those of the linear case obtained using the harmonic

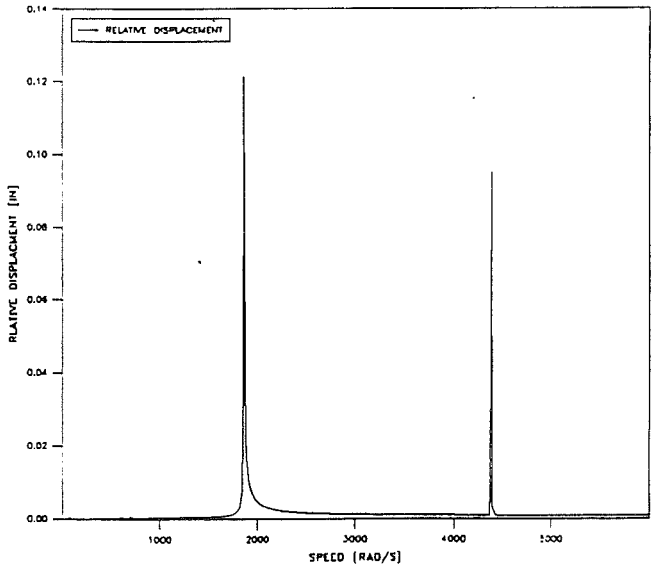

Fig. 3 Critical speed of generic model at left bearing side eccentricity = 0.5 mils, no damping, no gyroscopic, linear

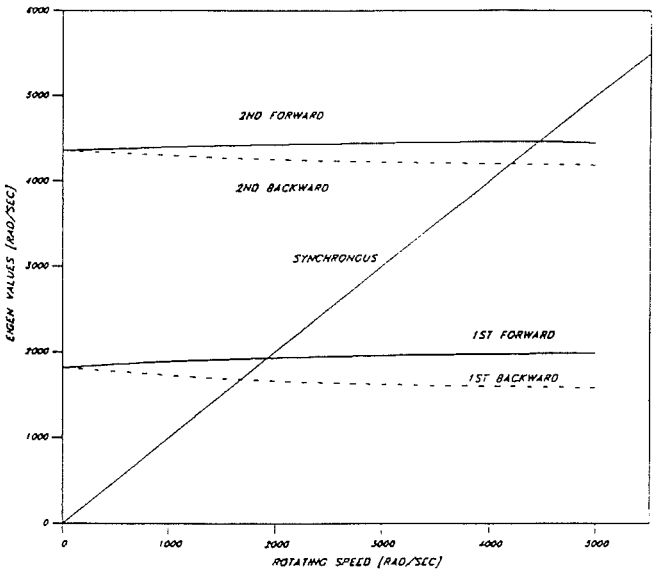

Fig. 4 Critical speed map for the generic model; no damping, linear

balance/FFT method. Numerical calculation is performed to investigate the existence of subharmonic responses.

The trajectory of the shaft center of a $1/n$ order subharmonic response lies in the region bounded by circles with radii, which are determined by the harmonic and subharmonic amplitudes. The trajectory touches the bounded circles at $(n - 1)$ points for forward whirl and $(n + 1)$ points for backward whirl (see Tondl, 1973). The shaft center trajectory is studied to identify the subharmonic responses and to compare the amplitude between the harmonic response and the $1/n$ order subharmonic response with various values of the side force, gap size, and rotor mass eccentricity (the term eccentricity will denote rotor mass eccentricity hereafter) near the critical speeds. To allow the occurrence of the subharmonic response, the damping is set to a small value for all cases. The results are shown in Figs. 5–8. These figures show that all subharmonic responses occur around the second critical speed and that all are of the order 1/2. In Fig. 5, the harmonic and subharmonic amplitudes are almost of the same magnitude for a small side force. In Fig. 6, the harmonic response becomes dominant when reducing

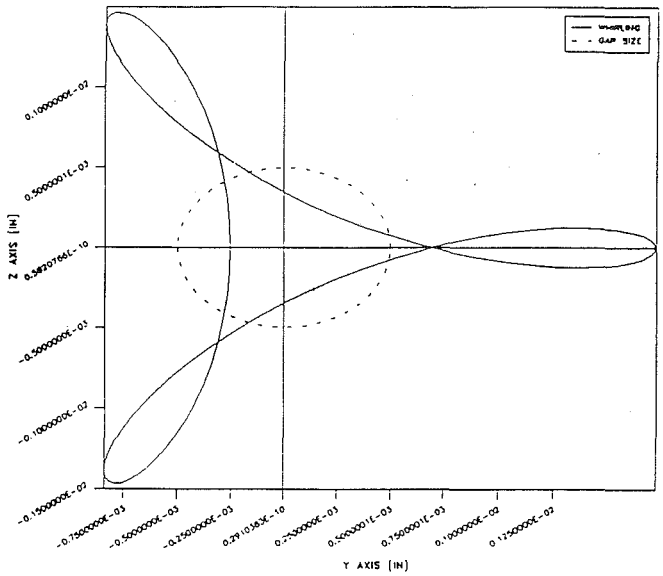

Fig. 5 Trajectory for subharmonic of order 1/2 gap = 0.5 mils, eccentricity = 0.5 mils, side force = 10 lb, speed = 4210 rad/s

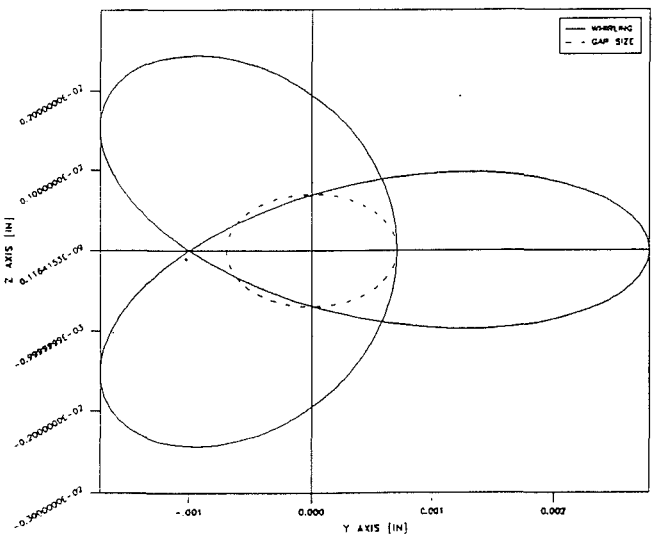

Fig. 7 Trajectory for subharmonic of order 1/2 gap = 0.7 mils, eccentricity = 0.5 mils, side force = 10 lb, speed = 4210 rad/s

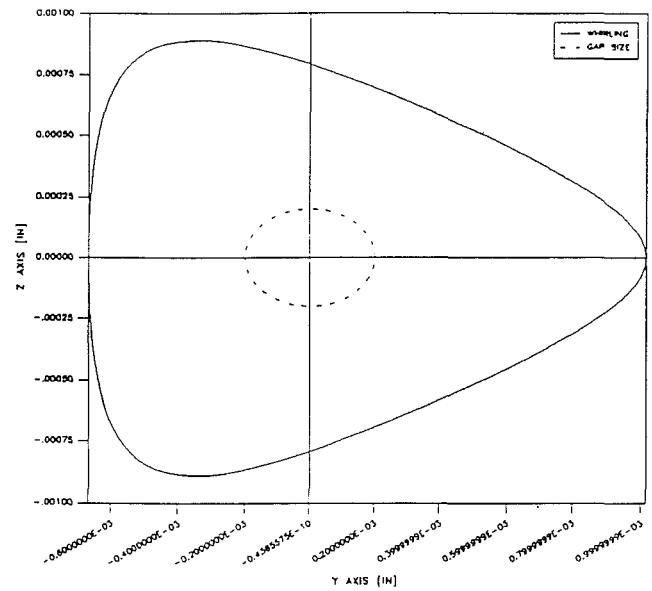

Fig. 6 Trajectory for subharmonic of order 1/2 gap = 0.2 mils, eccentricity = 0.5 mils, side force = 10 lb, speed = 4210 rad/s

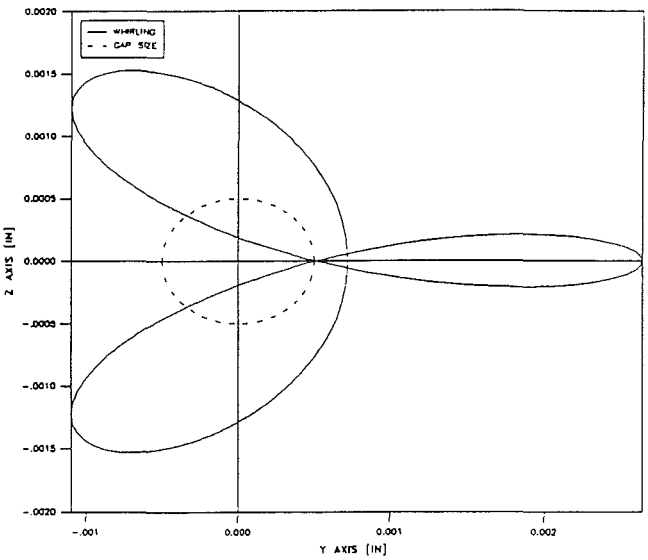

Fig. 8 Trajectory for subharmonic of order 1/2 gap = 0.5 mils, eccentricity = 0.5 mils, side force = 100 lb, speed = 4210 rad/s

the bearing clearance size. On the contrary, the 1/2 order subharmonic response becomes larger than the amplitude of the harmonic component by increasing the clearance size, as can be seen in Fig. 7. The gap size has a significant effect on the existence of the 1/2 order subharmonics in the HPOTP model regardless of the side force. In Fig. 8, the side force is raised to ten times that of Fig. 5. In that case, the results show the amplitude of the subharmonic response becoming slightly larger than that of the harmonic response. This result reveals that the side force also has some influence on whether any subharmonic response occurs.

A more detailed investigation comparing the effects of the side force and gap size is studied and the results are shown in Fig. 9. The figure shows that the side force has a significant effect on the existence of the 1/2 order subharmonic response. Around 200 lb side force and 0.5–0.7 mils of gap size is the region that induces the large amplitude of the 1/2 order subharmonic. Excessive side force, larger than 400 lb, will cause a reduction of the subharmonic responses. With constant gap size and eccentricity, there exists a certain range of side force region in which larger subharmonic response would occur. This agrees well with results presented by Choi and Noah (1987).

The effect of eccentricity on the existence of the 1/2 order subharmonic response with variation of the side force is studied and is shown in Fig. 10. The figure shows that the eccentricity has the effect of shifting the location of the maximum subharmonic response to the right. The side force ranges at which the maximum 1/2 order subharmonic response occurs are different for each eccentricity. The figure also shows that the larger eccentricity is, the lower the subharmonic response will be. This explains that the larger response amplitude due to the larger eccentricity induces more contact region than noncontact region and this effect reduces the amplitude of subharmonics since the system becomes relatively weakly nonlinear. It may then be necessary to reduce the gap size and side forces in any proposed design or maintenance criteria in order to eliminate dangerous subharmonic responses.

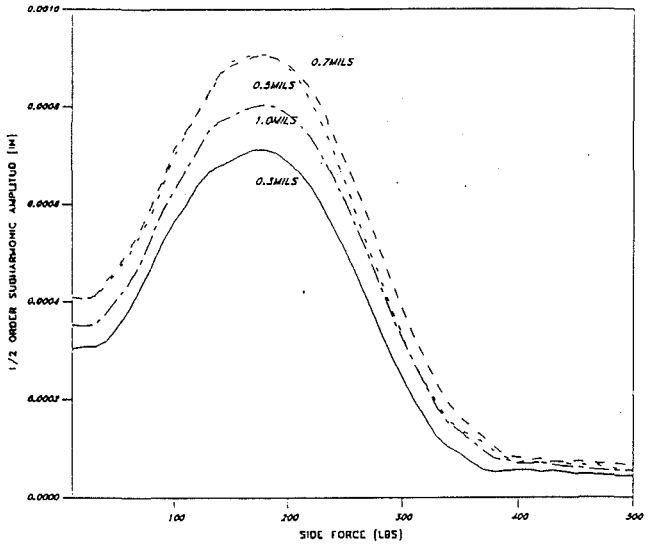

Fig. 9 Gap size effect on subharmonic of order 1/2 eccentricity = 0.5 mils, speed = 4210 rad/s

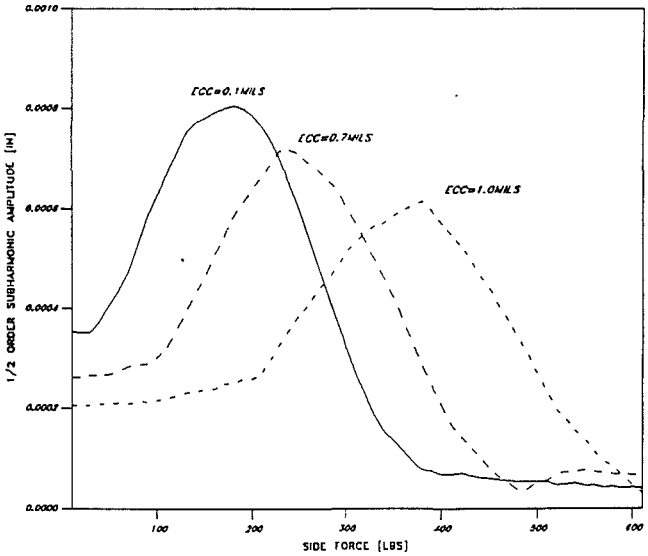

Fig. 10 Eccentricity effect on subharmonic of order 1/2 gap size = 0.5 mils, speed = 4210 rad/s

Conclusions

Based on the results obtained during the course of this study, the following conclusions can be made:

1 The harmonic balance/FFT method offers an effective and flexible method for determining the stable and unstable periodic response of nonlinear complex rotor-housing systems.

2 In comparison to the harmonic balance approach, a direct numerical integration method is used to obtain the steady-state periodic solutions:

(*a*) Will require much longer computational time for the relatively lightly damped rotor system to settle to a steady state.

(*b*) Will determine only stable periodic responses and not the unstable solutions, which may be used to indicate the onsets of transitions to chaotic responses.

(*c*) Might miss a close-by large steady-state solution from among multiple nonlinear solutions due to an unfortunate selection of initial conditions.

Acknowledgments

This work was carried out as part of a research project supported by NASA, Marshall Flight Center under contract No. NAS8-36293. The authors are grateful to Thomas Fox, the technical monitor, for his enthusiastic support and interest.

References

Beatty, R. F., 1985, "Differentiating Rotor Response Due to Radial Rubbing," ASME *Journal of Vibration, Acoustics, Stress, and Reliability in Design*, Vol. 107, pp. 151–160.

Bently, D., 1979, "Forced Subrotative Speed Dynamic Action of Rotating Machinery," ASME Paper No. 79-PET-16.

Childs, D. W., 1982, "Fractional-Frequency Rotor Motion Due to Nonsymmetric Clearance Effects," ASME JOURNAL OF ENGINEERING FOR POWER, Vol. 104, pp. 533–541.

Choi, Y. S., and Noah, S. T., 1987, "Nonlinear Steady-State Response of a Rotor-Support System," ASME *Journal of Vibration, Acoustics, Stress, and Reliability in Design*, Vol. 109, pp. 255–261.

Davis, L. B., Wolfe, E. A., and Betty, R. F., 1984, "Housing Flexibility Effects on Rotor Stability," *MSFC Advanced High Pressure O_2/H_2 Technology Conference Proceedings*, G. Marshall Space Flight Center, Huntsville, AL, June 27–29.

Ehrich, F. F., 1966, "Subharmonic Vibrations of Rotors in Bearing Clearance," ASME Paper No. 66-MD-1.

Ehrich, F. F., 1988, "High Order Subharmonic Response of High Speed Rotors in Bearing Clearance," ASME *Journal of Vibration, Acoustics, Stress, and Reliability in Design*, Vol. 110, pp. 9–16.

Fan, U. J., and Noah, S. T., 1989, "Vibration Analysis of Rotor Systems Using Reduced Subsystem Models," AIAA *Journal of Propulsion and Power*, in press.

Muszynska, A., 1984, "Partial Lateral Rotor to Stator Rubs," *Proceedings of the I. Mech. E. 3rd. Intl. Conf. on Vibrations in Rotating Machinery*, Univ. of York, Sept. 11–13, pp. 327–335.

Nataraj, C., and Nelson, H. D., 1987, "Periodic Solutions in Rotor Dynamic Systems With Nonlinear Supports: A General Support," presented at the ASME Design Conference, Oct.

Neilson, R. D., and Barr, A. D. S., 1988, "Response of Two Elastically Supported Rigid Rotors Sharing a Common Discontinuously Non-linear Support," *Proceedings of the Institution of Mechanical Engineers*, Heriot-Watt University, Sept. 13–15, pp. 589–598.

Noah, S. T., 1984, "Rotordynamic Analysis of the SSME Turbopumps Using Reduced Models," Final Report on NASA Contract NAS8-34505, Texas A&M University, Sept.

Saito, S., 1985, "Calculation of Nonlinear Unbalance Response of Horizontal Jeffcott Rotors Supported by Ball Bearings With Radial Clearances," ASME Paper No. 85-DET-33.

Tondl, A., 1973, "Notes on the Identification of Subharmonic Resonances of Rotors," *Journal of Sound and Vibration*, Vol. 31, No. 1, pp. 119–127.

Yamamoto, T. T., 1954, "On Critical Speeds of a Shaft," *Memoirs of the Faculty of Engineering, Nagoya (Japan) University*, Vol. 6, No. 2.

Development of an Efficient Oil Film Damper for Improving the Control of Rotor Vibration

Shiping Zhang

Litang Yan

Jet Propulsion Department,
Beijing University of Aeronautics and Astronautics,
Beijing 100083,
People's Republic of China

An efficient oil film damper known as a porous squeeze film damper (PSFD) was developed for more effective and reliable vibration control of high-speed rotors based on the conventional squeeze film damper (SFD). The outer race of the PSFD is made of permeable sintered porous metal materials. The permeability allows some of the oil to permeate into and seep out of the porous matrix, with remarkable improvement of the squeeze film damping properties. The characteristics of PSFD oil film stiffness and damping coefficients and permeability, and also, the steady-state unbalance response of a simple rigid rotor and flexible Jeffcott's rotor supported on PSFD and SFD are investigated. A typical experiment is presented. Investigations show that the nonlinear vibration characteristics of the unpressurized SFD system such as bistable jump phenomena and "lockup" at rotor pin-pin critical speeds could be avoided and virtually disappear under much greater unbalance levels with properly designed PSFD system. PSFD has the potential advantage of operating effectively under relatively large unbalance conditions.

Introduction

Modern gas turbine engines typically utilize squeeze film dampers (SFDs) as a flexible damped support to attenuate vibration amplitudes, and to reduce transmitted forces. In spite of the successful applications of SFDs, investigators have widely recognized that because of the nonlinear characteristics of squeeze film forces, the unbalance response of a rotor system using SFDs can be markedly dependent on rotor unbalance and the SFD design. Also, undesirable operation modes, characterized by high unbalance transmissibilities and rotor excursion amplitudes, are a possibility.

Squeeze film forces of conventional SFDs have a highly nonlinear dependence on whirl amplitudes and in turn on rotor unbalance. The highly nonlinear radial components of squeeze film forces for unpressurized SFDs are the decisive factor for SFD undesirable nonlinear performance, which can limit their effectiveness in controlling rotor vibration under certain unbalance conditions. The most remarkable nonlinear performance of SFDs is the existence of the so-called "jump" phenomena. For a rigid rotor on unpressurized SFD mounts, the value of the unbalance parameter $U>0.4$ would cause the "jump" bistable operation [1, 2]. For a flexible rotor on unpressurized SFD mounts, if $U>0.2$, bistable operation occurs for speeds below the first pin-pin critical speed and results in "lockup" of the bearing mounts [3, 4]. Therefore, improving the damping characteristics of squeeze film dampers for tolerating high rotor unbalance and favoring more effective rotor vibration control would be of considerable importance for practical applications of gas turbine engines and other high-speed rotating machinery.

Over the last two decades, many comprehensive theoretical and experimental investigations concerning the characteristics of SFDs and their effect on rotor dynamics have been contributed to the literature, and remarkable progress has been made in this field, which forwarded the understanding of the performance of SFD and its engineering applications. Nevertheless, although it has been well known that the effectiveness of SFDs can be limited by their highly nonlinear characteristics, few efforts have been made to improve the vibration control ability of the damper. Recently, San Andres and Vance [5] analyzed the effect of fluid inertia of SFDs. Their investigations show that for dampers operating at moderately large squeeze film Reynolds numbers, a significant reduction in amplitude response and transmitted force is possible. For unpressurized dampers the possibilities of bistable operation and jump phenomena are shown to be reduced and virtually disappear at sufficiently large operating Reynolds numbers. This work implies a possible way for more effective SFD performance with high-speed rotors. Although the effective direct damping coefficient increases in a wide eccentricity range, the effective cross-coupled damping coefficient (stiffness coefficient) remains little influenced when eccentricity $\epsilon>0.75$ ([5], Figs. 2 and 3). That means that the high nonlinear stiffness characteristics of unpressurized SFD bearings at large eccentricity ϵ are hardly improved by fluid inertia. Therefore, the potential advantages of SFDs operating under greater Reynolds numbers are limited. In addition, Adams and Zahloul [6] investigated the controlled-pressure hydrostatic squeeze film damper, which is shown to be one viable approach to reduce vibration significantly by

Contributed by the International Gas Turbine Institute and presented at the 35th International Gas Turbine and Aeroengine Congress and Exposition, Brussels, Belgium, June 11-14, 1990. Manuscript received by the International Gas Turbine Institute January 16, 1990. Paper No. 90-GT-257.

providing damping. The readily controlled variable resonance tuning benefited from the easily controlled variable stiffness. This also seems to be one promising approach for more effective rotor vibration control. At the present time, however, the availability of passive dampers that are inexpensive, reliable, and simple is still of greatest importance for turbomachinery applications. Thus, it appears to be of practical value to engineering applications for the conventional SFDs to be improved to operate with potential advantages for rotor vibration attenuation.

This paper develops an efficient oil film damper for more effective and reliable vibration control of modern gas turbine engines and/or other high-speed rotating machinery. The efficient oil film damper known as the Porous Squeeze Film Damper (PSFD) is developed based on the conventional squeeze film damper. The configuration of the PSFD is the same as that of the SFD, but the outer race of the PSFD is made of permeable sintered porous metal materials. The permeability of PSFD under the squeeze effect makes it possible for some of the oil to permeate into and seep out of the porous matrix, which remarkably affects the characteristics of squeeze film forces, especially when the amplitude eccentricity is greater. The nonlinearity of the squeeze film forces could be reduced with PSFD permeability and damping coefficients of squeeze film forces could be improved. Relatively greater damping forces could be achieved with PSFD. The nonlinear vibration characteristics of an unpressurized SFD system, such as bistable jump phenomena, could be avoided and virtually disappear under a much greater unbalance level with a properly designed PSFD system. PSFD could operate effectively under relative large unbalance loads as compared with SFD system.

The main intent of this paper is to provide investigators and machinery designers with a primary understanding of permeability effected porous squeeze film dampers, and a proposed manner to assess potential benefits of passive oil film dampers for rotor vibration control.

The characteristics of PSFD oil film stiffness and damping coefficients and permeability, and also the steady-state unbalance response of a simple rigid rotor and a modified flexible Jeffcott's rotor [3] supported on PSFD and SFD are investigated. Some additional extensive investigations concerning PSFD, such as attenuation of nonsynchronous motion, suppressing transient vibration response induced by sudden unbalance action, and detailed experimental research have been made [7, 12].

Theoretical Analysis

Figure 1 shows schematically a porous squeeze film damper with the dynamic forces and coordinates are defined. It is

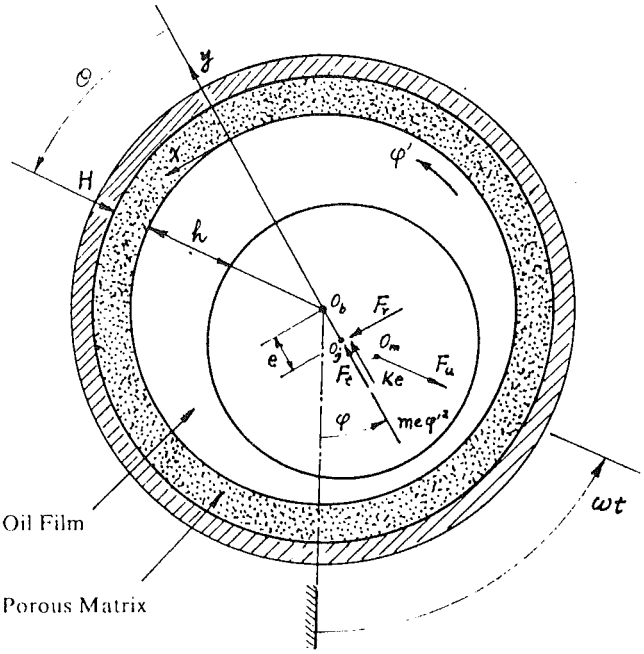

Fig. 1 Porous squeeze film damper with dynamic forces and coordinates

assumed that: (*a*) the oil journal surrounding a rolling element bearing is centrally preloaded with constant symmetric radial support stiffness, and prevented from rotating; (*b*) the short bearing approximation is valid; (*c*) the pressure gradient $\partial p/\partial y$ within the porous damper matrix is a linear function in the radial direction, and $\partial p/\partial y = 0$ at the porous outer boundary; (*d*) the porous material is rigid, homogeneous, and isotropic.

The lubricant flow through the porous bearing is assumed to be governed by Darcy's law [8].

$$q = -\frac{\Phi}{\mu} \cdot \nabla p \tag{1}$$

Thus, the permeability may be defined as:

$$\Phi = -\frac{\mu q_y}{\partial p/\partial y|_{y=0}} \tag{2}$$

Permeability Φ is generally determined by standardized experiments. The continuity equation governing the flow of an incompressible lubricant is

$$\nabla q = 0 \tag{3}$$

Substituting Eq. (1) into Eq. (3), the governing equation for

Nomenclature

a = mass ratio fraction of the total mass at the bearings
B = bearing parameter = $\mu RL^3/(MC^3\omega_r)$
C = radial clearance of bearing
e = journal eccentricity
f = resonance frequency ratio = ω_r/ω_c
F_r, F_t = nondimensional fluid film forces on journal in radial and tangential directions, respectively
g = rotor excursion amplitude at midspan with respect to static deflection line
G = nondimensional rotor amplitude at midspan = g/C
h = oil film thickness = $C(1+\epsilon\cos\theta)$
H = thickness of porous matrix
K_r = retainer spring stiffness per bearing station
$2K_s$ = rotor stiffness
L = axial width of bearing
$2M$ = rotor bearing system mass
p = oil pressure
q = rate of flow
R = radius of journal
T = transmissibility
U = unbalance = $(1-a)\rho/C$
α = permeability parameter = $12\Phi H/C^3$
δ = speed parameter = ω/ω_r
δ_r = retainer spring parameter = ω/ω_r (a speed parameter)
ϵ = eccentricity ratio = e/C
μ = absolute viscosity of lubricant at the mean lubricant temperature
ρ = unbalance eccentricity
φ = angular position of the bearing centerline = ωt
Φ = permeability
ω = rotor speed
ω_c = first pin-pin critical speed of rotor = $\sqrt{K_s/(1-a)M}$
ω_r = natural frequency of rigid rotor on retainer springs = $\sqrt{K_r/M}$
$(\,)'$ = $d/d(\omega t)$, operator

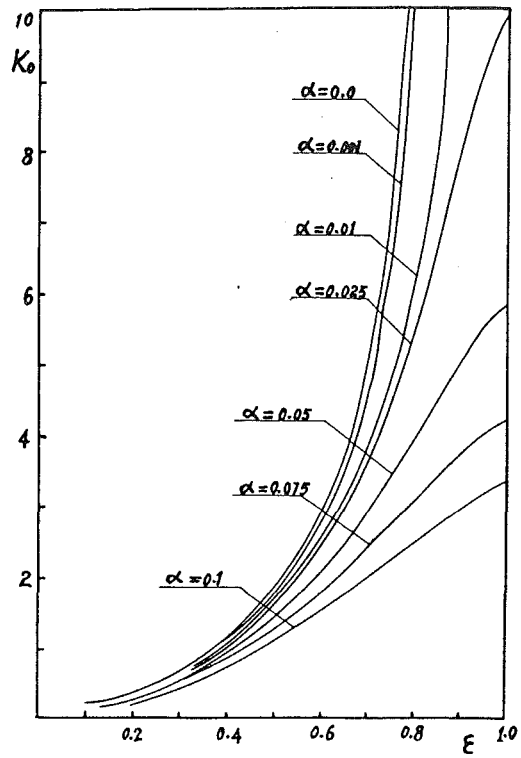

Fig. 2 Stiffness coefficients of PSFD

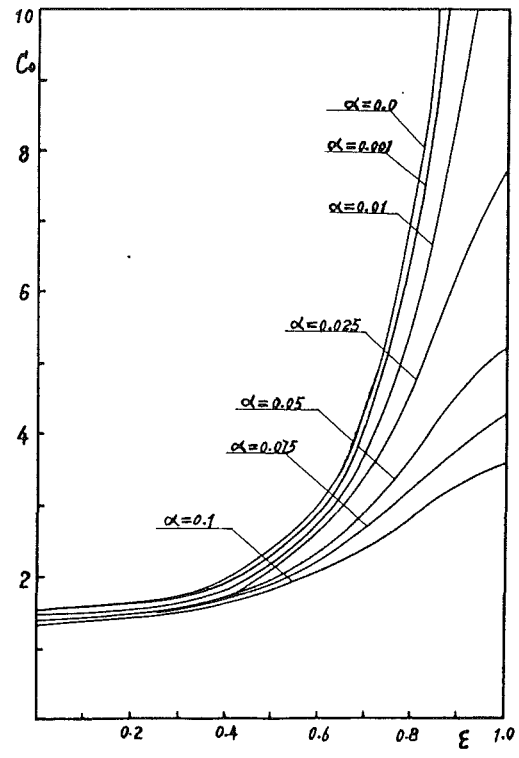

Fig. 3 Damping coefficients of PSFD

the flow of the lubricant within the porous bearing is obtained to be a Laplace equation:

$$\nabla^2 p = \frac{\partial^2 p}{\partial x^2} + \frac{\partial^2 p}{\partial y^2} + \frac{\partial^2 p}{\partial z^2} = 0 \tag{4}$$

The modified Reynolds equation governing the flow of the squeeze film lubricant, taking into consideration the mass exchange of lubricant between the bearing-film interface, may be written as [9]:

$$\frac{1}{6\mu}\left[\frac{1}{R^2}\frac{\partial}{\partial\theta}\left(h^3\frac{\partial p}{\partial\theta}\right)+\frac{\partial}{\partial z}\left(h^3\frac{\partial p}{\partial z}\right)\right] = -2\dot{\varphi}\frac{\partial h}{\partial\theta}+2\frac{\partial h}{\partial t}-2q_y \tag{5}$$

From assumption (*c*),

$$\frac{\partial^2 p}{\partial y^2} = \frac{1}{H}\frac{\partial p}{\partial y}\Bigg|_{y=H}^{y=0} = \frac{1}{H}\frac{\partial p}{\partial y}\Bigg|_{y=0} \tag{6}$$

$$\frac{\partial p}{\partial y}\Bigg|_{y=H} = 0 \tag{7}$$

Equation (7) suggests that there is no flow at the outer surface of the bearing, which implies that the porous bearing is encased in an impermeable housing. Substituting Eq. (6) into Eqs. (4) and (2):

$$q_y = -\frac{\Phi}{\mu}\cdot\frac{\partial p}{\partial y}\Bigg|_{y=0} = \frac{\Phi H}{\mu}\left(\frac{\partial^2 p}{\partial x^2}+\frac{\partial^2 p}{\partial z^2}\right) \tag{8}$$

Now from Eqs. (8) and (5), the modified short bearing Reynolds approximation equation takes the form:

$$\frac{\partial}{\partial z}\left[(h^3+12\Phi H)\frac{\partial p}{\partial z}\right] = 12\mu(e\dot{\varphi}\sin\theta+\dot{e}\cos\theta) \tag{9}$$

Squeeze film forces may be determined from integration of Eq. (9). For π-film unpressurized oil supply, the dimensionless squeeze film forces are obtained:

$$F_r = B(\epsilon\varphi' I_1+\epsilon' I_2)/\delta_r$$
$$F_t = B(\epsilon\varphi' I_3+\epsilon' I_1)/\delta_r \tag{10}$$

where

$$B = \frac{\mu R L^3}{MC^3\omega_c};$$

$$I_1 = \int_{\theta_1}^{\theta_1+\pi}\frac{\sin\theta\cdot\cos\theta}{(1+\epsilon\cos\theta)^3+\alpha}\cdot d\theta;$$

$$I_2 = \int_{\theta_1}^{\theta_1+\pi}\frac{\cos^2\theta}{(1+\epsilon\cos\theta)^3+\alpha}\cdot d\theta;$$

$$I_3 = \int_{\theta_1}^{\theta_1+\pi}\frac{\sin^2\theta}{(1+\epsilon\cos\theta)^3+\alpha}\cdot d\theta;$$

$$\theta_1 = \tan^{-1}\left(-\frac{\epsilon'}{\epsilon\varphi'}\right);\ \alpha = \frac{12\Phi H}{C^3} \tag{11}$$

The differential equations governing the motion due to rotating unbalance are well documented by [1, 2] and [3, 4] for rigid rotor and flexible rotor-oil film damper systems, respectively, and are not reproduced here for brevity.

Stiffness and Damping Coefficients

Referring to Eqs. (10) and (11), The dimensionless stiffness and damping coefficients of PSFDs for circular centered orbits can be expressed as

$$K_0 = \int_{\pi}^{2\pi}\frac{\sin\theta\cdot\cos\theta}{(1+\epsilon\cos\theta)^3+\alpha}\cdot d\theta$$

$$C_0 = \int_{\pi}^{2\pi}\frac{\sin^2\theta}{(1+\epsilon\cos\theta)^3+\alpha}\cdot d\theta \tag{13}$$

In addition, the stiffness and damping coefficients of the conventional SFDs may also be represented by Eq. (13) for zero permeability parameter, i.e., $\alpha = 0$.

For the unpressurized PSFD and SFD model, Figs. 2 and 3 show the dimensionless stiffness and damping coefficients,

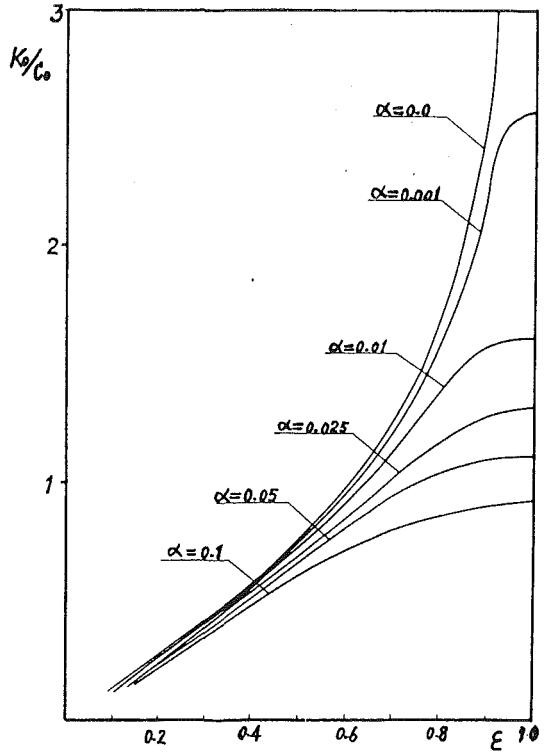

Fig. 4 Ratio of stiffness to damping coefficients of PSFD

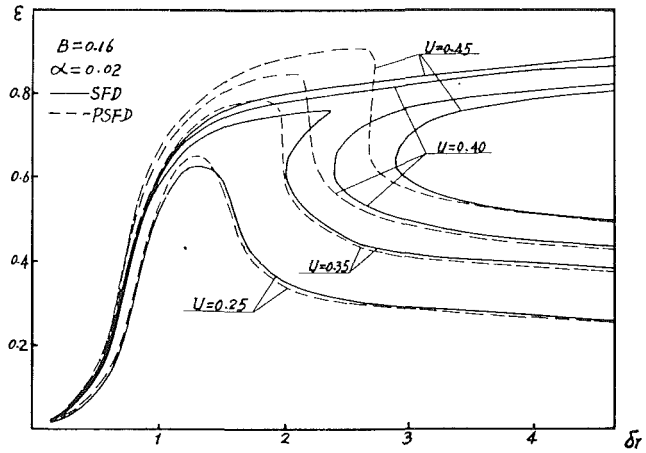

(a) Journal amplitude

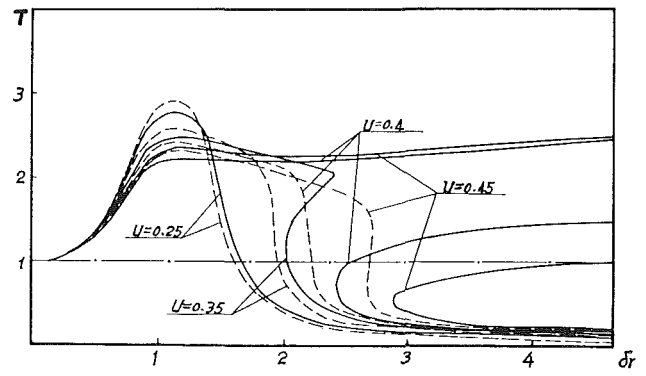

(b) Transmissibility

Fig. 5 Unbalance response of a rigid rotor on PSFD

respectively, for increasing orbit radii ϵ and permeability parameter α. With the increasing of PSFD permeability, the stiffness and damping coefficients decrease, which gradually becomes remarkable for an increased eccentricity ϵ. Thus the nonlinearity of squeeze film forces could be reduced with PSFD permeability. For example, considering the permeability parameter $\alpha = 0.025$, the stiffness and damping coefficients decrease very little for PSFD compared with SFD in the range $\epsilon < 0.6$. Thus, under this condition, PSFDs and SFDs could provide very similar damping characteristics for rotor vibration control. However, for eccentricity $\epsilon > 0.6$, a considerable decrease in the coefficients can be observed from Figs. 2 and 3 for $\alpha = 0.025$. That means that the characteristics of strict buildup of highly nonlinear oil film forces of SFD under sufficient eccentricity caused by abusive unbalance and possible instability could be satisfactorily improved by PSFD.

In order qualitatively to identify the difference of effect of permeability on stiffness and damping coefficients, the ratio of predicted stiffness coefficient to damping coefficient K_0/C_0 was taken into account, plotted as shown in Fig. 4. For conventional SFD, represented by $\alpha = 0.0$, $K_0/C_0 \to \infty$, as $\epsilon \to 1.0$, which means the squeeze effect of SFD produces more a stiffness force (directed radially inward) than a damping one (opposed to whirling motion) under sufficiently increased eccentricity. This highly nonlinear radial "stiffening" effect of SFD is responsible for the nonlinear response, such as jump phenomena and "lockup" of SFD mounts. In contrast to the abovedescribed properties of SFD, the permeability of PSFD makes the ratio K_0/C_0 decrease. Moreover, the greater the eccentricity is, the more the decrease, which causes the nonlinear "stiffening" effect to improve desirably with properly designed permeability parameter. The ratio K_0/C_0 approaches a limited value as $\epsilon \to 1.0$ rather than a limitless one. For example, considering the condition of $\alpha = 0.025$, the K_0/C_0 is approximately a linear function within the total eccentricity range, i.e., $\epsilon \in (0, 1)$. The K_0 and C_0 are of the same quantitative class as $\epsilon \to 1.0$ and thus, relatively greater damping forces can be achieved by PSFD as compared with SFD, under relatively large eccentricity conditions.

Rigid Rotor Unbalance Response

Figures 5(*a*) and 5(*b*) show the predicted amplitude and transmissibility unbalance speed response of an unpressurized SFD and PSFD supported rigid rotor system for the bearing parameter $B = 0.16$, and permeability parameter $\alpha = 0.02$. The response curves of PSFD and SFD system are represented by dotted lines and real lines, respectively. Under normal unbalance, $U = 0.25$, the response of amplitude and transmissibility of both PSFD and SFD system are of effectively attenuated conditions. When the rotating speed is below the critical speed, the amplitude and transmissibility of SFD are a little smaller than those of PSFD, while at supercritical speed, the phenomenon inverts and thus, PSFD provides smaller transmitted forces within working speed range. For unbalance mass eccentricity $U = 0.35$, the nonlinear stiffening effect of SFD stiffness coefficient produces a region of bistable operation within a speed parameter range $1.9 < \delta_r < 2.4$. However, the PSFD system with improved stiffness coefficient passes through critical speed smoothly at $\delta_r = 1.8$, with no bistable operation predicted. Moreover, under increased unbalance condition, $U = 0.4$, permanent bistable solutions of SFD exsit for the speed parameter $\delta_r > 2.4$. The higher whirling amplitude produces a force transmissibility large than the unbalance force ($T > 1.0$) and makes the damper ineffective in controlling such levels of unbalance. In practice under such conditions, high unbalance transmissibility and rotor excursion amplitude may remain in a wide speed range for speeds remarkably larger than $\delta_r = 2.4$. The dotted lines of Fig. 5 show that rotor vibrations can be effectively controlled by PSFD, in the case of unbalance $U = 0.4$. The mass center of the rotor on PSFD is sufficiently inverted when $\delta_r > 2.3$, with the transmissibility very much lower than the value obtained for the rotor mounted

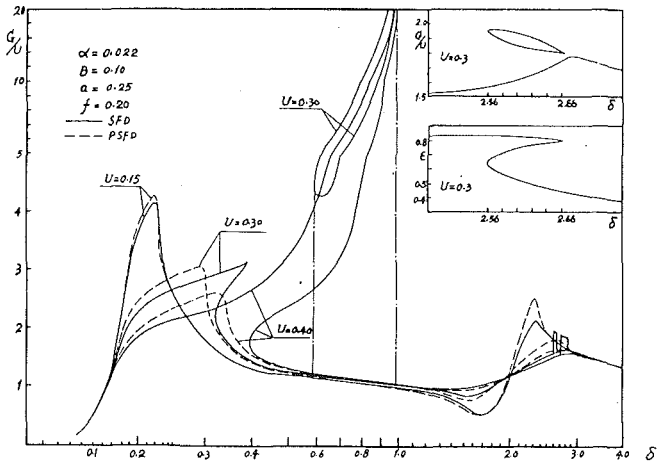

Fig. 6 Midspan unbalance response of a flexible rotor on PSFD

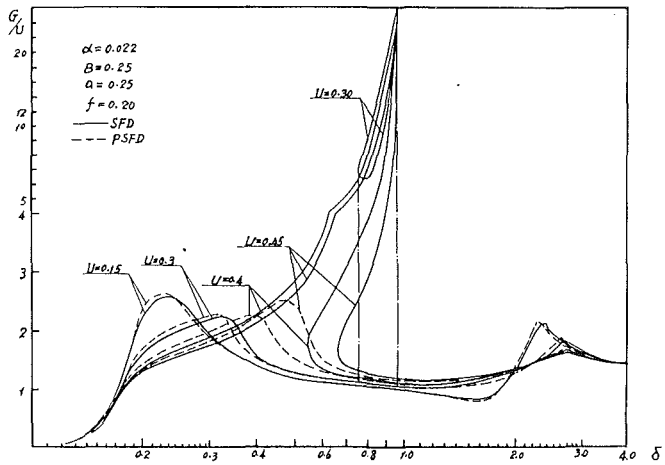

Fig. 7 Midspan unbalance response of a flexible rotor on PSFD

on rigid supports ($T = 1$). Further, in addition, under large unbalance conditions, $U = 0.45$, even worse performance of SFD supported rigid rotor is encountered, and destructive damage may be induced. However, PSFD of a permeability parameter $\alpha = 0.02$ still presents an effective vibration control ability, with the possibilities of jump phenomena and large transmissibility regions avoided.

The predicted results show that under normal unbalance conditions, both PSFD and SFD are of good vibration control ability. However, PSFD has the potential advantages to attenuate large rotor unbalance and thus, avoid nonlinear performance of a rotor on PSFD.

Flexible Rotor Unbalance Response

The unbalance response of a flexible rotor supported on SFDs has been investigated extensively concerning pressurized and unpressurized conditions [3, 4], of which the nonlinear response such as bistable operations and "lockup" phenomena of unpressurized SFDs were predicted to be a possibility for the unbalances exceeding $U = 0.2$.

A flexible rotor with a mass ratio $a = 0.25$, a resonant frequency ratio $f = 0.2$, and bearing parameters $B = 0.1$ and 0.25 approximately represent the conditions of some aircraft engines. For PSFDs with a permeability parameter $\alpha = 0.022$ and unpressurized SFDs, Figs. 6 and 7 show the dimensionless amplitude unbalance speed response at the rotor midspan for the bearing parameter $B = 0.1$ and 0.25, respectively. The curves of response at the damper journal and the force transmissibility are not presented here, but can be inferred from [3, 5].

Figure 6 shows the rotor midspan amplitude response for $B = 0.1$ and $U = 0.15$, 0.3, and 0.4. Under relatively small unbalance condition, $U = 0.15$, both PSFD and SFD system present effective vibration control ability, as indicated by the dotted line and the solid line, respectively, however, under conditions of remarkable unbalance, $U = 0.3$, bistable operation of the SFD system occurs for a speed range of $0.32 < \delta < 0.4$, and reappears for $\delta > 0.6$, and thus, the "lockup" of the SFD bearing mount is encountered when speeds approach the first pin–pin critical speed. Also, a possible bistable operation narrow speed range is predicted for $2.56 < \delta < 2.66$, where the highest amplitude response of G/U may be unstable, corresponding to the intermediate solution of the damper journal. For the same amount of unbalance, $U = 0.3$, and on PSFD, analysis shows that no possibilities of bistable operation and "lockup" phenomenon exist. Very smooth responses are favorable for rotor vibration control. Such ability of PSFD for vibration control remains effective for $U = 0.4$, as shown in Fig. 6. Nevertheless, when $U = 0.4$, rotor-SFD response predicts a region of bistable operation existing above $\delta = 0.4$, and results in SFD "lockup" at the pin–pin critical speed ($\delta = 1$), with excessive amplitude response at rotor midspan and large transmitted forces to the support structures.

Figure 7 shows, for bearing parameter $B = 0.25$, and unbalanced mass eccentricity $U = 0.15$, 0.3, 0.4, and 0.45, the rotor midspan amplitude responses on PSFD and SFD, respectively. Predicted results show that for unbalance $U = 0.3$, 0.4, and 0.45, bistable operations and "lockup" phenomena of SFD system are observed for rotor speeds less than and equal to the first pin–pin critical speed. The "lockup" phenomena correspond with the SFD bearing behaving like a rigidly contacted clearance in the vicinity of $\delta = 1$, e.g., with $\epsilon \approx 1.0$. The high nonlinear interaction between damper journal and radially "stiffened" squeeze film makes the rotor system suffer a bending resonant vibration model at the pin–pin critical speed. It can be deduced that "lockup" phenomena are a possibility for complex rotor–SFD systems at the first or higher pin–pin critical speeds under exceeded unbalance conditions due to the natural nonlinearity of SFDs. Such high rotor excursion amplitudes are unacceptably high in turbomachinery where blade tip clearances are to be kept at a minimum, not to mention the correspondingly high unbalance transmissibilities that could rapidly destroy the rolling element bearings.

In marked contrast, and in keeping with flexible rotor behavior, no bistable operation and "lockup" phenomena are predicted with permeable PSFD bearing supports, even for high unbalance condition, $U = 0.45$, as illustrated in Fig. 7. Hence, PSFDs with proper permeabilities will guarantee avoidance of bistable operation, and cancel out the "stiffening" effect of SFDs in the vicinities of pin–pin critical speeds. The high efficiency of rotor vibration control ability of PSFD benefits from its permeability, producing improved squeeze film force distribution, of which relatively greater damping forces can be achieved and radial "stiffening" film force can be linearized with proper permeability.

Experiment

The fundamental test rig used in this paper for rotors supported on squeeze film dampers was well documented by [10], and is not described here for brevity. Although systematic experiments about unbalance response of rotors supported on PSFDs and SFDs have been made [7], only a typical example is shown here in brief.

Figure 8 illustrates the oscillograms of a rigid rotor response supported on PSFD and SFD, respectively. The weight of equivalent mass lumped at the bearing station $W = 7.3$ kg; the damper radial clearance $C = 0.2$ mm; the squirrel-cage

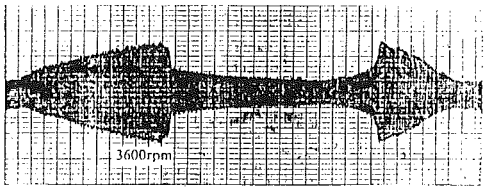

(a) PSFD response

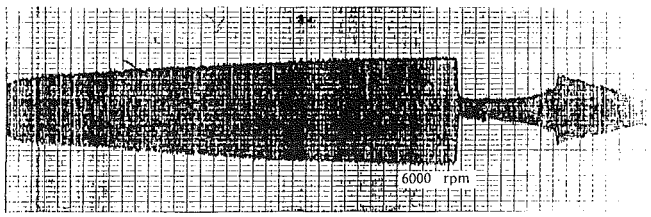

(b) SFD response

Fig. 8 Measured rigid rotor response

retainer spring stiffness $K = 820$ kg/cm; the unbalance amount $Q = 58.8$ g·cm and unbalance mass eccentricity $U = 0.41$; PSFD permeability parameter $\alpha = 0.016$; undamped critical speed $\omega_r = 3200$ rpm. As shown in Fig. 8, the right peaks of oscillograms indicated the response of slowdown passing through the critical speed, whereas the left remarkable response represents that of acceleration. Figures 8(*a*) and 8(*b*) are of the same scale. It can be seen from Fig. 8(*a*) that the rotor–PSFD system passes through the critical speed smoothly and approaches mass center inverted condition above $\omega = 3600$ rpm. However, the rotor–SFD system experiences high rotor excursion amplitude within a wide speed range as shown in Fig. 8(*b*), and a jump phenomenon occurs at $\omega = 6000$ rpm from a high excursion amplitude to a lower one, which corresponds with the predicted bistable operation. As before, the reason for more effective vibration controlling of PSFD is the substantial improved damping properties achieved from proper permeability of oil film housing.

Conclusions

1 From the work reported in this paper, it would appear that the vibration control ability of squeeze film dampers supporting both rigid and flexible rotors can be significantly improved by porous squeeze film dampers with permeable oil film outer race.

2 The configuration of the PSFD is the same as that of SFD, so the advantages of SFD such as lower production costs, structure simplicity, and little space requirement also remain with PSFD. The outer race of the PSFD is made of permeable sintered porous metal materials. The permeability of PSFD under squeezing effect makes it possible for some of the oil to permeate into and seep out the porous matrix.

3 The highly nonlinear characteristics of squeeze film stiffness coefficient (radial force coefficient) could be improved with the permeability of PSFD, and relative greater damping coefficient (tangential force coefficient) could be achieved. The fixed relation between stiffness coefficient and damping coefficient of SFD becomes adjustable to the designed permeability parameters of PSFD. Thus, more reasonable damping properties can be provided by PSFD.

4 Under normal unbalance conditions, the unbalance responses of both rigid rotors and flexible rotors supported on properly designed preloaded SFDs and PSFDs are well damped; similar response characteristics of rotor–SFD and rotor–PSFD systems are predicted.

5 Under abnormal unbalance conditions, however, bistable operation may occur over a wide speed range with undesirable high rotor excursion amplitudes and unbalance transmissibilities for rigid and flexible rotors supported on cavitated SFDs, and may result in "lockup" phenomena at the pin–pin critical speeds of flexible rotor–SFD systems with destructive flexural excursions. Nevertheless, under large unbalance extent, e.g., $U = 0.45$, no possibilities of bistable operations and so-called "lockup" phenomena are predicted for rotors supported on PSFD with proper permeability.

6 Experimental results verified the analytical results.

Acknowledgments

The authors wish to thank Prof. Li Qi-Han, director of structure/strength and vibration division of the Jet Propulsion Department of BUAA for his contributions to this work. The authors also wish to thank Dr. D. H. Hibner of Pratt & Whitney for his encouragement to the research.

This research project was supported by National Natural Science Foundation of China.

References

1 Mohan, S., and Hahn, E. J., "Design of Squeeze Film Damper Supports for Rigid Rotors," ASME *Journal of Engineering for Industry*, Vol. 96, 1974, pp. 976–982.

2 Gunter, E. J., Barrett, L. E., and Allaire, P. E., "Design of Nonlinear Squeeze Film Dampers for Aircraft Engines," ASME *Journal of Lubrication Technology*, Vol. 99, 1977, pp. 57–64.

3 Rabinowitz, M. D., and Hahn, E. J., "Steady State Performance of Squeeze Film Damper Supported Flexible Rotors," ASME JOURNAL OF ENGINEERING FOR POWER, Vol. 99, 1977, pp. 552–558.

4 McLean, L. J., and Hahn, E. J., "Unbalance Behavior of Squeeze Film Damped Multi-mass Flexible Rotor Bearing System," ASME *Journal of Lubrication Technology*, Vol. 105, 1983, pp. 22–28.

5 San Andres, L. A., and Vance, J. M., "Effect of Fluid Inertia on the Performance of Squeeze Film Damper Supported Rotors," ASME JOURNAL OF ENGINEERING FOR GAS TURBINES AND POWER, Vol. 110, 1988, pp. 51–56.

6 Adams, M. L., and Zahloul, H., "Attenuation of Rotor VIbration Using Controlled-Pressure Hydrostatic Squeeze Film Dampers," *Proc. 1987 ASME Design Technology Conf.-11th Biennial Conference on Mechanical Vibration and Noise*, Boston, MA, Sept. 27–30, 1987, pp. 99–108.

7 Zhang, S. P., "Development of High Efficient Oil Film Damper for High Speed Rotating Machinery," Ph.D. Dissertation, Beijing University of Aeronautics and Astronautics, Apr. 1989.

8 Morgan, V. T., and Cameron, A., "Mechanism of Lubrication in Porous Metal Bearing," *Proc. Conf. Lubrication and Wear*, Institute of Mechanical Engineers, London, 1957, pp. 151–157.

9 Marti, P. R. K., "Dynamic Behavior of Pure Squeeze Films in Narrow Porous Bearings," ASME *Journal of Lubrication Technology*, Vol. 96, July 1974, pp. 361–364.

10 Yan, L. T., and Li, Q. H., "Experiments on the Vibration Characteristics of a Rotor With Flexible, Damped Support," ASME JOURNAL OF ENGINEERING FOR POWER, Vol. 103, 1981, pp. 174–179.

11 Taylor, D. L., and Kumar, B. K., "Nonlinear Response of Short Squeeze Film Dampers," ASME *Journal of Lubrication Technology*, Vol. 102, 1980, pp. 51–58.

12 Zhang, S. P., and Yan, L. T., "Development of Porous Squeeze Film Damper Bearings for Improving the Blade Loss Dynamics of Rotor-Support System," *Proc. Third International Conference on Rotordynamics*, Sept. 1990, Lyon, France; ASME *Journal of Vibration and Acoustics*, in press.

Limit Cycle Vibration Analysis of a Long Rotating Cylinder Partially Filled With Liquid

J. Colding-Jorgensen
Department of Machine Elements,
The Technical University of Denmark,
DK-2800 Lyngby, Denmark

The dynamics of a long, stiff cylinder, flexibly suspended at the ends, partially filled with liquid, is analyzed for varying rotating speed. It appears from the analysis that in the absence of external damping, two distinct speed ranges with unstable whirl are present, as opposed to one instability region for the short cylinder, which has been analyzed by a number of authors (Kuipers, 1964; Wolf, 1968). This is in agreement with field experience with centrifuges, where several regions of instability are often encountered, each corresponding to a particular vibration mode. The results should also apply to a jet engine with oil accidentally trapped in the rotor, or any hollow rotor with liquid trapped in the cavity. When external damping is applied the linear theory predicts the rotor to be unstable at all speeds (Kuipers, 1964). This is clearly not in accordance with field experience, and other authors have suggested different types of nonlinear analysis that can give finite amplitude stable whirl or pulsating whirl (Berman et al., 1985). In the present analysis a simplified nonlinear analysis known as the hydraulic jump approximation is applied in the two unstable speed ranges predicted by the linear theory, and a stable whirl finite amplitude, dependent on the external damping, follows. It is argued that the amplitudes found this way should always be higher than those predicted by a more sophisticated analysis, and also higher than the amplitudes measured by other authors, so that the procedure described should give a safe worst case prediction of rotor whirl amplitudes for a given external damping. Finally, an experimental setup intended to verify the analysis in a quantitative way is presented.

Introduction

The dynamic instability caused by fluid trapped inside a hollow rotor, but not completely filling the cavity, has interested a number of authors over the past decades. It is of prime importance in a number of practical situations, for example when oil accidentally gets trapped in a jet engine, or during normal operation of a centrifuge. Kollmann (1962), Kuipers (1964), Wolf (1966) and Lichtenberg (1982) have described the phenomenon on the basis of experiments with simple one-degree-of-freedom short rotors, and linear theoretical models not including fluid internal damping. Within this context, the problem was found to be caused by a liquid wave, traveling on the surface of the spun-up liquid layer, in a direction opposite to the rotation. In a certain speed interval relative to the rotor natural frequency, this wave will interact with the rotor system to produce an unstable vibration with a frequency determined by the wave speed.

Already Kuipers (1964) had discovered the peculiar fact that within the framework of the linear, nonviscous model, external damping on the rotor will cause the system to become unstable at all speeds. This paradox was partly resolved by Hendricks and Morton (1979), who showed that including both external and internal damping would again produce a finite instability region. The boundaries of this instability region have been determined as depending on damping and mass parameters by Hendricks and Morton (1979), using a boundary layer approximation, and later by Holm-Christensen and Träger (1989), who obtained somewhat different results, using the full Navier–Stokes equations.

However, both of these models still predict the system to be unstable at some speed range, no matter what external and internal damping is applied.

If this were really the case, some kind of active control like that proposed in theory by Hendricks and Klauber (1984) and in practice by Matsushita et al. (1988), using an electromagnetically generated cross-coupling stiffness, would be the only way to control this vibration problem. However, Berman et al. (1985) have shown that if a nonlinear representation of the fluid is used, external damping is predicted to have a limiting effect on vibration amplitudes, even in the absence of internal damping. Furthermore they have provided a simple expression for a stable limit cycle vibration amplitude as a function of mass parameters and external damping.

The fluid model used is known as a hydraulic jump ap-

Contributed by the International Gas Turbine Institute and presented at the 35th International Gas Turbine and Aeroengine Congress and Exposition, Brussels, Belgium, June 11-14, 1990. Manuscript received by the International Gas Turbine Institute December 26, 1989. Paper No. 90-GT-40.

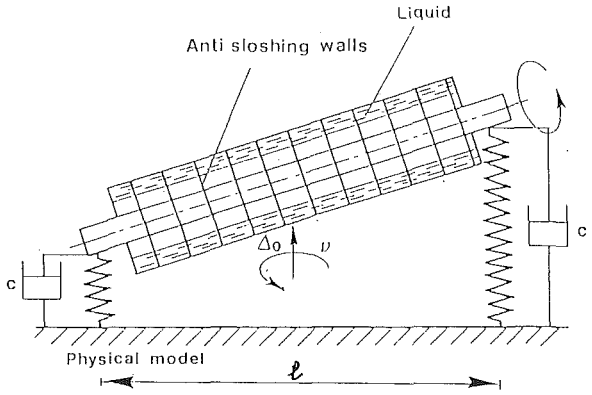

Fig. 1

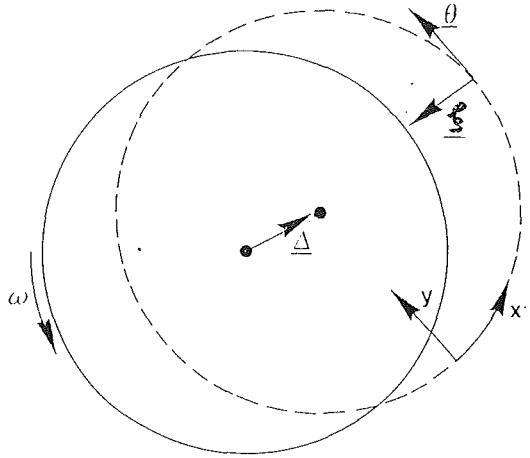

Fig. 2 Coordinate system and nomenclature

proximation. Such a model was also used by Inoue et al. (1985) to predict liquid wave profiles in a rotor undergoing forced vibrations, and experimental data have been provided to support the theory.

The present analysis is based on the model of Berman et al. (1985), but it has been extended to cover the two rotor vibration modes of a long, stiff, symmetrically suspended rotor (see Fig. 1).

The influence of external damping on the vibration amplitudes is discussed, and with the help of the theory and available experimental data, some conditions and guidelines are drawn up for the use of external damping to control this vibration problem.

Physical Model

The system analyzed, which is shown in Fig. 1, consists of a long, rotating, stiff cylinder, partially filled with liquid. It is suspended at the ends with identical springs. The springs also have the same stiffness in the vertical and horizontal directions. The effect of gravity on the spun-up fluid layer inside the rotor cavity is neglected.

Fluid axial velocity is set to zero, as if a number of walls separated the cavity into narrow compartments; see Fig. 1. This assumption is of minor importance in the first rotor mode, but of primary importance in the second rotor mode, where the rotor is yawing around the center of gravity, introducing axial pressure gradients into the liquid. This effect and the problem of the axial velocity assumption are discussed later in relation to projected experiments.

The fluid is assumed to be nonviscous in the present calculation. However, a fluid viscous term could be incorporated into the equations, for example, by using a boundary layer approximation at the wall.

Fluid Equations of Motion

In the x–y coordinate system moving with the rotating whirling cylinder, as shown in Fig. 2, the fluid equations become:

Tangential momentum balance:

$$\frac{\partial u}{\partial t}+u\frac{\partial u}{\partial x}+v\frac{\partial u}{\partial y}-2\omega v=-\frac{1}{\rho}\frac{\partial p}{\partial x}-\ddot{\Delta}\cdot\theta \tag{1}$$

Radial momentum balance:

$$\frac{\partial v}{\partial t}+v\frac{\partial v}{\partial y}+u\frac{\partial v}{\partial x}+2\omega u+R\omega^2=-\frac{1}{\rho}\frac{\partial p}{\partial y}-\ddot{\Delta}\cdot\xi \tag{2}$$

Continuity:

$$\frac{\partial u}{\partial x}+\frac{\partial v}{\partial y}=0 \tag{3}$$

The axial acceleration of the cylinder is neglected, and since the fluid axial sloshing is suppressed, this two-dimensional representation is sufficient to describe the fluid dynamics in any z plane with the local rotor axis deflection $\Delta(z)$.

Even in this two-dimensional form, these equations are quite

Nomenclature

A = integration constant
B = $\dfrac{3R^2(\omega-\Omega)^2}{h_0^2\omega^2}$ = whirl constant
C = damping coefficient
c = relative damping on first rotor mode
c_ν = relative damping on second rotor mode
F_r = radial force in system moving with whirl
F_t = tangential force in system moving with whirl
h = height of fluid layer
h_0 = height of undisturbed layer
h' = $h-h_0$
I = rotor moment of inertia around axis through center of gravity, perpendicular to rotational axis
l = length of rotor
M = rotor mass
p = pressure
R = inner radius of cylinder
S = hydraulic jump position
t = time
U = mean velocity in x direction
u = fluid velocity in x direction
v = fluid velocity in y direction
x = tangential coordinate in system moving with the cylinder; see Fig. 2
y = radial coordinate; see Fig. 2
z = axial coordinate
Δ = vectorial position of rotor axis at z
Δ = length of Δ
$\ddot{\Delta}$ = vectorial acceleration of rotor axis at z
ζ = angular coordinate in a system moving with the whirl
θ = unit vector in tangential direction at point on inner rotor wall; see Fig. 2
ν = yaw angle of rotor
ξ = unit vector in radial direction; see Fig. 2
ω = rotational angular frequency
ω_{01} = first rotor natural frequency
ω_{02} = second rotor natural frequency
Ω = whirl angular frequency

difficult to solve, but when the spun-up liquid layer is thin, they can be simplified considerably.

In Eq. (2), the body force $\Delta \cdot \xi$ is small compared to the pressure gradient, when the layer is thin, so it is neglected, as are the nonlinear terms in this equation. Also, in Eq. (2), we set $v = y(\partial h/\partial t)/h_0$, as is normally done in shallow water calculations. Then, Eq. (2) can be integrated between y and h, where $p = 0$ on the free surface, to give the pressure:

$$\frac{p}{\rho} = \frac{h_0^2 - y^2}{2h_0} \cdot \frac{\partial^2 h}{\partial t^2} + 2\omega \int_y^h u dy + R\omega^2 (h - y) \tag{4}$$

At the free surface, we have the boundary condition:

$$\frac{\partial h}{\partial t} + u \cdot \frac{\partial h}{\partial x} = v \tag{5}$$

Using Eq. (5) and the continuity Eq. (3), differentiating Eq. (4) with respect to x and inserting into Eq. (1), we get:

$$\frac{\partial u}{\partial t} + u \frac{\partial u}{\partial x} + v \frac{\partial u}{\partial y} + \ddot{\Delta} \cdot \theta = -R\omega^2 \frac{\partial h}{\partial x} + 2\omega \frac{\partial h}{\partial t} - \frac{1}{2} \frac{h_0^2 - y^2}{h_0} \cdot \frac{\partial^3 h}{\partial x \partial t^2} \tag{6}$$

Now, the equations will be put into a simplified depth-averaged form, setting:

$$U = \frac{1}{h} \int_0^h u dy \tag{7}$$

and

$$v_{(y=0)} = 0 \tag{8}$$

Also, in the following, the dispersion term $\partial^3 h/\partial x \partial t^2$ is neglected, in which case the solution always becomes a liquid wave synchronized to the rotor motion. The implications of neglecting the dispersion term are discussed later. Finally, we neglect terms of $(u - U)^2$, meaning that the Reynolds stresses caused by y gradients of the tangential velocity are small. With these simplifications, the fluid equations to solve become:

$$\frac{\partial h}{\partial t} + \frac{\partial}{\partial x}(hU) = 0 \tag{9}$$

$$\frac{\partial U}{\partial t} + U \frac{\partial U}{\partial x} + \ddot{\Delta} \cdot \theta = -R\omega^2 \frac{\partial h}{\partial x} + 2\omega \frac{\partial h}{\partial t} \tag{10}$$

Circular Whirl Solution: Hydraulic Jump

Consider a rotor motion where the local rotor deflection moves in a circle of radius $\Delta(z)$, with the angular frequency Ω.

With $\zeta = x/R + (\omega - \Omega)t$, we assume a solution of the form:

$$h = h_0 + h'(\zeta)$$

$$U = U(\zeta)$$

This describes a liquid wave synchronized to the rotor vibration. Equations (9) and (10) become:

$$\left(\omega - \Omega + \frac{U}{R}\right) \frac{\partial h'}{\partial \zeta} + \frac{1}{R}(h_0 + h') \frac{\partial U}{\partial \zeta} = 0 \tag{11}$$

$$(-\omega^2 + 2\omega\Omega) \frac{\partial h'}{\partial \zeta} + \left(\frac{U}{R} + \omega - \Omega\right) \frac{\partial U}{\partial \zeta} = -\Delta\Omega^2 \sin \zeta \tag{12}$$

The rotor whirl frequency is determined for small values of Δ, U, and h', where the determinant of the equations has to be zero. This gives:

$$\Omega = \omega \left(1 + \frac{h_0}{R} \mp \sqrt{\frac{h_0}{R} + \left(\frac{h_0}{R}\right)^2}\right) \tag{13}$$

The plus sign refers to prograde waves, the minus sign to retrograde waves, relative to the cylinder surface velocity.

This result is consistent with the resonant wave frequencies found by Miles and Troesch (1961). Only the retrograde waves are investigated in the following, since linear models and experimental evidence (Kuipers, 1964; Wolf, 1966) show that these waves can cause dynamic stability problems through interaction with the rotor resonances.

To determine the wave solution, Eq. (11) is integrated to:

$$\frac{dU}{dh'} = -R \frac{\omega - \Omega + \frac{U}{R}}{h_0 + h'} \tag{14}$$

With the initial conditions $U = 0$ for $h' = 0$, the exact solution of Eq. (14) is:

$$U = -\frac{R(\omega - \Omega)}{h_0} \frac{1}{1 + \frac{h'}{h_0}} \cdot h' \tag{15}$$

This is inserted into Eq. (12), and after integration, this becomes:

$$(\omega^2 + 2\omega\Omega)h' + R(\omega - \Omega)^2 \cdot \frac{1}{2} \frac{1}{1 + \left(\frac{h'}{h_0}\right)^2} = \Delta\Omega^2 \cos \zeta + A \tag{16}$$

where A is an integration constant.

This is now reduced to a second-order equation in h'/h_0.

A Taylor series expansion in h'/h_0 yields:

$$\frac{1}{1 + \left(\frac{h'}{h_0}\right)^2} \cong 1 - 2\, h'/h_0 + 3(h'/h_0)^2$$

When this is inserted into Eq. (16), the following equation results:

$$\frac{3}{2}(\omega - \Omega)^2 \frac{Rh'^2}{h_0^2} + \left(-\omega^2 + 2\omega\Omega - \frac{R}{h_0}(\omega - \Omega)^2\right) h' = \Delta\Omega^2 \cos \zeta + A \tag{17}$$

This has two solutions, and a hydraulic jump may be interpreted as a jump between the two branches. Since the solution must be periodic, the two branches must touch at $\zeta = \pm\pi$, by which we determine the constant A.

Consequently:

$$h' = h_0^2 \frac{\left(-\omega^2 + 2\omega\Omega - (\omega - \Omega)^2 \frac{R}{h_0}\right)}{3(\omega - \Omega)^2 R} \pm \frac{\sqrt{h_0^2 2\Omega^2 \Delta(1 + \cos \zeta)}}{3(\omega - \Omega)^2 R} \tag{18}$$

The jump height is:

$$\Delta h' = 2\sqrt{\frac{2\Delta(1 + \cos S)}{3R}} \cdot \left|\frac{h_0 \Omega}{(\omega - \Omega)}\right| \tag{19}$$

where S is the jump position. This is similar to the results of Berman et al. (1985).

Rotor Force and Coupled Rotor–Liquid Equations

In a coordinate system moving with the whirl, the fluid force per unit length is:

$$\frac{dF_r}{dz} = \rho(\Omega R)^2 \int_0^{2\pi} h' \cos \zeta d\zeta \tag{20}$$

in the radial direction, and

$$\frac{dF_t}{dz} = \rho(\Omega R)^2 \int_0^{2\pi} h' \sin \zeta d\zeta \tag{21}$$

in the tangential direction.

In order to simplify the rotor equations of motion, it is assumed that there exist two distinct speed ranges with high whirl amplitudes, one for each vibration mode. In the first interval, $\Delta = \Delta_0$, and in the second, $\Delta = z \cdot \nu$, because of the symmetry of the rotor (see Fig. 1). This is based on a linear analysis published elsewhere, experiments with centrifuges by Matsushita et al. (1988), and field experience indicating that there generally exists one speed range with high whirl amplitude for each vibration mode of the rotor.

For the first vibration mode, the equations of motion are:

$$(\omega_{01}^2 - \Omega^2) M \Delta_0 = F_r \tag{22}$$

$$2M\omega_{01} c \Omega \Delta_0 = F_t \tag{23}$$

For the second mode:

$$(\omega_{02}^2 - \Omega^2) I\nu = \int_{-l/2}^{l/2} \frac{dF_r}{dz} z dz \tag{24}$$

$$2I\omega_{02} c_\nu \Omega \nu = \int_{-l/2}^{l/2} \frac{dF_t}{dz} z dz \tag{25}$$

where ω_{01} and ω_{02} are the natural angular frequencies for each mode,

$$c = 2C/(2M\omega_{01})$$

and

$$c_\nu = \frac{1}{2} Cl^2/(2I\omega_{02})$$

F_r and F_t are found by integration of Eqs. (20) and (21), with $h'(\zeta)$ given by Eq. (18).

Then, the following coupled rotor–liquid equations result for the first mode:

$$\left(\frac{\Delta_0}{h_0}\right)^{\frac{1}{2}} \left(\frac{\omega_{01}^2}{\omega^2} - \frac{\Omega^2}{\omega^2}\right) = -\mu \left(\frac{\Omega}{\omega}\right)^3 \left(\frac{2}{B}\right)^{\frac{1}{2}} \frac{4(2)^{\frac{1}{2}}}{\pi} \left(\sin\left(\frac{1}{2}S\right) - \frac{2}{3}\sin^3\left(\frac{1}{2}S\right)\right) \tag{26}$$

and

$$\left(\frac{\Delta_0}{h_0}\right)^{\frac{1}{2}} \frac{\omega_{01}}{\omega} \frac{\Omega}{\omega} c = \mu \left(\frac{\Omega}{\omega}\right)^3 \left(\frac{2}{B}\right)^{\frac{1}{2}} \frac{4}{3\pi} (1 + \cos S)^{3/2} \tag{27}$$

where $\mu = \pi\rho R^2 l/M$ and $B = 3\frac{R}{h_0}\frac{(\omega - \Omega)^2}{\omega^2}$

This is similar to the results of Berman et al. (1985). Equations (26) and (27) can be solved for jump position S and whirl amplitude Δ_0.

For the second mode it is found in the same way that:

$$\left(\frac{\nu l}{h_0}\right)^{\frac{1}{2}} (\omega_{02}^2 - \omega^2) = -\left(\frac{\Omega}{\omega}\right)^3 \mu \frac{Ml^2}{I} \left(\frac{2}{B}\right)^{\frac{1}{2}} \frac{4}{5}\frac{1}{\pi} \left(\sin\left(\frac{1}{2}S\right) - \frac{2}{3}\sin^3\left(\frac{1}{2}S\right)\right) \tag{28}$$

and

$$\left(\frac{\nu l}{h_0}\right)^{\frac{1}{2}} \frac{\omega_{02}}{\omega} \frac{\Omega}{\omega} c_\nu = \left(\frac{\Omega}{\omega}\right)^3 \mu \frac{Ml^2}{I} \left(\frac{2}{B}\right)^{\frac{1}{2}} \frac{4}{15\pi\sqrt{2}} (1 + \cos S)^{3/2} \tag{29}$$

Equations (28) and (29) are solved for the yaw-whirl amplitude ν, and S, using the approximated whirl frequency Ω of Eq. (13).

Limit Cycle Results

Solving Eqs. (26) and (27) for the first mode, and Eqs. (28) and (29) for the second, a complete view of the rotor vibrations as a function of speed and external damping can be found. This is valid only when the two speed ranges, where high vibration amplitudes occur, are well separated, because of the simplifying assumptions concerning the mode shapes. If the two speed ranges with high vibrations approach each other and eventually overlap, as will be the case for high values of the mass relation μ, or if the rotor is not symmetric, so that Δ_0 and ν are not decoupled in the rotor modes, a more general and more complicated set of equations will have to be developed.

The present case is, however, sufficient to illustrate the effect of external damping, which is done for the case of a long cylinder with $I = (1/12)Ml^2$. In this case, the solutions for the whirl amplitudes have been calculated for various values of the relative external damping c, and the results are shown in Fig. (3), as a function of speed relative to the first rotor critical ω_{01}.

In the case calculated, $h_0/R = 0.13$. The whirl frequency is calculated as that of small amplitude whirl, given by Eq. (13) and the amplitude calculated is that of the end of the rotor: $\Delta_{(l/2)} = \Delta_0 + \nu \cdot l/2$.

Discussion

The results show that the whirl amplitude increases with the square of μ, which is the mass ratio, defined as the mass of the amount of fluid needed to fill the cavity completely, relative to the rotor mass. Also, the maximum whirl amplitude decreases approximately with the square of the external relative damping c, and the whirl amplitude curve flattens out for increasing damping; see Fig. 3.

While the linear analysis of Hendricks and Morton (1979) and Holm-Christensen and Träger (1989) cannot predict the finite amplitudes, the flattening of the curves is consistent with their findings of stability limits, and also with free whirl experiments by Cheng et al. (1985). The strong destabilizing influence of the external damping predicted by Hendricks and Morton (1979) is, however, contradicted by the present theory.

Within the range of the model, the whirl amplitude depends on a balance between the external relative damping c and the mass ratio μ. However, the range of the model also depends on this balance between μ and c: It has been calculated that for

$$\frac{\mu}{c} > 0.25$$

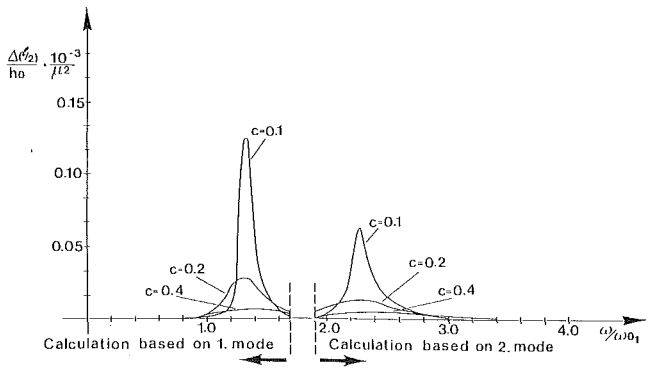

Fig. 3 Limit cycle amplitudes

Table 1 Comparisons of analysis predictions (present theory) and experimental data by Inoue

Δ/R	0.0033	0.0066	0.0115
$(\Delta h'/h_0)_{max}$, present theory	0.40	0.58	0.76
$(\Delta h'/h_0)_{max}$, measured	0.35	0.43	0.50
Fluid force$_{(max)}$, present theory	49	70	92
Fluid force$_{(max)}$, measured (Newton)	35	50	75

waves of approximately the same height as the liquid layer will be generated.

Judging from experimental results published by Inoue et al. (1985) and Cheng et al. (1985), waves of such height, and the resulting fluid force, will be limited by the thickness of the fluid layer and the cavity dimension, rather than the rotor dynamics, so on the basis of the present theory, it can be estimated that the balance between μ and c must be:

$$\frac{\mu}{c} < 0.25$$

for this external damping to have a significant limiting effect on whirl amplitudes.

The present analysis should be expected to overestimate wave height and whirl amplitudes, since both viscous and Reynolds stress terms in the equations have been neglected. This is confirmed by comparison to forced vibration experiments on a rotating cylinder partically filled with water by Inoue et al. (1985), who measured wave heights of 70 to 90 percent and forces of around 80 percent of those predicted by the present theory (see Table 1).

Berman et al. (1985) also reported that measured free whirl amplitudes were about half those calculated by a nonviscous hydraulic jump model, indicating a considerable damping influence from the viscosity of the fluid.

Table 1 presents measured maximum hydraulic jump height and associated fluid force reported by Inoue et al. (1985), compared to values calculated by the present theory. Correction has been made for the fact that the experiments were done with forced oscillation in one plane, instead of circular whirl, setting a whirl amplitude of Δ equal to an oscillation of 2Δ, as shown by the mentioned authors. The test fluid was water and other test parameters were:

$$l = 49 \text{ mm}, \; R = 152 \text{ mm},$$

$$h_0 = 20 \text{ mm}, \; \Omega = 63 \text{ rad/s}$$

If the dispersion term is retained in the equations, Berman et al. (1985) have shown that this will lead to a pulsating wave solution. However, the whirl amplitude resulting from this solution is smaller than that predicted by the simplified hydraulic jump solution. The measured pulsating whirl reported by Berman et al. (1985) is also generally smaller in amplitude than when the whirl is steady. Therefore, it seems that the present hydraulic jump calculation can be used as a guide when estimating the maximum whirl amplitudes resulting with a given external damping c and mass ratio μ, and to establish whether or not external damping can be used at all to limit the vibration amplitudes of the system.

An experimental setup is presently being constructed, and future experiments will focus on whirl amplitude measurements. Also, since the present theory does not take fluid axial sloshing into account, it is important to determine whether this has any effect on the second vibration mode of the rotor. This will be done, measuring with and without an antisloshing device, dividing the cavity into narrow compartments, as indicated in Fig. 1.

Conclusion

An analysis of a long, stiff, rotating cylinder, flexibly suspended and partially filled with liquid has been presented, using an extended version of the nonviscous hydraulic jump model of Berman et al. (1985).

This approach has an advantage over the different linearized models previously published, in that it is able to predict limit cycle vibration amplitudes in the speed ranges where even the most advanced linearized models including internal and external damping predict unstable whirl with amplitudes growing to infinity, regardless of the magnitude of the damping parameters.

The theory predicts a range of mass ratio relative to damping, μ/c, where external damping can be used to limit vibration amplitudes.

Within this range, comparison with available experimental results shows that the present calculation overpredicts destabilizing forces and whirl amplitudes with a factor of 1.1–2.0 for fluids with a viscosity in the same order of magnitude as that of water.

The calculation can be improved by including internal damping forces in the liquid. Also, the effect of fluid axial sloshing on higher rotor vibration modes should be studied, and a more general rotor configuration should be analyzed.

References

Berman, A. S., Lundgren, T. S., and Cheng, A., 1985, "Asynchronous Whirl in a Rotating Cylinder Partially Filled With Liquid," *Journal of Fluid Mechanics*, Vol. 150, pp. 311–327.

Cheng, C. A., Berman, A. S., and Lundgren, T. S., 1985, "Asynchronous Instability of a Rotating Centrifuge Partially Filled With Fluid," ASME *Journal of Applied Mechanics*, Vol. 52, pp. 777–782.

Hendricks, S. L., and Morton, J. B., 1979, "Stability of a Rotor Partially Filled With a Viscous Incompressible Fluid," ASME *Journal of Applied Mechanics*, Vol. 46, pp. 913–918.

Hendricks, S. L., and Klauber, R. D., 1984, "Optimal Control of a Rotor Partially Filled With an Inviscid Incompressible Fluid," ASME *Journal of Applied Mechanics*, Vol. 51, pp 863–868.

Holm-Christensen, O., and Träger, K., 1989, "A Note on Rotor Instability Caused by Liquid Motions," DCAMM Report No. 390, Technical University of Denmark.

Inoue, J., Jinnouchi, Y., and Araki, Y., 1985, "Forced Wave Motion of Liquid Partially Filling a High-Speed Rotor," ASME *Journal of Vibration, Acoustics, Stress, and Reliability in Design*, Vol. 107, pp. 447–452.

Kollmann, F. G., 1962, "Kritische Drehzahlen flüssigkeitsgefüllter Hohlkörper," *Forschung auf dem Gebiete des Ingenieurwesens*, Vol. 28, No. 4, pp. 115–123; No. 5, pp. 147–153.

Kuipers, M., 1964, "On the Stability of a Flexibly Mounted Rotating Cylinder Partially Filled With Liquid," *Applied Scientific Research*, Section A, Vol. 13, pp. 121–137.

Matsushita, O., Takagi, M., Yoneyama, M., Saitoh, I., Nagata, A., and Aizawa, M., 1988, "Stabilization by Cross Stiffness Control of Electromagnetic Damper for Contained Liquid Rotor Unstable Vibration," *Proceedings of IMechE International Conference: Vibrations in Rotating Machinery*, Sept. 13–15, pp. 77–84.

Miles, J. W., and Troesch, B. A., 1961, "Surface Oscillations of a Rotating Liquid," ASME *Journal of Applied Mechanics*, Vol. 28, pp. 491–496.

Wolf, J. A., Jr., 1966, "Whirl Dynamics of a Rotor Partially Filled With Liquid," ASME *Journal of Applied Mechanics*, Vol. 33, pp. 676–682.

Development of ODS Superalloy Technology in Japan for Turbine Blade Applications

K. Mino
Research Institute,
Ishikawajima-Harima Heavy
Industries Co., Ltd.,
Koto-ku, Tokyo

The strength of ODS superalloys has not been so satisfactory as to attract much attention for application in turbine blades. As one of the advanced materials programs supported by MITI, cooperative works were undertaken to develop ODS superalloys superior to monocrystalline alloys. Mechanical properties of new ODS alloys developed in Japan were summarized to evaluate their potentials for turbine blade applications. The project tasks included isothermal forging and diffusion bonding studies for blade fabrication.

Introduction

Oxide dispersion strengthening (ODS) has the advantage of extending creep properties to very high temperatures for long durations. Intermediate temperature creep strength is known to be more effectively improved by γ' phase precipitation than by oxide dispersion. Various alloys possessing high creep strength over a wide temperature range have been developed. Among them, MA6000, produced by the INCO International Co., is the first and only alloy commercially available. Other alloys containing higher volume fractions of γ' phase have been developed by Kang and Benn (1985), but the improved creep strength over MA6000 was not so large as to attract much attention. While some success has been achieved in producing a dispersion-strengthened corrosion resistant superalloy with a γ' phase strengthened matrix, the creep strength of MA6000 still suffers from low intermediate temperature creep strength as compared with monocrystalline cast superalloys.

The advanced materials programs supported by MITI were started in 1981. As one of the programs, the cooperative program on ODS superalloys was undertaken by the National Research Institute for Metals (NRIM), Sumitomo Electric Industries Co., and IHI from 1982 to 1988. It has aimed to develop advanced ODS alloys for a cooled gas turbine blade. Our biggest concern was improvement of intermediate temperature creep strength of MA6000 and evaluation of ODS alloys as an advanced material over monocrystalline alloys.

This paper summarizes some developmental work performed in Japan on ODS superalloy technology to evaluate their potentials for turbine blade applications.

Alloy Development

Most of the ODS alloy design has been made using knowledge of cast superalloys. In our previous work the modified Mar M247 was selected as the matrix phase composition of an advanced oxide dispersion strengthened alloy and the high-W, low-Al version of Mar M247 with no hafnium succeeded in obtaining a highly elongated grain structure (Mino, 1984). Tungsten was increased by about 3 wt% to strengthen the alloy and aluminum was decreased by about 1 wt% to improve the secondary recrystallization property. In the subsequent study by Kawasaki et al. (1989), a new experimental alloy TMO-2 developed at NRIM, containing more tantalum and slightly less aluminum than the above, has succeeded in giving higher creep strength than MA6000 over a wide temperature range. However, TMO-2 presents a density as high as 8.86 g/cm^3, since it contains a larger amount of tungsten and tantalum and a smaller amount of aluminum.

It was expected that further increase in tantalum content would improve the intermediate temperature creep strength of the previously studied alloys in the same manner as for the monocrystalline alloy. Alloy 98 was devised from these considerations (Mino and Asakawa, 1987). The matrix composition of Alloy 98 is close to the monocrystalline alloy CMSX-2.

The chemical composition, density, and crystal growth direction of TMO-2 and Alloy 98 are given in Table 1. MA6000 and CMSX-4 were also shown as the reference alloys. CMSX-4 is one of the second generation monocrystalline alloys, possessing 20 to 40°C higher temperature capability than the first generation alloys, which have been widely used.

Extruded billets were prepared by INCO's mechanical alloying process. Most of the billets were hot-extruded to round bars 18 mm in diameter, and several bars of TMO-2 had a larger size of 40 mm.

The extruded materials consist of extremely fine grains about 0.2 μm in size. They were zone-annealed to give an elongated and coarse grain structure along an extrusion axis by secondary recrystallization. This microstructural control prevents intergranular rupture and significantly improves high-temperature creep strength. In other words, the defect in directional recrystallization, i.e., the formation of equiaxial grains with grain boundaries perpendicular to the extrusion axis, leads to

Contributed by the International Gas Turbine Institute and presented at the 35th International Gas Turbine and Aeroengine Congress and Exposition, Brussels, Belgium, June 11–14, 1990. Manuscript received by the International Gas Turbine Institute February 12, 1990. Paper No. 90-GT-360.

Table 1 Nominal compositions (wt%, Bal: Ni), density, and crystal growth orientation of ODS and monocrystalline alloys

Alloy	C	Co	Cr	Mo	W	Ta	Al	Ti	B	Zr	Others	ρ(g/cm³)	Crystal Growth
Alloy 98	0.05	5.1	6.8	–	8.6	5.7	5.2	0.9	0.01	0.03	$1.1Y_2O_3$	8.60	<110>
TMO-2	0.05	9.7	5.9	2.0	12.4	4.7	4.2	0.8	0.01	0.05	$1.1Y_2O_3$	8.86	<110>
MA6000	0.05	–	15	2	4	2	4.5	2.5	0.01	0.05	$1.1Y_2O_3$	8.11	<110>
CMSX-4	–	10	6	0.6	6	6	5.6	1.0	–	–	3Re, 0.1Hf	8.70	<100>

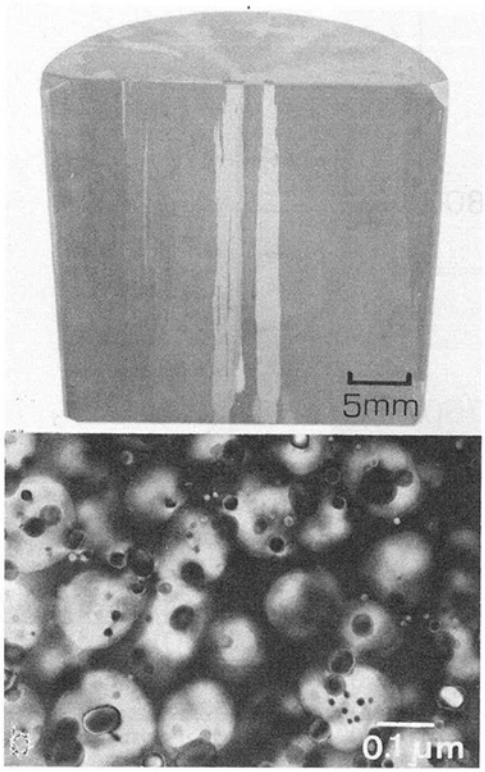

Fig. 1 Cross section of directionally recrystallized TMO-2 bar with transmission electron micrograph showing fine oxide dispersoids and γ' precipitates

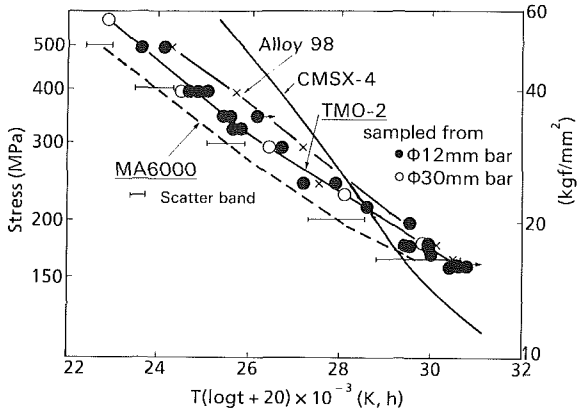

Fig. 2 Larson-Miller stress rupture curves of various ODS alloys; CMSX-4 is monocrystalline

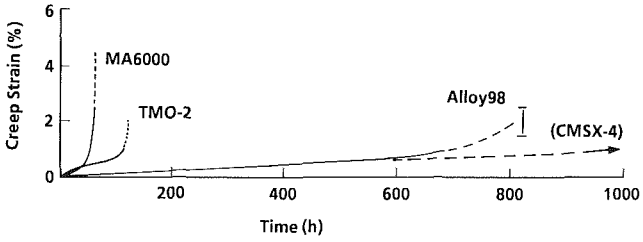

Fig. 3 Creep curves at 850°C, 392 MPa showing significant improvement in creep strength of Alloy 98; its creep rate is almost equal to that of CMSX-4 at intermediate temperature

a drastic decrease in creep strength. This situation is the same as recrystallized grain formation in monocrystalline superalloys.

Figure 1 shows the longitudinal macrostructure and transmission electron micrograph of TMO-2 zone-annealed at 1280 to 1300°C and the travel speed of 100 mm/h. The specimen aged at 850°C for 24 h had oxide dispersoids of 10 to 60 nm and γ' precipitates of about 100 nm in diameter.

Mechanical Properties

Creep Strength. Creep rupture tests of TMO-2 and Alloy 98 were carried out at 760 to 1050°C in air using the specimens of 3.5 mm in gage diameter. The results were plotted in Fig. 2 using the Larson-Miller parameter. The rupture curve of MA6000 was drawn based on the data by Benn and Kang (1984). Alloy 98 possessed the highest strength among the alloys in the figure, but was inferior to CMSX-4 under the stress above 200 MPa.

Comparative creep curves given in Fig. 3 show a significant increase of the intermediate temperature creep strength in Alloy 98. The creep strain was measured by the displacement of extension rods attached to the shoulders of creep specimens.

The dotted line in Fig. 3 is a creep cure of CMSX-4 estimated from extrapolated creep data at 1pct and 2pct strains. The ODS alloys ruptured at several pct strains, while the monocrystalline alloy ruptured after much larger deformations. Consequently, the difference of the time to reach 1pct strain between the ODS and monocrystalline becomes smaller than that of the time to rupture.

The stress for 1pct creep strain in 300 h was plotted in Fig. 4 for TMO-2, Alloy 98, and CMSX-4 as a function of temperature. Alloy 98 has higher strength than CMSX-4 over a wide range of stress. The advantage of temperature capability over CMSX-4 increased with the increase in temperatures. According to the current research at NRIM (Kusunoki et al., 1989), preliminary rupture data of a new TMO alloy are close to the goal indicated in Fig. 4. The broken line in Fig. 4 was drawn by shifting the abscissa of CMSX-4 curve by 80°C.

The effect of an aluminizing heat cycle on rupture strength was studied for TMO-2. TMO-2 was heat treated at 1050°C for 4 h or 24 h prior to aging treatment at 850°C. Effects of aging times on the rupture time at 760°C, 568 MPa were presented in Table 2. The intermediate aging coarsened γ' precipitates with decrease in the creep strength of TMO-2. However, the aluminizing heat treatment for 4 h was shown to be less detrimental to the 760°C rupture strength.

Fatigue Strength. Stress-controlled fatigue tests of push-pull type were done at 800°C and 1050°C with a frequency of 5 Hz. The cylindrical specimens of 6 mm in gage diameter were used. The 10^7 cycle fatigue strength of TMP-2 and Alloy

Table 2 Effect of intermediate heat treatment on creep rupture time of TMO-2 at 760°C, 568 MPa

Heat Treatment (Cooled in air)	Hardness (H_V)	γ' size (μm)	Rupture Time (h)
1290°C, 0.5h → 850°C, 24h	545	0.1	148
1290°C, 0.5h → 1050°C, 4h → 850°C, 24h	520	0.2	91
1290°C, 0.5h → 1050°C, 24h → 850°C, 24h	515	0.3	29, 37

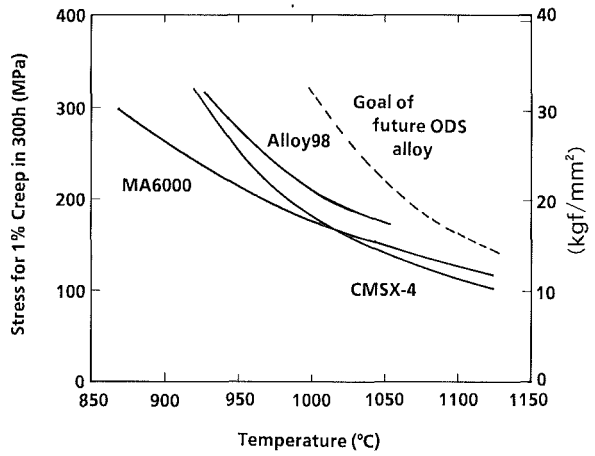

Fig. 4 1pct creep strength comparison of ODS alloys and CMSX-4; the broken line is a future strength goal of ODS alloys

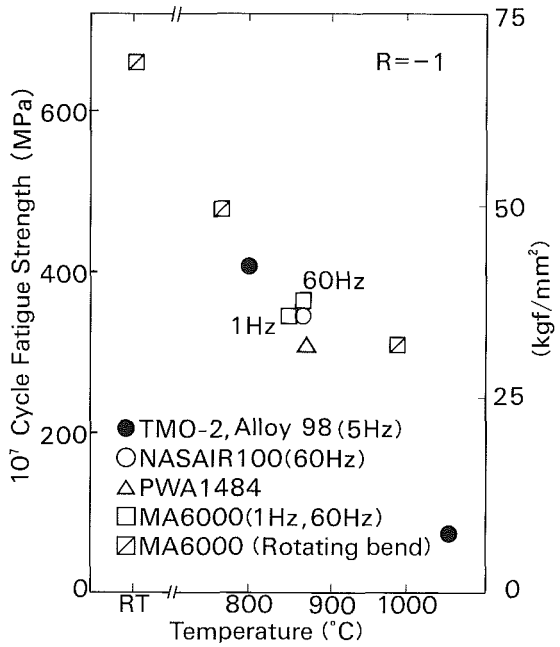

Fig. 5 High cycle fatigue strength

98 was compared in Fig. 5 with MA6000 and two monocrystalline alloys. Fatigue strength of MA6000 obtained by rotating bend tests is likely to give higher strength than that by push-pull tests. The high cycle fatigue strength of Alloy 98 at 800°C was almost equal to that of TMO-2, MA6000, and monocrystalline alloys. The fatigue strength at 1050°C is supposed to be strongly dependent on the testing frequency and careful examination will be needed for comparison.

Scattering of Materials Performance

The mechanical properties mentioned above are obtained

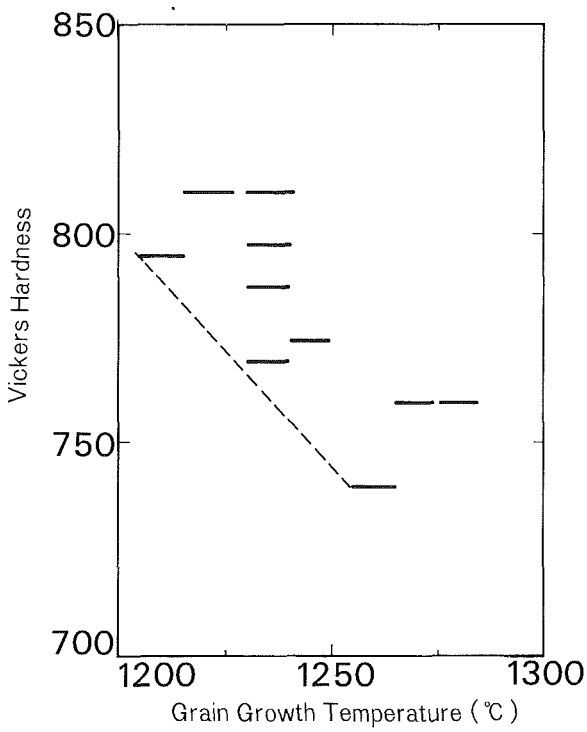

Fig. 6 Relationship between hardness of extruded TMO-2 bars and their recrystallization temperatures; heat to heat variation of recrystallization response was explained in terms of hardness before annealing

when the materials are processed properly. As described earlier, microstructural control for directional recrystallization severely affects materials performance of ODS alloys. Various factors influencing directional recrystallization have been fairly clarified in the past and present study.

Microstructures in the extruded condition determine the zone annealing response to secondary recrystallization. Secondary recrystallization or abnormal grain growth occurs when a small number of grains can consume other finer grains to grow much larger. The driving force for recrystallization is the grain boundary energy of fine grains. It has to be large enough to surpass the pinning force by oxide dispersoids. In other words, the grain size in extruded materials has to be less than the critical size determined by dispersoids.

Hardness of extruded materials was shown to be proportional to the inverse of grain size, which is similar to the Hall–Petch relationship (Mino et al., 1987). It was also shown by Mino et al. (1987) that the higher the hardness value in the extruded condition, the lower the secondary recrystallization temperature. This was found during the study of recrystallization response of preannealed or hot worked materials. As shown in Fig. 6, the above relationship explained the scattering of the recrystallization temperature of extruded TMO-2 bars. Much softer heats failed to recrystallize since the recrystallization temperature was too close to the melting point to be practicable.

Another important influence of grain size on the zone annealing conditions is the annealing speed. The zone travel speed

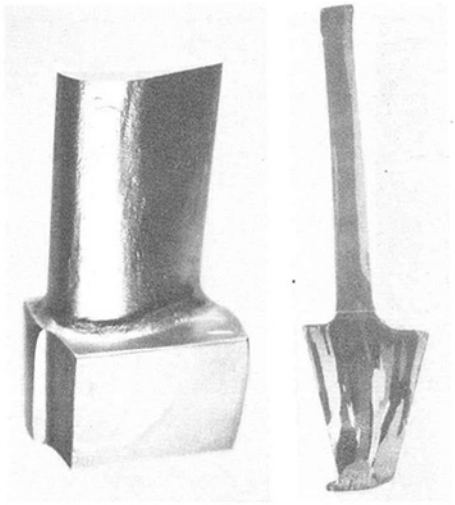

Fig. 7 Isothermally forged TMO-2 and cross-sectional macrostructure of subsequently zone annealed sample

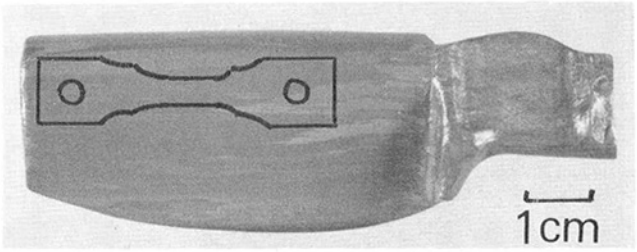

Fig. 8 Another isothermally forged sample; a configuration of rupture specimens is shown in the photograph

should be less than the migration rate of grain boundaries for directional recrystallization. The softer material had to be annealed at lower zone travel speed to obtain elongated grains. Faster annealing led to the same microstructure as for isothermal anneal.

Hot Forging

Near-net shape processing by hot forging will be necessary for improved material utilization and reduced machining cost in fabricating turbine blades. Hence, degeneration of directional recrystallization by hot forging becomes a serious problem from the practical viewpoint.

Hot forging tends to induce secondary recrystallized areas with a low grain-aspect ratio or unrecrystallized areas. Overly severe working derprives the material of recrystallizability. On the other hand, keeping high grain-aspect ratio tends to become difficult for forged parts for the following two reasons:

1 Direct induction heating becomes difficult in zone annealing of parts such as a forged turbine blade having a complex configuration. In this case, the temperature gradient across the specimen travel axis has to be sacrificed for overall temperature control.

2 Secondary recrystallized grains tend to be aligned parallel to the direction of plastic flow rather than that of the imposed temperature gradient.

As a countermeasure to (2), an appropriate design of preforms and/or forged shapes will be needed.

Figure 7 shows an example of isothermally forged TMO-2 samples. The zone annealed macrostructure is also shown. Transverse grains were found at the bottom and the left-hand side of the top in the root section. Fairly elongated grains were formed in the airfoil section. Another isothermal forging study,

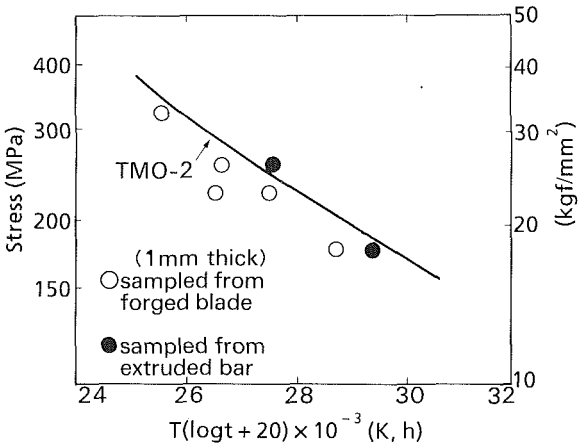

Fig. 9 Degradation of rupture strength of TMO-2 by isothermal forging

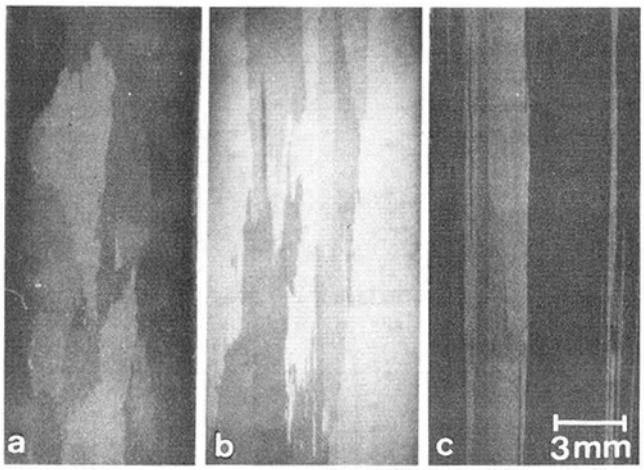

Fig. 10 Effect of temperature gradient on zone annealed macrostructures of TMO-2: (*a*) isothermal, (*b*) ~10°C/cm, (*c*) ~200°C/cm

aimed at developing a two-piece blade, was performed by Kobe Steel, Ltd., using a different preform design to get a forged sample as shown in Fig. 8. An elongated grain structure was observed in the airfoil section.

Creep rupture specimens of a plate form with a gage section of 1 t × 4 w × 10 l (mm) were sampled from the forged and zone annealed specimens as shown in Fig. 8. Figure 9 shows the result of rupture tests at 900 to 1050°C in air. Specimens having the same size were also machined from the nonforged TMO-2 bar and their test results were shown in the same figure. The forged materials had less strength than the nonforged. The strength reduction was also found not to be caused by the specimen size effect. Defects in directional recrystallization are considered to have led to the reduction in creep rupture strength.

In relation to (1), effects of temperature gradient across the zone travel axis were studied using TMO-2 bars 12 mm in diameter. The results are shown in Fig. 10. The small temperature gradient of zero to 10°C/cm has led to incompletely elongated grain structures. It was also found that the temperature gradient required for directional recrystallization was not so large as to be impracticable.

Diffusion Bonding

Diffusion bonding is necessary for manufacturing air-cooled turbine blades. Bonding of ODS alloys is known to be more difficult than that of conventional superalloys. The following methods were examined in this study.

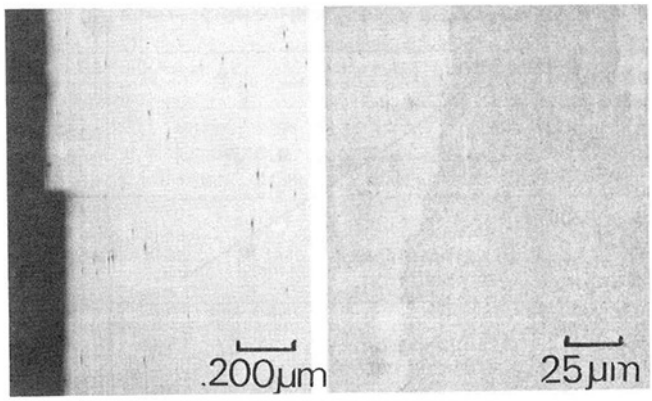

Fig. 11 Microstructures of directly diffusion-bonded TMO-2 after zone anneal

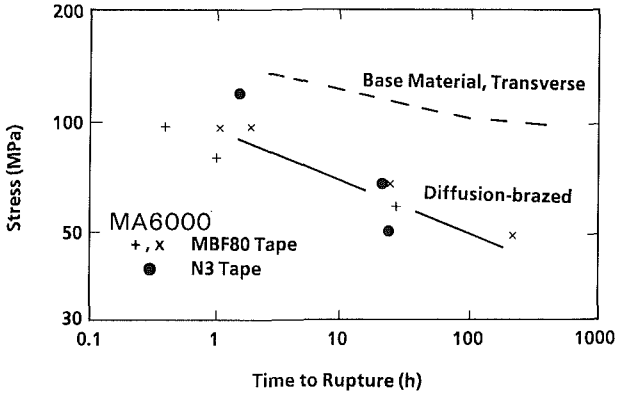

Fig. 12 Stress rupture data at 950°C of diffusion-brazed MA6000

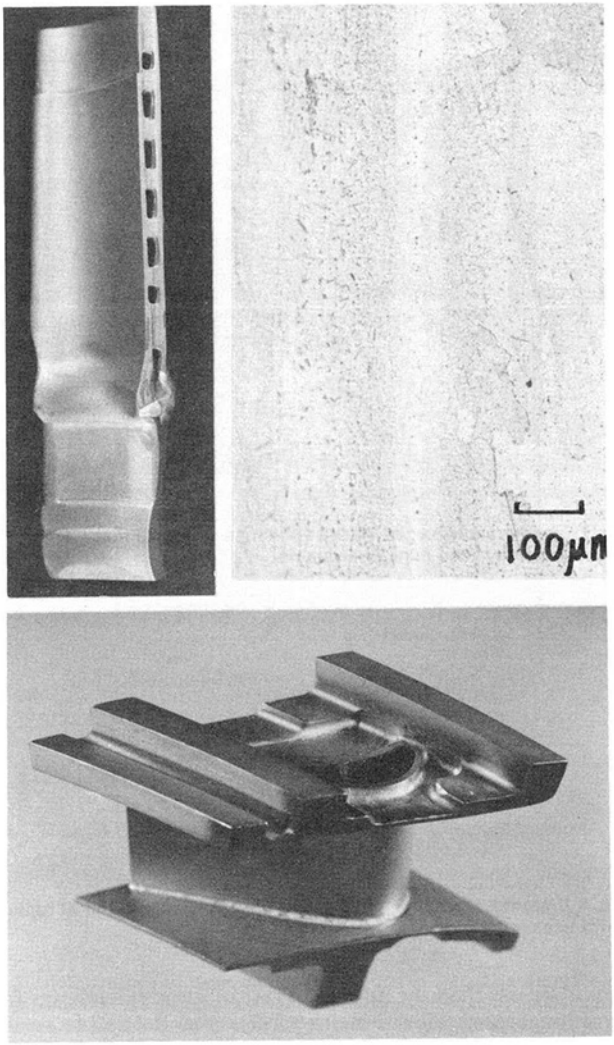

Fig. 13 Diffusion brazed samples of TMO-2 and MA754

1 Direct Solid-State Diffusion Bonding in Nonrecrystallized Condition. Fine-grained materials are easy to deform at elevated temperatures and suitable for direct bonding. TMO-2 bar specimens 12 mm in diameter were diffusion-bonded at 1230°C and 20 MPa for 2 h after degreasing in acetone.

2 Diffusion Brazing Using Amorphous Tapes. Two kinds of brazing tapes, MBF80 and N3, 40 to 50 μm in thickness, were used as an insert material between the mating surfaces of recrystallized MA6000 specimens. Heating conditions are 1150 to 1250°C, 1 to 5 MPa and 10 to 20 h. Layers deposited by plasma sputtering were also applied as an alternative insert material, but did not improve the bondability.

Microstructural examination of directly diffusion-bonded TMO-2 specimens revealed almost complete bonding, as shown in Fig. 11. The fatal defect was formation of unbonded areas at the near surface, which is considered to be caused by slight oxidation during heating in vacuum. Extremely high vacuum might be necessary for preventing it.

On the other hand, diffusion brazing using amorphous tapes has brought about a sound bonding under a slight bonding pressure. This can be beneficial to bonding of parts with a complex configuration. The trouble was its poor rupture strength, as shown in Fig. 12. Significant strength reduction was not found in a dispersoid-free superalloy MarM247LC brazed by exactly the same procedures. Some agglomeration of oxide dispersoid during diffusion brazing was found in the ODS alloy near the insert layer. However, the creep rupture surface did not coincide with this agglomeration layer. A different mechanism was likely to have operated in degrading the bonding strength of ODS alloys.

Both methods have shortcomings in manufacturing two-piece blades of ODS alloys. At present, diffusion brazing will be the only method for forming microstructurally defect-free bonding. Figure 13 shows diffusion-brazed samples. Mechanically machined parts of MA754 were used in assembling the vane model.

Summary

The MITI R&D program on ODS superalloys is believed to have substantially contributed to the knowledge of high-strength ODS alloys. One of the problems of ODS superalloys had been their poor creep strength at intermediate temperatures. The time to reach a usable creep strain of the development alloy has now been comparable to that of current monocrystalline alloys at those temperatures. Current research on ODS alloy development shows encouraging results of further increase in creep strength. These progresses in alloy development are believed to motivate a further study on several problems still remaining to be solved for manufacturing air-cooled turbine blades.

Acknowledgments

This work was performed in part under the management of

the Research and Development Institute of Metals and Composites for Future Industries as a part of the R&D project of Basic Technology for Future Industries sponsored by the Agency of Industrial Science and Technology, MITI.

References

Benn, R. C., and Kang, S. K., 1984, "Long-Term Mechanical Behavior of Some ODS Alloys," *Superalloys 1984*, M. Gell et al., eds., Metall. Soc. AIME, Warrendale, pp. 319–326.

Kang, S. K., and Benn, R. C., 1985, "Microstructural Development in High Volume Fraction Gamma Prime Ni-Base Oxide-Dispersion-Strengthened Superalloys," *Metall. Trans. A*, Vol. 16A, pp. 1285–1294.

Kawasaki, Y., Kusunoki, K., Nakazawa, S., and Yamazaki, M., 1989, "Development of Oxide Dispersion Strengthened Nickel-Base Superalloy," *Tetsu-to-Hagané*, Vol. 75, pp. 529–536.

Kusunoki, K., Kawasaki, K., Nakazawa, S., and Yamazaki, M., 1989, "Effect of the Amount of γ' Phase on the Creep Strength of the Dispersion Strengthened Ni-Base Superalloys," *Tetsu-to-Hagané*, Vol. 75, pp. 1588–1595.

Mino, K., 1984, "Directional Recrystallization of an ODS MarM247-1% Y_2O_3 Alloy," *Proceedings, PM Aerospace Materials*, I, MPR Publ. Serv. Ltd., United Kingdom, Paper No. 18.

Mino, K., and Asakawa, K., 1987, "An Oxide Dispersion Strengthened Nickel-Base Superalloy With Excellent High Temperature Strength," *Trans. Iron Steel Inst. Jpn.*, Vol. 27, pp. 823–829.

Mino, K., Nakagawa, Y. G., and Ohtomo, A., 1987, "Abnormal Grain Growth Behavior of an Oxide Dispersion Strengthened Superalloy," *Metall. Trans. A*, Vol. 18A, pp. 777–784.

Integrity Assessments of Components in the Creep Range

R. K. Penny
Professor.

M. A. Weber
Graduate Student.

Department of Mechanical Engineering,
University of Cape Town,
Rondebosch, South Africa

Robust methods for the predictions of deformations and lifetimes of components operating in the creep range are presented. The ingredients used for this are well-tried numerical techniques, combined with the concepts of continuum damage and so-called reference stresses. The methods described are derived in order to obtain the maximum benefit during the early stages of design where broad assessments of the influences of material choice, loadings, and geometry need to be made quickly and with economical use of computers. It is also intended that the same methods will be of value during operation if estimates of damage or if exercises in life extension are required. Results of the suggested method are amenable to tabular or graphic representation. To illustrate the use of these in parametric studies, three brief case studies are included. These involve a notched rod, a perforated plate, and a pipe for which lifetime estimates based upon failure criteria involving different degrees of conservatism are calculated. In addition, an illustration is given of the use of the charts presented in deciding inspection intervals and lifetime extensions. Finally, a brief excursion into the possibility for using the suggested methods for the mapping of designs within given regional constraints is given.

Introduction

Creep in high-temperature, highly loaded generating plants; which leads to microcracking and ultimate failure, is one of the main mechanisms that limits the life of components. Such components are often of complex geometry, and the service loadings produce multidimensional states of stress and stress redistribution in them. These factors, together with the complexities of material degradation, combine toward formidable problems in the assessment of the integrity of high-temperature plants. For this reason codes of practice are usually conservative in their design rules, but this conservatism can lead to the unnecessarily early retirement of a plant. Designers are therefore faced not only with the need to provide accurate, reliable predictions of operating lifetimes, but also with the need to incorporate in their designs a sound basis for updating and extending lifetimes during operation.

In addressing some of these issues, a range of methods has been developed over the past several decades of striving for higher temperatures and greater reliability. Generally speaking, these include techniques for stress analysis and, more recently, concepts to account for progressive material degradation. The coupling of stress analysis with material degradation is an attractive proposition and one that, if feasible, has promising capabilities for predicting reductions in strength, stiffness, toughness, residual and ultimate lives. In practice though, prohibitive computer costs and insufficient materials data are likely to impede progress toward its initial promise [1]. Perhaps even more important though, is the increasing recognition that what the designer needs is to be able to *decouple* the effects of geometry, loading, and materials characteristics. This is needed not only to be able to determine which factors are important and which are not, but also to be able to make decisions quickly and economically in ways that are within the scope of available tools. The call therefore, and it appears to be a desperate one [2], is for robust methods that are rigorously based, can be used flexibly, and provide solutions with accuracies commensurate with the quality of available data and the tolerances that usually have to be accepted in modeling geometries and loadings.

The basic ingredients for robust methods are available: well-tried numerical methods of analysis and the more recent concepts of *continuum damage* and *reference stresses*. The early work of Kachanov [3] and Rabotnov [4] in their studies of macroscopic damage variables during creep has developed continuously and forms a framework for a broader approach to other damaging mechanisms such as fatigue and large-scale plasticity [1]. Even more recently, reference stress approaches [5, 6] aim at the derivation of representative stress levels, which characterize the creep behavior of components from a minimum amount of data.

The aim of this paper is to contribute toward the generation of robust methods that have the following characteristics:

- cater to several interpretations of failure by creep which may be used by designers in assessing lifetimes;
- offer the means for parametric studies that enable the identification of essential features affecting component behavior with the smallest number of iterations;
- allow graphic representation of results for commonly occurring components wherever possible; and
- contribute to the furtherance of codes of practice.

Contributed by the International Gas Turbine Institute and presented at the 35th International Gas Turbine and Aeroengine Congress and Exposition, Brussels, Belgium, June 11-14, 1990. Manuscript received by the International Gas Turbine Institute January 31, 1990. Paper No. 90-GT-125.

Normalized Arrangement of Constitutive Laws for Creep Including Damage Effects

In order to maximize the potential for assessing the effects of dependent variables (loading, material, and temperature) on any calculated results of the creep response of a component, it seems sensible to cast the results in nondimensional form whenever possible. The numerical procedure must also be nondimensionalized, which, in itself, is not a bad thing anyway since the governing equations will then contain terms of like magnitudes and thus be less liable to meet with stability problems during solution procedures.

The best hope for such a procedure is to adopt the well-tried device of using a distorted time measure [6] and converting the creep and damage relationships [4] accordingly. Inherent in such a procedure is also the use of the time-hardening hypothesis as follows for the uniaxial case during which long term, low stress conditions leading to brittle failure apply:

$$\epsilon_c = A\sigma^m t^n \tag{1}$$

$$\epsilon_{cd} = A\sigma^m t^n (1-\omega)^{-p} \tag{2}$$

$$\omega = B\sigma^k t^n (1-\omega)^{-r} \tag{3}$$

where σ is the nominal stress at time t, which gives rise to creep strain ϵ_c in the absence of damage, ϵ_{cd} when damage occurs and at which time damage is ω. A, B, m, p, k, r, and n are material constants. If now these equations are converted with respect to stress, strain, and time measures defined respectively as:

$$\Sigma = \frac{\sigma}{\sigma_o}; \quad \lambda = \frac{\epsilon}{\epsilon_o}; \quad \epsilon_o = \frac{\sigma_o}{E}; \text{ and } \tau = AE\sigma_o^{m-1} t^n \tag{4}$$

where σ_o is some convenient normalizing value, then Eqs. (1), (2), and (3) become, after differentiation with respect to τ:

$$\dot{\lambda}_c = \Sigma^m \tag{5}$$

$$\dot{\lambda}_{cd} = \Sigma^m (1-\omega)^{-p} \tag{6}$$

$$\dot{\omega} = C\Sigma^k (1-\omega)^{-r} \tag{7}$$

where

$$C = \frac{B\sigma_o^{1+k-m}}{AE} \text{ and } \dot{(\,)} \equiv \frac{\partial}{\partial \tau}(\,) \tag{8}$$

If it is now assumed that the von Mises yield criterion and the Prandtl–Reuss relations are valid during creep [6] and that an equivalent stress criterion holds for damage accumulation [7], the multiaxial stress creep and damage laws are:

$$\dot{\lambda}_{ij,c} = \Sigma^{*m} \frac{d\Sigma^*}{d\Sigma_{ij}} \tag{9}$$

$$\dot{\lambda}_{ij,cd} = \Sigma^{*m} (1-\omega)^{-p} \frac{d\Sigma^*}{d\Sigma_{ij}} \tag{10}$$

$$\dot{\omega} = C\Sigma_\beta^k (1-\omega)^{-r} \tag{11}$$

where Σ_β is an equivalent stress given by:

$$\Sigma_\beta = \beta\Sigma^I + (1-\beta)\Sigma^* \tag{12}$$

In addition, Σ^* and Σ^I are the Mises effective and maximum principal stresses, respectively, while $0 \le \beta \le 1$. Integration of Eq. (11) gives:

$$(1-\omega) = [1-(1+r)C\Sigma_\beta^k \tau]^{1/(1+r)} \tag{13}$$

When $\omega = 1$, rupture occurs at time $\tau = \tau_R$ and then, from Eq. (13), there results:

$$(1-\omega) = (1-\tau/\tau_R)^{1/(1+r)} \tag{14}$$

and

$$\tau_R = \frac{1}{(1+r)C\Sigma_\beta^k} \tag{15}$$

Similarly, by integrating Eqs. (9) and (10) while using Eq. (15):

$$\lambda_{ij,c} = K\tau/\tau_R = K\Gamma \tag{16}$$

$$\lambda_{ij,cd} = aK[1-(1-\tau/\tau_R)^{1/a}] = aK[1-(1-\Gamma)^{1/a}] \tag{17}$$

where

$$a = \frac{1+r}{1+r-p} \tag{18}$$

$$K = \frac{\Sigma^{*m}}{(1+r)C\Sigma_\beta^k} \frac{d\Sigma^*}{d\Sigma_{ij}} = \tau_R \Sigma^{*m} \frac{d\Sigma^*}{d\Sigma_{ij}} \tag{19}$$

and

$$\Gamma = \tau/\tau_R \tag{20}$$

is a life fraction measure.

Finally, by differentiating Eqs. (16) and (17) with respect to the life fraction measure Γ, the creep strain rates with and without damage are:

$$\frac{d\lambda_{ij,c}}{d\Gamma} = K \tag{21}$$

$$\frac{d\lambda_{ij,cd}}{d\Gamma} = K(1-\Gamma)^{(1-a)/a} = (1-\Gamma)^{(1-a)/a} \frac{d\lambda_{ij,c}}{d\Gamma} \tag{22}$$

These equations form the basis for any stress analysis that aims to calculate the deformation and rupture characteristics of a component during creep. If the coupling between the progressive degradation of the material and its stiffness is to be taken into account, then Eqs. (17) and (22) must be used in stress analysis. When prohibitive computer costs make this an unattractive proposition, then material degradation is uncoupled for the purpose of the stress analysis and Eqs. (16) and (21) are used. If the latter course of action is taken then the analysis will not be capable of predicting the rupture characteristics directly. However, prudent manipulation of the results of the analysis, interpreted with the use of Eqs. (15), (17), and (22), is likely to provide a method of component assess-

Nomenclature

A, B = creep, damage constant
E = elastic constant (modulus)
k, m = damage, creep stress exponent
n = time exponent
p, r = damage exponents
R_1, R_2, R_3 = failure criterion factors
t, τ = real, distorted time
u, U = dimensional, normalized displacement
α = reference stress parameter
γ = upper bound deformation parameter
Γ = life fraction parameter
ϵ, λ = strain, normalized strain
σ, Σ = dimensional, normalized stress
σ_o, ϵ_o = normalizing stress, strain
$\bar{\sigma}$, $\bar{\epsilon}$ = reference stress, strain
ω = damage

Subscripts

c = creep strain component
cd = coupled creep damage strain component
el = elastic value
R = rupture
ss = stationary value
β = Hayhurst equivalent stress

Superscripts

I = maximum principal value
r, z = r, z component
$*$ = von Mises equivalent value

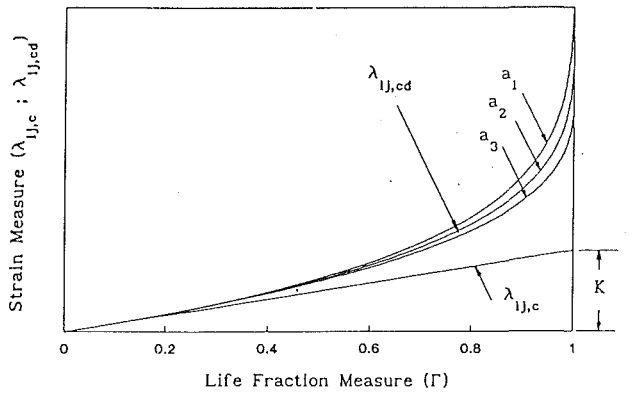

Fig. 1 Generalized representation of stationary and damaged strain measures as functions of the life fraction measure

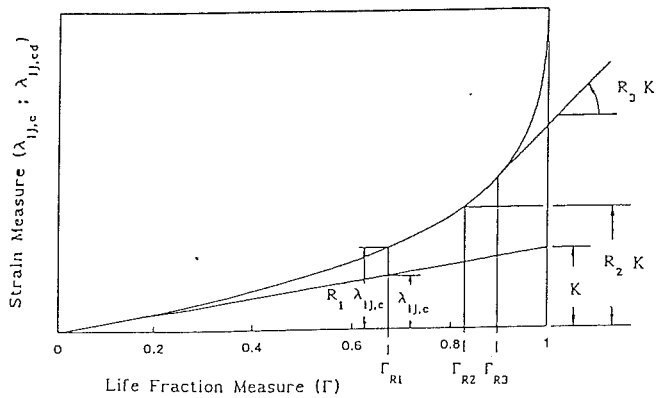

Fig. 2 Schematic representation of failure criteria based on strain measures

ment, which is particularly useful at the early stages of design and in which economy in computer processing time makes it viable.

Criteria for Component Failure

An analysis that couples progressive degradation with stiffness changes will allow calculation of all characteristics including the rupture time measure τ_R given by Eq. (15). A simpler approach is to estimate strains and rupture times based upon stationary state stresses.

This will underestimate the strains and, therefore, more conservative criteria need to be formulated. These can be managed in several ways by adjustment of the calculated stationary state strains and strain rates in the component, such that the effects of damage are taken into account. In this process, the judgment and experience of the designer will be crucial and much will depend on the intended use of the component. For example, a pressure vessel with a lifetime expectancy of 20–30 years can be monitored carefully and estimates of the remaining life can be made and updated against predicted values in a systematic way. Short of emergencies, which might include overloading, it is likely that changes in strain rate will be reasonable predictors of microstructural change and damage. On the other hand, in which lifetimes may be shorter and in which operating conditions contain more imponderables, predictions and measures of total strain will be more important; an example could be in turbine blade integrity assessment. Whichever the case, it is a relatively simple matter for stationary strain estimates to be adjusted to account for damage in current or forward predictions.

So far as rupture estimates are concerned, stationary state stress values are likely to be too conservative in most cases. This is because of the stress shedding from high stress regions to regions of lower stress that will happen, in the usual way, for statically indeterminate components. There are several analogies here. One is during instantaneous plastic flow leading to the spreading of high strains over large volumes of the component and eventual collapse as the loads increase. Another is the reduction of residual stresses during temperature soaking. If it is accepted that stationary state stresses are too conservative, then it is certain that initial elastic values are even more so, for creep conditions—a very restricting approach which has been suggested in some Codes. For uniaxial conditions, stress redistribution is constrained and net section stresses will most likely govern rupture. In this case, conservative lifetimes can be calculated on the basis of limiting strain rates to realistic values.

Figure 1 is a generalized representation of the strain measures $\lambda_{ij,c}$ and $\lambda_{ij,cd}$ as a function of the life fraction measure Γ for different values of a. The schematic representation of this is also shown in Fig. 2 for a given value of a, together with several conservative failure criteria, which could be used to calculate likely component retirement times from the point of gross deformation or deformation rate. The choice here will depend on the degree of conservatism thought necessary. In the first case, an acceptable value of creep strain that includes contributions from the *hardened* stationary state and the *softened* (void accumulated) state is chosen as a proportion R_1 of the hardened state. The corresponding life fraction measure Γ_{R1} to achieve this state is easily calculated from Eqs. (16) and (17) and is given by:

$$a[1-(1-\Gamma_{R1})^{1/a}]=R_1\Gamma_{R1} \tag{23}$$

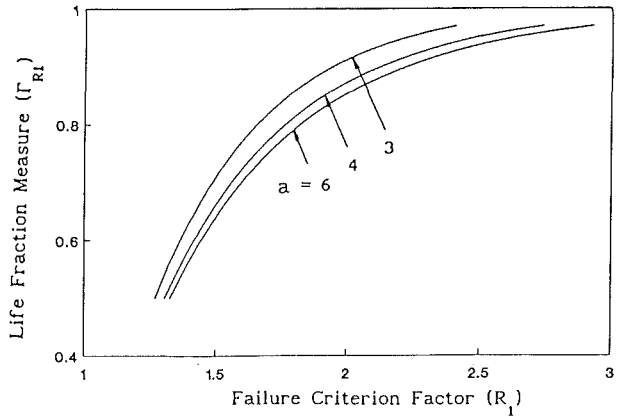

Fig. 3 Variation of life fraction using first failure criterion

This cannot be solved explicitly, but various life fraction measures corresponding to different values of R_1 are plotted in Fig. 3.

Another method based upon a strain measure would be in terms of a factored amount R_2 ($1 < R_2 < a$) of the stationary state creep strain at rupture. The life fraction measure Γ_{R2} corresponding to the choices of R_2 follow from Eq. (16) at $\Gamma = 1$ and Eq. (17):

$$a[1-(1-\Gamma_{R2})^{1/a}]=R_2 \tag{24}$$

Results for various values of R_2 are given in Fig. 4.

A third approach would be to regard the strain rate as a more critical measure of the imminence of failure. In this case a proportion R_3 of the stationary state creep rate is used to guard against the effects of excessive void formation. The life fraction measure Γ_{R3} at which this occurs is given by Eq. (22):

$$a[1-\Gamma_{R3}]^{(1-a)/a}=R_3 \tag{25}$$

These results are plotted in Fig. 5.

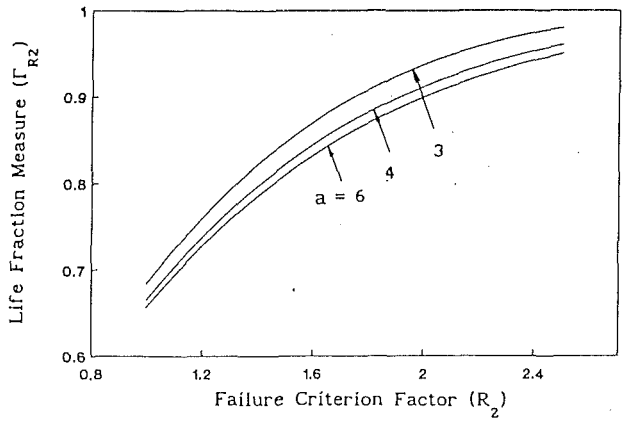

Fig. 4 Variation of life fraction using second failure criterion

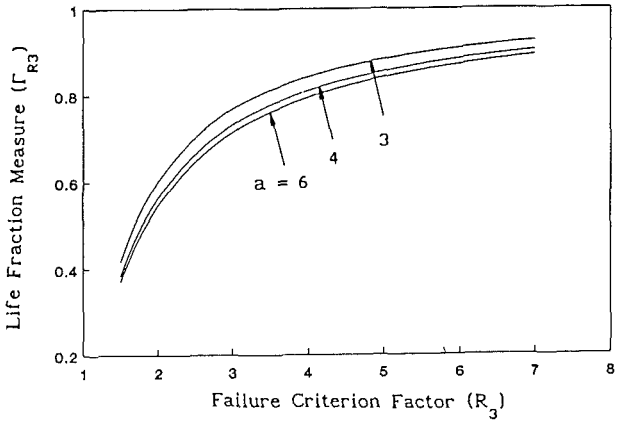

Fig. 5 Variation of life fraction using third failure criterion

Stationary State Analyses and Use of Reference Stress Techniques

Methods for calculating stationary state behavior of components are well known [6] and will only be summarized here. The stationary state differs from steady-state analyses in that it includes the effect of stress redistribution after first loading (Fig. 6 illustrates this qualitatively for steady loading). It is easier to perform a stationary state analysis in most cases and, whether this is accomplished through finite difference or finite element methods, the process is the same:

1 Solve the initial elastic (plastic) problem ($\tau = 0$).
2 Use the stresses from step (1) to calculate creep terms at $\tau = 0$; solve the rate problem and evaluate stress, strain and other rates.
3 Over a time interval $\Delta\tau$ evaluate new stresses by integrating forward: $\Sigma_{\tau+\Delta\tau} = \Sigma_\tau + \dot{\Sigma}_\tau \Delta\tau$, etc.
4 Repeat steps (2) and (3) until a state of stationarity is reached to within prescribed tolerances of $\dot{\Sigma} = 0$ and $\dot{\lambda}$ is constant.

In performing these calculations, the governing equations are all phrased in normalized terms as outlined earlier; this not only makes for more efficient computational routines but also gives the results in a form that is convenient in design. Stresses and strains are calculated as proportions of nominal values (stress/strain concentration factors) and these and other quantities can be studied and presented parametrically so that the effects of geometry or material constants can be easily evaluated. For example, if a power law is used to represent creep, then the results obtained from the stationary state calculations will quickly reveal the importance or otherwise of the creep exponent. Likewise, other material constants are

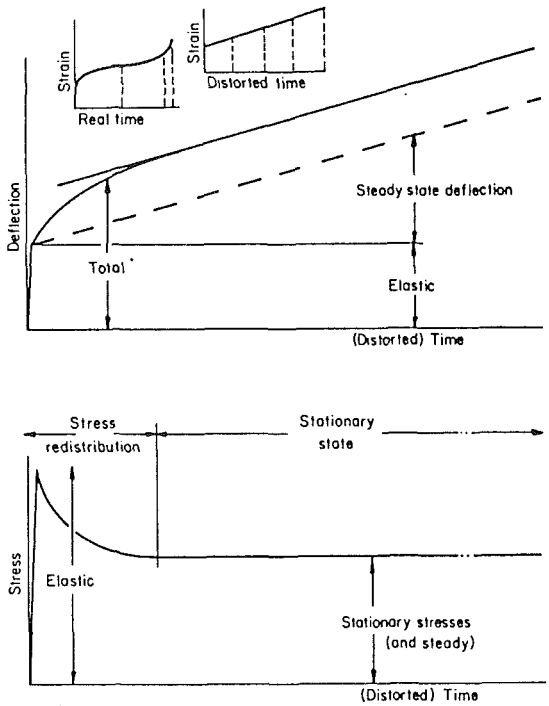

Fig. 6 Schematic representation of strain accumulation and stress redistribution following constant elastic loading [6]

embodied in the distorted time measure τ through Eq. (4) so that without performing new calculations every time the material is changed during early design studies; the effects can be judged from the amount of distortion that results in τ. In the same manner, if the component response is examined from a viewpoint of temperature changes, this can also be accommodated in the distorted time measure.

Another powerful concept in creep design is that of the so-called reference stress [5]. What this amounts to is that there exists for a given component, a unique stress level at which the stationary state creep response is relatively insensitive to the precise stress dependence of creep; in our case the response does not vary with the stress exponent m. The significance of this is manifold but, for the purpose of this paper, use of the reference stress as that value for normalizing the results of creep calculations means that all data can be computed once and for all for a given component. The results for standard components can then be catalogued for use in design in ways similar to those in which elastic stress concentration factors have been collected together; examples follow in the next section. The fuller uses of reference stress techniques, for example in assessing the effects of variable loading or as a means for deciding on critical sorting tests in laboratory data collection, are reviewed elsewhere [6]. For the present case, it is useful to give methods for calculating reference stresses. Any stationary state creep deformation u_c can be expressed as:

$$u_c = u_c(\sigma^m, g(\text{dimensions}))f(t) \tag{26}$$

Differentiating and choosing a convenient normalizing stress σ_o, a normalized rate equation can be derived, where $(\dot{}) = (d/d\tau)$:

$$\dot{U}_c = \dot{U}_c\left[\left(\frac{\sigma}{\sigma_o}\right)^m\right] \tag{27}$$

Here $f(t)$ is the usual time function, g(dimensions) is a function of the dimensions, and $\dot{U}_c$ is the normalized creep rate predicted by the numerical analysis. In general $\dot{U}_c$ will vary with the stress exponent m, and the degree of variation depends on σ_o. Letting $\bar{\sigma} = \chi\sigma_o$, where $\bar{\sigma}$ is the reference stress to be determined, σ_o is an initial estimate of the reference stress, and

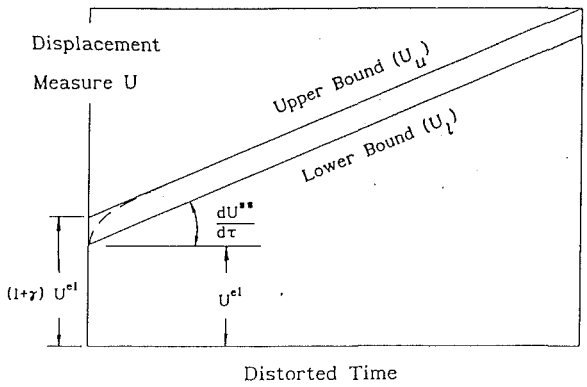

Fig. 7 Schematic representation of displacement characteristics

noting that $\dot{U}_c$ is a homogeneous m-degree function of σ, it follows from Eq. (27):

$$\dot{U}_c = \dot{U}_c\left[\left(\frac{\sigma}{\bar{\sigma}}\right)^{m1}\right] = \frac{1}{\chi^{m1}}\dot{U}_c\left[\left(\frac{\sigma}{\sigma_o}\right)^{m1}\right] = \dot{U}_c\left[\left(\frac{\sigma}{\bar{\sigma}}\right)^{m2}\right]$$

$$= \frac{1}{\chi^{m2}}\dot{U}_c\left[\left(\frac{\sigma}{\sigma_o}\right)^{m2}\right] \quad (28)$$

Computing $\dot{U}_c$ for an arbitrary choice of σ_o at two values of m, we can find two stationary state deformation rates $(\dot{U}_c)_{m1}$ and $(\dot{U}_c)_{m2}$. Using Eq. (28) an expression for χ can be obtained:

$$\chi = \left[\frac{(\dot{U}_c)_{m1}}{(\dot{U}_c)_{m2}}\right]^{1/(m1-m2)} \quad (29)$$

Typically, one would choose a high value and low value of m to ensure the closest estimate of χ; $m_1 = 3$ and $m_2 = 9$ for example.

A second method described by Sim [5] is based on the collapse load of a structure, P_{coll}, for a perfectly plastic material having a yield strength of σ_y:

$$\bar{\sigma} = \frac{P}{P_{\text{coll}}}\sigma_y \quad (30)$$

If a reference stress is used to normalize the stationary state analysis, the response of the component can then be expressed as in Fig. 7, the main ingredients of which are the initial elastic response and the stationary state rates; all of the quantities are dimensionless. The deformations U can then be bounded by:

$$U_l = U^e + \frac{dU^{ss}}{d\tau}\tau \quad (31)$$

$$U_u = (1+\gamma)U^e + \frac{dU^{ss}}{d\tau}\tau = U_l + \gamma U^e \quad (32)$$

with terms defined as in Fig. 7.

Problems Studied and Results

A number of problems were analyzed using the methods outlined above. A standard finite element package suited to nonlinear structural analysis (ABAQUS Version 4.7 [8]) was used; eight-noded quadratic elements were used in all cases, and mesh sensitivity analyses were performed. Where possible, results were compared with analytical solutions, and errors were found to be less than 3 percent. Use was made of the standard load and strain tolerancing of ABAQUS to prevent instability and numerical errors. All runs were allowed to continue well into the stationary state.

In each problem, the loading, P, or some nominal stress σ_{nom}, was normalized to a *reference stress parameter*, α, where:

Table 1 Plate with hole under equibiaxial tension: maximum normalized stresses and strain measures

Plate with hole : equibiaxial tension a/w = 1/10 ; a = 1 ; α = 0.9565				
	m = 3	m = 5	m = 7	m = 9
Σ^{*}_{el}	1.928 (1.0)	1.928 (1.0)	1.928 (1.0)	1.928 (1.0)
Σ^{*}_{ss}	1.313 (1.0)	1.184 (1.0)	1.127 (1.0)	1.095 (1.0)
Σ^{I}_{el}	1.933 (1.0)	1.933 (1.0)	1.933 (1.0)	1.933 (1.0)
Σ^{I}_{ss}	1.318 (1.0)	1.221 (1.4)	1.191 (1.6)	1.177 (1.6)
λ^{z}_{el}	1.930 (1.0)	1.930 (1.0)	1.930 (1.0)	1.930 (1.0)
γ	0.139	0.239	0.301	0.377
$\dot{\lambda}^{z}_{ss}$	2.221	2.278	2.263	2.214
τ_{ss}	≃ 2.6	≃ 2.0	≃ 1.9	≃ 1.8
Note : Locations in brackets are approximate values of r/a along the r-axis				

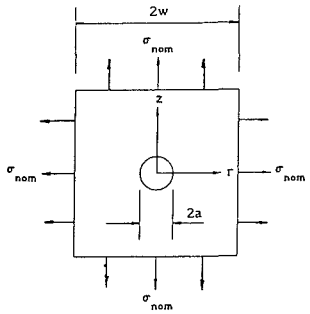

$$\bar{\sigma} = \frac{1}{\alpha}\sigma_{\text{nom}} \quad (33)$$

The reference stress parameter α gives the relationship between the loading and the reference stress, and is dependent only on the geometry. If the loading is expressed in the same units as the reference stress, α will be the same for similar geometries. Values for α were found using Eq. (29). Using this method, the results of a decoupled creep analysis based on Eqs. (16) and (21) will be normalized. They will be independent of the actual size (as long as similar geometries are used), the loading, and of all material parameters except the stress exponent m. However, if the reference stress is used, the results will be only weakly dependent on the stress exponent [6]. So it becomes feasible to present the results parametrically for different values of m in tabulated and graphic form. The designer can consult these tables, and use the relevant equations to calculate actual stresses, strains, strain rates, rupture data, etc., for different material parameters, loading levels, and, within limits, geometries, without having to reperform time-consuming structural analyses. Examples of the procedures are illustrated in the case studies that follow, and further possibilities of the approach are discussed later.

For the purpose of this paper, three simple problems were studied. A plate with a hole was subjected to equibiaxial tension, and 150 plane stress elements were used. Comprehensive results for the plate with a hole under equibiaxial tension are included in Table 1 for illustrative purposes. All results are maximal for the plate. By judicious data management, however, much more information can be extracted from the finite element analysis; but limited space has prevented inclusion of this. Nevertheless, the results in the table are sufficient to give

Table 2 Notched rod under uniaxial tension: maximum normalized stresses and strain measures

Circular rod with circumferential notch D = 2.0 ; d = 1.4 ; α = 0.7076				
	m = 3	m = 5	m = 7	m = 9
Σ^*_{el}	2.512 (0.7)	2.512 (0.7)	2.512 (0.7)	2.512 (0.7)
Σ^*_{ss}	1.460 (0.7)	1.266 (0.7)	1.181 (0.7)	1.133 (0.7)
Σ^I_{el}	2.787 (0.7)	2.787 (0.7)	2.787 (0.7)	2.787 (0.7)
Σ^I_{ss}	1.802 (0.6)	1.790 (0.6)	1.800 (0.6)	1.799 (0.6)
λ^z_{el}	2.579 (0.7)	2.579 (0.7)	2.579 (0.7)	2.579 (0.7)
γ	0.270	0.703	0.995	1.215
$\dot{\lambda}^z_{ss}$	2.919	3.013	2.989	2.877
Note : Locations given in brackets are approximate values of 2r/d along the r-axis				

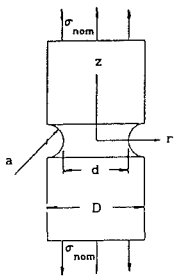

Table 3 Pipe with internal pressure: normalized stresses and strain measures

Pipe ; r_{inn}/r_{out} = 0.7 ; r_{inn} = 0.7 ; α = 0.4106				
	m = 3	m = 5	m = 7	m = 9
Σ^I_{el}	1.200 (0.7)	1.200 (0.7)	1.200 (0.7)	1.200 (0.7)
Σ^I_{ss}	1.035 (1.0)	1.086 (1.0)	1.109 (1.0)	1.122 (1.0)
U^r_{el}	0.703 (1.0)	0.703 (1.0)	0.703 (1.0)	0.703 (1.0)
γ	0.105	0.125	0.135	0.186
$\dot{U}^r_{ss}$	0.594	0.593	0.592	0.588
Note : Locations in brackets are across the wall				

the designer at least some idea of the maximum initial and stationary state values and to enable the initial calculation of design rupture data.

A circular cross section rod with a circumferential notch was subjected to uniaxial tension. A total of 100 axisymmetric solid elements were used, and condensed tabulated results for this problem are shown in Table 2. Lastly, a pipe was subjected to an internal pressure. Here 120 plane strain elements were used, and condensed tabulated results are shown in Table 3.

Case Study 1: Notched Rod. A circular-cross-section rod of diameter 20 mm with a circumferential notch of radius 3 mm is subjected to a constant axial nominal stress of 120 MPa at a temperature of 900°C. The bar is made from a conventionally cast nickel alloy MAR-M246. Short term experimental data from Harrison and Tilley [9] were used [10] to obtain the

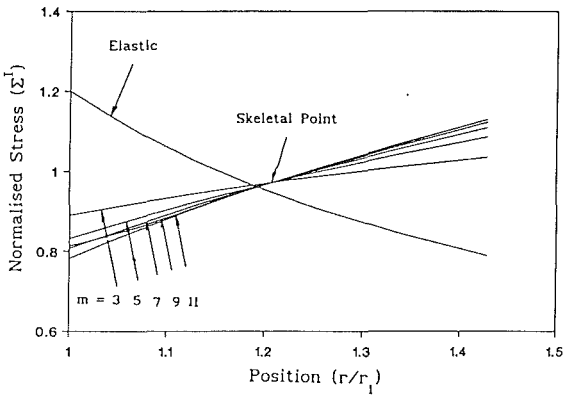

Fig. 8 Variation of normalized principal stress along *r* axis

following material parameters, described in Eqs. (2), (3), and (4):

$$m=8.4;\quad k=p=r=8.5;\quad n=1.076;\quad A=1.5\times10^{-76};$$
$$B=1.72\times10^{-76};\quad E=155\times10^{9}$$

the units being in N/m^2 and hours.

The results from the present method are given in Table 2. From the table we find that the maximum stationary state principal stress Σ^I_{ss}, for a stress exponent m = 8.4, is 1.799. From the material parameters and the given loading, using Eq. (33):

$$\bar{\sigma}=\frac{1}{\alpha}\sigma_{\text{nom}}=169.6\text{ MPa}$$

Using Eq. (8) the constant C is calculated to be C = 8.35 $\times$ 10^{-3}. Then from Eq. (15), and using the maximum stationary state principal stress as the equivalent stress in Eq. (12):

$$\tau_R=\frac{1}{C(1+r)\Sigma^k_\beta}=8.57\times10^{-2}$$

From Eq. (4):

$$t_R=\left[\frac{\tau_R}{AE\bar{\sigma}^{m-1}}\right]^{1/n}=302\text{ h}$$

This result compares with a value of 274 h by Sieburg [10], who performed an analysis that coupled the creep and damage accumulation. The coupled analysis took roughly ten times as long in CPU on a Vax 6230 as the decoupled approach suggested in this paper.

Case Study 2: Pipe Under Internal Pressure. A pipe with inner and outer wall diameters of 70 mm and 100 mm, respectively, operates at 60 MPa and 500°C. The material from which the pipe will be made has already been chosen. Estimates of the rupture time are required. The stationary state radial deformation of the pipe must be predicted and used in conjunction with the failure criteria to monitor the expended life fraction of the pipe so that the pipe will be retired not later than 85 percent of its useful life fraction. Safe inspection intervals to monitor the gross deformation of the pipe must be determined.

The material that will be used is a chromium-molybdenum steel. Long-term experimental data were obtained from Krisch [11] and the material parameters for the steel are listed below:

$$m=4.93;\quad k=p=r=3.27;\quad n=0.65;\quad A=7.83\times10^{-46};$$
$$B=3.40\times10^{-46};\quad E=160\times10^{9}$$

the units being N/m^2 and hours.

The normalized radial deformation characteristics of the pipe are listed in Table 3, while Fig. 8 shows the maximum

Table 4 Rupture times (pipe)

Stress	Distorted Rupture Time	Real Rupture Time (Hours)
Max Princ Stress in Pipe	13.49	34 100
Max Princ Stress at Mean Radius	19.10	58 200
Reference Stress	17.88	52 600

principal stress distribution throughout the pipe. Then using Eqs. (33) and (4):

$$\bar{\sigma} = \frac{1}{\alpha}\,\sigma_{\text{nom}} = 146 \text{ MPa}$$

$$\bar{\epsilon} = \frac{1}{E}\,\bar{\sigma} = 0.913 \times 10^{-3} \text{ mm/mm}$$

and, using Eq. (8):

$$C = \frac{B\bar{\sigma}^{(1+k-m)}}{AE} = 0.0131$$

The maximum stationary principal stress in the pipe is $\Sigma_{ss}^{I} = 1.09$, from Fig. 8, the maximum stationary principal stress at the mean radius (i.e., the skeletal point) is $\Sigma_{ss}^{I} = 0.98$, and the normalized stress corresponding to the reference stress is $\Sigma = 1.00$. These stress measures are used in Eq. (15) to calculate distorted rupture times, whence the real rupture times are calculated using Eq. (4). The rupture times are shown in Table 4, and a rupture time calculated from the reference stress is also shown. It is generally accepted that the maximum principal stress at the mean diameter (i.e., the skeletal point) gives the best estimate of rupture times. In order to be conservative, however, the rupture estimate based on the reference stress will be used.

The stationary deformation behavior of the pipe can be calculated using Eqs. (4), and (32) and the normalized deformation measures in Table 3. In the case of the outer wall radial deformation, the upper bound normalized displacement is, using γ at $m = 5$:

$$U_u = (\gamma + 1)U_e + \dot{U}_{ss}\tau = 0.791 + 0.593\tau$$

Then, using mm as the unit of length, and transforming to real time through Eq. (4):

$$u_u = 0.0361 + 384.4 \times 10^{-6} t^{0.65}$$

Relating real times to distorted times through Eq. (4), a real life fraction of 85 percent at retirement is equivalent to a distorted life fraction measure of 90 percent. From Figs. 3, 4, and 5 the failure criterion factors R_1, R_2, and R_3 are:

$$R_1 \simeq 2; \quad R_2 \simeq 1.9; \quad R_3 \simeq 5.5$$

This means that the pipe must be retired as soon as any of the following criteria have been met:

1 The actual outer wall creep deformation is 2 times the stationary creep deformation at that time.
2 The actual outer wall creep deformation is 1.9 times the stationary creep deformation at 52,600 hours (i.e., the rupture time estimated from the reference stress).
3 The actual outer wall creep deformation rate is 5.5 times the stationary creep deformation rate.

The gross deformation of the pipe must then be monitored at regular intervals, and checked against the failure criteria. The inspection intervals must be short enough that serious overshooting of any criterion is avoided, but long enough for measurable creep accumulation to occur. The remaining life fraction at retirement is to be 85 percent. If we choose, for example, one fifth of the remaining life fraction as a safe inspection interval to prevent late detection, then the corresponding interval, t_{int}, is one fifth of 15 percent of the rupture time from Table 4:

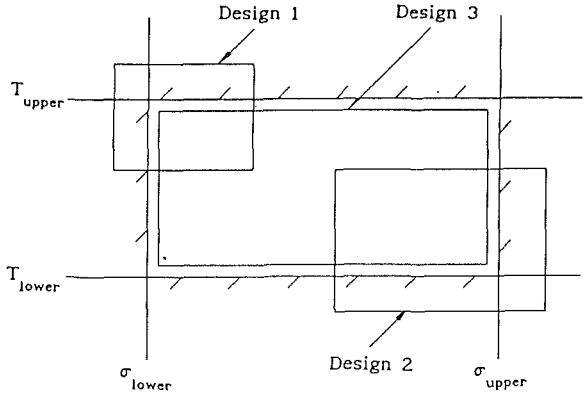

Fig. 9 Illustration of design envelopes

$$t_{\text{int}} = 0.05 t_R \simeq 1600 \text{ h}$$

The stationary state creep accumulation at the outer wall in that time is, using the above expression:

$$\Delta u = 0.047 \text{ mm}$$

This displacement is larger than the initial elastic displacement and will be suitable for measurement. An inspection interval of 1600 h can then be chosen.

Commentary

The case studies in the previous section have illustrated the ease with which the methods described in the paper and the tabulated results can be used by designers. In all cases, the material parameters and the loading were known. More often however in design, the material has to be chosen, the loading will not be known exactly, and it is in cases like this where the methods described here realize their highest potential. As all the nondimensional results are independent of the loading and of the material parameters (except for a weak dependence on the stress exponent m), calculations for different loading cases and different material parameters can be easily and quickly repeated.

The designer can see the effects of the stress exponent m on the stresses and strains from the tabulated results. The influence of other material parameters can be found from their effect on the distorted time measure τ and the normalized damage constant C; different temperatures can be included in the parameters τ and C. The effects of different loadings can be checked by their effect on the reference stress through Eq. (33). In this way, the designer can build up envelopes of safe designs when faced with uncertain temperature and loading extremes. This concept is illustrated in Fig. 9.

The initial outlay of computer time in developing the tabulated results is outweighed by the convenience to the designer. Especially in applications where similar geometries are regularly analyzed (e.g., pipework and other pressure vessels), the method will be extremely economical as the designer can build up catalogues of results.

The method described gives a rational basis for strain and damage accumulation monitoring and in situ inspection. The life fraction measure relationships apply to all geometries and loading cases. The relationships are derived here in their normalized forms, and the life fractions at failure are given in terms of normalized time measures. Similar relationships can be derived in dimensional form.

Conclusions

Achievement of the main aims has been demonstrated in the case studies through which the unifying themes presented have

been successfully applied. The case studies have shown that it is possible to make useful predictions of lifetimes and deformations from tabulated or graphic representations of normalized results. This can be done in ways in which the influences of geometry and materials can be easily and economically assessed. Critical issues such as lifetime extensions can be addressed by the same methods. Further demonstration of the potential of the use of these methods in the early stages of design is described in terms of regional constraints or design envelopes defined in terms of temperature levels and lifetimes.

Although the main techniques of the paper have been known for some time and their credibility continues to grow, there is still an urgent need for hardware testing to verify the ideas. It is noteworthy therefore that the themes of this paper would be powerful tools in the choice of an appropriate program of experimental work to be directed toward that end. Given these and any other verification it is hoped that the generic methods presented will be taken up by other workers who aim toward turning theoretical ideas into catalogues of results that are usable in design. A final accolade to be sought by all would be through successful incorporation in systematic assessment procedures employed in codes of practice.

References

1 Chaboche, J. L., "Continuum Damage Mechanics: Part 1—General Concepts," ASME *Journal of Applied Mechanics*, Vol. 55, 1988, pp. 59–64.

2 Jaske, C. E., "Predicting the Residual Life of Plant Equipment—Why Worry?" ASME *Journal of Pressure Vessel Technology*, Vol. 107, 1985, pp. 213–217.

3 Kachanov, L. M., "On Rupture Times Under Conditions of Creep," *Izvestia Akademii Nauk SSR, Otd. Tekhn. Nauk*, Vol. 8, 1958, pp. 26–31.

4 Rabotnov, Yu. N., *Creep Problems in Structural Members*, North-Holland Co., Amsterdam, 1969.

5 Sim, R. G., "Creep of Structures," Ph.D. Dissertation, Cambridge University, United Kingdom, 1968.

6 Penny, R. K., and Marriott, D. L., *Design for Creep*, McGraw-Hill, London, 1971.

7 Hayhurst, D., "Creep Rupture Under Multi-axial States of Stress," *J. Mech. Phys. Solids*, Vol. 20, No. 6, 1972, pp. 381–390.

8 Hibbitt, Karlsson and Sorensen, Inc., "ABAQUS User Manual Version 4.7," Providence, RI, 1989.

9 Harrison, G. F., and Tilley, G. P., "Static and Cyclic Creep Properties of Three Forms of a Cast Nickel Alloy," Paper No. C222/73, presented at the Int. Conf. on Creep and Fatigue in Elevated Temperature Applications, IMechE/ASME, Philadelphia, PA, 1973.

10 Sieburg, H. O., "Creep Predictions for Turbo-machinery Components," M.Sc. Dissertation, University of Cape Town, South Africa, 1989.

11 Krisch, A., "Creep Behaviour, Structural Changes and Cracks Observed in Creep Tests Lasting Several Years," Paper No. 62, presented at the Joint Int. Conf. on Creep, ASME/ASTM/IMechE, New York/London, 1963.

Analytical and Experimental Simulation of Fan Blade Behavior and Damage Under Bird Impact

H. C. Teichman

R. N. Tadros

Pratt & Whitney Canada Inc.,
Mississauga, Ontario, Canada

An extensive analytical and experimental program has been undertaken to investigate the Foreign Object Damage resistance capabilities of external components for small gas turbofan engines. A transient nonlinear impact analysis has been used to predict the structural response of fan blades under bird ingestion conditions. This analysis is based on finite elements, a three-dimensional bird load model, and an interactive structure-to-bird contact algorithm. Experiments were designed and carried out to record large blade deformations during bird impact, and were used to validate and calibrate the analytical models. The analytical models and testing program are described, and dominant fan blade response and failure modes are presented. Predicted results demonstrate good correlation with tests. Analysis application to fan blade design and other engine components is recommended.

Introduction

Many external aircraft components are susceptible to collision with birds, particularly during the critical takeoff phase. A bird impact on a vulnerable component, such as an engine or windscreen, can result in serious damage to the aircraft and even loss of life. Airworthiness standards require that these critical components be capable of withstanding bird strikes to a certain degree. All gas turbine engines, and particularly turbofan engines (where there is a significant increase in the probability of a bird strike because of the large fan inlet area), are designed to be safe and durable in order to withstand bird ingestion incidences.

Competitive engine markets and evermore increasingly stringent certification requirements place great demands on engineers to improve engine performance and safety. Engine component analytical design tools and criteria must be continuously improved and calibrated in order to meet these aggressive requirements. Currently, the design of impact resistant components is only partly amenable to analytical analysis due to the highly nonlinear and complex behavior of structures under transient impact loading. Thus, final design and acceptance predominantly depend on testing.

Better analytical simulation and improved design tool methodology lead to rapid and improved design optimization and to fewer and more successful engine tests, which reduce both development costs and delays. Some of the most difficult and costly engine tests involve Foreign Object Damage (FOD), such as bird ingestions, and Domestic Object Damage (DOD) such as that sustained from fan blade-off containment.

Pratt and Whitney Canada Inc. (P&WC) has undertaken an extensive analytical and experimental program to investigate the foreign and domestic object damage resistance capabilities of both external and internal components of small gas turbine engines. A transient nonlinear impact analysis computer program, called PW/WHAM (developed by Belytschko et al. [1] and adapted by all Pratt and Whitney Divisions), is used to simulate the engine component structural response to soft and hard body impacts. The use of PW/WHAM to simulate the behavior of small fan blades subjected to bird impact loading is specifically addressed in this paper. A small fan blade is representative of blades used in a turbofan engine in the 2000–7000 lb (9–35 kN) thrust class.

Background

Major factors affecting the structural response of fan blades under a bird strike are bird size (weight), blade size, bird velocity, fan blade rotational speed, fan blade spanwise location of impact, and bird orientation with respect to engine centerline.

The size of birds to be ingested successfully into an engine is set forth by certification authorities. The following is a brief summary of the Federal Aviation Administration (FAA) airworthiness certification requirements for turbofan engines [2].

For small (3 oz or 85 g) and medium (1.5 lb or 680.4 g) size bird ingestion, an engine design is rated acceptable providing it can demonstrate structural integrity and a level of operation after ingestion testing where the aerodynamics are capable of rapid thrust/power recovery to a minimum sustained level of 75 percent power.

For a large bird (4 lb or 1.814 kg) ingestion, an engine is rated acceptable if ingestion tests demonstrate that the engine can be shut down in a controlled and contained manner free of uncontrollable disintegration or fire, and presents no hazard to the aircraft.

The number of small and medium birds that must be ingested

Contributed by the International Gas Turbine Institute and presented at the 35th International Gas Turbine and Aeroengine Congress and Exposition, Brussels, Belgium, June 11–14, 1990. Manuscript received by the International Gas Turbine Institute January 31, 1990. Paper No. 90-GT-126.

by any engine is based on the fan inlet cross-sectional area. Compliance with these FAA standards is always demonstrated by tests.

Since the bird "size" standards are the same for all size engines, small engine fan blades generally are at a significant disadvantage compared to large fan blades based on their relative impact strength. In addition, the small fan blades are much more susceptible to damage from repetitive multiple bird impacts on the same blade as a result of a higher rotational speed than large fan blades. The transient behavior and resultant damage or failure modes differ dramatically for small and large fan blades under the same size bird impact loading. Large fan blades generally sustain "local" airfoil leading edge dents, curl-back, tears, or break-out from small, medium, or large size bird strikes, whereas small fan blades typically experience gross airfoil untwist, gross airfoil bending, or airfoil root fracture from medium or large size bird strikes. In a small engine, typically 10–15 blades may be impacted and/or damaged, whereas 3–5 blades may experience leading edge damage in a large engine from a similar single medium bird impact. Small engines do benefit from some load sharing among more individual fan blades, and from blade-to-blade interaction or contact compared to their larger counterparts. However, this does not overcome the combined advantages that large blades have over small blades.

The impact velocity on stationary (nonrotating) components is simply assumed to be the aircraft velocity since the bird's own velocity is negligible. In the case of a rotating engine fan rotor, the relative velocity between the bird and the local rotating blade section determines the resultant impact velocity and local impact incidence angle. Since the ratio of blade tangential speed to bird or aircraft speed is generally much greater than one over the entire airfoil span, any ingested foreign objects impact on the pressure or concave side of the airfoil. The response or damage experienced by small fan blades will vary dramatically with airfoil spanwise impact location mainly due to the high relative impact velocity gradient from blade root to tip. The relative impact velocity and blade spacing will govern the initial axial thickness of the bird "slice."

Bird orientation with respect to the engine centerline at initial impact will affect the initial size or mass of each bird slice, number of blades impacted, total time duration of bird slice contact with blade surface, and rate of bird mass ingestion with time. An axially oriented bird, whose major axis is parallel to the engine centerline, will generally cause the least amount of damage by spreading the slicing over many blades with a shorter impact time per blade. Although radially or circumferentially oriented birds will come into contact with fewer blades, they load each blade more heavily with a larger slice over a longer loading time period per blade than axially oriented birds.

Projectile behavior as a function of increasing impact speed can be characterized into the following categories: elastic, plastic, hydrodynamic, sonic, or explosive. Soft body impact on fan blades falls in the hydrodynamic regime where velocities are typically around 1200 fps (365 m/s) and less than 1700 fps (520 m/s). A projectile is considered a "soft body" when the internal stresses generated during the impact event substantially exceed the projectile material strength but are far below the target material strength. Peterson and Barber [3] concluded for impact velocities associated with bird strikes on aircraft and turbomachinery that birds behave essentially as a fluid during impact, birds do not bounce and impact load duration is approximately that of the "squash-up" time. This is the time for the bird to travel through its own length.

At the typical bird or ice strike velocities, the material density and not the material strength determines the projectile response. Various "dummy" bird substitutes were tested by Wilbeck and Rand [4]. It was found that gelatin, with the specific gravity of water, produced loading profiles similar to real birds.

Bird impact loading times are typically in the millisecond range. Local structural response is strongly coupled to the overall deformation of the structure. The gross structural response is dominated by the low-frequency components of the modal spectrum. In the case of a small unshrouded fan blade, first torsion and first bending dominate the dynamic structural response under medium or large bird impact loading. Transient strains in the deforming blade can range up to about 30 to 40 percent at strain rates of 1000 to 2000 in./in./sec. An unacceptable degree of blade damage is often characterized by an unacceptable level of plastic deformation, which does not necessarily result in fracture or material loss.

Design Approach

Optimization of structural geometry to improve ingestion damage resistance is generally in direct opposition to optimization for aerodynamic requirements. Thus, design tradeoffs and compromises must be carefully derived to satisfy all concerns, both performance and structural integrity. Low-aspect-ratio fan blades typically increase FOD resistance capability at the cost of increasing engine weight but do not directly compromise aerodynamic design considerations. The overall size and weight of the fan will strongly influence the design of the rest of the engine.

Designing an impact-resistant component necessitates a full understanding of the behavior of complex structures deforming under various impact loading environments. Testing of scaled components or full engines is extremely difficult, time consuming, and expensive. Consequently, the experimental technique alone is undesirable. Analytical computer techniques are needed that can adequately predict the nonlinear, large deflection, elastic-plastic material response and structural failure modes under bird impact loading interaction.

P&WC fan blades have very successfully demonstrated adequate and acceptable foreign and domestic object damage resistance capabilities. These capabilities are defined in the engine specifications. The design philosophy adopted ensures that fan blades do not suffer gross airfoil/blade fracture during a large bird strike, and will suffer only limited and controlled deformation without cracking, during small or medium bird ingestions in order to satisfy the minimum sustained thrust recovery requirement with much confidence.

Since the mid-1970s, the need to improve bird strike resistance capabilities, along with aerodynamic performance, has led to the design of low-aspect-ratio unshrouded fan blades. A low-aspect-ratio configuration has fewer blades per stage but of larger chord. Although midspan shrouds or snubbers provide the high-aspect-ratio blades with necessary FOD impact strength and vibratory margins, particularly on large engines through blade load sharing or coupling, the midspan shrouds provide only limited load sharing capability in small engines. Small engine fan blade midspan shrouds generally experience loss of bearing surface contact or "shingling" under medium and large bird or ice impact strikes. In unshrouded and low-aspect-ratio fan blades the large chord improves the impact strength dramatically. The P&WC JT15D-5 fan blade was one of the very first shroudless fan blades to enter production and has demonstrated excellent FOD resistance capabilities [5].

Engine durability requirements relative to ingestions are given important consideration from the very earliest stages of engine design. Empirical techniques based on test experience and analytical computer simulation are used to optimize and access the impact resistance of components in the design phase. Experimental rig and engine tests provide confirmation and failure mode data for validation of analyses.

During preliminary fan blade design, the soft body loading model involves simple impact force calculations based on the change in average momentum, which is applied to a static

cantilevered airfoil beam [3]. This empirical approach allows for a very rapid assessment of both gross airfoil spanwise bending and local chordwise leading edge strength. It should be noted that the impact force is not interactive with this deflecting beam analysis.

In the late 1970s, P&WC developed a Linear Dynamic Impact Analysis (LDIA) as an intermediate design tool based on work by Cornell [6] and Fulton [7]. Finite Element "shell" elements are used to model the airfoil. The Modal Superposition technique [8] is used to compute the transient structural response under an interactive bird "fluid" loading model The projectile loads are treated as a series of parallel, incompressible fluid jets, which impinge, turn, and flow along the compliant airfoil surface. The LDIA analysis simulates the maximum bird slice impact on a single, centrifugally stiffened fan blade. The bird model continuously interacts with the deflecting blade, thereby increasing the bird slice impact loading. Despite being limited to small target deflections, the computer code prediction of gross airfoil response in torsion and bending compare reasonably well with tests for medium bird impact. The LDIA has proven to be a very useful design tool, providing rapid results for parametric studies of airfoil geometry and bird impact parameters, and relative comparison of gross FOD strength for different fan blades.

A number of nonlinear finite element codes such as MAGNA [9], MARC [10], NONSAP-M [11], DYNA3-D [12], and PW/WHAM [13] have been adapted and linked to various bird load models. All codes are capable of predicting the nonlinear transient structural response to various levels based mainly on the degree of sophistication of the bird loading model. The MARC, MAGNA, and NONSAP-M codes make use of a simple empirical fluid jet impact model similar to that implemented in P&WC's LDIA described earlier. Niering [12] modeled the bird shape with DYNA3-D finite elements and various homogeneous material laws representative of fluid "stagnation" pressures. Belytschko et al. [14, 15] developed a transient structural analysis called WHAM, which included material and geometric nonlinearities. Pratt and Whitney selected the "WHAM" analysis based upon the solution procedure and adaptability to nonlinear impact problems, and initial procurement cost. Brown and Krahala [16] developed the first contact and impact force loading routines for hard body impact analysis together with nonlinear-to-linear boundary interface capability for large problems. Martin [13] developed a sophisticated three-dimensional finite element "fluid" impact load model, which makes PW/WHAM a unique and powerful program capable of predicting fan blade response to a bird strike.

PW/WHAM Capabilities

The development and tailoring of PW/WHAM for the design of engine components subjected to soft and hard body foreign or domestic object damage is a cooperative effort by all three Pratt and Whitney Divisions of United Technologies Corporation. Although development of the general multipurpose impact code is being pursued jointly, each division has rather unique applications based on engine size effects (large versus small engines) and mission (commercial, business, military) requirements.

PW/WHAM is an efficient Finite Element (FE) code, which employs an explicit central difference time integration scheme with lumped mass approximation. Geometric nonlinearity is introduced through a pseudo-Lagrangian coordinate approach by using a "convected" coordinate system attached to each element. The element coordinate system can undergo large translations and rotations, but it cannot deform. While large displacements are included in the element membrane plane, large displacements are not included in the out-of-plane bending effects, leading to the assumption of small curvatures and small strains. Local internal element nodal forces are computed directly from element stress at each time step, transformed to the global system and summed.

PW/WHAM currently employs a flat, uniform thickness, triangular plate element. This three-noded element has three in-plane integration points (constant strain) for each of the five through-the-thickness surfaces. A tapered thickness quadrilateral element and three-dimensional brick element will be available in the near future. Material nonlinearity is modeled with various elastic-plastic piecewise linear stress-strain curves which follow the isentropic harding law. The element failure model is initiated when the specified value for Von Mises stress is exceeded. Currently, only layer-by-layer element failure can be considered.

The impact forces are computed from the momentum transferred between moving structures while satisfying system momentum conservation or balance. Force equilibrium is maintained by applying equal and opposite impact forces normal to the contact surface between target and projectile. The contact procedure handles both bird-to-structure and structure-to-structure contact.

The contact algorithms do not correct for or reposition any penetrated node on the surface of the contacted element. Although a spring stiffness is available to limit the node penetrated, it has received limited use and mixed reviews. The artificial correction or repositioning of a penetrated node introduces additional external fictitious forces, which are not physically present in the original system equations of motion or a part of the momentum balance. Thus the impact force computation from the momentum transferred between moving structures alone is deemed to be completely adequate. Experience indicates the penetration is best controlled with time step size.

To simulate a soft body impact on a structure, the impacting projectile must undergo large deflection and segmentation (i.e., splash or cut-up) while interacting with the deforming structure. Martin's fluid finite element technique provides accurate macrofluid response and simple projectile geometry modeling. Prediction of the initial shock (Hugoniot pressure peak) or microfluid response is not required for such problems as bird strike on aircraft components. Validation of the three-dimensional FE fluid model with test data [17] yielded excellent agreement.

The three-dimensional projectile body is subdivided into spherical finite fluid elements or "segments." Each fluid segment reacts to external structural loads through a constitutive fluid material law and interacts with other neighboring segments based upon the current connectivity. Segment contraction or expansion under contact governs the segment's internal pressure. The segment's impact force on neighboring segments or structural elements is a function of its internal pressure and contact area. Projectile cohesiveness or intrasegment tensile strength is usually neglected in the model. The inviscid fluid assumption limits the segment to three translational degrees of freedom. The fluid element load model also uses the explicit integration technique, which simplifies the coupling link between the fluid and structure models.

PW/WHAM currently runs on the Micro VAX 2, IBM 3090 (with or without vector box option) and CRAY XMP28 computers. The code is nearly fully vectorized for the IBM and CRAY computers and runs in virtual memory. PW/WHAM is under constant development.

Analytical Modeling

Ingestion Idealization. Ingestion of a bird by a fan rotor stage can be simply thought of as a series of blades performing a "slicing" action and turning action of the incoming projectile. Figure 1 illustrates a projectile approaching a blade row at the resultant relative velocity. The blade spanwise chord

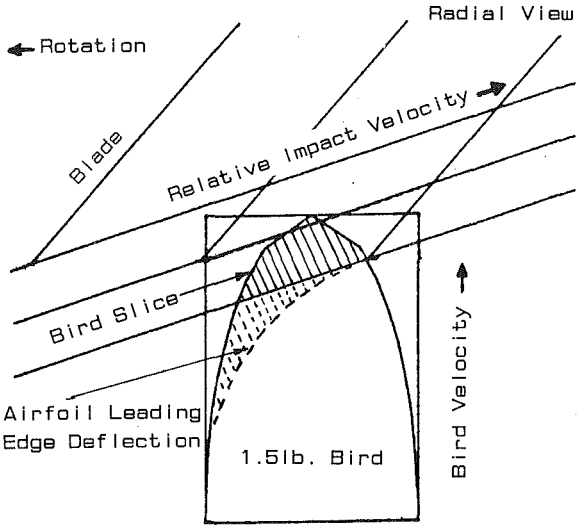

Fig. 1 Fan blade slicing of incoming bird

section corresponds to the location of the center of bird impact. During the simulation of bird impact, the blade FE model rotates circumferentially about the engine centerline while the bird FE model translates (axially) parallel to the engine centerline. The leading portion of the bird is "presliced" and removed due to the expected slicing action of the preceding nondeforming airfoil.

Current design analyses idealize and model impact on only a single blade or airfoil given the single largest slice that could possibly be cut from a bird, although multiblade impact analysis is possible. Experimental ingestion testing on small fan rotors has generally shown that one fan blade takes the brunt of the load and experiences the largest gross blade deformation, thus supporting the largest bird slice or "bite" size simplification.

Blade Model. The constant strain triangular plate FE is well suited to model the highly complex geometries of the compressor blade or airfoil provided the mesh is sufficiently fine. Figure 2 shows the airfoil finite element model used typically for small fan blades. An in-house preprocessor automatically interpolates and generates the FE model, given an aerodynamic data base and specific spanwise and chordwise element breakup commands. A finer mesh is required in the airfoil root region because of the high stress gradient that are expected due to gross airfoil response. This airfoil model contained 192 three noded elements, with a total of 117 nodes. An average element thickness is assigned to each pair of neighboring triangular elements, which form a quadralateral shape. All elements assume the same inelastic material behavior for simplicity. For Ti 6-4 material, a stress-strain curve corresponding to a strain rate of 1500 in./in./sec. is implemented.

The blade model rotation during impact is simulated by rigidly constraining the root to rotate at a specified constant speed while all other nodes are given the corresponding initial steady-state centrifugal displacement and velocity. The prescribed initial displacement vector and initial blade velocity ensure blade centrifugal stiffening and equilibrium from time zero. This approach avoids initial blade model transients under starting rotation and prior to bird impact. The initial steady-state blade displacements are computed incrementally under a centrifugal load in a separate finite element code and then input to PW/WHAM.

Viscous damping may be applied to the structural FE's impact deflection sometime after the projectile impact is completed in order to obtain a final deformed shape rapidly at minimal computer CPU time. The rigid body rotational velocity component of the blade is filtered out before viscous

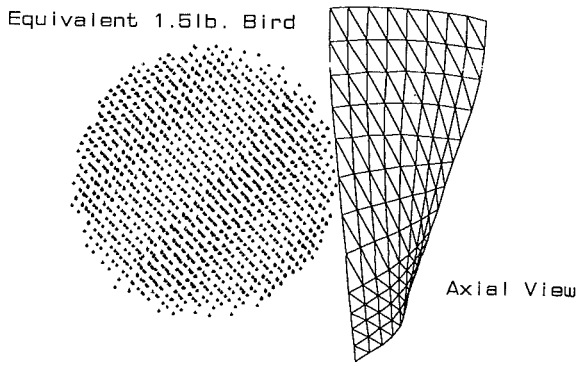

Fig. 2 Finite element model of blade and bird

damping is applied to the deflection response. This option has received limited application in small fan blade FOD analysis and has only been activated following the restoration of gross bending response.

Bird Model. The real bird is idealized as an ellipsoidal spheroid with a length-to-diameter ratio of 2.5. The density is assumed to be uniform throughout the bird with a specific gravity of 0.9 (i.e., 90 percent density of water). Experimental results show that "dummy" gelatin birds of this configuration produced very similar impact results on fan blades when compared to real birds.

The PW/WHAM code generates the entire bird model internally, given variables defining overall bird dimensions, density, segment size, velocity, and reference position in space. The three-dimensional bird projectile model is built up of small spherical fluid finite segments arranged in the closest packed construction. Each segment has the same initial radius and density, and is generally in contact with its 12 nearest neighbors except along the surface of the bird model. The segments are pictorially represented as a point at the segment's center of mass in Fig. 2.

The program preslices or cuts away any leading or trailing bird regions prior to the start of an impact simulation. The bird model axial length is reduced to include only the impact slice and sufficient additional bird length to avoid end effects, in order to reduce computer time. Adequate axial bird length must allow for an increasing slice thickness at increasing impact angles as the deflecting airfoil "climbs" axially deeper into the bird during impact. An interactive preprocessor is used to plot the bird and blade chord cross sections in order to define the bird preslice parameters (Fig. 1).

The mass of the segments is adjusted upward to account for the spatial voids between each spherical segment while preserving total bird mass and momentum transfer. Three-dimensional discretization of the bird into sufficiently small segments with adequate contact or momentum transfer capability typically requires between one and three thousand fluid segments. Consequently, the bird loading model is extremely CPU intensive in comparison to the structural model.

Contact Algorithm. At each time step, search routines automatically determine where contact exists between segments, and between segments and the structural target. Even though symmetry and vectorization techniques have been implemented, the search or contact routines require substantial CPU time. However, significant CPU investment can be saved with careful modeling. A restart option has also been used to reduce costs, but has limited capability of changing control parameters in subsequent restart runs.

Numerical Stability. An appropriately small time step size must be determined to maintain numerical stability in both the structural element and fluid segment models during the explicit temporal integration solution. The element size, density, and

stiffness affect the integration stability limits. Stability is generally maintained if:

$$\Delta t \leq 0.5 \frac{l_o}{c_1} \text{ (element)} \quad \Delta t \leq 0.4 \frac{R_o}{c_2} \text{ (segment)}$$

l_o = smallest initial element length
R_o = smallest initial fluid segment radius
c_1, c_2 = elastic wave speed in the material (function of density and element elastic modulus or fluid bulk modulus)

These time step requirements are necessary but are not always sufficient to guarantee conditional numerical stability because of the application's dependancy on the degree of nonlinearities. Experience has shown that in the analyses of small blades where high rotational (rpm) speed and high impact energy loading exist and result in significantly large deflections, a much smaller time step size is required to satisfy stability. In applications where large nodal rotations are inherent, the small angle per time step assumption in PW/WHAM may be violated and numerical inaccuracies build, eventually leading to instability before the simulation period ends. The selection of an adequate time step size is largely based on both experience and/or trial and error.

Since the bird model as a whole is less stiff due to the lack of fixed segment connectivity than the fixed connectivity blade, the blade time step size requirement will usually satisfy bird stability. However, individual segments during compression become much stiffer and consequently more susceptible to instability than blade elements, which become softer due to plasticity, and more stable. The PW/WHAM code currently uses the same time step size for both the structure and bird models in order to simplify bird-to-blade interaction.

Other local instabilities such as those occasionally observed at the extreme airfoil leading or trailing edge tip elements (generally very thin elements), are believed to be actual high-frequency effects, which may or may not lead to total analysis numerical instability.

Simulation Duration. The time required to simulate the local airfoil leading edge response to bird impact is generally equal to at least the bird's squash-up time. The formation of a large leading edge dent occurs as the blade cuts through the bird in a time usually of the order of 400 μs. This response is most common in large fan blades or when the bird size is small in proportion to blade size. In the case of small fan blades, the prediction of gross airfoil response about the airfoil root to medium or large bird impact requires the consideration of the blade fundamental modes/frequencies. The time required to allow the impact load to traverse the airfoil span and result in peak root response is usually of the order of the first mode period or 4000 μs.

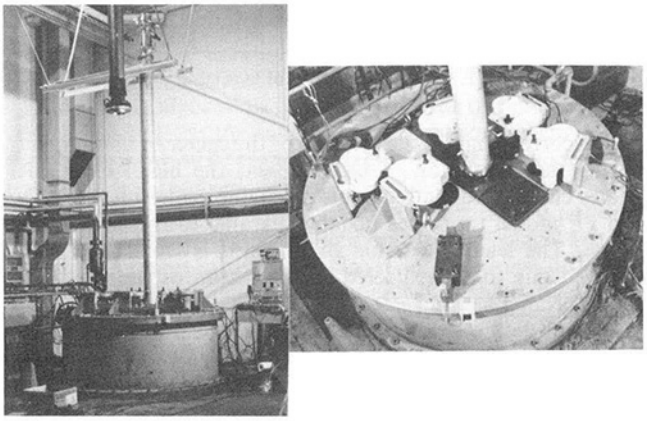

Fig. 3 Impact test "spin" rig with cannon and high-speed cameras

Table 1 Test and analysis comparison

Test Conditions	Static Shrouded Fan	Rotating Shrouded Fan	Rotating Shroudless Fan	Shroudless Fan Rotor
blade aspect ratio	2.6	2.6	1.7	1.7
blade speed (rpm)	0	8000	15,800	15,500
bird speed (in/sec)	3248	40	41	2832
bird density (lb/in3)	.024	.024	.024	.0325
bird shape	spherical	right cylinder	right cylinder	ellipsoid sphere
number of blades	1	1	1	25
bird diameter (in)	4.8	4.8	4.8	3.3
avg initial slice thickness (in)	.5	.2	.2	.44
impact centered (% of airfoil span)	50	60	60	60
resultant impact velocity (in/sec)	3248	6370	13,400	13,450
initial impact angle (degrees)	37.0	38.6	36.8	25.0
Analysis Parameters				
# node	144	144	117	351*
# element	238	238	192	576*
# bird segments	2997	2484	1883	1709
LE ref.mass location (%span)	50	60	60	60
time step (microsec)	.5	.20	.25	.25
"mass" ratio	.86	.5	.5	.5
simulation time (msec)	7.5	5.0	2.5	2.5
blade-to-blade friction	--	--	--	.2
Predicted slice mass ingested (lb)	.342	.371	.176	.522
Resultant Momentum (lb-sec)	1.45	2.15	3.57	4.94

* 3 blades

The CRAY or IBM vector-box computers lend themselves particularly well to the simulation of the long-term gross blade response.

Experimental Testing

Experimental data from real impact tests are required for verification and validation of analytical models, determination of structural failure modes, and calibration of design criteria. Tests also provide a direct comparison of the impact resistance strength of different blade materials and configurations. To that end, test programs to simulate soft and hard body impact on research and development fan blades have been conducted in various in-house facilities.

Existing FOD test facilities include rigs for impact testing on static or nonrotating single fan blades and impact on rotating single blades or fully bladed rotors. Full engine ingestion testing is mainly used to demonstrate compliance with engine certification requirements.

Static Blade Impact Testing. Impact tests on single nonrotating fan blades have successfully simulated the slicing mechanism and provided good assessment of relative blade strength. The tests proved to be simple, quick, and inexpensive to set up and conduct. Impact conditions were easy to control and good qualitative and quantitative data were provided for preliminary correlation with analyses.

Spherical gelatin "dummy" birds with phenolic microballoons were fired at fixed blades from a pressurized cannon. A wedge was positioned just in front of the blade to act as a leading dummy blade to preslice the incoming bird. Impact was targeted at the pressure side leading edge at an appropriate incidence angle. The bird and blade response were recorded on high-speed film. Airfoil tip deflections were measured from the films. Airfoil root suction surface strain gage responses were also recorded. Tests were conducted at low bird impact energy levels in order to avoid gross airfoil fracture. These impact tests excited only the gross bending response of the fan blades.

Spin Rig Impact Testing. In order to simulate possible engine fan rotor conditions best for bird impact, a dedicated "spin" or "whirligig" rig was developed for both FOD, DOD, and blade-off containment testing based on years of testing evolution. The photographs in Fig. 3 present the spin rig impact facility. Soft body impact on both single rotating fan blades and full rotor have been simulated. In the single blade tests, a specially designed "drop-pull back" mechanism introduced a dummy bird into the plane of the rotating fan blade and then pulled it back in order to simulate a single slice impact. Any secondary or repeated impacts on the fan blade were minor in nature. A compressed air cannon was used to fire a dummy bird at the fully bladed fan rotors. Five high-speed cameras recorded the impact events. The tests were conducted without a fan case in order to photograph the fan blade impact end on.

The very large gross torsion and bending deflections observed in some single fan blade impact tests were limited in degree by the blade-to-blade interaction in the fully bladed rotor impact tests. The single blade impact tests provided greater control over the bird targeting and more unobstructed views of the bird-to-blade interaction response than could be obtained in the fully bladed rotor tests.

Engine Ingestion Testing. Ingestion tests have demonstrated engine structure integrity and sustained engine power/thrust requirements. Limited damage to both the fan and compressor core was tolerated provided that overall engine power requirements were sustained. Real birds were fired into engines representing the most realistic conditions and targeted at the most vulnerable locations. Test conditions have satisfied impact at the critical fan location and provided for maximum bird debris ingestion into the engine core. High-speed cameras recorded the impact events. The irregular shape of real birds in flight tended to obscure the impact interaction to a greater degree than did the ellipsoid gelatin birds. At times, it was difficult to determine the blade spanwise location of bird impact, number of blades impacted, and leading edge or gross

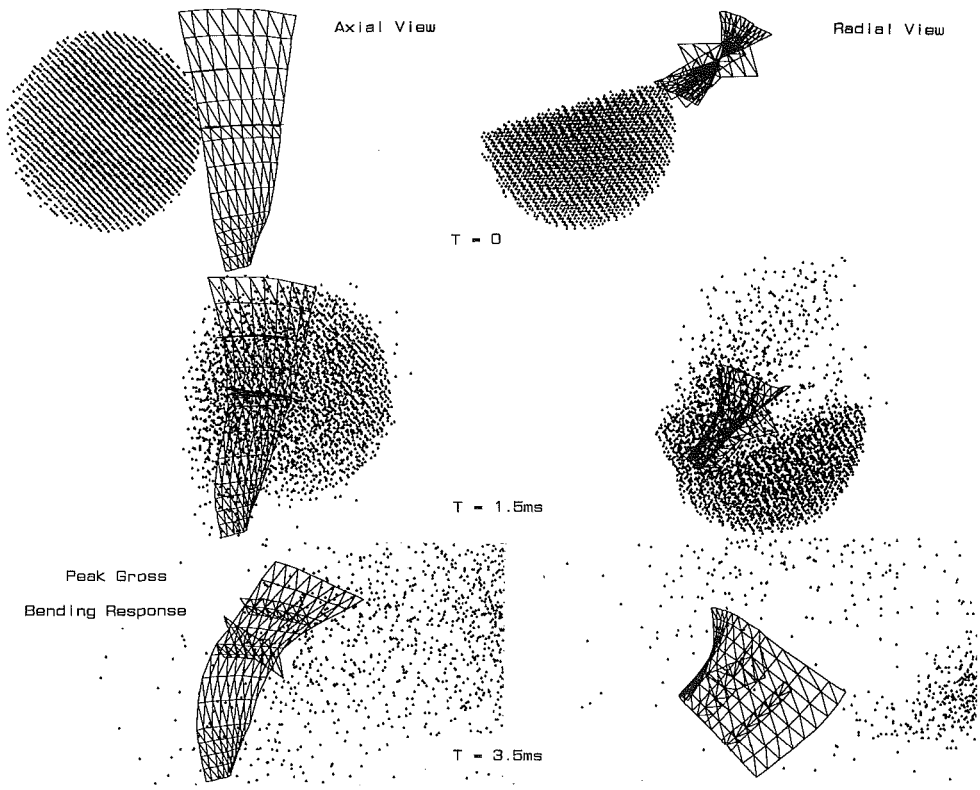

Fig. 4 PW/WHAM simulation of nonrotating blade response and bird behavior/interaction

blade tip response from the high speed films. Consequently, rig impact testing is preferred for research testing.

Correlation With Test

Four different PW/WHAM simulations of bird impact on small titanium fan blades were performed to demonstrate the code's capabilities. These predictions were compared to research test data for validation. Each test represented an increased degree of complexity. Soft body impacts representative of varying density "dummy" birds (gelatin with varying volumes of phenolic-microballoons) on both high-aspect-ratio shrouded and low-aspect-ratio shroudless fan blades were tested at increasing impact energy levels. Table 1 summarizes the blade and bird initial impact configurations along with analysis modeling parameters.

Static Shrouded Fan Blade Impact. A 4.8 in. (12 cm) diameter gelatin sphere with a specific gravity of 0.69 was fired at a velocity of 270 fps (82 m/s) at the blade midspan location. The upper frame in Fig. 4 shows the initial analysis configu-

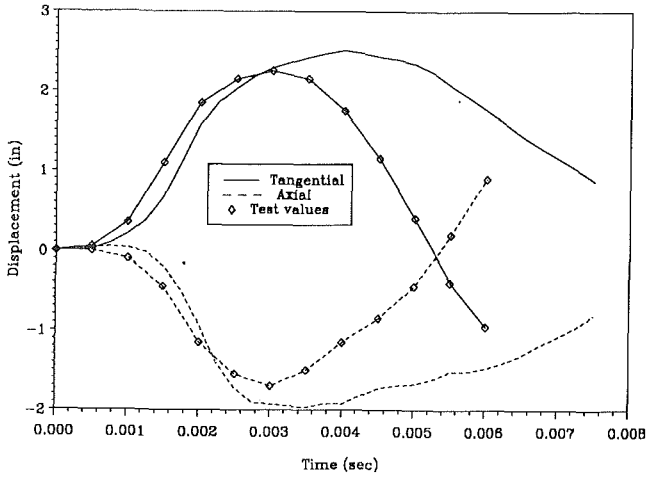

Fig. 5 Comparison of predicted and measured blade tip deflection, "static" shrouded fan blade impact

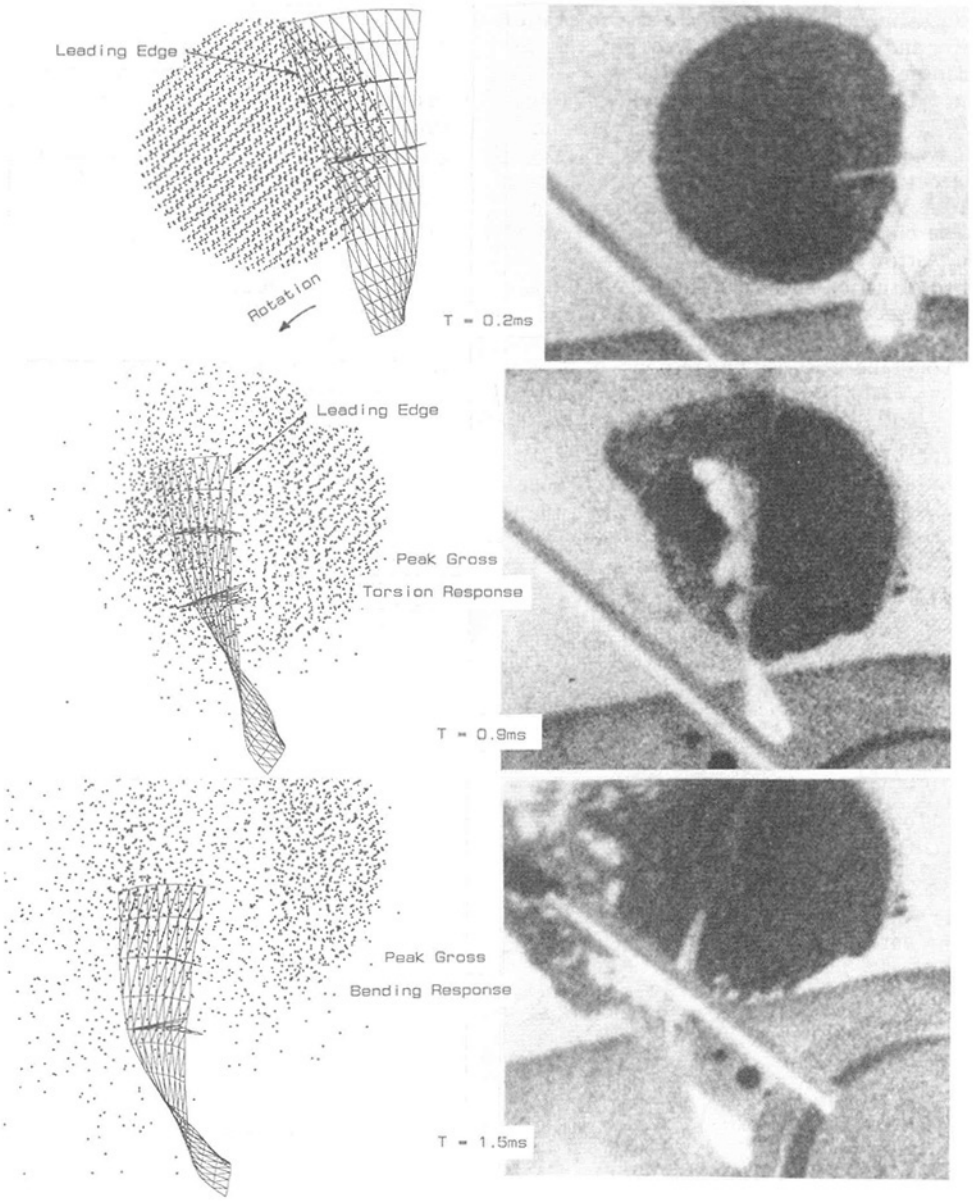

Fig. 6 Comparison of analysis with test high-speed photography, "rotating" shrouded fan blade impacted by gelatin bird

ration of the static shrouded fan blade and moving bird models. The leading portion of the bird was cut away to simulate a large slice impact on the compliant fan blade. A sequence of computer-generated graphics predicting blade deformation and bird behavior is presented in Fig. 4. It should be noted that the postprocessor connects the deformed airfoil nodes with straight lines. The analysis shows the increasing blade deformation with the growth of the bird slice thickness as the blade slices through the bird. Although a small degree of airfoil untwist occurred, only the gross bending response of the nonrotating blade was significantly excited in the analysis simulation and test. The gross bending response was primarily excited because of the lack of centrifugal stiffening, bird loading time corresponded to about a half-cycle of the first bending mode, and midspan shroud provided significant torsional stiffness. The time-history plots in Fig. 5 show that the predicted blade tip deflections correlate well with test data. The analysis deflections show a slightly longer period than test since material damping was not considered.

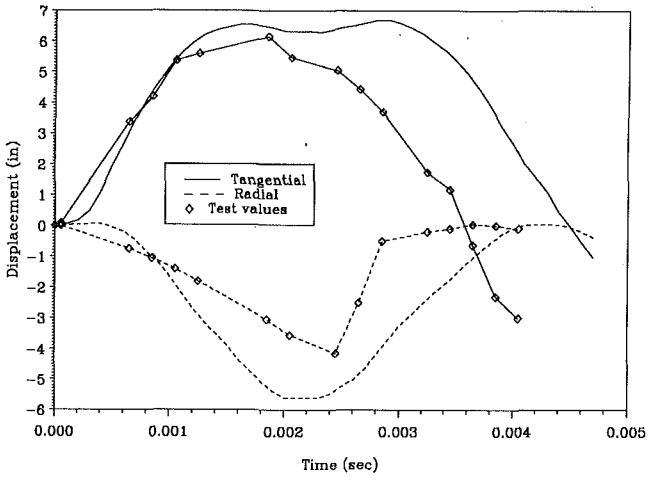

Fig. 7 Comparison of predicted and measured blade tip leading edge deflection, "rotating" shrouded fan blade test

Rotating Shrouded Fan Blade Impact. A single shrouded fan blade rotating at 8000 rpm simulated a high-energy impact condition as it sliced a gelatin right circular cylinder, 4.8 in. (12 cm) in diameter and 2 in. (5 cm) in height. Very large transient deflections occurred in the test without material failure. Figure 6 compares the predicted airfoil peak gross torsion and bending deflected geometries with high-speed photography. The agreement between analysis and test is very good. Even the bird response or "splash" is well modeled. The upper

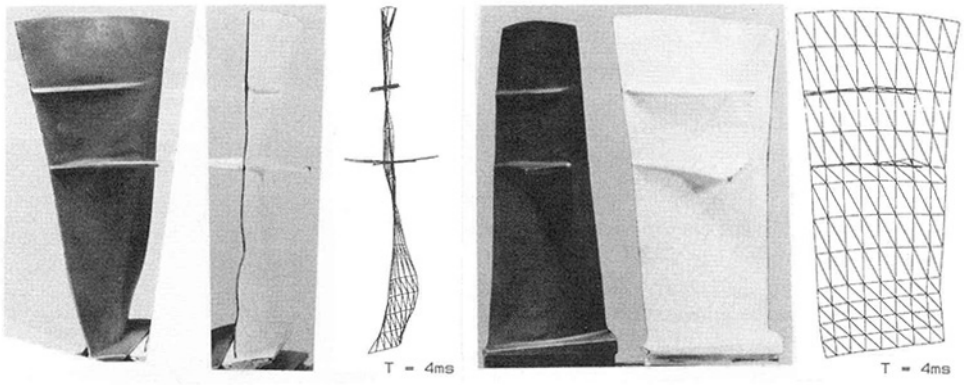

Fig. 8 Comparison of posttest blade deformation (middle blade) with analysis predicted deformation and undeformed blade

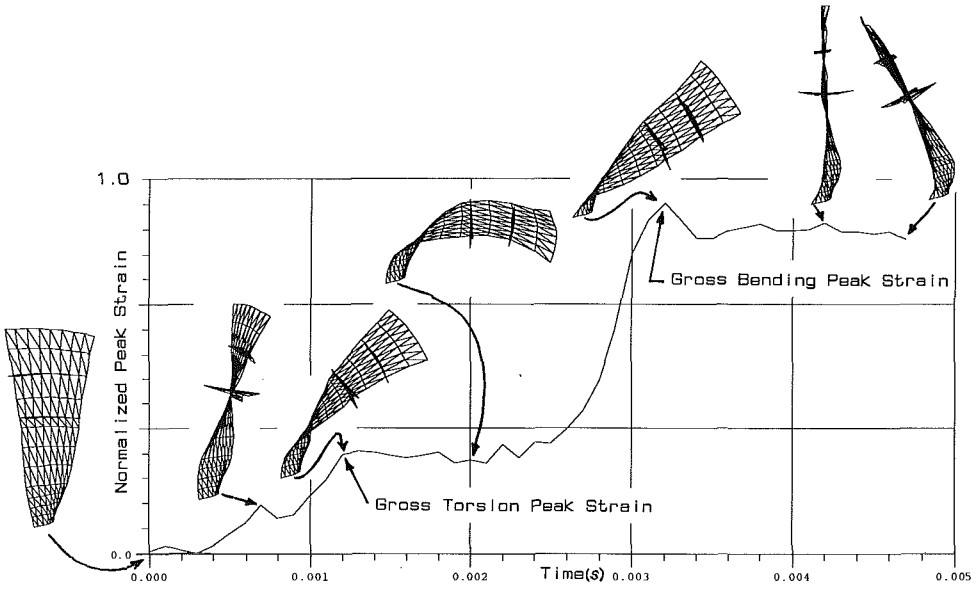

Fig. 9 Peak root leading edge region strain behavior with corresponding deflected geometry

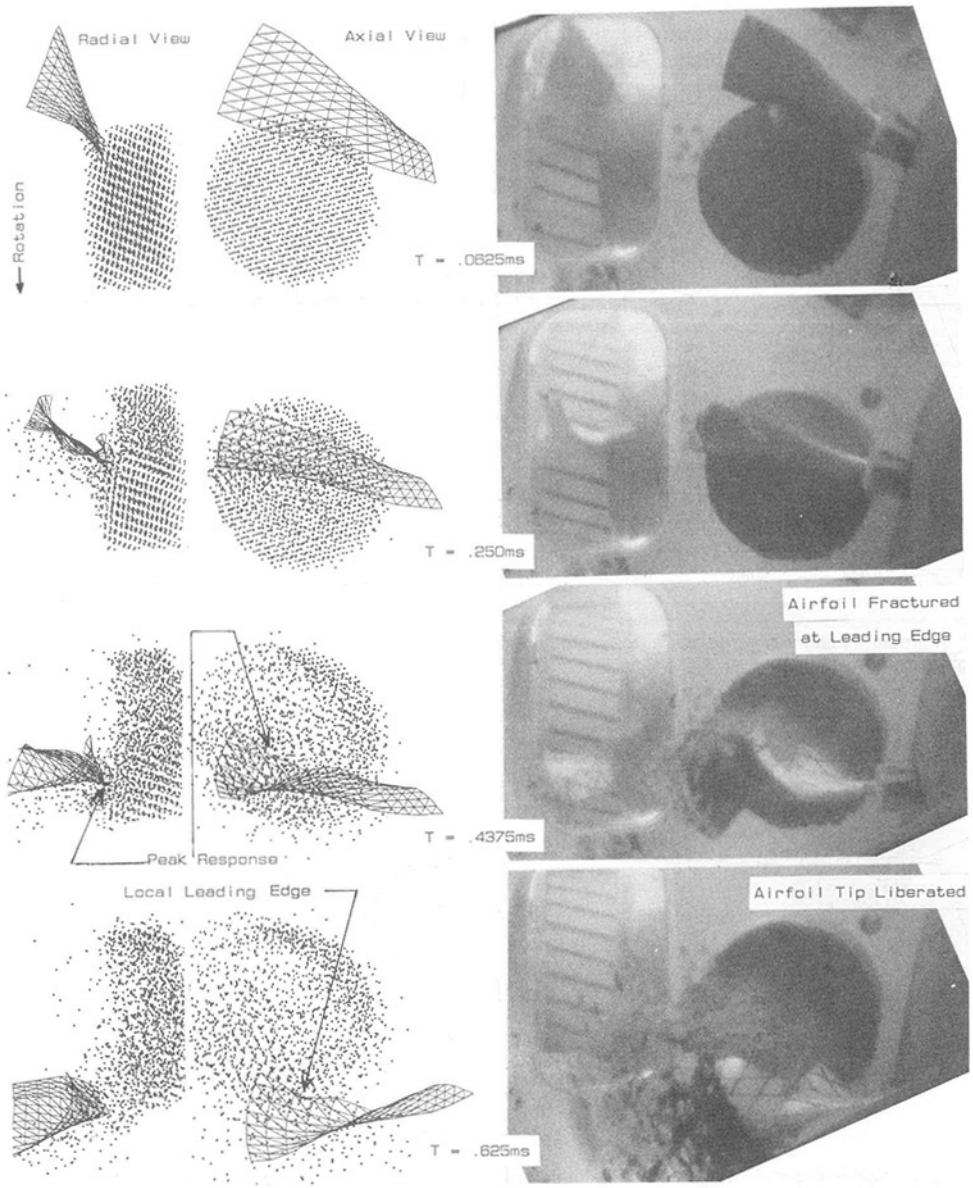

Fig. 10 Comparison of analysis with test high-speed photography, "rotating" shroudless fan blade impacted by gelatin bird

airfoil chordwise sections untwisted more than 90 deg to the extent that the leading edge trailed the true trailing edge (middle frame in Fig. 6) in the direction of blade rotation. While untwisted, the airfoil then experienced spanwise bending of nearly 90 deg (lower frame in Fig. 6). The comparison of predicted leading edge tip deflection time-histories with test is also shown in Fig. 7.

A posttest photo of the permanently deformed blade is compared to the analysis in Fig. 8. In both the analysis and test, the centrifugal force environment restored the gross bending response but had only little effect on the torsional untwist.

PW/WHAM predicted the peak strain response to occur at the airfoil leading edge root region at the time gross bending deflection is nearly fully restored. This time corresponds to approximately one period of the first bending mode. Figure 9 presents the typical strain time history behavior along with the corresponding superimposed airfoil peak deflected geometries. Two distinctive strain plateaus are generally observed. The first strain plateau corresponds to peak torsional response. The second following and highest strain plateau corresponds to peak bending behavior. The peak root strain response occurred some time after gross bending deformation because the energy imparted to the local impact zone must traverse the blade span before its full influence could be felt at the blade root. The analysis predicted the leading edge deflection "wave" response to propogate down the airfoil span during the restoration of the gross bending deflection.

The PW/WHAM analysis predicted no failure, which is consistent with test. The analysis also predicted the initial bird slice thickness of 0.2 in. (0.5 cm) to grow to about 1 in. (2.5 cm) as the deflecting airfoil climbed into the bird during slicing.

Rotating Shroudless Fan Blade Impact. An aerodynamically and structurally improved, shroudless, low-aspect-ratio (1.7) research fan blade was tested to compare its impact resistance to the high-aspect-ratio (2.6) shrouded fan blade. Due to the blade's vastly improved FOD design, the blade was impact tested at a much higher rotational speed in order to establish the uppermost bound of fracture free response. The shroudless fan blade was designed to be significantly stiffer than the shrouded fan blade, particularly below 50 percent span.

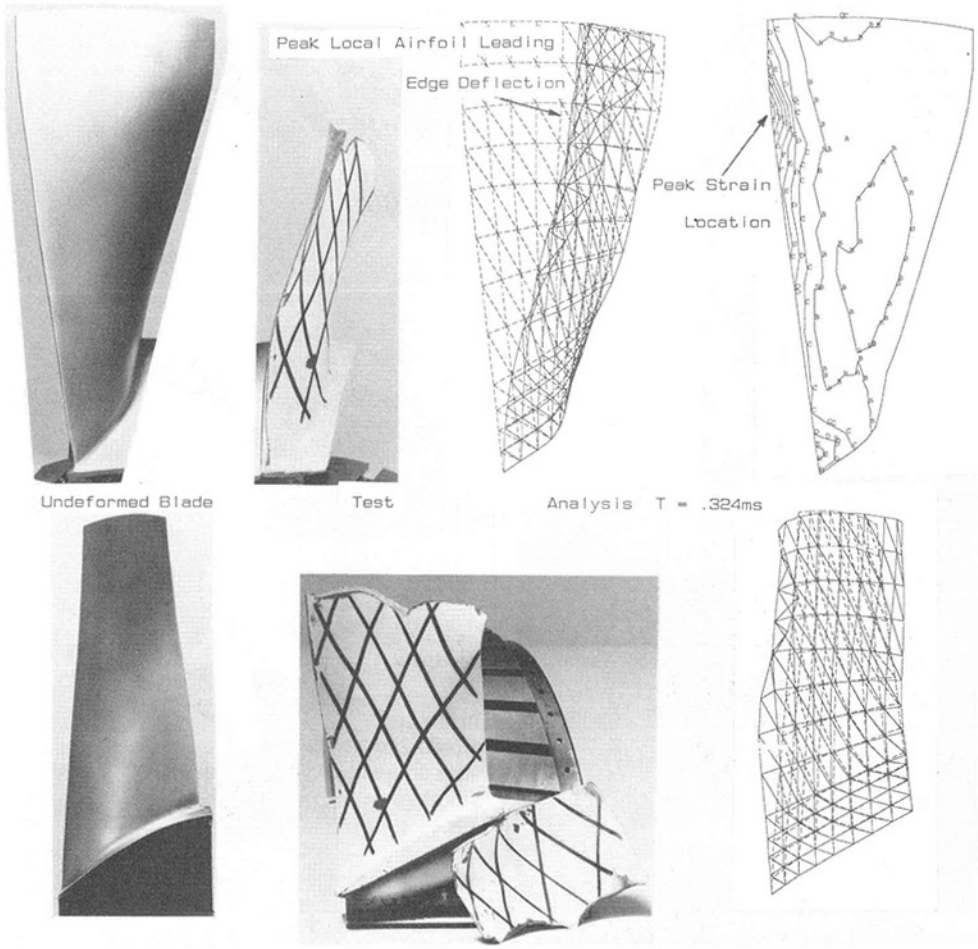

Fig. 11 Comparison of posttest blade with peak predicted deformation and dynamic strain

A single shroudless fan blade rotating at 15,800 rpm impacted a gelatin right circular cylinder of similar dimensions to that used in the shrouded blade test. The local dummy bird orientation angles and position at impact differed somewhat between the tests due to experimental test equipment variability. The impact location was biased toward the upper 50 percent airfoil span region and resulted in the subsequent fracture and liberation of the upper third of the airfoil.

Figure 10 compares the deflected geometry "movie" generated by the PW/WHAM analysis with high-speed film. Both the axial view (along the engine centerline) and the radial view (looking in on the tip by the means of a mirror) show the dummy bird being cut by the airfoil leading edge. The leading edge climbed into the bird and curled back, ingesting more bird slice mass at increased impact angles (frame 2 in Fig. 10). Both analysis and test showed that the initial upper airfoil tip section torsional untwist deformation was immediately compounded by following spanwise bending. Although no active element failure criteria were implemented in PW/WHAM, the analysis deflected geometries compare well with test to the point of airfoil fracture (Frame 3 in Fig. 10).

Furthermore, the predicted maximum dynamic strain and its location indicated the expected onset of cracking and possible material loss to occur in approximately the same location as experienced in the test. The analysis deflected shape plots also indicate the presence of a small local leading edge instability at the same location. The peak dynamic strain contour plot and deflected geometry plot at time 0.324 ms are compared to the fractured blade in Fig. 11. The actual airfoil leading edge fractured before the time of 0.43 ms. The fracture growth and tip section liberation were captured on high-speed film in the lower two frames of Fig. 10. Further, analysis mesh refinement of the leading edge tip region would result in a more localized deflection and drive the peak strain well above the crack prediction parameter (ratio of maximum strain to failure strain for the leading edge). The analysis prediction of critical location and time are consistent with tests demonstrating the code's capabilities of predicting the onset of failure.

Shroudless Fan Rotor Impact. The transient airfoil response observed in the single rotating blade impact cases essentially simulated the worst bird slice impact situation and provided an excellent comparison of individual blade strength to FOD. In addition, the very large transient airfoil deflection behavior demonstrated the tremendous degree of deflection that may be tolerated without material fracture or loss at high strain rate loading conditions. However, realistically in a fully bladed rotor, the large transient response of a fan blade would be limited to a degree by blade-to-blade interaction and multi-blade-to-bird load sharing. These effects are particularly significant in bird strikes on small fan rotors.

A research engine ingestion test was conducted where a real 1.5 lb (680 g) bird was fired at 236 fps (72 m/s) and impacted a shroudless fan rotor at 60 percent blade span with rotor speed at 15,500 rpm. The bird struck about 15 fan blades and imparted various levels of damage. The damage ranged from little-to-no visible deformation, to five blades with small degrees of local airfoil untwist or leading edge curl-back deformation, to only one blade, which was severely and permanently untwisted over its entire span. The engine continued to produce acceptable thrust following ingestion.

To correlate PW/WHAM anaylsis with the most severely

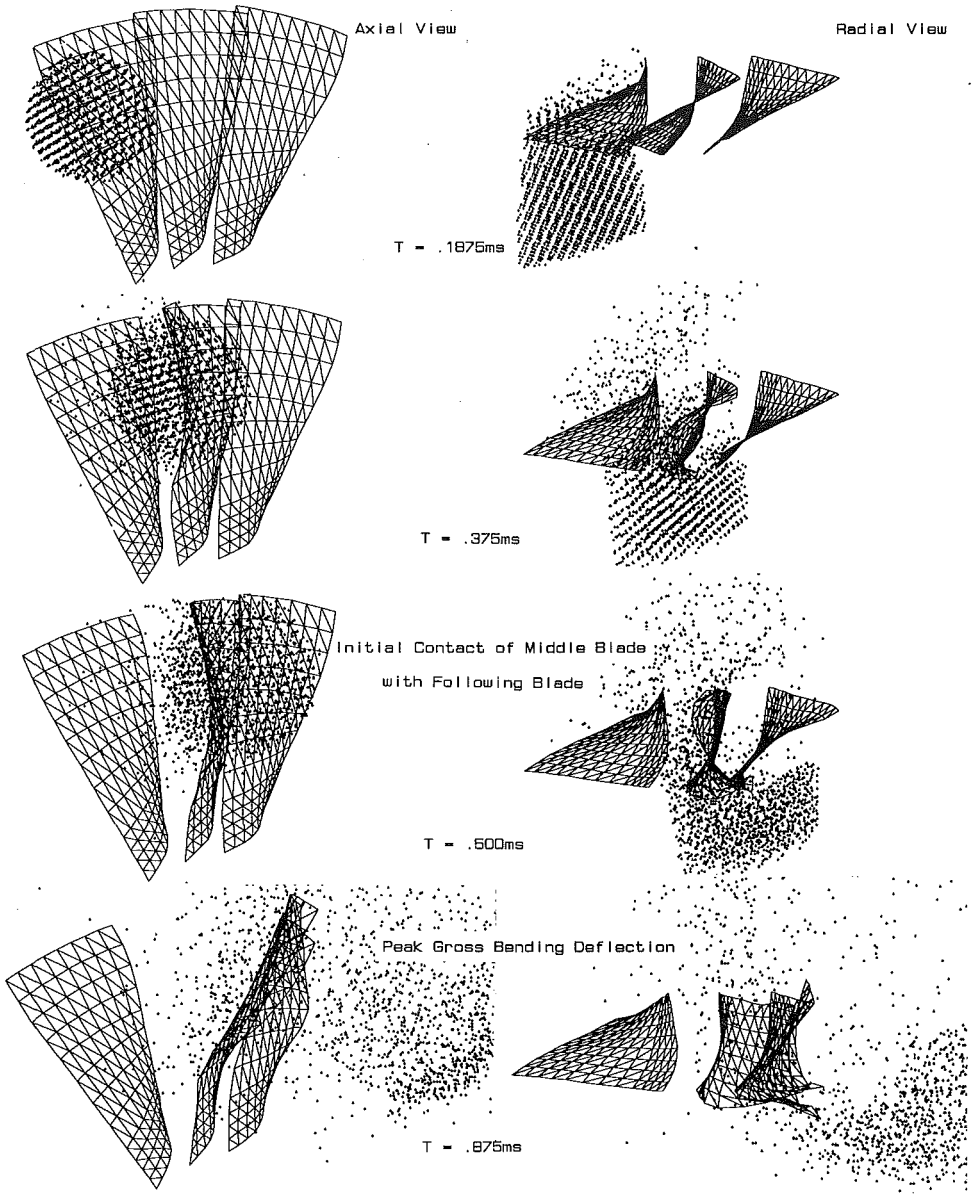

Fig. 12 PW/WHAM simulation of bird-to-multi-blade impact and blade-to-blade interaction (rigid body rotation removed)

deformed blade, a bird impact on multiple fan blades was simulated while accounting for blade-to-blade interaction. The analysis model in Fig. 12 depicts three shroudless fan blade airfoils rotating during impact with the axially translating bird model. The leading (left) blade was modeled as a "rigid" structure to preslice the leading portion of the bird (such that the largest slice could be ingested by the middle blade), while reducing computer time and providing a visual effect. The test showed that the blade directly in front of the most severely deformed blade exhibited very little deformation response. The following (right) blade was simulated for blade-to-blade interaction and bird load sharing behavior. The real bird was approximated by an ellipsoidal spheroid of uniform density.

The analysis generated movie presents the response of the blades to bird impact in Fig. 12. In both the axial and radial views, the blade rigid body rotational displacement was removed during postprocessing for ease of interpretation and illustration. The deflected geometry of the blades is noted at the time of initial contact of the middle blade with the following blade (0.500 ms) and the middle blade peak gross bending deflection (0.875 ms). Figure 13 highlights good agreement between the analysis predicted peak contact position of the middle blade with the following airfoil leading edge, and the posttest photograph of blade "I". A large spanwise contact mark or crease was left behind on the suction surface of blade "I" from the impact with the following blade "J" leading edge.

PW/WHAM predicted that the middle blade ingested about five times more bird mass than the following blade. This is qualitatively consistant with tests since the middle blade deformed and shielded the following blade by significantly reducing or cutting off its bird slice supply. Most of the following blade bending response was due to the impact from the middle blade and not from the bird. The load transferred to the following blade also relieved the middle blade, reducing its deflection and strain response. In a separate analysis where the following blade was not modeled, the middle blade deflection and root strain response were considerably greater.

The predicted maximum dynamic strain occurred in the root leading edge region of the middle blade and was sufficiently

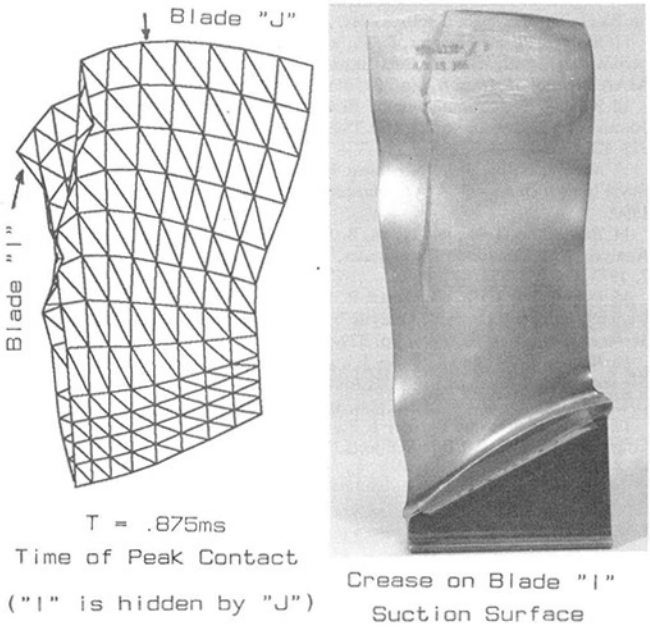

Fig. 13 Comparison of analysis at time of contract with posttest fan blade

large to suggest airfoil fracture. Blade "I" did not fracture in the bird ingestion test. However, a crack was found in the airfoil root region following a period of sustained engine running after bird ingestion. The predicted maximum dynamic strain in the following blade was about one-third that of the middle blade.

Figure 14 compares the predicted blade deformations, at the time gross bending response was initially restored following ingestion, to a posttest photograph of the permanently deformed blades I and J. The PW/WHAM successfully demonstrated the capability to predict multiple blade response, which agrees reasonably well with tests, especially when the "real" bird geometry was simply approximated by a dummy model.

Conclusions

PW/WHAM, a finite element based, transient nonlinear impact anaylsis, has been developed to analyze the response of fan blades or structures subjected to bird strikes. Research tests involving soft body impacts on single nonrotating blades, single rotating blades, and fully bladed rotors were performed over a wide range of impact velocities or energy levels. These tests included both shrouded and shroudless small titanium fan blades. Correlation of the analysis with test data generally resulted in very good agreement. The PW/WHAM analysis has very successfully demonstrated the capability of accurately predicting the large airfoil deflection response modes, bird-to-blade interaction, multiple blade impact, and blade-to-blade interaction. In addition, the analysis predicted the onset of blade cracking and possible fracture or material loss, which are consistent with tests. The test data provide a comparative basis for the continuing development, validation, and calibration of the analytical models for impact loading.

Salient conclusions with respect to the FOD response of small fan blade were also obtained. Generally, small fan blades experience gross torsional untwist, followed immediately by gross bending under medium and high-energy bird impact loading. Generally, low-aspect-ratio, shroudless fan blades demonstrate significantly improved FOD resistance or strength, over high-aspect-ratio shrouded fan blades. Modeling the "following" blade and blade-to-blade interaction are absolutely necessary for an accurate FOD analysis involving small fan blades.

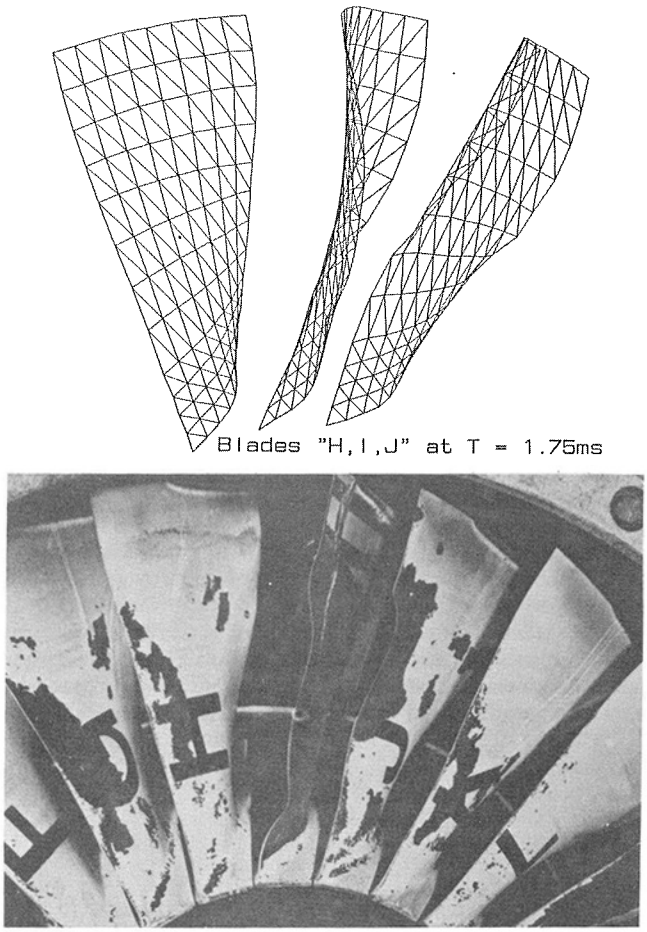

Fig. 14 Comparison of PW/WHAM deflected geometry (immediately following impact) with posttest blades "H, I, and J"

PW/WHAM has demonstrated its ability to be used as an effective analytical tool for designing FOD resistant structural components for soft body impact. However, since the analysis requires considerable engineering experience and the code currently utilizes significant computer resources and elapsed time, it can best be described as a "detailed" design tool used to verify near final designs. In addition, further experimental testing under both soft and hard body impacts must be pursued together with further refinements to the structure and bird models, in order to narrow down the crack initiation and failure modes for various components. The PW/WHAM analysis, through its generalized FE nature, has proved to be a very versatile code and is currently being applied to nose cone FOD, hard body fan blade-off DOD (released blade impact on first following blade), and containment (blade impact on case).

Acknowledgments

The presentation of this paper has been possible through the approval of Pratt and Whitney Canada Inc. The work reported herein was also in part funded by DRIE, the Canadian Department of Regional and Industrial Expansion. The authors wish to acknowledge the contributions, advice, and guidance of fellow Pratt and Whitney colleagues, especially N. F. Martin, P&WA, West Palm Beach, Florida, in carrying out this project. The contributions from the P&WC engineering test department are also appreciated.

References

1 Belytschko, T., and Mullen, R., "WHAMS, A Program for Transient Nonlinear Analysis of Structures and Continua," Northwestern University, Evanston, IL, 1978.

2 Code of Federal Regulations, Part 33—Airworthiness Standards: Aircraft Engines, Subpart E, Sec. 33.77, Foreign Object Ingestion, Jan. 1, 1988.

3 Peterson, R. L., and Barber, J. P., "Bird Impact Forces in Aircraft Windshield Design," Report #AFFDL-TR-75-150, Mar. 1976.

4 Wilbeck, J. S., and Rand, J. L., "The Development of a Substitute Bird Model," ASME JOURNAL OF ENGINEERING FOR POWER, Vol. 103, 1981, pp. 725–730.

5 Boyd, D. I., "Development of a New Technology Small Fan Jet Engine," *Canadian Aeronautics and Space Journal*, Vol. 33, No. 2, June 1987.

6 Cornell, R. W., "Elementary Three-Dimensional Interactive Rotor Blade Impact Analysis," ASME JOURNAL OF ENGINEERING FOR POWER, Vol. 98, Oct. 1976.

7 Fulton, G. B., "Design and Qualification of Foreign Object Damage Resistant Turbofan Blades," presented at the AIAA/SAE 11th Propulsion Conference, Anaheim, Sept. 1975.

8 Hirschbein, M. S., "Bird Impact Analysis Package for Turbine Engine Fan Blades," AIAA Paper No. 82-0696, 1982.

9 Smith, R. A., and McCarty, R. E., "Analytical Evaluation of Birdstrike Against an F-16A Laminated Canopy," presented at the AIAA/ASME/ASCE/AHS 29th Structures, Structural Dynamics & Materials Conference, Williamsburg, VA, Apr. 1988.

10 Engblom, J. J., "Coupled Fluid/Structure Response Predictions for Soft Body Impact of Airfoil Configurations," presented at the ASME Conference on Emerging Aerospace Technologies, Aug. 1980.

11 Storace, A. F., Nimmer, R. P., and Ravenhall, R., "Analytical and Experimental Investigation of Bird Impact on Fan and Compressor Blading," AIAA *Journal of Aircraft*, Vol. 21, No. 7, 1983, Paper No. 83-0954.

12 Niering, E., "Simulation of Bird Strike on Turbine Engines," ASME JOURNAL OF ENGINEERING FOR GAS TURBINES AND POWER, Vol. 112, 1990, pp. 573–578.

13 Martin, N. F., Jr., "Nonlinear Finite Element Analysis to Predict Fan Blade Impact Damage," AIAA *Journal of Propulsion and Power*, Vol. 6, Aug. 1990.

14 Belytschko, T. B., and Hsieh, B. J., "Nonlinear Transient Finite Element Analysis With Convected Coordinates," *Int. J. Numerical Methods Eng.*, Vol. 7, 1973, pp. 255–272.

15 Belytschko, T. B., Chiapetta, R. L., and Bartel, H. D., "Efficient Large Scale Non-linear Transient Analysis by Finite Elements," *Int. J. Numerical Methods Eng.*, Vol. 10, 1976, pp. 579–596.

16 Brown, K. W., and Krahula, J. L., "Linear–Nonlinear Interface for Finite Element Impact Analysis," ASME JOURNAL OF ENGINEERING FOR POWER, Vol. 104, 1982, pp. 23–27.

17 Bertke, R. S., and Barber, J. P., "Impact Damage in Titanium Leading Edges From Small Soft Body Objects," AFML-TR-79-4019, Mar. 1979.

A Proposed Method for Assessing the Susceptibility of Axial Compressors to Fouling

F. Seddigh
Research Associate.

H. I. H. Saravanamuttoo
Professor.
Fellow ASME

Department of Mechanical and Aerospace Engineering,
Carleton University,
Ottawa, Ontario, Canada

Although the overall effect of compressor fouling on engine performance has been recognized for many years, remarkably little has been published on the quantifiable effects. Mathematical modeling of compressors using stage stacking methods has recently been used for a systematic study of compressor fouling and earlier investigations led to an interest in the effects of engine size and compressor stage loading. This paper presents a proposed index showing the susceptibility of compressors to fouling, which could be useful in helping operators to determine cleanup intervals. Three engines of widely differing performance were used in developing this index and additional operator experience would be useful in confirming its validity.

Introduction

It has been well recognized for many years that the performance of industrial gas turbines can be significantly affected by compressor fouling (Upton, 1974). Fouling can result from operation in dirty industrial environments, which is to be expected, but can equally be found in remote rural locations due to problems such as insects, tree saps, pollen, etc. Another source of fouling can be due to oil leakage from bearings. Effective inlet filtration can alleviate, but not eliminate, the problem, and operators are still faced with the decision on what basis to schedule compressor cleaning. If cleaning is delayed too long full performance recovery cannot be obtained, but excessively frequent cleaning causes considerable disruption to operations.

Compressor fouling leads to reduction in both power output and overall efficiency of an engine. For example, a 1 percent reduction in axial compressor efficiency can account for a 1.5 percent increase in the heat rate for a given power output (Scott, 1977). Since neither the efficiency nor the power output of engines is usually measured directly, fouled engines can operate inefficiently for a long period of time. In the past, the operators did not consider the inefficient operation of an engine as a serious economic problem, mainly due to the availability of cheap fuels. However, rising fuel costs in the past two decades have caused the efficient operation of gas turbines to become a matter of prime importance. Presently, compressor fouling has been identified by both users and manufacturers of gas turbines as the most dominant factor contributing to performance deterioration in industrial applications. It is noted that the economic loss as a result of compressor fouling runs into millions of dollars annually (Reid, 1977).

In the last few years discussions have been held with a number of operators and it became clear that a better physical understanding of the fouling process was needed. In one case an operator claimed that fouling was not a problem, but the manufacturer recognized that the engine was extremely badly fouled and the problem did not show up simply because of the continuous operation at a relatively low power level.

Operators require a simple and reliable method for detecting fouling at a level where performance can be restored by compressor cleaning. Recent studies have been aimed at modeling compressor behavior so that a systematic study of fouling effects can be carried out to provide a knowledge base for further operations.

In order to run a gas turbine at a particular power setting at its best efficiency, some users have adopted the policy of compressor cleaning, regardless of local factors such as environment, season, and engine condition, on a fixed-interval basis such as approximately 250-hour interval for an on-stream washing and 1000-hour interval for a soak wash (Reid, 1977). An on-stream wash can return 75 percent of the lost efficiency. A soak wash can restore the engine virtually to "as-new" condition. Dry cleaning using nutshells, carried out at full speed, reduces the losses due to the fouling of the engine compressor by only approximately 20–30 percent and may clog up internal passages.

On-condition cleaning of the compressors is used by some users. This method requires a close monitoring of the engine parameters and development of a system that can predict performance degradation as a result of compressor fouling. The major obstacle in the way of successful on-condition cleaning is the development of a performance monitoring system, which has to be tailored to the needs of a particular user for a particular application and environmental condition; this puts considerable economic constraints on the development of such systems, which makes the adoption of the on-condition cleaning method practically impossible by some users. It is probable that if performance is allowed to deteriorate to the point where

Contributed by the International Gas Turbine Institute and presented at the 35th International Gas Turbine and Aeroengine Congress and Exposition, Brussels, Belgium, June 11–14, 1990. Manuscript received by the International Gas Turbine Institute January 24, 1990. Paper No. 90-GT-348.

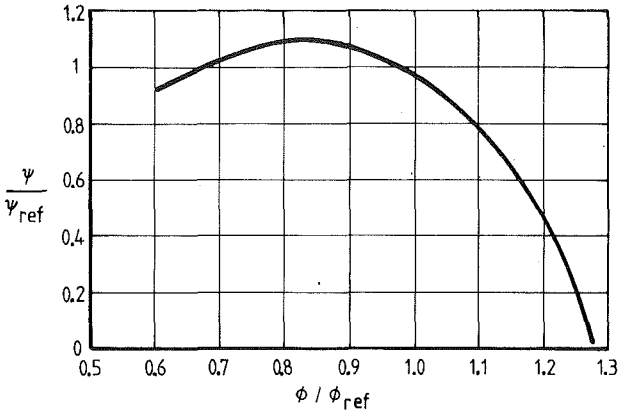

Fig. 1 Generalized stage pressure coefficient curve (Muir et al., 1988)

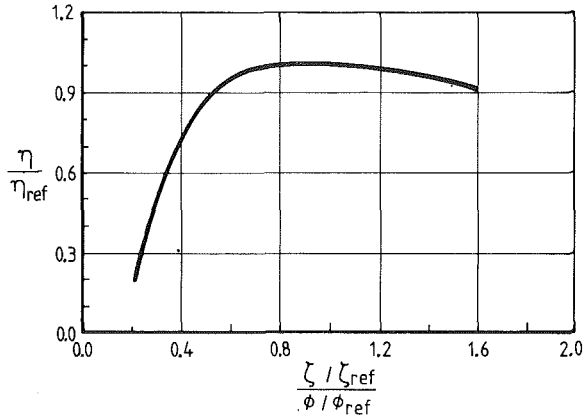

Fig. 2 Generalized stage efficiency curve (Muir et al., 1988)

it can be detected, a considerable waste of fuel will be incurred. Despite such difficulties, on-condition cleaning is gaining popularity with users. The programs developed for this purpose vary in their complexities as well as in their scope; some are completely automatic and others are semi-automatic. Also, the number of parameters that are monitored varies from one system to another. Scott (1977) reports on a simple system of monitoring the intake depression as a means of predicting the compressor fouling of two Avon powered units with satisfactory results. There are not enough data available on the complex automated monitoring systems to demonstrate their capabilities of reaching the required levels of accuracy and reliability for detecting the small changes in performance which could indicate compressor fouling. MacIsaac (1981) presents a vivid and comprehensive review of some of the well-known monitoring systems.

Some of the monitoring systems are nothing but trend monitoring and analysis of a few engine performance parameters. Saravanamuttoo (1974, 1979) describes a very simple and effective system for on-site monitoring of the engines. These systems are based on the premise that the test data are reliable. In order to isolate faulty reading, Agrawal et al. (1979) have published a method of identifying instrument faults. The method proposed by Williams (1981b) is similar to the gas path analysis of Saravanamuttoo (1979) except that he has assumed the compressor efficiency can be considered constant over a good part of the operating range. Several authors (Scott, 1979; Agrawal et al., 1979; Saravanamuttoo and MacIsaac, 1983) attempted to derive correlations that link the engine problems to changes in the monitored engine parameters.

Simulation of Compressor Performance. With the advent of faster and cheaper microcomputers the manual logging of engine data is gradually being replaced by remote data-acquisition systems. This has made it possible to extend the scope of research to predictive simulation techniques aimed at producing an accurate computer model of engines and their various components and processes. A systematic investigation of compressor fouling requires that the effect of fouling of a single stage be modeled correctly and hence the overall effects of all stages of an engine compressor can be obtained from the effects of the fouling of the constituent stages.

The stage stacking technique, which was extensively studied by Stone (1958) and improved by Howell and Calvert (1978), can be used as a tool to produce the compressor map for an engine from the performance of its individual stages. A successful application of the stage stacking technique depends to a great extent on the knowledge of the stage characteristics for all stages of a compressor. The stage characteristics for the compressor of an engine are in turn obtained by the engine manufacturer during its development phase; such information, if not published, would remain proprietary material of the manufacturer. When stage characteristics from test data are not available, there are alternate methods that can estimate them fairly accurately from the geometry of a stage, blade rows, and the flow pattern. The performance of a single stage is normally presented in the form of nondimensional stage characteristics as follows:

Flow coefficient:

$$\phi = \frac{C_a}{U}$$

Pressure rise:

$$\psi = \frac{C_p T_{os} (PR_s^{(\gamma-1)/\gamma} - 1)}{U^2}$$

Temperature rise:

$$\zeta = \frac{C_p \Delta T_{os}}{U^2}$$

Efficiency:

$$\eta = \frac{T_{os} (PR_s^{(\gamma-1)/\gamma} - 1)}{\Delta T_{os}} = \frac{\psi}{\zeta}$$

A set of parameters called "generalized characteristics" can be defined; these are the ratios of each characteristic parameter and the value of the same parameter at an arbitrary operating point, such as the point of maximum efficiency that may be designated by subscript ref:

$$\frac{\phi}{\phi_{ref}}, \quad \frac{\eta}{\eta_{ref}}, \quad \frac{\zeta}{\zeta_{ref}}, \quad \frac{\psi}{\psi_{ref}}, \text{ and } \frac{\zeta/\zeta_{ref}}{\phi/\phi_{ref}}$$

Figure 1 shows a plot of ψ/ψ_{ref} versus ϕ/ϕ_{ref} assembled from a number of openly published sources using stage pressure rise data (Muir et al., 1988). A generalized efficiency relation developed by Howell and Bonham (1950) as shown in Fig. 2, which has also been used by Muir et al. (1988), was found to

Nomenclature

C_a = stage inlet axial velocity
C_p = specific heat
$\dot{m}$ = mass flow rate
PR_s = stage pressure ratio
T_{os} = stage inlet total air temperature
ΔT_{os} = stage total temperature rise
U = tangential blade speed at mean radius
γ = ratio of the specific heats

Table 1 Design specification data for the three engines

DESCRIPTION		Engine # 1	Engine # 2	Engine # 3
$\dot{m}$	kg/s	17.2	65.8	115.7
PR		9:1	17.2:1	8.7:1
No. of Stages		11	16	17
Power Output	kW	2,850	20,134	28,200
N_{gg}	rpm	15,015	9,160	5,100
R_m	m	0.176	0.279	0.556
U	m/s	277	268	297

be adequate for modeling the off-design performance of gas turbines due to compressor fouling.

The stage characteristics for the compressor of an engine can be estimated by the use of a numerical search procedure; these characteristics with the aid of stage-stacking technique allow one to find the overall compressor map for the engine. At a given compressor speed and mass flow established by the operating line data points, the numerical search procedure begins by assuming specific values for the reference point of each stage. From the generalized characteristics curves (Figs. 1 and 2), the performance map for each stage is obtained and the performances of the individual stages are then stacked to find the overall compressor pressure ratio, *PR*, and the temperature rise ratio, $\Delta T/T$. If these values do not agree with the operating line data, the procedure is repeated. Muir et al. (1988) and Aker and Saravanamuttoo (1988) using the above procedure have produced the compressor performance maps for two industrial gas turbines that agree with the manufacturer's data. The present authors have also used the same procedure for producing the compressor performance map for another industrial engine whose specification data appear in Table 1; this is shown in Fig. 3, which is also in conformity with the manufacturer's data.

Simulation of Compressor Fouling. Lakshminarasimha and Saravanamuttoo (1986) simulated the fouling of individual compressor stages in the NACA five-stage compressor described by Sandercock et al. (1954). In order to reflect the loss in performance due to fouling, the inlet flow was reduced by arbitrary factors of 3 and 8 percent for light and heavy fouling, respectively, while the efficiency was lowered by 1 percent. Aker and Saravanamuttoo (1988) investigated the linear progression of fouling in compressor stages and how it could be best simulated. Basing their arguments on field data and on their discussions with the users of gas turbines, they noted that the impact of fouling on the front stages of a compressor is more than that on the rear stages. They concluded that it was more appropriate to adopt a model that could simulate linear progression of fouling into compressor stages. For this purpose, they reduced the flow coefficient, ϕ, by a certain percentage, say k_1 percent, through a linear progression from $n \times k_1$ for the first stage to k_1 for the nth stage. In a similar manner, the stage efficiencies were reduced using another factor k_2. They have referred to this model of fouling by the designation (k_1:k_2). After modifying the flow coefficients and efficiencies for the "clean stages," they applied a stage stacking technique in order to produce a compressor map for a fouled compressor whose match point with the existing turbines produced the modified operating point for the engine. In this way they were able to simulate fouling for two industrial engines; the stage stacking procedure gave excellent correlation with field data for clean engines and manufacturer's data, but no field results were available for fouled compressors. Similarly, the present authors simulated the fouling of an industrial gas turbine in the power range of 30 MW. The simulated compressor maps for the "clean and fouled" compressors for this engine, using the fouling model (1: 0.75), are shown in Fig. 3.

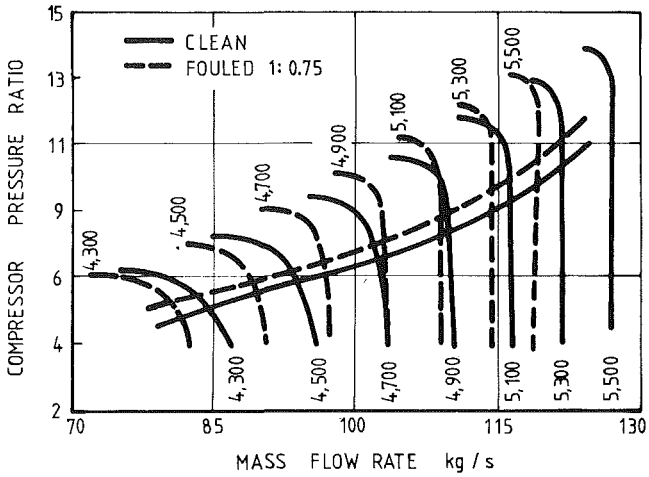

Fig. 3 Simulated clean and fouled compressor maps for engine No. 3

Fouling Severity. Quantifying the effects of compressor fouling has a number of obvious applications and benefits to the users for diagnostics, engine performance monitoring, maintenance, and operations. Such applications can be further extended by investigation of the sensitivity of engine performance to compressor fouling; this requires the identification of significant engine parameters, which can indicate the detrimental effects of compressor fouling. There have been references in the literature to stage loading as being one of the significant parameters in the impact of fouling on engine performance. Power output has also been mentioned. Saravanamuttoo and Lakshminarasimha (1985) were of the opinion that the performance of a small engine of less than 1 MW is expected to deteriorate more as a result of fouling than does a larger machine. Blauser and Gulati (1984) state that the performance loss due to fouling of the gas turbine compressor ranges from 3 to 10 percent of the output horsepower for axial design and substantially less for centrifugal designs. The amount of loss depends on the control parameters employed. If the gas generator's primary control parameter is speed, a lower degradation, in terms of power, will be observed than that which occurs if exhaust temperature is the primary control.

The existing knowledge concerning an engine's sensitivity to the fouling of its compressor has remained, to a large extent, speculative and suffering from contradictions; these conclusions were generally from observations of engine operation without examining the repeatability of such observations. Therefore this study is intended to fill the vacuum through the development of a *systematic method* for the examination of the likely parameters that could influence the severity of performance degradation due to fouling. For this purpose three industrial gas turbines, ranging in power output from 3 MW to 30 MW, were selected for fouling simulation. The significant parameters for these engines, which have been designated by numbers 1–3, are tabulated in Table 1.

Furthermore, the fouling model (1: 0.75) for the simulation of fouling of these engines was adopted. The fouling simulation results for engines Nos. 1 and 2 have already been reported by Aker and Saravanamuttoo (1988). Similar results for engine No. 3 have been produced, using the same fouling model. A critical examination of these results forms the basis for the investigation of engine sensitivity to fouling.

Results and Discussion

The computer model for the "clean compressor" of engine

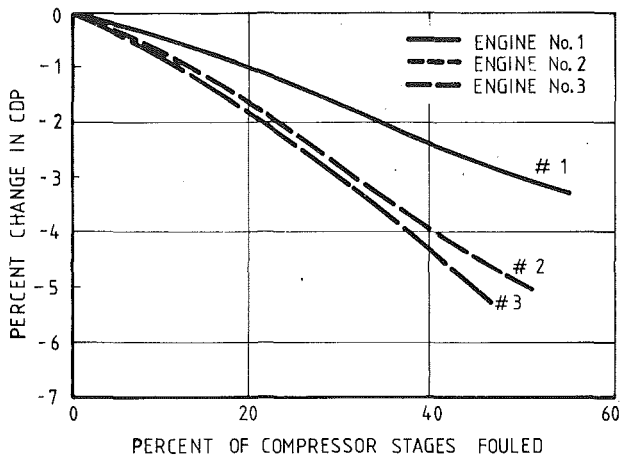

Fig. 4 Variations of the percentage CDP drop with the percentage of stages fouled for the three engines

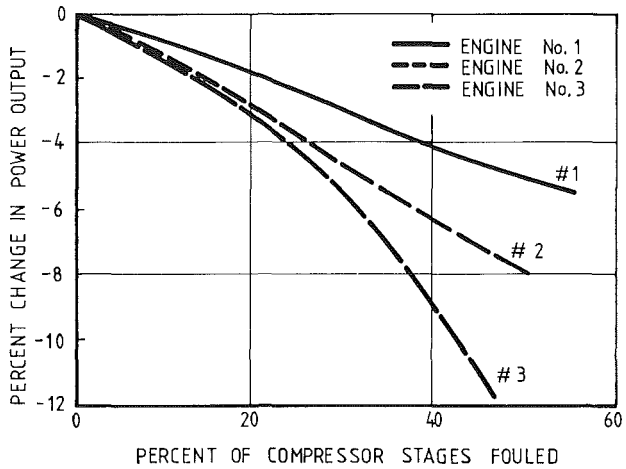

Fig. 5 Variations of the percentage power output drop with the percentage of stages fouled for the three engines

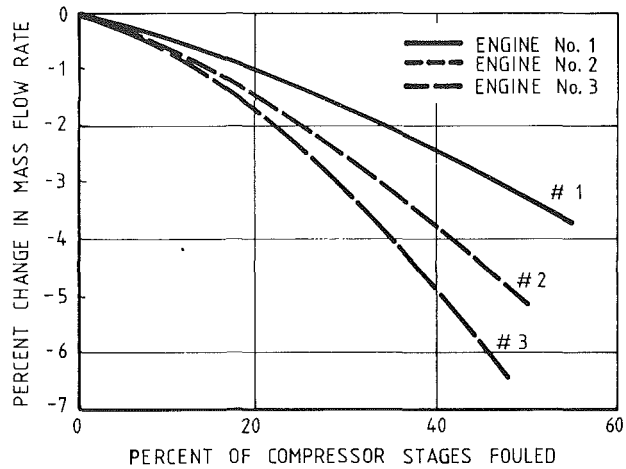

Fig. 6 Variations of the percentage mass flow rate decrease with the percentage of stages fouled for the three engines

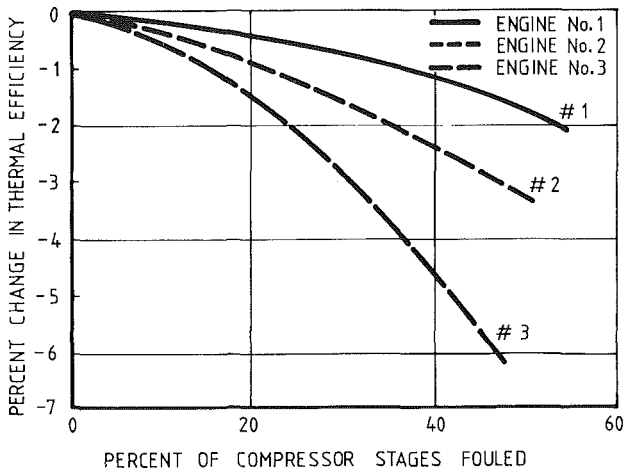

Fig. 7 Variations of the thermal efficiency drop with the percentage of stages fouled for the three engines

No. 3 was produced by stage stacking. The specifications for the compressor and the engine were obtained from its manufacturer and from published literature such as McQuiggan (1975). Figure 3 shows the simulation of the compressor map and the predicted operating line for this engine. A linear progressive fouling model of (1: 0.75) through the 8th stage of the compressor was applied and a compressor map for the fouled compressor was obtained and subsequently an operating line for the fouled engine was predicted. These results are also displayed in Fig. 3. Although a slight shift in the surge line is observed, the shift of the operating line is more significant and it is clear that the fouled engine operates at a lower surge margin. This engine actually makes use of variable power turbine nozzles, so the CDP can be maintained at a fixed value, making fouling hard to predict.

In Figs. 4–7, the simulation of the impact of the fouling model (1: 0.75) on compressor delivery pressure, power output, mass flow rate, and thermal efficiency for the three engines are shown. The general pattern exhibited in these graphs for various parameters is consistent, regardless of the performance parameter selected. The pattern indicates that the three engines can be listed on the basis of the severity of the performance degradation as a result of the compressor fouling in the ascending order of engine Nos. 1, 2, and 3. For further analysis Fig. 4, which shows the pattern in the compressor delivery pressure drop as a result of compressor fouling, is considered. Decreases in CDP for engines 2 and 3 are closer to each other compared to those for engines 1 and 2. The decrease in the

Table 2 Dimensionless groups and simulated results for the three engines

DESCRIPTION	Engine # 1	Engine # 2	Engine # 3
ΔT per Stage ° C	28.2	25.9	17.9
$\frac{C_p \Delta T_{stg}}{0.5U^2}$	0.737	0.724	0.407
$\frac{kW}{\dot{m}U^2}$	2.16	4.26	2.76
$\frac{kW}{\dot{m}C_p\Delta T_{stg}}$	5.88	11.77	13.56
CDP Drop at 40% fouling	2.40	3.95	4.45

CDP as a function of percent of number of stages fouled for the three engines is almost linear up to 25 percent progress into the compressor stages. For other performance parameters shown in Figs. 5, 6, and 7, more divergence from linearity at higher levels of fouling is observed, particularly for engine No. 3.

On the other hand some parameters calculated from the specification data for the three engines, as tabulated in Table 2, follow a pattern consistent with the abovementioned observations. This indicates that a likely relationship might exist

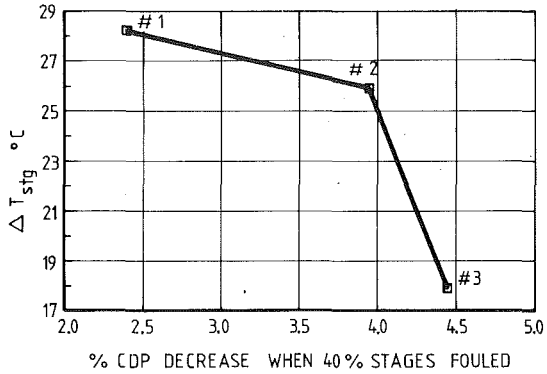

Fig. 8(*a*) Variations of stage temperature rise with percentage CDP decrease for the three engines when 40 percent of stages fouled

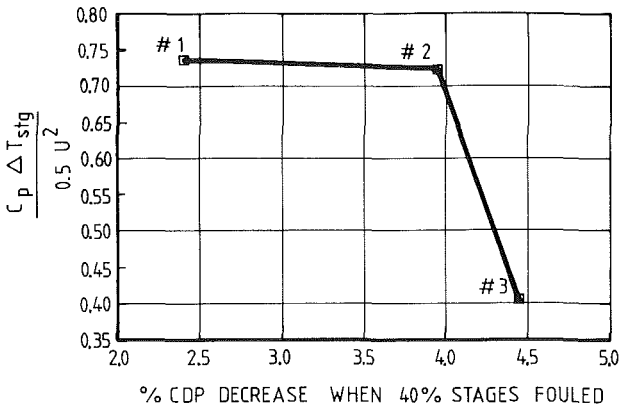

Fig. 8(*b*) Variations of stage loading coefficient with percentage CDP decrease for the three engines when 40 percent of stages fouled

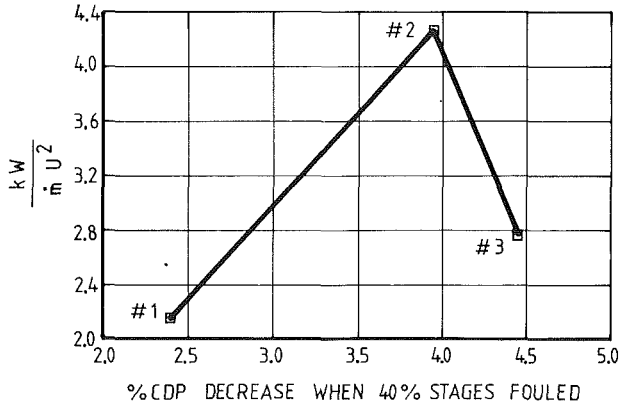

Fig. 8(*c*) Variations of the power coefficient, $kW/(\dot{m}U^2)$, with percentage CDP decrease for the three engines when 40 percent of stages fouled

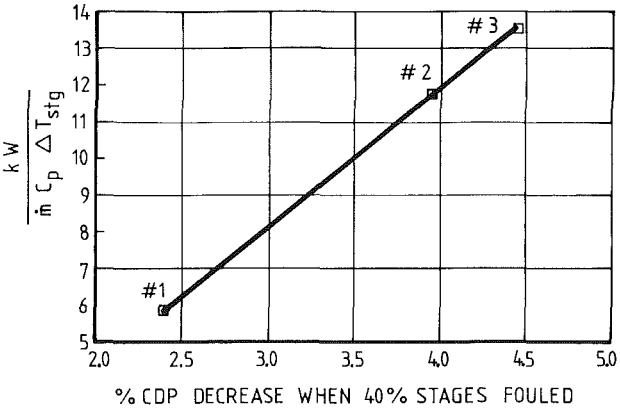

Fig. 8(*d*) Variations of $kW/(\dot{m}C_p\Delta T_{stg})$, with percentage CDP decrease for the three engines when 40 percent of stages fouled

between the corresponding parameters and the fouling sensitivity of the engines. A few dimensionless groups can be formed from the engine parameters, which in addition to the stage loading, ΔT_{stg}, are discussed below; the tangential velocity of the first row of blades at the meanline, the mass flow, and the power output are denoted by U, $\dot{m}$, and kW, respectively.

- ΔT_{stg}. This parameter is a measure of stage loading. For ease of reference and analysis, the percentage drop in CDP as a result of fouling 40 percent of the stages for all three engines have been recorded along with the other data in Table 2. The tabulated data indicate that on the basis of higher stage temperature rise, the engines follow the order of: engine No. 1, engine No. 2, and engine No. 3; while on the basis of sensitivity to fouling as apparent from the percent CDP drop, the engines follow a reverse order. The relationship between these data becomes more clear from a glance at Fig. 8(*a*). This figure shows that a clear-cut correlation between the stage loading of an axial compressor and its sensitivity to fouling does not exist, though it may be stated that the performance degradation of gas turbines with smaller stage loadings is more severe as compared to those with larger stage loadings.
- $C_p\Delta T_{stg}/0.5U^2$. This is the stage-temperature-rise coefficient based on the tangential velocity of rotor blades at their mean radius for the first stage, which is a nondimensional value for the stage loading. A glance at Table 2 and Fig. 8(*b*) reveals that practically what was said for stage temperature rise holds also true for this coefficient; all three engines had very similar values of U.
- $kW/\dot{m}U^2$. This nondimensional coefficient is the ratio of the specific power output and the square of the tangential speed of the frontal rotor blades at the mean radius. From the comparison of the tabulated results, as shown in Fig. 8(*c*), no consistent correlation between this parameter and the fouling sensitivity of the engines emerges.
- $kW/\dot{m}C_p\Delta T_{stg}$. This nondimensional coefficient is the ratio of the specific power output of an engine and the enthalpy rise for a stage. Figure 8(*d*) shows the variation of this parameter versus the percent CDP decrease due to fouling 40 percent of the stages. It appears that this parameter presents the best consistency among the dimensionless coefficients listed for these engines and the corresponding fouling sensitivity. The variation of this parameter with the sensitivity of an engine to fouling is linear and consistent. This parameter incorporates important specification data for an engine, i.e., the engine size manifested by its design power output, its design mass flow rate, and its stage loading.

As is evident from Figs. 4–7, the relationship between the progress of fouling in compressor stages and performance degradation is nonlinear for all of the engine parameters except for CDP. The nearly linear relationship exhibited in Fig. 4 and the ease of CDP measurement are the two factors for selecting CDP as the most suitable parameter in fouling studies, whose extent of degradation would determine the level of fouling progress in an engine. Further examination of the presented results indicates that the dimensionless quantity $kW/(\dot{m}C_p\Delta T_{stg})$ stands out as the most promising parameter for the comparison of different engines on the basis of their sensitivity to performance degradation due to compressor fouling.

It appears that susceptibility to compressor fouling is related to the parameter $kW/(\dot{m}C_p\Delta T_{stg})$, which could be referred to as a *fouling index*. The parameters are readily identifiable for any engine and the values for a wide range of commonly used gas turbines are shown in Table 3. The data in Table 3 were obtained from the 1989 Edition of "Gas Turbine World Performance Specifications," assuming a polytropic efficiency of 88 percent in all cases to estimate the overall compressor tem-

Table 3 Design specifications and estimated data for some industrial gas turbines

ENGINE	No. of Stages	Power kW	PR	Mass Flow kg/s	kW/kg/s	$\Delta T_{compressor}$ °C	ΔT_{stage} °C	$\frac{kW}{\dot{m}C_p\Delta T_{stg}}$
Mars	15	8,840	16.0	37.2	237.6	421	28.1	8.43
GT8	12	47,100	16.3	177.0	266.1	425	35.4	7.52
GT9	15	34,400	9.0	161.1	213.6	300	20.0	10.68
GT13E	17	147,900	13.9	491.4	301.0	389	22.9	13.14
501-KB5	13	3,924	15.1	15.7	249.9	408	31.4	7.96
570-KC	13	4,731	12.1	18.6	254.3	360	27.7	9.18
570-KA	13	5,910	12.7	19.6	300.8	370	28.4	10.59
PG 5371	17	26,300	10.2	122.5	214.7	325	19.1	11.24
PG 6541	17	38,340	11.8	136.6	280.7	354	20.8	13.50
PG 7191	17	150,000	13.5	416.5	360.1	383	22.5	16.00
PG 9161(E)	17	116,900	12.1	403.3	289.8	360	21.2	13.67
LM 2500	16	21,230	18.7	66.2	320.5	458	28.6	11.21
AVON	17	14,240	9.2	77.6	183.5	304	17.9	10.25
TORNADO	12	6,185	12.1	27.7	223.5	360	30.0	7.45
SATURN	8	1,080	6.7	6.4	168.8	246	30.8	5.48
CENTAUR	11	3,130	9.4	17.6	178.3	309	28.1	6.35
CENTAUR H	11	3,880	9.3	17.5	222.1	307	27.9	7.96
V-64	16	53,300	15.8	170.1	313.3	418	26.1	11.94
V-84	17	103,200	10.7	349.4	295.4	334	19.7	14.96
CW 251	19	42,500	14.7	159.7	266.0	402	21.2	12.55
W 501 D5	17	104,400	14.2	358.9	290.9	394	23.2	12.54
W 501 F	17	145,000	14.2	413.8	350.4	394	23.2	15.10
MW 701	17	130,550	14.0	444.6	293.6	391	23.0	12.77
CW 352 MAA	15	22,463	7.3	99.4	226.1	262	17.4	12.99
CW 352 MA	16	26,119	8.2	111.2	235.0	283	17.7	13.28
CW 352 MB	17	29,701	9.3	126.6	234.6	307	18.0	13.00

perature rise; engines with outputs from about 1000–150,000 kW are included, including both older designs and some of the latest designs. It is interesting to note that the larger units tend to have higher values of the fouling index than the smaller units; this may well be a controversial result, but has been arrived at from a systematic investigation without reliance on preconceived ideas.

Conclusions

From this investigation it appears that both the specific output of an engine and its compressor stage loading are important factors in determining its response to fouling effects. This study has been an attempt in the direction of quantifying the severity of performance degradation of an engine due to its compressor fouling; very little information is available on this topic. In the light of what has been presented and expressed, it warrants examining the simulated and field data for a few more engines similar to those in this study. Certainly, the validity of these results can be strengthened and the status of the presented hypothesis will be enhanced if more engines of diverse size are studied in the future, using the same methodology for their fouling simulation.

Acknowledgments

The authors would like to acknowledge the financial support of the Natural Sciences and Engineering Research Council (NSERC) of Canada. They would like also to thank GasTOPS Ltd. for their cooperation in providing software.

References

Agrawal, R. K., MacIsaac, B. D., and Saravanamuttoo, H. I. H., 1979, "An Analysis Procedure for Validation of On-Site Performance Measurements of Gas Turbines," ASME JOURNAL OF ENGINEERING FOR POWER, Vol. 101, pp. 405-414.

Aker, G. F., and Saravanamuttoo, H. I. H., 1988, "Predicting Gas Turbine Performance Degradation Due to Compressor Fouling Using Computer Simulation Techniques," ASME JOURNAL OF ENGINEERING FOR POWER, Vol. 111, No. 2, pp. 343-350.

Blauser, D. L., and Gulati, U., 1984, "Performance Considerations in Selection and Application of Gas Turbine Drivers for Centrifugal Compressors," ASME JOURNAL OF ENGINEERING FOR POWER, Vol. 106, pp. 952-960.

Freeman, C., and Dawson, R. E., 1983, "Core Compressor Development for Large Jet Engines," *Proceedings of the 1983 Tokyo International Gas Turbine Congress*, Oct. 23-29, pp. 361-368.

Howell, A. R., and Bonham, R. P., 1950, "Overall and Stage Characteristics of Axial-Flow Compressors," *Proc. Inst. Mech. Engrs.*, Vol. 163, pp. 235-248.

Howell, A. R., and Calvert, W. J., 1978, "A New Stage Stacking Technique for Axial-Flow Compressor Performance Prediction," *Trans. ASME*, Vol. 100, Oct., pp. 698-703.

Lakshminarasimha, A. N., and Saravanamuttoo, H. I. H., 1986, "Prediction of Fouled Compressor Performance Using Stage Stacking Techniques," *ASME Symposium on Turbomachinery Performance Deterioration*, FED-Vol 37.

MacIsaac, B. D., 1981, "A Review of Major Health Monitoring Techniques," presented at the Fourth Symposium on Gas Turbine Operations and Maintenance, National Research Council of Canada, Sept. 21-22, Toronto.

McQuiggan, G., 1975, "Prototype Testing Methods for Variable Geometry Industrial Gas Turbines," ASME Paper No. 82-GT-75.

Muir, D. E., Saravanamuttoo, H. I. H., and Marshall, D. J., 1988, "Health Monitoring of Variable Geometry Gas Turbines for the Canadian Navy," ASME JOURNAL OF ENGINEERING FOR POWER, Vol. 111, No. 2, pp. 244–250.

Reid, D. E., 1977, "Impact of Increased Fuel Prices on Gas Turbine Operation and Maintenance," presented at the Second Symposium on Gas Turbine Operations and Maintenance, National Research Council of Canada.

Sandercock, D. M., Kovach, K., and Lieblein, S., 1954, "Experimental Investigation of a Five-Stage Axial Flow Research Compressor With Transonic Rotors in All Stages; Part I: Compressor Design," NACA RM E54F24, Sept. 1954; "Part II: Compressor Overall Performance," NACA RM E54G01, July, 1954; "Part III: Interstage Data and Individual Stage Performance Characteristics," NACA RM E56G24, July 1956.

Saravanamuttoo, H. I. H., 1974, "Gas Path Analysis for Pipeline Gas Turbines," presented at the First Symposium on Gas Turbine Operations and Maintenance, National Research Council of Canada.

Saravanamuttoo, H. I. H., 1979, "A Low Cost, On-Site Performance Monitoring System," ASME Paper No. 79-GT-21.

Saravanamuttoo, H. I. H., and MacIsaac, B. D., 1983, "Thermodynamic Models for Pipeline Gas Turbine Diagnostics," ASME JOURNAL OF ENGINEERING FOR POWER, Vol. 105, pp. 875–884.

Saravanamuttoo, H. I. H., and Lakshminarasimha, A. N., 1985, "A Preliminary Assessment of Compressor Fouling," ASME Paper No. 85-GT-153.

Scott, J. N., 1977, "Improving Turbo Compressor Efficiency via Performance Analysis Techniques," ASME Paper No. 77-GT-53.

Scott, J. N., 1979, "Axial Compressor Monitoring by Measuring Air Intake Depression," presented at the Third Symposium on Gas Turbine Operations and Maintenance, National Research Council of Canada.

Southwick, R. D., 1974, "A Stage Stacking Simulation of Axial-Flow Compressors With Variable Geometry," ASD-TR-74-38.

Stone, A., 1958, "Effects of Stage Characteristics and Matching on Axial Flow Compressor Performance," *Trans. ASME*, Vol. 80, pp. 1273–1293.

Upton, A. W. J., 1974, "Axial Flow Compressors and Turbine Blade Fouling: Some Causes, Effects and Cleaning Methods," presented at the First Symposium on Gas Turbine Operations and Maintenance, National Research Council of Canada, Oct.

Williams, L. J., 1981a, "The Optimization of Time Between Overhauls for Gas Turbine Compressor Units," presented at the Fourth Symposium on Gas Turbine Operations and Maintenance, National Research Council of Canada, Toronto, Canada.

Williams, L. J., 1981b, "The Use of Mathematical Modeling in the Analysis of Gas Turbine Compression Unit Test Data," ASME Paper No. 81-GT-217.

J. Sawyer
Acurex Corporation,
Mountain View, CA 94039-7040

R. J. Vass

N. R. Brown

J. J. Brown

Center for Advanced Ceramic Materials
CIT TDC,
Virginia Polytechnic Institute &
State University,
Blacksburg, VA 24061-0256

Corrosion and Degradation of Ceramic Particulate Filters in Direct Coal-Fired Turbine Applications

High-temperature ceramic filters show considerable promise for efficient particulate removal from coal combustion systems. Advanced coal utilization processes such as direct coal-fired turbines require particulate-free gas for successful operation. This paper describes the various ceramic particulate filters under development and reviews the degradation mechanisms expected when operated in coal combustion systems.

Introduction

Direct Coal-Fired Turbines (DCFT) are under development by Solar Turbines, Inc., Allison Gas Turbines, and others. A typical process flow diagram is shown in Fig. 1. The economic viability, efficiency, and durability of these systems are largely dependent on the delivery of particulate-free hot gas to the power turbine. The materials of choice for efficient barrier-type particulate removal systems at operating conditions are ceramics such as SiC, Si_3N_4, mullite, cordierite, and others.

Typical operating conditions for a DCFT high-temperature filtration system are shown in Table 1. The filtration system will typically operate at approximately 1 MPa (10 atm) and 1000°C (1850°F). The filters will be subjected to a wide range of stress-inducing forces, including vibrations and thermal shock resulting from pulse cleaning of the filters. Severe chemical corrosion of the filters is expected from the steam and alkali present in the combustion gases. Lesser corrosion is also possible from SO_2, H_2S, CaO, and other low-level gas phase contaminants.

At the present time, no filter tests have been completed on DCFT systems. However, from filter operating experience on similar systems such as pressurized fluidized bed combustors (PFBC) and gasifiers, the filter degradation mechanisms that will be experienced in DCFT systems are becoming evident. In addition, a large amount of information on the performance of ceramic components relevant to coal-fired systems is available in the literature as well as from previous coal gasification research and experience. With this information, and examination of filters exposed in PFBC and gasification atmospheres, one can deduce the expected effects of DCFT exposure on the ceramic filter materials. Emphasis has been given to the performance of silicon carbide, silicon nitride, and aluminosilicate compositions.

Contributed by the International Gas Turbine Institute and presented at the 35th International Gas Turbine and Aeroengine Congress and Exposition, Brussels, Belgium, June 11–14, 1990. Manuscript received by the International Gas Turbine Institute January 25, 1990. Paper No. 90-GT-347.

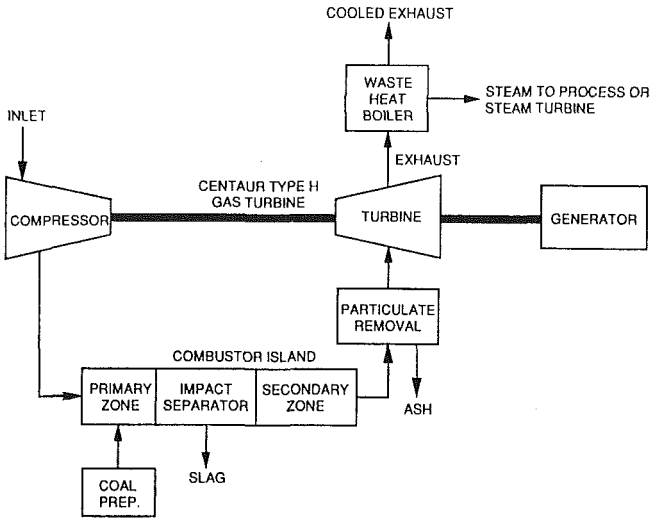

Fig. 1 Process flow diagram of direct coal-fired turbine systems

Types of Ceramic Filters

At the present time, three types of ceramic filter are being developed for advanced coal conversion processes: candle, crossflow, and fabric [1]. The candle filters are made by bonding ceramic fibers or grains to form a porous, hollow cylinder approximately 6 cm in diameter by 1–1.5 m long. The most common forms of candle filters are made using silicon carbide or alumina-silica grains and a clay binder. Some candles incorporate fibers or fine grains to form a "membrane" on the surface. Particulate-laden combustion gases enter a filter module containing a series of candles attached to a common tubesheet, as schematically shown in Fig. 2. The gases pass through the filters, trapping the particulates on the outside of the filter. As particles build up, the filter is cleaned periodically by jet pulsing through the filter in the reverse direction. The filter cake falls to the bottom of the chamber and is removed.

Table 1 Process system characteristics

System	Direct Coal-Fired Turbines
Combustor temperature, °C	1000 to 1350
Filter temperature, °C	980
Filter pressure, MPa	1
Atmosphere	Oxidizing
Gas Composition, Mole % (process)	
O_2	16
N_2	70
CO_2	8
SO_2	54 ppmv
H_2O	6
CH_4	trace
H_2S	trace
Particulate Loading, ppm	1000

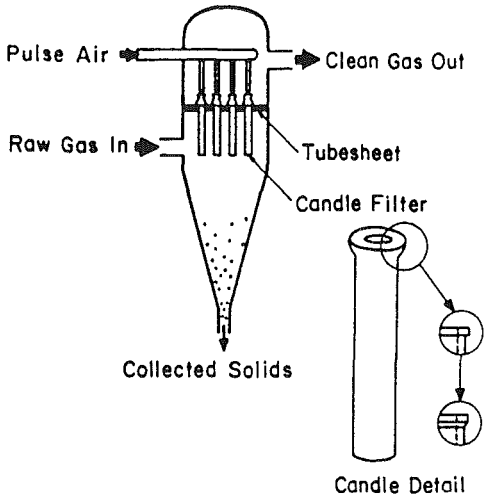

Fig. 2 Schematic of a candle filter module and ceramic candle filter element

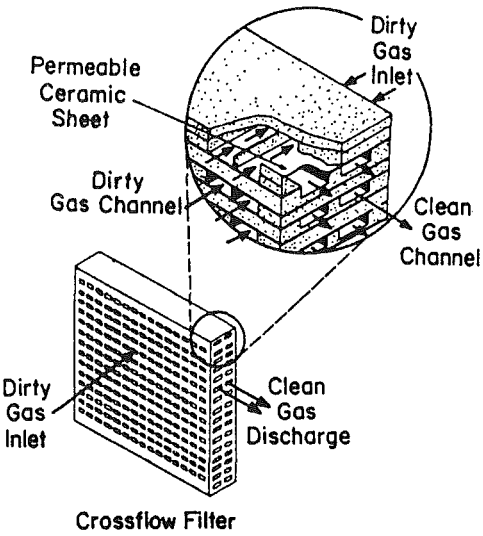

Fig. 3 Schematic showing operation of a ceramic crossflow filter element

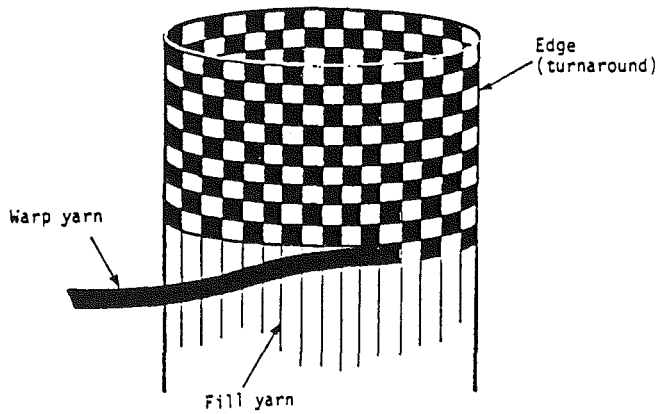

Fig. 4 Fabric filter tube

In an operating system, the filter will be pulsed (cleaned) from 3 to 20 times per hour.

The crossflow filter is the most compact of the filter geometries. These filters are fabricated by sintering together several layers of extruded cordierite or mullite. (Experimental Si_3N_4 crossflow filters are also under development.) The layers are corrugated and consist of porous, rectangular-shape channels. Alternating layers are offset 90 deg so that particulate-laden gases enter the channels in one direction, then filter to the channels on either side where the cleaned gases exit (see Fig. 3). Pulse cleaning gas is used to remove the dustcake deposited on the porous filter surfaces.

Fabric filters are flexible filters made from ceramic fibers formed into a mat or woven cloth, and fabricated into bag filters (see Fig. 4). The most common fibrous materials include silica-alumina-boria and alumina-silica. Fabric filters require the support of metallic screens or webs. The filters are configured into tubular shapes, and are also pulse cleaned.

Literature Review

Thermal-Mechanical Failure. Candle filters made from bonded ceramic grains are considered to be the strongest of the different types of ceramic filters available [1]. However, problems have been experienced with cracking of the candles, especially near the flange region, due to excessive mechanical and thermal stresses during operation. These stresses arise from several factors, including improper clamping arrangements, mechanical vibrations, stress concentrations from sharp contours on the candle surface, and thermal shock from cold pulse gas or during startup, shutdown, or upset conditions.

Proper clamping of the flanged candles has been a difficult design problem since the filter often operates at fairly high pressure differentials. The high pressure differential causes dust leakage at the flange/tubesheet interface unless significant force is used to hold the flange in place.

Recent candle failures have been experienced that have been determined to be caused by combinations of mechanical and thermal stresses. For example, at a gasifier test facility, candle filter failures were caused by unintentional water injection upstream of the filter module, resulting in thermal shock to the filters. Another set of failures occurred when filter elements were impacted by a slug of ash dislodged from upstream components [2].

A major problem encountered with the application of crossflow filters is delamination. The crossflow filter is composed of a series of individual filter "tiles," laminated together by sintering, usually with the addition of a ceramic cement. The cause of delamination is uncertain, although there are several possibilities including degradation of the cement, thermal or mechanical stresses, excess forces from the cleaning pulse, thermal shock from the cleaning pulse or during transient conditions such as startup and shutdown, and mechanical vibrations. The complicated structure of the crossflow-type filters results in a fairly complex and nonuniform stress distribution during transient conditions. Westinghouse estimated stress levels at the inside corner of the crossflow to be approximately equal to the material strength [3].

Besides delamination, other crossflow filter failures observed include flange breakage, breakage across the walls of

the filter, and collapse of the wall caused by excessive pressure drop across the filter. Although these failure modes are not frequently encountered, the occurrence of these failures points to a need for better understanding of the failure mechanisms involved [3].

Ceramic fabric filters are flexible and are, therefore, not susceptible to the thermal shock and plugging problems generally associated with rigid filter systems. However, the strength of the continuous filter materials is easily degraded by rough handling, excessive temperature, or corrosion. Fabric filters often experience failure due to excessive clamping forces on the filter, damages from the sharp edges of the clamp, thermal expansion differences of metal support cage and filter, improper tensioning of the filter bag, and the development of folds along the filter. The most frequently observed type of failure, however, is pinholing, with subsequent loss in particulate collection efficiency [4].

Chemical Degradation. Chemical attack is a primary limiting factor in long-term use of particulate filters at high temperatures. In general, ceramic or refractory materials are known to be chemically inert under a variety of conditions; however, elevated temperatures and pressures increase the susceptibility of most ceramics to chemical degradation. In addition, chemical reactivity tends to increase with temperature. In the case of alkali, considerable vaporization occurs at relatively low temperatures and becomes significantly greater as temperatures increase, as shown in Fig. 5. Thus, the potential chemical reactivities of candidate ceramic filter materials with the gaseous and particulate components of the coal combustion environment must be considered.

Alkali-Aluminosilicate Refractory Reactions. The corrosion of aluminosilicate materials by alkali compounds has been extensively studied. It has been found that refractory materials react with a number of alkali compounds, such as oxides, hydroxides, and carbonates or potassium and/or sodium [5]. A typical reaction proposed by Kennedy [6] is shown below:

$$11(Al_6Si_2O_{13}) + 26(NaOH) \rightarrow 22(NaAlSiO_4) + 4(NaAl_{11}O_{17}) + 13H_2O \quad (1)$$

The subsequent volume expansion (approximately 30 percent) associated with the reaction, results in degradation of the material. Similar reactions occur with potassium compounds. Calcium has also been found to cause degradation, but does not appear to be as reactive as sodium or potassium.

Wei et al. [7] studied the effects of coal combustion environments on high-duty fireclay refractories (approximately 37 percent alumina) using bricks from a coal-fired periodic kiln. The reaction products found on the exposed surface of the bricks consisted of a glassy phase with crystals of a sodium-calcium-alumina silicate. Other phases included corundum, mullite, and cristobalite. The glassy slag was high in alkali content, and likely resulted from the reactions of alkali oxides added with free silica to form low melting eutectics. Once formed, the glassy slag continued to dissolve free silica. Mullite was also attacked and dissociated into corundum and more free silica. The researchers concluded that the glassy slag protects the brick from further degradation as long as the slag viscosity is high, and that high-duty fireclay refractories perform satisfactorily at temperatures below 1260°C.

Hayden [8] studied the reactions of alkali vapors with various aluminosilicate (19 to 99 percent Al_2O_3) refractories. She concluded that resistance to alkali attack is increased by increasing alumina content up to 60 percent; however, increases of alumina content above 60 percent do not increase resistance to alkali attack. Hayden also stated that the resistance to alkali attack of aluminosilicates containing 60 percent or less alumina occurs because the reactions form a glassy phase on the surface, which tends to seal the surface of the ceramic and prevent deeper penetration of alkali compounds. Further, aluminosilicates with greater than 60 percent alumina do not form a surface glaze and thus limit the attack to the surface. These refractories are therefore susceptible to expansive reactions, which can cause spalling and/or catastrophic failure.

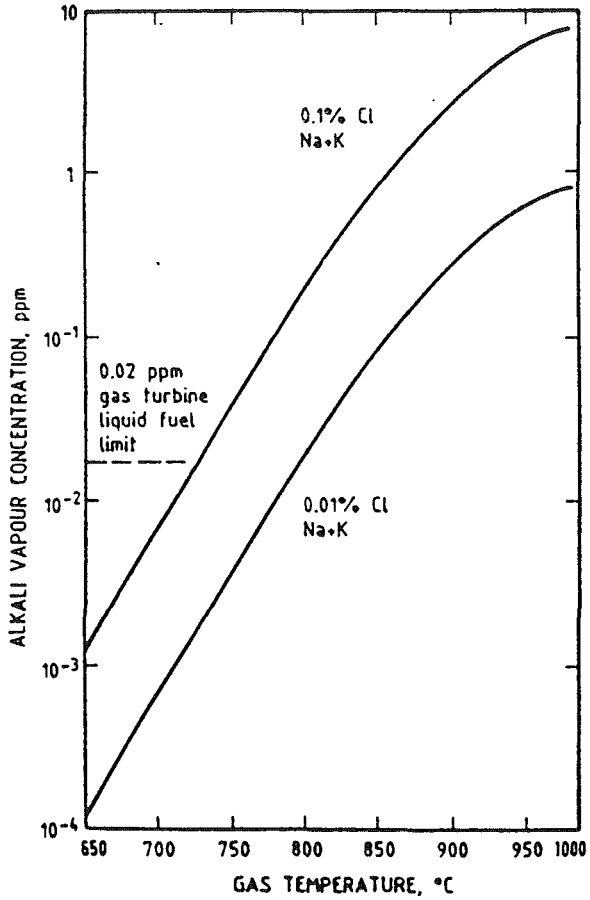

Fig. 5 Equilibrium alkali chloride (Na + K) vapor concentration as function of gas temperature for PFBC conditions [4]

Farris and Allen [9] studied alkali reactions with aluminosilicate refractory materials ranging from 42 to 90 percent Al_2O_3, using sodium and potassium carbonates. Reactions were found to occur between potassium oxide and the refractories at temperatures as low as 590°C, forming potassium aluminum silicates at low temperatures and potassium aluminates at temperatures above 1100°C. Similar reactions occurred with sodium oxide, forming sodium aluminum silicates at low temperatures and sodium aluminates at temperatures above 1100°C. The researchers concluded that refractories containing 42 to 70 percent alumina have the greatest resistance to alkali attack. Furthermore, to attain maximum alkali resistance, refractories containing less than 50 percent alumina require a mature microstructure and low porosity, whereas refractories containing more than 50 percent alumina require a fully bonded mullite matrix and minimum cristobalite and glass contents.

A study of alkali attack in blast furnaces by Havranek [10] covered several refractories, including aluminosilicates (45 to 90 percent alumina). Hot modulus of rupture data were obtained at different temperatures for refractory samples exposed to molten potassium carbonate in a reducing atmosphere for 5 h. Test results indicated that mullite-bonded alumina maintained good strength after alkali attack at 1400°C, whereas dense fireclay refractories maintained good strength after alkali attack only at low temperatures.

Rigby et al. [11] reported that high porosity and the presence of vanadium adversely affect the alkali resistance of refractories. The results of Federer and Tennery [12] support this conclusion. They also found that calcium sulfate along with

vanadium pentoxide causes [9] significant corrosion of mullite-based refractories.

Alkali–SiC and Si_3N_4 Reactions. Silicon nitride and silicon carbide refractories are generally coated with a layer of silica (usually cristobalite) or an aluminosilicate to prevent oxidation. The silica coating is actually a processing byproduct since it is difficult to eliminate all oxygen during the manufacture of the material [13].

Corrosion of silicon nitride and silicon carbide by molten salts was reported by Fox et al. [14] following experiments in which commercially availabe SiC and Si_3N_4 were exposed to combustion gas containing sodium sulfate at various temperatures. They found that corrosion occurred at temperatures as low as 885°C. Postexposure observation of the refractory surfaces revealed the presence of a glassy corrosion product that contained large bubbles. Upon removal of the glassy phase, extensive pitting was observed in both materials. The sodium appeared to have caused significant damage to the protective silica layer, thus allowing oxygen to react with the unprotected SiC and Si_3N_4. The proposed reactions are shown below:

$$SiC + 3/2O_2 \rightarrow SiO_2 + CO \quad (2)$$

$$xSiO_2 + Na_2SO_4 \rightarrow Na_2O \cdot xSiO_2 + SO_3 \quad (3)$$

$$Si_3N_4 + 3O_2 \rightarrow 3SiO_2 + 2N_2 \quad (4)$$

$$xSiO_2 + Na_2SO_4 \rightarrow Na_2O \cdot xSiO_2 + SO_3 \quad (5)$$

Smialek et al. [15] concluded that this type of corrosion causes significant loss of strength, up to 50 percent for SiC and up to 35 percent for Si_3N_4.

Federer's [16] work on the corrosion of SiC by halides (HCl, NaF, and HF) at 1200°C showed that HCl had little effect on SiC, but that the sodium-containing halides caused severe damage to the protective coating by forming a bubbly glaze and causing pitting in the SiC. A buildup of a glassy phase observed at the bottom of the test samples indicated that partial melting of the glaze had occurred at temperatures lower than 1200°C. The flexure strength of the samples was not affected. Several reaction mechanisms were suggested as follows:

$$2NaCl + SiO_2 \rightarrow SiCl_2 + Na_2O + 1/2O_2 \quad (6)$$

$$2NaF + SiO_2 \rightarrow SiF_2 + Na_2O + 1/2O_2 \quad (7)$$

Coating SiC with, for example, alumina was recommended to reduce the corrosion caused by sodium-containing halides.

Bourne and Tressler [17] performed strength tests at various temperatures on samples of Si_3N_4, both reaction sintered and hot pressed, after exposure to either molten NaCl or a NaCl–Na_2SO_4 eutectic at 1000°C. Large reductions in strength occurred in both types of Si_3N_4 for both molten salts. They concluded that corrosion by sodium-containing compounds causes increases in the size of critical flaws. Further, contaminants were believed to penetrate along grain boundaries in hot-pressed Si_3N_4 and through pores in the reaction sintered material.

Sato et al. [18] studied the effects of exposing Si_3N_4 and SiAlON of various types to potassium sulfate and potassium carbonate melts at temperatures ranging from 925 to 1300°C. Their results were similar to those observed by Bourne and Tressler [17] and Fox et al. [14] for sodium salts. However, they also found that the presence of aluminum and/or yttrium reduced the rate of corrosion for both potassium salts.

Easler et al. [19] examined the interactions of calcium and iron-rich coal slags with SiC in oxidizing and reducing atmospheres. They found that, at temperatures below 1150°C, no significant corrosion occurred. Corrosion at higher temperatures, however, was found to be extensive, particularly at temperatures above 1250°C. In addition, it was reported that at higher temperatures, basic slags are much more corrosive than acidic slags.

Becher [20] carried out experiments similar to those of Easler et al. [19]; however, Si_3N_4 ceramics were also included, and the slags were known to have lower concentrations of calcium and iron compounds and contained significant amounts of sodium and potassium oxides. Results of these experiments indicated that SiC was more resistant than Si_3N_4 to corrosion from the slag.

Steam-Refractory Reactions. Sadler et al. [21, 22] studied steam-induced silica volatilization in high-silica, alumina-containing refractories as a function of temperature and pressure. Their experiments were conducted at steam partial pressures up to 7 MPa (1000 psig) and at temperatures up to 1400°C. They concluded that steam-induced silica losses from silica-alumina refractories are insignificant below 1000°C at steam partial pressures up to 1000 psig, and that small weight losses (<3 percent) occur at higher temperatures if steam partial pressure is high (7 MPa). However, Sadler et al. [21] observed that SiC refractories (direct, silicate, and oxynitride-bonded) either severely bloated or completely disintegrated during exposures to high pressure (7 MPa) steam-containing environments at temperatures of 760 to 980°C. Horn et al. [23] suggested that this corrosion is caused by a two-step reaction where H_2O dissociates and the oxygen reacts with SiC. He recommends against the use of silicon carbide in steam-containing environments at temperatures above 1000°C.

Tressler et al. [24] found that water vapor greatly increased the rate of oxidation of SiC by acting as an oxidant at the reaction interface and reducing the viscosity of the SiO_2 layer by the presence of OH^- ions.

Adams et al. [25] investigated the effect of coal combustion environments on candidate structural ceramics for gas turbine applications. Environmental exposure tests of SiC, Si_3N_4, Al_2O_3–ZrO_2, $MgAl_2O$ spinel, AlN, SiC–Al_2O_3, and SiAlON refractories were conducted at temperatures ranging from 1000 to 1425°C. Test results showed that SiC, Si_3N_4, SiAlON, and SiC–Al_2O_3 materials were least affected by the exposures. Surface analysis showed the presence of S, Fe, Cu, Zn, Ca, and Ti in the exposed samples. Water vapor was found to cause oxidation in the silicon-based materials. Si_3N_4 and SiC–Al_2O_3 materials were found to have the greatest strength retention.

Combined Chemical and Thermal Degradation. The effects of chemical attack and thermal stresses are known to be detrimental to the service life and performance of ceramic materials. In the case of aluminosilicates, the formation of viscous melts due to alkali attack was found to reduce strength due to an increased rate of creep and loss of structural integrity. A more damaging effect is caused by the formation of expansive compounds, which, due to their volume expansion, cause cracking and spalling [6, 7, 26].

The formation of amorphous or glassy phase compounds, such as ternary glasses formed in the Na_2O–Al_2O_3–SiO_2 or K_2O–Al_2O_3–SiO_2 systems, combined with thermal cycling, can seriously damage ceramic materials due to strength reductions and increased thermal expansion coefficients causing spalling and cracking from increased thermal stress [24, 26, 27].

The formation of additional phases in a ceramic system can reduce mechanical strength in several ways. First, the new phase acts as a point stress concentration. The formation of expansive phases such as β–Al_2O_3 and the oxidation of SiC and Si_3N_4 along existing crack or grain boundaries are examples of this type of strength degradation. Second, the formation of viscous melts degrades the creep resistance of a material. Third, the formation of amorphous or glassy phases will cause the nucleation and growth of cracks and flaws due to the low strength and thermal expansion mismatch [27].

Pilot Plant Degradation Experience

Laboratory examination of filters exposed to PFBC and gasifier environments led the authors to the conclusion that

degradation of the ceramic materials occurred as a result of chemical attack or a combination of mechanical and thermal stresses. Visual inspection of candle filters exposed at high temperatures to PFBC and gasification atmospheres disclosed cracking either at the flange or in the body of the candle. Tensile strength measurements showed significant loss in strength of the SiC candle filters after only 500 h of operation compared to unexposed specimens. This marked decrease in strength results from binder depletion, chemical reaction between binder and gas phase compounds, and thermal shock during pulse cleaning.

Scanning electron microscopy and energy dispersive X-ray (SEM/EDX) analyses of failed candles indicated a marked decrease in binder content, probably due to liquification and flowing of the binder phase, as well as reactions between the binder phase and alkali metals, calcium, and sulfur. Thermal analyses of transients caused by pulse cleaning indicate that the candle can be subjected to stresses of approximately half the "as-received" strength, which over time can cause thermal fatigue [1]. Once the candle strength has degraded, the thermal transients can be approximately equal to the material strength.

The primary failures associated with the crossflow filter appeared to be flange cracking and delamination of the layers. Thermal analyses have indicated that the crossflow filter undergoes stresses during pulse cleaning, which are approximately equal to the "as-received" material strength [3].

Ceramic fabric filters examined showed splitting of the weave or pinholing. Pinholing is usually caused by a weave defect and can be prevented by adequate quality control. Weave splitting is usually caused by either handling of the material, improper filter mounting, or changes in the ceramic fabric strength. If the ceramic fabric materials are handled roughly, fibers are broken and the material is weakened. Improper filter mounting, causing folds in the fabric, can lead to broken fibers, and subsequent weakening of the material. SEM/EDX and XRD examinations of the ceramic fibers indicated that reactions with alkali materials in the gas stream and ash, as well as changes in crystalline structure, had occurred.

Conclusions

Ceramic materials or ceramic composites used in DCFT applications will be exposed to conditions that may degrade strength and limit service life due to chemical and thermal effects. Further, the mechanical limitations of ceramic materials pose significant problems when such materials are exposed to dynamic environments. The available information provides a guide to solving these problems but does not address the specific problems that will be encountered using ceramic filters for hot gas clean-up. The following conclusions can be drawn from the literature and filter examinations:

- Presently available ceramic filters have serious mechanical limitations, which limit their use in DCFT systems. Improved designs to reduce mechanical stresses within the filter device are needed. An improvement in thermal properties may be necessary to eliminate thermal shock and thermal degradation.
- Chemical attack by alkali metal compounds is a serious, long-term problem for the aluminosilicates. The rate of this degradation increases with temperature and is enhanced by the presence of vanadium compounds. The 45 to 60 percent alumina materials appear to be the most resistant to alkali attack.
- Chemical attack of SiC and Si_3N_4 by steam and alkali metal compounds appears to pose possible problems. Both reactions are generally temperature dependent.

The literature provides a significant amount of information concerning chemical attack in coal combustion environments. This information can in part be used to screen potential materials or combinations of materials. However, there appears to be a need to examine the chemical degradation of the non-oxide compounds further and to determine the effects of chemical degradation at temperatures below 1100°C. The thermal and mechanical data available provide only a general guide to material selection, and there is a need for further investigation in this area.

References

1 Sawyer, J., "Assessment of the Causes of Failures of Ceramic Filters for Hot-Gas Cleanup in Fossil Energy Systems and Determination of Materials Research and Development Needs," Oak Ridge National Laboratory, ORNL/Sub/86-57964/01, Oak Ridge, TN, Jan. 1989.

2 "Performance of Porous Sintered Ceramic Filters," Materials and Components in Fossil Energy Applications, U.S. Department of Energy Newsletter, DOE/FE-0080/80, Oak Ridge Operations, June 1989.

3 Ciliberti, D. F., Lippert, T. E., and Kleiner, R. N., "A Mechanical Analysis of a Ceramic Crossflow Filter," Westinghouse Report to DOE under contract No. DE-AC21-86MC23252.

4 Chang, R., Sawyer, J., and Lips, H., "Performance Evaluation of Ceramic Fabric Bag Filter on a Bench-Scale Coal Gasifier," Acurex Final Report to DOE under contract No. DE-AC21-84MC21337.

5 Diercks, D. R., and Stahl, D., "A Review of Refractory Materials for the Memphis Industrial Fuel Gas Demonstration Plant," Argonne National Laboratory, ANL/FE-81-60, Argonne, IL, Sept. 1981.

6 Kennedy, C. R., "Alkali Attack on a Mullite Refractory in the Grand Forks Energy Technology Center Slagging Gasifier," *J. Matr. Energy Systems*, Vol. 3, 1981, p. 27.

7 Wei, G. C., Tennery, V. J., and Harris, L. A., "Effects of Alternate Fuels Report No. 1, Analysis of High-Duty Fireclay Refractories Exposed to Coal Combustion," Oak Ridge National Laboratory, ORN/TM-5909, Oak Ridge, TN, Dec. 1977.

8 Hayden, R. F., M.S. Thesis, Virginia Polytechnic Institute and State University, Blacksburg, VA, 1976.

9 Farris, R. E., and Allen, J. E., "Aluminous Refractories—Alkali Reactions," *Iron Steel Eng.*, Vol. 50, 1973, pp. 67–74.

10 Havranek, P. H., "Alkali Attack on Blast Furnace Refractories," *J. Brit. Ceramic Soc. Trans.*, Vol. 77, 1978, pp. 92–97.

11 Rigby, G. R., and Hutton, R., "Actions of Alkali and Alkali-Vanadium Oxide Slags on Alumina-Silica Refractories," *J. Am. Ceram. Soc.*, Vol. 45, 1962, pp. 68–73.

12 Federer, J. I., and Tennery, V. J., "Effects of Alternate Fuels, Report No. 7: Analysis of Failure of a Mullite-Based Refractory Brick in an Industrial Oil-Fired Burner," Oak Ridge National Laboratory, ORNL/TM, Oak Ridge, TN, July 1979.

13 Evans, A. G., and Davidge, R. W., "The Strength and Oxidation of Reaction-Sintered Silicon Nitride," *J. Mater. Sci.*, Vol. 5, 1970, pp. 314–325.

14 Fox, D. S., Jacobson, N. S., and Smialek, J. L., "The Molten Salt Corrosion of SiC and Si_3N_4," Structural Ceramics Workshop held in Cleveland, Ohio; sponsored by NASA, Washington, DC, May 1986.

15 Smialek, J. L., Fox, D. S., and Jacobson, N. S., "Hot Corrosion Attack and Strength Degradation of SiC and Si_3N_4," NASA/89820, Apr. 1987.

16 Federer, J. I., Robbins, J. M., Jones, P. J., and Hamby, C., Jr., "Corrosion of SiC Ceramics in Synthetic Combustion Atmospheres Containing Halides," Oak Ridge National Laboratory, ORNL-6258, Oak Ridge, TN, Dec. 1985.

17 Bourne, W. C., and Tressler, R. E., "Molten Salt Degradation of Si_3N_4 Ceramics," *Am. Ceram. Soc. Bull.*, Vol. 59, 1980, pp. 443–452.

18 Sato, T., Koike, Y., Endo, T., and Shimada, M., "Corrosion and Strength Degradation of Si_3N_4 and Sialons in K_2CO_3 and K_2SO_4 Melts," *J. Mater. Sci.*, Vol. 23, 1988, pp. 14–51.

19 Easler, T. E., Tan, C., and Putz, L. M., "Influence of Oxidizing and Reducing Environments on Coal-Slag-Induced Corrosion of Silicon Carbide Ceramics," Argonne National Laboratory, ANL/FE-85-11, Argonne, IL, Oct. 1985.

20 Becher, P. F., "Strength Degradation in SiC and Si_3N_4 Ceramics by Exposure to Coal Slags at High Temperatures," *J. Mater. Sci.*, Vol. 19, 1984, pp. 2805–2814.

21 Sadler, L. Y., III, Heystek, H., Raymon, N. S., and Clancy, T. A., "Refractories for Dry Ash Coal Gasifiers," U.S. Bureau of Mines Report of Investigations 8913, 1984.

22 Sadler, L. Y., III, and Davis, E. G., "Steam-Induced Volatilization of Silica From Refractories," U.S. Bureau of Mines Report of Investigations 9052, 1986.

23 Horn, F. L., Fillo, J. A., and Powell, J. R., "Performance of Ceramic Materials in High Temperature Steam and Hydrogen," *J. Nuc. Mater.*, Vol. 85/86, 1979, pp. 439–443.

24 Tressler, R. E., Costello, J. A., and Zheng, Z., "Oxidation of Silicon Carbide Ceramics," *Indus. Heat Exch.*, Vol. 6, Nov. 1985, pp. 307–314.

25 Adams, J. W., Larsen, D. C., and Ruh, R., "Corrosion of SiC, Si_3N_4, and Oxide Ceramics in Coal Gas Combustion Products," *Indus. Heat Exch.*, Vol. 6, Nov. 1985, pp. 315–321.

26 Federer, J. I., "Corrosion of Materials by High Temperature Industrial Combustion Environments—A Summary," Oak Ridge National Laboratory, ORNL/TM-9903, Oak Ridge, TN, Feb. 1986.

27 Kingery, W. D., "Factors Affecting Thermal Stress Resistance of Ceramic Materials," *Amer. Ceram. Soc.*, Vol. 38, No. 1, 1955.

W. Tabakoff

A. Hamed

M. Metwally

Department of Aerospace Engineering and Engineering Mechanics, University of Cincinnati, Cincinnati, OH 45221

Effect of Particle Size Distribution on Particle Dynamics and Blade Erosion in Axial Flow Turbines

This work presents the results of an investigation conducted to study the effect of coal ash particle size distribution on the particle dynamics, and the resulting blade erosion in axial flow gas turbines. The particle dynamics and their blade impacts are determined from a three-dimensional trajectory analysis within the turbine blade passages. The particle rebound conditions and the blade material erosion characteristics are simulated using empirical equations, derived from experimental measurements. For the typical ash particle size distribution considered in this investigation, the results demonstrate that the size distribution has a significant influence on the blade erosion intensity and pattern.

Introduction

Gas turbines operating with working fluids containing solid particles are subjected to corrosion and erosion. A permanent loss of turbomachinery performance results from the change in the blade shape and the increased blade surface roughness as reported by Tabakoff (1984) for axial flow compressors. Experience with coal-burning gas turbines have shown that even small ash particles, of mean diameters from 1 to about 30 μm, can be very damaging to exposed turbine components. It is very difficult to remove these particles from the gas stream with conventional separation techniques. In order to minimize the adverse effects of particle erosion, a knowledge of the particle trajectory path, including the probable impact locations and the particle impact characteristics, is required. An analytical tool was developed by the authors to provide such knowledge of the particle behavior through the three-dimensional blade passages of axial flow turbomachinery.

Turbomachinery blade erosion has been the subject of many analytical and experimental investigations by the authors (Hamed and Fowler, 1983; Hamed et al., 1986; Tabakoff and Hamed, 1977; Tabakoff et al., 1988; Tabakoff, 1987, 1988). It has been shown that the particle characteristics significantly affect the blade impact patterns as reported by Tabakoff and Hamed (1986). In multistage axial flow turbines, the large sand particles were found to rebound after they impact the blade row leading edge, and re-enter the preceding blade row to impact its blade trailing edge suction side (Hamed, 1984). On the other hand, the small ash particle trajectories follow the gas flow field more closely.

Although it is well documented that the particle size has a strong effect on the particle trajectories and the impact patterns (Hamed, 1981), almost all blade erosion studies have been conducted assuming a uniform particle size based on the average diameter. The coal ash particle size distribution extends over a wide range of particle diameters as shown in Fig. 1. The study of the blade erosion using the actual particle size distribution will provide more accurate results. In this paper, the computation of the three-dimensional particle trajectory, and the resulting blade erosion, are conducted in a two-stage axial flow turbine using actual CG&E ash particle size distributions. The results are presented for the blade erosion parameter, impact frequency, impact velocity, and impingement angle contours on the blade pressure surfaces. The distribution of these erosion parameters over the blade surfaces provides valuable information that can be used in taking specific measures to alleviate the blade erosion problem. The computed results of the particle trajectories and blade erosion parameters for the actual size distribution are compared with those for a uniform particle size based on the weight average particle diameter.

Analysis

The equations governing the particle motion in the turbomachinery flow field written in cylindrical polar coordinates relative to a frame of reference fixed with respect to the rotating blade are:

$$\frac{d^2r_p}{d\tau^2} = F_r + r_p\left(\frac{d\theta_p}{d\tau} + \omega\right)^2 \tag{1}$$

$$r_p\frac{d^2\theta_p}{d\tau^2} = F_\theta - 2\frac{dr_p}{d\tau}\left(\frac{d\theta_p}{d\tau} + \omega\right) \tag{2}$$

$$\frac{d^2z_p}{d\tau^2} = F_z \tag{3}$$

where r_p, θ_p, and z_p define the particle location in cylindrical polar coordinates, and ω is the blade angular velocity. The centrifugal force and Coriolis acceleration are represented by the last term on the right-hand side of Eqs. (1) and (2). The

Contributed by the International Gas Turbine Institute and presented at the 35th International Gas Turbine and Aeroengine Congress and Exposition, Brussels, Belgium, June 11–14, 1990. Manuscript received by the International Gas Turbine Institute January 14, 1990. Paper No. 90-GT-114.

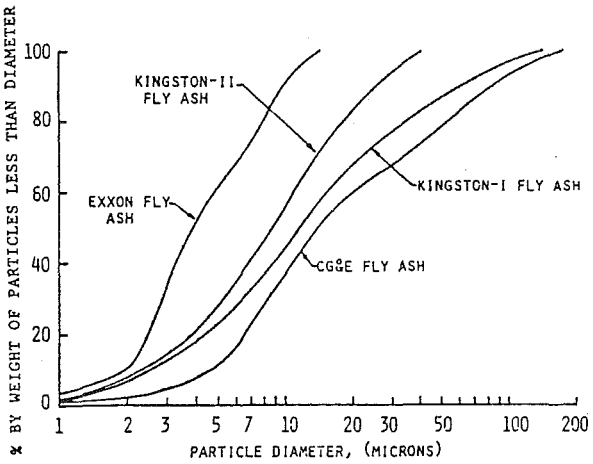

Fig. 1 Fly ash particle size distribution

first term on the right-hand side of Eqs. (1)–(3) represents the force of interaction between the two phases, per unit mass of particles. This force is dependent on the relative velocity between the particles and the gas flow, as well as the particle size and shape. Under the particulate flow conditions in turbomachines, the effects of the forces due to gravity and interparticle interactions are negligible, compared to those due to the aerodynamic and centrifugal forces. The force of interaction between the two phases is dominated by the drag due to the difference in velocity between the solid particles and the gas flow. The force of interaction per unit mass of solid particles is given by

$$\bar{F}=\frac{3}{4}\frac{\rho}{\rho_p}\frac{C_D}{d}\left[\left(V_r-\frac{dr_p}{d\tau}\right)^2+\left(V_\theta-\frac{d(r_p\theta_p)}{d\tau}\right)^2+\left(V_Z-\frac{dz_p}{d\tau}\right)^2\right]^{1/2}(\bar{V}-\bar{V}_p) \quad (4)$$

where V_r, V_θ, and V_z represent the relative gas velocities in the radial, circumferential, and axial directions, respectively, and ρ and ρ_p are the gas and solid particle material densities, d the particle diameter, and C_D the particle drag coefficient. This coefficient is dependent on the Reynolds number, which is based on the relative velocity between the particle and the gas. Empirical relations, as those presented by Tabakoff et al. (1985), are used to fit the drag curve over a wide range of Reynolds numbers.

Particle Trajectories. The particle trajectory calculations consist of numerical integration of Eqs. (1)–(3) in the flow field, up to the point of blade, hub, or tip impact. The magnitude and direction of particle rebounding velocity after these impacts are dependent on the impacting conditions and the particle and surface materials.

The particle rebounding conditions are determined from empirical correlations of the restitution parameters as shown by Hussein and Tabakoff (1973). These correlations are based on the experimental measurements of the particle's impacting and rebounding velocities near the metal surface. The LDV measurements are obtained for particle-laden flows over metal samples set at various angles to the flow in a special tunnel described by Tabakoff et al. (1980) and Tabakoff and Hamed (1982). The restitution ratios were found to be mainly dependent upon the impingement angle (Tabakoff et al., 1985; Tabakoff and Malek, 1987) for a given particle-material combination.

Empirical correlations are used in the present study to determine the magnitude and direction of the particle rebounding velocity after the surface impacts. The following empirical correlations were obtained by Tabakoff et al. (1985) for the restitution parameters in terms of the impingement angle for fly ash particles impacting a 410 stainless steel target:

$$V_{P_R}/V_{P_I}=1-0.90847\,\beta_I+0.3072\,\beta_I^2+0.05695\,\beta_I^3 \quad (5)$$

and

$$\beta_R/\beta_I=1-0.38746\,\beta_I+0.51442\,\beta_I^2+0.45094\,\beta_I^3 \quad (6)$$

where V_{P_I} and β_I represent the particle impact velocity and impingement angle, while V_{P_R} and β_R are the particle rebounding velocity and angle.

In the case of rotor blade impacts, the velocities and angles of impact and rebound are considered relative to the rotating blade. The particle trajectory after each blade impact and the particle distribution through the blade are influenced by the rebound correlations of the local turbine blade geometry as reported by Hussein and Tabakoff (1973). The blade airfoil, hub, and casing geometry must therefore be accurately represented in the trajectory analysis as it strongly influences the predicted particle dynamics. In particular, since a large number of particles impact the blunt leading edges of the turbine blades before entering the blade passage, the blade leading edge geometry has a strong influence on the rest of the trajectory calculations. In order to represent the radial variation in the blade shape on the particle trajectory, the blade surface coordinates are specified at a number of sections between the hub and tip.

Turbine Blade Passage Flow Fields. The large flow turning angles generally encountered in turbine blading produce large pitchwise as well as radial and axial flow field variations. The computed three-dimensional flow field data, on a representative grid in the blade-to-blade passage, are used to interpolate for the flow properties at each time step during the numerical integration of the particle equations of motion.

In the present study, the flow field in a blade passage is synthesized from a number of blade-to-blade stream surface solutions using the Katsanis code (1965). The pitchwise and streamwise variation in the flow properties are reflected in each flow field solution on a blade-to-blade stream surface. The influence of the hub and tip contours and the hub-to-tip variation in the blade shapes, on the other hand, are represented in the stream surface shapes and stream filament thickness, as determined from a midchannel hub-to-tip stream surface solution by Katsanis and McNally (1977).

Blade Erosion. Sample coupons from the blade material are tested in the erosion tunnel to provide experimental measurements of the erosion characteristics by the particles as reported by Hamed and Fowler (1983). The target erosion was found to be dependent upon the particle impact velocity, impingement angle, and on the flow and target temperatures for a given particle target material combination as shown by Tabakoff and Hamed (1977). Experimental measurements for fly ash particles impacting 410 stainless steel were used to obtain the following empirical equation. The erosion mass parameter, ϵ, is defined as the ratio of the eroded mass of target material to the mass of impinging particles

$$\epsilon=K_1\left[1+CK\left\{K_{12}\sin\left(\frac{90}{\beta_o}\beta_1\right)\right\}\right]^2 V_1^2\cos^2\beta_1[1-R_t^2]+K_3(V_1\sin\beta_1)^4 \quad (7)$$

where V_1 and β_1 are the impact velocity and impingement angle, respectively.

K_1, K_{12}, and K_3 are material constants, which are given below for fly ash particles impacting a 410 stainless steel target:

$$K_1=1.505101\times10^{-6}$$

$$K_{12} = 0.296077$$

$$K_3 = 5.0 \times 10^{-12}$$

CK is a parameter whose value depends on β_1 and the angle of maximum erosion, β_o, as follows

$$CK = 1 \quad \text{for} \quad \beta_1 \leq 2\beta_o$$

$$CK = 0 \quad \text{for} \quad \beta_1 > 2\beta_o$$

and

$$R_t = 1 - 0.0016 V_1 \sin \beta_1$$

The computation of blade erosion combines the empirical correlation for the mass erosion parameter (Eq. (7)) with the results of the particle trajectory calculations. The latter provide the impact velocities and impingement angles for a large number of particle trajectories.

Calculation Procedure

Two separate computer codes are used, one for calculating particle trajectories in the blade passages and another for predicting the blade erosion. The output of the particle trajectory code consists of three files. The first file provides the input for particle trajectory plots. The second particle trajectory output file contains all particle exit conditions from a given blade row, and is used as input to provide the initial conditions for the particle trajectories in the following blade row. These data are first adapted to a new frame of reference, which is fixed in each blade row. The particle axial and radial location is not affected by the relative motion between successive blade rows. The circumferential variation in the particle distribution at the exit of a given blade row is evened out at the entry to the following blade row due to the relative motion between successive blade rows. This effect is simulated in the computations by redistributing the particles randomly in the circumferential direction, in the new frame of reference, which is fixed relative to the subsequent blade row. The third file contains all computed particle impact data, including the impact locations, the impact velocity, and impingement angle relative to the solid surfaces, for use in the code for blade surface erosion predictions.

The code for blade surface erosion computations uses as input the particle impact data, and the various coefficients of the empirical equation for blade material erosion. The output from this program includes the blade erosion distribution, as well as the distribution of the impact velocity, impingement angles, and the frequency of particle blade surface impacts.

Results and Discussion

The particle trajectory and blade erosion analyses were carried out through a two-stage axial flow turbine, which was described by Roelke et al. (1966). The presented blade erosion results were obtained from the trajectories corresponding to 75,000 ingested particles or 22×10^{-5} grams of ash in the gas turbine for standard inlet air equivalent conditions at 1893 rpm and 7.071 lb/sec weight flow. The results are presented for the particle trajectories and the resulting blade erosion, for the CG&E particle size distribution shown in Fig. 1. For this purpose a histogram was constructed for nine different particle sizes contained within Fig. 1 and subsets of particle trajectories were obtained for the nine discrete particle sizes. The computed blade erosion is based on the cummulative erosion from the nine sets. The results of the particle trajectories and blade erosion computations are also presented for uniform particles, of a weight-average particle diameter. These results are used for comparison, to determine the effect of particle size distribution.

At the inlet to the gas turbine, the particles were assumed to have no velocity lag relative to the gas. Their spatial location

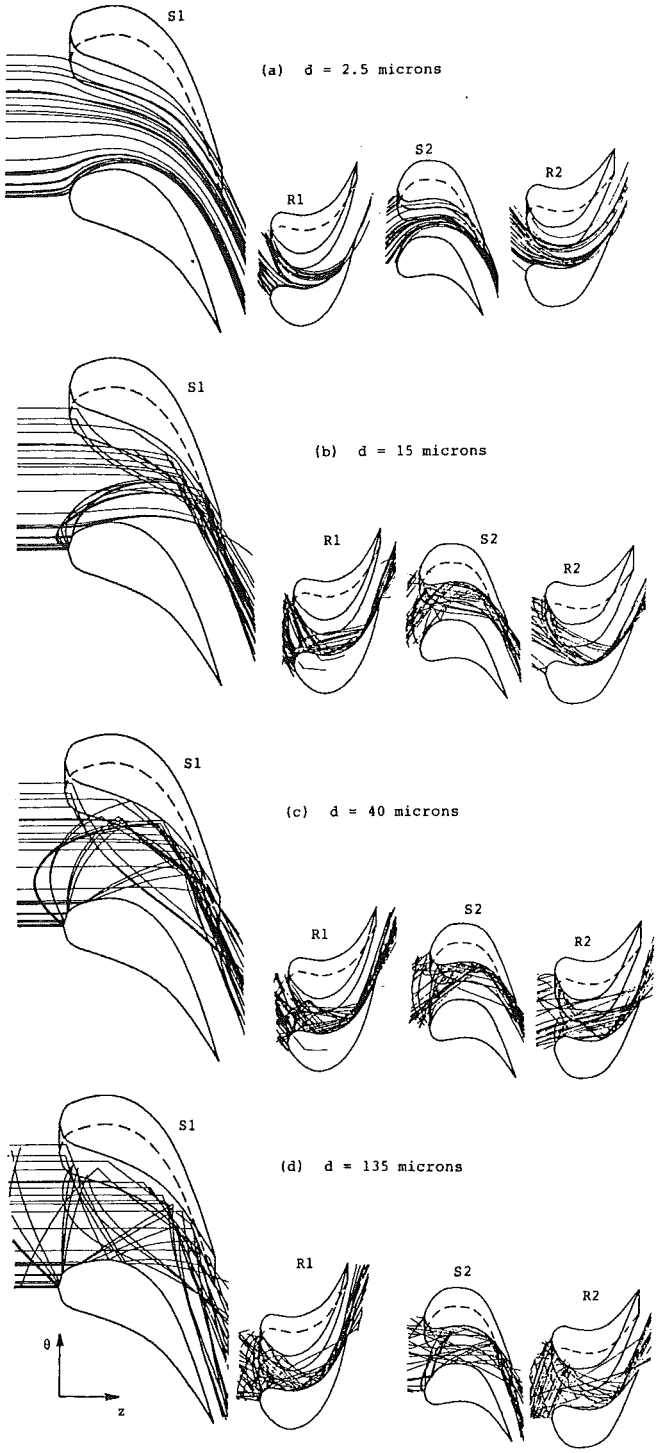

Fig. 2 Projection of particle trajectories in the θ-z plane

was randomly distributed, according to the mass flow, using statistical methods. The results presented here show typical particle trajectories and the associated blade erosion pattern. The results are also presented for particle blade impact data that influence erosion including the distribution of impact frequency, impact velocity, and impingement angle over the blade surface.

Figures 2 and 3 show sample projections of the particle trajectories through the blade rows in the z-θ plane and the z-r plane for four typical particle diameters of 2.5, 15, 40, and 135 μm. The effect of particle size on the trajectories can be clearly seen in these figures. Figure 2 shows that the deviation of the particle trajectories from the streamlines in-

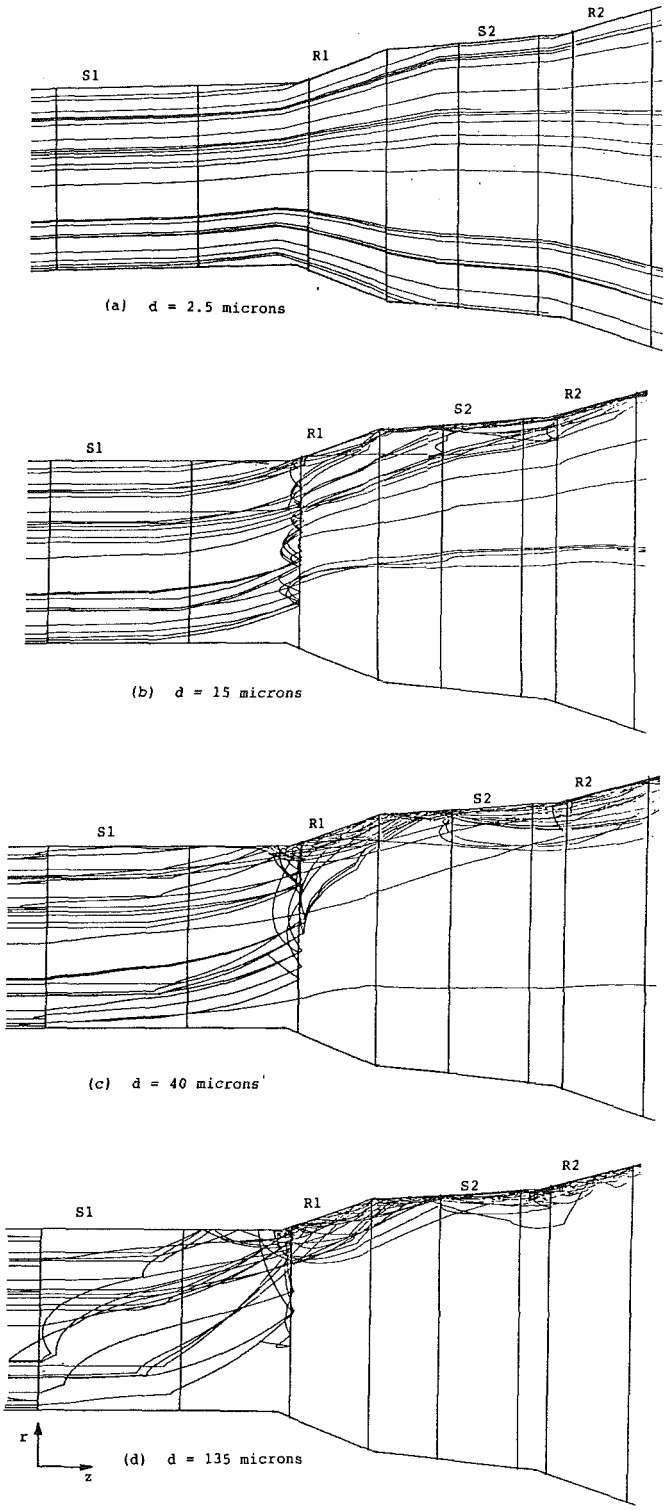

Fig. 3 Projection of particle trajectories in the r-z plane

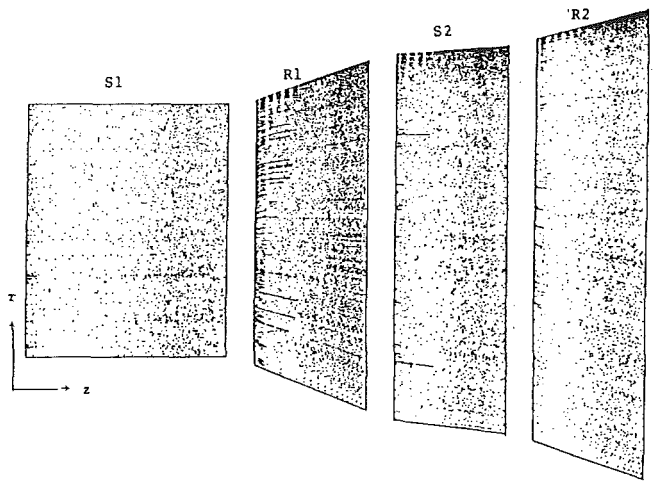

Fig. 4 Impact location for the nonuniform particles

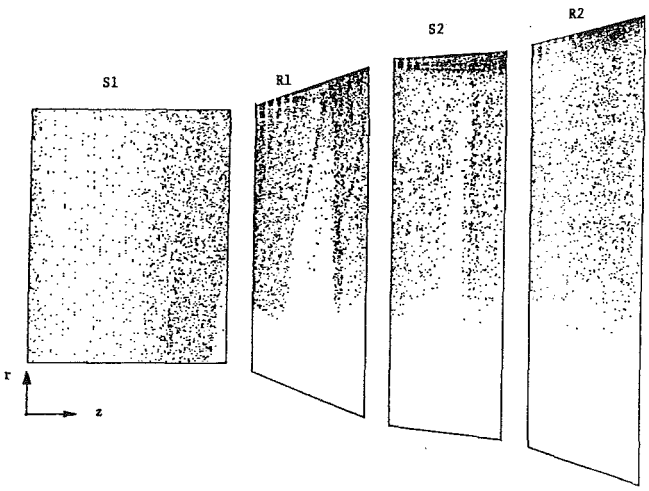

Fig. 5 Impact location for the uniform particles

creases with the particle size. Consequently, large particles have more impacts with the blade surfaces. The projection of particle trajectories in the r-z plane (Fig. 3) demonstrates the strong influence of blade impacts on the particle radial motion. The larger particles centrifuge faster after they impact the rotor blade suction surface near the leading edge. These impacts are caused by the negative incoming incidence angle of the larger particles relative to the rotor blade. This is caused by the fact that the large particles do not accelerate in the stator flow field as fast as the small particles. Their lower absolute velocities affect their inlet direction relative to the rotor blade rows.

The computed particle impact locations over the blade pressure surface in the two-stage turbine are presented in Figs. 4 and 5 for nonuniform and uniform particle size distribution, respectively. The results indicate that the particle centrifuging is more pronounced in the case of uniform particles as evidenced by the absence of impacts near the hub. This effort is less noticeable in the impacts of the actual nonuniform particle size. This is due to the negligible effect of blade impacts on the radial motion of the smaller particles, which continue to impact the entire blade pressure surface as shown in Fig. 6.

The blade erosion prediction is based on the particle computed impact data as determined from the particle trajectory calculations, and erosion empirical equation. The blade mass erosion parameter, ϵ_b, is defined as the blade mass removal per unit area of the blade surface per unit mass of ingested particles in (mg m^{-2} g^{-1}). The blade surface impact frequency, γ, is defined as the number of particle impacts per unit area of blade surface per unit mass of ingested particles (m^{-2}/g). The results are also presented for other parameters affecting the blade erosion, namely the weighted average particle impact velocity and impingement angles. The erosion results will only be presented for the blade pressure surfaces, since the blade suction surface erosion was found to be insignificant because of the small number of particle impacts.

The distribution of the blade erosion parameter, frequency of particle impacts, the particle impacting velocity, and their impingement angle, over the first stator blade pressure surface

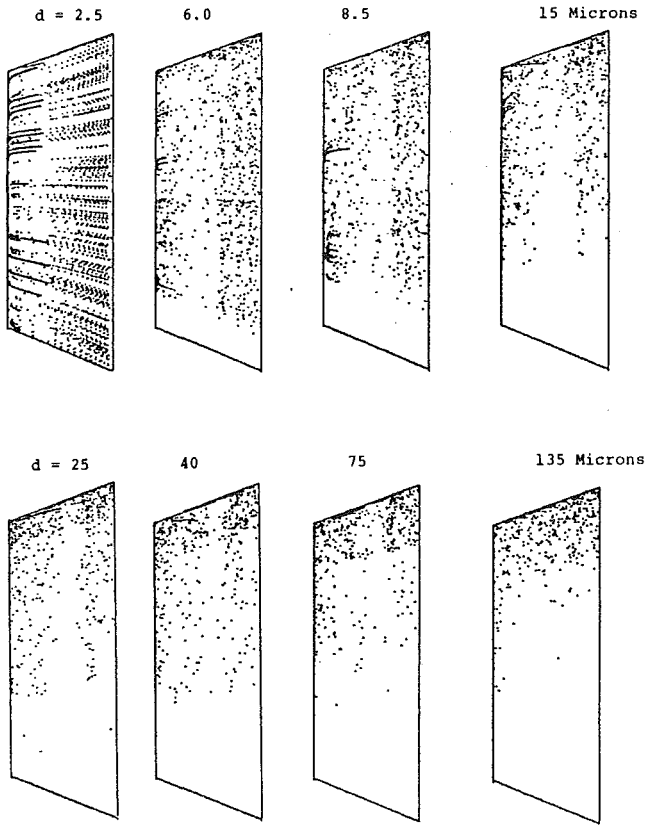

Fig. 6 Impact locations for the individual particle sets, first rotor

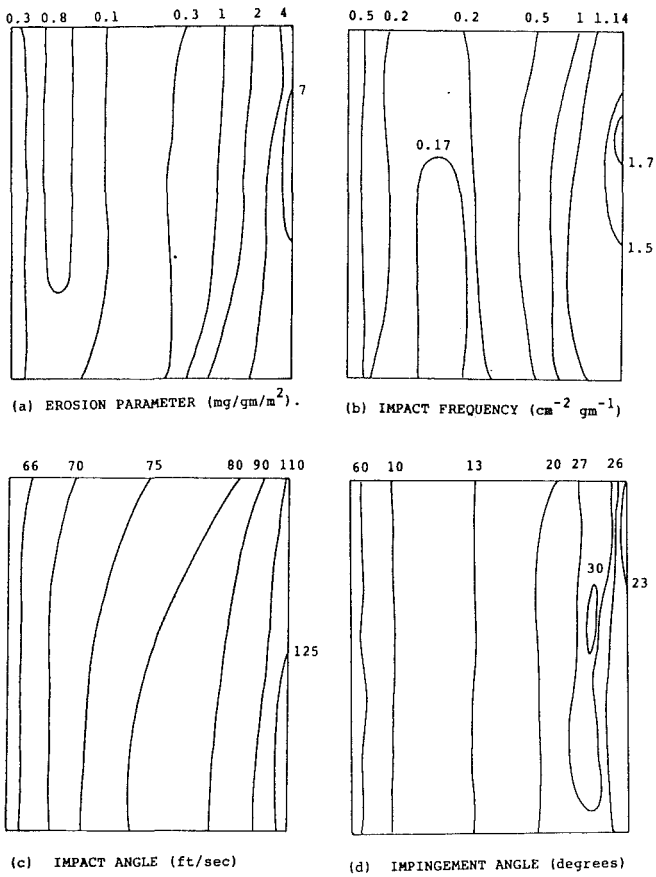

Fig. 8 Blade erosion parameters for the uniform particles, first stator

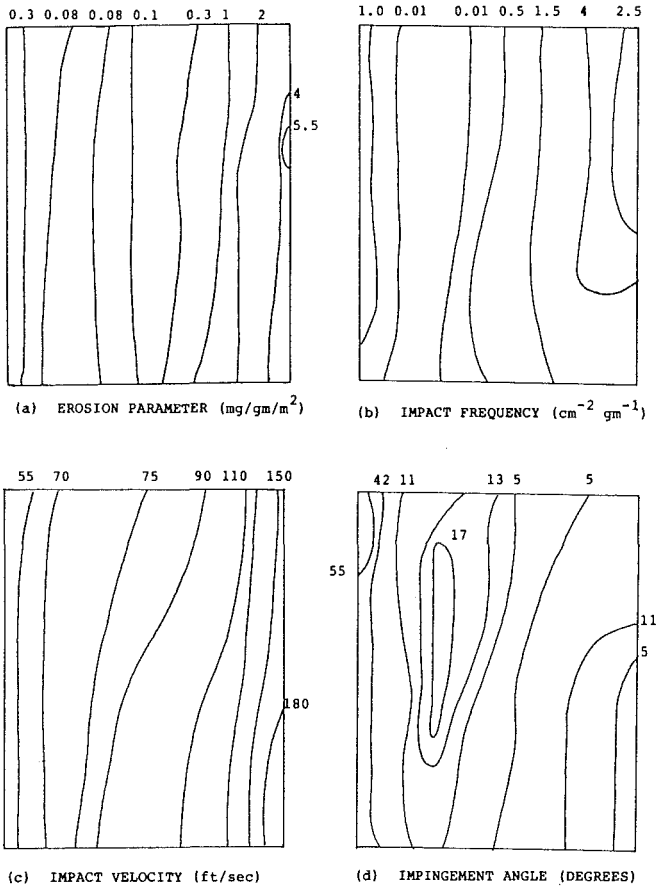

Fig. 7 Blade erosion parameters for the nonuniform particles, first stator

are presented for nonuniform and uniform particle sizes in Figs. 7 and 8, respectively. These figures show a low erosion zone near the middle of the first stator pressure surface, which can be attributed to the lower impact frequencies in this area as shown in Figs. 7(*b*) and 8(*b*). Inspection of these figures shows increased impact frequencies, high velocities, and higher erosion toward the trailing edge of the first stator pressure surface. The higher impact velocities in the case of nonuniform particles are attributed to the presence of the small particles, which accelerate faster due to their lower inertia. These small particles have repeated closely spaced impacts with the blade surface at small impingement angles. The first rotor blade erosion related parameters over the pressure surface are shown in Figs. 9 and 10 for nonuniform and uniform particle sizes. Figure 9(*a*) shows that the maximum erosion is at the leading edge and the minimum is at the corner between the hub and the trailing edge. It can be observed in the case of uniform particle size distribution that no erosion is predicted near the hub over a region extending from one-seventh of the blade span at the leading edge to two-sevenths of the span at the trailing edge. This is caused by the particles' radial migrations under the effect of the centrifugal force. The presence of small particles in the nonuniform particle distribution follows the gas flow streamlines more closely and hence their impacts with the blade surface continue to extend from the hub to the tip. From Figs. 9(*b*) and 10(*b*), one can observe that the impacting particle frequency increases toward the tip region, with higher values near the leading and trailing edges and lower values at midchord. Comparing these two figures, one can conclude that the particle nonuniformity increases the impact frequency. On the other hand, Figs. 9(*c*) and 10(*c*) show generally lower impacting velocities near the tip, with the highest impact velocities near the leading edges toward the hub. The impingement angle distributions of Figs. 9(*d*) and 10(*d*) show a gradual

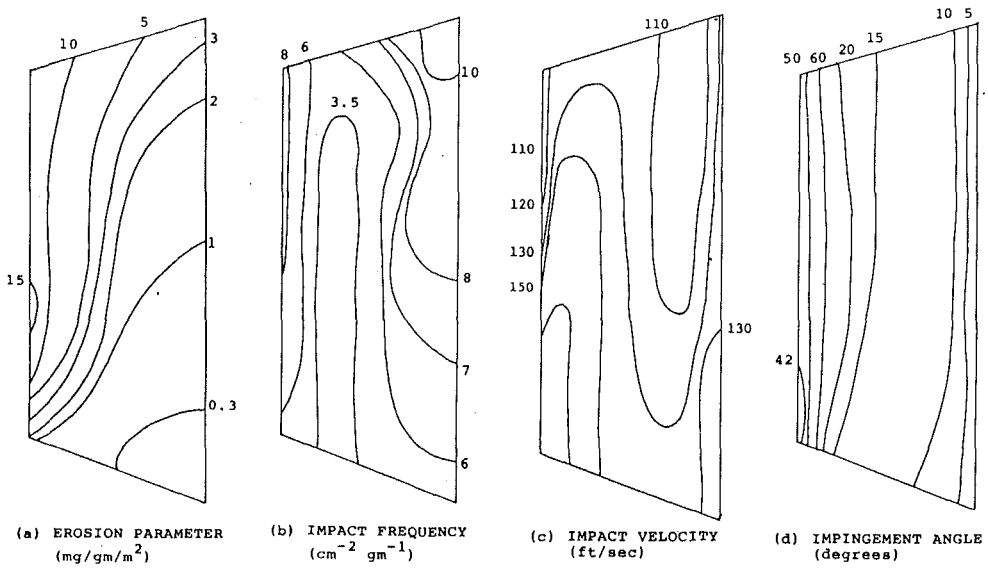

Fig. 9 Blade erosion parameters for the nonuniform particles, first rotor

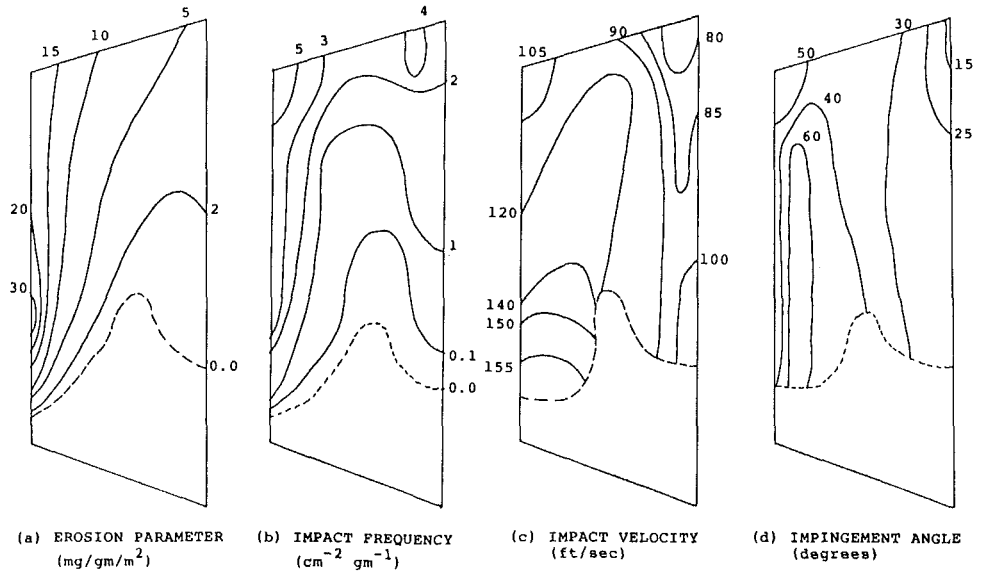

Fig. 10 Blade erosion parameters for the uniform particles, first rotor

decrease from the leading to the trailing edges over the blade height. Comparing the erosion results of Figs. 9(*a*) and 10(*a*) for the first rotor blade, it can be concluded that the uniform particle distribution overestimates the erosion of the first rotor blade.

The results of the blade erosion analysis for the second stator pressure surface are presented in Figs. 11 and 12. The maximum predicted blade erosion rates are at the tip-leading edge corner as shown in Figs. 11(*a*) and 12(*a*). The frequency of particle impacts, Figs. 11(*b*) and 12(*b*), shows similar trends as the blade erosion. It can be observed from the same figures that the maximum erosion in the second stator blade is higher in the case of uniform particle distributions (Fig. 12*a*). Less stator blade erosion is predicted with nonuniform particle distributions (Fig. 11*a*). Inspection of Figs. 11(*c*) and 12(*c*) shows that the average impact velocities are higher for the nonuniform case.

The erosion results for the second rotor blade pressure surface are presented in Figs. 13 and 14. The highest erosion rates are also close to the leading edge area with the maximum erosion at the tip leading edge corner (Figs. 13*a* and 14*a*). The values of the blade mass erosion parameters in these figures are much less than those in the first rotor. A comparison of Figs. 9(*b*), 10(*b*), 13(*b*), and 14(*b*) reveals that the particle impact frequencies are relatively lower than in the first rotor. Also, a large difference between the particle impacting velocities in the first and second rotors can be seen in Figs. 9(*c*), 10(*c*), 13(*c*), and 14(*c*).

Conclusion

The results presented provide a detailed description of the blade surface erosion pattern and intensity through multistage gas turbine engines for both nonuniform and uniform solid particle distributions. The location of the blade row influences not only the magnitude of blade erosion but also the erosion pattern and the location of maximum blade erosion. In the first stage, the maximum stator blade erosion is at the blade trailing edge and the maximum rotor blade erosion is not at the tip, but is located instead near one third the blade height

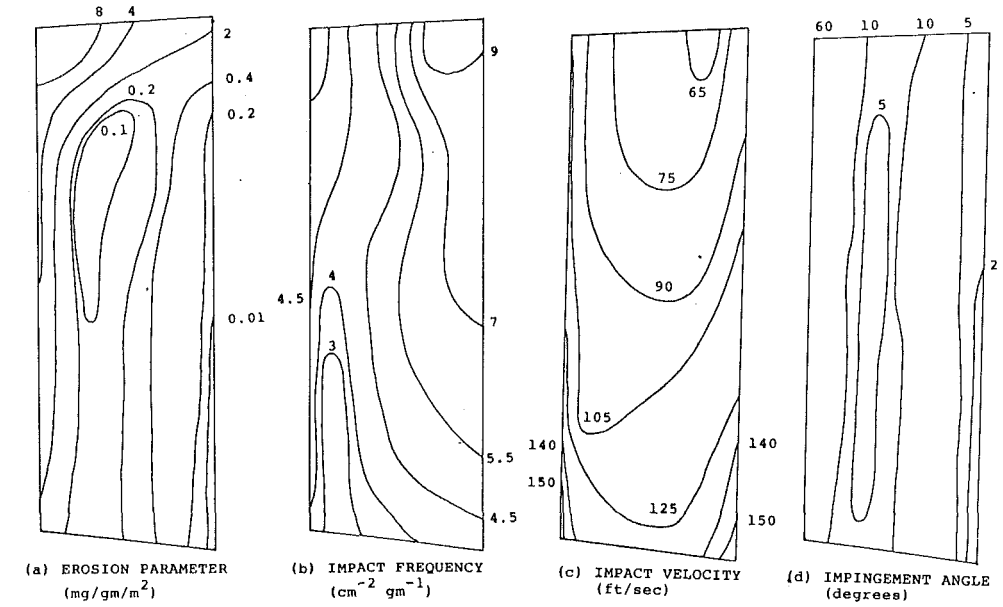

Fig. 11 Blade erosion parameters for the nonuniform particles, second stator

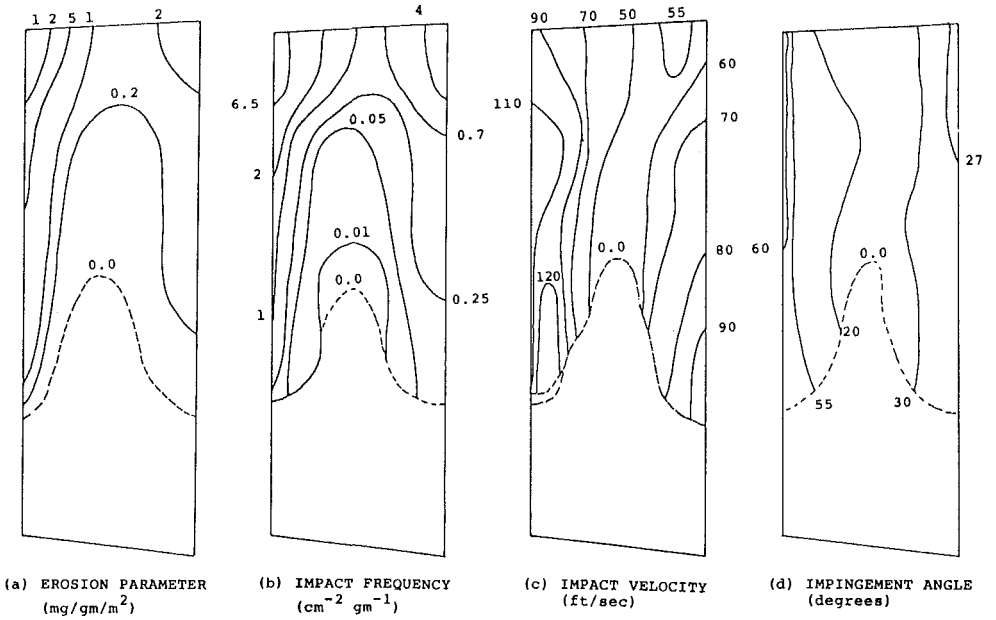

Fig. 12 Blade erosion parameters for the uniform particles, second stator

at the leading edge. The rest of the blade rows in the multistage turbines suffer the maximum erosion at the outmost radial location and the erosion pattern is quite similar to the impact frequency distribution over the blade surface. While generally lower blade erosion rates are predicted at the trailing edge than at the leading edge, except in the first stator, the blade trailing edge erosion can present a serious problem because of the smaller blade thickness. The maximum blade trailing edge erosions are generally at the blade outmost radius in all blade rows but the first stator. The first rotor represents the most critical blade row erosion in both maximum local and overall blade erosion. The overall blade erosion patterns are similar for both uniform and nonuniform distributions, but the erosion is generally lower for the nonuniform particle distribution. The nonuniformity of the particle distributions increases the impact frequency due to the multiple impacts of smaller particles. Although the impact velocities are higher for the nonuniform particles, the blade erosion level is lower because of the lower impact angles.

Acknowledgments

This research work was partially supported by the US Department of Energy, Contract No. 19X-89628C, Oak Ridge National Laboratory, Oak Ridge, TN.

References

Hamed, A., 1981, "Particle Dynamics of Inlet Flow Fields With Swirling Vanes," Paper No. AIAA-81-001.

Hamed, A., and Fowler, S., 1983, "Erosion Pattern of Twisted Blades by Particle Laden Flows," ASME JOURNAL OF ENGINEERING FOR POWER, Vol. 105, pp. 839–843.

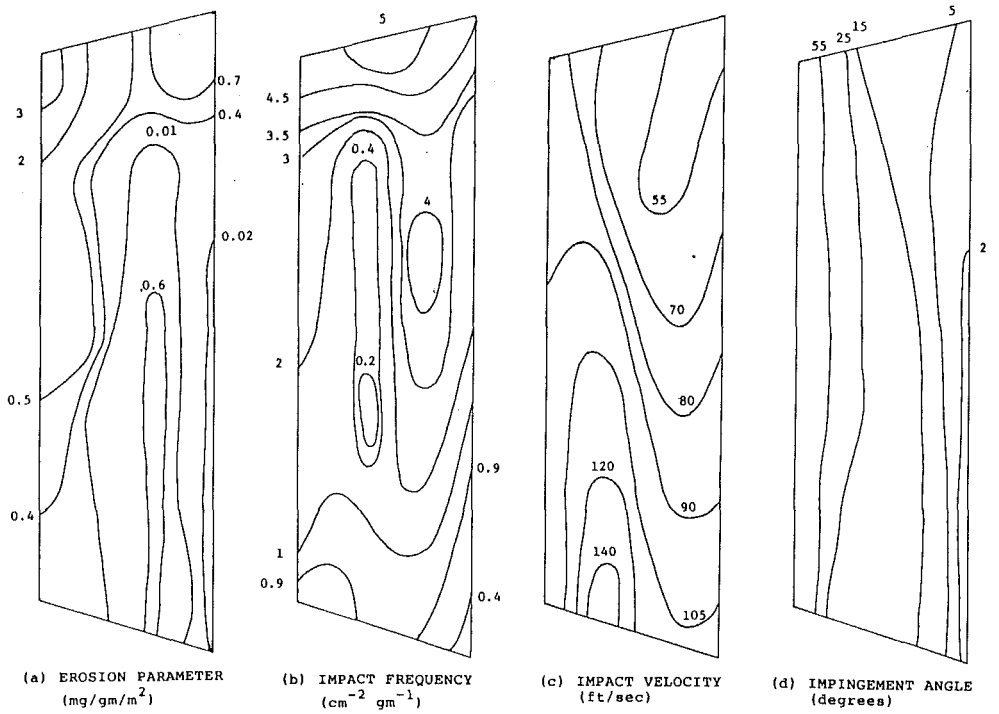

Fig. 13 Blade erosion parameters for the nonuniform particles

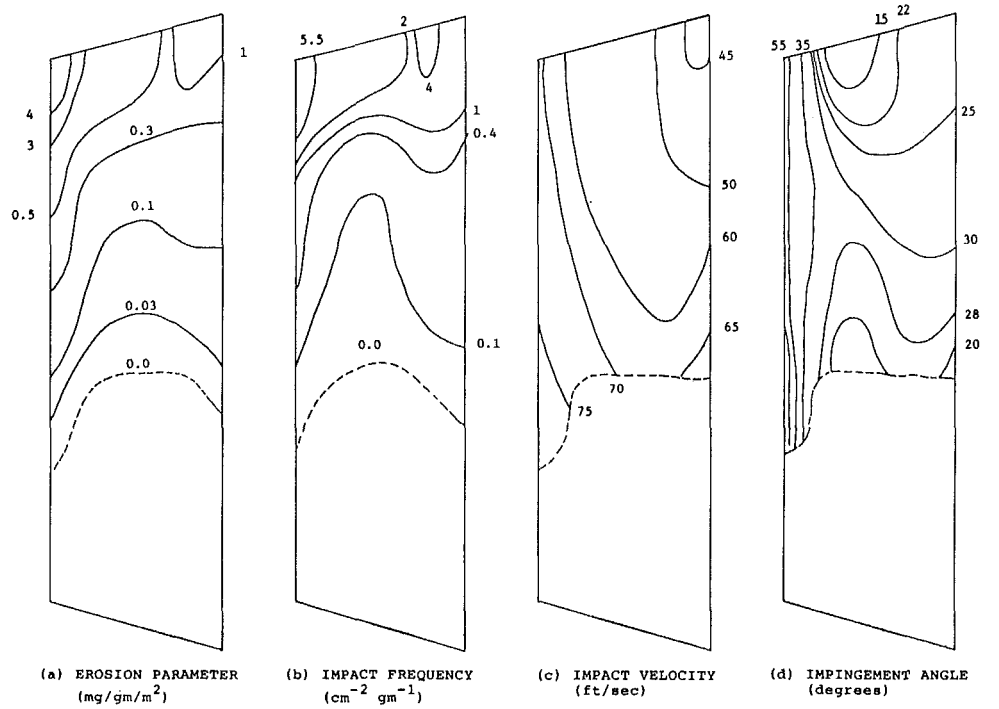

Fig. 14 Blade erosion parameters for the uniform particles, second rotor

Hamed, A., 1984, "Solid Particle Dynamic Behavior Through Twisted Blade Rows," ASME *Journal of Fluids Engineering*, Vol. 106, No. 3, pp. 251–256.

Hamed, A., Tabakoff, W., and Mansour, M., 1986, "Turbine Erosion Exposed to Particulate Flow," ASME Paper No. 86-GT-258.

Hussein, M. F., and Tabakoff, W., 1973, "Dynamic Behavior of Solid Particles Suspended by Polluted Flow in a Turbine Stage," *Journal of Aircraft*, Vol. 10, pp. 434–440.

Katsanis, T., 1965, "Fortran Program for Calculating Transonic Velocities on a Blade-to-Blade Stream Surface of a Turbomachine," NASA TND-2809, May.

Katsanis, T., and McNally, W. D., 1977, "Revised Fortran Program for Calculating Velocities and Streamlines in the Hub-Tip Mid Channel Stream Surface of an Axial, Radial, or Mixed Flow Turbomachine or Annular Duct, Vols. 1 & 2," NASA TND-8430 and NASA TND-8431.

Roelke, R. J., Stabe, R. G., and Evans, D. G., 1966, "Cold-Air Performance Evaluation of Scale Model Oxidizer Pump-Drive Turbine for the M-1 Hydrogen-Oxygen Rocket Engine—II. Overall Two-Stage Performance," NASA TND-3368.

Tabakoff, W., and Hamed, A., 1977, "Aerodynamic Effects on Erosion in Turbomachinery," JSME & ASME Paper No. 70, presented at the Joint Gas Turbine Congress, Tokyo, Japan, May.

Tabakoff, W., Hamed, A., and Ramachandran, J., 1980, "Study of Metals

Erosion on High Temperature Coal Gas Streams," ASME JOURNAL OF ENGINEERING FOR POWER, Vol. 102, pp. 148–152.

Tabakoff, W., and Hamed, A., 1982, "Investigation of Gas Particle Flow in Erosion Wind Tunnel," presented at the 7th Annual Conference on Materials for Coal Conversion and Utilization, National Bureau of Standards, Gaithersburg, MD, Nov.

Tabakoff, W., 1983, "A Study of the Surface Deterioration Due to Erosion," ASME JOURNAL OF ENGINEERING FOR POWER, Vol. 105, pp. 47–52.

Tabakoff, W., 1984, "Review—Turbomachinery Performance Deterioration Exposed to Solid Particles Environments," ASME *Journal of Fluids Engineering*, Vol. 106, pp. 106–125.

Tabakoff, W., Malak, M. F., and Hamed, A., 1985, "Laser Measurements of Solid Particles Rebound Parameters Impacting on 2024 Aluminum and 6A1-4V Titanium Alloys," Paper No. AIAA 85-1570.

Tabakoff, W., and Hamed, A., 1986, "The Dynamics of Suspended Solid Particles in a Two Stage Gas Turbine," ASME *Journal of Turbomachinery*, Vol. 108, pp. 298–302.

Tabakoff, W., 1987, "Compressor Erosion and Performance Deterioration," ASME *Journal of Fluids Engineering*, Vol. 109, pp. 298–306.

Tabakoff, W., and Malak, M. F., 1987, "Laser Measurements of Fly Ash Rebound Parameters for Use in Trajectory Calculations," ASME *Journal of Turbomachinery*, Vol. 109, pp. 535–540.

Tabakoff, W., 1988, "Turbomachinery Alloys Affected by Solid Particles," ASME Paper No. 88-GT-295.

An Approach to Describing the Simultaneous Erosion and High-Temperature Oxidation of Alloys

I. G. Wright

V. K. Sethi

V. Nagarajan

Battelle,
Columbus, OH 43201

The rate of wastage of an alloy surface subjected to erosion under conditions where high-temperature oxidation can occur can be significantly greater than that arising from erosion alone. This is because the erosion conditions can act to accelerate the oxidation process by causing regular shedding of the otherwise protective oxide scale. It is suggested that an important parameter in determining the rate of erosion-oxidation is the erodent flux, since the time available for oxide growth (or regrowth) in a given area is determined by the interval between successive erodent impacts. Using this simple premise, an approach is suggested by which the rate of erosion-oxidation can be related to the factors that control the alloy oxidation process, and those that describe the erosive environment. The assumptions made are examined, and some of the implications of this approach are discussed.

Introduction

The development of clean-coal utilization technologies, such as pressurized fluidized bed combustion (PFBC) and the direct firing of coal in gas turbines, results in the generation of hot, particle-laden gas streams, which must be expanded through or combusted in turbomachinery. For good system efficiency combined with acceptable component life, techniques must be developed to reduce the concentration of particulate matter in the hot gas stream and for accepting some level of particulate ingestion by the turbomachinery. It is also important that some capability for predicting the extent and rate of degradation of the turbine be available. Particle trajectory analysis techniques have been developed that allow the computation of the locations at which ingested particles will impact the hot gas path components. If the extent to which each impact will degrade the target component can be reasonably estimated, then it should be possible to predict with good accuracy the practical life of the turbomachinery as a function of the parameters that describe the incoming gas stream and the characteristics of the turbomachinery.

At relatively low gas and metal temperatures where the rate of oxidation/corrosion is slow, the interaction of impacting particles with the component surface can be described using the relationships derived for low-temperature erosion, which commonly involve the mass and velocity of the individual particles, and the hardness of the substrate acting as target. However, under the conditions where a significant corrosion component can be expected, as is the case for turbines that are fueled by coal-derived fuels or are expanding the flue gas from PFBC systems, then the rate of material removal from the metal surface under the action of impacting particles becomes a strong function of the oxidation characteristics of the alloy, and in fact the rate of material removal under these conditions can be significantly greater than that under conditions where erosion alone prevails. In this paper a simple approach is proposed to describe the erosion-oxidation response of an alloy in a high-temperature oxidizing environment (see also Sethi and Wright, 1989), and an attempt is made to incorporate both oxidation behavior and erosion-related parameters into a methodology that will allow a more realistic calculation of the rates of material loss under erosion-oxidation conditions. Any improvement in the ability to describe and eventually calculate the rate of material loss based on the actual response of an oxidizing metal surface to particle impacts has the potential to enhance significantly the realism of computation analysis of the response of turbomachinery to a wide range of conditions.

Erosion-Oxidation Interactions

When an alloy is subjected to erosion at temperatures at which surface oxidation can proceed at an appreciable rate, the way in which the corrosion process is affected by the erosion events must be taken into consideration if a reasonable basis for understanding the complex phenomena involved is to be established. A number of scenarios for the modification of the erosion processes by surface oxides have been proposed by, for instance, Hogmark et al. (1983), Stephenson et al. (1985, 1986a, 1986b), Kang et al. (1985), and Wright et al. (1986), as ways of rationalizing various observations of the phenomena involved. Typically, impacting erodent particles interact with the growing oxide scale on the metal surface and may lead to material loss by causing the oxide to spall from the metal surface, or by removing fragments of the oxide scale through typical erosion processes such as chipping or cracking. Depending upon the severity of the impact (particle kinetic en-

Contributed by the International Gas Turbine Institute and presented at the 35th International Gas Turbine and Aeroengine Congress and Exposition, Brussels, Belgium, June 11-14, 1990. Manuscript received by the International Gas Turbine Institute January 14, 1990. Paper No. 90-GT-361.

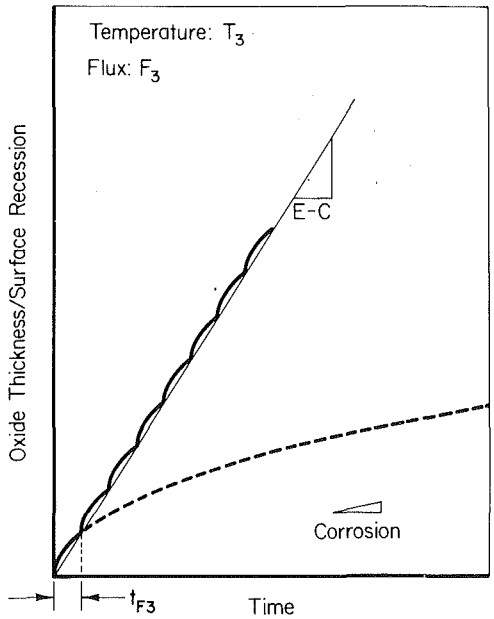

Fig. 1 Schematic representation of the erosion-parabolic oxidation process at temperature T_3 and erodent flux F_3, where each impact removes scale back to the metal surface; time interval between successive impacts is t_{F3}; the erosion-oxidation kinetics are given by a series of connected parabolas; the resulting rate of erosion-oxidation and oxidation alone are represented by the triangles

ergy), the thickness of the oxide scale, and the properties of the alloy substrate, the erosion event may lead to the removal of fragments of the oxide scale, or to shedding of the oxide over larger areas, or to the actual removal of substrate metal.

In the approach described here it is assumed that no metal is directly removed by the erosion process; instead, erosion accelerates the oxidation process, and the major mode of material removal is through loss of the oxide scale. This is demonstrated in Fig. 1, which shows the rate of thickening of the oxide scale on an alloy that is assumed to undergo oxidation at a parabolic rate at temperature T_3. A flux of erodent F_3 is assumed to be striking the oxidizing surface. Under fixed conditions of erodent velocity, particle size, and angularity, etc., the time interval between successive erosion events at a given location on the sample is inversely related to the erodent flux. For the erodent flux F_3 this interval will be t_{F3}. The amount of scale removed and the amount that reforms between successive impacts can be deduced from Fig. 1, in which the erosion-oxidation curve is represented by a series of connected parabolas, as the oxidation behavior is interrupted and restarted at intervals of t_{F3}. The parabolic oxidation rate in each case will be the same as that as for the initial part of the oxidation curve alone if the oxide is spalled back to the metal surface, as is the simplistic assumption made in Fig. 1. The rate of erosion-oxidation at any time may be approximated by the best line drawn through the point of inflection of the curve, and will be linear. Since the oxide at each impact point is removed from the surface, the alloy would actually experience a weight loss at a linear rate. The triangles drawn in Fig. 1 provide a comparison of the rates of metal loss by oxidation alone and by erosion-induced oxide exfoliation. If the impacting particles were sufficiently energetic to remove some substrate metal along with the oxide, the observed wastage rate would be even higher than that shown in Fig. 1. Conversely, if the erosion event results in incomplete removal of oxide, the rate of oxide regrowth in that area will be slower than that indicated in Fig. 1 since the rate will depend on the thickness of oxide remaining on the surface, hence the overall erosion-oxidation rate will be lower.

Under the conditions suggested above, the amount of oxide

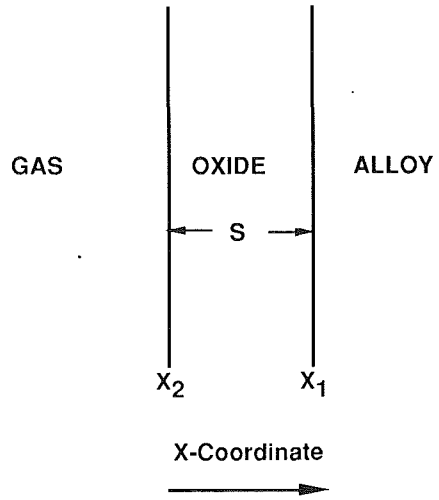

Fig. 2 Coordinates associated with growth of oxide scale

formed in the interval between erodent impacts can be readily related to factors that describe the oxidation behavior of the target material, and to some of the erodent parameters, by well-established principles of high-temperature oxidation.

The oxidizing alloy surface is described in terms of coordinates as shown in Fig. 2 (after Markworth et al., 1991). The illustrated surfaces are taken to be planar and aligned perpendicular to the X axis. Note that the convention used in which the X axis is directed into the metal is opposite to that which is often used in oxidation modeling, but was selected to yield an instantaneous rate of change in the position of the oxide/metal interface that was always positive.

In Fig. 2, the instantaneous thickness of the oxide layer is:

$$S = X_1 - X_2 \tag{1}$$

If X_1 changes as a result of oxidation, then the rate of oxidation is:

$$\dot{X} = \frac{a}{S^k} \tag{2}$$

where a is a temperature-dependent parameter, equivalent to the oxidation rate constant; k denotes the order of the oxidation kinetics (e.g., $k=0$ corresponds to linear kinetics and $k=1$ to parabolic kinetics), and the dot denotes differentiation with respect to time. When X changes by an amount dX_1, metal atoms are incorporated into the oxide, resulting in a change in oxide thickness of dS, which is proportional to dX_1:

$$dS = c\,dX_1 \tag{3}$$

where c is an alloy system constant—the ratio of the volume of oxide formed to the volume of metal consumed in the process—defined by the Pilling-Bedworth ratio. Combining Eqs. (1) and (3):

$$dX_2 = dX_1(1-c) \tag{4}$$

Since, given the scenarios in Fig. 1, the interval in any area available for oxidation to occur is controlled by the time between successive erodent impacts, t_F, the oxide thickness attained in this interval is given simply by differentiating Eq. (1) with respect to time, and combining the result with Eqs. (2) and (4):

$$\dot{S} = \dot{X}_1 - \dot{X}_2 = \frac{ac}{S^k} \tag{5}$$

Two special cases are of particular interest. These are as follows:

(a) All the scale is removed back to the metal surface by each successive impact; the area over which scale is removed

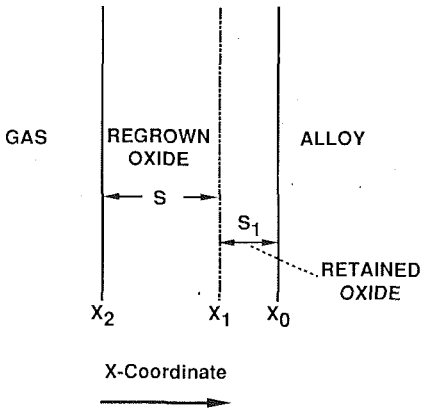

Fig. 3 Coordinates for case where oxide regrowth occurs on top of a layer of retained scale

is assumed to be directly proportional to the dimensions (such as projected area) of the impacting particle. This is obviously a very simplistic assumption, especially for high-temperature alloys, but serves as a starting point.

(*b*) Upon impact, separation occurs within the scale, so that some thickness of scale remains attached to the metal surface. Again, the area over which this damage occurs is assumed to be related to the particle size, as in case (*a*). This may be closer to the real situation, but still requires assumptions that the remaining layer has a uniform thickness and that its properties are unchanged by the impact.

If all the scale is removed by each impact as assumed in case (*a*), the initial conditions for Eq. (5) are $S(t=0)=0$, where t is time, and the solution is:

$$S^{(k+1)}=(k+1)act \tag{6}$$

so that the scale thickness formed (and removed) in the period between successive impacts is given by substituting t_F into Eq. (6).

However, if as suggested by case (*b*) only part of the existing scale is removed by the erosion event, leaving a scale of average thickness S_1 attached to the metal surface, as depicted in Fig. 3, then Eq. 5 may be rewritten:

$$\dot{S}_{\text{total}}=\frac{ac}{(S_{\text{total}})^k} \tag{7}$$

Since $S_{\text{total}}=S+S_1$, the rate of scale thickening upon regrowth is obviously slower than in the case where all the oxide was removed. This is illustrated schematically in Fig. 4 for an alloy oxidizing at a parabolic rate at temperature T_3 with an erodent flux of F_3, and where the retained scale thickness is equivalent to that grown in the interval 0.5 t_{F3}. This indicates that the resulting erosion-oxidation will occur at a linear rate that will be tangent to the parabolic oxidation curve at the value of the thickness of the retained oxide, S_1. Comparison with Fig. 1 shows that the rate of erosion-oxidation is only about 56 percent of that where the scale is removed back to the metal.

Using boundary conditions for the scale regrowth event of $S_{\text{total}}=S_1$ at $t=0$, and $S_{\text{total}}=(S+S_1)$ at $t=t_F$, the solution to Eq. (7) becomes:

$$S=act_F-\frac{S_1(1-S_1^k)}{(k+1)} \tag{8}$$

For linear oxidation kinetics ($k=0$), the scale thickness (S) regrown in both cases is the same, whereas for parabolic kinetics ($k=1$), S (Eq. (6)) is larger than S (Eq. (8)) by a factor determined by the thickness of the nonspalled scale.

Values for t_F, defined by the frequency of impacts, may be computed from trajectory analyses, or may be estimated from a knowledge of the particle size and loading in the gas stream. The number of impacts per second (N) is given by:

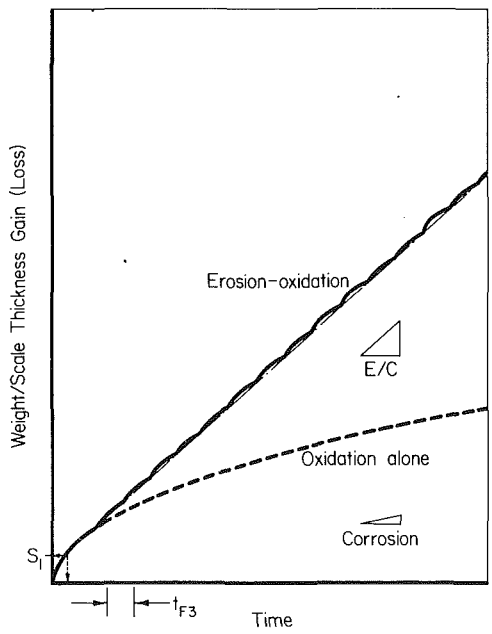

Fig. 4 Schematic representation of the erosion-parabolic oxidation process at temperature T_3 and erodent F_3, where a layer of scale of thickness S_1 is retained after each impact

$$N=\frac{6LvA}{\pi\rho_p d_p^3} \tag{9}$$

where L is the particle loading in the gas stream with units of mass/volume; d_p is the mean particle diameter; ρ_p is the density of the particle; v is the particle velocity, and A is the cross-sectional area over which the particle loading occurs. Also, the practical measure of material loss required is not oxide thickness (grown and removed), but thickness of metal removed, X_m, which is given by Eq. (3):

$$X_m=\frac{S}{c} \tag{10}$$

For the simplest case considered, case (*a*), substituting Eqs. (9) and (10) into Eq. (6), with $t=t_F=1/N$, gives:

$$X_m=B\left(\frac{ad_p^3\rho_p}{LAv}\right)^{\frac{1}{(k+1)}} \tag{11}$$

where

$$B=\frac{1}{c}\left[\frac{\pi c(k+1)}{6}\right]^{\frac{1}{(k+1)}} \tag{12}$$

and the rate of metal loss is

$$X_m N=B_1\left(\frac{LAv}{d_p^3\rho_p}\right)^{\frac{k}{(k+1)}} a^{\frac{1}{(k+1)}} \tag{13}$$

where

$$B_1=\frac{1}{c}\left[c(k+1)\right]^{\frac{1}{(k+1)}}\left(\frac{6}{\pi}\right)^{\frac{k}{(k+1)}} \tag{14}$$

Finally, since the oxidation rate constant usually has the form:

$$a=B_2 e^{-\frac{\Delta G}{RT}} \tag{15}$$

where B_2 is the Arrhenius constant; ΔG is the activation energy of the rate-controlling step in the oxidation process; R is the gas constant; and T is the reaction temperature, the rate of metal loss can be expressed as:

$$X_m N = B_3 \left(\frac{LAv}{d_p^3 \rho_p} \right)^{\frac{k}{(k+1)}} e^{-\frac{\Delta G}{RT(k+1)}} \tag{16}$$

where

$$B_3 = B_1 B_2^{\frac{1}{(k+1)}} \tag{17}$$

From Eq. (16) it can be seen that, if all other variables were held constant, an increase in particle velocity or loading would lead to an increase in the rate of metal loss through increasing the frequency of impacts. Conversely, increasing the particle size would reduce the number of particles available at a given solids loading, hence, would decrease the rate of metal loss. Increases in the oxidation (metal) temperature, or in the oxidation rate constant, would also increase the rate of metal oxidation.

Effects of Major Factors

Effect of Erodent Flux. The effect of changing the erodent flux is shown schematically in Fig. 5. Here the erosion-oxidation kinetic curves are drawn for erodent fluxes F_1, F_3, and F_5, where F_1 is 4 times F_3, and F_5 is 1/4 of F_3. The time intervals between impacts, t_{F1} and t_{F5}, will obviously be 1/4 and 4 times t_{F3}. The oxide thickness developed in the time between successive impacts would be correspondingly more or less, and the rate of oxide regrowth would always reflect the steep initial growth slope of the parabolic rate curve, the actual steepness depending on whether or not a fraction of the oxide scale was retained. The resulting linear erosion-oxidation rates can be visualized from the dimensions of the triangles drawn in Fig. 5. For the examples shown, changing the erodent flux from F_3 to F_1 (a fourfold increase) results in a twofold increase in the erosion-oxidation rate. Similarly, changing from F_3 to F_5 (a fourfold decrease) results in a 50 percent reduction in the erosion-oxidation rate. This square root dependence is a direct consequence of the assumed parabolic oxide growth kinetics, but nevertheless serves to show the magnitude of the effects possible.

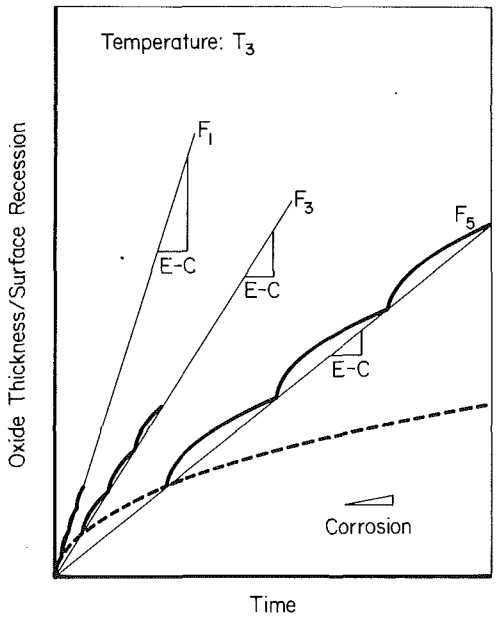

Fig. 5 Effect of changing erodent flux on erosion-oxidation at temperature T_3

Effect of Metal Temperature. The effect of changing the oxidation temperature is suggested in Fig. 6, which depicts the oxidation kinetics for the assumed alloy at temperatures T_1, T_3, and T_5. These temperatures are selected so that increasing the temperature from T_3 to T_5 results in a fourfold increase in the parabolic oxidation rate constant, while decreasing the temperature from T_3 to T_1 results in a fourfold decrease in the parabolic rate constant. Note that since the relationship of the parabolic rate constant to temperature typically has the form shown in Eq. (15), the chosen temperatures T_1, T_3, and T_5 do not represent linearly increasing values of temperature, but were simply chosen to show readily demonstrable effects of the parabolic rate constant. The erosion-oxidation kinetics shown in Fig. 6 for flux F_1 are correspondingly and substantially increased with increasing temperature. Therefore, even though a change in the gas temperature may or may not materially increase the erosion component, the overall contribution to material loss from erosion-oxidation can be significantly affected by change in the oxidation (gas or metal temperature). The previous considerations of the effect of erodent flux indicate that the influence of temperature would be larger with decreasing erodent flux.

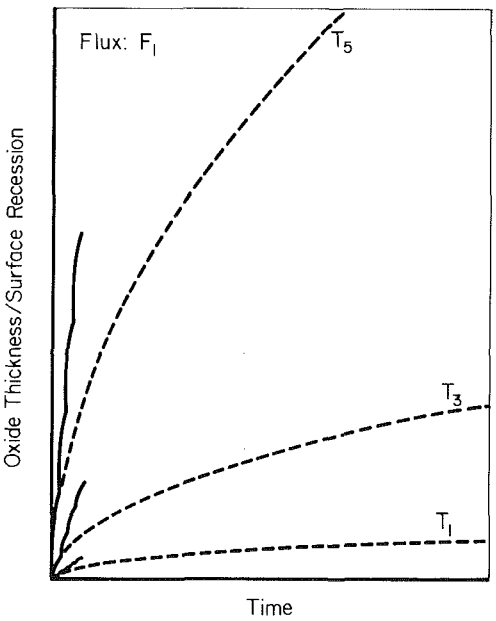

Fig. 6 Effect of increasing metal temperature on erosion-oxidation erodent flux F_1

Particle Size Dependence. It is generally held that erodent particles with a maximum size dimension of 2 μm may follow the fluid stream lines and not experience any contact with turbomachinery parts, while 4 μm particles probably contact the turbine surfaces but cause a tolerable amount of damage when the type of damage is assumed to be that from simple erosion or abrasion. In erosion-oxidation, in order for damage to occur, the erodent particle need not have sufficient energy to cut or abrade the metal surface but merely needs to cause the surface oxide scale to spall, which may require a considerably lower level of kinetic energy. Under these conditions, a change in particle size can have two effects: (1) at a fixed solids loading, an increase in the particle size leads to a decrease in the frequency of erosion events, hence to an increase in the time interval between erosion events; and (2) larger particles imply a higher level of kinetic energy, hence the extent or area over which spallation of the oxide scale occurs may be larger. Therefore, a strong dependence on the erodent particle size is expected under erosion-oxidation conditions where the major mode of material loss is by oxide scale exfoliation. It is also expected that the erosion-oxidation rates would increase with increased particle size.

Velocity Dependence. By essentially the same arguments used above, it would be expected that increasing the velocity

at a given particle size and loading in the gas stream would result in an increase in the frequency of impacts, hence a decrease in the time interval available for oxidation to occur. Hence the overall rate of erosion-oxidation would be expected to increase with increasing velocity.

Angle Dependence. At a given solids loading in the gas stream, the effect of changing the angle of incidence of the erodent onto the alloy target is to alter the effective erodent flux experienced by the target surface. For example, changing the angle from 90 to 30 deg results in a doubling of the target area intercepting a given volume of erodent stream, hence in a 50 percent reduction in the effective erodent flux in that area. Therefore, assuming that other conditions do not change, the arguments made earlier suggest that the erosion-oxidation rates will decrease with decreasing angle of impingement. Note that this may be overly simplistic, since the properties that affect the response of the oxide to an erosion event will doubtless vary with impact angle, so that the angle of impingement dependence of erosion-oxidation may be expected to be quite complex.

General Implications

This discussion of erosion-oxidation scenarios has pointed out that the rate of material loss under such conditions is likely to be significantly greater than under erosion alone, since most of the material loss will be the result of the shedding of oxide scale rather than by the cutting or abrasion of the actual metal surface, and the particle kinetic energies required to cause this material loss are likely to be lower under erosion-oxidation conditions. This suggests that this form of material degradation could be more severe in turbomachinery where the erodent particles are part of the hot gas stream, than under the conditions normally considered for turbomachinery erosion where the erodent particles are part of the much cooler gas stream in the compressor section. One of the major variables identified is the erodent flux impacting the surface experiencing erosion-oxidation. This can be very accurately calculated via the detailed particle trajectory modeling pioneered by Tabakoff and Hamed (1988), and it is expected that if this were combined with the approaches discussed here for describing the rate of material loss in terms of erodent flux, and essentially materials parameters that govern in the rate of oxidation, then improved estimation of the rate of degradation of turbomachinery components may be possible. Although a number of simplifying assumptions were made for expediency in explaining the overall approach, there is no practical barrier to obtaining the required parameters for typical alloys used in these applications. Note also that some of the implications developed in this description of erosion-oxidation are only expected where the metal temperatures are high enough for scale growth and exfoliation to be the dominant wastage mechanism.

References

Hogmark, S., Hammarsten, A., and Soderberg, S., 1983, "On the Combined Effects of Corrosion and Erosion," *Proc. 6th Int. Conf. on Erosion by Liquid and Solid Impact*, J. E. Field and N. S. Corney, eds., University of Cambridge, Paper No. 37.

Kang, C. T., Chang, S. L., Pettit, F. S., and Birks, N., 1985, "Synergisms in the Degradation of Metals Exposed to Erosive High-Temperature Oxidizing Environments," in: *Transport in Nonstoichiometric Compounds*, G. Simkovich and V. S. Stubican, eds., Plenum Press, New York, pp. 411–427.

Markworth, A. J., Nagarajan, V., and Wright, I. G., 1991, "An Approach to Modeling Simultaneous High-Temperature Oxidation and Erosion," *Oxdtn. Metals*, Vol. 35, No. 1/2, pp. 89–106.

Sethi, V. K., and Wright, I. G., 1989, "Observations on the Erosion-Oxidation Behavior of Alloys," in: *Corrosion and Particle Erosion*, V. Srinivasan and K. Vedula, eds., TMS Conf. Proc., pp. 245–264.

Stephenson, D. J., Nicholls, J. R., and Hancock, P., 1985, "The Erosion of Gas Turbine Blade Materials by Solid Sea Salt," *Corr. Sci.*, Vol. 25, No. 12, pp. 1181–1192.

Stephenson, D. J., Nicholls, J. R., and Hancock, P., 1986a, "Particle-Surface Interactions During the Erosion of a Gas Turbine Material (MarM002) by Pyrolitic Carbon Particles," *Wear*, Vol. 111, pp. 15–29.

Stephenson, D. J., Nicholls, J. R., and Hancock, P., 1986b, "Particle-Surface Interactions During the Erosion of Aluminide-Coated MarM002," *Wear*, Vol. 111, pp. 31–29.

Tabakoff, W., and Hamed, A., 1988, "Temperature Effect on Particle Dynamics and Erosion in Radial Inflow Turbine," ASME *Journal of Turbomachinery*, Vol. 110, No. 4, pp. 258–264.

Wright, I. G., Nagarajan, V., and Stringer, J., 1986, "Observations on the Role of Oxide Scales in High-Temperature Erosion-Corrosion of Alloys," *Oxdtn. Metals*, Vol. 25, No. 3/4, pp. 175–199.

G. Stürmer

M. Fundus

A. Schulz

S. Wittig

Lehrstuhl und Institut für Thermische Strömungsmaschinen, Universität Karlsruhe (T.H.), D-7500 Karlsruhe, Federal Republic of Germany

Design of Ceramic Gas Turbine Components

At the Institute for Thermal Turbomachinery (ITS), University of Karlsruhe, detailed theoretical and experimental studies concerning ceramic gas turbine components have been performed. For the analysis of the reliability of ceramic components by finite element calculations, the numerical code CERITS has been developed, which follows a strategy similar to that suggested by Gyekenyesi. CERITS determines the failure probability of ceramic components with reference to volumetric flaws. Different fracture criteria can be considered. CERITS is coupled to the finite element code ADINA, which facilitates the prediction of the required temperature and stress distributions. The procedure is demonstrated utilizing gas turbine combustor components.

Introduction

To improve the performance of gas turbines in general and the overall thermal efficiency in particular, it is necessary to increase the pressure ratio as well as the turbine inlet temperature (see Fig. 1). Consequently, the thermal load of the combustion chamber becomes extremely high. Despite the considerable achievements in cooling techniques, especially in small engines, e.g., automotive gas turbines, new materials for the flame tube must be used. For this application, modern ceramics are the best-suited materials, due to their excellent high-temperature strength and other attractive properties, which have been widely published.

In the Federal Republic of Germany, the development of ceramic components for automotive gas turbines was initiated about fifteen years ago by a project sponsored by the BMFT (German Federal Ministry of Research and Technology) (Bunk and Böhmer, 1978). In this field, mainly experimental investigations on combustion chambers with ceramic flame tubes were conducted. These flame tubes had a monolithic structure and showed designs similar to those of their metallic counterparts. The reliability was found to be insufficient under the operating conditions of the engine.

At the Institute for Thermal Turbomachinery (ITS), University of Karlsruhe, a completely different strategy was developed, based on segmentation of the flame tube. Special emphasis was put on the design of flame tube segments using mathematical models. The necessity of careful theoretical analysis follows from the specific behavior of ceramics at failure. This behavior is characterized by brittleness and large variations in fracture strength. Compared with metals, ceramics cannot reduce local stress maxima by plastic deformation. This requires both systematic material development to improve ductility and designs taking into account the characteristics of ceramics. However, the technique of subjecting ceramics primarily to compression stresses due to the higher fracture strength under pressure is not feasible in the case of combustion chambers because of the complex loading conditions. Therefore, careful analysis of the temperature and stress distributions within the component is imperative. A powerful tool in this context is the finite element technique. For the final prediction of the reliability of a component, the finite element method has to be extended to account for statistical fracture analysis of ceramics. Consequently, the numerical code CERITS was developed to predict the failure probability of ceramics. The code follows a similar strategy to that suggested by Gyekenyesi (1986). With the aid of CERITS, the critical areas within a ceramic component can be identified. Thus modifications to the geometry at the early stages in the design process will be easily achieved. Time and money consuming experimental investigations can be reduced and conducted more effectively.

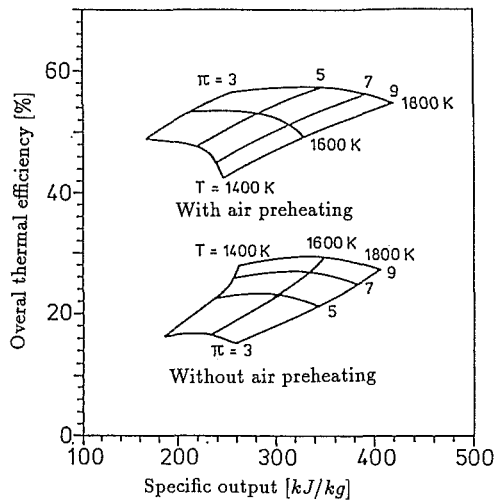

Fig. 1 Influence of turbine inlet temperature, pressure ratio, and air preheating on the overall thermal efficiency and the specific output of a small gas turbine

Contributed by the International Gas Turbine Institute and presented at the 35th International Gas Turbine and Aeroengine Congress and Exposition, Brussels, Belgium, June 11–14, 1990. Manuscript received by the International Gas Turbine Institute January 10, 1990. Paper No. 90-GT-48.

Theory

In order to predict ceramic failure, a combination of fracture mechanics and statistics is utilized. The theoretical models used in CERITS are all based on the weakest link theory (Batdorf, 1978; Shih, 1980), which is generally recognized to be appropriate for modeling failure of brittle materials. The basic principle of the weakest link theory is the comparison between the fracture of brittle materials and the failure of a chain under load. The chain is going to fail when the weakest link of the chain breaks. With respect to ceramics, this means that the failure of a component propagates from the point of the most disadvantageous combination of stress and flaw size. In other words, the whole component will fail if, at any location, the stress intensity factor becomes critical ($K_I \geq K_{Ic}$).

In the following, statistical models of fracture used in CERITS are briefly described. They are all appropriate to take influences of the polyaxial stress state into account. In the present analysis only volume flaws are considered to be responsible for component failure and subcritical crack growth is neglected.

Weibull Model. As a comparatively simple mathematical model for calculating failure probability of ceramic components, the Weibull model is used (Weibull, 1939). The well-known theory is based on extreme value statistics, and fracture mechanical aspects are neglected (Batdorf, 1978). The numerical code CERITS includes the Weibull theory with an extension for polyaxial conditions. To consider polyaxial stress states in Weibull's model, the principle of independent action (PIA) is applied. Assuming that the three principal stresses act independently with regard to fracture initiation, the probability of survival P_S is given by (Batdorf, 1977)

$$P_S(\sigma_1, \sigma_2, \sigma_3) = P_S(\sigma_1) \cdot P_S(\sigma_2) \cdot P_S(\sigma_3) \tag{1}$$

In the case of inhomogeneous stress distribution, the probability of survival for the entire component can be calculated from (Rufin et al., 1984; Gyekenyesi, 1986)

$$P_S = \exp\left\{ -\frac{1}{V_o}\int_V \left[\left(\frac{\sigma_1}{\sigma_o}\right)^m + \left(\frac{\sigma_2}{\sigma_o}\right)^m + \left(\frac{\sigma_3}{\sigma_o}\right)^m \right] dV \right\} \tag{2}$$

where σ_o represents the Weibull scale parameter of the unit volume V_o in dimensions of stress, m the Weibull modulus, and V the stressed volume. Equation (2) is only exact for spherical-shaped flaws, i.e., all principal stresses act as normal stresses. However, in real materials the flaws are far from being spherical. The orientation of the flaws is random and consequently most of them are exposed to a combined load of two or three principal stresses. This load can exceed the load caused by a single principal stress acting normal to the crack plane. Therefore, the model given by Eq. (2) overpredicts the probability of survival.

The normal tensile stress averaging method represents another extension of the Weibull model that accounts for polyaxial stress states. However, this method is not included in CERITS because it yields identical results to those of Batdorf's model with normal stress criterion. Instead of this, the normal stress criterion is added to the list of fracture criteria that can be used in connection with the Batdorf model.

Batdorf Model. In addition to the Weibull model, Batdorf's theory is implemented in CERITS. Using this theory, the overall probability of survival can be calculated from (Batdorf and Crose, 1974)

$$P_S = \exp\left[-\int_V \int_0^\infty \frac{\Omega}{4\pi} \frac{dN}{d\sigma_{cr}} d\sigma_{cr}\, dV \right] \tag{3}$$

where $N(\sigma_{cr})$ is the crack density function, σ_{cr} the critical stress, and Ω the solid angle in principal stress space containing all the crack orientations for which $\sigma_e \geq \sigma_{cr}$. Following Munz and Fett (1989), σ_{cr} is replaced by σ_{Ic} and σ_e by σ_{Ieq}, and subsequently Eq. (3) can be rewritten as

$$P_S = \exp\left[-\int_V \int_0^\infty \frac{\Omega}{4\pi} \frac{dN}{d\sigma_{Ic}} d\sigma_{Ic}\, dV \right] \tag{4}$$

The solid angle Ω used in Eq. (4) is defined as

$$\Omega = \int_{\sigma_{Ieq} \geq \sigma_{Ic}} \sin\alpha \, d\alpha \, d\beta = \int_{\beta=0}^{2\pi} \int_{\alpha=0}^{\pi} H(\sigma_{Ieq}, \sigma_{Ic}) \sin\alpha \, d\alpha \, d\beta \tag{5}$$

where

$$H(\sigma_{Ieq}, \sigma_{Ic}) = \begin{cases} 1 & \sigma_{Ieq} > \sigma_{Ic} \\ 0 & \sigma_{Ieq} < \sigma_{Ic} \end{cases} \tag{6}$$

The integration is illustrated in Fig. 2.

Using Eqs. (5) and (6) in Eq. (4) and integrating over σ_{Ic} by parts, the following relation can be obtained:

$$P_S = \exp\left[-\frac{1}{4\pi} \int_V \int_{\beta=0}^{2\pi} \int_{\alpha=0}^{\pi} N(\sigma_{Ic} = \sigma_{Ieq}) \sin\alpha \, d\alpha \, d\beta \, dV \right] \tag{7}$$

The crack density function $N(\sigma_{Ic})$ is expressed as a power function of σ_{Ic}, that is

$$N(\sigma_{Ic}) = \frac{1}{V_o}\left(\frac{\sigma_{Ic}}{\sigma_{Io}}\right)^m \tag{8}$$

Nomenclature

A = area
b_c = Weibull scale parameter (experimental data)
E = Young's modulus of elasticity
H = step function
K_I = stress intensity factor
K_{Ic} = critical stress intensity factor (mode I)
K_{IIc} = critical stress intensity factor (mode II)
m = Weibull modulus
N = crack density function
P_S = probability of survival
T = temperature
T_a = cooling air temperature at the outer surface
T_i = gas temperature at the inner surface
V = volume
V_o = unit volume
α = linear thermal expansion
α = angle used in integration of unit radius sphere
α_1 = parameter used in Richard criterion
α_a = heat transfer coefficient at the outer surface
α_i = heat transfer coefficient at the inner surface
β = angle used in integration of unit radius sphere
ϵ_i = emissivity at the inner surface
λ = thermal conductivity
ν = Poisson ratio
$\sigma_1, \sigma_2, \sigma_3$ = principal stresses
σ_o = Weibull scale parameter of the unit volume (uniaxial)
σ_{Io} = Weibull scale parameter of the unit volume (polyaxial)
σ_{Ic} = critical stress (mode I)
σ_{Ieq} = equivalent stress (mode I)
σ_{cr} = critical stress
σ_e = effective stress
Ω = solid angle for which $\sigma_e > \sigma_{cr}$

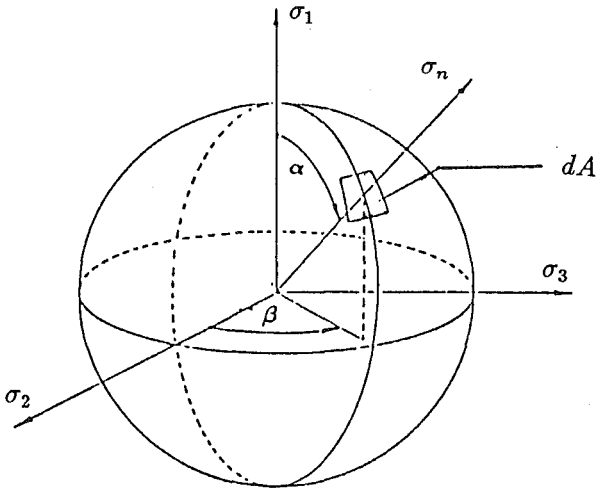

Fig. 2 Integration around the unit radius sphere

Finally, the crack density function in Eq. (7) is replaced by Eq. (8) at $\sigma_{Ic} = \sigma_{Ieq}$ and symmetric conditions are introduced. Then P_S is given by

$$P_S = \exp\left[-\frac{2}{\pi}\frac{1}{V_o}\int_V \int_{\beta=0}^{\pi/2}\int_{\alpha=0}^{\pi/2}\left(\frac{\sigma_{Ieq}}{\sigma_{Io}}\right)^m \sin\alpha\, d\alpha\, d\beta\, dV \right] \quad (9)$$

This relation is used in CERITS to calculate the probability of survival of ceramic components. For a detailed derivation of Eq. (9) see Munz and Fett (1989).

From a fracture mechanics point of view, Batdorf's model describes the physics of fracture rather than the pure extreme value statistics of Weibull. Furthermore, the introduction of the so-called equivalent stress σ_{Ieq} renders the Batdorf model extremely flexible. The equivalent stress σ_{Ieq} is a pure mode I stress (see Fig. 3), which has the same effect on the fracture initiation as the polyaxial stress state at the point under consideration. Different relations of equivalent stress, depending on fracture criterion and crack type, are given in the literature (Batdorf, 1978). Table 1 shows the relations available in CERITS. In the following, a short discussion of the shear insensitive as well as the shear sensitive criteria implemented in CERITS will be given.

Shear Insensitive Criteria. In CERITS, the normal stress criterion is applied for the shear insensitive model. In this case only normal stresses contribute to crack propagation and fracture initiation. Like Weibull's model with the principle of independent action, the Batdorf model with normal stress criterion leads to an underestimation of failure probability (Batdorf and Heinisch, 1978; Gyekenyesi, 1986).

Shear Sensitive Criteria. The coplanar strain energy release rate criterion (Batdorf, 1978) and the Richard criterion (Richard, 1985) are used as shear sensitive fracture criteria in CERITS. The coplanar strain energy release rate criterion is one of the most commonly used fracture criteria in the literature. Following this criterion, failure occurs if the strain energy release rate reaches a critical value, under the assumption that the crack propagation takes place in the plane of the original crack.

In contrast with other criteria, the empirical Richard criterion is more flexible. Here, the degree of shear sensitivity can be chosen according to the physical properties of the material under consideration through the introduction of the parameter α_1 in the equation for the equivalent stress (see Table 1). This parameter is defined as follows (Richard, 1985):

$$\alpha_1 = \frac{K_{Ic}}{K_{IIc}} \quad (10)$$

and depends only on the critical stress intensity factors K_{Ic} (mode I) and K_{IIc} (mode II), respectively (see Fig. 3). These factors can be determined experimentally. However, in the case of K_{IIc} the data available in the literature are insufficient.

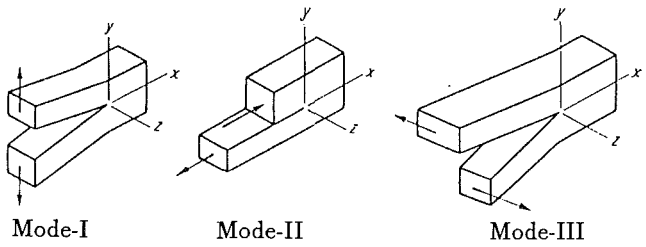

Fig. 3 Modes of crack surface displacement

Table 1 Different relations of equivalent stress

Symbol	Fracture criterion	Crack type	Equivalent stress
BATN	Normal stress criterion	Sphere	σ_n
BATGC	Strain energy release rate criterion	G.C.	$\sqrt{\sigma_n^2 + \tau^2}$
BATPSC	Strain energy release rate criterion	P.S.C.	$\sqrt{\sigma_n^2 + \frac{\tau^2}{(1-0.5\nu)^2}}$
RIPSC	Richard criterion	P.S.C.	$\frac{1}{2}\left[\sigma_n + \sqrt{\sigma_n^2 + \frac{4\alpha_1^2\tau^2}{(1-0.5\nu)^2}}\right]$

Crack Types. Two crack types, Griffith-Crack (G.C.) and Penny-Shaped-Crack (P.S.C.), are implemented in CERITS. The different combinations of crack type and fracture criteria are given in Table 1.

Weibull Scale Parameter. In Weibull's model as well as in Batdorf's model the Weibull modulus and the Weibull scale parameter are used to characterize the material strength. In CERITS, it is assumed that both parameters are derived from three or four point bending tests. The Weibull scale parameter is related to the test bar volume. In has to be reduced to the uniaxial Weibull scale parameter σ_o in the case of the Weibull model (see Eq. (2)) or to the polyaxial Weibull scale parameter σ_{Io} in Batdorf's model (see Eqs. (8) and (9)). In general, σ_{Io} depends on the applied fracture criterion. However, the use of a shear insensitive fracture criterion is justified when σ_1 is the only nonzero principal stress (Gyekenyesi and Wang, 1986). Consequently, this case is used in CERITS to calculate σ_o and σ_{Io} from three or four point bending test results including the effects of test type and test bar geometry.

Volume Integration. The volume integration of Eqs. (2) and (9) is achieved by subdividing the component into finite elements. Every finite element is divided itself into eight parts in each of which the stress state is to be considered constant. Equations (2) and (9) are solved for the subelements after approximating the volume integral through multiplication with the volume of the subelement. The probability of survival of a finite element can be calculated from the corresponding probabilities of the eight subelements. Finally, the joint probability of survival of the whole component is given by the multiplication of the finite element probabilities.

$$P_S = \prod_i (P_S)_i \quad (11)$$

Program Description

CERITS is a computer code for the prediction of failure probability of ceramic components. The necessary stress distribution within the component is provided by a preceding finite element analysis using the well-known computer codes ADINA and ADINA-T (N.N., 1984).

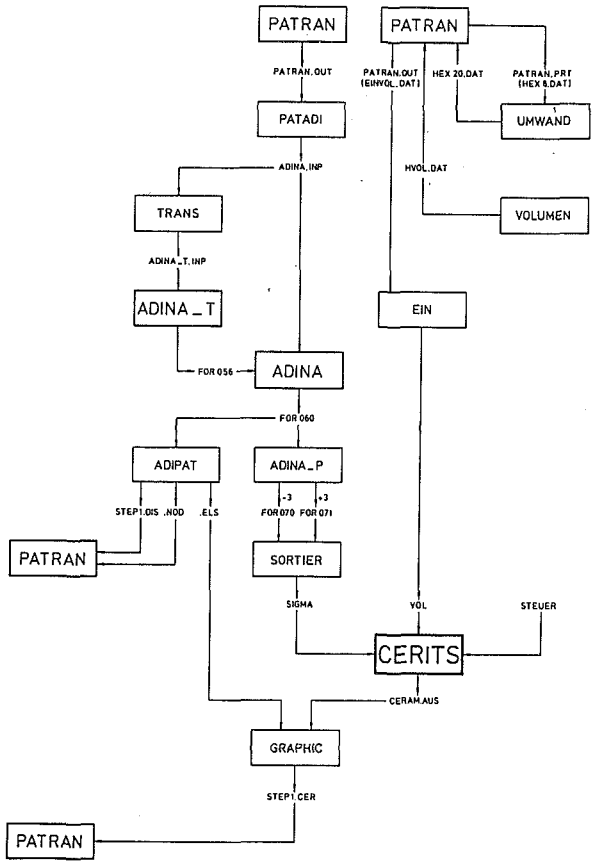

Fig. 4 Flow chart of the reliability analysis

Table 2 Required input control data

Variable	Entry	Format
NAME	Heading information	A20
WSTOFF	Material	A20
EMAX	Number of finite elements	I10
BK	Fracture criterion	I10
OUTPUT	Output control parameter	I10
ZAHL	Output control parameter	I10
TEST	Type of bending test	I10
M	Weibull modulus	F10.2
BC	Weibull scale parameter (experimental data)	F10.2
LI	Inner span	F10.2
LA	Outer span	F10.2
H	Height of test bar	F10.2
B	Width of test bar	F10.2
ALPHA1	Richard-parameter	F10.2
NUE	Poisson's ratio	F10.2
TEMP0	Reference temperature	F10.2

In addition to the stress distribution, the volumes of the finite elements are also necessary for the probability calculations. To get these volumes, we use the pre- and postprocessing system PATRAN (N.N., 1988), since finite element volumes are not available in ADINA. The sequence of analysis using CERITS together with other computer codes is depicted in Fig. 4. This figure also indicates that input and output of CERITS are managed by four logical units.

Logical unit 7 reads in the calculated stress distribution from ADINA. Under the assumption that the calculation has been performed by isoparametric 20-node elements with second-order integration, the data file contains three principal stresses at eight integration points of every finite element.

Logical unit 3 reads in the volumes of the finite elements from PATRAN.

Logical unit 5 reads a control file. This file contains the material properties, the fracture criterion, and some additional variables, such as the output control parameter, etc. Table 2 gives a summary of all required parameters.

The results are written on *logical unit 1*. This file contains all input control data and information on the convergence of the numerical integration. Finally, the failure probability and the probability of survival of the component are given (see Fig. 5). As an additional feature, the element probabilities can be printed in descending order. For reasons of clarity and for a better impression, the results can be illustrated by PATRAN. Thus, regions of insufficient reliability can be easily detected.

```
OUTPUT (CLASS 1)

NAME      : SEGMENT
MATERIAL  : SISIC

NUMBER OF ELEMENTS :    532

FRACTURE CRITERION (CRACK TYPE) : RICHARD-CRITERION (PSC)

NUMBER OF INTEGRATIONS                : 4256
INTEGRATIONS WITH REDUCED CONVERGENCE : 1650

TYPE OF BENDING TEST : 4-POINT BENDING

INNER SPAN        : 20.00
OUTER SPAN        : 40.00
HIGHT OF TEST BAR :  3.50
WIDTH OF TEST BAR :  4.50

WEIBULL SCALE PARAMETER BC (EXPERIMENTAL DATA) : 329.40
WEIBULL MODULUS (EXPERIMENTAL DATA)            :  12.40
WEIBULL SCALE PARAMETER SIGMA0 (CALCULATED)    : 310.96
REFERENCE TEMPERATURE                          : 293.00

POISSON'S RATIO                                :   0.20
RICHARD-PARAMETER ALPHA1                       :   1.30


OVERALL FAILURE PROBABILITY      :     0.162296D-02

OVERALL PROBABILITY OF SURVIVAL  :     0.998377D+00

END
```

Fig. 5 CERITS output

Table 3 Transversely loaded circular plate failure probabilities in percent (results from CERITS and SCARE)

	CERITS	SCARE
PIA	4.24	4.25
BATN	17.78	17.68
BATPSC	27.41	27.32

CERITS Code Verification

In order to verify the numerical code CERITS, comparative calculations were performed using the reliability analysis computer code SCARE developed by Gyekenyesi (1986). Gyekenyesi and Wang (1986) discussed a number of sample problems in order to validate the computer code SCARE. One of these examples is the analysis of a transversely loaded circular plate, which was used in the present studies to verify the numerical code CERITS. Table 3 summarizes the results of the comparison for different fracture criteria at an applied pressure of 1.52 MPa. An excellent agreement of the results can be observed.

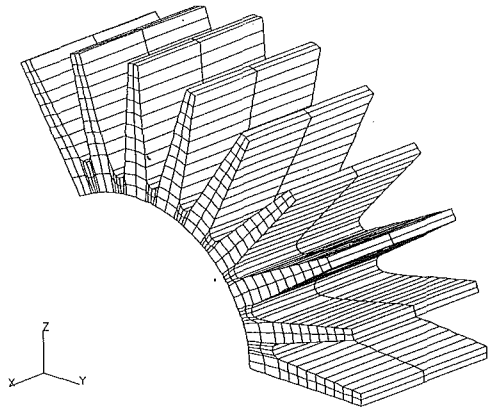

Fig. 6 Flame tube segment

Combustion Chamber Segment

The computer code CERITS is part of a research program at the Institute for Thermal Turbomachinery (ITS) concerning the development of a ceramic combustion chamber for a small gas turbine with a thermal power of about 300 kW. Before discussing the component design with the aid of CERITS in detail, the combustor conception is described.

In a first step to develop the combustion chamber, we require that only the highly loaded flame tube is made of ceramics. Previous investigations (Bunk and Böhmer, 1978) showed that flame tubes of monolithic design cannot satisfy the reliability demands. In our own preliminary investigations (Stürmer, 1987) we found that thermal stresses can be considerably reduced by dividing a monolithic component into small segments. Moreover, these calculations pointed out the advantages of circumferential as well as axial subdivision of the flame tube. Including thermodynamic and fluid mechanical aspects, the investigations led to flame tube segments, as depicted in Fig. 6. This figure shows the finite element model of the segment used in the first calculations. At present, the mesh is refined in the critical regions in order to improve the accuracy of the analysis. The segments have a 120 deg arc with an inner diameter of 45 mm and an outer diameter of 90 mm and an axial extension of 25 mm. To reduce the inner wall temperature, the segments are provided with cooling ribs along the outer surface. This is necessary due to the underlying thermal boundary conditions and the maximum permissible material temperature of about 1410°C for siliconized silicon carbide (SiSiC). If this temperature is exceeded, the elementary silicon would melt on the surface. Additionally sintered silicon carbide (SSiC) was taken into consideration. In this case the cooling ribs are unnecessary. However, to facilitate comparison, the analysis was done for the same geometry (with cooling ribs). To avoid mechanical stresses, the segments are elastically supported within a metal structure. Both radial and axial displacements are possible without constraints.

Boundary Conditions and Material Properties

The design process for a single flame tube segment will now be described. The boundary conditions of the finite element model satisfy rigid body motion constraints and permit a realistic description of the degrees of freedom of the segment in the real assembly. Especially the nodes within a contact surface of two parts are confined to avoid circumferential movement.

The thermal boundary conditions of the present calculations are summarized in Table 4. All calculations are performed under steady-state conditions. At the inner wall of the segment convective and radiative heat transfer are taken into account. Due to the relatively simple model in the finite element code ADINA-T, the radiative heat transfer is accounted for by a global coefficient only. The wavelength dependency of the emissivity of flue gas and soot and the absorption of the ceramic wall are not included. The heat transfer along the outer surface of the segment is assumed to be purely convective.

Table 4 Boundary conditions

Material	$T_i[K]$	$T_a[K]$	$\alpha_i[\frac{W}{m^2K}]$	$\alpha_a[\frac{W}{m^2K}]$	$\epsilon_i[-]$
SiSiC	1973	1073	245	566	0.6
SSiC	1973	1073	245	566	0.6

Table 5 Material properties

SiSiC

$T[K]$	$\lambda[\frac{W}{mK}]$	$E[GPa]$	$\nu[-]$	$\alpha[10^{-6}K^{-1}]$	$m[-]$	$b_c[MPa]$
293	140	380	0.2	5	12.4	329.4
873	70	350				
1673	40	290				

SSiC

$T[K]$	$\lambda[\frac{W}{mK}]$	$E[GPa]$	$\nu[-]$	$\alpha[10^{-6}K^{-1}]$	$m[-]$	$b_c[MPa]$
293	-	433.0	0.16	3.05	8.6	384.0
473	60.2	429.8		3.05		
673	51.0	426.2		3.03		
873	44.5	422.6		3.02		
1073	40.5	419.0		3.02		
1273	38.2	415.4		3.04		
1473	36.0	411.8		3.11		
1673	34.8	408.0		3.25		
1773	34.2	406.4		3.35		

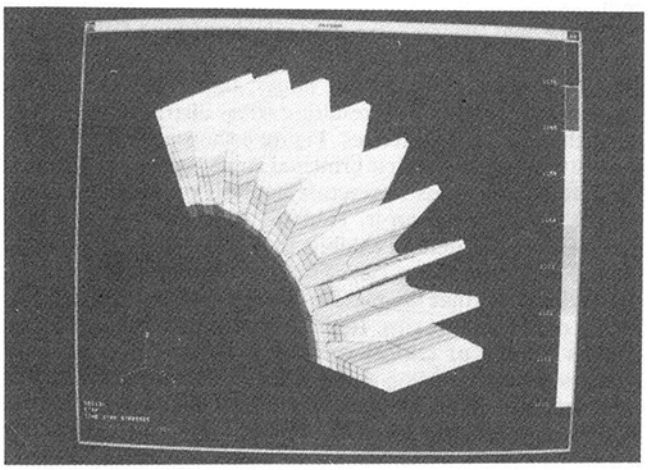

Fig. 7 Temperature distribution

The material properties of siliconized silicon carbide and sintered silicon carbide are given in Table 5. The temperature dependency of the material parameters is considered. However, the Weibull parameters are related to room temperature due to the lack of a satisfactory database for higher temperatures.

Results

Finite Element Analysis. As a first step in the design of the ceramic segments, the temperature distribution was calculated for both materials by ADINA-T. The thermal boundary conditions and material properties used have been previously introduced. The results are qualitatively demonstrated in Fig. 7, as generated by PATRAN. As expected, a

Table 6 Results of the finite element analysis

Material	$T_{min}[K]$	$T_{max}[K]$	$\sigma_{1max}[MPa]$	$\sigma_{3min}[MPa]$
SiSiC	1211	1582	149	-101
SSiC	1206	1596	168	-116

Table 7 Results of the failure probability analysis in percent

Material	PIA	BATN	BATGC	BATPSC	RIPSC $\alpha_1 = 0.5$	RIPSC $\alpha_1 = 1.3$
SiSiC	0.0098	0.0107	0.0191	0.0226	0.0147	0.1623
SSiC	0.1072	0.1162	0.2056	0.2318	0.1574	1.0012

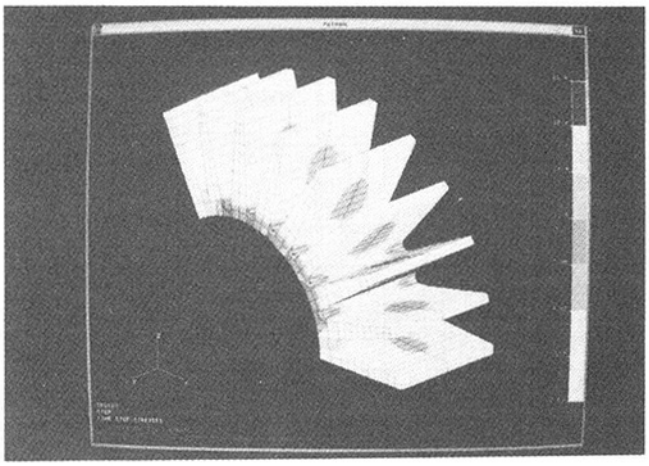

Fig. 8 Distribution of the first principal stresses

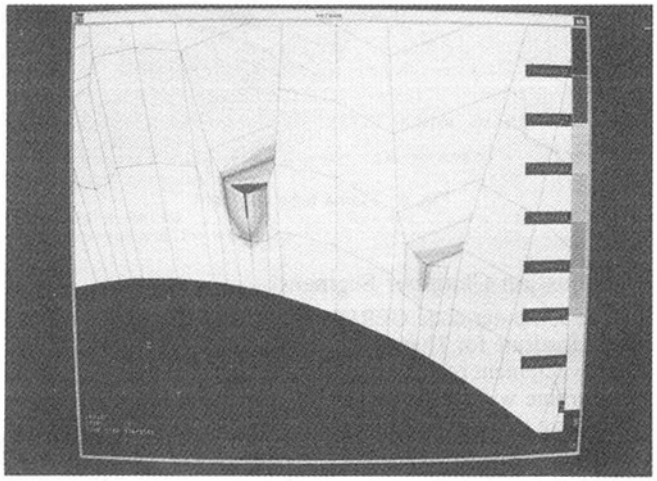

Fig. 9 Distribution of the failure probabilities

monotonic rise in temperature from the tips of the cooling ribs to the inner surface can be observed. In the axial direction, however, the temperature gradients are negligible. Table 6 contains some typical results of the thermal analysis.

The thermal stresses were thus calculated by ADINA using the calculated temperature distribution. Except for the above-mentioned constraints at some nodes, the model was not exposed to other loads. The resulting stress distribution is given through the principal stresses. Figure 8 shows, as an example, the distribution of the first principal stress, which is in general the determining stress in fracture analysis of ceramics. Some typical results are given in Table 6. As would be physically expected, the calculation exhibits the highest tensile stresses at the roots of the cooling ribs. For reasons of completeness, it should be noted that the highest compression stresses occur at the tip of the cooling ribs. In the present case the compression stresses are not of critical values. However, for a complete analysis the compression stresses have to be considered, even if the material strength of ceramics is much higher for compression than for tension. CERITS accounts only for failure under tensile stresses because compression contradicts the weakest link theory.

Reliability Analysis. The results of the failure probability analysis are demonstrated in Fig. 9. For clarity, only the critical region is shown. The advantages of using PATRAN as post-processing device are obvious. The originally colored failure probability distribution is given as a grey scale with darker areas representing critical regions of the segment. In the present case, the roots of the cooling ribs at both circumferential ends of the component are critical due to variations in wall thickness at this location. The absolute values of the failure probability are given in Table 7 for different fracture criteria. The failure probability of the component is about 0.02 percent using SiSiC. The results of SSiC are worse by a factor of 10. Moreover, it can be observed that the failure probability of both materials increases with the shear sensitivity of the chosen fracture criterion. In particular, the failure probability increases if the more shear sensitive Penny-Shaped-Crack is used instead of a Griffith-Crack in the same fracture criterion (please see BATGC and BATPSC results in Table 7). This trend is in accordance with the results given by Batdorf and Heinisch (1978) and Gyekenyesi (1986). The calculations including the Richard criterion were performed for various values of α_1. In the absence of the appropriate values of α_1 for the materials investigated, the highest and lowest values available in the literature were applied in the calculations.

Summarizing, it can be stated that in the case of SiSiC, the detected failure probability is satisfactory. However, in the case of SSiC the value is too high for running the present flame tube segments under operational conditions.

Conclusions

The new computer code CERITS for reliability analysis of ceramic components with respect to volume flaws is presented. Different fracture criteria based on the fracture statistical models of Weibull and Batdorf are discussed. CERITS is connected to the finite element code ADINA and uses the pre- and postprocessing system PATRAN for the demonstration of the results.

The design procedure is explained by its applicatiuon to a ceramic flame tube segment. Temperature and stress distributions are calculated by finite element techniques. The results are used to determine the failure probability of the component, including the effects of different fracture criteria and material properties. With the aid of CERITS, the critical regions of the segments can be easily identified. In the case of SiSiC the absolute values of the failure probability are satisfying. In the case of SSiC, however, future activities have to be concentrated on the improvement of the material parameters as well as on the design of the components.

References

Batdorf, S. B., and Crose, J. G., 1974, "A Statistical Theory for the Fracture of Brittle Structures Subjected to Nonuniform Polyaxial Stress," ASME *Journal of Applied Mechanics*, Vol. 41, pp. 459–464.

Batdorf, S. B., 1977, "Some Approximate Treatments of Fracture Statistics for Polyaxial Tension," *International Journal of Fracture*, Vol. 13, pp. 5–11.

Batdorf, S. B., 1978, "Fundamentals of the Statistical Theory of Fracture," *Fracture Mechanics of Ceramics*, R. C. Bradt et al., eds., Plenum Press, New York, Vol. 3, pp. 1–30.

Batdorf, S. B., and Heinisch, H. R., Jr., 1978, "Weakest Link Theory Re-

formulated for Arbitrary Fracture Criterion," *Journal of the American Ceramic Society*, Vol. 61, pp. 355–358.

Bunk, W., and Böhmer, M., eds., 1978, *Keramische Komponenten für Fahrzeug-Gasturbinen*, Springer-Verlag, Berlin.

Gyekenyesi, J. P., 1986, "SCARE: A Postprocessor Program to MSC/NASTRAN for Reliability Analysis of Structural Ceramic Components," ASME JOURNAL OF ENGINEERING FOR GAS TURBINES AND POWER, Vol. 108, pp. 540–546.

Gyekenyesi, J. P., and Wang, A. J., 1986, "SCARE—A Post-processor Program to MSC/NASTRAN for the Reliability Analysis of Structural Ceramic Components," NASA Technical Report TR-2654.

Munz, D., and Fett, T., 1989, *Mechanisches Verhalten keramischer Werkstoffe*, Springer-Verlag, Berlin.

N. N., 1984, "ADINA Theory and Modeling Guide," Report AE 84-4, ADINA Engineering Inc., Watertown, MA.

N. N., 1988, "PATRAN Plus User Manual," P/N 2191020, PDA Engineering, Costa Mesa, CA.

Richard, H., 1985, "Bruchvorhersagen bei überlagerter Normal- und Schubbeanspruchung von Rissen," VDI-Forschungsheft 631/85, VDI-Verlag, Düsseldorf.

Rufin, A. C., Samos, D. R., and Bollard, R. J. H., 1984, "Statistical Failure Prediction Models for Brittle Materials," *AIAA Journal*, Vol. 22, pp. 135–140.

Shih, T. T., 1980, "An Evaluation of the Probabilistic Approach to Brittle Design," *Engineering Fracture Mechanics*, Vol. 13, pp. 257–271.

Stürmer, G., 1987, "Theoretische Untersuchung der Temperatur- und Spannungszustände keramischer Brennkammerbauteile," Diplomarbeit, Institut für Thermische Strömungsmaschinen, Universität Karlsruhe, Federal Republic of Germany.

Weibull, W., 1939, "A Statistical Theory of the Strength of Materials," *Ingeniörsvetenskapsakademiens Handlingar*, No. 151.

W. P. Parks, Jr.
R. R. Ramey

Babcock & Wilcox Co.,
Lynchburg, VA 24506

D. C. Rawlins
J. R. Price
M. Van Roode

Solar Turbines Inc.,
San Diego, CA 92138

Potential Applications of Structural Ceramic Composites in Gas Turbines

A Babcock and Wilcox–Solar Turbines Team has completed a program to assess the potential for structural ceramic composites in turbines for direct coal-fired or coal gasification environments. A review is made of the existing processes in direct coal firing, pressurized fluid bed combustors, and coal gasification combined cycle systems. Material requirements in these areas were also discussed. The program examined state-of-the-art ceramic composite materials. Utilization of ceramic composites in the turbine rotor blades and nozzle vanes would provide the most benefit. A research program designed to introduce ceramic composite components to these turbines was recommended.

Introduction

A research team from Babcock and Wilcox Co. and Solar Turbines Inc., working under a program sponsored by the US DOE AR&TD Fossil Energy Program, has assessed the potential for structural ceramic composites in turbines for direct coal-fired or coal gasification systems (Parks et al., 1989). The program goal was to identify potential improvements to overall system efficiency and performance over current designs through the implementation of ceramic composites.

This was accomplished by reviewing current designs for coal-based turbine systems, assessing state-of-the-art structural ceramic systems, and by identifying those areas in a turbine that would most benefit from the utilization of ceramics.

A research program to incorporate ceramic composites in a gas turbine to best advantage was also recommended.

Background

Land-based gas turbines are currently being used by domestic electric utilities to generate power during peak demand times and by industrial concerns such as offshore oil platforms for electrical generation. Only about one percent of the baseline power in the United States is generated from gas turbines; however, a time can be foreseen when large amounts of power will be derived from combined gas turbine/steam turbine systems as they have an overall efficiency greater than that of a conventional steam plant. Furthermore, with the development of coal gasification, pressurized fluidized bed combustion, and direct coal-fired gas turbines, it is possible that combined cycle plants will be coal based. It can also be anticipated that the turbines will be operated at higher temperatures because of the increases in specific output and unit efficiency that can be gained (EPRI, 1986). Increasing the turbine firing temperature to the 1675 K range or higher could raise the net integrated system efficiency by 2–3 percentage points depending upon the actual system (Horner, 1980).

This work focused on direct-coal-fired gas turbines (CFGT) and turbines in integrated coal gasification combined cycle systems (IGCC) rather than gas turbines in general. CFGT and IGCC systems are both under development, but have not yet achieved commercialization. The degree to which these systems will impact the global energy scene and affect oil usage and supply will depend on the rate at which the remaining technical barriers of these systems can be overcome and on the number of systems installed. A preliminary forecast of approximately 200 2–10 MWe coal-fired gas turbines to be installed in the United States over the next 10–15 years was estimated as part of Solar's CFGT program (Smith et al., 1987). The major markets for CFGT were determined to be industrial cogeneration, military installations, and enhanced oil recovery sites. The expected market for IGCC appears to be in the 100–500 MWe range; however, no forecast on the number of potential units has been identified (Wieber and Halow, 1987; Cornett, 1987).

Industrial gas turbines generally operate at turbine inlet temperatures in the 1035 to 1435 K range, although engines with advanced cooling designs have been able to achieve a current maximum turbine inlet temperature of approximately 1525 K. The maximum adiabatic flame temperature of most common fuels is approximately 2275 K, so further increases in turbine inlet temperature would be feasible if materials could be developed to withstand higher operating temperatures.

Marginal improvements in performance can be achieved through the use of advanced metallic alloys such as directionally solidified single crystal components. However, these materials have several disadvantages, including high costs, utilization of strategic materials, special fabrication requirements, and cooling in service, which reduces system efficiency.

Recently, efforts have been made to use low-grade fuels,

Contributed by the International Gas Turbine Institute and presented at the 35th International Gas Turbine and Aeroengine Congress and Exposition, Brussels, Belgium, June 11–14, 1990. Manuscript received by the International Gas Turbine Institute January 30, 1990. Paper No. 90-GT-251.

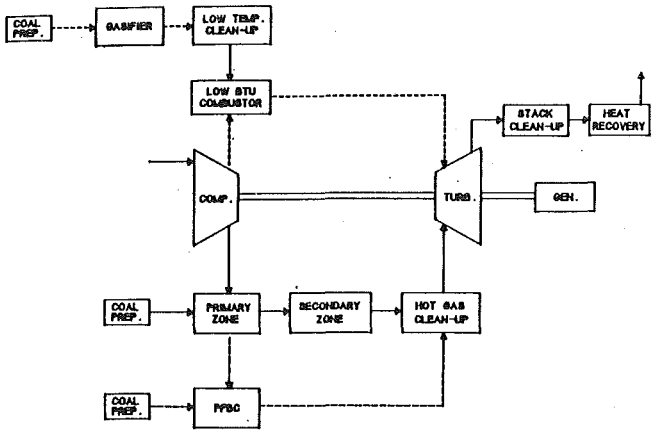

Fig. 1 Similarities between direct coal-fired gas turbines, IGCCs, and PFBCS

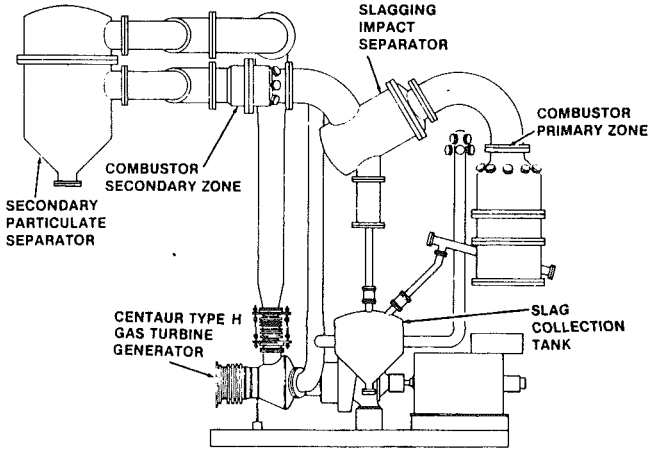

Fig. 2 Solar's coal-fueled Centaur model H gas turbine system arrangement

such as coal, to power the gas turbine. This necessitates that either the turbine hot end components be hardened to withstand the corrosive and erosive nature of the hot gases from the coal combustor or that the hot combustion gases be sufficiently cleaned of ash and slag particulates and other corrosive species prior to entering the turbine hot end.

The combustion of coal presents several potential hazards to both the turbomachinery hardware and the environment. The ash contained in coal is relatively inert during combustion; however, it can cause accelerated erosion and corrosion of the turbine if it is not removed from the gas stream. Fly ash is also a potential health hazard, and its concentration in the turbine exhaust streams will likely be regulated by federal and state governmental agencies. The sulfur and nitrogen contained in the coal present potential hazards since they are major contributors to the formation of acid rain.

This overview focuses on those systems that are currently being designed or are in demonstration scale testing. Three types of coal-fired gas turbine system were studied. Figure 1 shows their similarities and common major components. The basic goal of these systems is to burn coal for the production of electricity and to recover the exhaust thermal energy in a steam bottoming cycle for additional power. The three types are:

1 Direct coal-fired gas turbines utilizing entrained flow combustors (CFGT)

2 Integrated coal gasification combined cycles (IGCC)

3 Pressurized fluidized bed combustors (PFBC) in combined cycle systems

Direct Coal-Fired Gas Turbines. The Department of Energy (DOE) through the Morgantown Energy Technology Center (METC) is currently supporting several programs for the development of an environmentally sound, integrated heat engine system that will produce cost-competitive energy from coal (Byam and Markel, 1987). Three gas turbine manufacturers have been awarded contracts through METC for the development of a direct coal-fired gas turbine: Solar Turbines Incorporated, Allison Gas Turbine, and Westinghouse.

These contracts are now in the third year of a five-year program, with coal-fired engine demonstrations planned for the mid-1990s. Solar and Allison are developing coal-fired engines of approximately 4 MWe. Westinghouse plans to develop a 100 MWe coal-fired gas turbine after an initial subscale development of a 0.5 MWe turbine. All three contractors plan to use coal–water slurry as fuel. Modifications to the gas turbine hardware are focused on the combustion zone, with the aerodynamic design and the materials of construction of the turbine hot end remaining unchanged. One of the proposed systems is shown in Fig. 2.

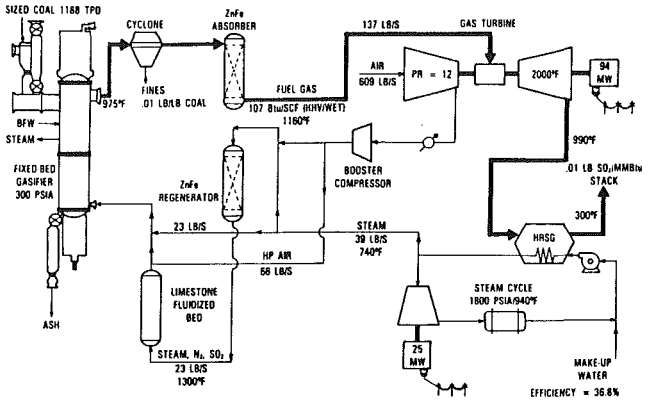

Fig. 3 Schematic of fixed-bed gasifier system (Wieber and Halow, 1987)

Integrated Coal Gasification Combined Cycles. Integrated coal gasification combined cycle (IGCC) systems for electric power generation are very attractive since they allow utilities to add power output incrementally to existing power plants, first by installing a gas turbine fired by natural gas, then by adding a coal gasifier and gas cleanup system, and finally by adding a steam turbine. High thermal efficiencies can be obtained because of the combination of efficient combustion turbines with steam turbines (Penner et al., 1987). The gas turbines normally used in IGCC systems are large industrial engines ranging from approximately 35 to 140 MWe. Complete IGCC power plants may include several gas turbines along with a steam turbine. Total power output for planned IGCC plants range from about 50 to greater than 400 MWe.

In IGCC, coal is reacted with air or oxygen under reducing conditions to produce a fuel gas that normally has high concentrations of hydrogen, carbon monoxide, and sometimes methane. A low-Btu fuel gas is obtained in air-blown gasifiers, and a medium-Btu gas is obtained in oxygen-blown systems.

There are three main types of gasifiers: entrained flow, fluidized bed, and fixed bed reactors. An example is shown in Fig. 3.

Pressurized Fluidized Bed Combustors. Pressurized fluidized bed combustors (PFBC) differ from fluidized bed gasifiers in that sufficient air is fed into the combustion zone to provide complete combustion of the coal rather than the formation of a fuel-rich syngas. These systems operate at pressures up to about 10 atm, with bed temperatures maintained below 1145 K. Sulfur control is obtained by injecting calcium-based sorbents into the fluidized bed. One of the remaining technical

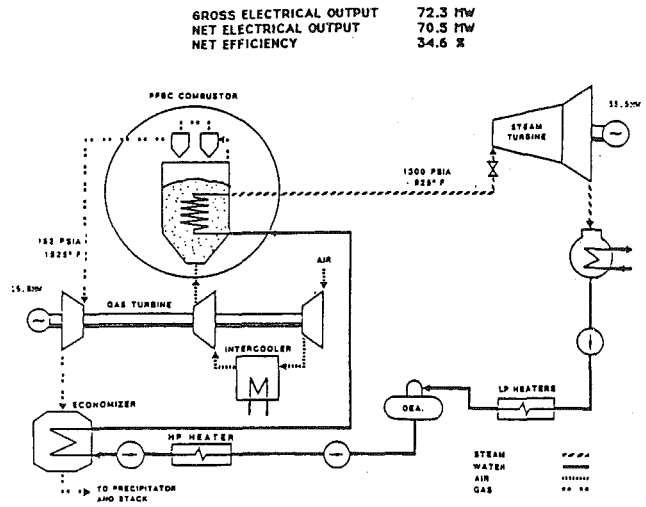

Fig. 4 Schematic of Tidd PFBC demonstration plant (Mudd and Strogran, 1988)

difficulties in PFBC systems is the development of hot gas clean-up methods that will provide adequate protection for the gas turbine hardware. Two or three stages of high-efficiency cyclones are currently used to reduce particulate loadings. Environmental protection standards for particulates are met using postturbine particulate control methods. There are no commercial PFBCs in operation today; however, several utility-scale demonstration projects are under construction, and several pilot-scale plants are in operation (Smith, 1985). Plans for second generation PFBCs include a topping combustor to heat the gas exiting the PFBC to 1425–1475 K prior to entering the gas turbine (McClung, 1988). One example is shown in Fig. 4 (Mudd and Strogran, 1988).

Ceramic Component Development for Gas Turbines

In recent years, a rapid growth in research and development activities aimed at improving turbine engine performance through increased turbine inlet temperature has occurred. The two major design approaches to achieve the higher turbine inlet temperature are to utilize advanced cooled superalloy components and high-temperature monolithic ceramic or ceramic composite components. The two approaches are diverse with respect to design, manufacturing methods, capabilities and limitations (Bornemisza and Napier, 1988). The metal alloy approach is more mature and presents less risk in all areas, while the ceramic approach represents a high-risk alternative but with much greater potential benefits to engine performance and cost savings. This is largely due to elimination, or reduction of cooling air, higher turbine inlet temperatures, and reduction of erosion and corrosion problems. All of these will contribute to increased overall efficiency and durability.

In a review of the development of ceramic automotive gas turbines, Carruthers and Wimmer (1988) reported that high-performance ceramics, in conjunction with heat recovery cycles and improved aerodynamics, promise fuel savings on the order of 50 percent in a variety of gas turbine applications by the year 2000. This savings is mainly attributable to the higher turbine inlet temperatures (TIT) achievable using ceramic components. Such dramatic increases in fuel savings may not be realizable with coal-fired industrial gas turbines; however, it is evident that increased firing temperatures will increase the overall efficiency of the integrated system. The degree to which these savings can be achieved is highly dependent upon the ongoing development of ceramic matrix composite components with improved fracture toughness and reliability.

Several specific components in a coal-fired industrial gas turbine can potentially benefit from the use of structural ceramics. These are summarized below:

Slurry Transport and Atomization. The inside walls of the transport piping and the atomization nozzles are subject to wear due to the abrasive nature of coal slurry; however, temperature is not a problem since the slurries are water based. Abrasion-resistant materials to line the interior of the transport pipes and to manufacture nozzles are readily available from numerous suppliers.

Combustor. Combustors and gasifiers for coal firing will be subject to severe operating conditions since they will face temperatures of 1800–2140 K under reducing conditions. Experience has shown that high chromium refractories have performed well in coal gasifiers. The combustors designed for coal-fired gas turbines will also be refractory lined vessels; thus satisfactory performance can be expected.

Transfer Ducting. The transfer ducting between an off-base cylindrical combustor and the annual turbine section (i.e., the scroll) will be subjected to high temperatures, although not as high as those in the combustor. It is expected that the conditions encountered in the transfer ducting can be resisted by the same refractories used in the combustor.

Hot Gas Clean-Up. Due to their erosive and corrosive nature, the products of coal combustion will be very detrimental to gas turbine hot end materials. Thus hot gas clean-up is critical to success. Numerous projects are currently being funded by DOE, EPRI, and several other organizations (Furlong and Shevlin, 1981; Ciliberti and Lippert, 1981; Saxena et al., 1985). Due to this high level of effort, hot gas clean-up was considered to be beyond the scope of this project.

Gas Turbine Hot End (Nozzle Vanes and Rotor Blades). The gas turbine hot end is primarily concerned with the first-stage nozzle vanes and first-stage rotor blades since these areas are exposed to the highest temperatures. The vanes and blades in subsequent stages will be subjected to lower temperatures due to work extraction. The first-stage components are currently made from cooled superalloy materials, and elimination of this cooling would permit increased turbine efficiencies.

For both the nozzle vanes and rotor blades, replacement of the currently used metallic components with ceramic materials would yield several significant advantages. These include increased efficiency due to higher temperature capability and reduced cooling requirements. However, when using ceramics, the designer must be concerned with maintaining stresses to values substantially less than the nominal fracture stress of the ceramic, and avoidance of high-stress concentrations that in a metal component could be reduced by local plastic deformations.

The first-stage nozzle vanes experience the highest gas temperatures within the gas passage, and are also exposed to temperature spikes, which can be several hundred degrees higher than the average inlet temperature. First-stage superalloy nozzle vanes are usually coated, and are aggressively cooled as the gas temperatures can be greater than the melting point of the metal. Subsequent stages of nozzles are at lower temperatures due to work extraction and additions of cooling air.

Additional air cooling of the superalloy nozzle vanes could be used to allow for higher inlet gas temperatures; however, this extracts a penalty on the overall cycle efficiency. Improved thermal barrier coatings offer the potential of higher firing temperatures at the price of higher manufacturing costs. Ceramics might permit increasing the inlet air temperatures into the 1620–1970 K range without the need for air cooling or additional coatings.

Rotor blades are typically exposed to slightly lower temperatures than the nozzle vanes; however, they are subject to

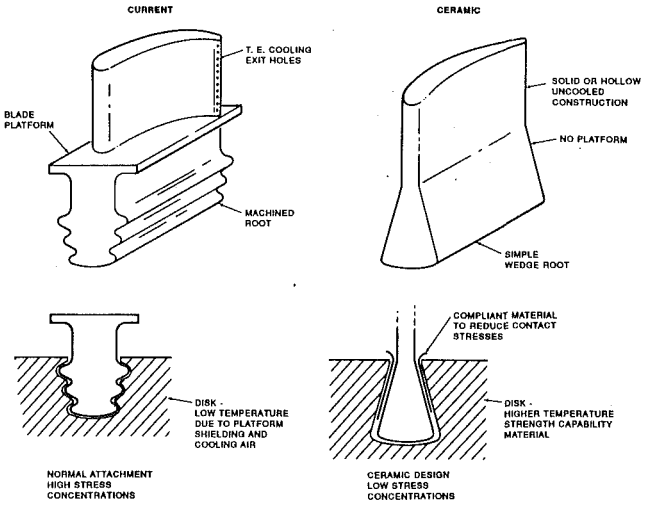

Fig. 5 Schematic representations of current superalloy and a potential ceramic turbine blade root design

high tensile loads created by the high-speed rotation. In industrial turbine applications, metal temperatures are limited to about 1175 K for conventional superalloys, and to about 1325 K for advanced directionally solidified and single crystal alloys. Ceramics offer the potential for uncooled operation at temperatures up to about 1675 K. For separately bladed metallic disks, design considerations must include potentially higher temperatures due to the use of uncooled blades. High cycle fatigue properties of the ceramic materials need to be established before successful application in rotating components can be achieved.

Ceramic research to date has concentrated mainly on small radial engine components, i.e., technology has not progressed to the point where all ceramic integral rotors are feasible in the size range required of medium to large sized industrial gas turbines. In addition, a blade root design for attachment to the metal disk that would avoid contact stress initiated failures remains one of the critical issues yet to be solved. Composite systems with high fracture toughness and more predictable properties may provide part of the solution. It is believed that the recent advances in ceramic technology may be sufficient to design and fabricate ceramic composite turbine blades successfully in the near future (Fig. 5).

For both rotor blades and nozzle vanes, the potential advantages and design considerations/limitations of ceramics are similar. Some of the most significant advantages are:

- Higher temperature capability, which translates directly to higher firing temperatures and accompanying efficiencies.
- Reduced cooling requirements for the same firing temperature, which also translates directly to improved efficiency.
- Reduced sensitivity to combustor pattern factor problems (streaking or temperature spikes) as a result of flatter strength versus temperature and oxidation versus temperature behavior of ceramics.
- No need for protective coatings, thereby reducing the number of processing steps, except for unusually severe environments (coatings may be required to reduce contact stress problems).
- No strategic element content.

The support disk will continue to be made from metal alloys; however, the temperature capabilities of these alloys will be greater than those currently used.

Material Assessment

This section examines the state of the art in ceramic material development. The materials addressed are shown in Table 1, while materials recommended for further study are listed in Table 2. Key systems are described in the following sections; however, considerable other work is ongoing world-wide.

Table 1 Systems reviewed for possible application to coal-based gas turbines

Monolithic Systems
- Silicon carbide
- Silicon nitride
- Zirconia

Composite Systems
- Silicon nitride matrix
  - SiC whiskers
  - Continuous SiC fibers
  - SiC particulate
  - BN particulate
- Silicon Carbide matrix
  - CVI/CVD of continuous fiber preform
- Alumina matrix
  - SiC whiskers
  - SiC continuous fibers or particulates made using DIMOX process
  - Continuous fibers
- Zirconia matrix
  - Continuous Al_2O_3/ZrO_2 fibers
- Mullite matrix
  - Continuous SiC fibers
  - SiC whiskers
  - Continuous alumina fibers
  - Continuous mullite fibers
  - Alumina whiskers
- Glass ceramic matrix
  - Continuous SiC fibers
- Carbon matrix
  - Continuous graphite fibers

Structural ceramics can be divided into two major classifications: monolithics and composites. Major efforts have been pursued by companies such as GTE, Norton, and Garrett to produce useful monolithics for structural applications; however, one basic flaw remains in their structural use: These materials fail catastrophically with minimum reliability. Weibull statistical studies have helped to characterize risk but performance is still limited.

Ceramic composite materials have expanded the capabilities of structural ceramics as they offer improved toughness, impact resistance, and greater strain to failure than monolithic materials, all of which lead toward greater reliability than previous ceramics. There is considerable ongoing work in different types of reinforcement for ceramic composites, including particulates, whiskers, chopped fibers, and continuous fibers. In general, composites with particulates, whiskers, and chopped fibers yield greater strain to failure than monolithic ceramics. Continuous fiber-reinforced composites show the greatest strain-to-failure and also show nonbrittle failure.

The database for ceramic composites is limited, especially when applied to corrosive conditions in coal-fired turbines. Many systems have been characterized for unidirectional flexural strengths, but complete tensile and sheer data are lacking. Indeed, work is needed to understand the failure mechanisms in ceramic composites. Few data on long-term properties, such as creep, cyclic fatigue, and corrosion, have been reported.

A stress-strain curve comparing flexural data for monolithic SiC and a Nicalon/CVI SiC composite is shown in Fig. 6. Initial failure strain for the composite material is about seven times greater than that of the monolithic. This behavior translates to greater tolerance to mechanically or thermally induced strains and perhaps more predictable performance.

Non-Oxide Structural Ceramic Systems. Silicon nitride matrix composites have been produced with various reinforce-

Table 2 Recommended ceramic composites for evaluation as candidates for coal-based gas turbines (these composites will be tested against currently used metallic components)

Fabricator	Composite
Babcock & Wilcox	Oxide-oxide
	SiC reinforced CVI SiC
Corning	Continuous fiber reinforced
	Calcium-alumino-silicate
	Glass ceramics
DuPont/SEP	SiC reinforced CVI SiC
Lanxide	Composites
Oak Ridge National Laboratory	SiC whisker reinforced Al_2O_3
	SiC reinforced CVI SiC
3M	Nextel reinforced CVI SiC (Siconex TM)
GTE	Si_3N_4 based composites
Carborundum	SiC based composites

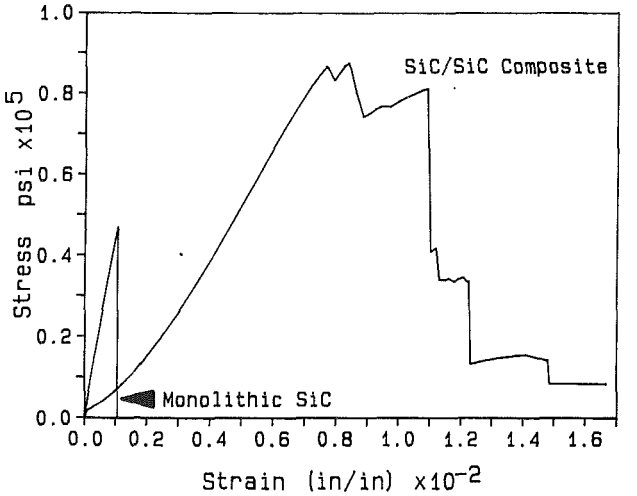

Fig. 6 Stress-strain curves contrasting monolithic SiC with a SiC composite containing continuous SiC fibers

ments, including SiC whiskers (Taheto, ARCO, Los Alamos) and continuous fibers (Nicalon, Tyrano, Nextel 312, Dow Corning fibers). Processing methods include hot-pressing (Shalek et al., 1986; Buljan et al., 1987, 1988), hot isostatic pressing (Yeh and Schienle, 1987) or reaction-bonding (Lundberg et al., 1987; Bhatt, 1985; Corbin et al., 1986).

In hot-pressed composites, a 30 v/o SiC_w loading yielded the best strength and fracture toughness at both ambient and elevated temperatures. The strengths of reaction bonded silicon nitride (RBSN) were considerably lower; however, unlike the hot-pressed materials, they fractured in a nonbrittle manner. Norton (Corbin et al., 1986) has produced RBSN specimens with a strength (110 ksi) 230 percent over that of their monolithic RBSN. The work of fracture of this material was also significantly improved.

Chemical vapor deposited (CVD) SiC/SiC composites have been made by several groups including SEP, ORNL, DuPont, TECO, and RCI. Both ORNL and SEP have shown composites with strength retention to 1275 K (Lamicq et al., 1986; Stinton, 1989). Tensile data from ORNL have shown failure stress of 33 ksi and strain of 0.75 percent. Unreinforced SiC exhibited strain to failure around 0.1 percent (Caputo et al., 1987).

Corrosion tests on monolithic SiC and Si_3N_4, and a few composites with these matrices, have been performed by ORNL, B&W, and TECO. In alkali-rich environments, such as coal-fired applications, these materials perform poorly. For example, SiC at 1425 K was consumed after 48 hours in sodium carbonate (Federer, 1990).

Oxide Matrix Composites. Alumina, mullite, zirconia, and glass ceramic matrix systems have also been examined. Alumina has been successfully reinforced with silicon carbide whiskers and particulates, and DuPont's alumina/zirconia continuous fiber (PRD-166). Forming techniques have been hot-pressing, pressureless sintering, direct oxidation process (DIMOX), and sol-gel impregnation. Some of the earliest work on hot-pressed composites was done at Oak Ridge where specimens containing up to 50 v/o whiskers were made successfully (Becher and Wei, 1984; Wei and Becker, 1985; Tiegs and Becher, 1985, 1986). Fully dense (>99 percent theoretical density), fine grained ($<\mu$m), alumina matrix composites were attained when hot-pressing was done at 2125 K. Moreover, SiC_w were found to be compatible and stable in the presence of alumina. At 20-30 v/o SiC_w loadings, toughness was approximately double that of pure alumina. However, of greater importance was that it was retained to 1275 K, i.e., to the projected use temperature of coal-based gas turbines currently under development. Flexural strength increased with increasing whisker content.

Hot-pressed shapes are generally limited to simple geometries, are costly, and have anisotropic properties due to preferred whisker orientation. For these reasons, use of pressureless sintering techniques are desirable; however, sintering under pressureless conditions is difficult as the whiskers inhibit particle rearrangement and shrinkage.

Mechanical properties of pressureless sintered composites are strongly dependent upon the fired density and the best fracture toughness (7.5 MPa•$m^{1/2}$) is found in composites with a 10 v/o whisker loading at a 92 percent theoretical density. This value is comparable to the fracture toughness of hot pressed composites with the same whisker loading; however, the strength is poorer.

Lanxide Corporation produces ceramic composites via direct oxidation of molten aluminum metal baths, and they have reported data on alumina matrix composites reinforced with Nicalon or Avco silicon carbide fibers and SiC particulates (Barron-Antolin et al., 1988; DuPont, 1989). The Nicalon fiber containing composites exhibited room temperature four-point bend strengths of 145 psi and toughness values up to 29 MPa•$m^{1/2}$; however, high-temperature properties were not reported. At 1275 K, both strength and fracture toughness of SiC particulate containing composites were approximately half their room temperature values.

The mechanical properties of mullite can be improved through additions of SiC_w and also SiC continuous fibers. With increasing whisker loadings, flexural strength increased with the maximum increase occurring at the 30 w/o level (Samanta and Musikant, 1985). In addition, limited data have shown that fracture toughness can be improved from 2.4 to 3.52/3.60 MPa•$m^{1/2}$ by a 30 w/o whisker addition.

Continuous fiber zirconia matrix composites show moderate strength at room temperature and good strength retention at elevated temperatures. Failure occurs noncatastrophically. In addition, PRD-166 zirconia composites offer the good corrosion and stability in air of monolithic zirconia. Corrosion testing in both sodium carbonate and municipal refuse environments showed improved corrosion resistance in comparison to metals or monolithic silicon carbide (Parks, 1989).

In comparison to more traditional crystalline materials, composites that have a glassy matrix can be densified without damaging the reinforcing fibers as the matrix is able to flow at temperature. In addition, glass ceramics provide a means whereby the matrix can be densified in the glassy state then crystallized to a refractory material. Early work on fiber-reinforced glass matrices was done at United Technologies Research Center (Brennan and Prewo, 1982; Prewo and Brennan, 1982; Prewo et al., 1986) where SiC fibers were used to rein-

Table 3 Ranking of ceramic systems for potential application in direct-fired turbines for coal or coal gasification processes; range is from a low of 1 (poor) to a high of 5 (good)

System		Criteria								
Fiber	Matrix	Oxidation	Erosion	1000°C Strength	Thermal Stability	Toughness	Development State	Ease of Processing Complex Shapes	Suspected Reliability	Rank
Oxide	Alumina	5	4	2	5	4	2	3	4	33
Oxide	Zirconia	5	4	3	4	4	2	3	4	33
SiC whisker	Alumina	3	3	4	4	4	3	2	3	31
SiC	SiC	2	3	4	3	4	3	3	4	30
SiC	SiC/oxide coating	4	4	4	3	4	1	2	4	26
SiC	Mullite	3	2	3	2	3	2	3	4	25
SiC	Glass	2	2	3	2	3	3	3	4	24
Graphite	Carbon	1	2	2	2	3	4	3	4	23
—	Zirconia	5	5	3	3	3	4	3	2	31
—	SiC	3	3	3	3	2	5	3	2	27
—	Silicon	2	3	3	3	2	5	3	2	27

force both glass and a lithium aluminosilicate (LAS) glass ceramic. Other work by Corning using a SiC whisker-reinforced cordierite matrix has yielded a promising glass matrix composite (Gadkaree and Chung, 1986). Strengths (46 ksi) at 1175 K were only slightly less than those at room temperature and 60 percent of the room temperature strength (53 ksi) was retained at 1475 K.

In corrosion testing, dense alumina and zirconia perform substantially better than SiC or Si_3N_4 in oxidizing conditions. Corrosion resistance often decreases with silica content.

Material Assessment Conclusions. A review of the existing ceramic systems has indicated that there are several promising systems that could find application in turbines:

- Alumina reinforced with SiC whiskers
- Mullite reinforced with continuous SiC fibers or whiskers
- Zirconia reinforced with continuous alumina-zirconia fibers
- Silicon nitride reinforced with SiC continuous fibers or whiskers
- CVI SiC reinforced with continuous SiC fibers
- Glass ceramics reinforced with continuous SiC fibers

Although there are several promising systems, the current database is insufficient to apply them directly to design of turbine components. The database must be expanded to include processing enhancements, component design, joining techniques, ability to produce complex shapes, and reliability assessment. Based on recent work (Luh et al., 1989) at Lawrence Berkeley Laboratory, which has shown substantial reduction in life for some ceramic materials exposed to cyclic as opposed to static loading, the effect of cyclic loading (high cycle fatigue) needs to be established on potential ceramic turbine materials.

When potential ceramic systems are compared, it becomes apparent that tremendous differences exist between the current state of the art in the various systems. In an effort to highlight areas of difficulty and strength, a ranking scheme was devised as shown in Table 3. This ranking is subjective, and addressed only the application of these materials to turbines for direct firing or coal gasification; ranking for other applications would be different.

Conclusions

Ceramic composites are still in their infancy, having received intensive development only since the mid-1970s. The difficulties of bringing this new generation of materials to technical and economic viability are evidenced by the fact that they have not yet found widespread use. The work addressed herein focused on ceramic composites for coal-fired gas turbines; however, future research on these materials will also be applicable to conventionally fired gas turbines as well as other ceramic applications.

This work showed that several material systems are potentially applicable to gas turbines. However, because of limited property characterization in many cases, additional research to prove their suitability is warranted. The ultimate goal of this research program is long-term testing of ceramic components in an actual coal-fired gas turbine system. This goal will only be achieved through a sustained research effort over several years with the financial backing of both government and industry. The benefits to be obtained from this research include increased system efficiency for coal-fired gas turbine systems due to increased firing temperature capabilities, and increased component life due to the superior erosion and corrosion characteristics of ceramics.

References

Barron-Antolin, P., Schiroky, G. H., and Anderson, C. A., 1988, "Properties of Fiber-Reinforced Alumina Matrix Composites," *Ceram. Eng., Sci. Proc.*, Vol. 9(7-8), pp. 759-766.

Becker, P. F., and Wei, G. C., 1984, "Toughening Behavior in SiC-Whisker-Reinforced Alumina," *Am. Ceram. Soc. J.*, Vol. 67(2), pp. C267-C269.

Bhatt, R. T., 1985, "Mechanical Properties of SiC Fiber-Reinforced Reaction-Bonded Si3N4 Composites," NASA Technical Report #85-C-14.

Bornemisza, T., and Napier, J. C., 1988, "Comparison of Ceramic vs Advanced Superalloy Options for a Small Gas Turbine Technology Demonstrator," ASME Paper No. 88-GT-228.

Brennan, J. J., and Prewo, K. M., 1982, "Silicon Carbide Fiber Reinforced Glass-Ceramic Matrix Composites Exhibiting High Strength and Toughness," *J. Mater. Sci.*, Vol. 17, pp. 2371-2383.

Buljan, S. J., Baldoni, J. G., and Huckabee, M. L., 1987, "Si_3N_4-SiC Composites," *Am. Ceram. Soc. Bull.*, Vol. 66(2), pp. 347-352.

Buljan, S. J., Baldoni, J. G., Neil, J., and Zilberstein, G., 1988, "Dispersoid-Toughened Silicon Nitride Composites," ORNL Report #ORNL/Sub/85-22011/1.

Byam, J. W., and Markel, K. E., 1987, *Proceedings of the Annual Heat Engines and Gas Stream Cleanup Systems Contractors Review Meeting*, U.S. Department of Energy, Morgantown Energy Technology Center.

Caputo, A. J., Stinton, D. P., Lowden, R. A., and Besman, T. M., 1987, "Fiber-Reinforced SiC Composites With Improved Mechanical Properties," *Am. Ceram. Soc. Bull.*, Vol. 66(2), pp. 368-372.

Carruthers, D., and Wimmer, J., 1988, "Gas Turbines Challenge Ceramic Technology," *Aerospace America*.

Ciliberti, D. F., and Lippert, T. E., 1981, "Evaluation of Ceramic Fiber Filters for Hot Gas Cleanup in Pressurized Fluidized-Bed Combustion Power Plants," EPRI Report CS-1846.

Corbin, N. D., Rossetti, G. A., and Hartline, S. D., 1986, "Microstructure/Property Relationships for SiC Filament-Reinforced RBSN," *Ceram. Eng. Sci. Proc.*, Vol. 7(7-8), pp. 958-968.

Cornett, M. S., 1987, "Process Improvements Make Integrated Gasification Combined Cycle Viable," *Modern Power Systems*, Vol. 7(10), pp. 25-31.

DuPont, 1989, Preliminary Engineering Data, DuPont Lanxide Composites.

EPRI, 1986, "Materials for Large Land-Based Gas Turbines," EPRI Report #AP-4476.

Federer, J. I., 1990, Oak Ridge National Laboratory, Private Communication.

Furlong, D. A., and Shevlin, T. S., 1981, "Fabric Filtration at High Temperature," *Chemical Engineering Progress*, Vol. 77(1), pp. 89-91.

Gadkaree, R. P., and Chung, K., 1986, "Silicon-Carbide-Whisker-Reinforced Glass and Glass-Ceramic Composites," *Am. Ceram. Soc. Bull.*, Vol. 65(2), pp. 370-376.

Horner, M. W., 1980, "High-Temperature Turbine Technology Program:

Turbine Subsystem Design Report—Low Btu Gas," Topical Report for US DOE Contract Number DE-AC01-76ET-10340.

Lamicq, P. J., Bernhart, G. A., Dauchier, M. M., and Mace, J. G., 1986, "SiC/SiC Composite Ceramics," *Am. Ceram. Soc. Bull.*, Vol. 65(2), pp. 336–338.

Luh, E. Y., Dauskardt, R. H., and Ritchiee, R. O., 1989, "Cyclic Fatigue-Crack Growth Behavior of Short Cracks in SiC-Reinforced LAS Glass-Ceramic Composite," *J. Mater. Sci.*, Vol. 8, in press.

Lundberg, R., Kahlman, L., Pompe, R., and Carlson, R., 1987, "SiC-Whisker-Reinforced Si_3N_4 Composites," *Am. Ceram. Soc. Bull.*, Vol. 66(2), pp. 330–333.

McClung, J. D., 1988, "Clean, Cost-Effective Kilowatts From Coal," *Proc. 1988 Seminar on Fluidized-Bed Combustion Technology for Utility Applications, Vol. 2: Pressurized Fluidized-Bed Combustion*, Palo Alto, CA.

Mudd, M. J., and Strogran, H. K., 1988, "Tidd PFBC Demonstration Plant: Status as of the Start of Construction," *Proc. 1988 Seminar on Fluidized-Bed Combustion Technology for Utility Applications, Vol. 2: Pressurized Fluidized-Bed Combustion*, Palo Alto, CA.

Parks, W. P., Ramey, R. R., Rawlins, D. C., Price, J. R., and Van Roode, M., 1989, "Potential Applications of Structural Ceramic Composites in Gas Turbines," ORNL/Sub/88-SA798/01.

Parks, W. P., 1989, "Research and Development of a Ceramic Fiber Composite Heat Exchanger, Phase 2, Final Report." DOE/ID/12536-2.

Penner, S. S., Alpert, S. B., Beer, J. M., Denn, M., Haag, W., Magee, R., Reichl, E., Rubin, E. S., Solomon, P. R., Wender, I., and Woodcock, K., 1987, "Coal Gasification: Direct Applications and Syntheses of Chemicals and Fuels," *Energy*, Vol. 12(8–9).

Prewo, K. M., and Brennan, J. J., 1982, "Silicon Carbide Yarn Reinforced Glass Matrix Composites," *J. Mater. Sci.*, Vol. 17, pp. 1201–1206.

Prewo, K. M., Brennan, J. J., and Layden, G. K., 1986, "Fiber Reinforced Glasses and Glass-Ceramics for High Performance Applications," *Am. Ceram. Soc. Bull.*, Vol. 65(2), pp. 305–313, 322.

Samanta, S. C., and Musikant, S., 1985, "SiC Whiskers-Reinforced Ceramic Matrix Composites," *Ceram. Eng. Sci. Proc.*, Vol. 6(7–8), pp. 663–672.

Saxena, S. C., Henry, R. F., and Podolski, W. F., 1985, "Particulate Removal From High-Temperature, High-Pressure Combustion Gases," *Progress in Energy and Combustion Science*, Vol. II, pp. 193–251.

Shalek, P. D., Petrovic, J. J., Hurley, G. F., and Gac, F. D., 1986, "Hot Pressed SiC Whisker/Silicon Nitride Matrix Composites," *Am. Ceram. Soc. Bull.*, Vol. 65(2), pp. 351–356.

Smith, D. J., 1985, "Advances in Fluidized Bed Combustion and Cogeneration," *Power Engineering*, Vol. 89(10), pp. 26–32.

Smith, K. O., LeCren, R. T., and Hasan, A. M., 1987, "Advanced Coal-Fueled Industrial Cogeneration Gas Turbine System, Topical Report," DOE-METC Contract No. DE-AC21-86MC23166.

Stinton, D. P., 1989, Oak Ridge National Laboratory, Private Communication.

Tiegs, T. N., and Becher, P. F., 1985, "Particulate and Whisker Toughened Alumina Composites," *Proc. Auto. Tech. Dev. Contractors' Coord. Meet.*, Vol. P-155, Society of Automotive Engineers, Inc., Warrendale, PA.

Tiegs, T. N., and Becher, P. F., 1986, "Alumina–SiC Whisker Composites," *Ceram. Eng. Sci. Proc.*, Vol. 7(9–10), pp. 1182–1186.

Wei, G. C., and Becher, P. F., 1985, "Development of SiC-Whisker Reinforced Ceramics," *Am. Ceram. Soc. Bull.*, Vol. 64(2), pp. 298–304.

Wieber, P. R., and Halow, J. S., 1987, "Advanced IGCC Power Systems for the United States," *Energy Progress*, Vol. 7(2), pp. 119–125.

Yeh, H., and Schienle, J., 1987, "SiC-Whisker-Toughened Silicon Nitride," Ceramic Technology for Advanced Heat Engines Project, Semiannual Progress Report for Apr. 1987 through Sept. 1987, pp. 27–49.

Experimental and Computed Performance Characteristics of High-Speed Silicon Nitride Hybrid Ball Bearings

G. W. Hosang
Sundstrand Power Systems,
San Diego, CA 92123

Development testing of hybrid bearings with M.50 rings and HIPed silicon nitride balls in small high-speed turbojet engines was carried out for several minutes at speeds up to 110,000 rpm. The main rotor system comprised an overhung radial compressor and turbine monorotor assembly with a pair of preloaded 101-size bearings. Estimated aerodynamic thrust of up to 750 N (170 lb) was added to the 200 N (45 lb) preload on the bearing adjacent to the compressor. Some testing was carried out with MIL-L-7808 air/oil mist and some with JP-10 fuel supplied in a similar fashion. After each test phase the bearings were removed for examination and re-used or replaced. Four of the bearings were submitted to inspection with special equipment to measure operating contact angles, as evidenced by the visible ball tracks, and any wear present. Contact angles and other operating characteristics estimated with the Jones, "SHABERTH," and "ADORE" computer codes were compared with the experimental data.

Introduction

During development of the small "Gemjet" turbojet engine for potential application to the U.S. Army Missile Command (MICOM) fiber optic guided missile (FOG-M) (Jones et al., 1987), testing of hybrid bearings with hot-isostatic-pressed (HIPed) silicon nitride balls was undertaken. The main rotor system, as can be seen in Fig. 1, comprised an overhung radial compressor and turbine assembly mounted with a pair of preloaded angular-contact ball bearings. One particularly attractive feature that commends use of hybrid bearings in such an application is the immunity of the ceramic ball to corrosion. Small, simple, expendable, short-life engines most likely would not incorporate bearing sump systems seals, thereby exposing the bearings to corrosion from the widely varying environmental conditions in which the missiles could be stored (for periods up to 10 or 15 years) and operated. While the races of the bearings can be plated reliably nowadays with thin chromium for corrosion protection, the same is not true of balls. Other advantages of the hybrid over the steel ball bearing include reduced inertial and centrifugal ball loads at the very high speeds of these small engines, reduced ball thermal expansion effects on operating internal clearance, and improved frictional characteristics at the ball-race contacts. While the primary reason for evaluating hybrid bearings involved corrosion considerations, impetus was provided by occasional very short-life failures from uncertain cause(s) of all-steel bearings in the #2 position.

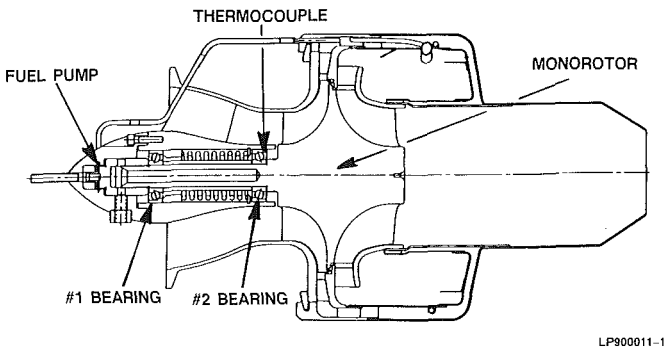

Fig. 1 Gemjet cross section

Preliminary engine testing with all-steel bearings had been carried out with MIL-L-7808 oil lubrication supplied by an industrial air/oil mist system and the same approach was used for the hybrid bearings except that JP-10 fuel (Burdette et al., 1978) was substituted for the lube oil during some of the testing. It was thought that the availability of leakage fuel from the nearby shaft-mounted fuel pump to lubricate, or at least cool, the bearings might obviate having to supply oil or grease lubrication or cooling air.

The hybrid bearings were removed at convenient points in the engine development program for visual assessment. Examination after disassembly revealed ball running tracks on the raceways that were, in most cases, easily visible. Estimation of the contact angles, while fairly straightforward on some races, was not possible on others. Cross-race tracing had been

Contributed by the International Gas Turbine Institute and presented at the 35th International Gas Turbine and Aeroengine Congress and Exposition, Brussels, Belgium, June 11–14, 1990. Manuscript received by the International Gas Turbine Institute January 30, 1990. Paper No. 90-GT-110.

employed on a routine basis as a quality assurance procedure to verify compliance to specification conformity requirements. Since the test hybrid bearings had all been checked in that fashion prior to assembly, it was decided to repeat the measurements in efforts to determine as accurately as possible the contact angles and to characterize any wear. These data could then be compared to values estimated with the following computer codes:

- A. B. Jones' classical analysis, which can model single bearings or systems of up to six ball and roller bearings (takes no account of lubrication or cage effects).
- "SHABERTH" (Crecelius and Pirvics, 1976) analysis, which can model single bearings or systems of up to five ball and roller bearings taking account of lubrication, cage, speed, and thermal effects.
- "ADORE" (Gupta, 1984) performance simulation analysis, including component wear prediction, for single ball or roller bearings, taking account of lubrication, cage, speed, and thermal effects.

To conduct analyses with the codes "SHABERTH" and "ADORE," it was necessary to ascertain lubricant-type physical properties for the fuel. This proved somewhat problematic, particularly in the case of "ADORE," because of the number of properties that required definition.

Experimental Procedures

Four 101-size hybrid ceramic bearings were tested as three pairs in a "Gemjet" turbojet during the engine's development as shown in Table 1. Features of the bearings were as follows:

- Counterbored outer race angular contact type bearing.
- 12 mm bore, 28 mm outside diameter, 8 mm width.
- 11 HIPed silicon nitride Anti-Friction Bearing Manufacturers Association (AFBMA) Grade 5 dimensional accuracy 4.76 mm (0.1875 in.) diameter balls.
- AMS 6490 M.50 tool steel races.
- AMS 6415 (AISI 4340) steel pitch riding, outer-land piloted, AMS 2412 silver-plated cage.
- Diametral internal clearance 0.0178–0.0203 mm (0.0007–0.0008 in.).
- Spring-preloaded "back-to-back" mounted system with 200 N (45 lb) preload.

The bearings were created by substituting ceramic balls for the standard steel balls in previously unused AFBMA precision class 7 turbomachinery bearings after measurements of raceway curvatures had been made with Form Talysurf precision tracing equipment.

The first pair was operated with the same commercial air/oil mist supply of MIL-L-7808 oil at a rate of 1 to 2 cc/min. as had been used in prior testing with otherwise similar all-steel bearings. Initial operation consisted of cautious step increases in speed to determine whether thermally stable operation, as evidenced by the outer race temperature of the more heavily loaded #2 bearing, could be attained. Subsequent testing included "slam" accelerations and decelerations between 65,000 and 103,000 rpm using simple rapid manual throttle movements during this phase of the development program. During testing of the second pair of bearings, "slam" starts to approximately 107,000 rpm were also successfully carried out. Then JP-10 fuel was substituted for the oil. The quantity supplied (15–25 cc/mm) was approximately an order of magnitude greater since it was intended to bracket the estimated leakage flow anticipated from the shaft-driven fuel pump, illustrated in Fig. 1. After the second test series and examination of the bearings, it was decided to re-use the two bearings that had been in the more lightly loaded #1 position, sustaining only the 200 N (45 lb) preload, as a third "pair" for the remaining testing since they showed very little, if any, wear or micropitting in the raceways. At the start of the third test the fuel lube flow was inadvertently set to the oil lube value of 2 cc/min. While thermal equilibrium was established at the initial test speed of 67,000 rpm, #2 bearing outer race temperature rose rapidly when operation at 103,000 rpm was attempted. Immediate shutdown was initiated with bearing temperature peaking at approximately 160°C. Satisfactory operation was restored at 15 cc/min. fuel lube flow for the final run (at speed).

During operation at 103,084 rpm, an estimated aerodynamic rotor thrust of 667 N (150 lb) was added to the 200 N (45 lb) preload on the #2 bearing. At 109,956 rpm this thrust rose to 756 N (170 lb). With MIL-L-7808 oil steady-state temperatures as measured by a thermocouple on the #2 bearing outer race were generally in the range 100°–115°C (210°–240°F). At 109,956 rpm they were at the upper end of that range. With JP10 fuel at 103,084 rpm temperatures ranged between about 72°–100°C (160°–210°F).

The four bearings were then carefully disassembled and resubmitted to Form Talysurf cross-race tracing to determine whether the ball paths could be detected, the angles determined, and any wear characterized. In addition, three balls from each set were checked for roundness and, in one case, the wear depth measured. Unfortunately specific measurements of ball and raceway surface finishes were overlooked and it was necessary to review prior quality assurance data to estimate values for use in the analyses: inner raceway 0.073 μm (2.87 μin.), outer raceway 0.030 μm (1.17 μin.), balls 0.0025 μm (0.10 μin.).

Table 1 Details of testing of ceramic hybrid bearings

Test No.	Bearing Position	Bearing Serial No.	Radial Play mm	Radial Play in	Run No.	Lube Type	Mist Lube System: Air Pressure kPa	Air Pressure PSI	Mist Quantity* Drops/Sec	Mist Quantity* CC/Min	Run Length Min	Comments
1	1	0382	.018	.0007	1	7808 Oil	240	35	1	1.0	24	Thermocouple attached to rear face of #2 outer race.
	2	0317	.020	.0008	2	7808 Oil	240	35	2	2.3	6	
					3	7808 Oil	515	75		2.1	6	
2	1	0446	.018	.0007	4	7808 Oil	515	75	2		33	Thermocouple touching outside diameter of #2 outer race.
	2	0485	.020	.0008	5	JP10 Fuel	515	75		15	8	
					6	JP10 Fuel	515	75		25	4	
3	1	0446	.018	.0007	7	JP10 Fuel	240	35	2		2	68% speed only only run 7.
	2	0382	.018	.0007	8	JP10 Fuel	240	35	2		6	68% speed; temperature #2 brg. over 150°C (300°F) on accel run 8; thermocouple same as test 2.
					9	JP10 Fuel	515	75		15	2	

*NOTE: For some runs lube flow was measured and for some only the droplet count was made. 100% speed = 103084 RPM

Analytical Procedures

The engine main shaft rotor two-bearing system was modeled with the Jones and "SHABERTH" computer codes while the bearings had to be modeled individually with "ADORE." Inasmuch as the Jones analysis does not automatically account for differential thermal and centrifugal growth effects while the others do (with suitable input data), they had to be estimated separately. As noted above, the only measured bearing temperature was that of the #2 bearing outer race. The operating fits and clearance of a bearing are very sensitive to the (assumed) race rolling element and supporting structure temperatures, in particular any temperature gradients. It was therefore decided in the interests of simplicity to assume that all bearings components and the outer housing were isothermal. The only other temperature that could be in any way inferred was felt to be that of the rotor shaft. The aerodynamic net forward thrust load from the monorotor blading was estimated to be quite high from approximately 672 N (151 lb) at 103,000 rpm to 756 N (170 lb) at 109,956 rpm, the two speeds at which most of the subject testing was being carried out. Because the room temperature fit of the inner race on its shaft journal was only a nominal 0.005 mm (0.0002 in.) interference, and absolutely no evidence of race creepage or frettage was noted on any of the #2 bearings in spite of the comparatively high loading, it was therefore presumed that the shaft was approximately 10°C (18°F) hotter than the bearing components. This would serve to increase the press fit and further obviate frettage. This approach also seemed intuitively acceptable considering the unimpeded heat flow path through the solid monorotor from the turbine to the shaft. The usual Lamé-type equations for interference-fitted cylinders were used to estimate the centrifugal growth effects at the two speeds mentioned above. Parametric analyses with variations in both aerodynamic thrust load and radial clearance to bracket the estimated operating values were run with the Jones code to permit their verification.

For "SHABERTH" it was necessary to supply viscosities at 38°C (100°F) and 99°C (210°F), density at 15.5°C (60°F), coefficient of thermal expansion, and thermal conductivity for JP-10 fuel to permit its "use" as a lubricant. These data were found to be readily available (CRC, 1983) and are reproduced in Table 2.

One problem arose with the analysis (Fresco, 1966) used in "SHABERTH" for estimating the pressure coefficient of viscosity. It apparently provides a relationship that decreases linearly with increasing temperature and can predict values equal to or less than zero that cause run failure. Such a case occurred when simulation of the 160°C (320°F) temperature "spike" with JP10 lube was attempted. A solution was not obtained until the bearing temperatures were reduced to 140°C (284°F). It is to be noted also that (CRC, 1983) data show a continuous smooth variation of JP10 viscosity with temperatures at least to 180°C (356°F).

For "ADORE" analyses, considerably more data were required for input definition of the JP-10 fuel as an undefined, special lubricant. There are, in fact, options available involving specification of viscosity-related properties and/or traction versus slip characteristics. It was decided to pursue evaluation of all the data, enumerated in Table 3.

Table 2 JP-10 fuel lubricant properties for "SHABERTH" computer code

Kinematic Viscosity, cs @ 37.78°C (100°F)	2.35
Kinematic Viscosity, cs @ 98.89°C (210°F)	1.13
Density, gm/cc @ 15.56°C (60°F)	0.94
Thermal Conductivity, W/m/°C	0.108
Thermal Coefficient of Expansion, 1/C°	6.93 E–4

It will be observed in Table 3 that there are two different units (*) for the temperature coefficient of viscosity β. In the absence of measured data for both, conversion of one to the other can be accomplished by noting their theoretical equivalence from solution of the two constitutive viscosity relations employing them and used in "ADORE," assuming all other values are identical.

$$\text{Type I: } \mu = \mu_0 \exp[\alpha p + \beta_I (T_0 - T)] \tag{1}$$

$$\text{Type II: } \mu = \mu_0 \exp[\alpha p + \beta_{II} (1/T - 1/T_0)] \tag{2}$$

where μ is the lubricant viscosity at a pressure p and temperature T, μ_0 and T_0 are reference values at ambient conditions, and α is the pressure coefficient of viscosity.

Thus,

$$\frac{\beta_I}{\beta_{II}} = \frac{1}{T \times T_0} \tag{3}$$

In spite of many bearing and oil industry-wide personal contacts, not much more data were found beyond those listed

Table 3 Lubricant properties required by "ADORE" computer code

- Lubricant Film Thickness Computations (low pressure) at Race/Rolling Element Contacts
  - Dynamic Viscosity, PaS
  - Pressure–Viscosity Coefficient, 1/Pa
  - Temperature–Viscosity Coefficient, K° *
  - Thermal Conductivity, W/m/°K
- High Pressure Traction Computations at Race/Rolling Element Contacts
  - Low Pressure Range Atmospheric Value of Viscosity, PaS (corresponds to first value of each coefficient below)
  - High Pressure Range Atmospheric Value of Viscosity, PaS (corresponds to second value of each coefficient below)
  - Low Pressure Range Pressure–Viscosity Coefficient, 1/Pa
  - High Pressure Range Pressure–Viscosity Coefficient, 1/Pa
  - Low Pressure Range Temperature–Viscosity Coefficient, 1/K° *
  - High Pressure Range Temperature–Viscosity Coefficient, 1/K° *
- Traction/Slip Characteristics (Traction = Friction) at Race/Rolling Element Cage/Race Contacts
  - Traction coefficient at zero slip
  - Maximum Traction Coefficient
  - Traction coefficient at Infinite Slip
  - Slip at Maximum Traction Coefficient, m/sec

At any known, common reference temperature.

in Table 2. From Jackson (1989) an estimate of the pressure coefficient of viscosity at the two common reference temperatures of 40° and 100°C based on an extrapolation of a proprietary relationship using the viscosities and densities from CRC (1983) yielded the values in Table 4.

A more recently developed method (Wu et al., 1989) of estimating the pressure coefficient of viscosity utilizes the viscosity and the slope of the ASTM viscosity-temperature characteristic (ASTM, 1985)

$$\alpha = (0.1657 + 0.2332 \log \mu_0) \times m_0 \quad (4)$$

where α = pressure-viscosity coefficient, $kPa^{-1} \times 10^5$; m_0 = viscosity-temperature property from the ASTM-Walther equation and equal to (ASTM slope)/0.2; μ_0 = atmospheric kinematic viscosity at the temperature of interest, mm^2/s.

This was an outgrowth of their earlier work, which produced the correlation, reputed to be accurate within 7 percent for 197 data points for 102 different fluids:

$$\alpha = 1.030 + 3.509 (\log \mu_0)^{3.0627} + 2.412 \times 10^{-4} m_0^{5.1903} (\log \mu_0)^{1.5976} - 3.387 (\log \mu_0)^{3.0975} \rho^{0.116} \quad (5)$$

where, additionally, ρ = atmospheric density at the temperature of interest, $kg/m^3 \times 10^{-3}$.

By measurement on the usual ASTM viscosity-temperature chart, the slope of the JP10 characteristic was found to be 0.650. Thus the value of m_0 in the foregoing is 3.25.

Roelands (1966) gives a very extensive treatment of the subject of viscosity, including computation of many properties required for analysis, starting with a minimum of actual data not only for petroleum-based lubricants but for a host of other fluids as well. Admittedly, the validity of computations for "other fluids" may be less certain. However, by careful study of this monumental work, much can at least be inferred. Rather than the common ASTM (American Society for Testing Materials) kinematic viscosity-temperature relationships, Roelands (1966) relied on a somewhat similar dynamic viscosity-temperature relationship and was able to develop a host of other relationships with significantly better correlations to much actual experimental data than most if not all other investigators. The basic relationship he proposed was:

$$\log (\log \eta_0 + 1.200) = -S_0 \times \log (1 + t/135) + \log G_0 \quad (6)$$

η = atmospheric dynamic viscosity, cP
T_0 = temperature, °C
S, G = dimensionless characteristic constants

To assist in definition of JP-10 properties, it was found useful with Roelands' approach to consider viscosity versus pressure data for "kerosene" (Bridgman, 1971), for "white gas," and "HO-1" (a light hydraulic oil) and a mixture of the two (Dill, 1989), and MIL-F-5572A AVGAS (Barnett and Hibbard, 1956) along with other more familiar lubricant data. For the purposes of this work it was assumed that JP5 fuel and "kerosene" were identical, as were AVGAS and "white gas."

These data are shown plotted in Roelands-type Figs. 2 and 3, the latter a similar viscosity versus pressure relation. The strength of these presentations, from an analytical standpoint, is that they yield linear graphic and mathematical relationships over surprisingly wide temperature ranges. By assuming (with Roelands' considerable justification not presented here) "families" of fluids to have similar characteristics, it is possible to infer and estimate desired properties. Most importantly and not too surprisingly, the pressure coefficient of viscosity is related to the slope of the fluid's viscosity versus pressure characteristic, "Z," and the temperature coefficient of viscosity is related to the slope of the viscosity versus temperature characteristic, "S." Figures 4 and 5 show Roelands' S and Z data, respectively, with those for "new" fluids mentioned here added.

Table 4 Proprietary relationship, JP-10 pressure-viscosity coefficients (Jackson, 1989)

Temperature, °C	Coefficient, 1/kPa (1/psi)
40	1.549 E-5 (1.068 E-4)
100	1.430 E-5 (0.986 E-4)

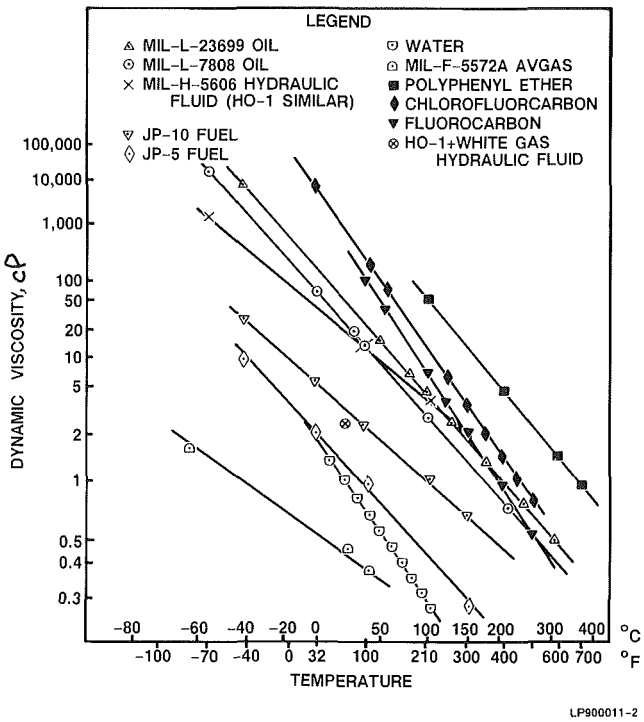

Fig. 2 Dynamic viscosity-temperature characteristics per Roelands (1966)

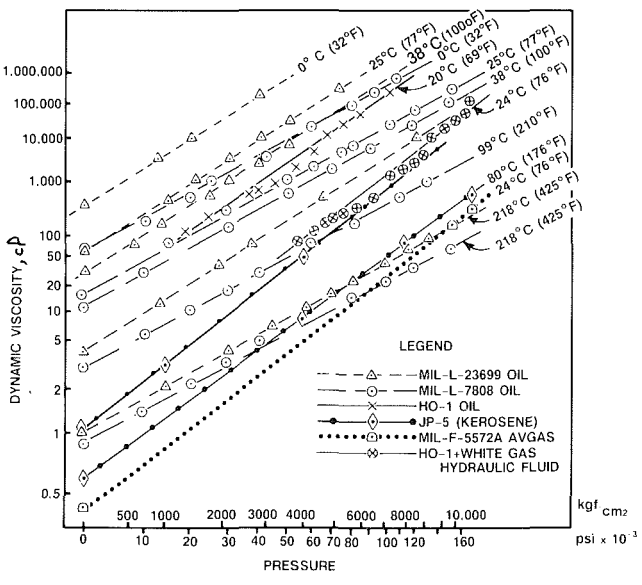

Fig. 3 Dynamic viscosity-pressure characteristics per Roelands (1966)

The other key relationships proposed by Roelands (1966) in his classic work are listed below:

$$\alpha = 1.151 \times 10^{-3}\, Z\, (\log \eta_0 + 1.200)\, (1 + p/2000)^{z-1} \quad (7)$$

α = pressure-viscosity coefficient, cm^2/kgf
Z = slope of Roeland's pressure-viscosity relationship
η = atmospheric dynamic viscosity at the temperature of interest, cP
p = contact pressure, kgf/cm^2

A version of Eq. (7) with the pressure set to zero is termed the "initial" coefficient and gives representative values up to 1000 kg/cm^2 (14,000 psi). Thus,

$$\alpha_i = 1.151 \times 10^{-3}\, Z\, (\log \eta_0 + 1.200)^{z-1} \quad (8)$$

Also,

$$\beta = 2.303\, S\, \frac{(\log \eta_0 + 1.200)}{(T + 135)} \quad (9)$$

β = temperature-viscosity coefficient, 1/K
S = slope of Roelands' temperature-viscosity relationship
η = dynamic viscosity at temperature
T = temperature, °C

and, for an isothermal condition, the variation of viscosity with pressure is

$$\log \eta + 1.200 = (\log \eta_0 + 1.200)\, (1 + p/2000)^z \quad (10)$$

η = viscosity at temperature and pressure of interest, cP
η_0 = atmospheric viscosity at temperature of interest, cP
p = pressure of interest, kgf/cm^2

It has been noted by many that the simple Barus exponential relationship describing viscosity variation with pressure fails at high pressure. "ADORE" input permits two values of pressure and temperature viscosity coefficients as noted in Table 3. Thus, α_i can be conveniently used for the low pressure range and the second value computed for a representative contact pressure (high), along with appropriate temperature coefficient(s) β and elevated-pressure viscosity η.

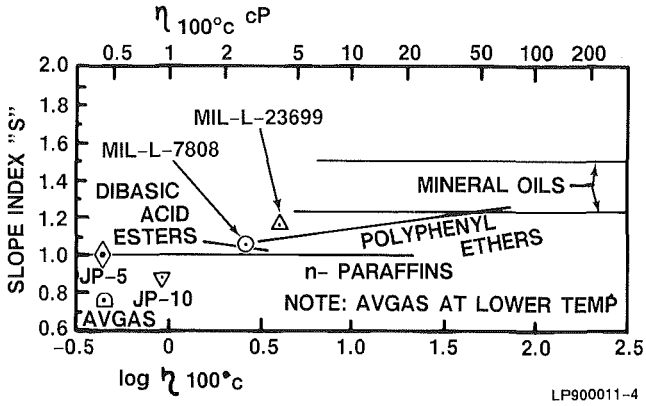

Fig. 4 Slope indices of various liquids per Roelands (1966)

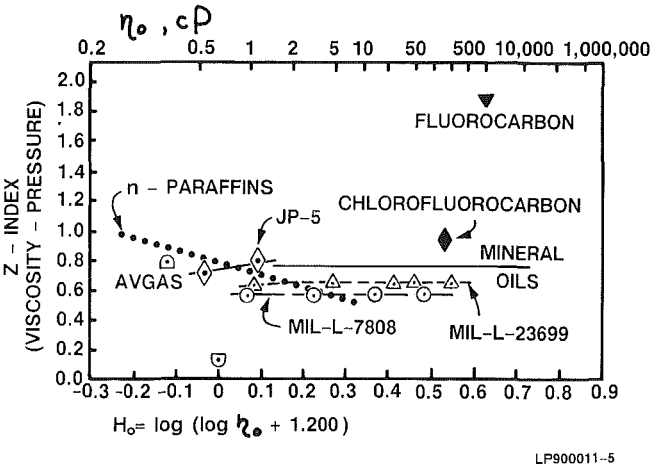

Fig. 5 Viscosity-pressure indices of various liquids per Roelands (1966)

Results and Discussion

Table 1, again, shows details of the hybrid bearing testing carried out in the turbojet engine. Tables 5 and 6 present the results of the inspection, including the measured contact angles, carried out on the bearing components after removal from the engine and careful disassembly. As can be seen in Table 5, significant wear of the inner raceway of bearing *S/N* 0382 was detected. Most, if not all, of the wear was believed to have occurred during test 3 since it was not apparent during visual inspection after test 1. All of the balls in bearing *S/N* 0485 were found to have a groove worn in them. It is worthy of note that both races of that bearing had a band of fine fatigue pitting over 360 deg and there was fairly heavy cage pocket wear. There was, however, no "failure" as such and the evaluation of hybrid bearings was considered successful, including their ability to complete a simulated mission profile (test 3) with JP10 fuel as the lubrication.

Table 7 lists the newly derived numerical values of the "lubrication" properties of JP10 fuel needed as input for the computer code "ADORE." Since the output of the latter code includes estimated wear rates of the inner and outer raceways, the balls (from contact with the races but not the cage), and

Table 5 Ball track curvature and wear measurements

Pair/ Position No.'s	Bearing Serial No.	Raceway	Contact Angle, Degrees Upper Edge	Mean	Lower Edge	Wear Type [1]	Calc. Wear Depth [2] µm	µin	Profile Waviness Run µm	µin	New µm	µin	Curvature % of Ball Dia Run	New
1/1,3/2	0382	Outer	32.4	13.6	-5.2	Abr.	-0.78	-31	7.92	312	0.18	7	52.7	52.6
		Inner	45.9	26.3	6.7	Abr.	15.4	606	4.88	192	2.72	107	51.5	53.4
1/2	0317	Outer	28.6	17.5	6.4	P&D	0.13	5	0.94	37	0.46	18	53.7	53.8
		Inner	29.0	16.0	3.0	P&D	-2.0	-78	1.88	74	1.42	56	53.9	53.3
2/1,3/1	0446	Outer	29.0	17.8	6.6	P&D	-0.43	-17	0.66	26	0.23	9	53.4	53.4
		Inner	30.7	18.6	6.5	P&D	-0.61	-24	3.15	124	1.80	71	53.1	52.9
2/2	0485	Outer	30.4	18.9	7.4	S.F.,B	-1.1	-43	1.68	66	0.20	8	53.3	52.9
		Inner	30.7	18.0	5.4	S.F.,B	-.69	27	1.73	68	1.45	57	53.1	53.3

Equipment Used = Rank Taylor Hobson Form Talysurf.

Notes: 1. Abr. = Abrasive wear, e.g. from contaminant in lubricant, including cagelands and ball pockets, slight heat discoloration on inner race.
P&D = Fine microscope pitting and denting, but generally excellent condition
S.F. = Shallow surface fatigue pitting.
B = Balls all feature continuous circumferential wear band, cage pockets polished from ball contact.
2. Negative values for raceway wear are a measure of uncertainty in the calculation procedure due to assumptions regarding radius of curvature and profile waviness.

the cage guiding land(s) and ball pockets, considerable effort was devoted to defining them as accurately as possible in hopes of predicting the wear that had actually occurred.

The values for JP10 computed using Roelands' relationships were selected for use with "ADORE" primarily because the pressure coefficient of viscosity fell between the values suggested by Jackson in Table 4 and those computed with the Wu et al. Eqs. (4) and (5). Also, both required sets of pressure and temperature viscosity coefficients were easily obtainable. As recommended by Gupta (1989), identical traction characteristics were utilized for both lubricants.

Figures 6 and 7 show examples of the contact angles computed with the three codes and the measured values as well. In Fig. 6 are data for the test 3 #1 bearing, which sustained only the preload of 200 N (45 lb). The curves illustrate the variation in contact angles with diametral clearance as computed with the Jones code. As noted above, any effects of speed and temperature have to be accounted for in that analysis by input adjustment of the clearance. It was estimated that a reduction of about 0.002 mm (70 μ in) from the room temperature value was obtained in the engine, as suggested by the vertical dashed line. Again, the "SHABERTH" and "ADORE" codes account for such changes automatically with input of appropriate temperatures. Only single-point data sets are therefore shown for them, with "SHABERTH" output including only the mean contact angles. Agreement of actual and computed values is seen to be reasonable, actually good in about half the cases.

It was also mentioned above that bearing component operating temperatures were assumed isothermal for simplicity.

Table 6 Sample ball roundness measurements

Bearing Serial No.	Average		Ball 1		Ball 2		Ball 3	
	μm	μin	μm	μin	μm	μin	μm	μin
0382	0.15	6	0.08	3	0.20	8		
0317	0.08	3	0.10	4	0.08	3	0.08	3
0446	0.10	4	0.15	6	0.10	4	0.08	3
0485	1.14	45	1.14	45	1.04	41	1.22	48

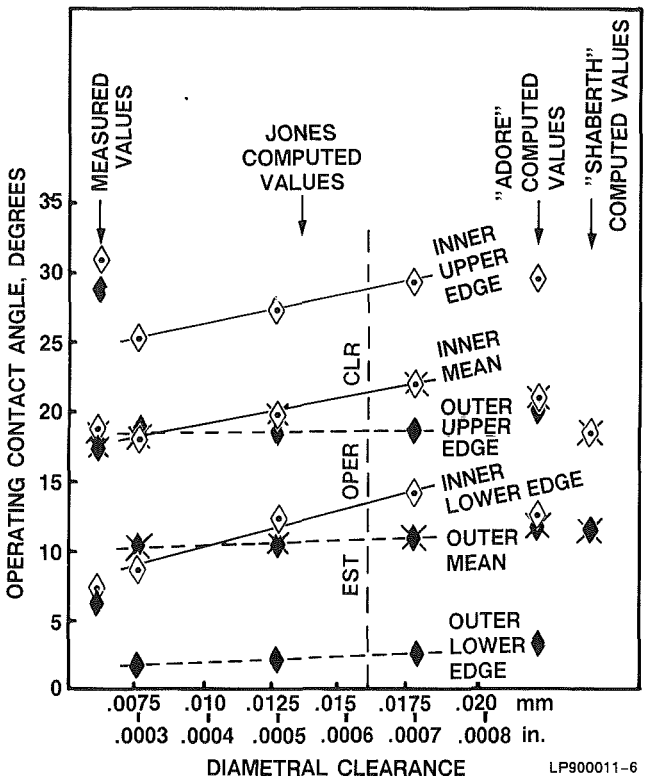

Fig. 6 Comparison of actual and computed operating contact angles: bearing 0446 as pair 3, #1; thrust load 200 N (45 lb)

Table 7 Example derived JP10 lubrication properties for "ADORE" computer code input

PROPERTY	VALUE	SOURCE
Pressure Coefficient of Viscosity, α, 1/k Pa (1/psi)		
40°C (104°F) – low pressure range	1.352E-5 (.9323E-4)	Equation (8)
– high pressure range	.9284E-5 (.6401E-4)	Equation (7) 7,000 kgf/cm² (100,000 psi)
100°C (212°F) – low pressure range	1.053E-5 (.7257E-4)	Equation (8)
– high pressure range	.7227E-5 (.4983E-4)	Equation (7) 7,000 kgf/cm² (100,000 psi)
Temperature Coefficient of Viscosity, β, 1/K° (1/F°)		
40°C (104°F) – low, high pressures	1.70 E-2 (9.44E-3)	Equation (9)
100°C (212°F) – low, high pressures	9.84 E-3 (5.47E-3)	Equation (9)
Roelands Temperature – Viscosity "Slope Index", S	0.84	Slope of JP10 fuel characteristic in Figure 2.
Roelands "Pressure – Viscosity Index", Z	0.75	Estimated as similar to fuels family (see Fig. 5) from slopes in Fig. 3: – JP5 (30°C).774, (80°C).708 – AVGAS (20°C).74 – H0-1 (20°C).713 – H0-1 + White gas (24°C).78
Viscosity at 7,000 kgf/cm² (100,000 psi), cP		
40°C (104°F)	3630	Equation (10)
100°C (212°F)	319	Equation (10)
Traction (Friction) Coefficients – rolling element/race = dry contact	0.20 for boundary lube situations	Reached at and maintained constant above sliding velocity of 0.5 m/sec (20 in/sec) [Gupta, 1989]
– rolling element/cage – race/cage } Same relation used for 7808 oil lube	0.05 for boundary lube situations	Constant at all sliding velocities [Gupta, 1989]

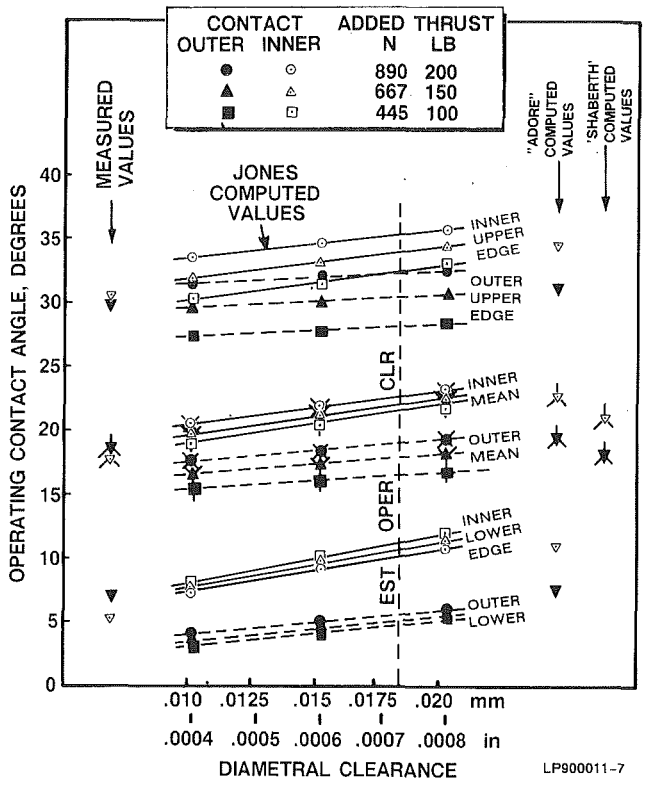

Fig. 7 Comparison of actual and computed operating contact angles: bearing 0485 as pair 2, #2; total thrust load 867 N (195 lb)

Table 8 Comparison of measured and computed data

Pair/Position No.	Bearing Serial No.	Raceway	Mean Contact Angle, Degrees			
			Measured Actual	Computed		
				Jones	"SHABERTH"	"ADORE"
1/1	0382*	Outer	13.6	10.8	11.7	12.8
		Inner	26.3	20.7	18.3	21.4
1/2	0317	Outer	17.5	18.1	17.7	18.8
		Inner	16.0	21.3	20.5	22.0
2/1	0446*	Outer	17.8	10.5	11.6	12.8
		Inner	18.6	21.5	18.9	21.7
2/2	0485	Outer	18.9	18.4	18.3	19.5
		Inner	18.0	22.5	21.2	22.9
3/1	0446	Outer	17.8	10.7	11.6	12.0
		Inner	18.6	21.3	18.6	21.2
3/2	0382	Outer	13.6	18.3	17.9	18.8
		Inner	26.3	21.7	20.6	21.6

*Re-used in test 3.

Figures 6 and 7 offer some justification for that approach since the variation of contact angles can be seen to be relatively insensitive to internal clearance. Operating clearance is, however, sensitive to the individual temperatures of the bearing components.

Figure 7 shows similar data for the test 2 #2 bearing except that the Jones code output includes three thrust loads, additive to the 200 N (45 lb) preload, of 445, 667, and 890 N (100, 150, and 200 lb). This was intended to permit some verification of the estimate of 667-756 N (150-170 lb) for the aerodynamic rotor thrust. Again, the actual and computed results are seen to be in fairly good agreement. Table 8 presents a summary of all the contact angle data including the Jones code results at the estimated operating diametral clearances. It may be that some of the discrepancies resulted from reuse of two of the bearings in the third test.

A host of other output was obtained from some much longer "ADORE" runs than was used simply to develop the contact

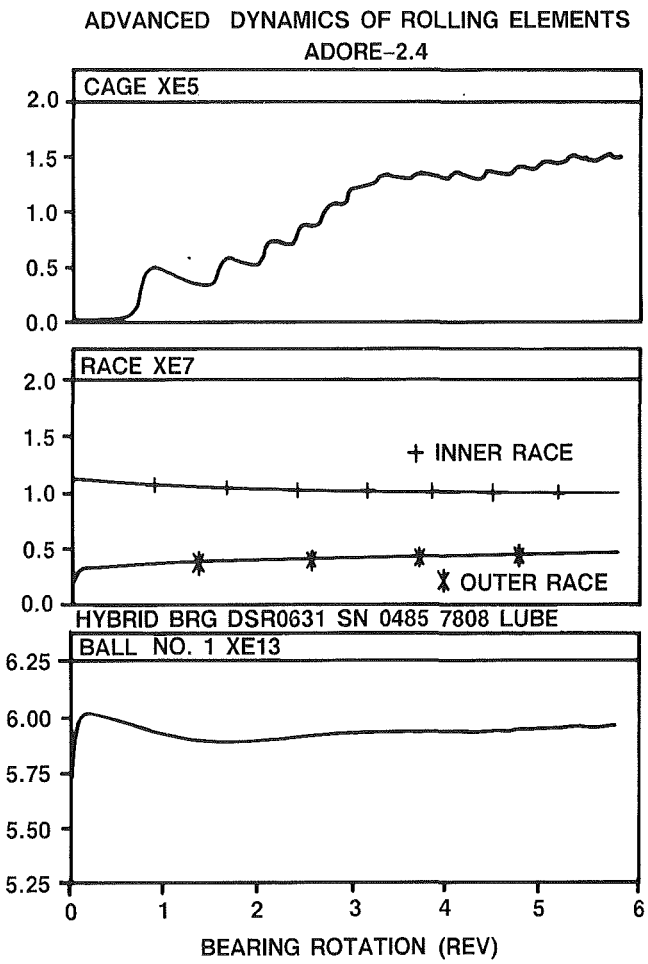

Fig. 8 Time average wear rates (in **3/s), bearing 0485, test 2, #2

angle data. Wear predictions with "ADORE" are based on the Archard equation and are therefore sensitive to the wear coefficients assumed. The same values were used in all the runs so the results may be compared to each other. Figures 8, 9, and 10 show the wear prediction plots for tests 2, #2 and 2, #1 with 7808 oil and 2/3, #1 with JP10, respectively. The first two produced cage wear predictions about an order of magnitude larger than any of the other cases computed. The last one, however, is seen to have a pronounced "saw-tooth" characteristic, which appears to display an increasing trend. Unfortunately, however, the wear predictions, as far as they were taken, did not seem to reflect actuality, particularly the inner raceway wear in 0382. It may be that, as suggested by the wear characterization in Table 5, abrasive foreign material from an external source was responsible. Also, no correlation of assumed wear coefficients with experimental data was attempted or possible.

Conclusions

Evaluation of the hybrid bearings with both MIL-L-7808 oil and JP10 fuel lubrication was successful.

The computation of operating contact angles for high-speed bearings was found to produce reasonable agreement with actual values measured with sophisticated profilometer equipment. Measurement was possible because lubrication of the bearings was only marginally satisfactory giving rise to burnishing and wear marks where the bearing balls had run. Each of the three bearing sets had only run in the engine for a comparatively short period of several minutes and the oper-

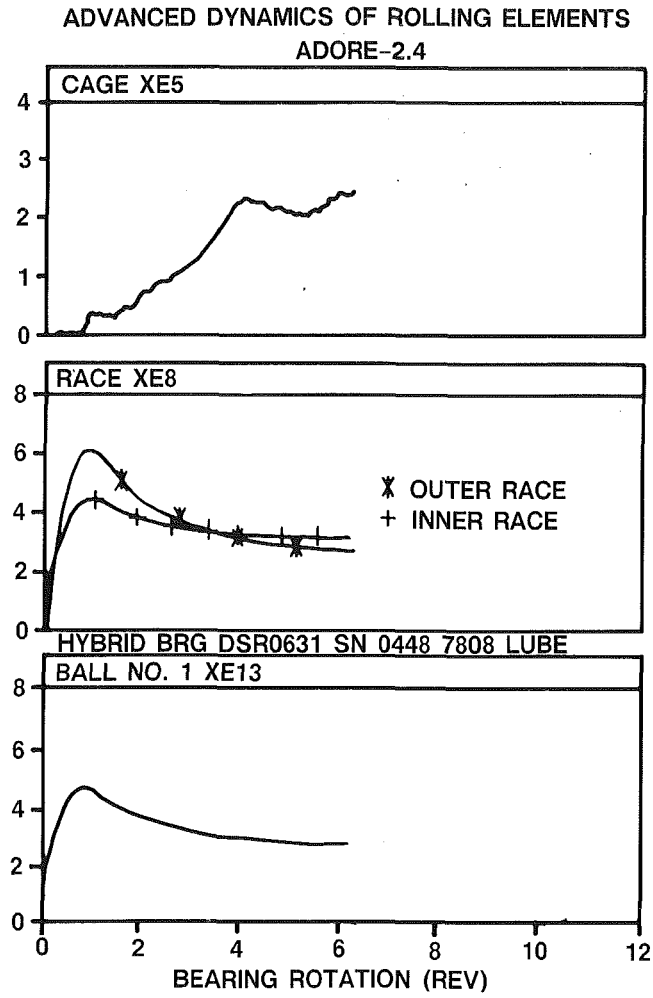

Fig. 9 Time average wear rates (in **3/s), bearing 0446, test 2, #1

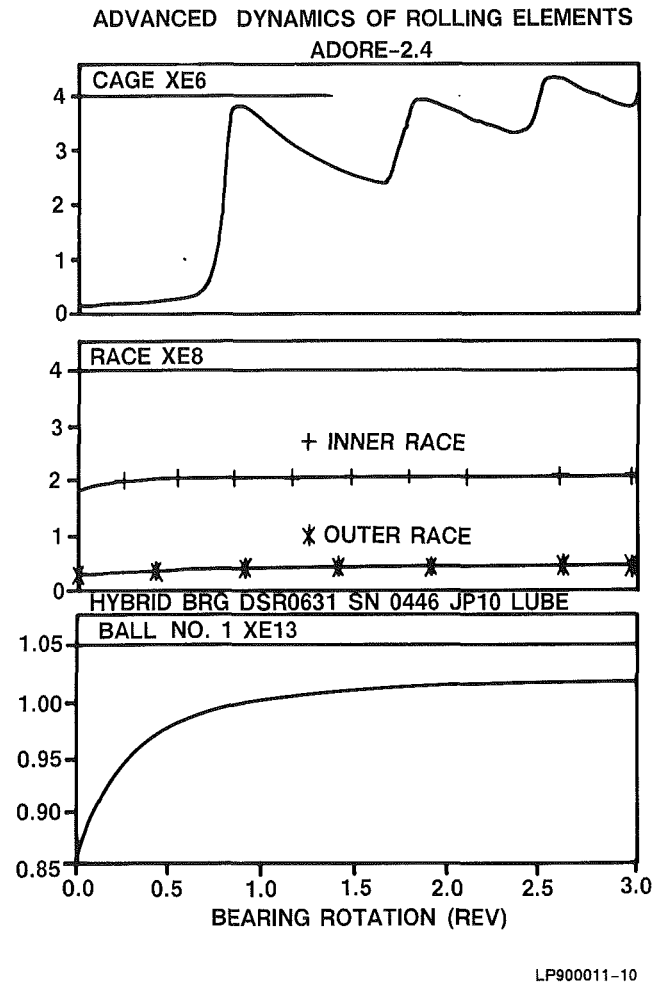

Fig. 10 Time average wear rates (in **3/s), bearing 0446, tests 2, 3, #1

ating conditions were known about as accurately as possible. This permitted fairly precise modeling of the bearings with the Jones, "SHABERTH," and "ADORE" computer codes. The three sets of computed data were also in quite close agreement.

The performance simulation code "ADORE," it was hoped, would provide wear predictions that matched the hardware observations. In spite of the great pains taken to develop appropriate "lubrication" properties of the JP10 fuel used as the bearing lubricant in some of the testing, the wear predictions were not accurate, although suggesting some interesting trends affecting the cage. Perhaps greater familiarity with the code will in the future permit improved agreement. Certainly the monumental work of Roelands proved of great value in defining the "lubrication" properties of JP10 fuel for use in the analyses.

Acknowledgments

The author would like to express his appreciation to the following individuals whose cooperation and assistance was invaluable: Mr. Andrew Jackson of Mobil Oil Corporation, Mr. W. R. Jones of NASA-Lewis, Mr. J. Dill of Mechanical Technology Inc., and Mr. S. Matheson of Bearing Inspection Inc., and to Sundstrand Power Systems for permission to publish this work.

References

ASTM, 1985, "Viscosity-Temperature Charts for Liquid Petroleum Products," *ASTM Standards*, Section 5, Vol. 05.02, D341.

Barnett, H. C., and Hibbard, R. R., 1956, "Properties of Aircraft Fuels," NACA TN3276.

Bridgman, P. W., 1971, *The Physics of High Pressure*, Pub. Dover (Orig. Pub. Bell, London, 1931).

Burdette, G. W., Lander, H. R., and McCoy, J. R., 1978, "High-Energy Fuels for Cruise Missiles," *Journal of Energy*, Vol. 2, No. 5, pp. 289–292.

CRC, 1983, "Handbook of Aviation Fuel Properties," Report No. 530, Coordinating Research Council Inc., Atlanta, GA (Sustaining Members American Petroleum Institute and Society of Automotive Engineers, Inc.).

Crecelius, W. J., and Pirvics, J., 1976, "Computer Program Operation Manual on 'SHABERTH,' a Computer Program for the Analysis of the Steady State and Transient Thermal Performance of Shaft-Bearing Systems," USAF and USN NAPTC Technical Report AFAPL TR-76-90, Oct.

Dill, J. F., 1989, Mechanical Technology Inc., Personal Communication.

Exxon, 1973, "Data Book for Designers," Exxon International Co., Florham Park, NJ.

Fresco, G. P., 1966, "Measurement and Prediction of Viscosity-Pressure Characteristics of Liquids," M.S. Thesis, Report PRL-3-66, Dept. of Chemical Engineering, The Pennsylvania State University, University Park, PA.

Gupta, P. K., 1984, *Advanced Dynamics of Rolling Elements*, Springer-Verlag, New York.

Gupta, P. K., 1989, Personal Communications.

Jackson, A., 1989, Personal Communications.

Jones, A., Weber, H., and Fort, E., 1987, "Gemjet—A Small, Low Cost, Expendable Turbojet," AIAA-87-2140.

Roelands, C. J. A., 1966, "Correlational Aspects of the Viscosity-Temperature-Pressure Relationship of Lubricating Oils," Doctoral Dissertation, Technical University of Delft, The Netherlands.

Wu, C. S., Klaus, E. E., and Duda, J. L., 1989, "Development of a Method for the Prediction of Pressure-Viscosity Coefficients of Lubricating Oils Based on Free-Volume Theory," ASME *Journal of Tribology*, Vol. 111, pp. 121–128.

G. Bandyopadhyay

K. W. French

D. J. Sordelet

GTE Laboratories Inc.,
Waltham, MA 02254

K. D. Moergenthaler
Daimler-Benz Aktiengesellschaft,
7000 Stuttgart 60,
Federal Republic of Germany

Fabrication and Development of Axial Silicon Nitride Gas Turbine Rotors

Since 1984, GTE Laboratories Inc. has performed research to develop net shape fabrication technology for axial silicon nitride rotors for the Daimler-Benz research gas turbine engine. The initial effort was focused on the fabrication of injection-molded profile disks. Subsequently, efforts were shifted to develop injection molding and slip casting technology for the bladed gasifier rotors. This joint activity has demonstrated that the ceramics technology has improved significantly over the last five years, as is evidenced by a major improvement in properties and performance of silicon nitride components. The evolution of the ceramics fabrication technology at GTE and the role of improved process and NDE methods on components fabricated in recent years are described in this paper.

Introduction

Development and demonstration of high-density silicon nitride components for use in turbine engines are major objectives of several government and industrial heat-engine activities [1–6]. In one such program, Daimler-Benz AG (DB) is pursuing research for developing gas turbines for automotive applications [5, 6]. A specific goal in this continuing activity at Daimler-Benz is to demonstrate the net shape fabricability of reliable axial rotors by high-volume manufacturing processes.

Since 1984, GTE Laboratories Inc. (GTEL) has performed research to develop net shape fabrication technology for axial silicon nitride rotors specifically for the Daimler-Benz research gas turbine engine. The initial effort was focused on the fabrication of injection-molded profile rotor disks (Fig. 1*a*) to demonstrate the feasibility of the forming approach. Subsequently, efforts were shifted to develop injection molding and slip casting technology for fabrication of the bladed gasifier rotors (Fig. 1*b*). In this paper, a brief description of the profile disk activities is given first, followed by a more detailed discussion of the bladed rotor fabrication program.

The profile rotor disk program demonstrated the viability of net shape fabrication of axial rotors by injection molding and provided test samples for evaluation. However, it was evident that at the time of this activity (1984–85), the materials properties and component quality were not sufficient for use in the gas turbine engine environment. The axial bladed rotor fabrication program was designed to investigate two forming methods, injection molding and slip casting, with the objective that a preferred method of fabrication could be selected and pursued for fabrication of engine quality rotors. Major progress was made in understanding the fundamental issues related to the two forming approaches. However, only the results from the injection molding program are described in this paper, primarily because GTEL selected injection molding as the preferred method based on having significantly more success with this approach.

Profile Rotor Disk Fabrication

For this activity, GTE SN502 silicon nitride, which is a fine, high-surface-area powder with crystalline and amorphous phases, was used. The powder was prepared in a ball milling operation where silicon nitride was blended with 6 w/o yttria and 2 w/o alumina to produce GTE AY6 composition. The injection molding process used for fabrication of these parts has been described in several earlier publications [7, 8]. It consisted of (*a*) compounding, which involved high shear mixing of the powder with a molten wax-based binder; (*b*) injection molding, by which the powder/binder mix was formed into the profile disk shape using a two-piece metallic mold; (*c*) binder removal, which must be accomplished without disrupting the ceramic structure; and (*d*) consolidation of the part by sintering or glass-encapsulated hot isostatic pressing (HIPing) [9].

Substantial internal and external cracking difficulties similar to those observed in the initial AGT 100 radial rotor fabrication effort [7] were encountered in the early stages of this program. The cracking problem was resolved through the development of a special processing method for large cross section components. The new process included significant starting powder control and modifications in the binder burnout and densification procedures. With these changes, several sintered and HIPed disks with >98 percent theoretical density (3.262 g/cc theoretical density) were successfully fabricated. The feasibility of forming an axial rotor hub by injection molding was thus demonstrated.

Contributed by the International Gas Turbine Institute and presented at the 35th International Gas Turbine and Aeroengine Congress and Exposition, Brussels, Belgium, June 11–14, 1990. Manuscript received by the International Gas Turbine Institute January 10, 1990. Paper No. 90-GT-47.

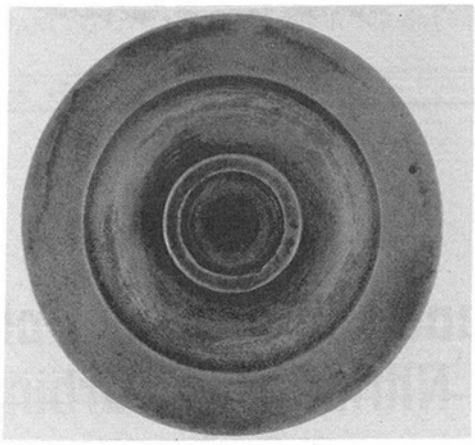

(a) Profile Rotor Disc

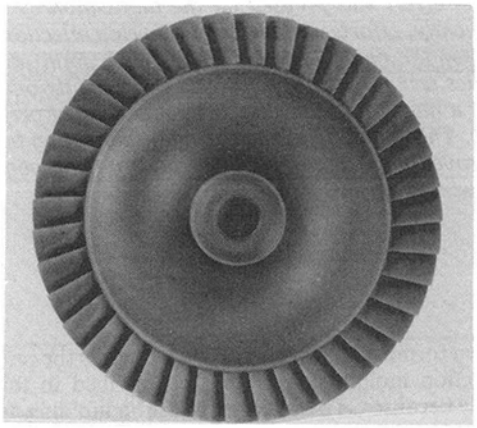

(b) Bladed Axial Rotor

Fig. 1 GTEL AY6 silicon nitride components for Daimler-Benz AG program

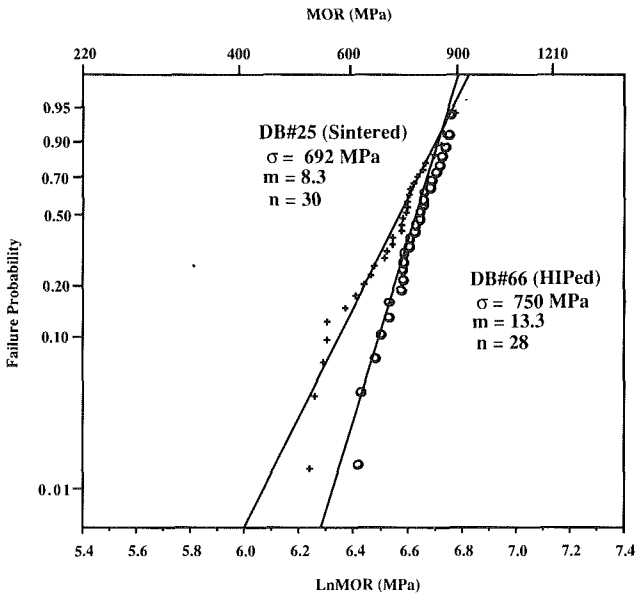

Fig. 2 Four-point bend strength of MOR bars machined from sintered and HIPed injection-molded AY6 profile disks fabricated in 1985: σ is the average strength, m is the Weibull modulus, and n is the number of specimens tested

Table 1 Types and sources of defects in structural ceramics components

Defect Categories	Defect Sources	Defect Types
External Contaminants	• Impurities in starting powder • Environmental contamination	• High density inclusions • Voids • Surface pits
Process Related	• Contamination from equipment • Poor processing method • Poor finishing techniques	• High density inclusions • Voids • Cracks • Surface fold lines, packing problems, etc. • Machining defects

Room temperature four-point bend strengths of MOR bars ($1.27 \times 2.54 \times 25.0$ mm)[1] machined from these disks are shown in Fig. 2. The data are representative of the material properties achieved at GTEL in the 1984–85 time frame. The HIPed material showed superior strength (σ) and Weibull modulus (m) compared to those obtained from the sintered material. The majority of the subsequent effort was therefore focused on component densification by the HIPing process.

The primary concerns at this stage of parts fabrication were related to defects coming from two sources: the processing environment, and the process itself (Table 1). Environmental defects consisted of those related to external contaminants from the laboratory or factory environment. They appeared in the form of high-density inclusions, voids (from organic contaminants), and surface pits. In the "laboratory process" used for fabrication of the profile disks, powder processing was done in limited quantities in conventional laboratory space (i.e., no clean room). Although strict attention was given to protecting the powder from foreign contamination, the desired level of cleanliness necessary for high-reliability structural ceramic components was difficult to achieve. Foreign contamination was sometimes detected in processed powder as well as in densified components. Batch-to-batch variations in the processed powder also limited the reproducibility of mechanical properties. The process-related defects, on the other hand, were caused by contamination from the equipment as well as by poor processing. These defects appeared in the form of cracks, high-density inclusions, and a high level of finely dispersed metallic contamination (from processing equipment), and surface defects such as fold lines, poor packing, etc. The metallic contamination in the profile disks sometimes exceeded 2500 ppm Fe as compared to 200 to 500 ppm in the normal processing environment. Dark flowlines indicative of such contamination were noted in some sectioned components, as shown in Fig. 3. This figure also shows a typical example of a process-related crack in the component section.

It is expected that a high level of undesirable metallic contamination could significantly impact the high-temperature properties. Typical examples of high-temperature strength data

[1]All strength data measured at GTEL and discussed in this paper were obtained in four-point bend tests in a SiC fixture [10] whose inner and outer loading points were 10.16 and 22.86 mm, respectively. The strength data obtained at Daimler-Benz used fixtures whose loading points were 15 mm and 30 mm with specimen size of $3 \times 3.5 \times 35$ mm. Crosshead speed was constant (unless specified otherwise) at 0.5 mm/min for all standard measurements at GTEL and Daimler-Benz.

Table 2 High-temperature strength of MOR bars machined from HIPed profile disk (DFL indicates the deviation from linearity on the load-deflection curve)

Crosshead Speed (mm/min)	800°C σ (MPa)	800°C n	800°C DFL (%)	1000°C σ (MPa)	1000°C n	1000°C DFL (%)	1200°C σ (MPa)	1200°C n	1200°C DFL (%)
0.5	641	5	0	513	6	0	432	3	0
0.05	–			–			376	3	25
0.005	–			493	5	0	299	2	192

Table 3 Key controls for injection molding process

Powder	Starting powder specification, environmental controls for processing, particle size, size and shape distribution, surface area.
Compounding	Rheological behavior, contamination.
Molding	Visual and microfocus x-ray inspection for defects.
Binder Removal	Visual inspection.
Densification	Density, visual and microfocus x-ray inspection, phase composition.
Finishing	Dimensional inspection, visual examination.

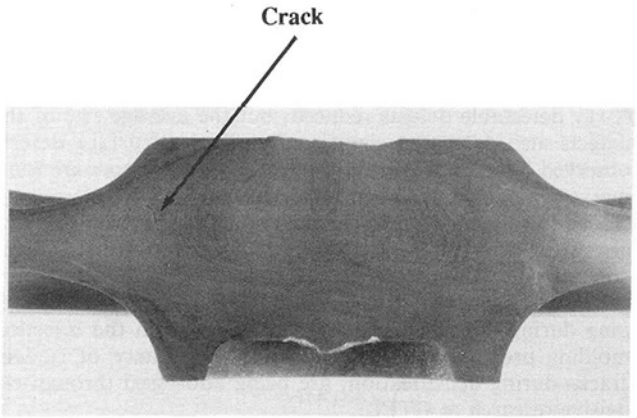

Fig. 3 Dark flow lines in the component cross section are indicative of metallic contamination from equipment during the molding step. The arrow shows the defect formed during the binder burnout and densification process.

obtained from MOR bars machined from a representative HIPed disk are shown in Table 2. The significant strength drop and associated increase in deflection from linearity at 1200°C with the decrease of cross-head speed is indicative of substantial slow crack growth at this temperature.

The "Laboratory Process" Versus the "Prototype Process"

A majority of the defect types observed in components such as the profile disks that were fabricated by the "laboratory process" have now been eliminated through improvements incorporated in the "prototype process." The "prototype process," as referred to in this paper, includes powder handling and processing in specially designed clean room facilities, improved binder removal and densification processes, and implementation of stringent quality-control measures for process

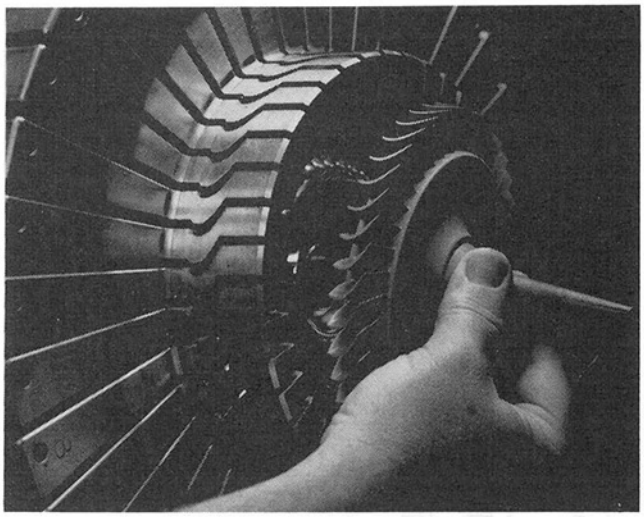

Fig. 4 Injection molding tool and a molded rotor

control and development. Typical examples of controls used for injection molding process are summarized in Table 3.

The "prototype process" benefited significantly through extensive use of nondestructive methods, which have been developed for process controls, as well as to ensure final quality of components. The NDE methods included extensive microfocus and conventional X-ray and visual inspection of components at various stages of processing. GTEL has developed the microfocus X-ray system for evaluation of a wide range of components and has established flaw detection limits in silicon nitride ceramics [11]. The effectiveness of this inspection method has already been demonstrated for small cross section parts such as MOR bars, as well as for large and complex shapes such as turbocharger rotors [12]. Other inspection methods include visual examination at 20× magnification and dye penetration tests for cracks and other surface defects.

The impact of the "prototype process" on turbocharger rotor fabrication was discussed in an earlier publication [12]. In the current paper, the impact of these improvements on axial gas turbine Daimler-Benz rotors are described.

Axial Rotor Fabrication, Properties, and Performance

Rotor Fabrication and NDE. Two silicon nitride powder sources have been used for fabrication of axial bladed rotors: GTE SN502 and a blend from Ube Corp. (Japan) termed here as Ube A. The GTE AY6 formulation was changed slightly; the updated composition contained 6 w/o yttria and 1.5 w/o (instead of 2 w/o) alumina. The alumina level was decreased to improve the high-temperature properties [8] without significantly influencing the densification characteristics.

The injection molding tool (Fig. 4) used in this program is a high-quality, production-ready tool with a high degree of flexibility built into the design, which has served to make it a powerful technology development tool as well. The following special features were incorporated in the design:

- Cavity evacuation system
- Additional inserts for the test molding of thicker blades

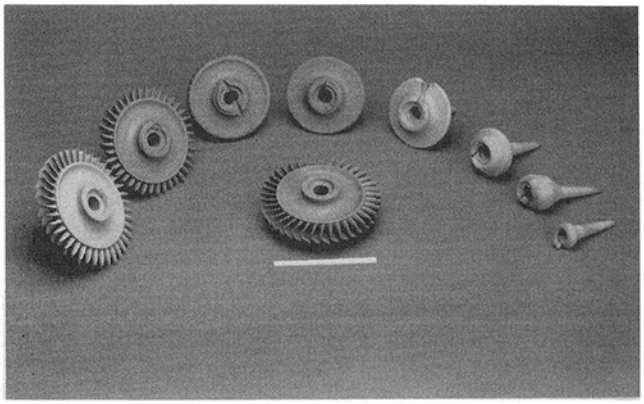

Fig. 5 Cavity-filling pattern for the Daimler-Benz axial turbine rotor

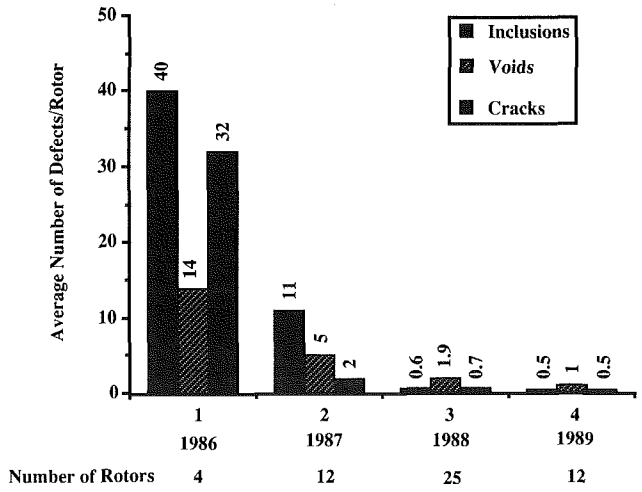

Fig. 6 Quality improvement as indicated by microfocus X-ray in Daimler-Benz rotors. Detection limit in the thick section is ~150 μm and in the thin section ~50 μm.

- A hydraulically activated scrolling mechanism
- Interchangeable rotor hub contour inserts

The attempts to mold silicon nitride rotors with this tool showed excellent fill pattern, as evidenced by the short shots of the rotor (Fig. 5). Clearly, the gating and the mold design allowed uniform mold filling including the blade area.

The rotor fabrication procedures evolved over several iterations of molding, binder removal, and densification of components. The first-generation rotors were fabricated in 1986 by the "laboratory process." Initial optimization was carried out with the starting powder, compounding and molding parameters, the binder removal conditions, and the HIPing parameters. The primary areas of difficulties at this stage were defects from environmental contamination and formation of cracks in the thin section of the rotor hub as well as in the central bore region of the rotor. The cracks generally formed after molding and after binder burnout. It appeared that the thin section of the rotor could contract before the thicker sections at two stages during the fabrication process: when cooling in the mold after injection molding, and during the binder removal cycle. This type of nonuniform shrinkage resulted in circumferential cracking within the thin area of the hub. Continued adjustments with the molding parameters and the burnout cycle to eliminate the cracking problems resulted in some improvements, and several product-of-the-mold densified rotors were fabricated for evaluation.

The second-generation rotors were fabricated in 1987 with several improvements in processing equipment specifically to eliminate metallic contamination. A stringent process control through NDE was also implemented at this stage. Visually, however, cracks in the hub and in the bore region could be detected in these parts. The cracking problem could not be eliminated by process modification alone.

Table 4 Improvement in the surface quality of Daimler-Benz axial rotors

Year	Number of Rotors	Average Number of Visually Detectable Defects/Rotor		
		Cracks	Pits	Chipped/Broken Blades
1987	12	4	3	5
1988	25	0.8	0.2	1
1989	12	0.3	0.2	2

The third-generation rotors fabrication in 1988 and 1989 included a change in the hub configuration profile in order to reduce/eliminate the tendency of circumferential cracking. The thickness of the thin section of the hub was increased to reduce the cross-sectional variation in the hub profile. In addition, the "prototype process" and the related facilities and process improvements were fully exploited with the third-generation rotors.

The surface and the internal qualities of Daimler-Benz rotors have improved significantly since the first-generation rotors were fabricated. Figure 6 shows the dramatic reduction of microfocus X-ray detectable defects in components with time. Both environment- and process-related defects were reduced. Similar quality improvements have been demonstrated in other GTEL component fabrication activities, such as silicon nitride turbocharger rotors [12]. It has been demonstrated in the turbocharger program that as a result of the process improvements during 1986 through 1988, not only was the total number of X-ray detectable defects reduced, but the average size of the defects also decreased significantly. Typical surface defects observed in second- and third-generation DB rotors are summarized in Table 4. Other detectable surface defects not included in this table are fold lines or packing problems, which are difficult to quantify. Despite major improvement in the component quality, some surface flaws remained in the recent generation parts. These remaining defects, such as blade chipping during handling, residual fold lines from the injection molding process, and the occasional appearance of surface cracks during densification, are being addressed through extensive research at GTEL.

Rotor Properties and Performance. The component quality improvement as observed through the NDE has also been confirmed through the mechanical properties improvement of MOR bars machined from rotors as well as from the cold spin test results of the rotors.

The room-temperature and high-temperature (to 1200°C) strengths of MOR bars machined from the axial rotors fabricated at various stages of the program (1986 through 1988) are summarized in Table 5. During this time period, the room-temperature strength of the rotor material improved from 750 MPa to over 1000 MPa, whereas the 1200°C strength improved from 435 MPa to over 700 MPa. The quality improvement observed in these parts is similar to those observed in other components fabricated at GTEL [12].

The time-dependent strength of materials similar to that used for Daimler-Benz rotors was measured at 1000°C [12]. These data are critical because of known susceptibility of silicon nitride ceramics to time-dependent strength degradation at elevated temperatures. Generally, under an applied load, the stress intensity at a crack tip causes the crack to grow at a rate described by

Table 5 MOR strength improvement of injection-molded and HIPed AY6 (Si_3N_4 + 6 w/o Y_2O_3 + 1.5 w/o Al_2O_3) Daimler-Benz rotors

Rotor No.	Date	RT σ (MPa)	RT m	RT n	1000°C σ (MPa)	1000°C m	1000°C n	1200°C σ (MPa)	1200°C m	1200°C n	Data Source
66*	1986	750	13.3	28	510	—	28	435	—	3	GTEL
33A	1986	752	5.6	29		—			—		DB
127	1987	897	16.6	15	593	11.7	8	490	11.4	6	GTEL
142	1987	910	11.6	12		—			—		DB
128-2	1988	979	11.3	13	779	26.3	7	483	11.6	7	GTEL
77-2	1988	993	15.0	15	786	—	5	538	—	5	GTEL
43-2	1988	1028	14.0	15	876	—	5	703	—	5	GTEL

*Profile Disc

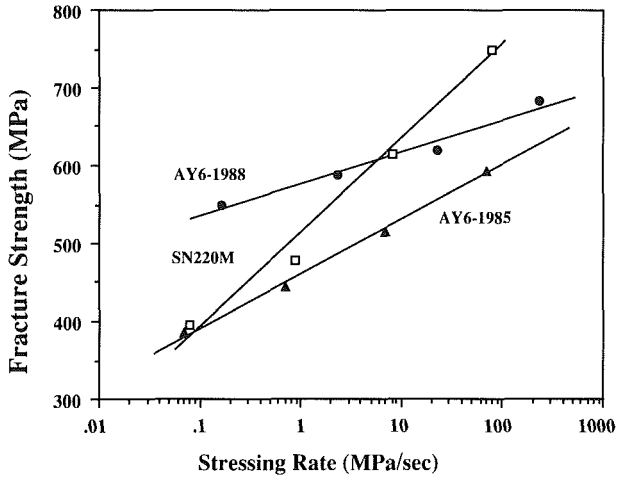

	TEST ATM.	N
AY6-1985	Air	15
AY6-1988	Argon	33
SN220M-1985	Air	9

Fig. 7 Comparison of subcritical crack growth data from GTEL AY6 Turbocharger material [12] and data obtained from [15, 16]

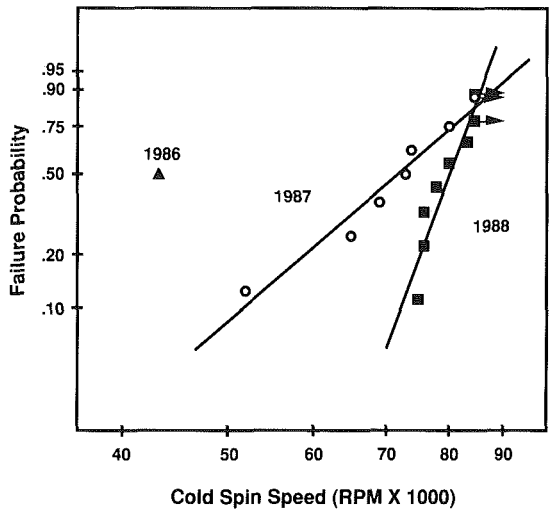

	Spin Speed for 50% Probability of Survival	Weibull Modulus
1987	77,443	4.3
1988	81,713	14.5

Fig. 8 Cold spin test results of GTEL AY6 rotors for Daimler-Benz show significant improvement in quality. The arrows in the graph indicate tests suspended prior to burst. Probability of survival and Weibull modulus calculations include results from both failed rotors as well as from tests suspended prior to burst.

$$V = A(K_I/K_{IC})^N, \quad (1)$$

where V is the crack velocity; K_I is the stress intensity at the crack tip due to the applied load; K_{IC} is the critical stress intensity factor of the material (fracture toughness); and A and N are material constants. If the stress is maintained, the crack will grow subcritically to a size large enough ultimately to cause failure; the larger the crack grows, the more the strength of the material degrades.

From fracture mechanics, it can be shown that the fracture strength (σ) of a material is related to the applied stressing rate ($\dot{\sigma}$) as follows:

$$\sigma_f = C\dot{\sigma}^{(1/(N+1))}, \quad (2)$$

where C is a constant. The parameter N is the same constant as in Eq. (1) and is a measure of the material sensitivity to subcritical crack growth; low values of N indicate low resistance to subcritical crack growth. A linear regression of the slope of a log–log plot of the fracture strength versus stressing rate will therefore provide evidence of a material's resistance to time-dependent strength degradation. These data can also be used to predict the lifetime of components in specific stress conditions [13].

Figure 7 shows the fracture strength as a function of stressing rate at 1000°C for several silicon nitride materials. The SN220M and AY6-1985 data are taken from tests conducted at Allison Gas Turbine Division of General Motors Corporation [14, 15]. The AY6-1988 data are from material machined from GTEL turbocharger rotors fabricated by the prototype process. The significant increase in the N value shows the excellent resistance to subcritical crack growth (and therefore strength degradation) attained in recently fabricated components at GTEL. Although tests at GTEL were conducted in an argon environment, the high oxidation resistance of GTE silicon nitride and the relatively short duration of the tests (3 second to 1.5 hours) show that a significant improvement has indeed been attained in the crack growth resistance of materials similar to that used for fabrication of Daimler-Benz rotors.

The cold spin results from GTEL AY6 axial rotors tested by Daimler-Benz AG are shown in Fig. 8. The figure also shows the spin speed at which 50 percent survival probability can be achieved and the corresponding Weibull modulus calculated for second- and third-generation rotors. The calculation included the results from failed tests as well as from tests suspended prior to burst. The data clearly show the impact of

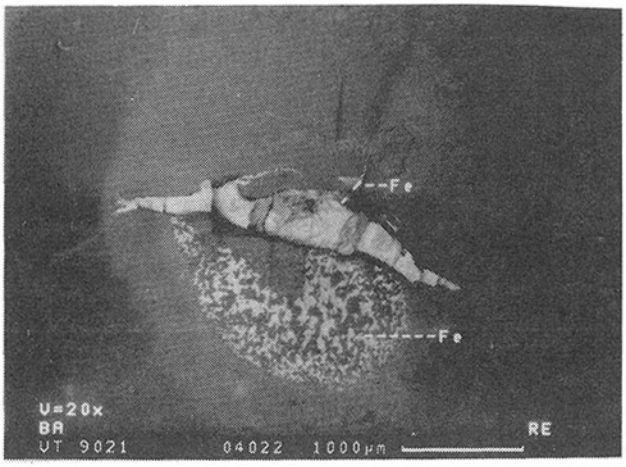

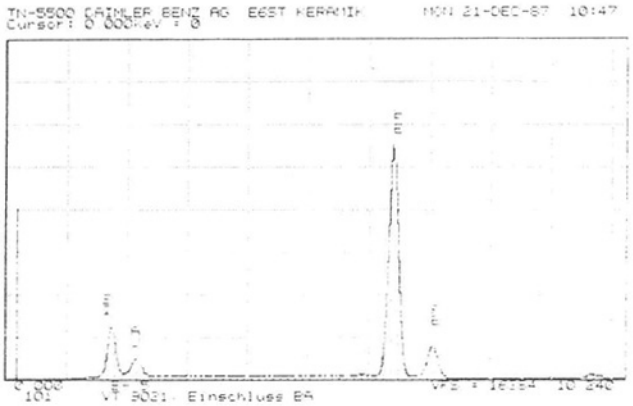

Fig. 9 SEM photograph and EDX data of the defect that caused failure in a rotor at 52,000 rpm. The outline of the metallic-contaminated area matched well with the microfocus X-ray radiograph.

the improved processing on component performance. Both spin speed and the Weibull modulus showed a significant improvement. This improvement is also in agreement with the reduced number of defects detected through the NDE methods.

Although the NDE results and the component performance show a strong correlation, the failure origin could rarely be traced to a specific NDE detected defect. Only in one case (Rotor #124, which failed at 52,000 rpm) was an NDE-detected large inclusion identified as the primary failure origin. Figure 9 shows the SEM photograph of the defect after fracture. The outline of the reacted zone seen in the SEM photograph matched well with the microfocus X-ray detected defect. The EDX analysis shown in Fig. 9 clearly identified the inclusion as a large iron-containing particle. In the majority of the rotors, the failure originated from the high stressed bore area. Thus it is speculated that fold lines, visually detectable surface cracks, or machining-induced flaws caused rotor failures. Inclusions or voids ($< 300\ \mu m$) found in the internal surfaces of fractured components were believed to have only secondary effects on failure during component testing. Figure 10 shows an example of a 30 μm metallic defect, which acted as a secondary failure origin in a rotor at 73,000 rpm.

Hot spin test results of GTEL rotors have been performed by Daimler-Benz with some significant success. The results will be described by Moergenthaler et al. [6] in another paper.

Summary

Axial silicon nitride profile disks and gas turbine rotors for Daimler-Benz research gas turbine engines have been fabricated by the injection molding process. The fabrication procedure evolved over several iterations of molding, binder removal, and densification of components. The results from this development are summarized below:

1 Injection molding and hot isostatic pressing can be used to fabricate high-quality axial silicon nitride rotors.

2 Major quality improvements in components have been achieved through implementation of process and environmental control and NDE methods. Cold burst speeds of rotors have improved significantly as a result of this quality improvement.

3 Excellent material properties have been demonstrated in rotors. Further improvement in component performance is expected with continued improvement of the surface quality of parts.

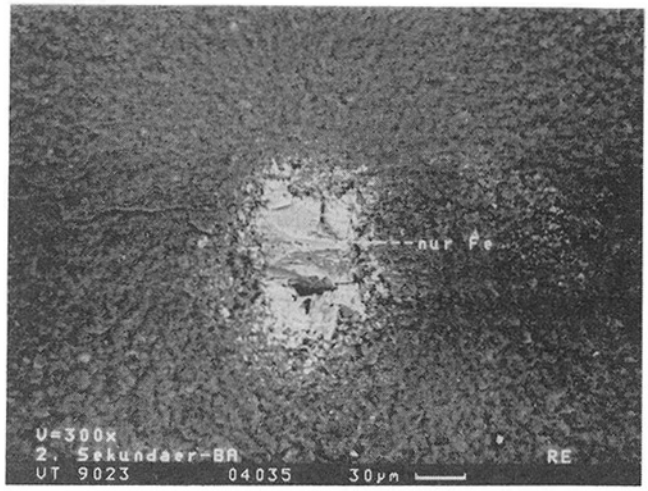

Fig. 10 An example of a 30 μm metallic defect, which acted as a secondary failure origin in a rotor at 73,000 rpm

Acknowledgments

The authors gratefully acknowledge P. Fuce, J. Gagne, S. Quinn, D. Thomas, and J. Neil of GTE Laboratories Inc. and S. Butscher of Daimler-Benz AG for their help and support at various stages of this program.

References

1 Helms, H. E., "AGT 100 Project Summary," ASME Paper No 88-GT-223.

2 Boyd, G. L., and Kreiner, D. M., "AGT101/ATTAP Ceramic Technology Development," ASME JOURNAL OF ENGINEERING FOR GAS TURBINES AND POWER, Vol. 111, 1989, pp. 158–167.

3 Bornemisza, T., and Napier, J., "Comparison of Ceramic vs Advanced Superalloy Options for a Small Gas Turbine Technology Demonstrator," ASME Paper No. 88-GT-228.

4 Yamagishi, K., et al, "Current Status of Ceramic Gas Turbine R&D in Japan," ASME Paper No. 89-GT-114.

5 Hempel, H., and Wiest, H., "Structural Analysis and Lift Prediction for Ceramic Gas Turbine Components for the Mercedes Benz Research Car 2000," ASME Paper No 86-GT-199.

6 Moergenthaler, K. D., et al., "Development and Testing of an Axial Silicon Nitride Gas Turbine Rotor," ASME Paper No. 90-GT-96.

7 Bandyopadhyay, G., and French, K. W., "Fabrication of Near-Net-Shape Silicon Nitride Parts for Engine Application," ASME JOURNAL OF ENGINEERING FOR GAS TURBINES AND POWER, Vol. 108, 1986, pp. 536–539.

8 Mahoney, F. M., French, K. W., and Bandyopadhyay, G., "Fabrication and Evaluation of AGT 100 Injection Molded Silicon Nitride Gasifier Rotors," *Proc. of 25th Automotive Technology Development Contractors' Coordination Meeting*, Society of Automotive Engineers, Warrendale, PA, Apr. 1988, pp. 85–89.

9 Larker, H. T., "Hot Isostatic Pressing of Ceramics," in: *Progress in Nitrogen Ceramics*, F. L. Riley, ed., Martinns Nijhoff Publishers, 1983, pp. 717–724.

10 Smith, J. T., and Quackenbush, C. L., "Phase Effects in Si_3N_4 Containing Y_2O_3 or CeO_2: I. Strength," *Bull. Am. Ceram. Soc.*, Vol. 59, No. 5, 1980, pp. 529–532.

11 Cotter, D., and Koenigsberg, W., "Microfocus Radiography of High Performance Silicon Nitride Ceramics," *Proc. of the Conf. on Non-destructive Testing of High Performance Ceramics*, Boston, MA, Aug. 25–27, 1987, pp. 233–253.

12 Bandyopadhyay, G., et al., "Fabrication and Evaluation of Silicon Nitride Heat Engine Components," *Proc. of 3rd Int. Symp. on Ceramic Materials and Components for Engines*, Las Vegas, NV, Nov. 27–30, 1988, pp. 1397–1406.

13 Wiederhorn, S. M., and Ritter, J. E., Jr., "Application of Fracture Mechanics Concepts to Structural Ceramics," *Fracture Mechanics Applied to Brittle Materials*, ASTM STP 678, S.W. Freiman, ed., 1979, pp. 202–214.

14 Khandelwal, P. K., Chang, J., and Heitman, P. W., "Slow Crack Growth in Sintered Silicon Nitride," *Fracture Mechanics of Ceramics 8*, R. D. Brandt, A. G. Evans, D. P. H. Hasselman, and F. F. Lange, eds., Plenum Press, New York, 1986, pp. 351–362.

15 Chang, J., Khandelwal, P. K., and Heitman, P. W., "Dynamic and Static Fatigue Behavior of Sintered Silicon Nitrides," *Ceramic Eng. Sci. Proc.*, Vol. 8, No. 7–8, 1987, pp. 766–777.

Journal of Engineering for Gas Turbines and Power

Technical Briefs

Thermal Cycling of High-Temperature Industrial Steam Turbine Rotors

N. Adinarayana[1] and R. S. Alwar[2]

Introduction

The turbine rotor is often the critical component that fixes the limits for transient operation of the turbine because of cyclic thermal strains. The common mode of failure of components subjected to cyclic stress-strains is fatigue. Particularly for high-temperature rotors, which are subjected to high inelastic strains at critical locations like notches, the rotor life is limited by low cycle fatigue strength. To predict the fatigue life for crack initiation, it is necessary to evaluate the local stress-strain history of a material element at the notch root for comparison with smooth bar fatigue data.

The essential steps to evaluate thermal stresses in steam turbine rotors are reviewed by Hohn (1975) and Dawson and Neill (1964). These methods are undergoing continuous development, including development of sophisticated finite element software and approximate methods. In the present investigation a 15 MW high-speed industrial turbine rotor is subjected to detailed thermal stress analysis using finite element technique.

Thermal Stresses on Startup

Generally industrial steam turbines operate with constant inlet steam parameters and are partial admission turbines, having one impulse stage as the first turbine stage with subsequent stages as reaction stages. The wheel chamber is the area where the steam first comes into contact with the rotor. The variation of steam temperature in a wheel chamber with load, idealized for startup calculations, for a typical turbine is shown in Fig. 1. The startup diagram (Fig. 1) is a provisional startup schedule fixed during the design stage. The objective of the analysis is to check that under normal operating conditions the strain levels reached are not excessive for the startup schedule.

Transient Temperature Distribution

To investigate the thermal behavior of the rotor during startup, the first problem is to calculate the transient temperature distribution in the rotor with time and change in steam temperature. This is a heat conduction problem and convective heat transfer coefficients are specified on the rotor surface. A realistic estimation of the heat transfer coefficient, which is a function of steam flow, location, and time, is essential. Generally empirical relations obtained from model experiments or by experiments on the actual turbine are used to estimate heat transfer coefficients. Figure 2 shows the heat transfer coefficients estimated at different zones of the front section of a typical 15 MW industrial steam turbine rotor.

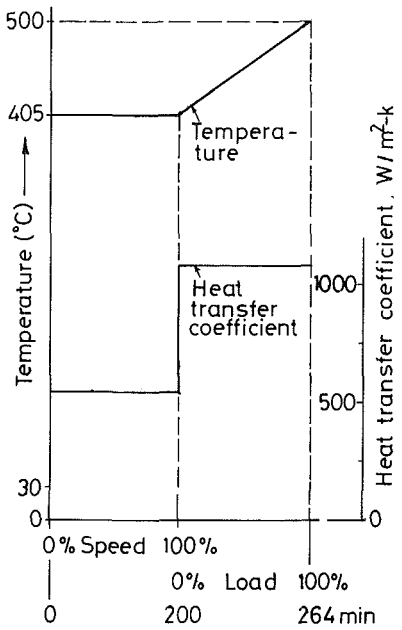

Fig. 1 Variation of wheel chamber steam temperature and heat transfer coefficients during cold startup

A finite element mesh configuration for a typical industrial steam turbine rotor is shown in Fig. 4. For a heat conduction problem, one important aspect is the contact between moving blade root and rotor, to take into account the heat flow from the blade to the rotor. Generally for reaction blading, a hammerhead root is used with partial contact between the blade root and rotor groove. If it is assumed that the blade root is in full contact with the rotor, the temperature distribution is not much different, as shown in Table 1. Hence in the finite element analysis for transient temperature distribution, the rotor can be considered as solid at the blade grooves. However, for thermal stress analysis, the details of the blade grooves are to be considered as shown in Fig. 4.

Elastic Thermal Stress Analysis

Finite element stress analysis for axisymmetric bodies is well documented (Zienkiewics, 1977). For a typical industrial steam turbine rotor, during startup from cold, the maximum stress is observed at the first reaction blade groove fillet. The variation of axial stress and strain calculated by linear elastic finite

[1]Bharat Heavy Electricals Ltd., Hyderabad, India.
[2]Indian Institute of Technology, Madras, India.

Contributed by the Power Division of The American Society of Mechanical Engineers. Manuscript received by the Power Division September 15, 1990.

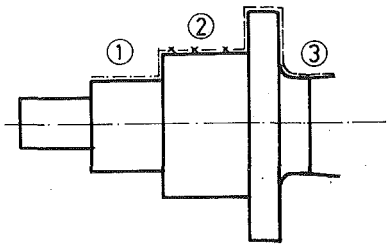

TIME	HTC AT ZONE $\left(\frac{W}{m^2\text{-}k}\right)$		
	①	②	③
SPEED 0%	350	605	582
SPEED 100%	350	814	582
LOAD 14%	350	1948	1164
LOAD 30%	350	4500	1164
LOAD 100%	350	14290	1164

Fig. 2 Heat transfer coefficients at the rotor front section

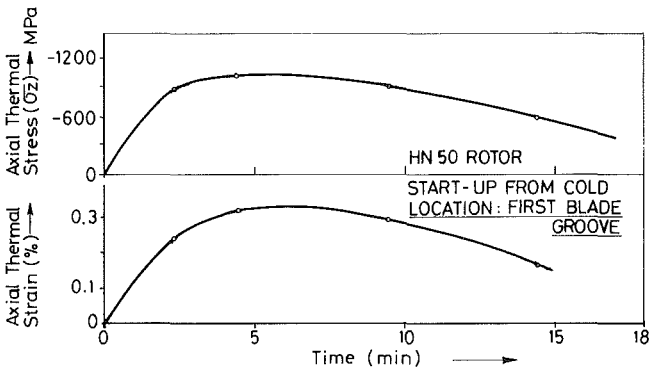

Fig. 3 Variation of axial thermal stress and strain with time

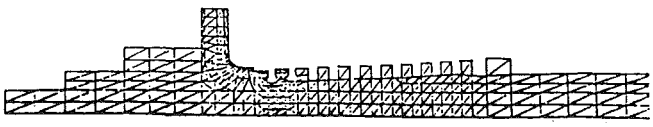

Fig. 4 Finite element mesh for rotor thermal stress analysis

Table 1 Temperature (°C) in rotor with and without full contact

Time, s	Location	Partial contact	Full contact
62.0	A	92.83	93.11
	B	85.43	86.41
	C	115.87	106.80
	D	148.20	138.64
	E	170.80	162.90
	F	66.05	66.11

element computer programs at this location is shown in Fig. 3.

Notch Strain Analysis

When cyclic external loads are applied to a notched component, the behavior of the material at the notch root can be considered better in terms of strain rather than stress because the fatigue life of notched parts can be estimated from the fatigue life of unnotched specimens that are cycled to the same strains as the material at the notch root by strain-controlled tests. Hence the accurate evaluation of stresses and strains at notches is very important. Usually thermal stresses obtained by elastic thermal stress analysis exceed the elastic limit of the material at notches like blade grooves on the surface of the rotor. Generally as a next step, an elastic-plastic residual strain is calculated. In the present analysis, the software GNATS is used to calculate the residual elastic-plastic strains in the rotor. As the elastic-plastic finite element analysis is expensive and time consuming, an approximate method proposed by Molski and Glinka (1981), and Glinka (1985) is examined. The method, which is energy based, is very promising, and its application to rotor residual stress analysis is discussed below.

Table 2 Residual strains

Transient	Elastic strain invariance	Molski-Glinka rule	Elastic-plastic finite element mesh
Startup from cold of a 15 MW rotor			
Residual strain, percent	0.3340	0.3824	0.3830

Molski-Glinka Rule. Assuming uniaxial conditions at the notch root and linear elastic behavior of the material, the strain energy density at the notch root can be expressed as

$$W_\sigma = \int_0^t \sigma(t)\,dt = \sigma^2/2E$$

where σ is the local stress at notch and E is the modulus of elasticity. The strain energy density due to nominal stresses can be expressed as

$$W_S = S^2/2E$$

where S is the nominal stress. If the stress concentration factor K_t is defined as σ/S, it can be easily seen that

$$K_t = [W_\sigma/W_s]^{0.5} \tag{1}$$

The above equation is strictly valid only when the region around the notch root is behaving elastically. Molski and Glinka (1981) assumed that this is true even when the localized plasticity exists at the notch root. Using the above equation and representing the material property in the plastic region by the relation

$$\gamma = \frac{\sigma}{E} + \left(\frac{\sigma}{K}\right)^{1/n} \tag{2}$$

where γ is the local strain at the notch, n is the cyclic strain hardening exponent, and K is the strength coefficient, the following relation is obtained:

$$\frac{(K_tS)^2}{2E} = \frac{\sigma^2}{2E} + \frac{\sigma}{1+n}\left(\frac{\sigma}{K}\right)^{1/n} \tag{3}$$

The left-hand side of the equation can be expressed as

$$\frac{(K_tS)^2}{2E} = (K_tS)\,(K_tS/E)/2 = (K_tS)\,(K_te)/2$$

where e is the nominal strain.

The values for (K_tS) and (K_te) can be taken as the peak stress and strain obtained by elastic finite element analysis and hence the left-hand side of Eq. (3) is known. Therefore, the residual stress σ can be computed from Eq. (3) and notch root strain γ can be computed from Eq. (2).

Residual Stress and Strains. The peak strains are calculated by detailed elastic-plastic finite element analysis and also by the Molski-Glinka method. Also, as a first approximation, the strains obtained by linear elastic analysis can be assumed as plastic strains according to the elastic strain invariance hypothesis (Manson, 1978). The strains calculated by the above three methods for a typical 15 MW industrial steam turbine rotor are given in Table 2. The strain according to the elastic

strain invariance hypothesis is the lowest and the strain predicted by the Molski–Glinka rule is very near the actual value evaluated by detailed elastic–plastic analysis. Therefore, it is more convenient to use the Molski–Glinka rule to estimate the local inelastic strains rather than the rigorous elastic–plastic finite element analysis.

Acknowledgments

The authors thank M/s Bharat Heavy Electricals Limited, Hyderabad, India, for sponsoring a research project to conduct the above studies and permission to publish the paper.

References

Dawson, R. A. T., and Neill, D. A., 1964, "The Application of Thermal Fatigue Analysis to Turbine Components," *Thermal Stresses and Thermal Fatigue*, CEGB conference proceedings.

Glinka, G., 1985, "Energy Density Approach to Calculation of Inelastic Strains Near Notches and Cracks," *Engineering Fracture Mechanics*, Vol. 22, No. 3, pp. 485–508.

Hohn, A., 1975, "Steam Turbines on Start-up," *Brown Boveri Review*, No. 6-75, pp. 231–241.

Manson, S. S., 1978, *Thermal Stresses and Low Cycle Fatigue*, McGraw-Hill, New York.

Molski, K., and Glinka, G., 1981, "A Method of Elastic–Plastic Stress and Strain Calculations at Notch Root," *Materials Science and Engineering*, Vol. 50, pp. 93–100.

Zienkiewics, 1977, *The Finite Element Method*, McGraw-Hill, New York.